UNIVERSITY OF COPENHAGEN

Complex Dynamics in Cell Signalling

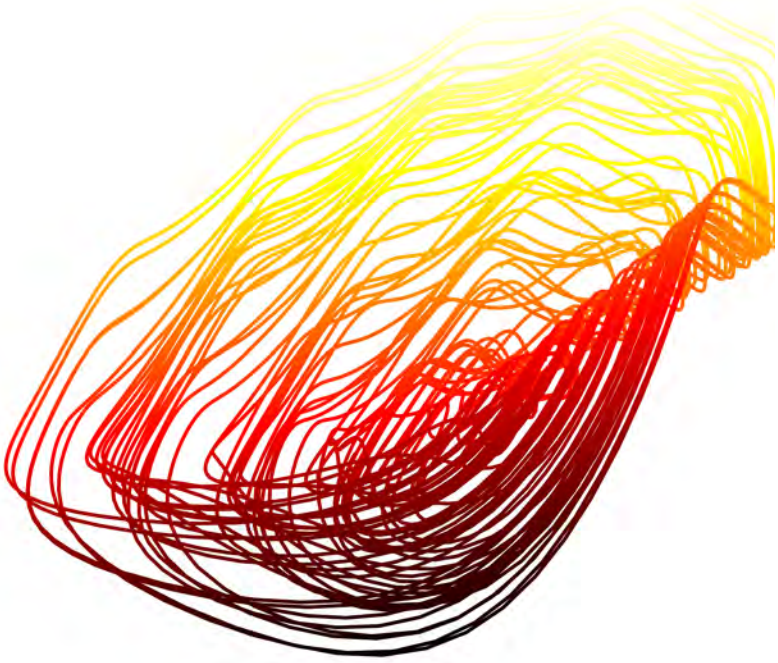

Mathias Luidor Heltberg

Thesis submitted for the degree of PhD

Supervisor: Mogens H. Jensen

February 1, 2019

Contents

List of Figures

Abbriviations

Abbreviation in thesis	Full name
NF-κB	Nuclear Factor kappa B
TNF	Tumor Necrosis Factor
HAG/LAG	High/Low Affinity Gene
p53	Tumor Protein 53
Mdm2	Mouse double minute 2 homolog
ATR	Ataxia telangiectasia and Rad3 related
Vm	Membrane Potential
DA	Dopamine
PD	Parkinsons Disease
DITA	Density Induced Translation Arrest
RBS	Ribosome binding site
GFP	Green Fluorescent Protein

Declaration

This thesis presents the results I have obtained during the last four years, where I worked in the biocomplexity group at the Niels Bohr Institute. It is divided into six chapters, starting with an introduction, in which I focus on presenting some important concepts that will be used throughout the thesis. In the chapters 2-6, I present the results for different projects, that each examine a separate biological system. My work has been theoretical and I have throughout this period worked my work has mainly been consisting of construction of mathematical models, analytical arguments, construction of simulation algorithms and data analysis. Part of the work has been done in collaboration with experimental groups, and is based on experimental results, but I have not performed any experiments myself. Thus in chapter 2, 3 and 6 there are results from experiments, that I have not performed, but these are important for the theoretical arguments, and is therefore also included. The chapters 2-6, are all founded on papers in which I have been first- or shared first author, and in the preface of each chapter I explain my own contribution to the project.
The thesis are founded on the papers I have published in this period, and therefore it is expected that overlaps between the articles and the chapters in this thesis. Generally the content from the papers, has been rewritten in this thesis, some results and figures have been left out, whereas other results that has not yet been a part of papers are included.
Parts of the subsections, especially in chapter 2, have been presented in my master thesis, though they have been rewritten in the current thesis. Subsections having some overlap with figures or data presented in the master thesis are marked by (M).
I will in the following, when referring to my own papers mark these as **paper X**, references to all other papers will be in normal reference style.
Even though this is a presentation of my own work, I will write the chapters using *we* form in almost all arguments.

Acknowledgements

I feel truly blessed to have been given a chance to spend the last four years in an absolute fantastic environment at the Niels Bohr Institute; my home away from home. The main reason for this has been my supervisor Mogens H. Jensen who has been a great inspiration and part of the entire work I have done. From day one, he involved me in all his research and treated me as a fellow scientist, and I cannot thank him enough for believing in me even in the early and difficult phases of this PhD. I remember one episode during my first months, where I asked for permission to work on a new project to which he replied: *"Science is not something you can order in advance or produce on a factory. You need to follow your heart and if you find that project interesting, then it is what you got to do!"*. This has been a guideline for me ever since. Our countless discussions in front of his blackboard has more or less led to all the main results in this work. So to sum up I can name few people who has given me more support and been there for me more, during the last four years. For this, I will always be grateful. I am also truly thankful to my colleagues at the biocomplexity group - you have generated the best atmosphere one could ever wish for.

My assistant supervisor, Sandeep Krishna, has always been a great help and source of inspiration. Troels C. Petersen, who has taught me what I know about data analysis and been an extra supervisor, a travel companion and good friend for me. Yonatan Chemla has been an invaluable collaborator and our work and discussions have been among the most inspirational moments of this period. Rune Rasmussen has been an extraordinary colleague for me, and our collaboration turned out to be a very efficient and fruitful process in which he shaped my way of writing and thinking scientifically. Jakob Dreyer has been a great collaborator who has always dedicated time to discuss our scientific projects. It has been a pleasure to work with Galit Lahav and her abilities as a leader and her strength to always stand up to what she believes in is admirable. Her high standards for scientific writing proved a strong motivation for me. Alba Jimenez has also been very important for the work, and her direct thinking and happy spirit has been fantastic. Finally, Hussein Awada has been an amazing colleague in work and through our numerous inspirational discussions. However first of all he has always been extremely supportive, helpful and had my back without ever asking for anything in return. He has taught me a great deal about life and been a true brother for me.

A special thanks goes to my family. "Manuel", "Mc", and "Mogens"; We form a fantastic team and thank you for always being ready to help me no matter whether it is about lost car keys, correcting my thesis, or just showing interest in my life during both difficult and happy times. For help with both the master and PhD thesis, and for being the person I usually go to whenever I have a question, a special thanks to my sister - she plain out rocks. Even though she truly hates it, I have to thank Signe Hansen - I cannot create an apt expression for my feelings anyway, so I just hope you know why.

Finally, the work in this thesis could not have been done without being supported by a grant from the Danish Council for Independent Research, or StemPhys DNRF Center of Excellence (DNRF116), who have supported the research and publications of several papers.

From the bottom of my heart, thank you one and all.

Abstract

This thesis consists of five results sections, in which biological systems are examined through mathematical modelling.
The first section examines how the transcription factor NF-κB is affected by oscillations in the ligand TNF. Since the presence of a constant level of TNF induces oscillations in NF-κB, they create a system of two coupled oscillators that can lead to entrainment depending on the coupling strength between them and the ratio between their original frequencies. For a range of parameters, this led to two stable limit cycles, and in the presence of noise transitions between the two cycles occurred and we termed this modehopping. We measured the distribution of transition times, and found this to be the sum of two exponentials we described by a simple 1D model. Next we considered how this affects downstream genes, and constructed a model that separates genes depending on the affinity and cooperativity of the NF-κB binding to the promoter region of the gene. We found that the transitions in NF-κB oscillations creates multiplexing between different families of genes. Then we increased the amplitude of TNF further and observed chaotic dynamics in NF-κB, with statistical properties similar to the trends found in modehopping. The chaotic dynamics created a variety of different amplitudes, and we realized that this was a mechanism to enhance low affinity genes. We found that this led to a significant raise in protein complex formation and that chaos enhanced both the efficiency and economy of this process. Finally we found that chaotic dynamics creates a population of heterogeneous cells that individually changes state in time. This was found to increase the survival rate in various toxic environments.
The second project investigates the dynamics of another transcription factor, p53, following depletion of the protein Mdmx. The dynamics of p53 is believed to be important for the cellular control of processes as division and DNA repair. and previous reports have shown that p53 starts to oscillate following γ-radiation. Here we analyzed experimental data of p53 before and after Mdmx depletion, which revealed a typical response characterized by a large transient pulse followed by sustained oscillations. We used these experimental markers as guidelines to construct a simple mathematical model, and considered the different hypotheses by introducing impact parameters to represent each individual hypothesis. In this way we found that the main results was explained by an enhanced degradation of p53 caused by Mdmx. We then used the model to predict how cells depleted of Mdmx would respond to UV exposure in terms of p53 dynamics. By comparing the predictions to experimental results, we found a strong agreement between the two.
The third project investigates how the dynamics of the membrane potential in neurons are affected by changes in extracellular ion concentrations. Inspired by previous experimental findings, showing different ion compositions in sleep than in awake, we extended an existing model to include extracellular ion concentrations. We then examined how the dynamics changed, if previously reported ion concentrations from sleep and awake were inserted into the model. By solely changing the ion concentrations a state transitions did not occur, but by changing ion concentrations accompanied by a perturbation in one of the gating channels, a transition occurred. We examined this further, by introducing an active ion composition, and found that this was enough to drive the neurons to a third state that we termed active awake. We argue that while the transition between sleep and awake is robust and needs perturbations in both ions and the gating channel, the transition between quiet awake and active awake does only need ion changes and can thus be done more

quickly. Finally, we investigated the nature of the dynamics in the observed states and found that the quiet awake state was governed by chaotic dynamics whereas the sleep state was a closed limit cycle which allows the possibility of neuronal synchronization.

The fourth project investigates how the dynamics of extracellular dopamine in the human brain is affected when the dopaminergic neurons are dying. It is well known that the correct stimulation of dopamine is fundamental for processes as memory, learning and movement, and it has been shown that at the onset of Parkinsons disease, a large fraction of all dopaminergic neurons are gone. We started by considering a previously published model for extracellular dopamine in a small subspace of striatum, and examined the dynamical properties as the density of neurons decreased. We then constructed a stochastic model for neuronal firing which were included in the dynamical model. Inspired by experimental findings, we introduced three different compensation mechanisms, and found many measures to differ, but for all models the signal to noise ratio was significantly lowered. From this examined the landscape of remaining neurons in the entire striatum, after severe levels of denervation. Again we used previously suggested hypotheses from the literature as inspiration and based on this we constructed three different models for dopamine neuron denervation in a network. We found that these models can give rise to completely different signal transmission properties, but at severe levels it was a common feature that the network was divided into small communication classes and regions completely deprived of dopamine started to exist.

The fifth project investigates how the protein production of GFP in bacteria is affected by incorporation of a strong promoter, a strong RBS and non canonical amino acids. Since transcription and translation in bacteria occurs simultaneously, we hypothesized that there could be limits to the transcriptional-translational density. In experiments we found that a system with a strong promoter and a strong RBS had almost no protein expression, but this expression was rescued if a codon for a non canonical amino acid was inserted early in the sequence of the gene. From this we constructed a model that allowed interaction of ribosomes from neighbouring mRNA strands during the time of transcription, in a process we termed Density Induced Translation Arrest. From the model we could reproduce the trends in the data, and predict how the rescue effect would disappear if the mutation was placed in the late part of the genome. This prediction was confirmed from the experiments. We then predicted an increased production if either the promoter or the RBS was decreased, which was also confirmed in experiments. Finally we used the model to predict the production from other genes depending on their length and sequence, which was again found to match what was found in the experiments.

Resume

Denne afhandling består af fem kapitler, hvori biologiske systemer studeres gennem matematisk modellering.

Det første kapitel undersøger hvordan transkriptions faktoren NF-κB påvirkes as oscillations i liganden TNF. Idet et konstant niveau af TNF inducerer oscillationer i NF-κB, skaber de sammen et system af to koblede oscillationer, der kan medføre synkronisering afhængigt af koblingsstyrken mellem dem og forholdet mellem deres indbyrdes frekvenser. For et interval af parametre, dette medførte to stabile grænse cykler, og gennem tilstedeværelsen af støj, kunne overgange mellem de to cykler forekomme, og vi navngav dette tilstandshop. Vi målte fordelingen af overgangs-tider og fandt at denne kunne beskrives af summen af to eksponential functioner og vi beskrev dette ved hjælp af en simpel 1D model. Derefter overvejede vi hvordan dette ville påvirke gener der påvirkes af NF-κB, og vi lavede en model der opdeler gener efter deres affinitet og cooperativitet for NF-κB bindingen til deres promoter region. Vi opdagede at overgangene i NF-κB skabte en tidsopdeling mellem stimulation af forskellige gener. Derefter hævede vi TNF amplituden og fandt kaotisk dynamik i NF-κB, der havde de statistiske egenskaber lignende dem vi såved tilstandshop. Kaotisk dynamik skabte en bred fordeling af forskellige amplituder, og vi indsåat dette var en mekanisme til at øge produktionen fra lav-affinitets gener. Vi opdagede at dette medførte en signifikant forøgelse af formationen af protein komplekser og at kaos dermed forbedrede både effektiviteten of økonomien af denne proces. Sidst opdagede vi at kaotisk dynamik skaber heterogene populationer af celler der individuelt kan skifte tilstand som tiden går. Dette viste sig at forøge overlevelses raten i forskellige giftige miljøer.

Det andet projekt undersøger dynamikken af en anden trankriptions faktor, p53, efter fjernelse af proteined Mdmx. Dynamikken i p53 anses for at være vigtig for cellens kontrol med processer som deling og DNA reparation, og tidligere studier har påvist at p53 har en svingende koncentration når efter gamma bestråling. Vi startede med at analysere eksperimentel data for p53 før og efter fjernelsen af Mdmx, og dette viste et typisk respons karakteriseret af en høj, transient puls, efterfulgt af vedvarende svingninger. Vi benyttede disse eksperimentelle markører som retningslinjer, til at skabe en simpel matematisk model og vi undersøgte forskellige hypoteser ved at introducere We used these experimental markers as guidelines to construct a simple påvirknings-parametre til at repræsentere hver individuel hypotese. Pådenne måde opdagede vi at hoved resultaterne kunne forklares gennem at Mdmx forøger nedbrydningen af p53. Derefter brugte vi modellen til at forudsige hvordan celler uden Mdmx, ville reagere påUV bestråling gennem deres p53 dynamik. Ved at sammenligne forudsigelserne med de eksperimentelle resultater kunne vi finde en stærk overensstemmelse mellem de to.

Det trejde projekt undersøger hvordan dynamikken membran potentialet i neuroner påvirkes af ændringer i de de extracellulære ion koncentrationer. Vi var inspirerede af tidligere studier der påviste forskelle i ion kompositionerne mellem søvn og vågen tilstand, og vi udvidede en eksisterende model til at inkludere ion koncentrationer. Vi undersøgte hvordan dynamikken ændrede sig, hvis de tidligere rapporterede ion koncentrationer fra søvn og vågen tilstand indsattes direkte i modellen. Hvis man kun indsatte ionerne skete der ikke en overgang, men hvis ion koncentrationerne ændrede sig kombineret med ændring i en af ion kanalerne kunne en overgang forekomme. Vi undersøgte dette yderligere ved at indføre en aktiv vågen ion komposition, og opdagede at dette

var nok til at drive neuronerne ind i en tredje tilstand som vi kaldte aktiv vågen. Vi argumenterede for at mens overgangen mellem søvn og vågen tilstand var robust og behøver flere ændringer for at forekomme, kan overgangen mellem de vågne tilstande klares udelukkende med ioner og kan derfor klares hurtigere. Slutteligt undersøgte vi den underliggende årsag til dynamikken i de forskellige tilstande, og vi opdagede at den normale vågne tilstand var domineret af kaotisk dynamik mens søvn tilstanden var præget af en lukket grænse cykel der kan give mulighed for synkronisering mellem neuroner.

Det fjerde projekt undersøger hvordan dynamikken af extracellulær dopamin i den menneskelige hjerne påvirkes når dopamin neuronerne dør. Det er accepteret at den korrekte stimulering af dopamin er fundamentalt for processer som hukommelse, indlæring og bevægelse og det er påvist at omkring begyndelsen af Parkinsons sygdom, er størstedelen af neuronerne forsvundet. Vi startede med at betragte en tidligere publiceret model for ekstracellulær dopamin i et lille område af striatum, og undersøgte de dynamiske egenskaber mens tætheden af neuroner formindskedes. Derefter lavede vi nu en stokastisk model for neuroners fyring, og vi inkluderede denne i den dynamiske model. Inspireret af eksperimentelle resultater, introducerede vi nu tre forskellige kompensations mekanismer og opdagede at mange mål var forskellige mellem disse modeller, men at signal til støj forholdet blev mindre for alle modeller. Fra dette undersøgte vi nu landskabet for de tilbageværende neuroner i hele striatum, efter svær denervering. Ogsåher brugte vi tidligere foreslåede hypoteser fra litteraturen som inspiration, og påbaggrund af dette lavede vi tre forskellige modeller for dopamin neuron denervering i et netværk. Vi opdagede at disse modeller kan give anledning til fuldstændig forskellige forhold for signallering, men ved svær denervering er det et fællestræk at netværket bliver opdelt til småklynger og at der opstår regioner der er helt udtømt for dopamin.

Det femte projekt undersøger hvordan protein produktionen af GFP i bakterier påvirkes af indførslen af en stærk promoter, en stærkt ribosom binding og ikke-kanoniske aminosyrer. Idet transkription og translation i bakterier forgår simultant, forestillede vi os at der kunne være en øvre grænse for transkriptions-translations tætheden. Gennem eksperimenter opdagede vi at et system med en stærkt promoter og en stærk ribosom binding nærmest ingen protein ekspression havde, men at denne ekspression blev genskabt hvis man indførte et codon der kodede for en ikke-kanonisk aminosyre tidligt i gen-sekvensen. Herfra skabte vi en model, der tillod interaktioner mellem ribosomer fra nabo mRNA strenge, under transkriptionen i en process vi navngav tætheds induceret translations anholdelse. Fra denne model kunne vi genskabe de tendenser vi havde set i de eksperimentelle resultater, og forudsige hvordan denne rednings mekanisme ville forsvinde hvis mutationen var placeret sent i gen sekvensen. Denne forudsigelse var bekræftet gennem eksperimenter. Slutteligt brugte vi modellen til at forudsige produktionen fra andre gener afhængigt af deres længde of sekvens og dette var endnu en gang i overenstemmelse med hvad blev fundet i eksperimenterne.

List of papers

Published papers

I. **Heltberg, M**., Kellogg, R. A., Krishna, S., Tay, S., & Jensen, M. H.
Noise induces hopping between NF-κB entrainment modes.
Cell systems, 3(6), 532-539 (2016). (Shared first author)

II. **Heltberg, M. L**., Krishna, S., & Jensen, M. H.
Time Correlations in Mode Hopping of Coupled Oscillators.
Journal of Statistical Physics, 167(3-4), 792-805 (2017). (First author)

III. Chemla, Y., Friedman, M., **Heltberg, M**., Bakhrat, A., Nagar, E., Schwarz, R., ... & Alfonta, L.
Expanding the genetic code of a photoautotrophic organism.
Biochemistry, 56(16), 2161-2165 (2017). (Contributing author)

IV. Schlesinger, O., Chemla, Y., **Heltberg, M**., Ozer, E., Marshall, R., Noireaux, V., ... & Alfonta, L.
Tuning of Recombinant Protein Expression in Escherichia coli by Manipulating Transcription, Translation Initiation Rates, and Incorporation of Noncanonical Amino Acids.
ACS synthetic biology, 6(6), 1076-1085 (2017). (Shared first author)

V. Rasmussen, R., Jensen, M. H., & **Heltberg, M. L**.
Chaotic Dynamics Mediate Brain State Transitions, Driven by Changes in Extracellular Ion Concentrations.
Cell systems, 5(6), 591-603 (2017). (Shared first- and corresponding author)

VI. **Heltberg, M. L.**, Krishna, S., & Jensen, M. H.
On chaotic dynamics in transcription factors and the associated effects in differential gene regulation.
Nature Communications, 10(1), 71 (2019). (First author)

In preparation

VII. **Heltberg, M. L.**., Chen, S, Jimenez, A., Jensen, M. H. & Lahav, G
Using live single-cell dynamics combined with mathematical modeling to identify functional interactions in complex networks (Preprint)

VIII. **Heltberg, M. L.**, Awada, H. N.,Rasmussen, R., Jensen, M. H. & Dreyer, J. K.
On the spatial and temporal landscape of dopaminergic denervation in the striatum

IX. Jensen, M. H., Kadanoff, L. P., **Heltberg, M. L.** & Krishna, S.
Chaotic dynamics and interacting rhythms: lessons for biology

1 Introduction

Life is complex, dynamic, and includes a great variety of components that are interacting in many different ways. Thus a mathematical attempt to describe living systems, will involve many different variables, a high degree of nonlinearity and an enormous number of parameters. Therefore we must accept that it is not possible to describe a living system with mathematical tools, and obtain the same precision as we can describe interacting physical objects as for instance planetary motion or single particles interacting. However, life is not just a complete mess of chaos, and it seems structured and organized, is characterized by having well defined responses to a variety of external stresses. An example of this is the immune system, where different cells are specialized use the input signals as information to generate an output and possible another signal to other types of cells. To obtain this level of control, cells need to have a fine tuned registration of the surrounding environment and a variety of responses according to the situation. From a scientific point of view, it is therefore of great interest to understand these processes and discover the key factors that ensures that living organisms can generate their desired output and maintain their function. Furthermore, a thorough understanding of these biological systems, opens the gates for creation of better medicine and to harvest the cellular machinery in advantageous ways. An interesting aspect of the response and signalling mechanisms in cells, is the dynamical properties of specific systems. This could be the sudden emergence of oscillatory dynamics in transcription factor dynamics, or the change in the firing pattern of neurons. First of all this gives an important fingerprint about the underlying network, of which the studied entity is part. Furthermore it is a tempting hypothesis that cells can use dynamical features to carry information and generate a correct output. This is the main question that is investigated in this thesis. The main approach to the problems in this thesis, is to use the interplay between creating a mathematical model that captures essential features of a biological system, and then create an external perturbation and study the response of the system, and dissect the reasons for or the effects of the response. This is schematically shown in Fig. 1. Since the majority of the results is centered around the effects of complex dynamics, we start by introducing the theory of dynamical systems, that is the result of the pioneering work of Henri Poincare in the last part of the 19th century. Here we aim at capturing some essential and qualitative effects of the system under examinations and see what can be learned from the general properties of this [1].

1.1 Dynamical Systems (M)

One of the great steps in modern science, is the many experimental tools that allow studies of the dynamical evolution of different proteins, molecules and signals. Thus we can study not only if a cell increases or decreases in the value of a specific protein after some time, but we can map the exact trajectory and take dynamical features as responses and fluctuations into account. This opens the door to much new insight into biological systems, and to work alongside the experiments from a mathematical point of view, we usually work in the framework of dynamical systems. Here we consider a vector field in n dimensions, defined by a set of n differential equations:

$$\dot{x_i} = f_i(x_1, ..., x_n, t) \tag{1}$$

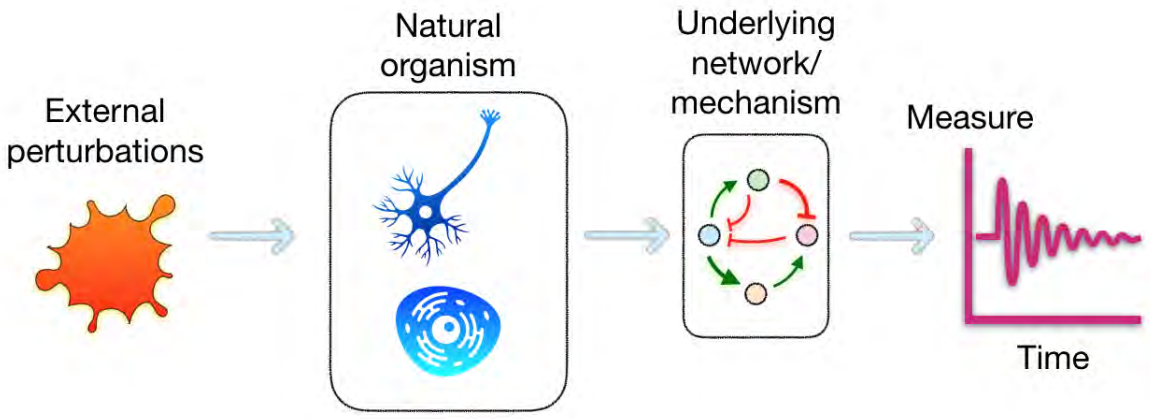

Figure 1: *Schematic figure showing the way we study systems biology and a method that is the basis of the projects in this thesis. We study a biological system (bacteria, eucaryotic cell or neurons), by considering some properties of the system, and examine how this changes when it is perturbed by external factors. Then we either use the network to predict the response, or use the response to try and predict the structure of the underlying system.*

From a theoretical point of view, we wish to describe the evolution in time of the system in consideration where the resulting dynamics is a trajectory in an n dimensional phase space. However, finding an exact solution for a set of coupled differential equations is almost always impossible to find, unless the system is very simple. However today we have an arsenal of techniques at which we can obtain information about the evolution of dynamical systems, and most of all we can use fast computers to perform numerical integration, which gives us a solution for the system from a specific initial condition. An important point to consider is the uniqueness of the solution to the differential equations: $\dot{\mathbf{x}} = \mathbf{f}(\mathbf{x})$ with $\mathbf{x}(\mathbf{0}) = \mathbf{x}_0$. There the uniqueness theorem states that if $\mathbf{f}$ is continuous and all partial derivatives are continuous in a subset P, then $\mathbf{x}(\mathbf{t})$ has a solution on this subset and this is unique. From this it follows that trajectories in the phase space can never intersect. This is easy to accept, because if they did, how to decide when it should follow one way or another, being at the intersection of two trajectories?

Mathematical definition of dynamical system

The study of dynamical systems, aims at describing the vector field defined in a specific domain U of the complete space V, so in one dimension

$$\dot{x} = f(x) \quad x \in U \subset V \tag{2}$$

We define U as the phase space of the autonomous dynamical system. In some cases the system depends on time explicitly, for instance when perturbed by an external oscillation, so $\dot{x} = f(x,t)$, and this is defined as non-autonoumous and we can define the extended phase space $\mathcal{R} \times U$, where $\mathcal{R}$ is the axis of time.
We define a solution to the system of $\dot{x}$, to be a differentiable map

$$y : I \mapsto U, \qquad \text{where} \qquad I = t \in \mathcal{R}, a < t < b \tag{3}$$

so:

$$\frac{dy(t)}{dt}\Big|_{t=\tau} = f(y(\tau), \tau) \tag{4}$$

for all $\tau \in I$. [2]

However, even if we are armed with analytical techniques and fast computers, we quickly face a problem when trying to model biological systems. The number of possible interactions of molecules is terrifyingly large, and even if we could consider all the relevant interactions this would lead to an enormous parameterspace. Since we are hoping to use experimental signatures of the system, as our foundation to model the underlying system and obtain fundamental information about this, we want to restrict the number of degrees of freedom as much as possible. In this process, we are truly missing a uniqueness theorem relating dynamics to the underlying network. This means that given we observe some feature from experiments, a large peak, oscillations etc., we we could construct an infinite number of models to mimic this characteristic feature, which does not lead to any progress in our understanding of the system. However, just naively introducing the simplest model in terms of for instance nonlinearity of dimensionality, to fit the experimental signature can as well be dangerous if we do not take the nature of the biological system into account. Therefore systems biology is a vivid and difficult field, filled with temptations of introducing too many free parameters and fear of constructing models that fails in predicting anything further from the trajectory of the experimental signature, to which it was built in the first place. Therefore we aim at capturing some essential features of the system, without adding too many unnecessary assumptions, following the physical tradition of reductionism, inspired by the principle of "Occams razor".

1.1.1 Fixed Points and Limit cycles (M)

In the theory of dynamical systems, a fixed point $\mathbf{f}(x^*)$, is a steady state value, from which the system does not evolve. This can be found by solving the differential equations:

$$\mathbf{f}(x^*) = \mathbf{0} \tag{5}$$

Fixed points can be attracting, repellant or a combination of these. The stability of these can (except in a few situations) be determined by linearization around the fixed point, by introducing the jacobian. If we now consider a two dimensional nonlinear system written as:

$$\begin{aligned} \dot{x} = &\quad f(x,y) \\ \dot{y} = &\quad g(x,y) \end{aligned} \qquad with \begin{cases} f(x^*,y^*) = 0 \\ g(x^*,y^*) = 0 \end{cases} \tag{6}$$

At the fixed point we now have: We now make the substitution $u = x - x^*$ and $v = y - y^*$ and write

$$\begin{aligned} \dot{u} &= f(u + x^*, v + y^*) \\ &= f(x^*,y^*) + u \left.\frac{df}{dx}\right|_{x^*,y^*} + v \left.\frac{df}{dy}\right|_{x^*,y^*} + \mathcal{O}^2 \\ &= u \left.\frac{df}{dx}\right|_{x^*,y^*} + v \left.\frac{df}{dy}\right|_{x^*,y^*} \end{aligned} \tag{7}$$

Here we have neglected terms of second order and higher, because v and u are very small close to the fixed point. If we do the same for $\dot{v}$ we can write it in matrix notation:

$$\begin{pmatrix} \dot{u} \\ \dot{v} \end{pmatrix} = \begin{pmatrix} \frac{\partial f}{\partial x} & \frac{\partial f}{\partial y} \\ \frac{\partial g}{\partial x} & \frac{\partial g}{\partial y} \end{pmatrix}_{x^*,y^*} \begin{pmatrix} u \\ v \end{pmatrix} \tag{8}$$

From this we can characterize the dynamics around the fixed points based on the trace and determinant of the matrix. With this we only define the dynamics around a point, but if we move up to dimensions two or higher, the dynamics can also generate oscillations. For a nonlinear system, the steady state dynamics be a one-dimensional line with a non-zero flow, known as a limit cycle [1]. Limit cycles are isolated trajectories, meaning that points in the vicinity of the limit cycle get either attracted or repelled by this trajectory - which is contrary to a linear center, that also has oscillations but is not attracting or rappelling. A perturbation to a center (as the harmonic oscillator) would lead to oscillations with a new amplitude, whereas a perturbation to a stable limit cycle would would decay back to the fixed trajectory. Limit cycles can arise through various bifurcations, but the canonical way, is when the stability of fixed point with complex eigenvalues changes from stable to unstable (Fig. 2A). This new unstable point could of course lead to a diverging trajectory, but due to the nonlinearities in many systems, the trajectory will still be bounded around the same region and at this point we say that a *Hopf bifurcation* has occurred.
There is no general way to determine if a system has a limit cycle, and the most important theorem that can be used in some situations is the Poincare-Bendixon theorem which can pragmatically be used in the following way (Fig. 2B):

- Define the region R, where at the boundary all flow is towards R
- Find a region inside R (white) where the flux goes outwards.
- Then a limit cycle must exist inside R (green)

Here the second point would very often be to find an unstable fixed point, from where all flow goes away from that point. In this case, one can determine the range for which the limit cycle exist by determining the stability if the fixed point. It is often extremely difficult to calculate the flow of a closed boundary over R, and furthermore we note that the theorem is only valid in the plane. This is easy to imagine, since one could in 3D construct a subset R, where trajectories would never leave, but they could be for instance chaotic like the Lorenz attractor. Thus a trajectory would stay

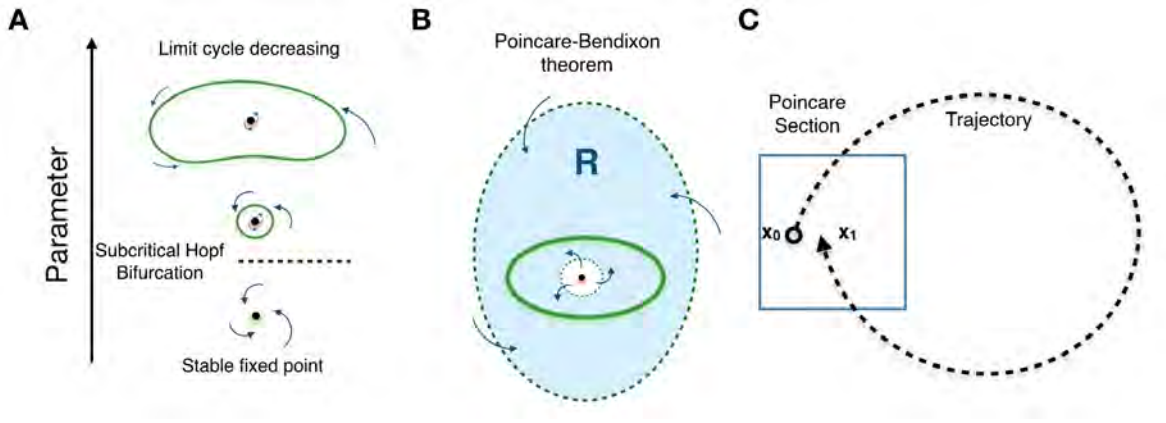

Figure 2: *A) Schematic figure showing how a limit cycle can arise following a change in parameters. At the point when the limit cycle starts to exist, it is very small and circular, but as it grows the shape in phase space can be highly irregular. B) Schematic figure showing the concept of the Poincare-Bendixon theorem C) Schematic figure showing the concept of a Poincare section.*

inside R, but it would not be closed. A useful way to study limit cycles in a dynamical system is through the introduction of a Poincare section. In an system of n dimensions, we define a Poincare section to be a subspace, S of dimensions $n-1$ that is traverse to the flow of the system, meaning that the trajectory passes through S after each rotation (Fig. 2A). In this way the Poincare section is a map of S onto itself, and we can this way transform the problem of studying a continuous, n-dimensional problem into a discrete, $n-1$-dimensional problem. Therefore we can write the map:

$$x_{n+1} = P(x_n) \tag{9}$$

And in this, a fixedpoint given by $x^* = P(x^*)$ represents a closed cycle and thus a limi cycle for the dynamical system.

1.1.2 Oscillatory Networks in Biology (M)

Proteins can oscillate in concentration, and in the last decades some of the most important proteins has been found to oscillate in living cells under specific conditions. [3, 4, 5] The general observation that some proteins oscillate is not that surprising, since systems with circadian clocks have been known for centuries. However, it has been found that many proteins oscillate in concentration with a natural frequency of hours [6], but why these proteins oscillate on these timescales and what effect on the biological system this might induce, is not clearly understood. Since genetic expression is regulated by proteins called transcription factors, that are themselves products of the protein synthesis, one could easily that a genetic network can form a nonlinear dynamical system that can give rise to oscillatory behaviour. There are some essential features, that are required for a biochemical network can oscillate. First of all there must be a negative feedbackloop, that ensures that the trajectory in phase space remains bounded, and can be carried back to some point creating a cycle. Secondly the system must be nonlinear for limit cycles to arise, and thirdly there must a time delay, for otherwise a negative feedback mechanism would merely bring the system towards a steady state. Therefore we can imagine the simplest mechanism giving rise to

oscillations in a genetic network is a negative feecbackloop with a "proper" time delay, τ (Fig. 3A). An classical example of such a model was used to model the protein synthesis [7] through the

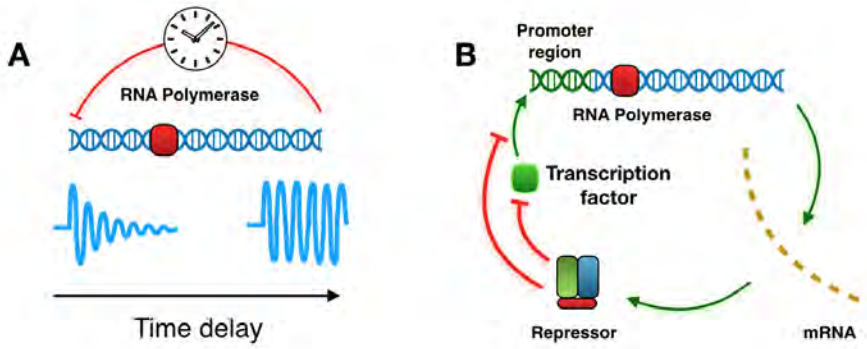

Figure 3: *A) Schematic figure showing negative feedbackloop with a time delay. B) Schematic figure showing a typical genetic network that can lead to oscillatory dynamics if the created protein either degrades the*

dynamical system:

$$\dot{Y(t)} = k_1 S \frac{K_d^p}{K_d^p + Y(t-\tau)^p} - k_2 E_T \frac{Y(t)}{K_m + Y(t)} \tag{10}$$

This inserted time delay is of rather abstract character, but if we consider a biological system, there would be subsequent processes that would generate a time delay large enough for oscillations to occur [8], for instance the transcription and translation of a protein that degrades or inhibits its own transcription factor (Fig. 3B). Transcription factors are therefore an essential element of genetic network models, and they can often lead to nonlinear reactions. In the simplest picture, transcription of a protein is started when the RNA polymerase binds to the promoter region of a gene. In reality this process includes numerous steps, but for this thesis, we will focus on the regions that can control transcription by binding transcription factors. These are the cis-acting elements and can be positioned quite far from the genes they are controlling. For this thesis we will refer to these regions as part of the promoter, that thereby is a regulating region. Transcription factors that can be either activators of repressors, for a specific gene, and normally the bound fraction of transcription factors can be described through the a Hill function:

$$\dot{m} \propto \begin{cases} \frac{T_F^h}{T_F^h + K^h} & \text{for an activator} \\ \frac{K^h}{T_F^h + K^h} & \text{for a repressor} \end{cases} \tag{11}$$

The control of transcription is a ubiquitous means of regulating gene expression, but it has only recently been appreciated that transcription factor dynamics might be important for gene regulation. Given the nonlinearities in the negative feedbackloops, and the built in time delay, one could argue that it is no surprise that many networks oscillate, since they can originate from basic network structures. For instance, oscillations have been observed in key transcriptional factors, such as the p53 tumour suppressor or NF-κB, which regulates numerous genes involved in immune response [9, 10, 5, 11]. Debate continues about the functional role, if any, of these oscillations [12], but it is clear that altering the dynamics of these transcription factors differentially affects downstream genes [4, 3, 13, 14].

1.1.3 Coupled Oscillators (M)

That oscillators can couple couple to each other is well known, even for people with no knowledge in dynamical systems and non-linear mathematics. For instance the daily rhythm couples to the position of the sun, not only for humans but almost any higher level organism. The history of synchronization, begins in 1665, when the dutch physicist Christian Huygens, by chance observed that pendulum clocks hanging on the same wall tended to oscillate with exactly the same frequency. Being a great experimentalist he conducted several experiments using clocks suspended from a beam as seen in Fig. 4A, and realised that the synchronization of the clocks depended on the distance between them.

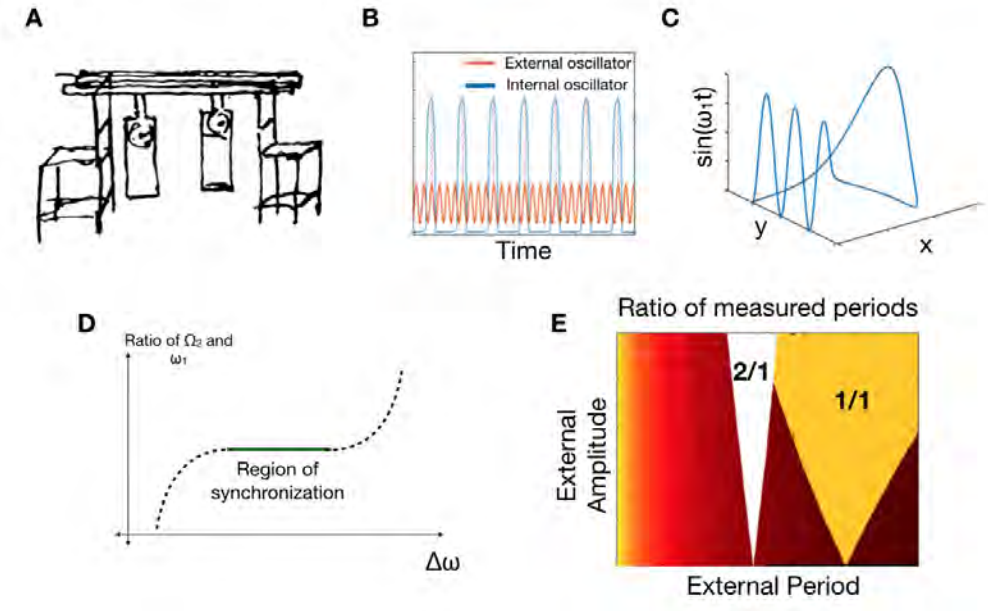

Figure 4: *A) Original drawing from Huygens in a letter to his father. B) Trajectories of internal and external oscillators. Dotted lines are to point out the same position for the peak in the external oscillator C) Phase space of two variables in the external oscillator and* $sin(\omega_1 t)$*. D) Schematic figure showing that changing the internal frequency can in specific regions lead E) Arnold tongues in the system:* $\dot{x} = a - x(1 - \frac{4y}{1+x^2}) + Asin(\omega t)$ *and* $\dot{y} = bx(1 - \frac{y}{1+x^2})$

In this we will consider two oscillators with different self sustained frequencies ω_1 and ω_2. We now assume they are coupled so the oscillator with ω_1 is controlled and this affect the frequency of the oscillator with natural frequency ω_1 and measured frequency Ω_2 If two oscillators synchronize, this means that they are locked to each other, and there will be no phase drift, i.e. when one oscillator is at its peak, the other will always be in a specific position (Fig. 4B). This means that if we consider this in the phase space they will form a closed loop. If we consider two variables of the external oscillator (x and y), and plot these as a function of $sin(\omega_1 t)$ this will form a closed trajectory in the phase space (Fig. 4C). Depending on the strength of the coupling we can now have regions of synchronization, where we can change ω_1 and then Ω_2 will automatically follow.

Mathematically speaking:

$$\frac{d(\Omega_2/\omega_1)}{d\omega_1} = 0 \tag{12}$$

These regions we define as synchronisation regions, and depending on the strength of the coupling, these plateau regions can be of significant length (Fig. 4D). Since the plateaus depend on the strength of the coupling we can make a synchronization map, by calculating the ratio Ω_2/ω_1 for all values of all values of the coupling strength (amplitude of external oscillator) and the frequency of the external oscillator. By doing this, plateaus of growing width become visible as we increase the coupling strength, and these regions are known as Arnold tongues (Fig. 4E). These have interesting features, for instance it turns out that all rational numbers form a synchronization region, and this is discussed in greater detail in Appendix C. Finally we mention that it is important that the internal oscillation is a stable limit cycle. We furthermore restrict the definition of coupled oscillators, to *weak* couplings between oscillators, since for very strong couplings, the phenomena are not that interesting. One can imagine that if the clocks in Huygens experiments were connected by a rod, (very strongly coupled) they would off course oscillate with same frequency and phase, and not exhibit interesting effects of synchronization.

1.1.4 Chaos

From coupled oscillators, chaotic dynamics can arise. Chaos is a fascinating phenomena that has been widely studied since the sixties, but it is difficult to define it unambiguously. When we refer to chaos, we refer to a dynamical system that has the property to have a positive Lyapunov exponent in the deterministic limit. Deterministic is a system without any stochastic randomness, which means that if one knows the initial state of the system exactly, then the trajectory in the phase space will be the same every time it is initiated in that state. For dynamical systems that is not chaotic, an uncertainty in the initial conditions does not influence the trajectory much and two trajectories starting in almost the same points, will remain close to each other. Take for instance a system with a stable limit cycle as the only attractor, then a small difference in the initial conditions might lead to a minor phase difference in the oscillations, but this phase difference will be constant in time. For a system that is chaotic however, any two initial conditions infinitesimally apart will have exponentially diverging trajectories as time proceeds. This is mathematically defined by the Lyapunov exponent λ:

$$|y_1(t) - y_2(t)| \approx e^{\lambda t}|y_1(0) - y_2(0)| \tag{13}$$

which gives an approximation of the separation rate between trajectories. This divergence makes it practically impossible to predict the future dynamics, and therefore the phenomena has been named chaos [15, 16, 17, 1]. In order to generate the unpredictable trajectories, without any crossing of trajectories, the phase space need to be at least three dimensions and furthermore the attractor needs to have a complex stucture, which is found to have fractal nature. As a last remark, we note that in contrast to deterministic systems, we have stochastic systems that will be treated below. We note that a system with noise, will have uncertainty in every step, and thus by integrating all this uncertainty over a trajectory, will lead to a divergence between trajectories related to the spread in the noise. Thus, both deterministic chaotic and noisy systems exhibit unpredictability in their future trajectories, but for very different underlying reasons.

1.2 Noise in Biology (M)

All biological systems is the result of an interplay between deterministic forces, driven mainly by electromagnetic forces, and the random fluctuations, that mainly exists due to the random nature of molecular motion. In the process of modelling protein dynamics, stochasticity can therefore often be vital to include in the considerations. It is highly dependent on the system how noise should be treated. For some systems in the thermodynamical regime, noise can be neglected due to the very large number of molecules if the system is in equilibrium, where the fluctuations can be regarded to scale as $\frac{1}{\sqrt{N}}$ [18]. However in living cells, the system is out of equilibrium and usually the number of specific proteins and mRNAs is low, and therefore fluctuations play a great role [19]. A standard way to describe dynamics in the presence of noise is through the Langevin equation that takes the form:

$$m\frac{d^2x}{dt^2} = -\lambda\frac{dx}{dt} + \eta(t) \tag{14}$$

Here the dynamics of the particle is governed by Stokes and the noise term $\eta(t)$ which has the correlation function $\langle \eta_i(t)\eta_j(t')\rangle = 2\lambda k_B T\delta_{ij}(t-t')$. However for biological systems, we are often interested in the noise arising from fluctuations in the interacting molecules.

1.2.1 Intrinsic Noise in Molecular Systems (M)

In 1977 Thomas D. Gillespie presented the so called Gillespie algorithm [20], that in many cases represents the most exact way to implement molecular noise into the system. In this we consider a volume V, with a spatially uniform mixture of N chemical species, that is represented by the number of molecules $X_1...X_N$, and these can react through M different reactions, $R_1...R_M$. Starting from $t = 0$ we make a small time step dt and assume that the probability of a reaction, i, occurring is in this interval $P_i = R_i dt$. Thereby we draw random numbers at each time step and update the system every time a reaction occurs. This speed of this can be significantly enhanced if we directly calculate the time until the next reaction. Now returning to the problem of N molecules and M reactions, we consider the probability that the next reaction is of type ϵ, and it occurs in the time-interval $[t+\tau, t+\tau+dt]$. We therefore consider:

$$P(\tau,\epsilon)d\tau = \overbrace{P_{not}(\tau)}^{\text{No reaction in } [t,t+\tau]} \cdot \overbrace{R_\epsilon d\tau}^{\text{Reaction } \epsilon \text{ occurs}} \tag{15}$$

Therefore we want to describe $P_{not}(\tau)$ in terms of the rates. Since at each timestep ϵ, the probability for no reaction to appear is:

$$P_{not}(dt) = 1 - \sum_{i=1}^{N} R_i dt \tag{16}$$

We can thus define $\tau \equiv n \cdot dt$ and then:

$$P_{not}(\tau) = P_{not}(dt)^n = \left(1 - \sum_{i=1}^{N} R_i \frac{\tau}{n}\right)^n = e^{-\sigma\tau} \tag{17}$$

$$\text{where} \quad \sigma \equiv \sum_{i=1}^{N} R_i \tag{18}$$

Now we use the transformation method, that is a way to generate random numbers following a specific PDF, f(x), from random numbers uniformly distributed in the interval $[0;1]$.

Mathematically we wish to find a random number in the interval $[r; r+dr]$, that equals to the probability of obtaining a number in the interval $[x(r); x(r+dr)]$ of the original PDF. This means we can set up the integral equation:

$$\int_{-\infty}^{x(r)} f(x'(r))dx'(r) = \int_{0}^{r} g(r')dr' = r \tag{19}$$

We need to solve $\int_{-\infty}^{x(r)} f(x'(r))dx'(r)$, and invert the obtained function which we can rarely do. In the above example where all rates are constant and we have an exponential PDF we can do exactly this:

$$\int_{0}^{t} f(t')dt' = 1 - e^{-t/\tau} = r \quad \Rightarrow t(r) = -\frac{ln(1-r)}{\tau} \tag{20}$$

We can then the update process, where at each iteration step we update the time by

$$t_{n+1} = t_n - \frac{ln(1-r)}{\sigma} \tag{21}$$

where σ is the sum of all the rates. Schematically the Gillespie algorithm can be described as:

- Pick two random numbers, ν_1 and ν_2.
- Calculate time until next reaction:

$$\tau = -\frac{ln(\nu_1)}{r} \tag{22}$$

- Pick the next reaction:

$$\epsilon = \frac{\sum_{i=1}^{k-1} r_i}{\sum_{j=1}^{n} r_j} < \nu_2 \leq \frac{\sum_{i=1}^{k} r_i}{\sum_{j=1}^{n} r_j} \tag{23}$$

- Update the system according to the chosen reaction.

In this way the system can be updated, and the reactions adjusted at each time step which makes it is a very precise way of updating the system. Note that the larger the volume, the more molecules will be present, and the closer we are to the deterministic limit. If we compare simulations with different noise levels, to a deterministic simulation in an oscillatory system, we find that the smaller the volume, the faster it goes out of phase with the deterministic oscillation (Fig. 5A). When the number of molecules gets very high, it takes a lot of steps to make any significant changes to the system, and since there are many molecules, reactions happen all the time and the step sizes gets microscopic. A way to avoid this, is through the τ-leap method, that starts from the direct Gillespie method, but compromises a little on the accuracy, by making a poisson approximation to increase the step size [21]. Finally it should be mentioned that the Gillespie algorithm can be used in other situations than simulating molecular dynamics. For every system that is updated by the next step and where all rates are constant we con use the method. An example is the TASEP system, that is a ladder of length L, divided by N steps, where a particle of size S, can enter at region 1 with rate r_i and move along the ladder with rate Nr_0, given that there is not another particle in front of it (Fig. 5B). Applying the Gillespie algorithm to this, we can count the number of particles leaving the ladder, and find that this also depends on N (Fig. 5B), which in an abstract way represents a noise level, even though this is not as trivially defined that for the molecular systems.

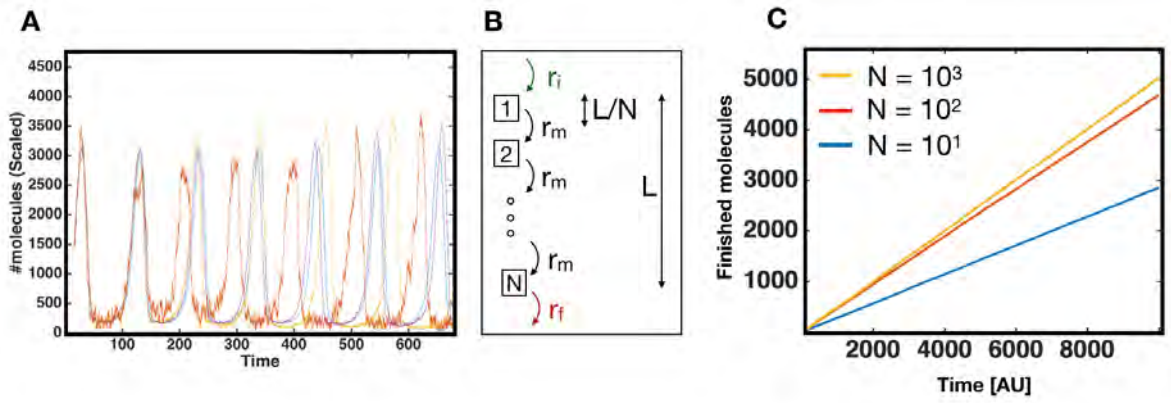

Figure 5: *A) Gillespie algorithm for different volumes. B) Schematic figure of the TASEP model C) Number of finished particles, for different number of steps N*

1.2.2 Specific Mechanisms Arising From Noise

As we claimed above, life is the result of an interplay deterministic laws and stochasticity, so in this way life itself is an indirect result of the fluctuations in the biochemical particles. However stochasticity can give rise to some specific features in dynamical systems. One of these is bistability, in which a dynamical system has two stable fixed points. If we consider the dynamical system:

$$\dot{x} = x(1 - x^2) + \epsilon\mathcal{N} \tag{24}$$

It is obvious that this has two stable fixed points for $x = 1$ and $x = -1$. For a deterministic system, the trajectory would move towards one of the fixed points and then stay there forever. However in the presence of noise, this is governed by transitions between the two stable states (Fig. 6A) and the rate between the changes is governed by the noise level, which in this example is determined by ϵ. Another interesting phenomena that that is induced by noise, is the arise of oscillations in systems with a stable fixed point but with complex eigenvalues. If we consider the Brusselator system:

$$\dot{x} = a - (b + d)x + cx^2y \tag{25}$$

$$\dot{y} = bx - cx^2y \tag{26}$$

Then this will not have oscillations for $b < 2$. This means that for the deterministic system, the trajectory would settle in the fixed point, but in the presence of noise the trajectory will be "pushed" out of this point, and in this region, it will have oscillatory motion with clear signal in the power spectrum (Fig. 6B). Furthermore the larger the noise level, the larger the oscillations will be, which can be estimated by calculating the maximum value in the power spectrum (Fig. 6C). Thus we have seen that noise in dynamical systems can lead to complex behaviour of the system, and the proper control of noise in the cell is therefore very important.

1.3 Overview of Projects

Finally, we present an overview of the chapters as presented in the thesis which is presented as a timeline in Fig. 7. Since the projects are of different character and since the work was carried out

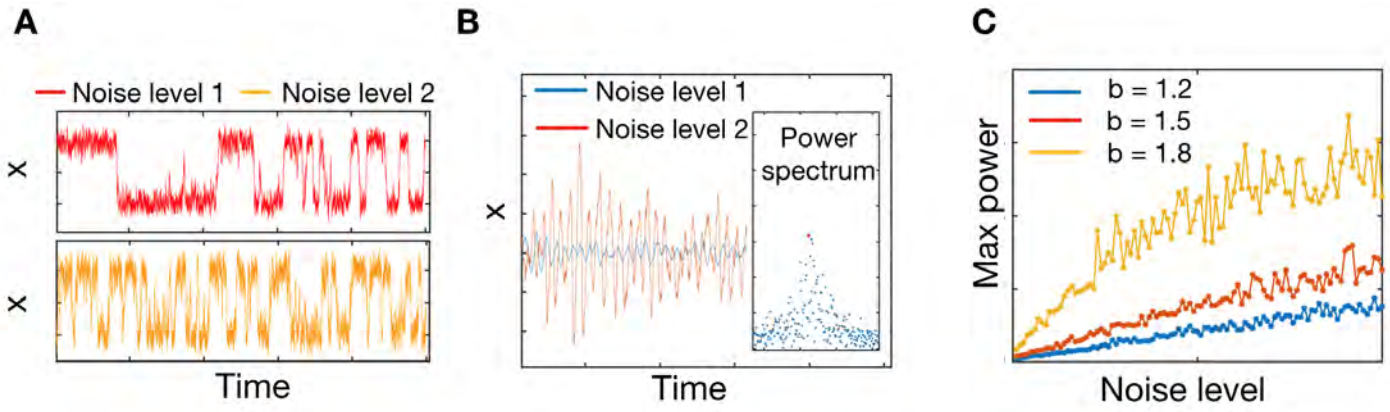

Figure 6: *A) Value of x as a function of time. Above: small noise level. Below: large noise level. B) trajectory showing x as a function of time. Blue: small noise level. Red: small noise level. Inset: Power spectrum for the red data series. C) The peak value in the power spectrum as a function of the noise level. Here b represents the parameter that leads to a Hopf bifurcation for $b \approx 2.0$.*

at different stages of the PhD, it is the hope that the reader in the projects should also find some development in the ideas and ways to find solutions to the problems. In chapter 2, we present the

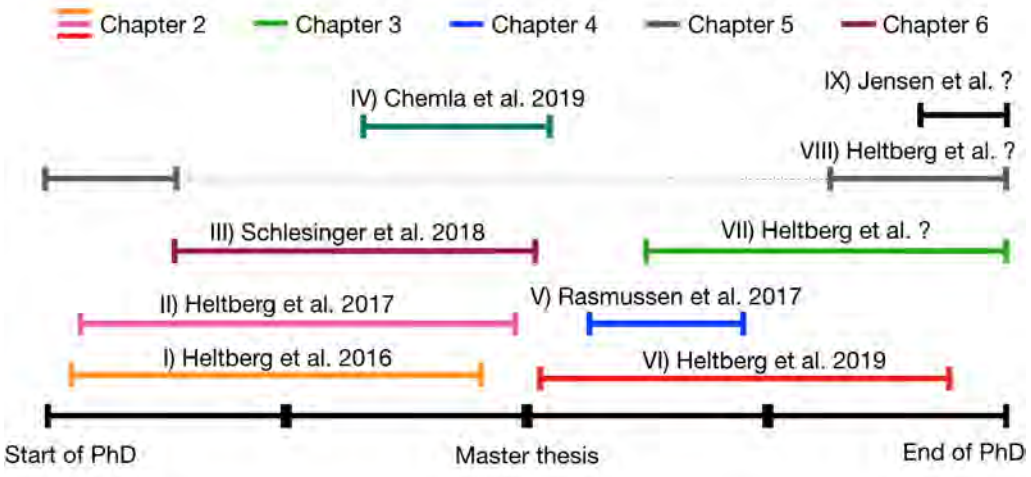

Figure 7: *Schematic figure showing the time of creation of the different projects. Note that the results of paper IV and IX is not part of this thesis.*

work on oscillations, modehopping and chaotic dynamics in NF-κB and the effects on downstream genes. This work was initiated in April 2015 during my visit to Bangalore where we realized that modehopping could occur. We worked a lot on the transition to chaotic dynamics, but in the end the most interesting aspect was the downstream gene model. We developed this further, which led to the results presented in paper VI. In chapter 3, we move on to describe the results on another transcription factor: p53. Here we start by presenting the experimental results and from this we construct a mathematical model that investigates which mechanisms can and cannot lead to the observed experimental behaviour. We extend this, by including the response stimulation of UV

radiation and test the limits of the model. In chapter 4, we move on to the description of neurons, and introduce the extended averaged neuron model. Here we test the dependency on external ion levels in a mathematical model of the neuron, and find that this can help the state transitions between sleep and awake, and we hypothesize that the awake state is governed by chaotic dynamics. In chapter 5, we investigate the dependencies on dopamine in parts of the human brain, and how the systems breaks down when the neurons are removed as is found in Parkinsons disease. We test this for different models of compensation mechanisms, and from this we move on to model the global landscape of dopaminergic neurons, depending on the ways they are removed from a network. In chapter 6, we study the protein production of GFP inside E. coli, for a specific line of bacteria that has an unnatural amino acid encoded. We find that if the system is tuned by too strong promoters this does not lead to an large expression, but if a codon for an unnatural amino acid is inserted a large expression is seen. We create a mathematical model for this and test the model predictions with experiments.

2 The Effects of Complex Dynamics in NF-κB on Gene Regulation

In this chapter the results of paper I, II and VI is presented and discussed, along with a few other ideas that could be part of future projects. This work has been ongoing since the start of my PhD and can therefore be regarded as the main results of my work. The project was originally founded on experimental work carried out by Savas Tay and Ryan Kellogg, where they found oscillations with different frequencies in NF-κB. We then used the model, proposed in 2012 by Mogens H. Jensen and Sandeep Krishna to describe observed the phenomenon. In these projects, I have done the mathematical modelling and created numerical simulations and analytical arguments, with great help and inspiration from Sandeep Krishna and Mogens H. Jensen.
In this project we observe experimentally that NF-κB oscillates with different frequencies when perturbed by oscillating TNF. We use an exiting model to examine this and find that that transitions between limit cycles can occur in the presence of noise, and we term this modehopping. We then investigate the time correlations in modehopping and characterize the distribution of times in each state through a 1D model. From this we examine the downstream effects of the dynamics in NF-κB, and create a model that defines a gene based on the affinity and cooperativity in its binding with NF-κB. We find that modehopping can stimulate genes and different times, in a process we term multiplexing. We extend this to consider chaotic dynamics which we find by increasing the TNF amplitude even further, and we find that chaotic dynamics has some statistical properties that we also found in modehopping and that chaotic dynamics can enhance low affinity genes. Finally we use this to investigate the effects of chaos further and we find that it enhances the efficiency and economy of protein complex formation and increses the average lifetime for populations of cells in specific stressed environments.

2.1 Introduction to the Network of NF-κB and its Role as Transcription Factor

NF-κB (nuclear factor kappa-light-chain-enhancer of activated B cells) is a family of protein complexes that function as transcription factors. There are 5 different subunits (p65/RelA, RelB, c-Rel, p52/NF-κB2, p50/NF-κB1) that can form dimers and work as different versions of NF-κB [22, 23]. These subunits can combine both in homo- and heterodimers, and they use the structure of the two subunits to form a complex with DNA [24]. In this thesis we will consider all complexes of NF-κB as one, since there is no evidence that the different versions of NF-κB should have different functionality for the problems we consider.
When not stimulated, NF-κB is located in the cytoplasm forming a complex with proteins from a family of inhibitors named IκB (inhibitor of κB). Like for NF-κB, we will in this treat all versions of IκB as one. The role of this inhibitor is to keep the NF-κB proteins in the cytoplasm, as they mask the Nuclear localisation sequence, and thus stopping the transport into the nucleus where it can function as transcription factor [25]. Thus to activate NF-κB IκB should be degraded and main pathway for this activation is stimulated by Tumor Necrosis Factor (TNF). TNF is a ligand, that has shown to be essential in different processes as cell death and inflammation, and maintaining the correct regulation of TNF is crucial[26], since dysregulation of TNF has been related

to outbreaks of Alzheimer's disease [27] and cancer [28]. In the activation of NF-κB, it binds to a receptor, and this causes the adaptor protein TRADD to recruit the proteins TRAF2 and RIP. This will in turn activate the protein kinase IKK, that can then phosphorylate IκB, which leads to degradation thereby activation NF-κB [24]. Since NF-κB activates IκB, this creates a negative feedbackloop, and it has previously been shown that NF-κB can oscillate after stimulation with TNF [3].

NF-κB is present in (almost) all mammalian cells, and is believed to be very important in the process of cellular responses to external stimuli. It is a "rapid-acting" primary transcription factor, since it it is always present in the cell, but usually in the inactive state that can quickly be made active [29]. This is in contrast to other transcription factors that should undergo protein synthesis before they can work which significantly limits the time before the cell can react to external stimuli. The mammalian immune system can be divided into the innate and the adaptive response [30], and NF-κB is believed to be important for both. In the innate system, a key component of eliminating foreign pathogens, is macrophages and these cells can activate NF-κB to induce expression of proinflammatory cytokines, chemokines and anti-apoptotic proteins, to remove the antigen [31]. When the macrophages cannot remove the pathogens themselves, T-cells are stimulated as part of the adaptive immune system and in this activation, NF-κB is also an essential transcription factor [32]. This highlights NF-κB has a variety of very important features that control basic response mechanisms in living organisms, and due to the many interactions its full significance is still far from understood.

2.2 Experimental Results (M)

The original idea of modehopping in NF-κB came following the very interesting results from Savas Tay and Ryan Kellogg, with whom we have collaborated. In their paper from 2015 [13] they showed that entrainment of $NF-\kappa B$ appeared when cells were stimulated with periodically modulated TNF.

2.2.1 Connections Between NF-κB Oscillations and Protein Production (M)

Periodic inputs may lead to entrainment of oscillators, a phenomenon where the oscillatory process locks, in frequency and phase, to the external signal. The classical examples of entrainment comes from physics where for instance pendulum clocks or lasers can cause modelocking; in these systems there exists well-developed theory describing how two oscillators can couple so one external, periodic oscillator affects an internal oscillator. The output of the internal oscillator depends on the coupling between them, and to the difference in frequency between the two. The extracellular ligand TNF can cause the fraction of NF-κB localized within the nucleus, to oscillate with a natural period of 90-100 min [13]. Accordingly, it was previously shown that NF-κB oscillations can synchronize in time to the TNF input, but only at specific frequencies of TNF stimuli. For TNF stimulation with periods of 120 minutes the cells synchronized in time and showed large oscillation amplitudes (Fig. 8A, [13]), whereas for TNF stimulation with periods of 60 minutes, the cells did not synchronize and showed smaller oscillation amplitudes (Fig. 8B, [13]). Here it was also shown that individual genes had different expression depending on the oscillations of NF-κB and for all the cells studied it was highest on the synchronized case where the amplitudes were

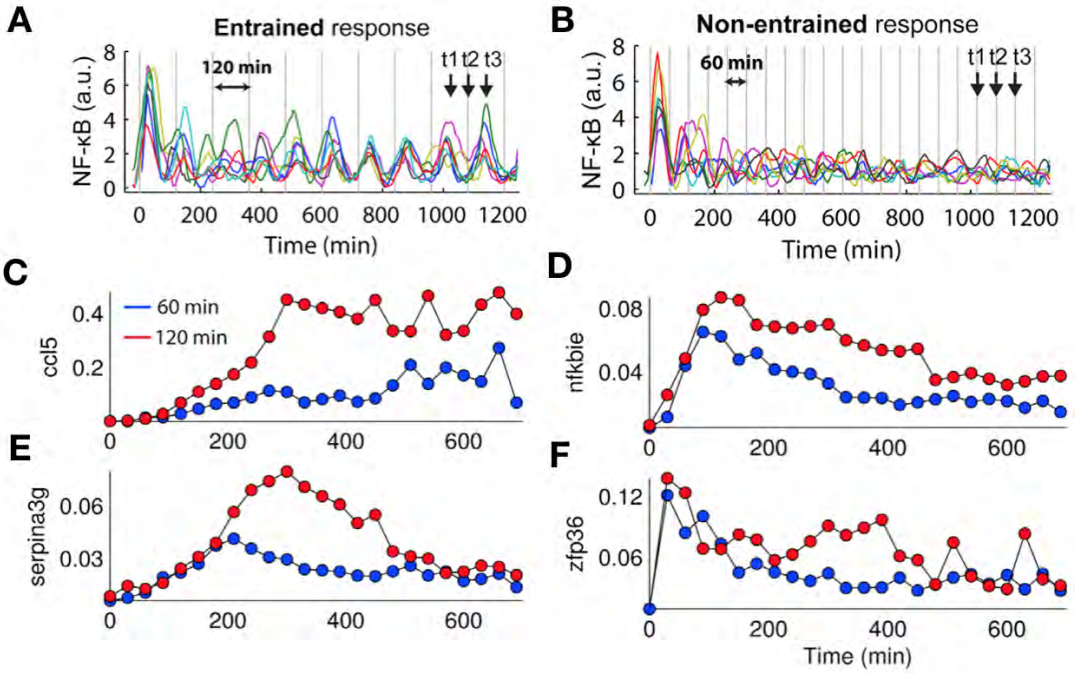

Figure 8: *A) NF-κB oscillations at TNF period 120 min. B) NF-κB oscillations at TNF period 60 min. C-F) Protein production for each TNF stimuli from four independent genes. (All subfigures are originally from [13])*

highest (Fig. 8C-F, [13]). From this expermental motivatiom, we conclude that synchonization in protein oscillations can depend on the external frequency and the downstream gene production are affected by the modes of oscillation in NF-κB.

2.2.2 Observation of Cells With Dynamically Changing Frequency (M)

This project began with repeating the observations described in Kellogg and Tay 2015. Using microfluidic cell culture, we delivered periodic TNF stimulation to fibroblasts and recorded dynamics of NF-κB nuclear localization by live cell fluorescence microscopy. We hereby confirmed that NF-κB oscillations occur, but we also observed that they show spontaneous frequency jumps and transitions between locking modes during the time course of periodic stimulation for some external forcing periods (Fig. 9A). We investigated this more thoroughly by considering these apparent transitions in a frequency space. Here we observed that the oscillations involve apparently spontaneous changes in frequency, but that the frequency seem to be close to either the 1/1 or 1/2 ratio between internal and external periods. We wished to investigate this further and see if we could find a signal when examining all the cells. For these traces, we now found the individual peaks by smoothening the data using the Matlab function *smooth*, followed by peak detection, using the Matlab function *mspeaks*. The peaks were then filtered based on reaching a threshold 10% of maximum intensity. Gathering all the data from these oscillations, we calculated the frequencies and compared them to the applied TNF frequency. Compared to 90 min TNF input where cells entrain almost exclusively at the 1:1 locking mode, at 150 min the average cell

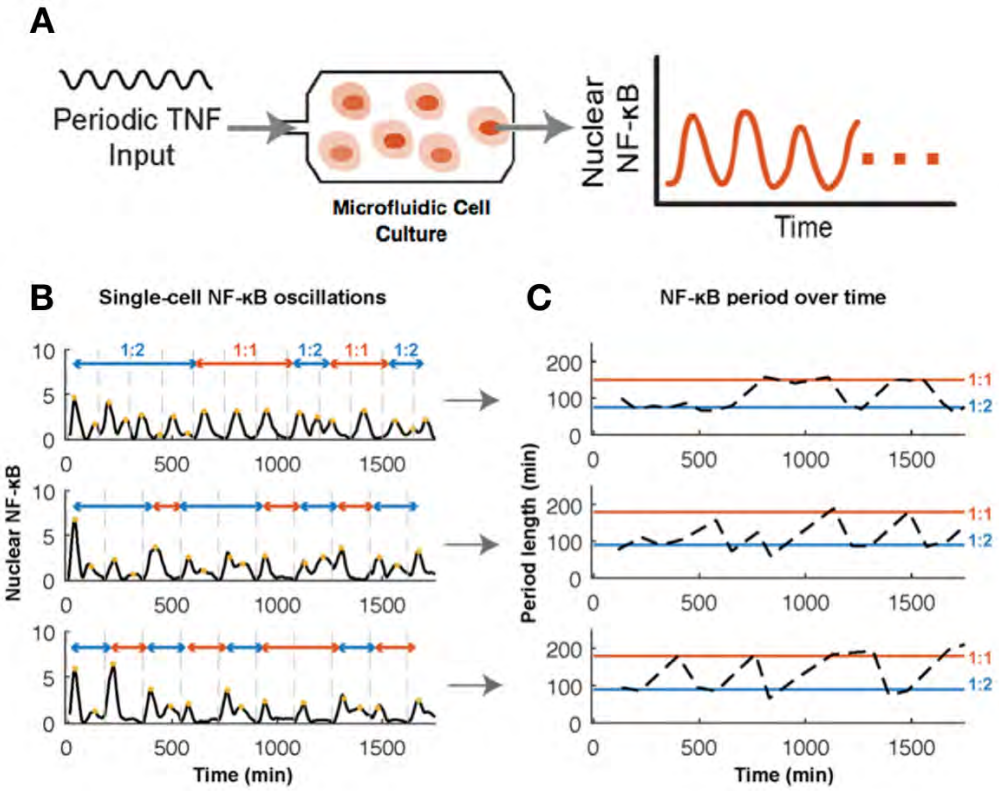

Figure 9: *A) Schematic figure showing the setup of experiments. B) 3 representative single cell traces showing oscillatory NF-κB level. C) Corresponding traces showing the frequency of oscillations in time.*

spends equal time in 1:1 and 1:2 modes. For 180 min input, the average cell spends most time in the 2:1 mode but also about 30% of time in the 1:1 mode (Fig. 10A). Therefore this suggests that multiple entrainment modes occurs during the time course. This suggests that the system for this external amplitude, can be in one of two states depending on the frequency of TNF (Fig. 10B) or in the overlapping Arnold tongue regions where both solutions co-exist (Fig. 10C). In deterministic systems, spontaneous transitions between locking modes cannot occur before the multiple overlaps within the Arnold tongue regions will cause a transition into chaos [33]. We therefore wanted to investigate whether and how transitions between entrainment modes can spontaneously occur in a noisy system like the NF-κB network and what drives them.

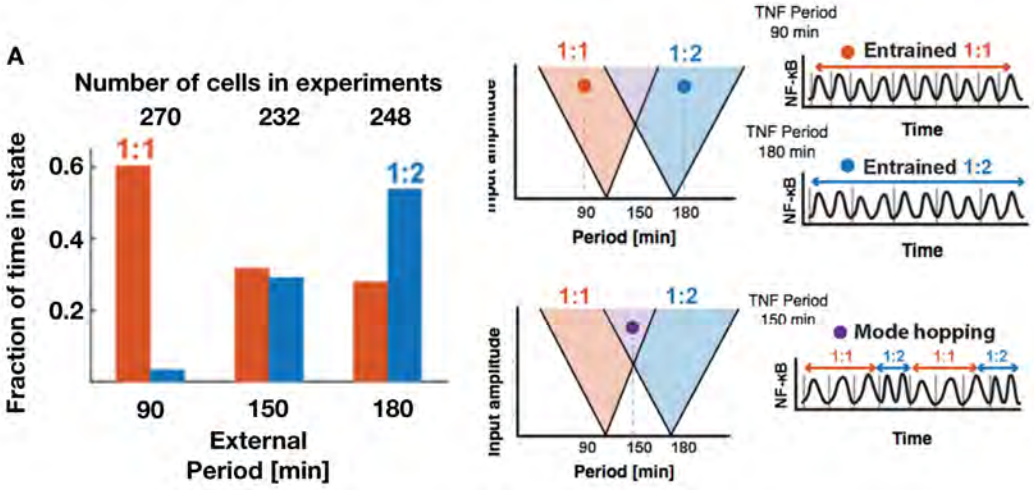

Figure 10: *A) Comparison of time an average cell spends in each entrainment mode, for differing TNF input frequencies. B) Periodic forcing in an oscillator leads to entrainment visualised by regions called Arnold tongues. In the 1:1 NF-κB entrainment mode (orange region), the NF-κB period matches the 90 min period of the fluctuating TNF input. In the 1:2 entrainment mode (blue region), there is one TNF input cycle for every two cycles of the NF-κB oscillation. C)In overlapping Arnold tongue regions, multiple entrainment modes are possible. Here noise may enable spontaneous transitions between entrainment modes, as observed in experiments.*

2.3 Overlapping Arnold Tongues Leads to Modehopping Phenomena (M)

When an external driving signal oscillates, it can couple and thereby entrain or synchronize another nonlinear oscillator. In our system this means TNF is varied in frequency, and within certain ranges it will force the NF-κB oscillations to occur with the externally imposed frequency [34, 13]. As the amplitude of TNF oscillations is increased, the range of frequencies for which it can entrain NF-κB becomes larger - and we thus have regions of parameter space that will lead to entrainment. These expanding synchronization regions, defined by the external amplitude-frequency parameter space are called Arnold tongues [35, 36, 33, 37]. A full investigation of these in the classical sine circle map, along with some analytical theorems is found in Appendix C. Entrainment has been observed in many different physical systems, from fluids [38] to quantum mechanical devices [39, 40], and in biological processes such as cell cycles [41, 42, 43], and gene regulatory dynamics in synthetic populations [6]. We are now interested in studying the effects as the external amplitude is increased and regions of synchronization should start to overlap.

2.3.1 Mathematical Model for NF-κB With External Forcing (M)

We started out by considering the model of NF-κB dynamics inside the nucleus, previously published by Jensen and Krishna 2012. In this deliberately simplified model, the oscillations arise from a single negative feedback loop between NF-κB and its inhibitor IkBα, and can be triggered by TNF via the activation of the IkB kinase (IKK). This is described through five coupled differential

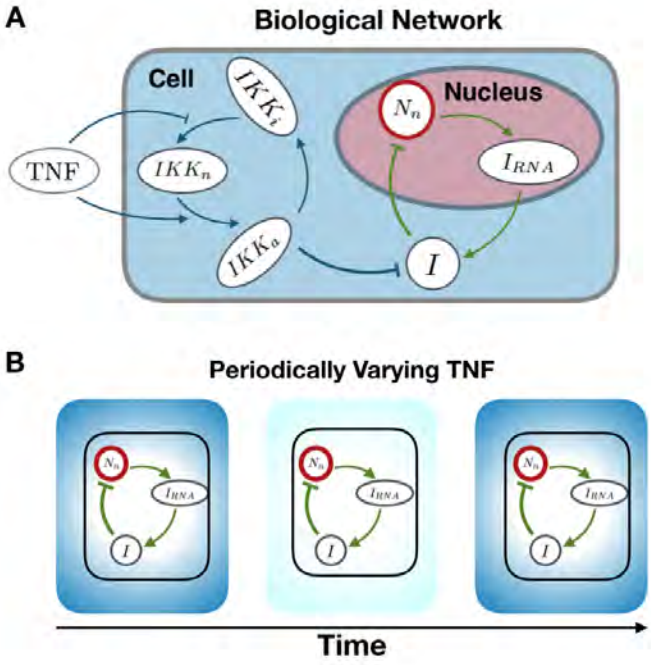

Figure 11: *A) Schematic picture of a simplified NF-κ B network with a single negative feedback loop which can generate oscillations. B) Schematic picture of oscillations in the external TNF concentration, represented by the changing shade of blue.*

equations as can be seen below, and a full discussion of the model is found in Appendix B.

$$\dot{N_n} = k_{Nin}(N_{tot} - N_n)\frac{K_I}{K_I + I} - k_{Iin} I \frac{N_n}{K_N + N_n} \tag{27}$$

$$\dot{I_{RNA}} = k_t N_n^2 - \gamma_m I_{RNA} \tag{28}$$

$$\dot{I} = k_{tl} I_{RNA} - \alpha I K K_a (N_{tot} - N_n)\frac{I}{K_I + I} \tag{29}$$

$$\dot{IKK_a} = k_a \cdot TNF \cdot IKK_n - k_i IKK_a \tag{30}$$

$$\dot{IKK_i} = k_i IKK_a - k_p IKK_i \frac{k_{A20}}{k_{A20} + [A20] \cdot TNF} \tag{31}$$

$$IKK_n = [IKK]_{tot} - IKK_a - IKK_i \tag{32}$$

$$TNF = 0.5 + A\sin(\frac{2\pi}{T}t) \tag{33}$$

This is shown schematically in Fig. 11A, where the position of the components can be seen as well. We now let the concentration of surrounding TNF oscillate, so it affects the cells on single cell level. This is shown schematically in Fig. 11B.

2.3.2 Overview of Dynamics Resulting From Arnold Tongues

We now studied the system of two coupled oscillators, where TNF affected NF-κB, and we now examine the resulting dynamics when we change the amplitude of TNF. In this description we will use Fig. 12 as a guide. At first we consider the situation where the TNF amplitude is infinitely small, which is shown at point 0 in Fig. 12. Here the TNF and NF-κB oscillations do not couple, which means that in their combined phase space the trajectory will be quasiperiodic. A thorough

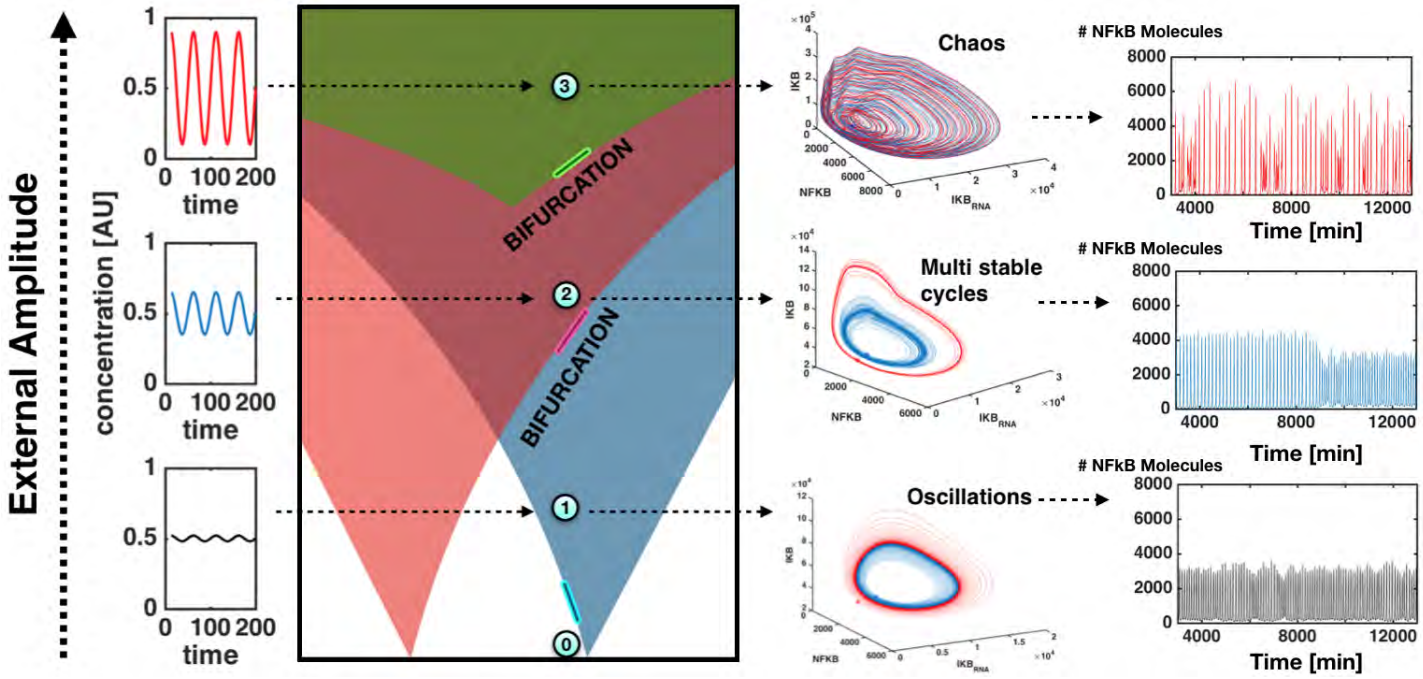

Figure 12: *Dynamics that emerges when the NF-kB system is driven by a periodic TNF signal. The left panel shows schematically that there are Arnold tongues, triangular regions of the TNF amplitude-period parameter space where NF-kB oscillations can be synchronized to the TNF signal. Outside the Arnold tongues, e.g. point 0, there is no synchronization. As TNF amplitude increase the Arnold tongues start overlapping and the behaviour becomes more complex. Keeping the TNF period fixed (here we used T=50 min), as we increase the the TNF amplitude we enter three distinct states: Point 1: A single Arnold tongue, only allowing one oscillation state. Point 2: Overlap of Arnold tongues, allowing two stable oscillation states. The presence of noise can cause transitions (mode-hopping). Point 3: Chaotic dynamics, with apparently unpredictable trajectories. The trajectories corresponding to these points are shown in in the middle panels. Red and blue trajectories correspond to two different initial conditions in a deterministic simulation. The rightmost panels show the dynamics of NF-κB vs time in stochastic simulations where intrinsic noise is implemented using the Gillespie algorithm.*

discussion of this is found in Appendix C. Here it is important to remember, that their combined phase space has quasiperiodic trajectory, but this does not mean that NF-κB show quasiperiodic behavior - NF-κB oscillates through the dynamics of a limit cycle that is unchanged by the small oscillations in TNF. If we increase the TNF amplitude, we find that entrainment occurs, where the internal oscillator locks to the external signal in frequency and phase. For the NF-κB dynamics, this means that there exists one stable limit cycle (Fig. 12, point 1). Therefore the dynamics will be attracted to the stable cycle, characterized by a fixed frequency and amplitude, independent of initial conditions (Fig. 12 right panel below, blue and red trajectory). Thus, when we simulate the dynamics in a stochastic simulation, by adding noise to our simulations using the Gillespie algorithm [20], we find that the oscillations will deviate in amplitude and frequency according to the noise level but that they always will be around the entrained oscillation state (Fig. 12 below to the right, black trajectory). Thus the frequency and thereby amplitude of NF-κB, can within some

range be dictated by the TNF oscillation parameters. As the TNF amplitude increases further, we the expanding Arnold tongues now can start to overlap, which means that we have crossed a bifurcation point(Fig. 12, point 2). As expected, we observed that when NF-κB oscillations are simulated deterministically within the overlapping Arnold Tongue regions of parameter space, oscillations settle in different entrained states depending on the initial conditions (Fig. 12 right panel center, blue and red trajectory). Mathematically speaking this means that more than one limit cycle exists, and depending the basins of attraction, a trajectory can be attracted to one of the limit cycles. Modehopping was however not observed, since transitions between stable states do not occur for the deterministic system. Now we turned to the stochastic simulations, and here we find that transitions between entrained states do indeed occur. This can be understood as a transition in amplitude and frequency space. We conclude that noise mediates hopping between entrainment modes and could serve as a mechanism in the cell to produce quick switching of NF-κB oscillation frequency. Finally, for large amplitudes of TNF, we reach the transition into deterministic chaos, which refers to complex, apparently unpredictable, dynamics that even simple deterministic dynamical systems can produce. Chaotic dynamics can arise in nonlinear systems of dimension higher or equal to three, but a universal way to achieve chaos is by driving a nonlinear oscillator by an external periodic signal (Fig. 12, point 3) [36, 33]. In the chaotic system, two trajectories starting from almost identical initial positions, will evolve completely different in time and since a trajectory will never repeat itself, they will both expand visited part of the phase space compared to other dynamics (Fig. 12 right panel above, blue and red trajectory). From the point of view of NF-κB this means that there will be a large spread in the height of the amplitudes which is happening for the deterministic system but also in the presence of noise (Fig. 12 above to the right, black trajectory). Therefore we conclude that NF-κB dynamics can become chaotic, and leads to a variety of different amplitudes and frequencies.

2.4 Investigation of The Time Correlations of Mode Hopping (M)

From the stochastic simulations on the NF-κB system, we found that transitions between limit cycles did occur and we termed this phenomenon Modehopping. Now we turned to describe the quantitative features of this, in order to figure out how the frequency of transitions depended on parameters in the system.

2.4.1 Introducing a Poincare Section to Study the Transitions (M)

The phase space in the NF-κB model is spanned by the five variables plus time, and that makes it tricky to visualize the trajectories in a meaningful way. In order to study the system, we introduced a Poincare section at NF-κB = 1500 (Fig. 13A), that would allow us to perform a discrete analysis [1]. Within this section we could study the state of the system after each oscillation. Inside this section there were however still several variables to take into account, but to simplify this further we assumed that the period of each oscillation would be a sound measure that would be defined by a combination of all these variables, and we will often use this as a measure in the following section. Therefore we measured the period of each oscillation and had thus transformed the problem into a discrete, one-dimensional study (Fig. 13B).

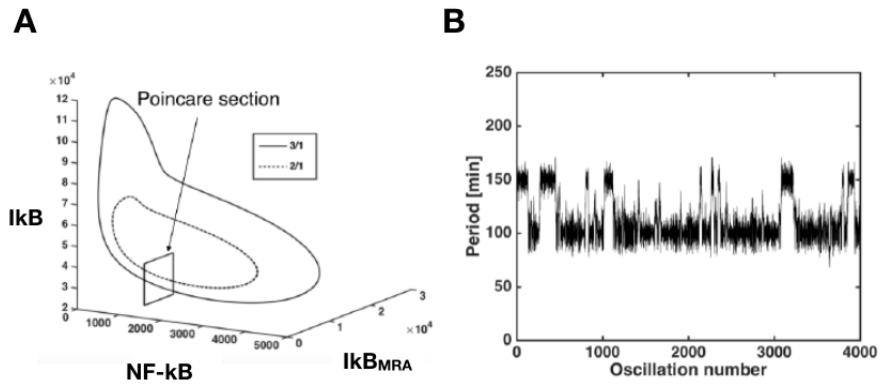

Figure 13: *A: The two stable limit cycles for the deterministic system with external oscillator parameters $T = 50$ min and $A = 0.1$. Shown here is the phase space of variables $NF - \kappa B$, IKB_{RNA}, and IKB, and the Poincare section we use in our analysis. B: 1000 trajectories, making exactly one oscillation, started from the same initial condition. TNF Period = 50 min, TNF Amplitude 0.1.*

2.4.2 Defining Three Key Characteristics of the System

From a mathematical point of view, we now want to find the distribution

$$P(x_i^n \mid x_i^{n-1} = \mu_i) \tag{34}$$

where x_i^n is the position of the i^{th} variable on the Poincare section after n periods of the oscillation, given that the position in the Poincare section after $n-1$ oscillations was μ_i (the period is also regarded as a variable). To use this model we needed to estimate the nature of three key measures:

- The noise inside the Pojncare section after one oscillation
- The deterministic decay into the limit cycle
- The geometry of the basins of attraction

We found the distribution of time periods after one oscillation to be gaussianly distributed and that its standard deviation, σ, to a good approximation, could be treated as independent of the initial position (Fig. 14A).

Thus, in the Poincare section, the system could be described as a deterministic trajectory with gaussian noise. We now studied how a deterministic trajectory with initial position perturbed from the limit cycle, was attracted to the cycle. We calculated the absolute value of the difference between the present period and the period of the previous oscillation in a deterministic simulation and found that this quantity exhibits complex behaviour, but overall went to zero as an exponential decay (Fig. 14B). The non-smooth structure in the decay comes from the coupling between several variables, but we will in the rest of this part, treat these deviations as a negligible effect on top of the basic exponential decay. The decay constant was dependent on the parameters of both TNF and the NF-κB system but for fixed parameters, this was a characteristic measure for each basin of attraction. To finish the investigation, we tried to define the boundary between each basin of attraction. To do this we ran a stochastic simulation of 10^4 oscillations, where we recorded all variables inside the Poincare section. We then used these as initial conditions for deterministic

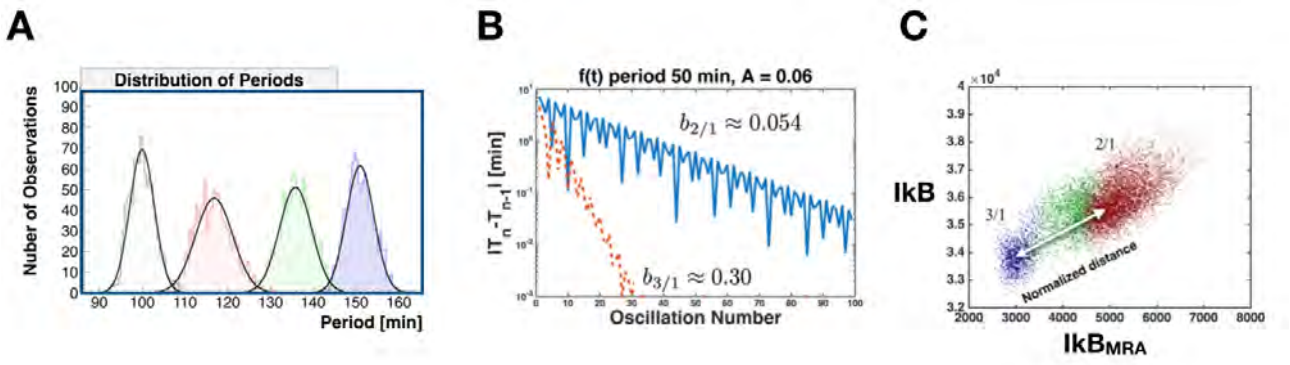

Figure 14: *A) Four distributions of the period after one oscillation; all with gaussian fits. B) Absolute value difference between period and previous period, as the trajectories decay into the limit cycle. The parameter b is the exponential decay constant. C) Stochastic simulation found* 10^4 *points inside the Poincare section. These were used as initial values for deterministic simulation. After 10 oscillations blue has period greater than 145 min (3/1 tongue) and red has period smaller than 105 min (2/1 tongue). Green refers to points between these values.*

simulations and map the period after 100 oscillations. After 10 oscillations, we found that the majority had settled into one of the two limit cycles (Fig. 14C blue and red), but some were still unsettled (Fig. 14C green). This seemed to be a result of a semi-stable 5/2 Arnold tongue. We note that the to good approximation can be regarded as divided in groups depending on a linear distance. This breaks as we move closer to the transition into chaos, where fractal structures start to emerge as there are two stable limit cycles. However, in the modehopping regime, we can approximate the one dimensional system to follow an exponential decay with gaussian noise, once inside the defined basin of attraction. If the noise kicks the trajectory out of the basin of attraction it jumps to the other limit cycle. We now wished to transfer these conclusions into a simple mathematical model

2.4.3 Introducing a 1D Model to Explain the Distribution of Transition Times (M)

To understand how the transitions are related to the observations inside the Poincare section, we imagine a point inside the basin of attraction of a specific limit cycle. We consider the map:

$$d_n = d_{n-1}\Delta + \mathcal{N}(0,\sigma) = \mathcal{N}(d_{n-1}\Delta, \sigma), \tag{35}$$

where $\mathcal{N}$ defines the normal distribution with parameters given in the argument. A schematic version of this simple model, is shown in (Fig. 15A). We are now interested in knowing the probability density function, $P(d_n)$. This can thus be described as:

$$P(d_n) = P(d_n|d_{n-1})P(d_{n-1}) \tag{36}$$

We start by considering the position after one jump, given the initial position is d_0, described by:

$$P(d_1) = \frac{1}{\sqrt{2\pi}\sigma} e^{-\frac{1}{2}\left(\frac{d_1 - \Delta d_0}{\sigma}\right)^2} \tag{37}$$

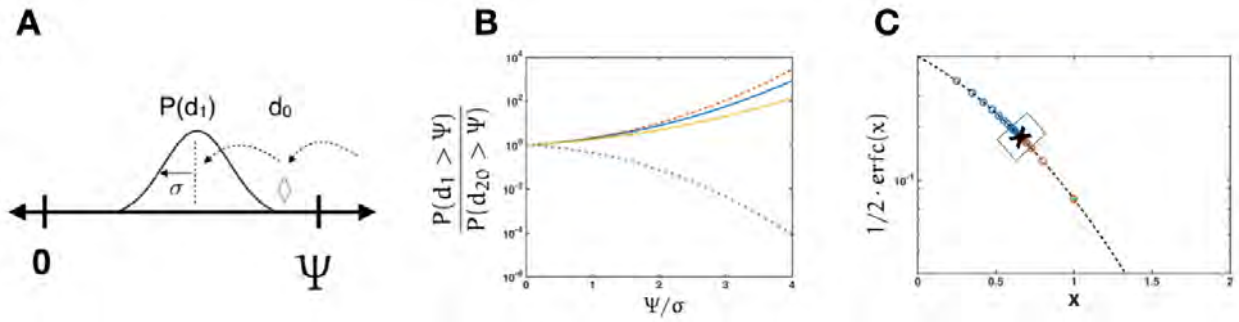

Figure 15: *A) Schematic cartoon of the 1D model. B) Ratio between the probability to leave the state after the first jump and after 20 jumps (in steady state), plotted for the different parameters and initial positions in the model. C) The probability to leave the state, plotted on the error function. Orange starting from* $d_0 = 0$ *and blue starting from* $d_0 = \Psi$*.* $\Psi/\sigma = 1$*. The cross indicates the steady state.*

Now we want to calculate the distribution for the position after the second step. To calculate this we are (to avoid too many ds we define $d = d_0$, $y = d_1$ and $x = d_2$) solving the integral:

$$P(x) = \frac{1}{\sqrt{2\pi}\sigma_1\sigma_2}\int_{-\infty}^{\infty} e^{-\frac{1}{2}\left(\frac{x-\Delta y}{\sigma_1}\right)^2} e^{-\frac{1}{2}\left(\frac{y-\Delta d}{\sigma_2}\right)^2} dy = \mathcal{N}\Big(\Delta^2 d, \sqrt{\sigma_1^2 + \sigma_2^2\Delta^2}\Big). \tag{38}$$

As this holds for every step, we can iterate from the first jump d_1. That is, the PDF of the nth jump becomes:

$$P(d_n) = \frac{1}{\sqrt{2\pi}\sigma_n} e^{-\frac{1}{2}\left(\frac{d_n - \Delta^n d_0}{\sigma_n}\right)^2} \quad \text{where} \quad \sigma_n = \sigma\sqrt{\sum_{i=0}^{n-1}\Delta^{2i}} = \sigma\sqrt{\frac{1-\Delta^{2n}}{1-\Delta^2}}. \tag{39}$$

Now in order to consider transitions between basins of attraction, we must consider the probability that the distance d is larger than the boundary of the basin, defined as Ψ. Thus:

$$P(d_n > \Psi) = \int_{\Psi}^{\infty} \frac{1}{\sqrt{2\pi}\sigma_n} e^{-\frac{1}{2}\left(\frac{x-\Delta^n d_0}{\sigma_n}\right)^2} dx = \frac{1}{2}\mathrm{erfc}\Big(\frac{\Psi - \Delta^n d_0}{\sigma_n}\Big) \tag{40}$$

From this we can also see that this will always reach a steady state, where the probability of leaving (i.e., a transition out of the basin of attraction) will be:

$$\lim_{n\to\infty} P(d_n > \Psi) = \lim_{n\to\infty}\Big(\frac{1}{2}\Big[\mathrm{erfc}\Big(\frac{\Psi - \Delta^n d_0}{\sigma_n}\Big)\Big]\Big) = \frac{1}{2}\Big[\mathrm{erfc}\Big(\frac{\Psi}{\sigma}\sqrt{1-\Delta^2}\Big)\Big] \tag{41}$$

This means that the probability of leaving will, in steady state, be highly dependent on the relation between Ψ and σ, but independent of the initial position d_0. The probability to leave the state in the first jump will always be dependent on the initial position. If we assume $d_0 = \Psi$ we obtain:

$$P(d_1 > \Psi | d_0 = \Psi) = \frac{1}{2}\Big[\mathrm{erfc}\Big(\frac{\Psi}{\sigma}(1-\Delta)\Big)\Big] \tag{42}$$

showing that the probability to leave in the first jump is higher than in the steady state. If we consider $d_0 = 0$ we obtain:

$$P(d_1 > \Psi | d_0 = 0) = \frac{1}{2}\Big[\mathrm{erfc}\Big(\frac{\Psi}{\sigma}\Big)\Big] \tag{43}$$

showing the probability to leave in the first jump is lower than in the steady state.
With these results, we have an interesting measure, the ratio between the probability of leaving in the first iteration, divided by the probability of leaving in the steady state. This ratio is plotted in Fig. 15B for different values of Δ and different initial positions. Another visualization of this is the probability to leave for each step, depending on the initial condition, for $\Psi/\sigma = 1$ (Fig. 15C). We now proceed to calculate the probability distribution for the first time to leave the entrained state, J_1, meaning the first time the distance will be greater than Ψ:

$$P(J_1 = n) = \frac{1}{2^n}\Big[1 - \mathrm{erf}\Big(\frac{\Psi - \Delta^n d_0}{\sigma_n}\Big)\Big] \prod_{j=1}^{n-1} \mathrm{erf}\Big(\frac{\Psi - \Delta^j d_0}{\sigma_j}\Big) \tag{44}$$

Assuming that $d_0 = \Psi$ we can reduce the above expression:

$$P\Big(J_1 = n | d_0 = \Psi\Big) \quad = \frac{1}{2^n}\mathrm{erfc}\Big(\frac{\Psi}{\sigma}\sqrt{1-\Delta^2}\sqrt{\frac{1-\Delta^n}{1+\Delta^n}}\Big) \prod_{j=1}^{n-1} \mathrm{erf}\Big(\frac{\Psi}{\sigma}\sqrt{1-\Delta^2}\sqrt{\frac{1-\Delta^j}{1+\Delta^j}}\Big) \tag{45}$$

From this expression, it should be deduced, that the argument depending on n will converge to one, meaning that the probability to jump out will quickly reach a steady state. In the steady state there is always the same probability to jump out, and the distribution describing a discrete event with the same probability will be the exponential distribution.

From Fig. 15C, we observe that it takes several iterations to reach the steady state, and we assume that these initial probabilities can be described by a single exponential distribution. Therefore, we expect that the distribution of oscillations in one limit cycle before transition, can be described by a sum of two exponential distributions:

$$f(n) = \overset{\text{Initialposition}}{Ae^{-bn}} + \overset{\text{SteadyState}}{Ce^{-dn}} \quad \text{where} \quad n \equiv d_n > \Psi \wedge d_{n-1}..d_1 \leq \Psi. \tag{46}$$

2.4.4 Comparing the 1D Model to the Statistical Properties of Transitions (M)

Now we want to test if the dynamics of modehopping can be described by the model predictions. We let the system start inside the basin of attraction for one of the limit cycles and measure the number of oscillations before it leaves this state. In these simulations, we define that the trajectory leaves the entrained state when the period becomes closer to the period in the other limit cycle. We start by testing for a situation like $d_0 = \Psi$, i.e., when the initial position is on the border of the basin of attraction and at $d_0 = 0$, i.e., at the center of the limit cycle (Fig. 16A-B). In both cases we find that the distribution follow the sum of two exponentials, and if the trajectory start around the boundary there will be an increased probability to escape in the first oscillations(Fig. 16A), which is opposite to the results if the trajectory starts right at the limit cycle (Fig. 16B). The effect of the initial conditions is thus captured in the first part of the fit, where we find that these effects can be estimated by adding another exponential function. From our predictions, the two situations should have the steady state distribution. We therefore compare the values of λ_2 in the two fits (Fig. 16A-B). Here we obtain:

$$\lambda_2(d_0 = \Psi) = 0.0181 \pm 0.0019 \tag{47}$$

$$\lambda_2(d_0 = 0) = 0.0178 \pm 0.0006 \tag{48}$$

We want to compare these numbers by dividing their difference with the square root of the sum of their errors:

$$\frac{\lambda_2^0 - \lambda_2^\Psi}{\sqrt{\sigma_{\lambda_2^0}^2 - \sigma_{\lambda_2^\Psi}^2}} = 0.15\sigma \tag{49}$$

This means that they are 0.15 standard deviations from eachother and thus in very good agreement with the hypothesis.

Now we want to study the long term dynamics, and estimate the distribution of number of oscillations in one limit cycle, before leaving for the other limit cycle (As can be seen in Fig. 13B). We use Fisher's discriminant, implemented in MATLAB, to separate the points, and classify them between different states [44]. From the model we expect the distribution to reach a steady state after some oscillations inside one basin of attraction, but having much higher probability to leave the state in the early rounds. This is because the trajectory usually enter a new basin of attraction close to the boundary of this. We confirmed this for the 3/1 limit cycle (Fig. 16C), and show that the distribution is different than the 2/1limit cycle (Fig. 16C), that had a smaller decay constant. Thus we conclude that we can describe the time distributions of modehopping depending on the decay constant of the basin of attraction (dependent on the basin), the noise level (dependent on the volume V) and the geometry of the basin of attraction (dependent on the TNF amplitude).

2.5 Creation of Downstream Model for Protein Production (M)

Given the NF-κB-dynamics and the now to some extent understood time correlations in the modehopping, we consider the significance for the downstream genetic networks. Since NF-κB, is a very important transcription factor, regulating more than 100 genes, we now considered how these dynamics could be of importance.

2.5.1 Affinity and Cooperativity Based Downstream Model (M)

We assume that NF-κB can bind to an enhancer or operator region, and can form complexes to bind the RNA polymerase, with different affinity, depending on the gene As a simple model we now consider two genes, both regulated by NF-κB. Gene 1 has a high affinity, and needs a few number (two) of NF-κB molecules to bind to the promoter (Fig. 17A left) whereas Gene 2 has low affinity and needs a higher number (four) of NF-κB molecules to bind to the promoter (Fig. 17A right). For these two arbitrary genes we consider the following model for their protein production:

$$\dot{m}_i = \gamma_i \frac{N^{h_i}}{N^{h_i} + K_i^{h_i}} - \delta_i m_i \tag{50}$$

$$\dot{P}_i = \Gamma_i m_i - \Delta_i P_i \tag{51}$$

To keep the model as general as possible, we are using the same parameters for both genes, but let them differ only in the parameters for affinity, K_i and the coorperativity given by the Hill coefficient h_i. We define genes with small values of K as high affinity genes (HAGs) and those with large values of K (≥ 4) as low affinity genes (LAGs). The use of Hill functions to describe the protein production for genes governed by transcription factors has often been used in systems biology [45, 46, 47, 48]. A derivation of the Hill function is found in Appendix A. All the parameters can

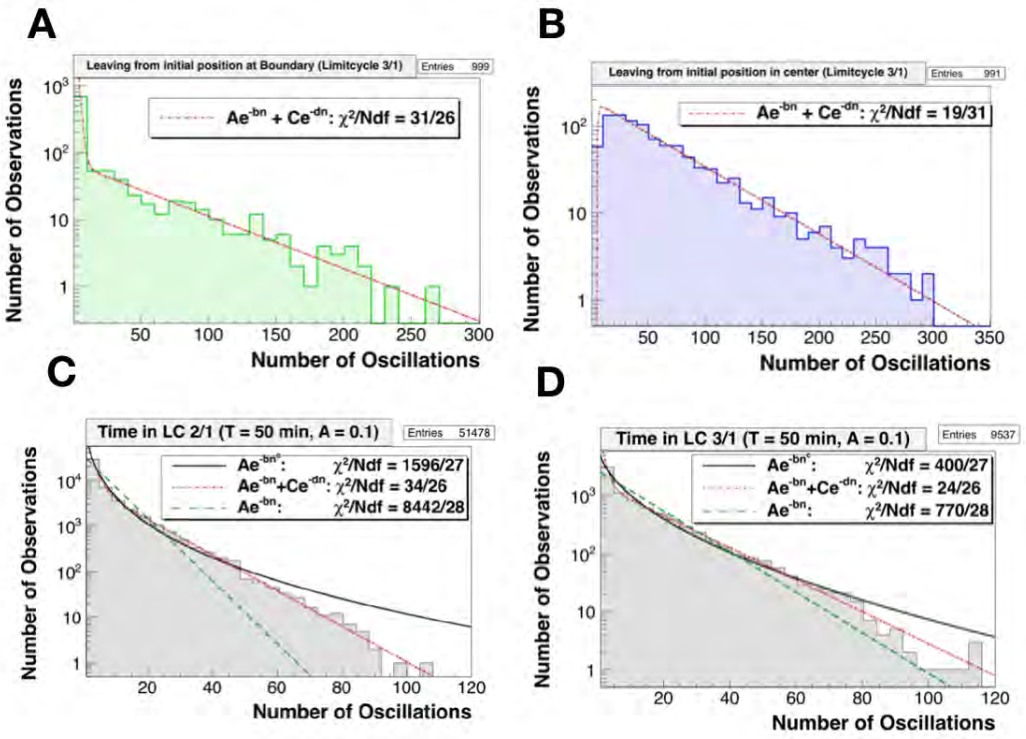

Figure 16: *A) Distribution of number of jumps before leaving the state for the simulated system. Initial position around the boundary. B) Distribution of number of jumps before leaving the state for the simulated system. Initial position in the center of the limit cycle. C) Distribution of oscillations in 3/1 state for totally* $6 \cdot 10^5$ *oscillations. Parameters of external oscillator is* $T = 50$ *min and* $A = 0.1$*. V* $= 2 \cdot 10^{-14} L$*. D) Distribution of periods for the 2/1 limit cycle. From the model perspective this distribution is different from A) in the value of* Δ*. Same parameters used.*

be found in the table below

	Gene 1	Gene 2
γ_i	4.0	4.0
h_i	2	4
K_i	1.0	$\sqrt{20.0}$
δ_i	2.0	2.0
Γ_i	2.0	2.0
Δ_i	0.3	0.3

We now consider the situation where NF-κB can oscillate in two different states defined by frequency and amplitude. We observe the average NF-κB level is greatest for the high frequency state (2/1) since this state always has a substantial NF-κB level, which is not the case for the low frequency state (3/1), where the concentration drops to almost zero at some points (Fig. 17B). From this we learn that the gene with high affinity and low cooperativity, will benefit from a high average level of NF-κB and thus small amplitudes. This is because there is not a great difference in the output level reached by the small or large amplitude oscillation (Fig. 17C) and therefore it is advantageous to have more peaks and thus a higher average level. If we instead consider the

gene with low affinity and high cooperativity, then a pulse of very high concentration is required to generate a production. If we study Fig. 17C, we see that the magenta curve is in generally yielding a lower output than the cyan, but that the height of the peak in the 3/1 state yields many times more than the 2/1 state. Therefore it is advantageous for this gene to have very high peaks which is possible in the 3/1 state.

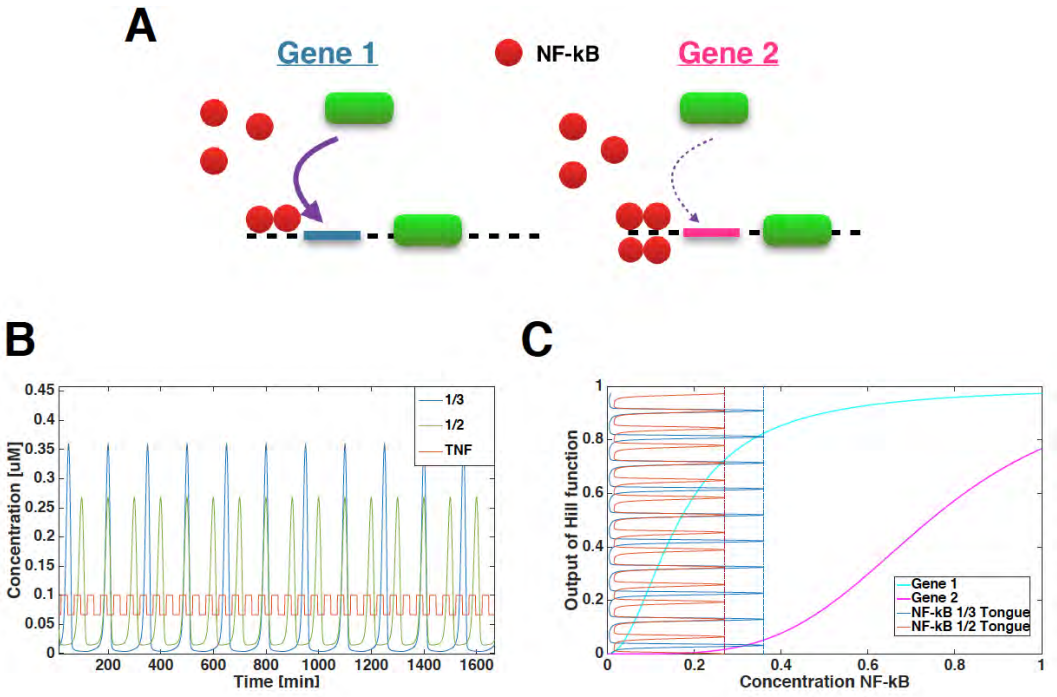

Figure 17: *A) Schematic figure of the two types of genes B) Visualization of the two oscillating states C) Visualization of the Hill functions governing the mRNA production. Vertically is seen the NF-κB oscillations, showing the relevant levels.*

2.5.2 Differential Gene Control From Suggested Model (M)

Since these two genes react oppositely to a change in state for the NF-κB oscillation we have a polar gene expression. We now consider how modehopping will affect this. We find that the protein level being produced from Gene 1, is highest in the 2/1 state (Fig. 18A red) compared to the 3/1 state (Fig. 18A blue) and we see that in the stochastic simulation, modehopping (Fig. 18A yellow), causes these to change in time. Similar results are found for Gene 2, where the highest production is in the 3/1 state. (Fig. 18B) Combining these two arbitrary genes, modehopping now serves as a mechanism of gene regulation, where it can facilitate management of amino acids or other metabolic factors. Since only one of the genes is in a high production state at a time, the cell can be dedicating extra resources to synthesis of a defined subset of proteins at a time. As shown Fig. 18C, the oscillations of NF-κB causes one family of genes to be upregulated, on times where other families of genes are down regulated. In this way modehopping can be an efficient way to change the production of different genes according to their affinity and cooperativity.

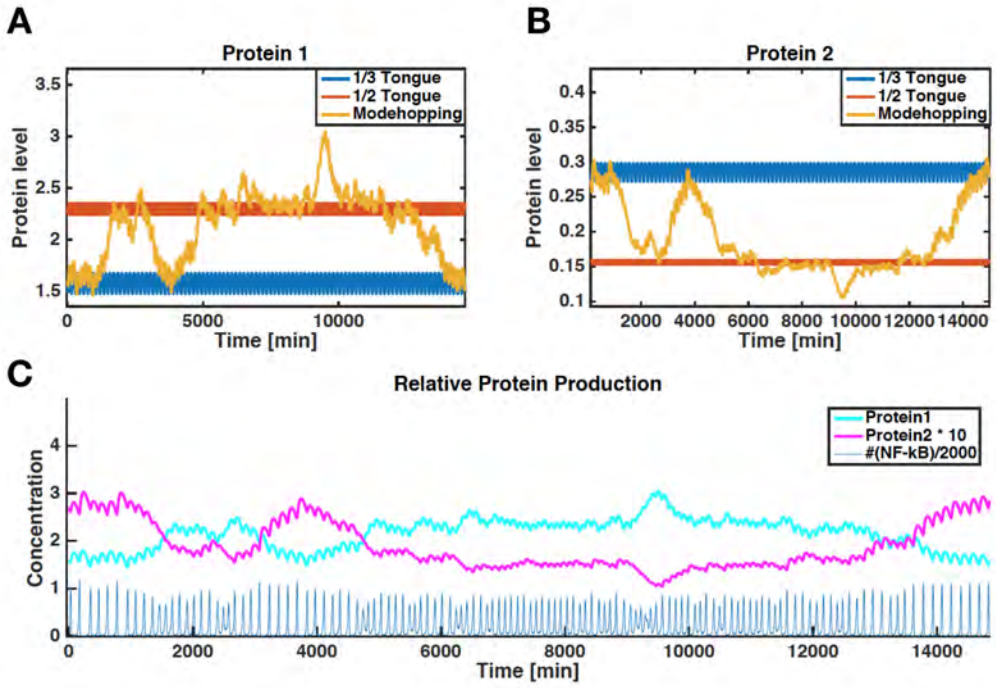

Figure 18: *A) The protein level of Gene 1, shown for 1/2 state, 1/3 state and the stochastic simulation. B) The protein level of Gene 1, shown for 1/2 state, 1/3 state and the stochastic simulation. C) Simulation of the levels of both proteins for a timeseries. In the bottom the corresponding NF-κB oscillations are shown.*

2.6 Chaotic Dynamics in NFκB Regulates Downstream Genes

Having thoroughly investigated the dynamics in the overlapping Arnold tongue regime, we increased the external TNF amplitude even further to move into the chaotic regime. We hypothesized that chaos could have some interesting effects for a transcription factor as TNF, and sought to investigate this phenomenum in detail.

2.6.1 Statistical Properties of the Chaotic Dynamics in NF-κB (M)

As a test, to make sure that the dynamics observed in the upper panel of Fig. 12 was really chaotic, we started three simulations, that in initial conditions, differed in only one molecule. We observed all three trajectories oscillate, but diverged after only a few oscillations (Fig. 19A). This is typical for chaotic systems and defined by the positive Lyapunov constant. This constant is usually calculated as the average over a large sample of diverging trajectories, but for this work we do not know the exact value of the lyapunov exponent and are satisfied with the observation of diverging trajectories. In the study of this chaotic attractor, we were particularly interested in the statistical properties, when intrinsic noise was present. We therefore calculated the distribution of periods deep inside the chaotic regime, where the periods were determined from the flow through a Poincare section. Here we surprisingly found a structure in the distributions, with peaks around several of the integer values of the external period (Fig. 19A). Thus inside the chaotic regime of this attractor, there were structures in the dynamics, that was reminiscent of modehopping, but for many states instead of two states. However where modehopping would usually spend several

oscillations in each state before transitions, we found that inside the chaotic regime, transitions are recurring very frequently, and once inside the chaotic region, the frequency of transition grows (Fig. 19C). Interestingly, the deeper we move into the chaotic regime, the more independent the results are from the noise level, and thus chaotic dynamics can look like a high frequency version of modehopping that is independent of noise. We note that the underlying mechanisms in modehopping and chaotic frequency transitioning are of completely different character though.

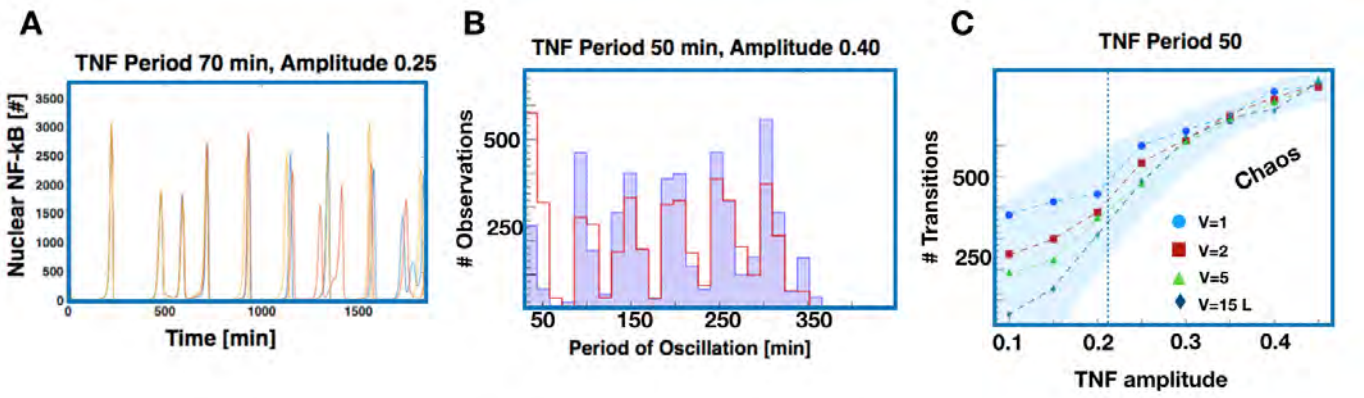

Figure 19: *A) Trajectories starting from initial conditions that differ in only one molecules diverge quickly in time. The different colours show trajectories for initial conditions differing only in one molecule; they remain close for a while but eventually diverge exponentially. B) G) Distribution of time periods for a simulation of 1000 oscillations. The red indicates the distribution of periods for the deterministic simulation, and the blue indicates the distribution for stochastic simulation. Same parameters were used in the simulations. C) The number of transitions (over an interval of thousand oscillations) between entrained states for different noise levels, as a function of the external amplitude. Blue:* $V = 1 * 10^{-15}L$*, Red:* $V = 2 * 10^{-15}L$*, Green:* $V = 5 * 10^{-15}L$*, Cyan:* $V = 15 * 10^{-15}L$*. Transitions are defined whenever a trajectory period are closer to another integer value*

2.6.2 Chaotic Dynamics Enhances Low Affinity Genes

Next we wanted to test the protein production from genes with different affinities and cooperativities. Running a long simulaiton, we then measured the average protein concentration associated with each gene over timescales much longer than the half-lives of the mRNA and proteins. This average is the simplest measure of the effect of NF-κB oscillations on gene expression, and could quite plausibly be important for living cells. We find that as TNF amplitude increases, we obtain very different behaviour for HAGs, LAGs and genes with intermediate affinity (MAGs) (See Fig. 19A-C). As described above and in Fig. 12, as TNF amplitude is increased, while keeping the frequency constant, the NF-κB dynamics is first a single-mode oscillation (point 1 in Fig. 12), then exhibits mode-hopping (point 2 in Fig. 12) and finally chaos (point 3 in Fig. 12) for high amplitude TNF. The ranges of TNF amplitude which exhibit these three qualitatively different dynamics are indicated in Fig. 19A-C.

We find that the chaotic regime shows the differential behaviour of the different genes most clearly. The HAG has a linearly decreasing average protein level as TNF amplitude is increased, while the

LAG shows exactly the opposite. The MAG exhibits much less variation with TNF amplitude and we believe that this can be regarded as a constant production over changing NF-κB dynamics. We stress that it is interesting that genes under control of NF-κB can be designed to have increasing, decreasing, as well as relatively flat response to variation of a single parameter. Overall, we see that both HAGs and LAGs could exhibit fold-changes on the order of two-fold, which we believe should be observable in experiments, while MAGs could lie within experimental error and thus appear effectively unresponsive to TNF amplitude.

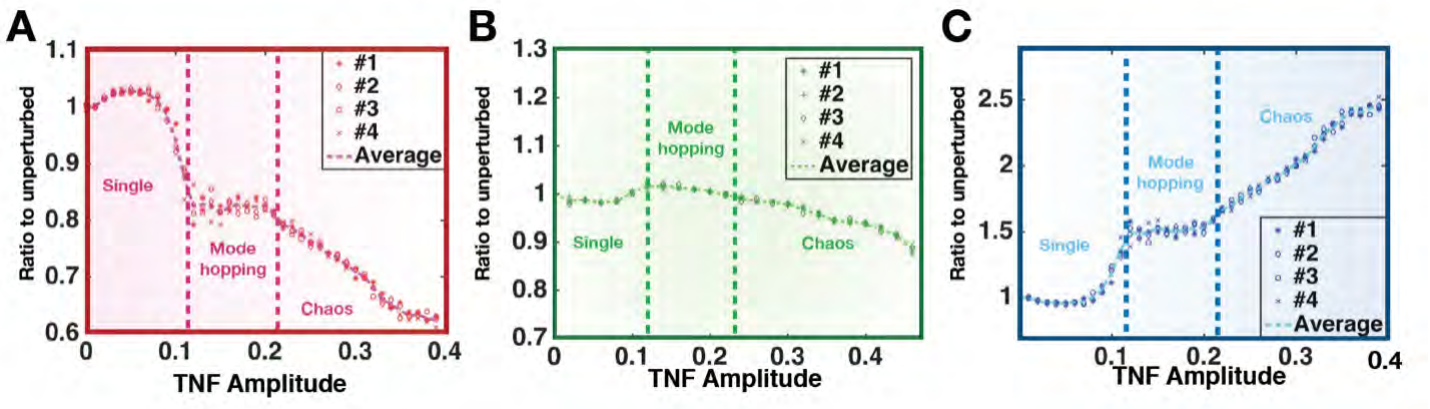

Figure 20: *A) The average protein level from an HAG ($K = 4.5, h = 4$), for different values of the TNF amplitude. We performed 4 separate simulations of duration $5 * 10^5$ min. and show their individual means and the mean of these four combined. We used $V = 2 * 10^{-14} L$ and $T = 50$ min. Results for other periods are found in SI. B) Same as A) but for MAG ($K = 2, h = 3$). C) Same as A) but for LAG ($K = 1, h = 2$).*

2.6.3 Robustness to Variations in Parameters and Noise

Finding that genes could be upregulated by chaotic dynamics was surprising and interesting, but we needed to test the robustness of this result - both in terms of noise levels as well as parameters for the external oscillator. Since biological systems are often characterized by large fluctuations and much noise, we therefore started by varying the level of intrinsic noise in the NF-κB system. This is done in the Gillespie simulation, by varying the effective volume of the system. We find that the average protein levels are quite robust to such increases of intrinsic noise (Fig. 21A-B). The mode-hopping region is the most affected by the changes in noise level, since these affect the rate at which the system jumps from one entrained state to another. The chaotic regime, in contrast, already exhibits many hallmarks of randomness even in the absence of noise, so adding noise does not affect the behaviour much.

Next, we also wanted to include extrinsic noise into the variation of TNF, since in experimental procedures, as well as in vivo, there will always be considerable stochasticity in the TNF signal. Could these fluctuations mask the differential control of genes, especially in the chaotic regime? We added Langevin noise to the periodic TNF waveform at a sufficiently high level to smear out the predominant frequency in a Fourier spectrum of the noisy waveform. Furthermore we also

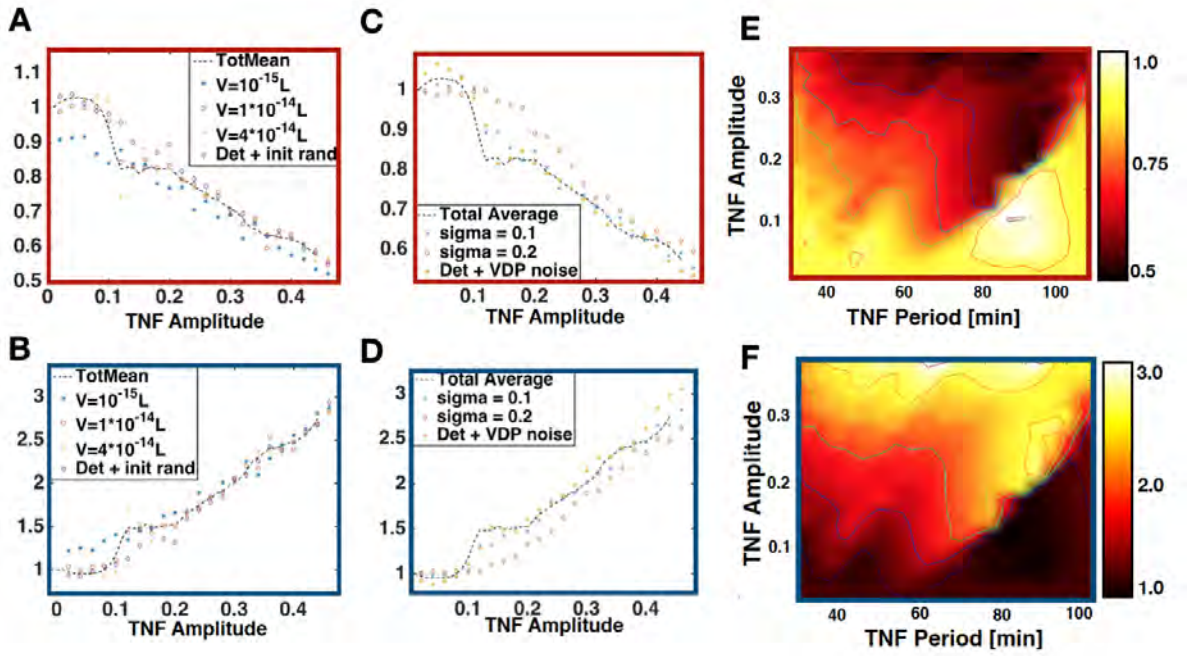

Figure 21: *A) The average production from the HAG for different intrinsic noise levels. We performed simulations of duration* $1*10^5$ *min each datapoint and used the Total mean as calculated in Fig. 20. Here* $T = 50$ *min. B) Same as A) but for the LAG. C) The average production from the HAG for different extrinsic noise levels. We performed simulations of duration* $1 * 10^5$ *min each datapoint and used the Total mean as calculated in Fig. 20. We added Langevin noise to the oscillator and used* $\dot{r} = r(1 - r)$ *and* $\dot{\theta} = \nu$*, and in the last dataseries (yellow *) we used the Van der Pol oscillator with noise as a perturbation to TNF. Here* $T = 50$ *min. D) Same as C) but for the LAG. E) The average production from the HAG, for different values of the TNF amplitude and period. The bright colours indicate the maximal average protein levels, while the dark colours correspond to low average protein levels. F) Same as E) but for the LAG.*

oscillated TNF as a Van der Pol oscillator with Langevin noise. This is described by the dynamical system:

$$\dot{x} = y + \eta(t) \tag{52}$$

$$\dot{y} = -x + \mu(1 - x^2)y + \eta(t) \tag{53}$$

With $\eta(t)$ being uncorrelated white noise. We found that this did not affect the results results significantly and NF-κB still showed the same transition from single-mode oscillation to mode-hopping to chaos as TNF amplitude was increasing (Fig. 21C-D). As with intrinsic noise, the extrinsic noise had most effect in the mode-hopping regime and minimal effect in the chaotic regime.

We now tested our central result for TNF frequencies, with a time period in the range 30 - 120 min. Here we also found the overall same trends, with the characteristic increase/decrease in average protein levels, as a function of TNF amplitude. Thus we conclude from this investigation that even in the presence of intrinsic and extrinsic noise, and in the range of different TNF frequencies chaotic dynamics will up regulate low affinity genes.

2.6.4 Analytical Arguments for Explains the Downstram Effects of Chaos

From the above section we were convinced that the results were quite robust. We therefore just focused on the ratio between the produced level in the chaotic region and the non-perturbed region. We therefore tested the results for completely different TNF waveforms in order to see if this could stop the effects inside the chaotic regime. Here we found that for all the tested wave forms, chaotic up regulates the protein production with at least a factor of 2 for LAGs and note that the highest effect is found when TNF is oscillated as a square pulse (Fig. 22A).
So far in this work, we have mainly focused on two genes defined by a specific value of h and K. Now we wanted to draw the full picture, and calculated the ratio produced in chaos vs produced in unperturbed for different values of h and K. Here we find that for for increasing hill coefficients and decreasing affinity the this ratio is growing. Thus for a large interval of parameters, especially as $K \mapsto \infty$, chaotic dynamics results in increased protein levels and the results are even more significant. For instance the production for a gene with $h = 6$ and $K = 7\mu M$ has a 6 fold increase in chaos versus for flat TNF (Fig. 22B).

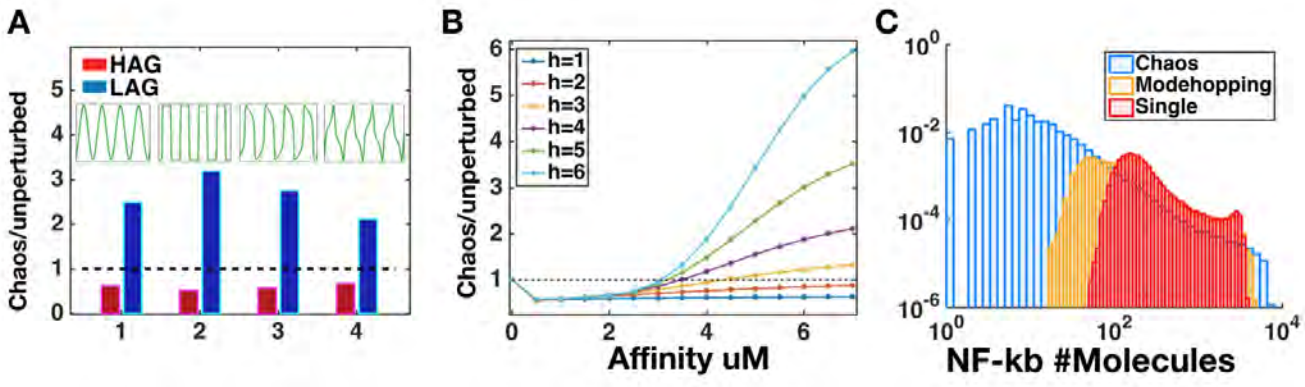

Figure 22: *A) The ratio of Proteins at* $TNF = 0.5 + 0.4sin(2\pi\omega t)$ */* $TNF = 0.5$ *for different wave forms. B) Protein level for* $TNF = 0.5 + 0.4sin(2\pi\omega t)$ *for genes defined by different levels of K and h. C) Distribution af NF-κB at different time levels inside the different regimes.*

We wanted to investigate some of the the underlying mechanisms of how the distribution of NF-κB acutally changes in the different affinity regimes. We see that as we move into the chaotic regime, the distribution of NF-κB gets broader in both ends and therefore NF-κB in the chaotic regime spends more time around zero, but does also have the very large peaks that affects the low affinity genes (Fig. 22C).
A mathematical analysis of this behaviour provides some intuition to understand why HAGs and LAGs respond so differently: The long-term average protein level is essentially proportional to the average of the Hill function over the same long timescale: $\langle P \rangle \sim \left\langle \frac{N^h}{K^h + N^h} \right\rangle$. For HAGs, K is small, and to lowest order in K/N, $\langle P \rangle \sim 1 - K^h \left\langle \frac{1}{N^h} \right\rangle$. In contrast, for LAGs, K is large, and $\langle P \rangle \sim \frac{\langle N^h \rangle}{K^h}$. To carry out the analytical calculations we start out with the equation for the m_{RNA}:

$$\frac{dm}{dt} = f(t) - \delta m \quad \text{where} \quad f(t) = \frac{N(t)^h}{N(t)^h + K^h} \tag{54}$$

Because the NF-κB concentration N(t) is periodic in time with period T, therefore f(t) is also periodic with period T. To begin, let us examine the case where f(t) is composed of only a single

mode with a non-zero average σ:

$$f(t) = \sigma + Ae^{i\omega t} \quad \text{with } \omega = 2\pi/T \tag{55}$$

In that case, the solution of the equation for m_{RNA} is:

$$m(t) \approx \frac{\sigma}{\delta} + \frac{A}{\delta + i\omega} e^{i\omega t} \tag{56}$$

In general of course f(t) is a Fourier sum of many modes, but since the equation for m_{RNA} is linear in m, the resultant solution is:

$$m(t) = \sum_{-\infty}^{\infty} \frac{\sigma}{\delta} + \frac{A_k}{\delta + i\omega_k} e^{i\omega_k t} \tag{57}$$

Here, the k = 0 term takes care of the σ term in the previous single-mode case. The argument can be easily extended to the protein, because the dP/dt equation is also linear in P and so each mode in m(t) will contribute additively to P(t) (just like each mode in f(t) contributes additively to m(t)). In order to understand how average expression of the gene depends on various parameters, we simply need to look at the k = 0 term, because averaged over time:

$$\langle m \rangle = \frac{A_0}{\delta} \tag{58}$$

$$\text{with} \tag{59}$$

$$A_0 = \frac{\gamma}{T} \int_0^T \frac{N(t)^h}{N(t)^h + K^h} dt = \frac{\gamma}{T} \int_0^T \frac{1}{1 + (\frac{K}{N})^h} dt \tag{60}$$

Now we consider the two cases where K is very small and very large respectively. For small K we expand the fraction:

$$A_0 \approx \frac{\gamma}{T} \int_0^T \Big(1 - \Big[\frac{K}{N(t)}\Big]^h + \mathcal{O}\Big) dt \tag{61}$$

$$= \gamma(1 - \langle (K/N)^h \rangle) \tag{62}$$

Therefore this will be dominated by the smallest values of N(t). As we see in Fig. 22C these occurs in the chaotic state, and therefore the average production in total will be smaller for chaotic than for the limit cycle case. If we instead consider the case with very large K, we make the expansion

$$A_0 = \frac{\gamma}{T} \int_0^T \frac{(\frac{N}{K})^h)}{1 + (\frac{N}{K})^h)} dt \tag{63}$$

$$\approx \frac{\gamma}{T} \int_0^T \Big(\Big[\frac{N(t)}{K}\Big]^h + \mathcal{O}\Big) dt \tag{64}$$

$$= \gamma \langle (N/K)^h \rangle \tag{65}$$

This will clearly be dominated by the largest values of N(t) and as can be seen in Supplementary Figure 2K these also occurs for the chaotic state. In this case the chaotic dynamics thus increases the average production of genes with large K. These arguments forms an analytical argument behind the results we find in Fig. 20 derived from the extreme cases for the affinities of genes.

2.7 Chaos Increases Efficiency in Protein Complex Formation

In eukaryotic cells, many functions are carried out by complexes of proteins that are constructed from multiple subunits, for instance haemoglobin, that consists of 4 subunits from 2 genes that

are located on different chromosomes. A study of the NF-κB interactome found that amongst 384 genes that are regulated by NF-κB there were 572 protein-protein interactions [49]. Therefore we wanted to test how the variety of amplitudes found in chaotic dynamics, affected the formation of protein complexes whose subunits all was regulated by NF-κB.

2.7.1 Small Homogenous Complexes Show Similar Trend as Single Proteins

The full importance of protein complexes formed by smaller subunits is still far from understood, and in mathematical modelling one usually consider the production of the individual subunits. The introduction of NF-κB affected complexes have likewise not been deeply investigated, but we expect that they will have a functional role. For instance, there seems to be evidence that NF-κB controls autophagy via multiple pathways, including the up-regulation of both Beclin 1 and A20, which interact with each other inhibiting Beclin 1 ubiquitination, and thereby repressing autophagy [50]. We therefore tested how the concentration of protein complexes, whose subunits were encoded by NF-κB controlled genes, was altered as the NF-κB dynamics became chaotic.
We first considered the simplest complex that consists of two subunits (Fig. 23A). In this case, the model has the following additional equations, where P_1 and P_2 represent the concentrations of the two proteins and $C_{2,1}$ the concentration of the complex:

$$\dot{P}_1 = \Gamma_1 m_1 - \lambda_C P_1 P_2 - \Delta_1 P_1, \tag{66}$$

$$\dot{P}_2 = \Gamma_2 m_2 - \lambda_C P_1 P_2 - \Delta_2 P_2, \tag{67}$$

$$\dot{C}_{2,1} = \lambda_C P_1 P_2 - \Delta C_{2,1}. \tag{68}$$

Here $C_{2,1}$ refers to a complex consisting of two subunits, with one HAG. At this points we will test both homogeneous and heterogeneous complexes, and we consider that subunits can be either HAG or LAG.Furthermore we will, in order to keep things as simple and transparent as possible, keep the values of the parameters λ and Δ fixed even though these could easily differ between complexes. An exploitation of the effects of the entire parameter space will be interesting to pursue in future work, but is beyond our scope. Even though chaotic dynamics creates large fluctuations in the production, then if we consider a complex consisting of two subunits are both HAG proteins, the complex has the highest average level in the oscillatory regime since both subunits will be in their highest production regime (Fig. 23B). The same argument can be used for complexes consisting of two LAG proteins, though they have the highest production level in the chaotic regime (Fig. 23C).

2.7.2 Chaos Enhances Small Heterogeneous Complexes

Now if we consider the production of a two subunit complex that is heterogeneous and therefore consists of one HAG and one LAG subunit. Here both proteins fluctuate up and down (Fig. 24A), and therefore the result is not as obvious as above. Simulating the above equations for a heterogenous complex, we find a significantly higher level of the complex in the chaotic regime Fig. 24B. We now move on to test larger complexes of different combinations of subunits. We describe the concentration of the protein complex C_{n,n_H} consisting of n subunits, of which n_H are from an

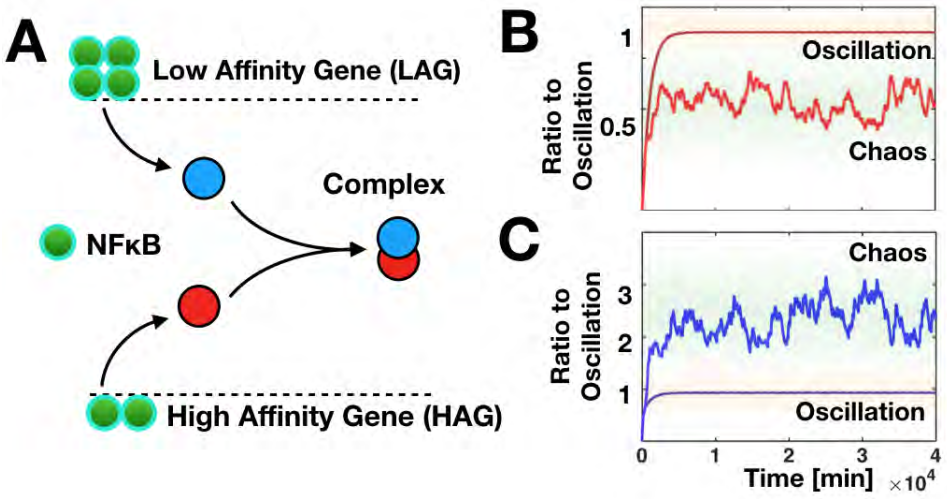

Figure 23: *A) Schematic picture of how LAG and HAG encoded proteins may form protein complexes. B) Protein concentration for HAG ($K = 1, h = 2$) with oscillatory and chaotic dynamics respectively. $T_{TNF} = 50$ min. C) Protein concentration for LAG with ($K = 4.5, h = 4$) oscillatory and chaotic dynamics respectively. $T_{TNF} = 50$ min.*

HAG and the rest from an LAG, is modelled by:

$$\dot{C}_{n,n_H} = \lambda \prod_{i=1}^{n} P_i - \Delta_n C_{n,n_H}. \tag{69}$$

For $n = 3$ and $n_H = 2$, we found that the production was also highest in the chaotic regime and, before moving further, we tested whether the outcome was different if all complexes combined randomly (yellow curve in Fig. 24C), or if there was a hierarchical structure in the assembly (blue and red curves in Fig. 24C). We found no difference in the outcome, and we could therefore move on and focus on the non-hierarchical assembly of complexes, calculated as shown above.

2.7.3 Chaos Increases Efficiency in Protein Complex Formation

Now we were ready to test all compexes for $n \in [2-10]$ and in each case we tried with all different different combinations of HAG and LAG subunits. We calculate the ratio between the production in the chaotic state and in the oscillating state. Thus if this has a value of one, means that there is no difference between the two states. Unexpectedly, we find that all heterogeneous complexes exhibit a higher average level in the chaotic regime (Fig. 25A). This means that only homogenous HAG complexes would be present at a high level in the single-mode oscillatory regime. One might ask, whether this is simply the result of higher mean levels of NF-κB. Therefore, we normalized the concentration of the complexes by the mean NF-κB concentration - when this ratio is large we will say the complexes are produced more efficiently. As seen in Fig. 25B, all complexes are produced more efficiently in the chaotic regime – even the homogenous HAG complexes. Therefore chaos seem to be a generally cheap way to produce protein complexes, in terms of NF-κB molecules. If the cell wish to build a specific type of complex, and do not care about the individual subunits, then from an economical argument, it is necessary to minimize the number of unused subunits. In

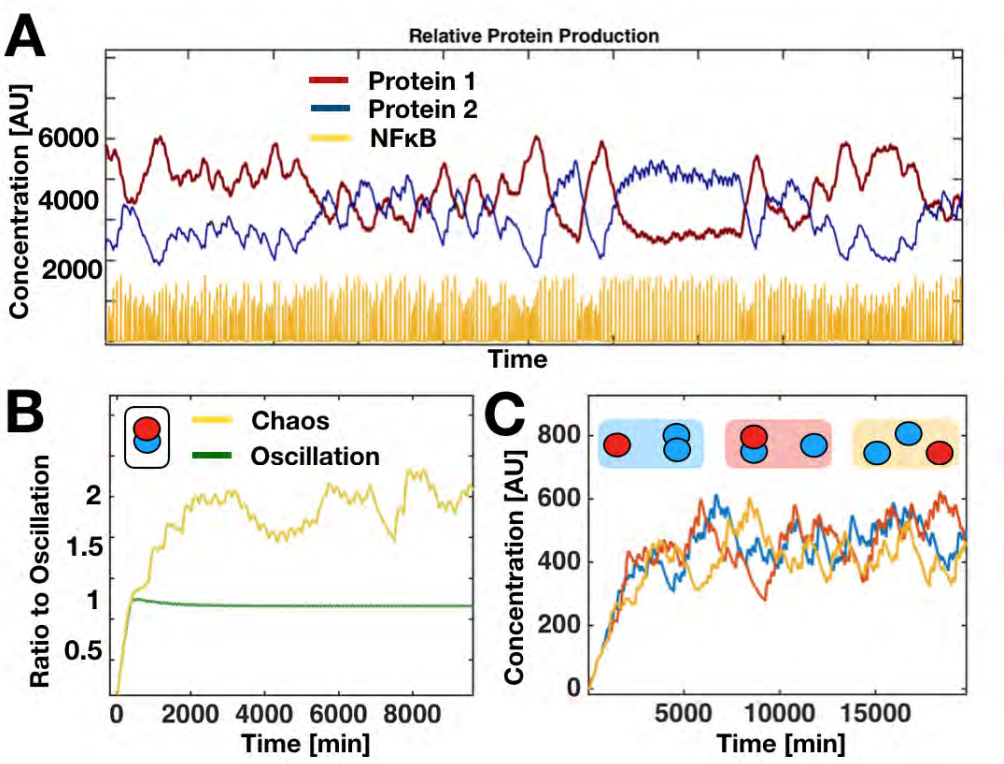

Figure 24: *A) Time series of NF-κB (yellow) and the corresponding protein level. Red: Level of HAG protein. Blue: Level of LAG protein (multiplied by 20).* $T_{TNF} = 50$ *min. B) Concentration of a heterogenous two-protein complex (shown upper left) with oscillatory and chaotic dynamics respectively. C) Concentration of a heterogenous three-protein complex in chaotic dynamics depending on the hierarchical assembly (shown above).*

Fig. 25C we show the ratio between the average concentration of complexes to the concentration of unused subunits, calculated as $\frac{\langle C_{N,n_H} \rangle}{\sum_{i=1}^{N} \langle P_i \rangle}$. This ratio too is largest in the chaotic regime for all complexes, except those made only from HAG proteins. Thus, a chaotically varying transcription factor not only up regulates low affinity genes, but also results in higher and more economical production of protein complexes composed of subunits from different genes.

2.8 Chaos Generates Advantageous Population Heterogeneity

We now consider how the dynamics of NF-κB can affect a population of cells. In the following, we consider only the deterministic NF-κB system, started from a broad distribution of initial points, so the cells are not initially synchronised. We will then study a population of N independent cells that are affected by the same oscillating TNF stimulus. Within each cell, we will track one LAG and one HAG. Here we have chosen the parameters so that the two corresponding proteins have the same average protein level.

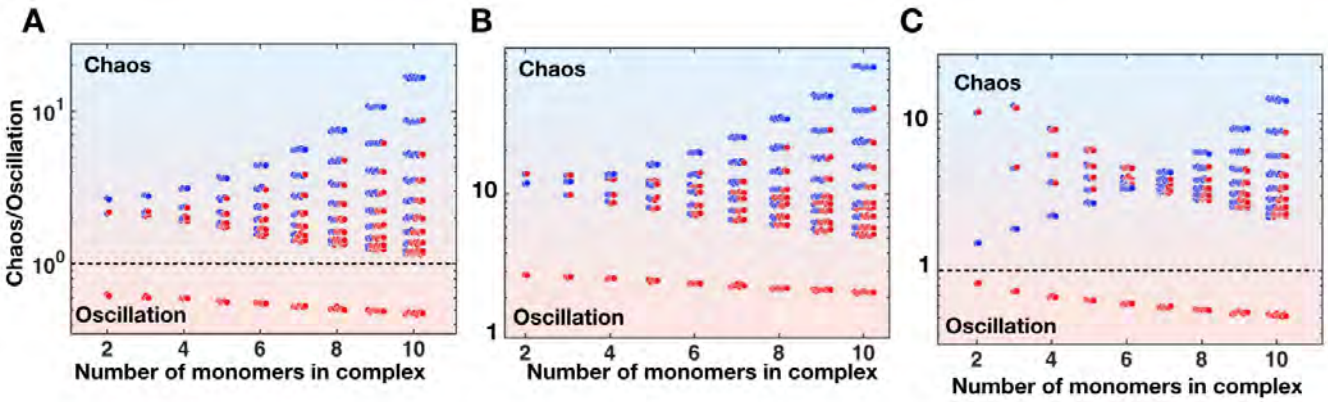

Figure 25: *A) Relative concentration for complexes of different compositions. The y-axis show the concentration in chaos divided by the concentration in the oscillatory regime, and the black line show where these are equal. B) Relative concentration per NF-κB for complexes of different compositions measured by the fraction* $\frac{\langle C_{N,n_H} \rangle}{\langle NF-\kappa B \rangle}$*. Same axis as in A). C) Relative concentration per unused subunits for complexes of different compositions measured by the fraction* $\frac{\langle C_{N,n_H} \rangle}{\sum_{i=1}^{N} \langle P_i \rangle}$*. Same axis as in A).*

2.8.1 Dynamically Heterogeneous Populations Arise From Chaos

We have described how chaotic dynamics exhibit never repeating trajectories since trajectories, from just slightly perturbed initial conditions, will diverge in time. Therefore it is evident that one might find a population, where the individual cells states follow chaotic dynamics, to be heterogeneous. This, combined with the mechanisms of entrainment between the external and internal oscillator, gives the oppertunity for a population to switch between homogeneous and heterogeneous states by changing the external amplitude. We simulated a population of cells and observed that when NF-κB is in a single-mode oscillatory state, the average level of both Protein 1 and Protein 2 is homogenous across the population. We also found that if NF-κB is in the mode-hopping regime, then the distribution of protein levels across the populaiton is bimodal. Finally we found that in the chaotic regime, the distribution is heterogenous for both proteins (Fig. 26A-D). Following the structure of Fig. 26, we indeed find that population can generate different states by tuning the external amplitude and we note that this process is noise independent. For the heterogeneous state inside the chaotic region, we also note that not only is the population heterogeneous, but it is also dynamic in the sense that if one cell is in a high production state of Protein 1 at time t_1 it might just as well be in a high production state for Protein 2 at some later time t_2. We imagined that such heterogeneity in a cell population, could provide a selective advantage when the population is exposed to some potentially lethal stresses and we therefore went on to study this.

2.8.2 Chaos Increases the Number of Surviving Cells in Toxic Environment

We now imagine that each cell in the population can be exposed to two toxic drugs at concentrations D_1 and D_2. The effects of each of these drugs can be opposed by the presence of proteins P_1 or P_2. Thus we assume that if the toxic is present in the population, then at each time step, each cell

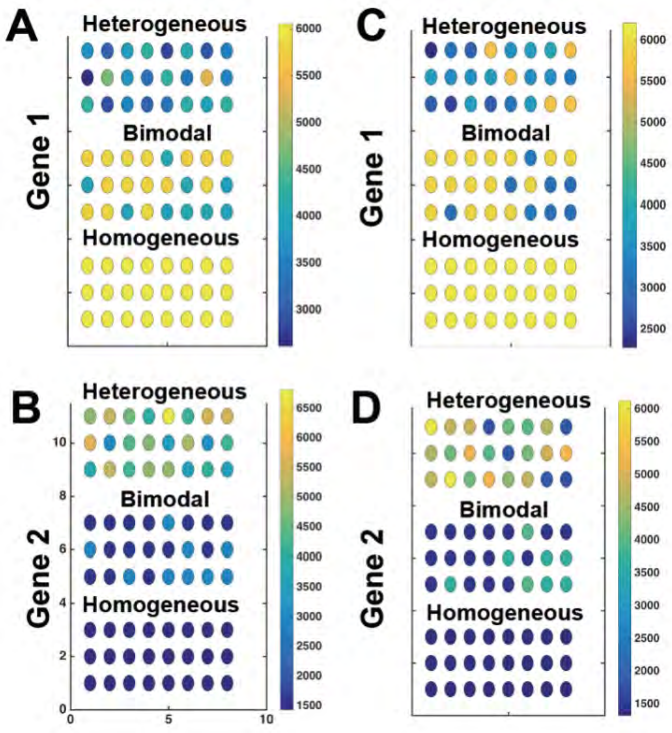

Figure 26: *A) Protein concentration from an HAG with $K = 1, h = 2$ and external TNF period 50 min. Bottom: The concentration corresponding to a single-mode oscillation; TNF amplitude: 0.04. Middle: The concentration corresponding to mode-hopping; TNF amplitude: 0.12. Top: The concentration corresponding to chaos; TNF amplitude: 0.36. B) Protein concentration from an LAG with $K = 4.5, h = 4$. TNF period 50 min. TNF amplitudes are identical to those used in A. C) Protein concentration from the HAG. TNF period 95 min. Bottom: The concentration corresponding to a single-mode oscillation; TNF amplitude: 0.1. Middle: The concentration corresponding to mode-hopping; TNF amplitude: 0.2. Top: The concentration corresponding to chaos; TNF amplitude: 0.4. D) Protein concentration from the LAG. TNF period 95 min. TNF amplitudes are identical to those used in C.*

is killed with probability

$$\mathcal{P}_{Die} = \mathcal{P}_0\Big(\frac{D_1^h}{D_1^h + P_1^h} + \frac{D_2^h}{D_2^h + P_2^h}\Big). \tag{70}$$

Thereby we imagine that P_1 and P_2 are stress-responders that can help the cell survive stressed conditions. We define a constant $\mathcal{P}_0$ to represent the probability that the drugs kill in the absence of the protective proteins. Following the model in the sections above, we consider the case where P_1 is encoded by a HAG and P_2 by a LAG, both regulated by NF-κB.

First we consider the situation where only one of these drugs is present. When only Drug 1 is added in a high amount, cells where NF-κB is in a single-mode oscillating state will have a higher survival rate than cells where NF-κB is mode-hopping or chaotic. This is exactly what one would expect from Fig. 20, since HAG proteins are on average at higher levels in the single-mode oscillatory state. When only Drug 2 is added in a high amount, cells in chaotic states will have a slightly higher survival rate, but due to large fluctuations, these cells will also eventually die due to temporary low

levels of Protein 2. Now we consider what will happen to the system if both drugs are added in a comparable amounts. We therefore tested four different patterns of adding the drugs (Fig. 20C-F), so that they have dynamical fluctuations but have the same mean (cyan and black traces in Fig. 20C-F). Here we find that the cells in the chaotic state will have significantly higher survival rate compared to the others for all the different dynamics applied. From this we conclude that in the presence of multiple toxic drugs, a population of cells is better off having a large heterogeneity in gene expression and up regulating the low affinity genes and thus up regulating the product of genes. This is obtained in the chaotic regime for NF-κB dynamics and this enhances the survival rate. We found these results rather surprising and went on to investigate the mechanisms behind this result.

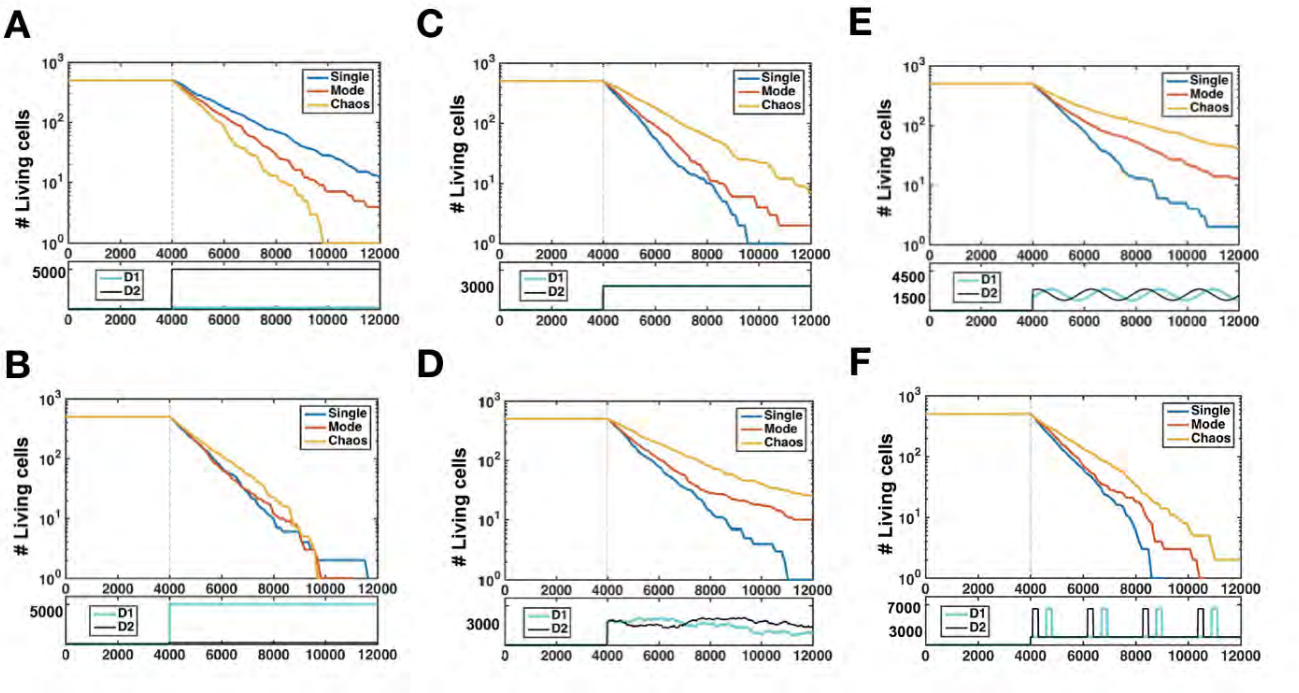

Figure 27: *All figures show the number of surviving cells vs time (Drug is added at T=4000 min). A) D1 = 6000, D2 = 0. B) D1 = 0, D2 = 6000. C) D1 = D2 = 3000. D)* $\dot{D}_{1+2} = \mathcal{N}(0, 100.0)$ *and* $D_{1+2}(0) = 3000$. *The panel below shows a specific trajectory on this pattern. In general* D_1 *is above* D_2 *50% of the times and vice versa. E)* $D_{1+2}(t) = 3000 + 1500 \cdot sin(\frac{t}{5000} + \Omega)$ *F)* $D_{1+2}(t) = 7000$ *if* $sin(\frac{t}{5000} + \Omega) > 0.95$ *and otherwise* $D_{1+2}(t) = 3000$

2.8.3 Analytical Arguments Explains Increased Survival Rate

In order to explore the results shown in Fig. 20, we analyzed the distribution of proteins for the single limit cycle dynamics and for chaotic dynamics. We find that the distribution of proteins inside the chaotic regime is much broader than for the oscillatory dynamics. As described in the above section, we fixed the production ratios so the average sum of the two proteins are be equal, but we find that in the chaotic region the mixture is broader and therefore the product of the two proteins is significantly higher in this region (Fig. 28A-B). This is one of the explanations of why chaos increases the survival rate when several external stresses are present, which can be seen if

we consider the removal rates once again.

$$r = \mathcal{P}_0\Big(\frac{D_1^h}{D_1^h + P_1^h} + \frac{D_2^h}{D_2^h + P_2^h}\Big) \tag{71}$$

As we defined in the text we normalized the proteins, and by adjusting their production profiles we fixed the number of total proteins. This can be seen in Fig. 28C, where we see that the sum of proteins has the same mean, even though the spread in the chaotic distribution is larger. Expanding the death rate (and just setting h=1), we find that:

$$r = \mathcal{P}_0\Big(\frac{2D_1D_2 + P_1D_2 + P_2D_1}{D_1D_2 + P_1D_2 + P_2D_1 + P_1P_2}\Big) \tag{72}$$

Here we note that the terms in the nominator and denominator are almost identical, but there is a product of the proteins only occurring in the denominator. Looking at the distribution of this (Fig. 28D) we see that this is significantly larger for the chaotic dynamics, since there is a mixture of represented proteins. Therefore the denominator will be larger in the chaotic regime and thus the death rate will in general be lower for the cells if they have chaotic NF-kB dynamics. Therefore the intuitive explanation comes from the fact that since there is a spread of proteins then there are some outliers that will have a small rate of dying. And since these change dynamically in time, a larger fraction of the cells will have decreased death rate compared to the case for a stable limit cycle. We also believe that part of the explanation from the increased survival rate comes from fact that there, in the chaotic population, always will be some cells that are in the low removal rate range. And since these vary in time, the cells could have very robust subpopulations if there suddenly comes a burst in one of the drugs. Therefore we wanted to investigate if the survival rate for a population could depend on the diversity in the population.

2.8.4 Diversity Increase the Average Lifetime of a General Population

Inspired by these results, we wanted to study whether there were some advantage by having a heterogeneous population, in a more general setting. We therefore consider a situation where the a single toxic is added in a high dose so cells die with a rate r. This dose is delivered in a time interval, τ We define that at time $t = 0$ we have N_0 living cells. Now the number of surviving cells after a dose must be:

$$N = N_0 \int_{-\infty}^{\infty} e^{-r\tau}\mathcal{P}(r)dr \tag{73}$$

Here $\mathcal{P}(r)$ denotes the probability distribution to have a specific r. In the case of all cells being in a single state we have:

$$N = N_0 \int_{-\infty}^{\infty} e^{-r\tau}\delta(r - r_\mu)dr = N_0 e^{-r_\mu\tau} \tag{74}$$

If we now consider the chaotic state, we assume that the distribution could be given by a normal distribution so: $\mathcal{P}(r) = \mathcal{N}(r_\mu, \sigma)$ (Fig. 29A). It should be noted that the rates from this distribution are far from zero so the integral of the negative axis can be assumed to be zero. Thus we calculate:

$$N = \frac{N_0}{\sqrt{2\pi}\sigma}\int_{-\infty}^{\infty} e^{\frac{1}{2}\left(\frac{r-r_\mu}{\sigma}\right)^2} dr \tag{75}$$

$$= \frac{N_0}{\sqrt{2\pi}\sigma} e^{-\frac{1}{2}\left(\frac{r_\mu}{\sigma}\right)^2} \sqrt{2\pi\sigma^2} e^{\left[\left(\frac{r_u}{sigma^2}\right)^2 + \tau^2 - 2\tau\frac{r_u}{\sigma^2}\right]\frac{\sigma^2}{2}} \tag{76}$$

$$= N_0 e^{\frac{1}{2}\tau^2\sigma^2 - r_\mu\tau} \tag{77}$$

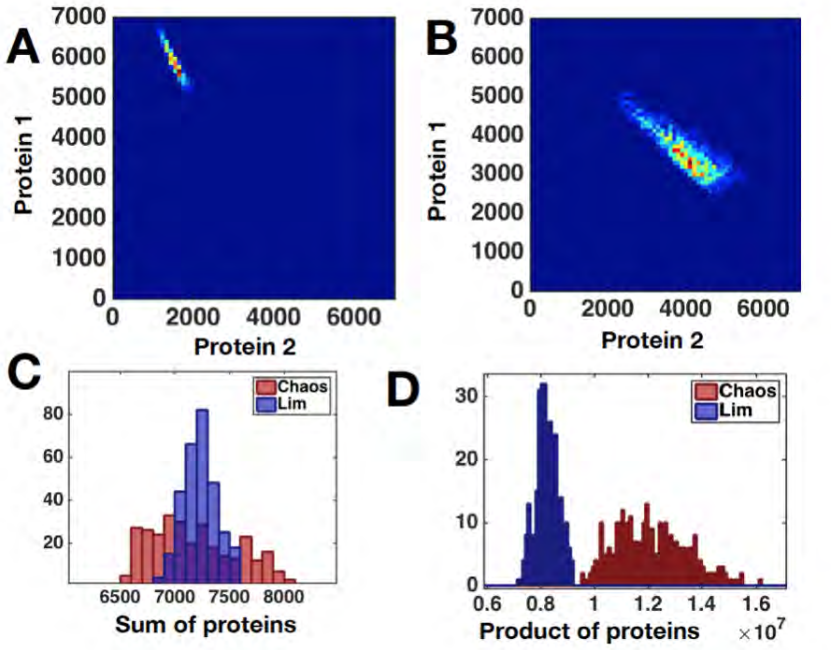

Figure 28: *A) Heat map showing Protein levels during stochastic simulation when dynamics is a limit cycle. B) Heat map showing Protein levels during stochastic simulation when dynamics is chaotic. C) Sum of proteins in stochastic simulations when dynamics is in chaotic and limit cycle regime. D) Product of proteins in stochastic simulations when dynamics is in chaotic and limit cycle regime.*

This means that the benefit from having a spread of your rates can be calculated by:

$$\frac{e^{-r_\mu t_0}}{e^{-r_\mu t_0}} e^{1/2(t_0\sigma)^2} = e^{1/2(t_0\sigma)^2} \tag{78}$$

Let us term the mean value of the gaussian distribution r_{μ_1} and the mean of the delta function r_{μ_2} and assume that $r_{\mu_1} \neq r_{\mu_2}$. The size r_{μ_2} in order for $N_2 > N_1$ to hold should then be:

$$r_{\mu_2} < r_{\mu_1} - \frac{1}{2} t_0 \sigma^2 \tag{79}$$

We simulate this and find as predicted, that the number of surviving cells is higher for the population with large diversity (Fig. 29B). Normally it is argued that populations of bacteria have large diversity so some of them can be immune to different toxicities they might be faced by. While this is of course still true, then the above argument shows that even if no cells in the population are close to being immune, a diverse population will generally have a higher survival rate than a completely homogeneous one.

2.9 Discussion and perspectives

Transcription factors are known to have different dynamics, depending on external conditions and it has previously been argued that oscillations in gene regulatory networks can control transcriptional specificity and efficiency [9, 13, 51]. However the mechanisms behind how this may be exploited to differentially control of downstream genes is not well understood. In this chapter,

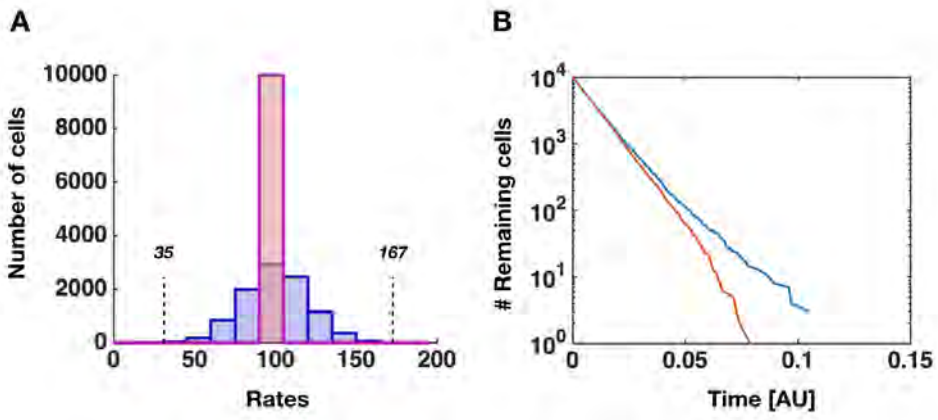

Figure 29: *A) Distribution of removal-rates for both populations. The numbers refers to the min and max level from the gaussian distribution. B) Number of surviving cells as a function of the time at which the dose is given.*

we have shown how an oscillatory network can lead to multi stability of limit cycles and how the presence of multiple entrainment modes may diversify biological functions and to control gene expression output and specificity [52, 53] NF-κB activates hundreds of genes, requiring mechanisms for controlling relative expression level and specificity under fluctuating environmental signals. As we show, noise-induced jumps in NF-κB oscillation frequency can cause temporal switching between genes with diverse promoter characteristics over time.

Our model uses periodic variation of TNF to produce complex dynamics of NF-κB. Uncovering conditions where TNF naturally varies periodically and thereby entrains the NF-κB oscillations would add substantial weight to our results. Oscillatory dynamics is believed to be of importance to several processes in the immune system [54] and there exists evidence that TNF does indeed very in a pulsatile or periodic manner in some situations [55, 56, 57, 58], as well as mathematical models that attempt to explain the underlying mechanisms [55, 59], but it is unclear whether these natural oscillations entrain NF-κB. The positive feedback between NF-κB and TNF that has been hypothesised to produce travelling waves of TNF is perhaps the most promising scenario we are aware of where periodic TNF modulation may occur naturally [59].

In this project we show how bi-stability in frequency space can arise from an externally oscillating ligand that couples to a protein network that is has limit cycle. This means that in the deterministic system we found to two distinct oscillatory states and in the presence of noise, this allowed dynamical switching between the states. We investigated how the statistics for the transitions between limit cycles can be controlled by changing the parameters of the external oscillator. Here we developed a simple 1D system, derived from the behaviour inside a Poincare section, and found that the distribution fo transition times, can be approximated as a sum two exponential functions. From the properties of modehopping, we should consider the benefits of this mechanism in gene regulation. Without going in to great detail about other mechanisms, the following will instead focus on the complex outcome of regulation, by simply perturbing the external amplitude, and thus climbing up the Arnold tongue diagram.

We start by considering the very low coupling. This is the limit where only one limit cycle ex-

ist and thus no matter the noise level, no transitions will occur and the $NF-\kappa B$ will oscillate with the same amplitude and frequency. In this limit one of the families is always in the high production state. If we now increase the amplitude a little more, keeping the period of oscillation constant, we reach the early limit of overlapping tongues, but where the basins of attraction can still be assumed to be approximately linear. In this limit modehopping will occur, but the system will spend relatively long time in each state, and to a good approximation following the statistics previously described. Therefore this work uncovers a new function for noise in gene regulation. If the cell is in the modehopping regime, then if it can control the level of intrinsic noise, the rates of transitions can change rapidly and thus it can fine tune the output. Furthermore, this method of gene regulation could facilitate management of amino acid or other metabolic factors by dedicating resources to synthesis of a defined subset of proteins at one time. Cellular mode hopping therefore expands the toolbox of single cells to control the dynamics, specificity, and efficiency of gene expression and protein production.

If we want to increase the frequency of modehopping we can increase the TNF amplitude to the limit, where the linearity of the basins break down and each limit cycle can be attracted from many positions in phase space. Here the magnitude of the decay constant is also larger, meaning that even in the presence of noise, the trajectories will be attracted to the limit cycles quickly, but they can also leave the limit cycle quickly due to complex geometry of the basins.

If we now increase the amplitude even further we move into the chaotic regime. We showed that from a frequency point of view, chaos shows some of the traits from modehopping, and the deeper into the chaotic regime we get, the more states can be visited. Chaotic dynamics has in general been underestimated as a means for controlling genes, maybe due to its unpredictability. This work shows that deterministic chaos potentially further expands the toolbox available for single cells to control gene expression dynamically and specifically. Since chaotic behaviour within overlapping Arnold tongues is a fundamental feature of driven nonlinear oscillators [33, 36, 60], we are confident that NF-κB driven by sufficiently large TNF amplitudes will exhibit deterministic chaos. However, an experimental realisation of this model, through microfluidics experiments [61, 62], would necessarily be subject to various sources of noise, and it is not obvious that deterministic chaotic can be determined from these traces. Many sophisticated methods exist, that allow chaos to be found without requiring unreasonably long time series; see for example [63, 64]. However as the noise gets large the normal traces from chaos as lyapunov exponents, fractal dimension of attractor etc. gets smeared out, and one need to use statisctical properties. The next step is to test whether HAGs respond differently from LAGs, and this can be investigated using genes that have previously investigated in the regime where NF-κB shows single-mode oscillations [4, 13]. Since the expression level of some of these genes track NF-κB oscillations closely, while others track the mean NF-κB levels, it is likely that these genes already span a range of affinity values [14]. If this is the case, we can start to consider "polar" gene regulation, where some genes are up regulated and others down regulated from the same trace of dynamics. From the test of the robustness of these results, where we investigated many parameter values, we are comfortable in arguing, that these genes may be directly used to study the chaotic regime, without worrying too much about details such as their maximal transcription/translation rates or the stabilities of the mRNA and proteins they encode. Therefore we suggest that chaotic dynamics can produce differential control of high vs. low affinity genes, down regulating the former while simultaneously up regulating the latter

and that this can be used not only to control single non-interacting genes, but also for upregulating specific complexes of proteins and generating useful heterogeneities in cell populations.
To sum up, one can achieve a great complexity in the regulation of genes, by coupling two oscillatory dynamics, and in from there regulate only the external amplitude. Whether this is actually something the cells are using is up for tests in a number of experiments, but this has great potential in future research, not only for the NF-κB system but for transcription factors that has the ability to show oscillatory behaviour in general. It is the hope, that this will inspire theoretical and experimental exploration of the presence and utility of modehopping and chaos in transcription factors of living cells.

3 Mdmx as a Modulator on the p53-Mdm2 Network

In this chapter the results of **paper VI** is presented and discussed, along with some other results that will be part of future projects in this field. This work was mainly carried out during my stay in the Lahav lab at Harvard Medichal School in the final part of 2018. The project was guided by Galit Lahav and was based on results from experiments carried out by Sheng-hong Chen. The ideas for the background theory, was done in a great collaboration with Galit Lahav and Mogens H. Jensen. The data analysis and the mathematical modelling I carried out myself. Parts of the figures were created in coorperation with Alba Jimenez.
In this section, we will present a simple mathematical model of the p53/Mdm2/Mdmx system and use this to investigate which of their known interactions quantitatively affects p53 dynamics. We show that the Mdm2-dependent degradation of p53, facilitated by Mdmx, is the most critical interaction regulating p53 dynamics. Next, we used this model to predict p53 behavior following DNA damage in Mdmx depleted cells. and use the experimental results to constrain the model and identify the mechanisms responsible for the UV dose dependent and independent features of p53 dynamics.

3.1 Introduction to the Network of Tumor Protein p53

The tumor suppressor protein p53, is a transcription factor, that can bind to specific sequences on the DNA [65]. The protein is found in slightly various forms across species, but the human p53 protein has 393 amino acids. It has been divided into four domains according to structure and functionally. Here the first 42 amino acids at the N-terminus constitute a transcriptional activation domain that interacts with the basal transcriptional machinery in positively regulating gene expression [66, 67]. The protein has a central role in the coordination of the cellular responses to a broad range of external stress factors [68] and therefore it has been called a "cellular gatekeeper" [67] and "the guardian of the genome" [69]. Specifically the p53-mediated transcription is of great importance in tumor suppression, the vast majority of tumor derived mutations have taken place in the region encoding p53's DNA binding domain [66]. Therefore, the dynamics of p53 play an important role in cell fate decision and therefore a quantitative understanding of the signaling network underlying p53 dynamics is important to decode cellular decision process. In normal conditions, p53 protein is maintained at low levels by a series of regulators, most famously Mdm2. This protein is produced from p53 transcriptional activity and functions as a p53 ubiquitin ligase to facilitate the degradation of p53 [70, 71, 72]. This forms a typical negative feedback loop that is often found in genetic networks. In response to various cellular stresses including DNA damage and replication stress, p53 can be stabilized which leads to a sudden up regulation of the nuclear concentration. Mechanisms leading to p53 activation can be initiated by DNA damage, where ATR or ATM can promote p53 phosphorylation and thus block the Mdm2-mediated degradation [73, 74]. Here there is an important distinction between the responses of p53 following recruitment of ATM or ATR. The first is typically enhanced in relation to double strand breaks (DSB) following for instance γ-radiation and can lead to oscillations in p53 [5]. The second is enhanced in relation to single strand breaks (SSB) following for instance UV-radiation and can lead to a large transient pulse [75]. Since Mdm2 has such an important regulatory effect on regulation of p53 levels, it is of great interest that another protein Mdmx, a homolog of Mdm2, has also been found to have an

important impact on the p53 regulation [76, 77, 78]. However Mdmx itself cannot cause degradation or nuclear export of p53 [79], and therefore it is an open question what the most important role is of Mdmx [80]. Some studies indicate that Mdmx represses the p53-mediated transcriptional activation [81, 76], where others claim that the major role of Mdmx lies in its ability to enhance degradation of p53 [82, 83, 84].

3.2 Analysis of Experimental p53 Dynamics Reveals Three Key Characteristics

My work on this project started out with the experimentally generated time series of p53 concentrations inside the nucleus of single cells. The first objective was to characterize the specific quantitative features of the p53 dynamics which should later be used for the mathematical model construction. At this point it was known that the depletion of Mdmx leads to a characteristic response, that can qualitatively be separated into two distinct phases of p53 dynamics - a transient pulse and sustained oscillations [85]. Mdmx suppression is initiated right after mitosis, and since this occur at different times (Fig. 30A red region), we needed to create a common time frame for all the cells. Therefore we started out by generating an algorithm to align the traces of single-cell p53 dynamics to the time of cell division, so this could serve as our initial time point (Fig. 30B). Following immediately after Mdmx is suppressed in the cells, p53 undergoes a transient high-amplitude pulse (Fig. 30B, orange region). After this, the system enters the second phase, where p53 shows a series of low amplitude oscillations (Fig. 30B, red region), which seem to be a steady state, since these oscillations continue for longer time than the experiments can last. Our first goal was therefore to quantify the two phases, by using all the traces and calculate some statistical properties.

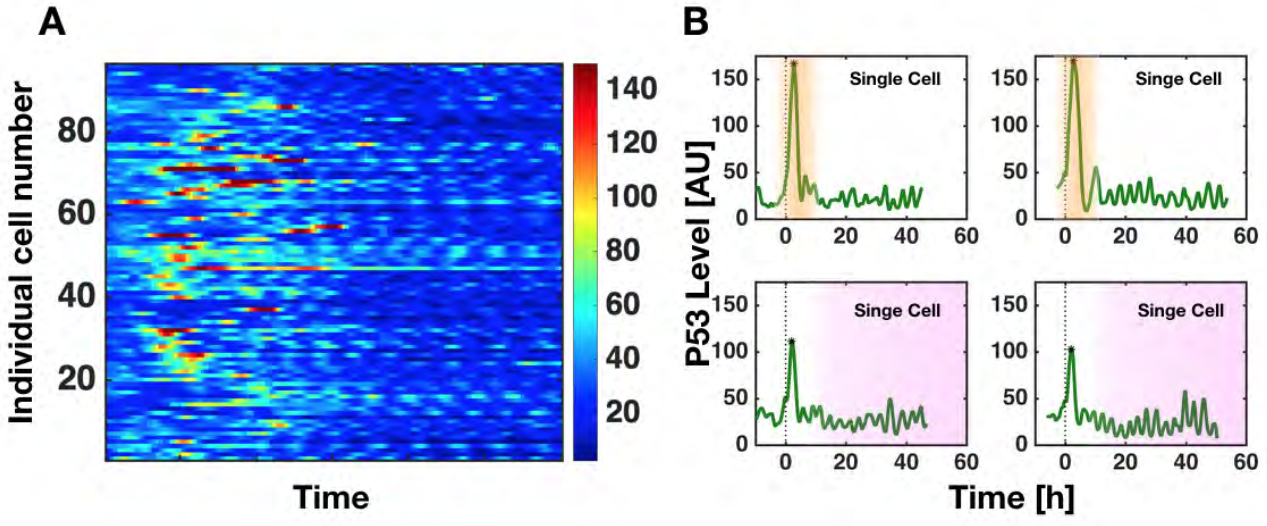

Figure 30: *A) Heatmap showing p53 traces for all cells when not aligned. B) Four representative p53 traces, aligned by time of mitosis*

3.2.1 Transient Pulse Follows Right After Mdmx Depletion

We first characterized the p53 pulse, which represents an important fingerprint of the role of Mdmx on p53, since it captures the initial response of the system before other potential secondary complex responses emerge. We calculated the population average trace (Fig. 31A, green trace), from which one can clearly see the post-mitotic phase-one pulse (Fig. 31A yellow region), while the sustained oscillations are masked by the mean value and stochastic fluctuations. It should be noted, that there is a drop in the average value of p53 with a minimum around 25 hours. After discussing this, we realized that this was most probably due to external effects in setup of the experiment, and we will in the following part neglect this. Using the alignment to characterize the average initial pulse (Fig. 31B), we found this to be symmetric, i.e. showing the slopes during increase and decrease (Fig. 31C), and to have a maximal value of the amplitude around three times larger than the mean level of p53 before Mdmx depletion (Fig. 31D). We wanted to know whether the obtained data for the height of the amplitude had some statistical properties or just was randomly distributed. We found that this distribution were quite smooth, and could be well described by fitting it to a gamma distribution (Fig. 31D). The small peak preceding mitosis is due to an increase in auto-fluorescence seen in all channels.

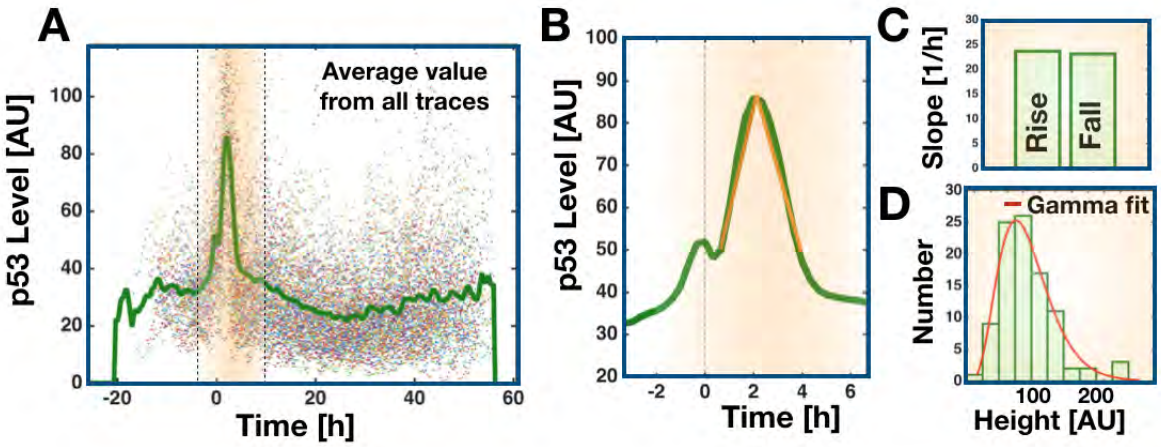

Figure 31: *A) All traces and the calculated mean value (green) at all time points. B) Zoom on the transient pulse. Yellow lines correspond to fitted lines of increase and decrease. C) Barplot showing the increase and decrease. D) Distribution of heights of the peak and a fitted gamma distribution (red)*

3.2.2 Sustained Oscillations Follow Transient Pulse

From the transient pulse, we moved on to characterize the p53 dynamics after the initial response (Fig. 30B yellow region), where the dynamics seem to be oscillatory (Fig. 30B magenta region). First of all we needed to define the properties of the oscillations, and to check whether the observations seemed to follow similar kinds of oscillations. We therefore calculated the Fourier spectrum, using the FFT algorithm in MATLAB, for each cell trace individually. The resulting power spectrum show a surprisingly strong signal for a frequency of approximately 0.3/hour (Fig. 32A). This is an important fingerprint convincing us that the p53 oscillations are well defined and is

a characteristic of the system. While this power spectrum (Fig. 32A, y-axis) in some cases can provide an estimate of the amplitude of the oscillations, we wished to define this better and used an independent algorithm to calculate the distance from each peak to the two neighboring valleys. From this method, we plotted the distribution of amplitudes for all oscillations, and found that this was very smooth. We once again fitted this to a gamma distribution (Fig. 32B) to obtain the best fitted values, which should be used for later comparisons. With the most probable amplitude and frequency defined from the methods described above, we could show that a sinusoidal with these parameters follow the experimentally observed oscillations quite well (Fig. 32C). From this one can observe, that the amplitude showed substantial variations due to noise, while the frequency of the oscillations was surprisingly stable, which is in agreement with previous observations for p53 oscillations following DNA damage [86, 87].

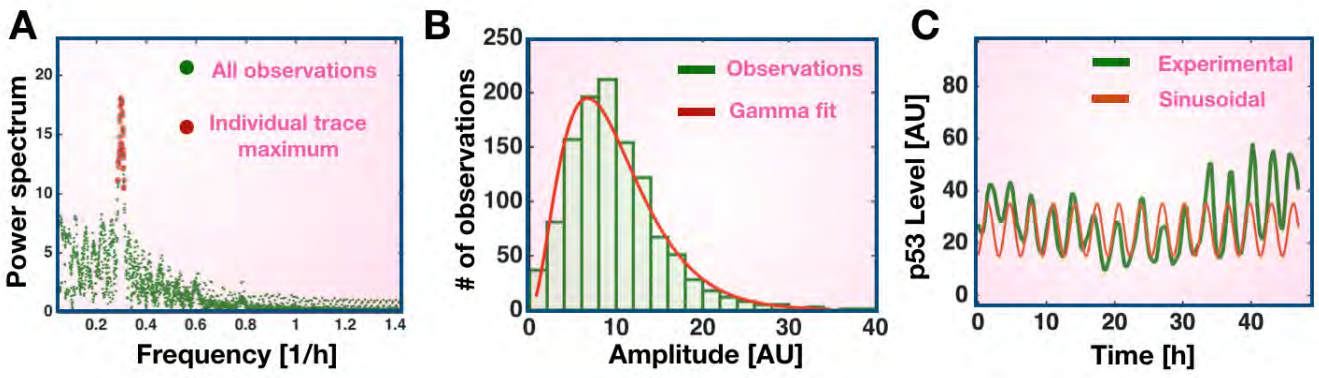

Figure 32: *A) Fourier spectrum of the sustained oscillations calculated using a Matlab FFT algorithm. The red dots mark the highest Fourier signal for each individual cell. The height of the peak correspond to the amplitude of the most dominant frequency of oscillation. B) Histogram showing the distribution of amplitudes of the oscillatory phase. C) Comparison of a single cell oscillatory expression (green) to a modelled sinusoidal oscillation (red) with amplitude and frequency corresponding to the most probable values of the Fourier spectrum in A).*

3.2.3 Examination of the Nature of p53 Oscillations

In the process of understanding the underlying dynamical system as well as possible, an important question was to consider whether the oscillations that we observed, came from a deterministic limit cycle or a deterministic spiral that would look like sustained oscillations due to the noise in the system. The latter we term stochastically induced oscillations, and they are known to produce clear signals in the Fourier power spectrum, which for some systems can be calculated analytically [88]. We wanted to investigate if it was possible to determine whether the observed experimental data represented an underlying limit cycle. To do this, we gathered all the datapoints from the oscillatory phase (i.e. after the transient pulse). We divided each individual trace by its own mean, and placed the individual traces following each other (Fig. 33A). Next we needed to merge all the individual traces together, in a way that could minimize the differences between the end of one trace and the beginning of the next. We decided to combine them by letting each trace end at its last peak and let the next trace begin with its first peak (Fig. 33B). We defined the height of the

two merged peaks to be the mean of these two points. Furthermore the dataseries were influenced by a large background noise as discussed in Fig. 31A. In order to align the oscillations we therefore took this background noise into account, by subtracting a running mean from each datapoint (Fig. 33C red trace). The running mean was calculated at each point by taking the average of an array containing the point itself, the n previous points and the n future points. We tried different values of n, which did not show any conclusive difference, and in the following is shown for $n = 6$. Having aligned all the datapoints, we transformed the data into a two-dimensional phase space, by adding an embedding dimension (Fig. 33D). This is done by dividing the data into two dataseries, where the second dataseries is translated in time. For a vector of datapoints, p, containing N datapoints, this can be written as:

$$p(t) \mapsto [p(1; N - \tau), p(\tau; N)] \tag{80}$$

The value of τ was decided to be the first value for which the correlation coefficient between of the data was below 0.5. It is clear that this is densely packed, and to see the most visited regions of the phase space, we constructed the corresponding heat map (Fig. 33E). If this was a limit cycle we would assume that the most visited regions would be in a circle around the center. If this was a stochastically driven oscillation, we would expect that the most visited regions would be at the center and decay as the distance to the center increased. From (Fig. 33E) it seems that there is a line around the center that represents the most visited regions, suggesting a shape for the limit cycle as drawn in blue in Fig. 33E. However this data is so noisy that it is not sufficient to make a definite conclusion on whether this is a limit cycle. We therefore use the above arguments, to conclude that this system is extremely close to the Hopf bifurcation, and for the rest of this chapter we will assume that the oscillations in p53, induced by Mdmx suppression, is a limit cycle, but very close to the Hopf bifurcation.

3.2.4 The Ratio of Mdm2/p53 Reveals a Slight Shift

The experimental data we obtained from the experiment is measured from the fluorescence and thus the concentrations of p53 are in arbitrary units. In order to create further constraints to the mathematical modelling we wanted to quantitatively determine the effect Mdmx has on p53's transcriptional activity. Therefore we calculated the ratio of Mdm2 to p53, with and without Mdmx present in the system. The measurements were taken at different time points in order to make correlations between datapoints disappear. First we calculated the correlation between the value of p53 and Mdm2 in the all the cells (Fig. 34A) and we find that the values of p53 and Mdm2 have a higher correlation coefficient ρ, in the control compared to the Mdmx suppressed cells. We then plotted the distribution of the ratio Mdm2/p53 in both the control and the suppressed traces, and we found that depletion of Mdmx creates a broader distribution (Fig. 34B), which is what we would assume from Fig. 34A. The broadening of the distribution is explained by the occurrence of oscillatory dynamics in the Mdmx suppressed cells, where the correlation can be shifted at extremum points. Furthermore we observed that Mdmx depletion moves the mean of the distribution to a slightly larger value, which indicates that the Mdm2 production per p53 protein is higher, when Mdmx is depleted. This is in agreement with previous studies suggesting that Mdmx suppresses p53 transcriptional activity [89, 90], even though this effect is quite small. From all these observations and measurements, we conclude this section by identifying three char-

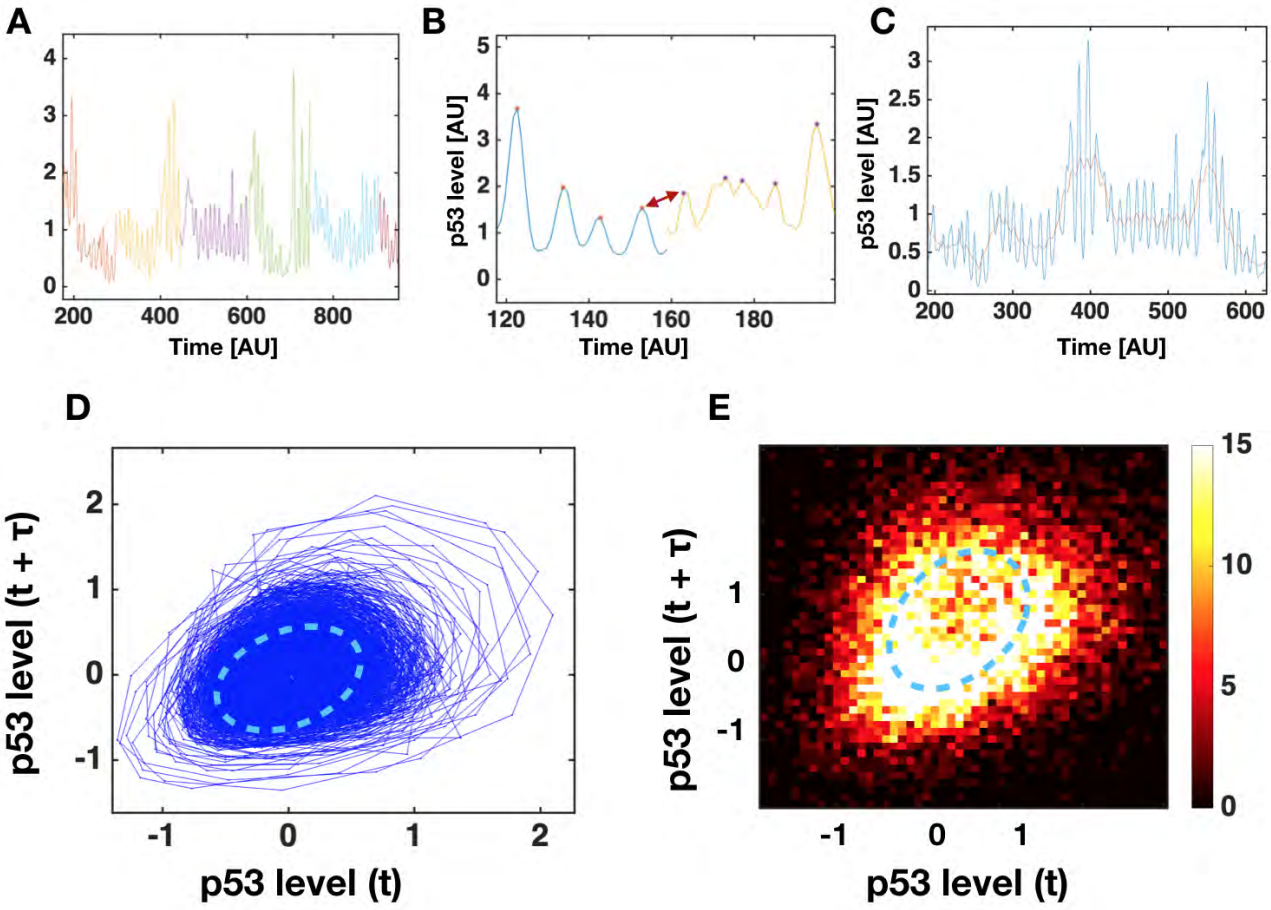

Figure 33: *A) 6 different oscillatory traces represented by separate colors, following each other. B) Example of how two traces are merged together at the end, by combining their last and first peak respectively. C) Representative data series showing the merged dataset (blue) and the running mean (red). D) Phase space of the time embedded data. The blue ellipse shows a suggested position for an underlying limit cycle. E) Heat map generated from the phase space in D). The blue ellipse shows a suggested position for an underlying limit cycle.*

acteristic features of p53 dynamics and activity following Mdmx depletion: (I) an initial large amplitude pulse; (II) sustained oscillations; (III) a perturbation in the Mdm2/p53 distribution (Fig. 34C). With this, we wanted to investigate if these quantitative features could be explained by a mathematical model of p53 and Mdm2 regulation by Mdmx.

3.3 Mathematical Model Captures the Effects of Mdmx on p53 Network

Our aim was to investigate what role of Mdmx could lead to the dynamics observed in the experiments. In order to do this we wanted to create a minimal model that would have a steady state when Mdmx was present and was oscillating when Mdmx was depleted. Since we do not measure the values of Mdmx in time, we decided to treat Mdmx as a perturbation to the parameters of the

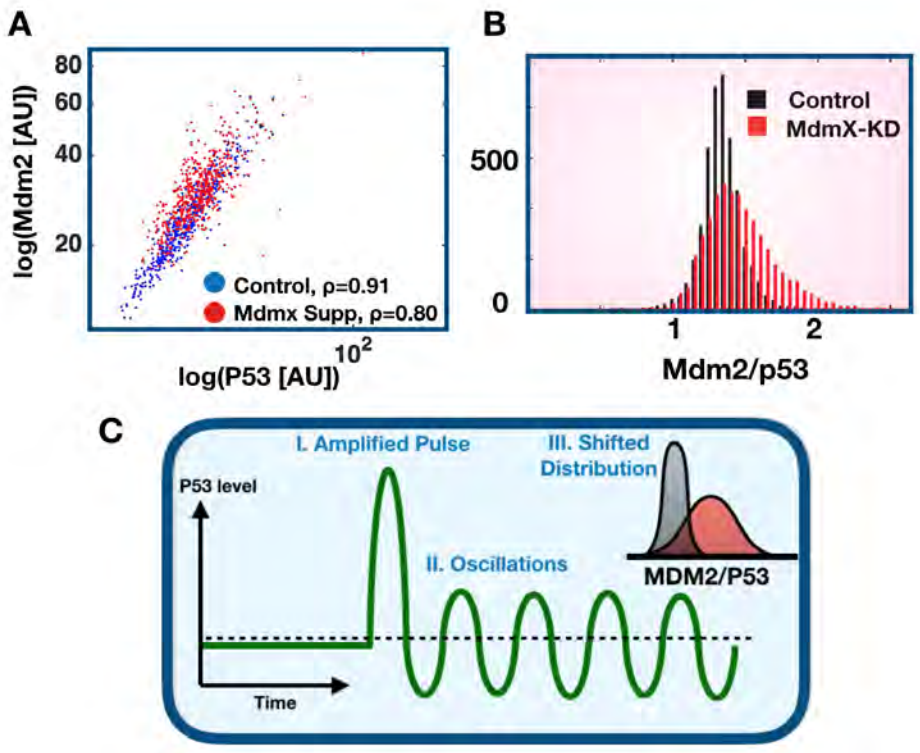

Figure 34: *A) Correlation plot showing p53 in the x-axis and Mdm2 on the y-axis. B) Distribution of the Mdm2/p53 ratio before (black) and after (red) Mdmx suppresion based. C) The Characteristic features of p53 dynamics following Mdmx depletion: I) initial pulse, II) sustained oscillations and III) a perturbation in the Mdm2/p53 ratio.*

system. Thus we assume that Mdmx is constant in time, but changes upon suppression:

$$Mdmx = \begin{cases} 1 \text{ in contol} \\ 0 \text{ in suppressed cells} \end{cases}$$

It should be noted that even though the Mdmx level is non-zero in the suppressed cells, since this just represents a perturbations in the parameters, the following results are valid for any perturbation in Mdmx. Therefore we created a model with so few parameters, that we could easily study the effects from a single parameter, following Mdmx depletion.

3.3.1 Construction of Minimal Model and Introduction of Impact Factors

We consider the well-known p53-Mdm2 feedback-loop using the two ordinary differential equations:

$$\frac{d}{dt}(p53) = \alpha - \beta \cdot Mdm2 \frac{p53}{\gamma + p53}$$
$$\frac{d}{dt}(Mdm2) = \psi \cdot p53(\tau_{Del}) - \delta \cdot Mdm2$$

In this model, p53 is produced at a constant rate α and degraded upon binding to Mdm2 through a saturated degradation process with parameters β and γ. The production of Mdm2 is proportionally to the p53 level with parameter ψ and it is degraded through a standard decay process with decay

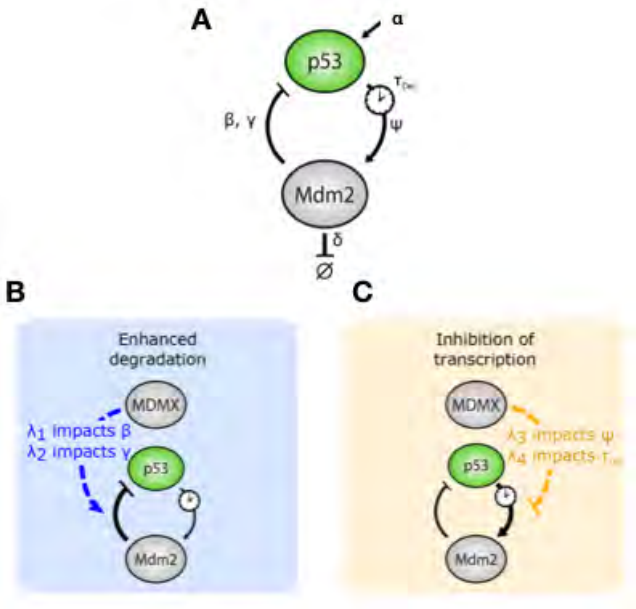

Figure 35: *A) Schematic figure showing the p53-Mdm2 network and the associated parameters B) Suggested mechanism of enhanced degradation and the affected parameters C) Suggested mechanism of inhibited transcription and the affected parameters*

constant δ. This is shown schematically in Fig. 35A. We stress that this simple model is restricted only to include a minimal number of parameters, as no cooperativity is assumed (e.g. use of Hill coefficients) since this will include more free parameters, and we do not have any experimental data suggesting that this is a necessary assumption. Thus, these two equations serve as a minimal model for p53 oscillatory behavior. Next we investigated how each of the potential regulatory interactions between Mdmx and the p53-Mdm2 feedback (increase in Mdm2-mediated p53 degradation, and decrease in p53 transcriptional activity) would affect p53 dynamics. We introduced a set of impact parameters λ_i that account for the various effects Mdmx has on the p53-Mdm2 system:

$$\begin{aligned} \beta &\mapsto \beta(1+\lambda_1 \cdot Mdmx) \\ \gamma &\mapsto \gamma(1+\lambda_2 \cdot Mdmx) \\ \psi &\mapsto \psi(1-\lambda_3 \cdot Mdmx) \\ \tau_{Del} &\mapsto \tau_{Del}(1+\lambda_4 \cdot Mdmx) \end{aligned}$$

The impact parameters λ_1 and λ_2 account for Mdmx's impacts on the maximum activity (β) and p53-Mdm2 association (γ) for p53 degradation respectively (Fig. 35B). λ_3 and λ_4 account for differential Mdmx's impacts on p53 transcriptional activity (ψ) and time delay (τ_{Del}) respectively.

3.3.2 Mathematical Analysis of the Phase Space

Before introducing Mdmx into the system, we needed to understand the properties of the dynamical system. First we considered the boundaries of the phase space, to find out where the trajectory of p53 and Mdm2 would go. It is easy to show that this is always found in the 1st quadrant meaning that p53 and Mdm2 are always positive as they should be. In the same way the variables does not

run off to infinity since:

$$\begin{aligned}
&\frac{d}{dt}Mdm2\Big|_{(Mdm2=\infty)} < 0 \\
&\frac{d}{dt}p53\Big|_{(p53=\infty,Mdm2=\infty)} < 0 \text{ and} \\
&\frac{d}{dt}p53\Big|_{(p53=\infty,Mdm2=0)} > 0 \text{ but} \\
&|\frac{d}{dt}p53\Big|_{(P=\infty,M=0)}| << |\frac{d}{dt}Mdm2\Big|_{(P=\infty,M=0)}|
\end{aligned}$$

We now consider the fixed points of the system, which are defined by:

$$\frac{d}{dt}(p53) = \frac{d}{dt}(Mdm2) = 0$$

In a fixed point there is no dynamics and we can thus in the following derivations neglect the time delay τ_{Del} leading to:

$$Mdm2^* = \frac{\psi}{\delta}p53^*$$

This is the fixed point of the system. It already represents an essential feature of the system studied in the experiments; the relation between the concentrations of Mdm2 and p53. From this we can see that only the parameter controlling the transcriptional activity of p53, ψ, and the one controlling the degradation of Mdm2, δ, affects the ratio between these two. By comparing this to the results found in the experiments (Fig. 34B) we use this to already put a bound on these parameters. Since we expect that Mdmx could effect the transcriptional activity ψ, we keep δ fixed, and obtain:

$$\psi = \langle\frac{Mdm2}{p53}\rangle_{obs}^{supp} \cdot 0.1 \approx 0.15 \quad \text{and} \quad \delta = 0.1$$

With this we can also directly determine the impact of Mdmx, since we know the mean value of the distribution in the WT (Fig. 34B (black))

$$\begin{aligned}
\frac{\psi}{\delta}(1-\lambda_1) &= \langle\frac{Mdm2}{p53}\rangle_{obs}^{WT} \\
&\Rightarrow \lambda_1 = 1 - \frac{\delta}{\psi}\langle\frac{Mdm2}{p53}\rangle_{obs}^{WT} \approx 0.15
\end{aligned}$$

From this we can derive an equation for the steady state level of p53 in this system:

$$\begin{aligned}
0 =& \alpha - \frac{\psi\beta}{\delta}\frac{(p53^*)^2}{\gamma + p53^*} \\
=& {p53^*}^2 - \frac{\alpha\delta}{\psi\beta}p53^* - \gamma\frac{\alpha\delta}{\psi\beta} \\
=& {p53^*}^2 - \mathcal{K}P^* - \gamma\mathcal{K} \\
\Rightarrow& p53^* = \frac{\mathcal{K}}{2}\left(1 + \sqrt{1 + 4\gamma\mathcal{K}^{-1}}\right) \\
\text{With } \mathcal{K} &= \frac{\alpha\delta}{\psi\beta}
\end{aligned}$$

This result is the analytical result of the p53 steady state concentration as a function of the five parameters in the system, where we for simplicity fix $\alpha = 0.1$. From this we learn that the p53

steady state increases by decreasing the Mdm2 mediated degradation through the parameter β and that it decreases by increasing transcriptional activity of p53 through the parameter ψ Using this we can consider a linear stability analysis of the system in order to investigate the onset of oscillations in the system. In order to do the analytical calculations we still neglect the time delay and set up the Jacobian that has the form:

$$J = \begin{pmatrix} -\frac{\gamma\beta Mdm2^*}{(\gamma+p53^*)^2} & -\beta\frac{p53^*}{\gamma+p53^*} \\ \psi & -\delta \end{pmatrix}$$

From this we calculate the trace and the determinant:

$$\tau = -\gamma\beta \cdot \frac{Mdm2^*}{(\gamma + p53^*)^2} - \delta$$
$$\Delta = \gamma\beta\delta \cdot \frac{Mdm2^*}{(\gamma + p53^*)^2} + \beta\psi\frac{p53^*}{\gamma + p53^*}$$

Since the oscillations are an essential part of the experimental observations, we want to study if oscillations can occur, by calculating the eigenfrequency of the system. This describes the frequency of the oscillatory dynamics around the fixed point, where the linearization should hold. This is given by:

$$\omega = \frac{1}{2}\sqrt{4\Delta - \tau^2}$$

It exists only when the value of τ squared (not to confuse with the parameter τ_{Del}) is smaller than 4Δ which is of course also the criteria for the eigenvalues to be complex. Thus there can be a spiral in the system, but in order to have a real oscillations, we need not only complex eigenvalues, but also a non-decaying system. We are thus searching for a Hopf bifurcation, which occurs when τ calculated from the Jacobian, changes from negative to positive and the fixedpoint thereby becomes unstable. We can reorganize τ, and show that this system can never have a stable limit cycle since:

$$\tau = -\Big(\frac{\gamma\beta M^*}{(\gamma + P^*)^2} + \delta\Big)$$

is strictly negative. Therefore, for this system without a time delay, the existence of a limit cycle is impossible. It should be noted however, that since there is a well defined eigenfrequency in the system, oscillatory dynamics generated solely by the presence of noise can still occur as discussed in Fig. 33.

3.3.3 The Existence of a Limitcycle Through Inclusion of a Time Delay

At this stage we had learned that no limit cycle can exist in the proposed dynamical system without a time delay. In this section we study the effect of the time delay, and how this can initiate oscillations. When a dynamical system moves closer to the Hopf bifurcation, the absolute level value of the effective decay constant τ decreases until it reaches zero which is when the bifurcation occurs. If the time delay should be able to create oscillations in the system, it must effectively add something to the decay constant. Thus we expect that the decay in a system with a time delay (τ_{Eff}) to take the form:

$$\tau_{Eff} = \tau + f(\tau_{Del}) \tag{81}$$

We study this perturbation to the effective decay by introducing a Poincare section as a line in the p53-Mdm2 phase plane from $[(0, Mdm2*); (p53*, Mdm2*)]$ (Fig. 36A). In this way we can estimate the distance the trajectory moves closer to the fixed point inside this section. We start out by considering the system with no time delay. Theoretically this decay distance can be approximated by:

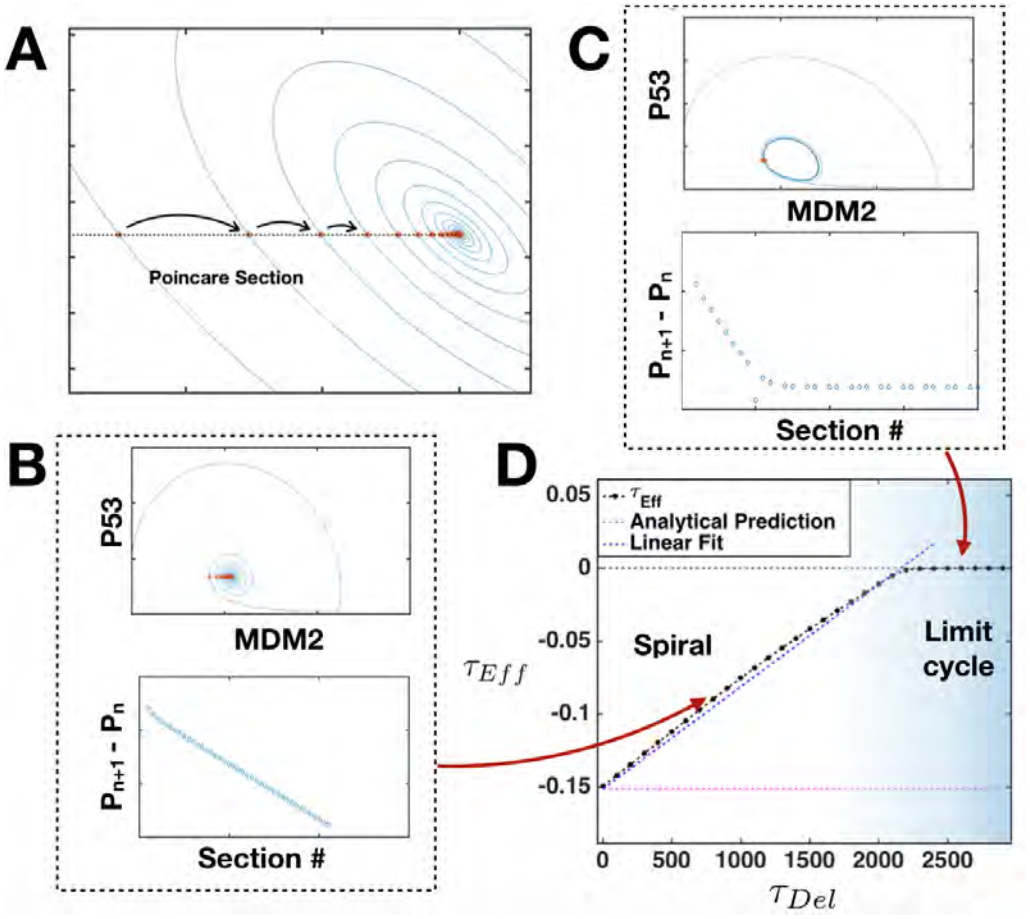

Figure 36: *A) Schematic picture of the Poincare section where we study the decay in the stable spiral B) Above: Phase space of p53 and Mdm2 and the trajectory decays to a stable fixed point. Below: The difference between two points at the Poincare section. C) Above: Phase space of p53 and Mdm2 and the trajectory decays to a limit cycle. Below: The difference between two points at the Poincare section. D) How the effectively measured τ increases linearly as we increase the time delay T_{del}, and at some point it becomes positive at which point the limit cycle comes into existence.*

$$P(n) \approx P\Big(t = \frac{2\pi}{\omega}\Big) \tag{82}$$

$$= P_{n-1} e^{-\frac{\tau 2\pi}{2\omega}} \tag{83}$$

$$= P_0 e^{-n\frac{\tau}{\omega}\pi} \tag{84}$$

$$\tag{85}$$

This means that we can estimate the decay at each Poincare section as:

$$P_{n-1} - P(n) \approx P_0\Big(e^{-(n-1)\frac{\tau}{\omega}\pi} - e^{-n\frac{\tau}{\omega}\pi}\Big) \tag{86}$$

$$= P_0 e^{-n\frac{\tau}{\omega}\pi}\Big(-e^{\frac{\tau}{\omega}\pi} - 1\Big) \tag{87}$$

$$= Ce^{-n\frac{\tau}{\omega}\pi} \tag{88}$$

Thus the value of τ will be the slope at which the decay is observed in a logarithmic plot, since the value of ω turned out to be approximately constant. In Fig. 36B we observe the decay as a line, with decay constant τ / ω * π. In Fig. 36C the decay is observed when the limit cycle has occurred. By fitting a linear fit to the points in a logarithmic plot we get a relation shown in Fig. 36D, where the decay rate is shown on the y-axis as a function of the increasing time delay. Thus we can use this to predict when the limit cycle sets in due to the time delay, depending on the parameters in the system.

3.3.4 The Effects of Mdmx Impact Parameters

We now turned back to the original problem: Investigating the effects of the impact from Mdmx. We started by testing the impact parameter λ_1. Here we found that by only incorporating this, the dynamics of p53 showed almost all the observed characteristics from the dynamics pre- and post Mdmx depletion in the experiments.

For non-zero values of λ_1 we observed a steady state level of p53 (Fig. 37A, before Mdmx depletion) and thus no oscillations. However once Mdmx is depleted, a single, transient pulse was observed, and this was followed by sustained oscillations (Fig. 37A, after Mdmx depletion). It is noted that, as λ_1 increases, so does the height of the initial pulse. However there was no effect on the amplitude of the sustained oscillations (Fig. 37A). In addition, λ_1 controls basal levels of p53, with higher λ_1 leading to lower basal levels of p53 before Mdmx depletion. From this we moved on to test impact parameter λ_2. This also affects the basal levels of p53 but in an opposite way, i.e. higher λ_2 leads to higher basal levels of p53 (Fig. 37B, before Mdmx depletion). Interestingly λ_2 only leads to p53 oscillations post Mdmx depletion without the initial high-amplitude pulse of p53 (Fig. 37B). Finally we tested the effects of the impact parameters that was connected to the inhibited transcription λ_3 and λ_4. Introduction of either of these result in oscillatory p53 behavior before Mdmx depletion, which does not fit with our experimental observations (Fig. 37C and37D). Therefore, based on these simulations, we concluded that Mdmx role in enhancing p53 degradation by Mdm2 (impact parameter λ_1) is critical for generating p53 biphasic dynamics after Mdmx depletion.

To understand these effects further, and to consider combinations of impact parameters, we tried to investigate the trajectories in the phase space spanned by Mdm2 and p53. This represents alternative way to characterize the effects of Mdmx on p53 is to visualize the dynamics of the p53 before and after Mdmx perturbation. Before Mdmx depletion (Fig. 38A), increasing values of the impact parameter λ_1 causes dampening of the p53 oscillations in equillibrium, though progressive narrowing of the limit cycle (As can be seen by the decreasing amplitude in Fig. 37A). To visualize the transient pulse, we observe that after Mdmx depletion (Fig. 38B), the trajectory takes a longer path from the fixed point (green zone) to reach the oscillatory regime (red zone) for increasing values of λ_1. The stretching of the trajectory corresponds to the height of the initial pulse, and

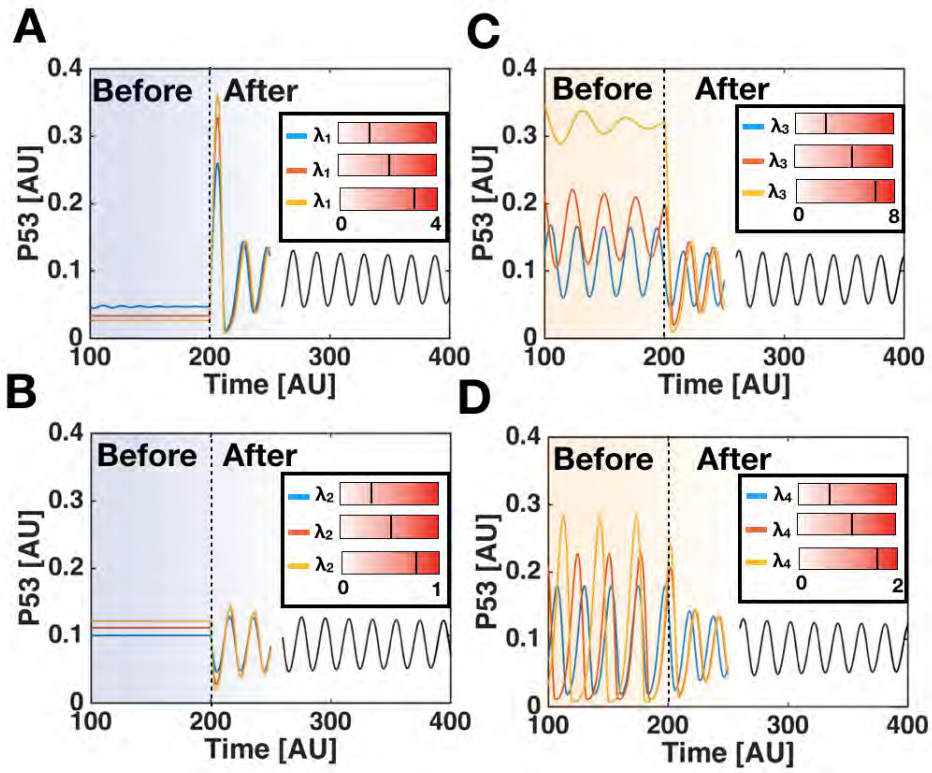

Figure 37: *A) Effects of Mdmx through impact parameter λ_1 on parameter β. Before Mdmx depletion, λ_1 values for blue, red and yellow curves respectively: (1; 2; 3). After Mdmx depletion, λ_1 is set to zero. B) Effects of Mdmx through impact parameter λ_2 on parameter γ. Before Mdmx depletion, λ_2 values for blue, red and yellow curves respectively: (0.25; 0.5; 0.75). After Mdmx depletion, λ_2 is set to zero. C) Effects of Mdmx through impact parameter λ_3 on parameter ψ. Before Mdmx depletion, λ_3 values for blue, red and yellow curves respectively: (2; 4; 6). After Mdmx depletion, λ_3 is set to zero. D) Effects of Mdmx through impact parameter λ_4 on parameter τ_{Del}. Before Mdmx depletion, λ_4 values for blue, red and yellow curves respectively: (0.5; 1; 1.5). After Mdmx depletion, λ_4 is set to zero.*

this shows why increasing values of λ_1 lead to higher amplitudes of the initial pulse. Therefore we can conclude that the role of Mdmx, modelled with only impact parameter λ_1 can explain the first two features of p53 biphasic dynamics; an initial high amplitude pulse followed by sustained low-amplitude oscillations. Thus λ_1 was an essential part of the explanatory model, however it could be in combination with some of the other impact parameters. As we learned in the mathematical analysis, the ratio of Mdm2/p53 in the steady state was determined by the ratio ψ/δ, and since ψ was affected by inhibited transcription through impact parameter λ_3, we were tempted to study the effects of this in greater detail and see if this could inhibit the oscillations as well. We studied the steady state dynamics in the phase space as λ_3 was increasing and we found that this could in fact also inhibit oscillations for at large values (Fig. 38C). However this would indicate that p53 would be much larger than Mdm2 (2-3 times) and this would be contradictory to the ratio between these two found in the experiments. Thus λ_3 cannot explain neither the transient pulse nor the sustained oscillations alone. We therefore tested combinations of λ_1 and λ_3 to see how they this

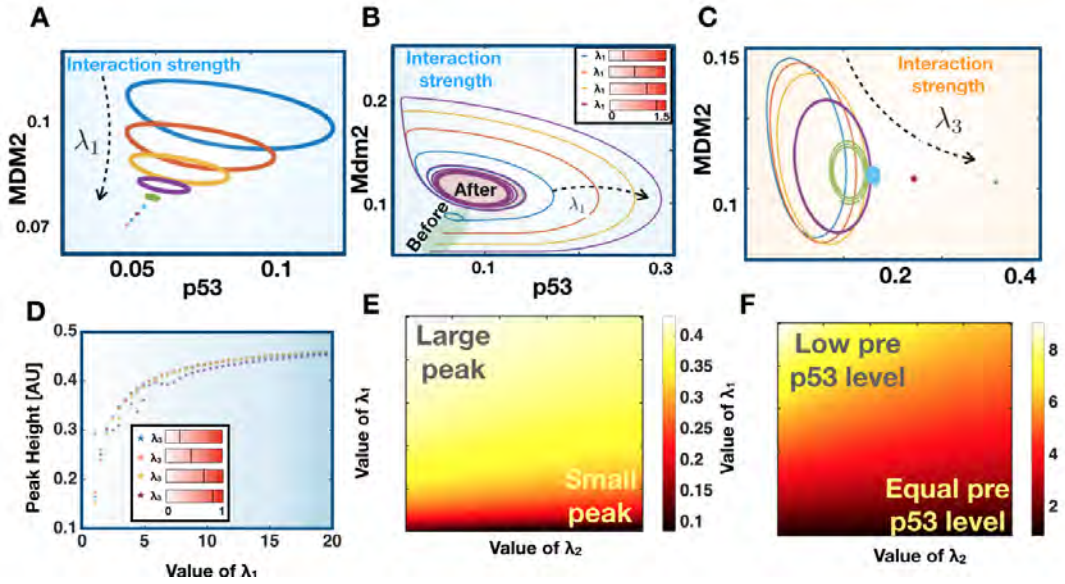

Figure 38: *A) Equillibrium dynamics in the p53-Mdm2 phase space as λ_1 increases. B) Trajectory from equillibrium dynamics pre- and post Mdmx depletion C) Equillibrium dynamics in the p53-Mdm2 phase space as λ_3 increases. D) Height of the transient pulse as λ_1 increases for different values of λ_3 E) Heatmap showing the height of the transient pulse for combinations of values for λ_1 and λ_2 F) Heatmap showing the mean p53 level pre Mdmx depletion divided with the mean p53 level post Mdmx depletion for combinations of values for λ_1 and λ_2*

affected the the amplitude of the initial p53 pulse. We found that the amplitude of the pulse is almost solely defined by the value of λ_1 (Fig. 38D), and the presence of λ_3 does not significantly change this. Finally we wanted to test the effects of λ_2 in combination with λ_1. The motivation for this comes from the fact that while λ_1 decreases the steady state level of p53, λ_2 increases it. From the experimental observations (Fig. 31A), it can be argued that the mean value of p53 does not change significantly after Mdmx depletion. Therefore the antagonistic role of λ_1 and λ_2 could be an important aspect in the full description of the effects of Mdmx. We tested the amplitude of the transient pulse for combinations of values for λ_1 and λ_2 and found that λ_2 significantly decreases the amplitude of the pulse (Fig. 38E). Likewise we calculated the ratio between the steady state level after and before Mdmx depletion (Fig. 38F) and once again observed that the steady state before Mdmx depletion can only be around the same level as the as after Mdmx depletion for high values of λ_2. Therefore we conclude that by combining λ_1 and λ_2 one can obtain both a large transient pulse and a steady state level around the same level, but since the steady state level was not one of the characteristic features of the experiment, we will in the following neglect any effect of λ_2 and consider only combinations of λ_1 and λ_3.

3.3.5 The Slope Following Mdmx Depletion

From the experimental observations, the occurrence of a large transient pulse following the Mdmx suppression should be an essential part of the dynamical system. In this section we calculate what parameters can lead to a sudden pulse following a perturbation. We start by consider the fixed

point of p53. When Mdmx is suppressed, we should have oscillations around the fixedpoint:

$$p53^* = \frac{1}{2}\mathcal{K}\Big(1 + \sqrt{1 + 4\gamma\mathcal{K}^{-1}}\Big)$$

For the Mdmx suppressed cells we have:

$$\begin{aligned}
\mathcal{K} =& \frac{\alpha\delta}{\beta\psi} \approx \frac{1}{15} \\
\Rightarrow \quad & \text{p53}^* = \frac{1}{30}\Big(1 + \sqrt{1 + 4 \cdot 0.15}\Big) \approx 0.075. \\
\Rightarrow \quad & \text{Mdm2}^* \approx 0.075 \cdot 1.5 = 0.11
\end{aligned}$$

For the control cells, where Mdmx is present, we have:

$$\begin{aligned}
\mathcal{K} =& \frac{\alpha\delta}{\beta_{Mdmx}\psi} \approx \frac{1}{50} \\
\Rightarrow \quad & \text{p53}^* = \frac{1}{100}\Big(1 + \sqrt{1 + 4 \cdot 0.5}\Big) \approx 0.027 \\
\Rightarrow \quad & \text{Mdm2}^* \approx 0.027 \cdot 1.25 = 0.035
\end{aligned}$$

Now as we remove Mdmx, we make a transition so $\mathcal{K} = \frac{1}{50} \mapsto \frac{1}{15}$. Therefore the slope will be:

$$\frac{dp53}{dt}|_{t=0} = \alpha - \frac{1}{15}0.034 \cdot \frac{0.0268}{0.0268 + 0.01} \approx 0.075$$

With this we can understand that the generated pulse after Mdmx removal arises due to the parameter change causing a sudden out-of-equilibrium state, which leads to a positive value for $\frac{d}{dt}(p53)$.

3.3.6 Stochastic Simulations Captures the Mdm2/p53 Ratio

We next tested whether parameter λ_1 can also capture the third characteristic feature of p53 dynamics; the increase in the ratio between Mdm2/p53 after Mdmx depletion (Fig. 34B). We learned from the analytical considerations, that this ratio was determined inside the fixed point by the ratio of ψ/δ, but since the limit cycle has a trajectory slightly away from this, we needed to test this through numerical simulations. We found that incorporating parameter λ_1 alone is insufficient for accounting this shift as was observed experimentally (compare Fig. 39A to Fig. 34B). We then tested the impact of parameter λ_3, which accounts for the direct effect of Mdmx on Mdm2 transcription by p53 (parameter ψ) and therefore is predicated to affect the ratio of Mdm2/p53. Based on the experimental immunofluorescence data, we could then calculate the average ratio of Mdm2/p53 both in the control and Mdmx depleted cells and use these values to set the bounds for the value of λ_3 based on the analytical calculations. We predicted that values of λ_1 equal to 3 (From (Fig. 37A) and λ_3 equal to 0.15. This could capture the shift in the Mdmx/p53 distribution. Indeed, the resulting distribution was shifted after Mdmx depletion as was experimentally observed, when including parameters λ_1 and λ_3 (compare Fig. 39B to Fig. 34B). Finally, by combining both impact parameters (λ_1 and λ_3), we simulated the system with internal noise (applying Chemical Langevin equation) and external noise (by applying gaussian uncertainty to the parameters at each simulation). This was done to examine the robustness of the system. We confirmed a robust biphasic dynamics of p53 after Mdmx depletion in the presence of noise that quite accurately captured the experimental behavior in single cells (Fig. 39C). Taken together,

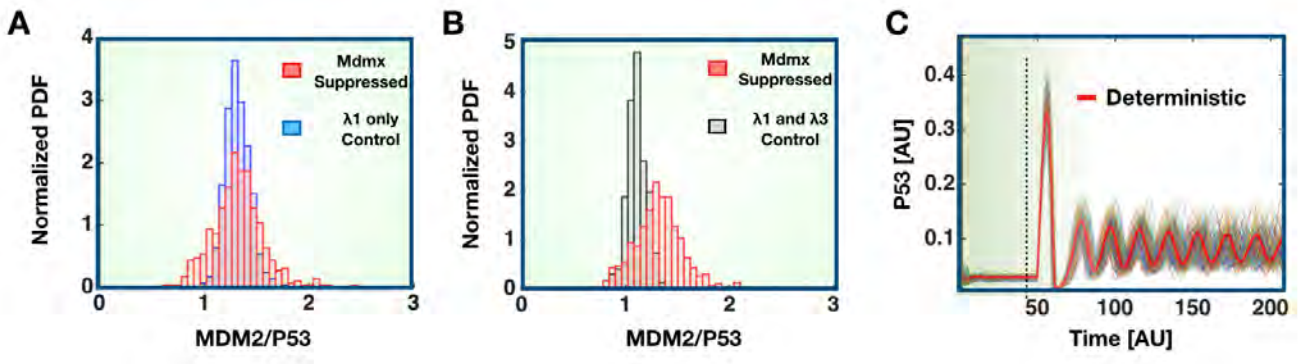

Figure 39: *A) Distribution of Mdm2/p53 pre Mdmx depletion (blue) and post Mdmx depletion (red) when only λ_1 is used. B Distribution of Mdm2/p53 pre Mdmx depletion (black) and post Mdmx depletion (red) when both λ_1 and λ_3 is used. C) Stochastic simulation showing dynamics of 100 independent cells.*

the mathematical analysis shows that the Mdmx-mediated p53 degradation through parameters λ_1 and Mdmx-mediated regulation of p53 activity through paramater λ_3 is sufficient for capturing the three quantitative features of p53 biphasic dynamics following Mdmx depletion including the initial high amplitude pulse, the low amplitude oscillations and the shifted distribution of Mdm2/p53 with increased variance. Furthermore we can conclude that the most important effect of this system is the enhanced degradation of p53 through Mdmx, and the inhibited transcriptional activity can be observed, but that this signal is significantly smaller.

3.4 Mdmx Suppressed Cells Following Exposure to UV Radiation

To further validate and constrain the model, we now wanted to test whether we could expand it to predict the effect of DNA damage on p53 dynamics. Again we wanted to have cells with and without Mdmx and compare the simulations to new experimental results.

3.4.1 Introduction of ATR to the Model and its Impact on p53

We introduced the DNA damage sensor ATR to our p53-Mdm2-Mdmx model and investigated the resulting p53 dynamics. ATR is a PI3 kinase-related kinase that senses DNA damage after UV-radiation. Activated ATR stabilizes p53 through inhibitory phosphorylation of Mdm2; which in turns activates the Mdm2-p53 negative-feedback loop (Fig. 40A). ATR activation in wild-type cells was shown to lead to a dose-dependent single pulse of p53, and ATR is introduced following a similar description as shown in [75], where we introduce a single dose dependent parameter, θ:

$$\frac{d}{dt}ATR = \theta - ATR$$

$$\theta = \begin{cases} 0 & \text{if } t < T_{UV} \\ 2\sqrt{D_{UV}} & \text{if } t \geq T_{UV} \text{ and } t < T_{UV} + \Omega \\ 0.1 & \text{else} \end{cases}$$

Here T_{UV} is the time of UV exposure, and Ω a parameter in units of time. Therefore the model can be understood the following way: ATR concentration reaches a dose dependent level after UV-

radiation and then decays exponentially (Fig. 40B). For simplicity we fixed the decay parameter to unity.

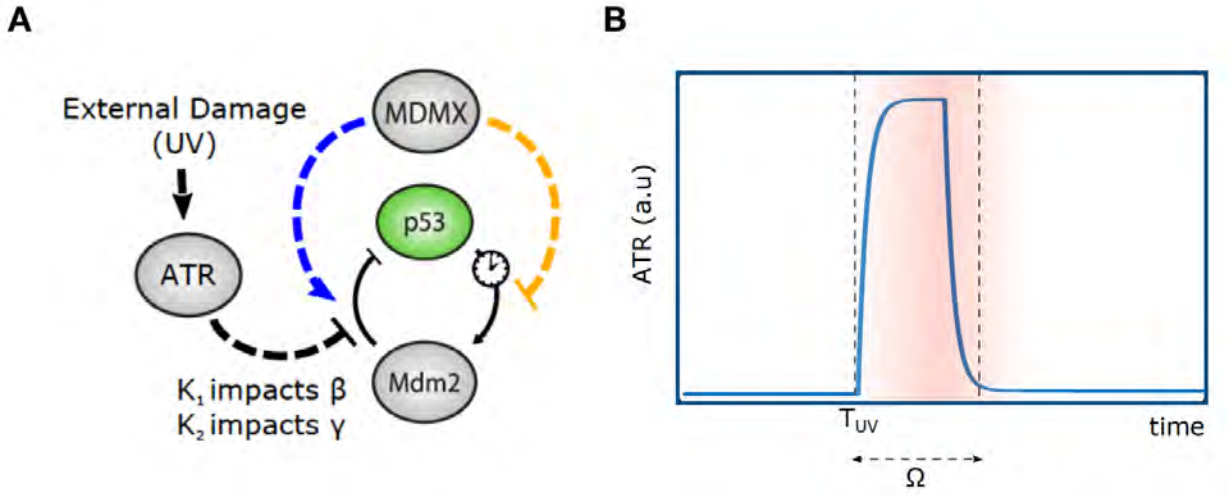

Figure 40: *A) Schematic figure showing the suggested effects of ATR on the p53 network. B) Example of ATR dynamics following UV radiation.*

Like we studied the effects of Mdmx on p53, we wanted to follow the same strategy and let ATR affect p53 through a set of impact parameters. We therefore modelled ATR inhibition of Mdm2-mediated p53 degradation through two parameters (κ_1 and/or κ_1) (Fig. 40A):

$$\beta_{Mdmx} \mapsto \beta_{Mdmx} \frac{\kappa_1}{\kappa_1 + ATR}$$
$$\gamma_{Mdmx} \mapsto \gamma_{Mdmx} \frac{\kappa_2}{\kappa_2 + ATR}$$

We used the values from previous simulations (Fig. 39C), where β_{Mdmx} refers to the dependency on Mdmx of this parameter. We compared the effects of UV-radiation alone (Fig. 41A, C) to that of Mdmx depletion followed by UV-radiation (Fig. 41B, D). We introduced three doses of UV-radiation through three different values of κ_1 and κ_2. In Fig. 41A to 41D, we observed that only parameter κ_1 did have a strong effect on the amplitude of the UV-triggered p53 pulse. Specifically, ATR activation (through its effect on κ_1) led to a single p53 pulse with an amplitude that scaled with κ_1 value (Fig. 41A). In contrast to this, activation of ATR through the other parameter κ_2 led to oscillations with no initial p53 pulse across all tested parameter values (Fig. 41B, D). This suggests that ATR inhibition of Mdm2-mediated p53 degradation occurs through parameter κ_1 that affects β (i.e. the degradation of p53 by Mdm2). Interestingly, when we consider the effect of ATR through parameter κ_1 in cells with Mdmx suppression, we found the amplitude and duration of the UV-induced pulse to be higher (Fig. 41B) compare to those with UV-radiation alone (Fig. 41A). Furthermore, the model predicted that in Mdmx depleted cells the initial pulse caused by UV-radiation is followed by a series of p53 oscillations, and that these have a larger amplitude than the ones induced by Mdmx alone (Fig. 41B).

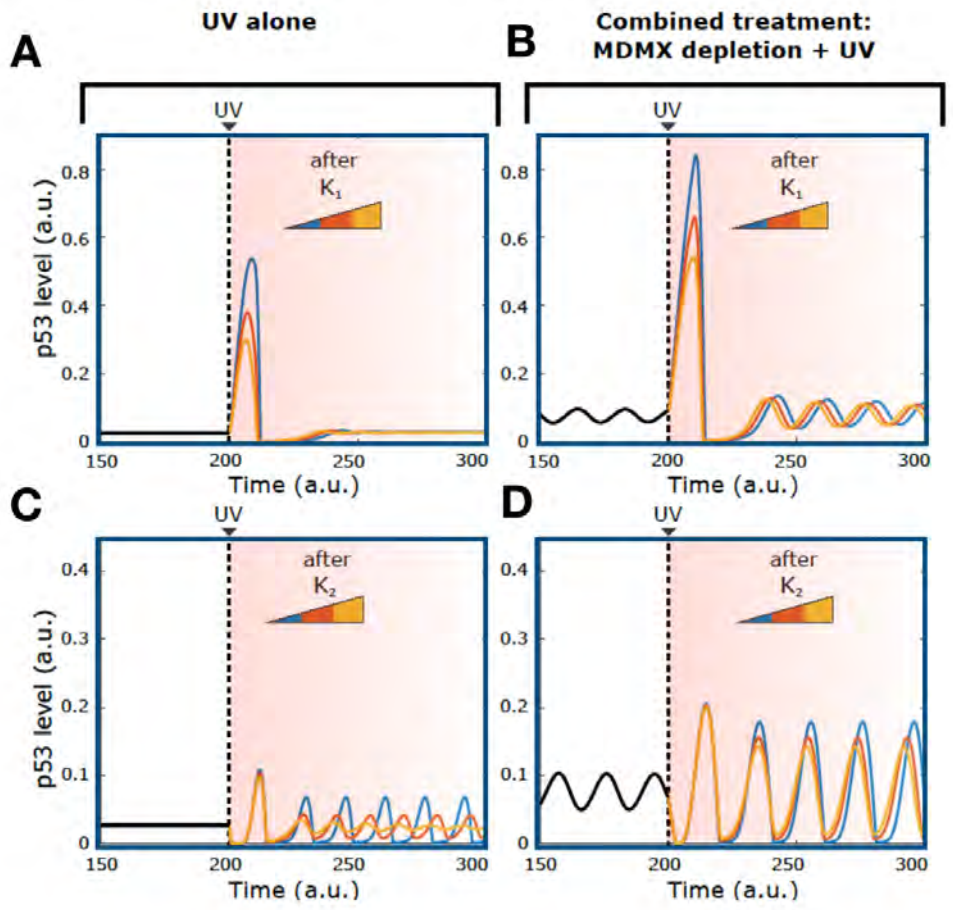

Figure 41: *A) Before UV,* $\kappa_1 = 0$*, after UV* κ_1 *values for blue, red and yellow curves respectively: (0.1; 0.25; 1).* $\lambda_1 = 3$ *and* $\lambda_3 = 0.15$ *B) Before UV,* $\kappa_1 = 0$*, after UV* κ_1 *values for blue, red and yellow curves respectively: (0.1; 0.25; 1).* $\lambda_1 = \lambda_3 = 0$ *C) Before UV,* $\kappa_2 = 0$*, after UV* κ_2 *values for blue, red and yellow curves respectively: (0.01; 0.025; 0.1).* $\lambda_1 = 3$ *and* $\lambda_3 = 0.15$ *D) Before UV,* $\kappa_2 = 0$*, after UV* κ_2 *values for blue, red and yellow curves respectively: (0.01; 0.025; 0.1).* $\lambda_1 = \lambda_3 = 0$

3.4.2 Depency of UV Induced Response on Applied Dose and Parameters

We next analyzed how different UV doses might affect the slope (Fig. 42A) and amplitude (Fig. 42B) of the UV-triggered initial p53 pulse. Simulation of the model using a range of values for κ_1 suggests that both the slope and height of the initial p53 pulse increase with the dose of UV-radiation (Fig. 42A, B). A similar trend was predicted for Mdm2 depleted cells, and the model predicts that the slope and amplitude of the p53 initial pulse will be higher in these cells (Fig. 42A, B; blue curves). This can be logically explained since ATR has an antagonistic role compared to Mdmx and therefore if no Mdmx is there, the effects of ATR will be even greater. Finally, we tested how different UV doses did affect the amplitude of p53 oscillations following the initial p53 pulse in response to UV in Mdmx depleted cells. Based on simulations from the model, we measured the relative increase in the oscillatory amplitude after UV as we vary κ_1 and κ_2 independently (Fig. 42C). Here we observed, that parameter κ_2 holds a stronger effect in changing the oscillatory

amplitude. Furthermore, for all values of parameters κ_1 and κ_2, the amplitude of p53 oscillations following UV is independent of the UV dose. Taken together our model suggests that a combined treatment of Mdmx depletion followed by UV radiation will lead to a large p53 pulse (Fig. 41B, Fig. 42B) followed by oscillations (Fig. 41B, Fig. 42C). In addition, our model predicts that the UV-triggered p53 oscillations will have higher amplitude compared to the oscillations prior to UV (Fig. 41B, Fig. 42B). At this stage we therefore predicted that κ_1 would be important for describing the system, but did not know whether the effects of κ_2 was also necessary. Furthermore we concluded that our model had three predictions for the Mdmx depleted cells:

- The transient pulse would have a larger amplitude and steeper slope.
- UV radiation would lead to increased, but dose-independent oscillations after the transient pulse.

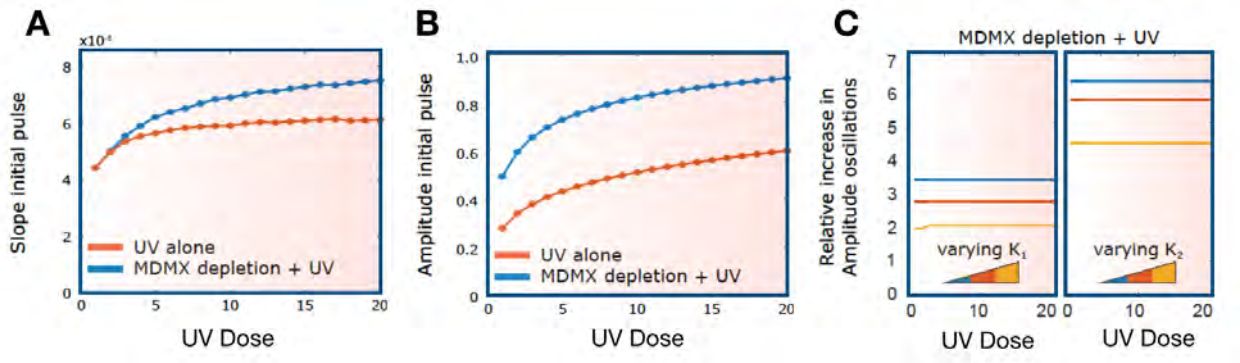

Figure 42: *A) Slope of the p53 initial pulse following the increasing UV dose for both control (red) and Mdmx depleted cells (blue). B) Amplitude of the p53 initial pulse following the increasing UV dose for both control (red) and Mdmx depleted cells (blue). C) Amplitude of the p53 sustained oscillations after the initial pulse for different levels of κ_1, blue, red and yellow curves respectively: (0.1; 0.25; 1) and κ_2 blue, red and yellow curves respectively: (0.01; 0.025; 0.1)*

3.5 Comparing Experimental Data to Model Predictions in Response to UV Radiation

To test the predictions from the model, we now moved to experiments. The single cells were exposed to UV in two different doses 8 J/m^2 or 16 J/m^2 for both control (upper single-cell p53 traces in Fig. 43A and Fig. 43B) and Mdmx depleted cells (lower single-cell p53 traces in Fig. 43A and Fig. 43B). Based on these figures we could clearly divide the dynamics into three phases and colored them according to their dynamic behavior: before treatment (blue), initial response (red) and long-term response (yellow).

3.5.1 Analysis of the UV Induced Pulse Reveals Dose Dependency

First of all we observed that for the cells subjected to UV-radiation alone, p53 shows a single pulse with an amplitude that increases with dose (upper single-cell traces Fig. 43A and Fig. 43B). Second, when UV-radiation is combined with Mdmx depletion, this initial pulse shows a larger

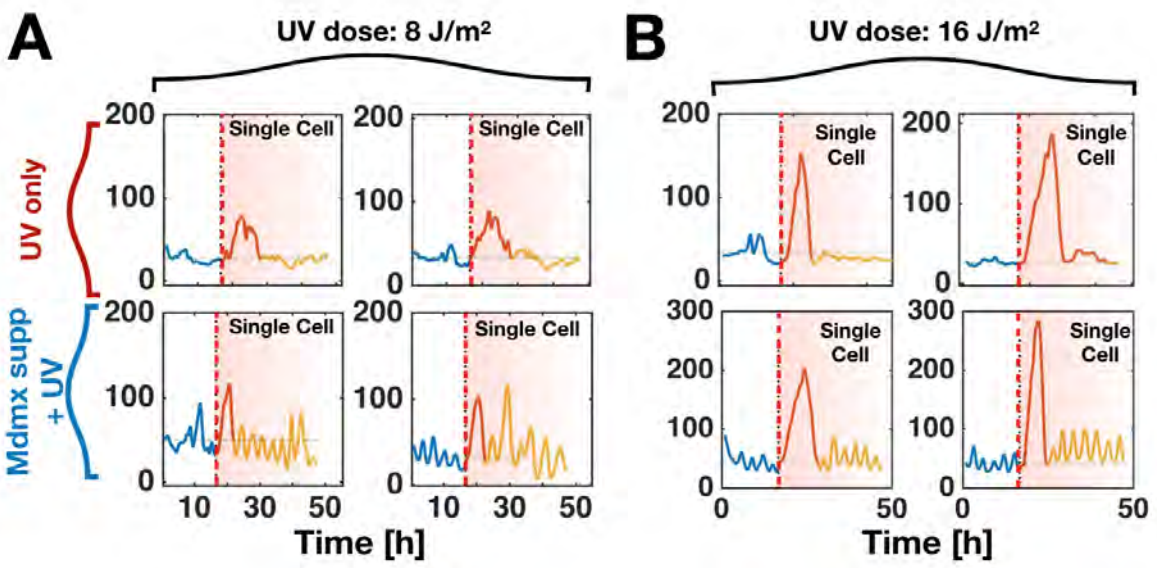

Figure 43: *A) Four representative single-cell time series of p53 dynamics following UV-radiation of 8 J/m^2 The bottom two panels show prior Mdmx depletion. Blue corresponds to pre-UV dynamics, red is transient response and yellow is steady state dynamics. B) Four representative single-cell time series of p53 dynamics following UV-radiation of 16 J/m^2 . The bottom two panels show prior Mdmx depletion. Blue corresponds to pre-UV dynamics, red is transient response and yellow is steady state dynamics.*

amplitude (Fig. 43A). To test this further, we calculated the average p53 level for each group of cells (Fig. 44A, B). Here we observe that for the low dose of UV radiation, the height of the peaks are of similar size (Fig. 44A), whereas for the large UV dose, the Mdmx suppressed cells show a much larger amplitude (Fig. 44B). To quantify these observations more thoroughly, we calculated the values of both the height and the slopes for the peaks following both doses. From these we can conclude that the Mdmx depleted cells show a larger slope in both conditions (Fig. 44C, Fig. 44D), and a significantly larger amplitude following the large UV dose (16 J/m^2) (Fig. 44F). These results are in agreement with the predictions from the model. For the small UV dose (8 J/m^2), the amplitudes are of similar height and this is not predicted from the model (Fig. 44E). We expect that this discrepancy might be due to some other mechanisms in the complicated ATR feedback system, that is beyond the scope of this model. We note that, as predicted by the model, an increase in the UV dose leads to a larger slope (Fig. 44C, Fig. 44D) and higher amplitude of the pulse (Fig. 44E, Fig. 44F), and thus these features are dose-dependent.

3.5.2 Analysis of the UV Affected Oscillations Reveals Enhanced Amplitudes

From the single cell traces we observe that for both UV doses, that in the combined treatment (UV and Mdmx depletion), the initial single pulse was followed by oscillations with higher amplitude compared to before UV treatment (lower single-cell traces (Fig. 43A, B). We therefore wanted to quantify the series of oscillations observed in Mdmx depleted cells following the initial UV-triggered pulse. As we did for the Mdmx induced oscillations, we calculated the Fourier spectrum (Fig. 45A,

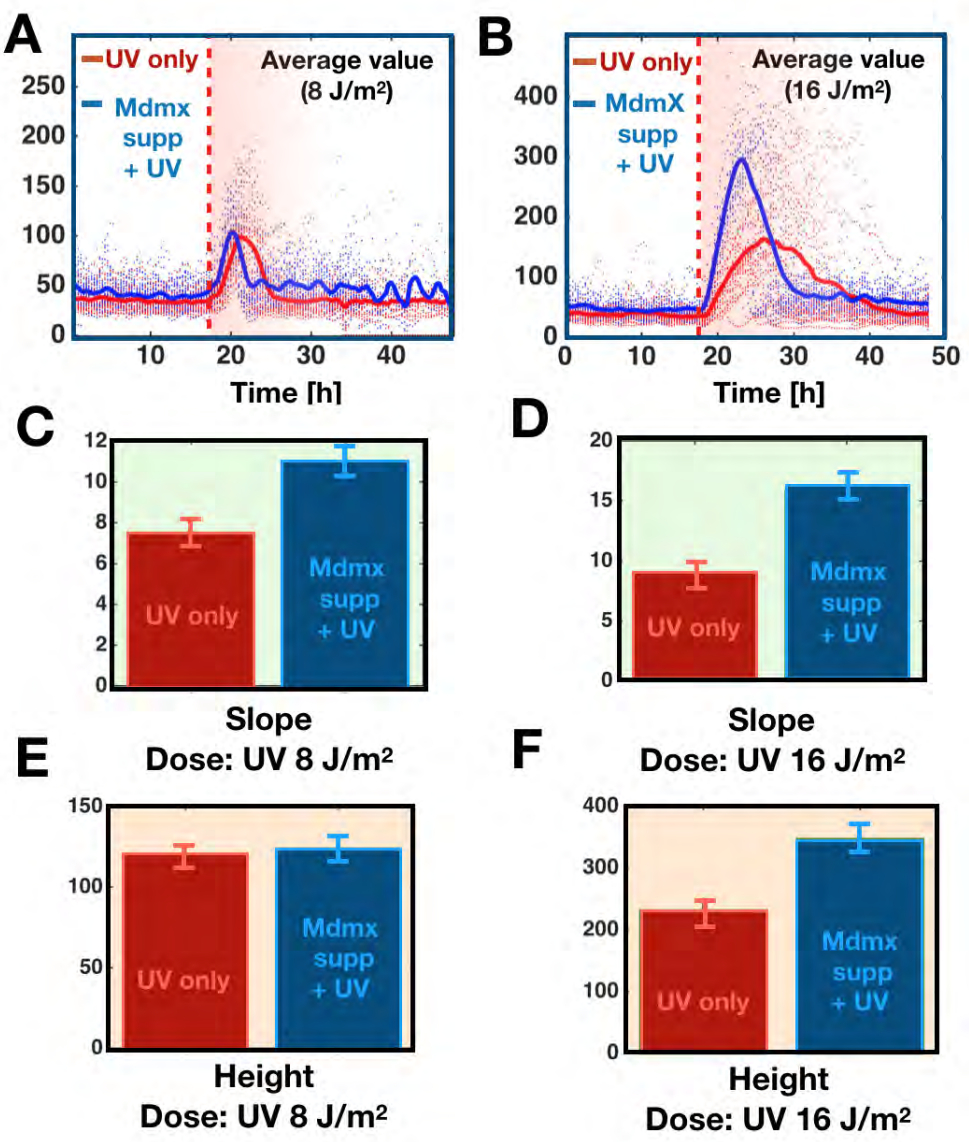

Figure 44: *A-B) Mean p53 dynamics obtained by averaging individual cell traces over time before and after UV-radiation (8 and 16 J/m2 respectively). The red trace corresponds to p53 dynamics before and after UV. The blue trace is p53 dynamics with prior Mdmx depletion followed by UV. C) Slope of the p53 initial pulse after UV-radiation ($8J/m^2$) without (red) and with Mdmx depletion (blue). D) Slope of the p53 initial pulse after UV-radiation ($16J/m^2$) without (red) and with Mdmx depletion (blue). E) amplitude of the p53 initial pulse after UV-radiation ($8J/m^2$) without (red) and with Mdmx depletion (blue). F) amplitude of the p53 initial pulse after UV-radiation ($16J/m^2$) without (red) and with Mdmx depletion (blue).*

B). This could not be determined as clearly as for the oscillations following Mdmx depletion (Fig. 32A) which is because the traces are shorter and the number of cells are fewer. Despite this uncertainty in the data, we observe that the frequencies are around the same value as the Mdmx depleted cells. From this we needed to characterize the amplitudes, and therefore we calculated the distribution of all amplitudes (Fig. 45C, D) for both UV doses. While the frequencies of the

oscillations were similar to the oscillations resulting from Mdmx depletion alone, the amplitude of oscillations was approximately two times larger compared to the amplitude resulting from Mdmx depletion alone (in Fig. 45C, D compare gamma fits in red from of Fig. 32B with current gamma fits in green). We also note that for both observations, the oscillatory frequency and the increase in oscillatory amplitude, were independent of the UV-dose. This is in agreement with the model predictions, and from this we can also conclude that only κ_1 is needed in order to describe the effects of ATR on the p53 dynamics. Had the amplitudes of oscillation been much larger, we would have needed κ_2 but since this is not the case, only a single impact parameter will be sufficient to describe the effects on p53.

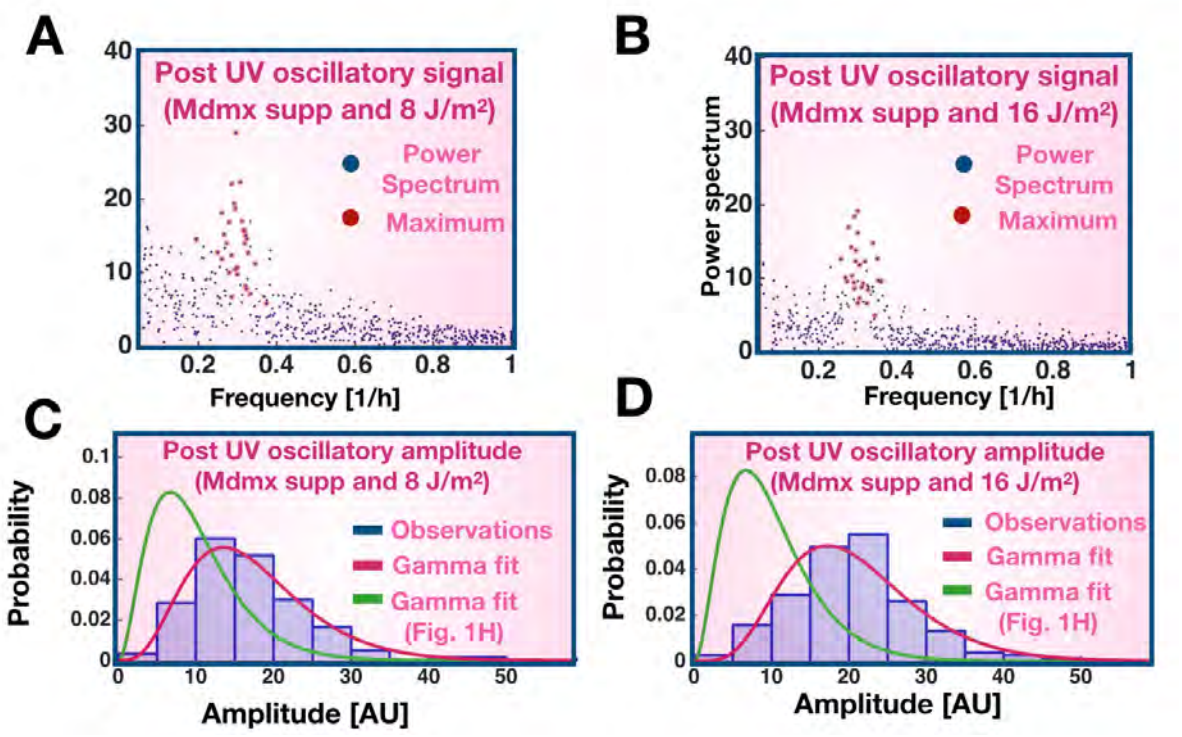

Figure 45: *A) Fourier spectrum of the sustained oscillatory phase after UV-radiation ($8J/m^2$). B) Fourier spectrum of the sustained oscillatory phase after UV-radiation ($16J/m^2$). C) Distribution of amplitudes of the p53 oscillations following UV-radiation ($8J/m^2$). D) Distribution of amplitudes of the p53 oscillations following UV-radiation ($16J/m^2$).*

3.5.3 Conclusions From Experimental Findings

Based on these experimental findings, we conclude that the main features of p53 dynamics in response to Mdmx depletion combined with UV-radiation (an enhanced UV-triggered initial pulse followed by large-amplitude oscillations) were all captured in our model. Even though there was a small discrepancy for the small UV dose, we did not find this strong enough to change the model in order to describe the experimental data. Thus following the agreement between our model and experimental results, we concluded that the effect ATR has on Mdm2-mediated degradation of p53 through impact parameter κ_1 is the function that dominates the p53 dynamical response following DNA damage. Indeed, we found that the Mdm2-dependent degradation of p53 (facilitated by

Mdmx and hindered by ATR) is the most critical interaction regulating p53 dynamics both in non-stressed conditions and following DNA damage.

3.6 Discussion and Perspectives

In this project we have investigated the regulation of p53 dynamics through a combination of single-cell imaging, data analysis and mathematical modeling. The focus was to determine the role of Mdmx in regulating p53 dynamics in both non-stressed conditions and after DNA damage. The approach was to make the data analysis as detailed and clear as possible, so we could extract the most important features, and use these to make constraints for a mathematical model. In order for this interplay to function optimally, we made it a top priority that the model should be as simple as possible, and include as few parameters as possible. Furthermore, wanted this study not only to be able to reproduce experimental data and claim that one hypothesis can achieve that, but to test several hypotheses and reject many of these based on the interplay between the model and the experimental data. Therefore we also believe that the results have more weight, in the sense that the thorough investigation can explain why so many of the hypotheses fail to explain the experiments. This approach has been widely used in physics throughout the years, but has vaguely been applied to biology since the experimental data have rarely been good enough to put up restrictions for the models. However as the quality of biological data has improved immensely, this approach will hopefully be vividly applied in the future.

The overall conclusions from this project was that we could extract three prototypic features of the p53 dynamics in vivo. Based on existing literature we constructed a minimal model, and we used the experimental conclusions as guidelines to simulate the impact of each Mdmx-mediated molecular mechanism in regulating p53 dynamics. By comparing experimental results with simulations, we proposed that Mdmx-mediated p53 degradation plays the major role in regulating p53 biphasic dynamics. Therefore it is tempting to speculate that the main function of Mdmx could be to perturb the dynamical system, by suppressing p53 oscillations through the enhanced Mdm2-mediated p53 ubiquitination. After Mdmx suppression, we observed in the experimental data, how a transient p53 pulse showed higher slope and amplitude following UV-irradiation. By applying the same modelling strategy as before, we tested different impact parameters. Our results suggested once again an inhibitory role of Mdmx via modulation of the slope and height of p53 pulse. Our simple model could reproduce the experimental results, but surpriisingly, this effect was not obvious when a low UV dose was applied to the cells. Therefore it is possible that there is a technical challenge in quantifying a mild increase in amplitude due to the low basal level of p53. Alternatively, the amplitude could be dampened by unknown signaling proteins and this dampening effect is relieved at high UV dose. It has previously been claimed that p53 oscillations are flexible in amplitude but robust in period [85]. Our results substantiate this claim, which therefore can be a very important fingerprint towards a still improved understanding of the underlying p53 network. A very important question, which still remains unclear, is if different amplitudes of p53 oscillations (or other transcription factor proteins), can activate distinct transcriptional programs and therefore encode various biological information for cell state determination [91]. The fact that ATR activation leads to a higher amplitude of p53 oscillations provides a plausible approach to further dissect functions of p53 amplitude in future experiments. From the systems biology point of view, Mdmx acts as a key suppressor of p53 oscillations in both non-stressed conditions and after

gamma-irradiation [85]. Therefore it is tempting to believe that Mdmx is serving as a major regulatory target for other cellular signals to modulate p53 dynamics and cellular behavior. Clinically, Mdmx overexpression is observed in multiple cancers [92, 93, 94]. Thus, it would be interesting to further investigate the role of Mdmx in regulating p53 dynamics in Mdmx overexpressed cancers as well as cancers with wild type TP53.

How dynamics of signaling molecules emerge through interacting components in space and time remains an unresolved question. It is an important problem in the field of systems biology to understand how signal-specific dynamics emerge and specify downstream transcriptional programs for cellular decision. Oscillatory dynamics are widely observed in a variety of different biological processes including circadian rhythm [95, 96], immune response [4, 3], stress response [97, 5] and development [98, 99]. To understand how these oscillations emerge and what biological functions are encoded in these oscillations, it is critical to take multifaceted approaches. This work took an integrative approach combining single-cell quantitative imaging through detailed and quantitative analysis with mathematical modelling to identify key regulatory mechanisms underlying p53 dynamics. This project therefore provides an example of how to examine fine tuned mechanisms responsible for signaling dynamics. This was done by developing a minimal mathematical platform based on quantitative perturbations of signaling dynamics in single cells. This platform can be the basis to study p53 dynamics in various biological contexts in the future.

4 Chaotic Dynamics Mediate Brain State Transitions

In this chapter the results of **paper V** is presented and discussed, along with some other results that has not yet been published. The main part of this work was carried out in the spring of 2017 in a vivid collaboration with Rune Rasmussen. It started when we discussed how concentrations of extracellular ions could affect the dynamics of the membrane potential. This was inspired by the experimental findings published in Ding et al. 2016. The parts on chaotic dynamics was greatly improved through discussions with Mogens H. Jensen.

In the this section, we will extend a previously published model (Averaged-Neuron model) to explicitly treat the changes in extracellular ion concentrations that occur during the sleep-wake cycle. We demonstrate that by inducing changes in $[K^+]o$, $[Ca^{2+}]o$ and $[Mg^{2+}]o$ in combination with decreasing the conductance of the Ca^{2+}-dependent K^+ channel, we can generate state transitions in neuronal firing patterns. We show that sleep is dominated by a stable limit cycle, resulting in self-sustained, stable firing patterns, whereas wakefulness is governed by irregular oscillations and chaotic dynamics and we discuss how the properties of chaotic dynamics define transitions between brain states.

4.1 Background to Neurons and Membrane Potential

Action potentials are in general believed to be formed as a result of electrical currents that pass through ion channels. The neuronal cell has a membrane that consists of a bilayer of lipids that forms an almost perfect electrical insulator. This leads to the possibility of having different ion concentrations between the inside of the cell and the surrounding extracellular space. In the membrane, there is a number of different proteins embedded and these act as ion gates, which is the foundation for creating a dynamically changing ion difference. The ion gates are divided into two subcategories, ion channels that, when open, passively let the ions run towards the lower concentration, and ion pumps that actively transport ions from one side to the other of the membrane [100].

4.1.1 Description of the Hodgkin-Huxley Model

In their seminal work, Hodgkin and Huxley investigated the membrane potential on the giant axon the squid [101]. In this they measured three different types of currents, sodium (Na^+), potassium (K^+) and a leak current. They now used the theory of electrical circuits to construct a model where the current could run through a passive resistor (for leak), or two variable resistors (for K^+ and Na^+). From Fig 46, it is clear that using Kirchoffs law, the applied current must be split on the different channels so:

$$I(t) = I_C(t) + \sum_k I_k \quad \text{where we sum over the three different channels} \tag{89}$$

Now since we are interested in modelling the membrane potential, and assume that this acts as a capacitor, we can write the current on the capacitor as $I_C = C\frac{dV}{dt}$ so we end up with the differential equation:

$$C\frac{dV}{dt} = -\sum_k I_k + I(t) \tag{90}$$

Where C is the membrane capacitance per unit area. Now we need to model the specific gating channels. They all take the general form:

$$I_k = g_k(V - E_K) \tag{91}$$

Here g_k is the specific conductance for the k'th channel. In the original formulation the full differential equation took the form:

$$C\frac{dV}{dt} = -(g_L(V - E_L) + g_K n^4(V - E_K) + g_{Na} m^3 h(V - E_{Na})) + I(t) \tag{92}$$

where n, m and h, are called gating variables and they control the voltage dependency of the gate and they are again modelled by differential equations.

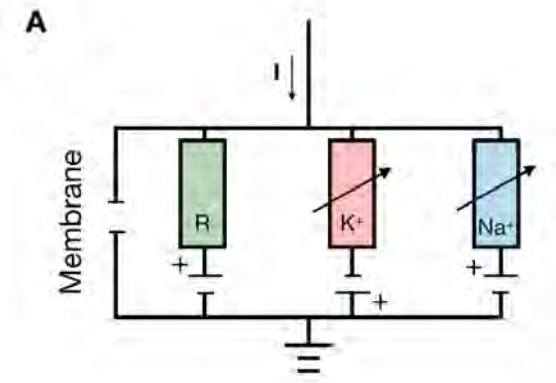

Figure 46: *Schematic figure showing electrical circuit in the Hodgkin-Huxley setup.*

4.1.2 Definition of Neuronal States

During transition from sleep to awake, the brain transitions from a state that attenuates sensory inputs to one that often amplifies them [102, 103, 104]. How this transition between states occurs is incompletely understood, both a the level of the brain and at the level of the neurons that must implement the transition in a smooth and robust way. Cortical Neurons exhibit three distinct physiological and behavioral states that characterize the transition from sleep to active wakefulness. Specifically, slow-wave sleep is characterized by oscillating periods of synaptic barrages (called "upstates") and silence (called "downstates") [105]. It is understood that this behavior reflects oscillations in membrane potential (Vm) and therefore the neurons susceptibility to input. In wakefulness, these downstates are suppressed and Vm is maintained closer to threshold. Although the classic view holds that oscillations are restricted to slow-wave sleep, recent studies have demonstrated that a quiet-awake state is also characterized by low-frequency Vm oscillations. Once actively awake, however, movement and arousal suppresses these oscillations and Vm is depolarized tonically, making neurons sensitive to inputs and prone to firing. Despite our understanding of the neuronal behaviors that are indicative of transitions from slow-wave sleep to quiet-awake to active-awake, the underlying mechanisms that initiate these transitions remain unclear.

4.1.3 Extracellular Ion Concentrations Changes Between Neuronal States

Recently it was proposed that changes in extracellular ion concentrations ($[K^+]o$, $[Ca^{2+}]o$ and $[Mg^{2+}]o$) control activity patterns during sleep and wakefulness, and that ionic changes are sufficient to shift the state from sleep to awake [106]. However, given that changes in neural activity also strongly affect extracellular ion concentrations [107, 108, 109, 110, 111], it is not possible to unequivocally distinguish cause and consequence in vivo. For example, both spiking and excitatory barrages, which originates within the neuron itself, increase $[K^+]o$ [108, 112], making it difficult to experimentally assess causality. A remedy for solving this issue is modeling and simulations [113, 114, 115, 116]. The ability to maintain parameters constant, thereby reducing variable space dimensionality, is a powerful tool for interrogating the impact of changes in both intracellular and extracellular ion concentrations on Vm dynamics and state transitions, as well as for formulating hypotheses and predictions for future experimental investigations.

4.2 Creation of the Extended Averaged Neuron Model

An important step towards successfully modeling the neuronal dynamics in a simple manner, is the "Averaged-Neuron" model, which recently has been proposed [116]. This model is inspired by previously constructed neural-network models [117, 118, 119, 120, 121, 122]. The framework of these models is based on currents running through different ion channels which are mathematically described in a Hodgkin-Huxley manner. These all affect and contribute to the total change in the menbrane potential Vm, which typically measured in experiments. The new model simplifies the enormous complexity of these models, by performing a mean-field approximation of a population of neurons to construct an "Averaged-Neuron" model. Our purpose with this project was to investigate how varying extracellular concentrations could affect the dynamics in the membrane potential, and therefore we decided to use the Averaged neuron model and by implementing dependencies on the extracellular concentration we could investigate this.

4.2.1 Introduction of Extracellular ions Dependencies

We therefore first implemented and extended the Averaged-Neuron model so the extracellular concentrations were taken into account. In this model, it is assumed that the neuron can interact with itself (directly or indirectly) through excitatory or inhibitory synaptic currents, depending on the conductances of the channels and the reversed potential that depends on the concentrations. The intrinsic currents are governed by the following intrinsic conductances, either depolarizing or hyperpolarizing Vm: Voltage-gated (NaV) and persistent (NaP) Na^+ channels, voltage-gated (CaV) Ca^{2+} channels, voltage-gated (KV), leak (KLeak), fast A-type (KA-type), inwardly rectifying (KIR), slowly inactivating (KSI) and Ca^{2+}-dependent (KCa) K^+ channels, and finally a Ca^{2+}-pump/exchanger expelling Ca^{2+} ions from the intracellular compartment (Fig. 47). Extrinsic currents exist through the AMPA, NMDA and GABA receptors [116]. To summarize, in this model, the currents affects the membrane potential Vm through nine different intrinsic channels and three extrinsic channels (Fig. 47).

For all of these conductances we adapted the full parameter set from the original Averaged-Neuron model. The original Averaged-Neuron model did not consider changes in extracellular ion concentrations as variables, but as fixed constants. We extended the Averaged-Neuron model

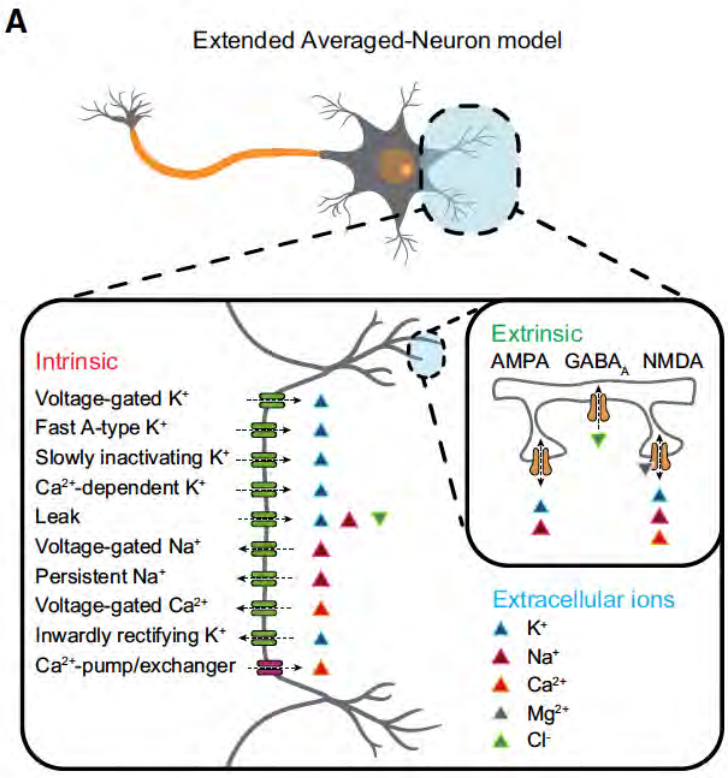

Figure 47: *Schematic diagram of the extended Averaged-Neuron model containing intrinsic ion channel conductances and Ca^{2+}-pumps, extrinsic synaptic ion channel conductances and extracellular ion concentrations.*

by introducing extracellular and intracellular ion concentration dependencies, by implementing Nernst and Goldman-Hodgkin-Katz equations for calculating reversal potentials for all receptors and channels. The reverse potential thus takes the form:

$$V_i = \frac{RT}{zF} ln\Big(\frac{\text{ion outside cell}}{\text{ion inside cell}}\Big) \tag{93}$$

We also added a Mg^{2+} dependency for the NMDA receptor, that satisfies the criteria that higher Mg^{2+} leads to lower current [123, 124] (Fig. 47). A detailed mathematical description of the extended Averaged-Neuron model is provided in Appendix D.

4.2.2 Analysis of Firing Patterns in Sleep Reveals Two Different Frequencies

Based on experimental measurements we sought to use the initial extracellular ion concentration parameter set found in sleep:

- $[K^+]o = 3.5mM$
- $[Ca^{2+}]o = 1.5mM$
- $[Mg^{2+}]o = 0.8mM$

The remaining intra- and extracellular ion concentrations were maintained constant and values were based on previous in vivo and in vitro experimental measurements [125, 126, 127, 128, 129, 130]. With this we found that the membrane potential showed a spiky, oscillatory pattern, in a way

that remarkably closely recapitulated previous recordings obtained from neurons during slow-wave sleep [105] (Fig. 48A). This model generated wave forms of slow oscillatory patterns, consisting of alternating periods of Vm depolarization and spiking (termed upstates) and Vm hyperpolarization and silence (termed downstates). This oscillatory pattern is coupled to the dynamics of intracellular Ca^{2+} concentration, and therefore we also found oscillations in this trajectory, with upstates generating a $\approx 8\mu M$ rise in $[Ca^{2+}]i$ (Fig. 48B). The preferential slow Vm oscillations were evident when analyzing frequency components for 10 simulations, showing a high prevalence of 1-4 Hz delta power (Fig. 48C). To investigate this further we also calculated the moving standard deviation (SD) of the mean Vm (window size 20 ms). In this way the spikes are effectively smeared out, and we found this measure varied between 0.1 and 3 mV (Fig. 48D), similar to the seminal recordings obtained [105]. Finally, we calculated the distribution of the running mean, and found that this showed a clear bi-modal distribution, with peaks around -70 and -50 mV, reflecting the equal presence of up- and downstates separated by 20 mV (Fig. 48E).

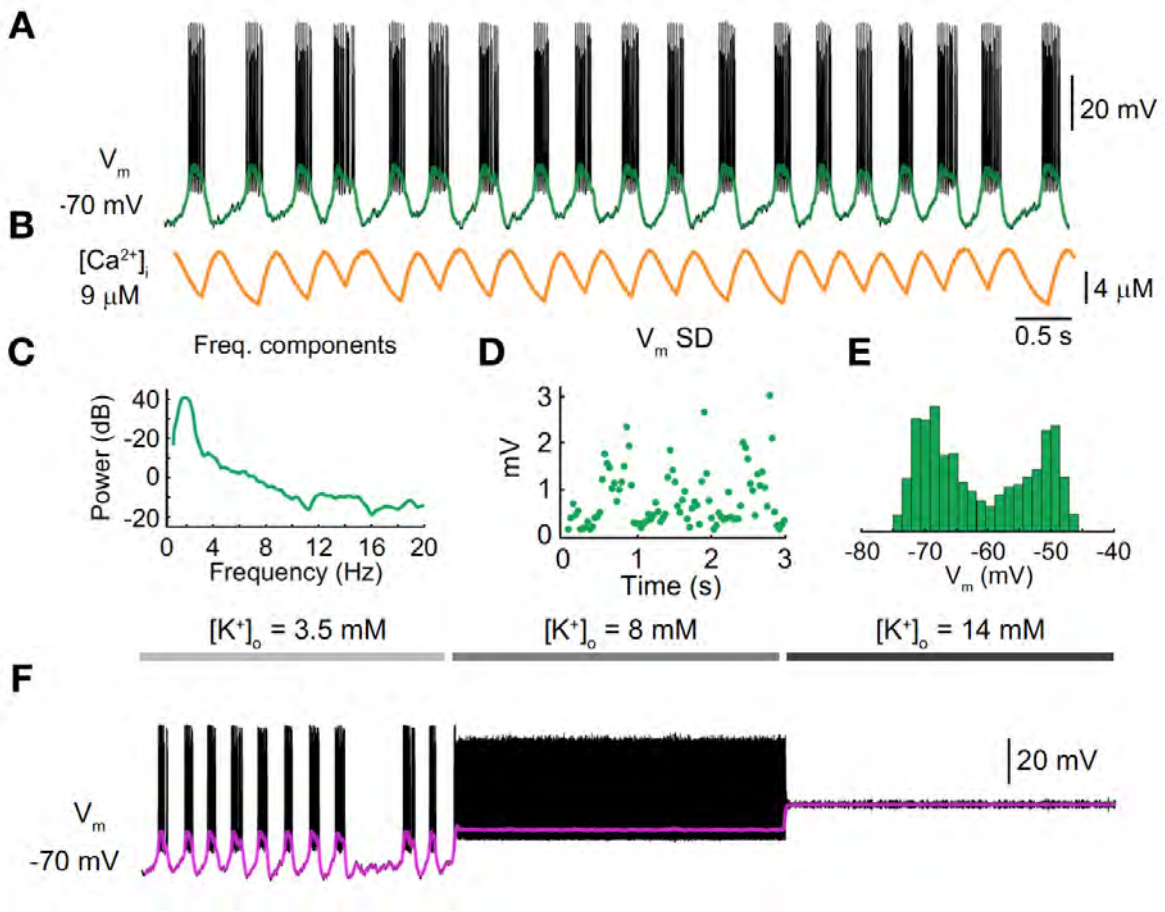

Figure 48: *A) Representative slow-wave-sleep membrane potential (Vm)firing pattern. B) Intracellular Ca^{2+} concentration ($[Ca^{2+}]i$) with initial extracellular ion concentration parameter set ($[K^+]o = 3.5mM$, $[Ca^{2+}]o = 1.5mM$ and $[Mg^{2+}]o = 1.1mM$). C) Vm frequency spectra. D) Standard deviation (SD) of mean Vm. E) Mean Vm distribution. F) Representative Vm firing pattern with 3.5, 8 or 14 mM $[K^+]o$.*

To assess the validity of our implemented ion concentration dependencies in the model, we

sought to test the effect of variations in external increasing $[K^+]o$ from 3.5 to 8 to 14 mM. The resting Vm of neurons is mainly determined by K^+-permeable conductances, and Vm is known to be highly sensitive to changes in $[K^+]o$ from experiments [113]. Thus, we would expect drastic Vm changes when pushing $[K^+]o$ to extremes if the model should be valid. When increasing $[K^+]o$ from 3.5 to 8 mM we observed a qualitative change in Vm dynamics and the alternating up- and downstates disappeared and instead Vm was maintained depolarized and the neuron fired continuously at rates of $100Hz$, giving rise to a tonic elevation in $[Ca^{2+}]i$ at $9\mu M$ (Fig. 48F). This finding is in congruence with in vitro slice experiments, inducing epileptic seizure activity by increasing $[K^+]o$ to 7.5 or 8.5 mM in the external media [131, 132]. We now further elevated $[K^+]o$ to 14 mM and observed completely abolished action potential firing, releasing the tonic $[Ca^{2+}]i$ elevation (Fig. 48F). This effect is likely explained by depolarization-induced conductance blockage, where NaV channels are kept hostage in the inactivated configuration, resulting in the inability of the neuron to fire [133, 134]. This observed effect appears similar to what is seen during in vivo cortical spreading depression, where $[K^+]o$ reaches levels above 12 mM [135], leading to annihilation of neural activity in the affected brain area [136, 137]. Therefore these results demonstrate that the model very closely recapitulates cardinal properties of Vm dynamics during sleep and is expectedly sensitive to changes in extracellular ion concentrations. We now went on to test how the experimentally measured values would affect the firing patterns in the neurons.

4.2.3 Changes in Ion Concentrations Does Not Lead to State Transition

It was recently suggested that changes in extracellular ion concentrations ($[K^+]o$, $[Ca^{2+}]o$ and $[Mg^{2+}]o$) could control state-dependent activity patterns during sleep and wakefulness, and that the measured shifts in ion concentrations, are sufficient to mediate the transition from sleep to awake [106]. However, due to the intimate relation between neural activity and ionic changes, establishing causality in vivo is non-trivial. Therefore it is interesting to investigate this through mathematical modelling, and to investigate the effect of ion concentration changes on the sleep to awake transitions in the model, we used the previously measured extracellular ion concentrations during sleep [106] (Fig. 49A).

$$[K^+]o = \begin{cases} 3.9mM \text{ for sleep} \\ 4.5mM \text{ for awake} \end{cases}$$

$$[Ca^{2+}]o = \begin{cases} 1.35mM \text{ for sleep} \\ 1.2mM \text{ for awake} \end{cases}$$

$$[Mg^{2+}]o = \begin{cases} 0.8mM \text{ for sleep} \\ 0.7mM \text{ for awake} \end{cases}$$

With sleep ions, Vm dynamics closely recapitulated sleep with alternating up- and downstates as we just have observed. When we switched to awake ions no apparent change in Vm dynamics was obvious, except a subtle tendency to have more spikes per upstate (Fig. 49B), which results in longer upstate $[Ca^{2+}]i$ (Fig. 49C). To quantify this, we analyzed Vm frequency components, we found no significant difference in 1-4 Hz delta power between sleep and awake ions (Fig. 49D). Also mean Vm SD, a frequently used indicator for neuronal state [103, 105, 138], was similar for sleep

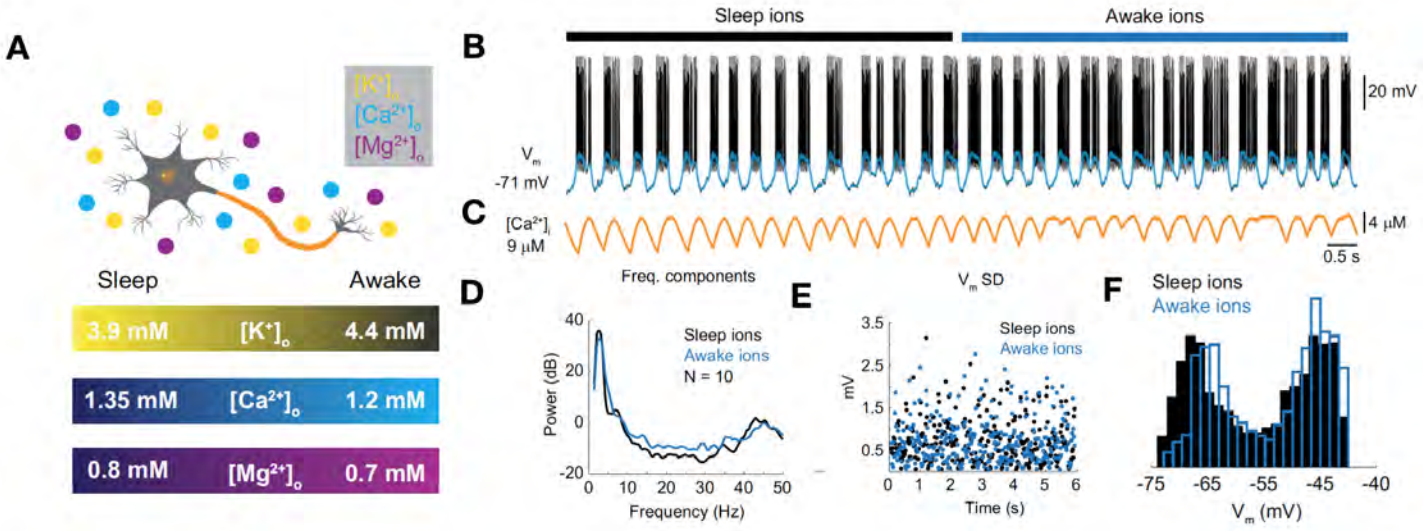

Figure 49: *A) Representative slow-wave-sleep membrane potential (Vm)firing pattern. B) Intracellular Ca^{2+} concentration ($[Ca^{2+}]i$) with initial extracellular ion concentration parameter set ($[K^+]o = 3.5mM$, $[Ca^{2+}]o = 1.5mM$ and $[Mg^{2+}]o = 1.1mM$). C) Vm frequency spectra. D) Standard deviation (SD) of mean Vm. E) Mean Vm distribution. F) Representative Vm firing pattern with 3.5, 8 or 14 mM $[K^+]o$.*

and awake ions (Fig. 49E). Finally, mean Vm showed a clear bi-modal distribution with both sleep and awake ion concentrations (Fig. 49F). Taken together, shifting the extracellular concentrations of K^+, Ca^{2+} and Mg^{2+} with the same magnitude as measured in vivo failed to induce a significant state transition. This suggests that ion changes of this magnitude alone is not sufficient to produce a transition from sleep to awake. We evaluated the effect of switching from sleep to awake ion concentrations, for several values of initial parameters, but these analyses showed the same overall result.

4.3 Inhibition of Gating Channels Combined with Ion Changes Lead to State Changes

Early seminal, and more recent work, has implicated the KCa channel in Vm activity patterns observed during sleep and wakefulness [105, 116]. After a rise in $[Ca^{2+}]i$ this channel generates an outward K^+ current that hyperpolarizes Vm. In this way, the KCa channel has been proposed to be a key component for generating downstates during sleep [105]. Opposite, with elevated levels of neuromodulators such as norepinephrine and histamine, which is found during wakefulness [102], the KCa channel is partially inhibited [139, 140] and this could potentially induce the sleep to awake transition by preventing the occurrence of downstates [105] (Fig. 50A-B). From our simulations of membrane potential during sleep, we observed a close relation between mean Vm and $[Ca^{2+}]i$ oscillations with a 0.12 s lag for $[Ca^{2+}]i$ (Fig. 50C). This led us to analyze the relation between $[Ca^{2+}]i$ and the KCa current. Not surprisingly, we found a -0.013 s lag between $[Ca^{2+}]i$ and KCa currents (Fig. 50D). The largest KCa currents occurred when mean Vm was at the peak of depolarization, and Vm rapidly hyperpolarized following a peak KCa currents. This suggested

that KCa mediated outward currents could be key for generating downstates.

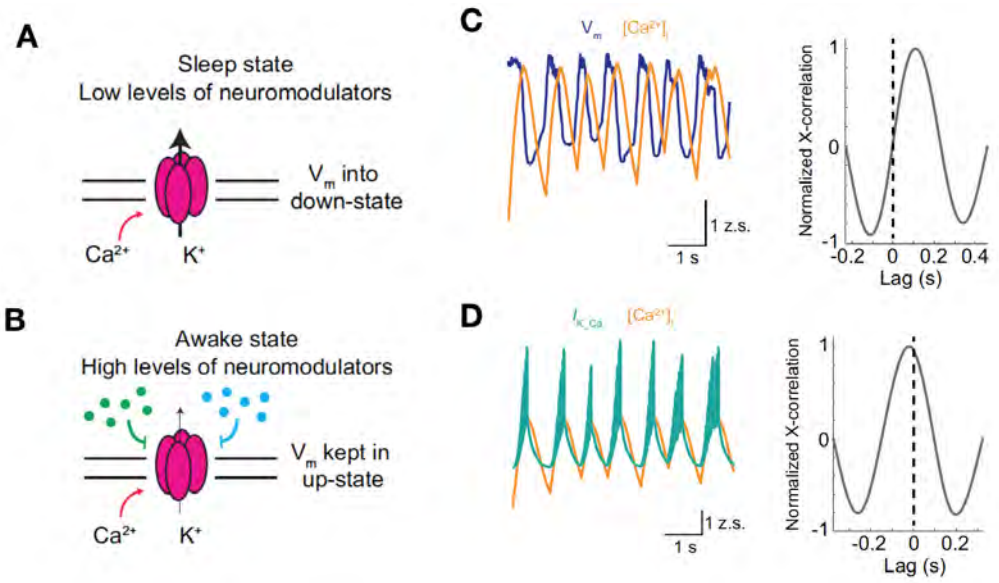

Figure 50: *A-B) Schematic diagram of speculated sleep and awake state and neuromodulator-mediated decrease of Ca^{2+}-activated K^+ channel conductance ($gKCa$). C) Left: Relation between membrane potential (Vm) and $[Ca^{2+}]i$. Right: Cross-correlation between Vm and $[Ca^{2+}]i$. D) Left: Relation between Ca^{2+} -activated K^+ channel current (IK_{Ca}) and $[Ca^{2+}]i$ Right: Cross-correlation between IK_{Ca} and $[Ca^{2+}]i$.*

4.3.1 Inhibition of the KCa Channel Can Induce a State Transition

We now investigated the role of the KCa channel and to mimic the elevation in neuromodulator levels seen during wakefulness [102, 139], we reduced the conductance parameter of the KCa channel ($gKCa$) over time (100% = 2.3 mS/cm^2, 75% = 1.73 mS/cm^2 and 50% = 1.15 mS/cm^2). In this the sleep ion concentrations are being kept constant throughout. When $gKCa$ was reduced to 75% we observed only a tendency toward a state change, with longer upstates and fewer downstates, whereas reducing gKCa to 50% produced a definite state change, almost completely preventing Vm from entering downstates, thereby producing tonic firing (Fig. 51A). This was also observed for $[Ca^{2+}]i$ that was kept at a high level in the tonic firing state (Fig. 51B). This was investigated further, and we found a non-significantly reduced 1-4 Hz delta power for the 75% inhibition, whereas 50% induced a significantly reduced delta power (Fig. 51C). Mean Vm SD did not give a clear signal, with less than one standard deviation between the states (0.74 ± 0.55 mV for 100% and 0.590.32 mV for 50%) (Fig. 51D). Finally, mean Vm distributions for 100% and 75% $gKCa$ appeared bi-modal whereas the 50% $gKCa$ distribution was clearly uni-modal (Fig. 51E). We performed a bifurcation analysis, making gradual changes in the other conductance parameters. This revealed that the parameter of$gKCa$ was the most important parameter for creating state change in firing dynamics. Changing the conductance of almost all other channels had very little effect, except for the parameter $gCaV$ that also had the potential to create a transition, but this was still less potent than $gKCa$ (Fig. 51F). Overall, this demonstrates that the KCa channel most likely plays a dominant role in sleep Vm activity patterns and inhibiting this channel, assumedly

via increased levels of neuromodulators, can be sufficient to induce a transition to a state governed by high frequency firing patterns. However, decreasing the conductance of this channel by 25% was not sufficient to invoke a full state transition, which suggests a threshold level for when the state is shifted from sleep to wakefulness.

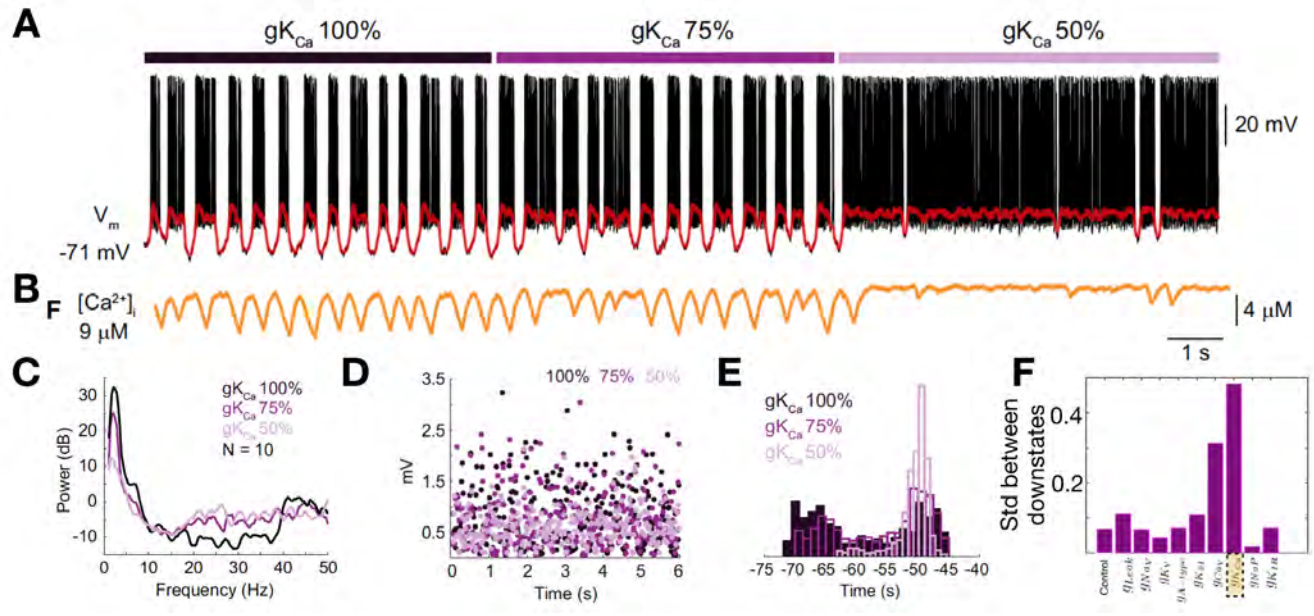

Figure 51: *A) Representative Vm firing pattern and with 100, 75 or 50% gKCa. B) Representative $[Ca^{2+}]i$ with 100, 75 or 50% gKCa. C) Vm frequency spectra for 100, 75 and 50% gKCa. D) Standard deviation (SD) of mean Vm (spikes removed) with 100, 75 and 50% gKCa. E) Mean Vm distribution for 100, 75 and 50% gKCa F) The standard deviation in the time between down states. Each gating parameter at 70%*

4.3.2 Ion Concentrations Controls the Threshold For State Transition

As we observed in the section above, changing extracellular ions from sleep to awake concentrations was not in itself sufficient to induce a state transition. However, we speculate if awake ions could affect the threshold for invoking the KCa channel-dependent state change, and in this way be permissive and modulatory on state changes (Fig. 52A-B). To investigate this, we changed the extracellular ions from sleep to awake concentrations, while reducing gKCa to 75 and 50% as in the previous section. In contrast to what we found in Fig. 51, when we reduced gKCa to 75% and included the awake ions, we observed a state transition with Vm kept in the upstate for long periods and with few downstates (Fig. 52C). This was also seen for $[Ca^{2+}]i$ that never reached low levels (Fig. 52D). We note that this state has the promising feature that it is not tonically firing with high frequency even though it clearly represents a state different from sleep since the neurons fire with higher frequency in longer periods. Thus we believe this could represent an important state of wakefullness. As before, when reducing gKCa to 50% the state change was pronounced, with Vm tonically depolarized and the neuron continuously firing (Fig. 52C). We found a significant reduction in 1-4 Hz delta power with the combination of 75% gKCa and awake ions, as well as with 50% gKCa and awake ions (Fig. 52E-F). The prevalence of delta power was

significantly smaller with 50% gKCa compared to 75% gKCa. We believe that this represents two different states of wakefullness, quiet awake and active awake, which has previously been reported experimentally [141, 142]. Finally, mean Vm distribution was shifted towards uni-modality with 75% gKCa and awake ions and this was even more apparent with 50% gKCa and awake ions (Fig. 52G). Taken together, these data suggest that the awake ion concentrations reduces the threshold for invoking a sleep to awake state transition. We found that $[K^+]o$ is the most potent mediator of this ion concentration mediated effect, but the combined concurrent shift in all three ion species triggers the greatest sleep to awake state change (Fig. 52H). What is more, the results points to and supports current in vivo evidence that the awake state comprise multiple sub-states, with differences in delta oscillations and mean Vm dynamics.

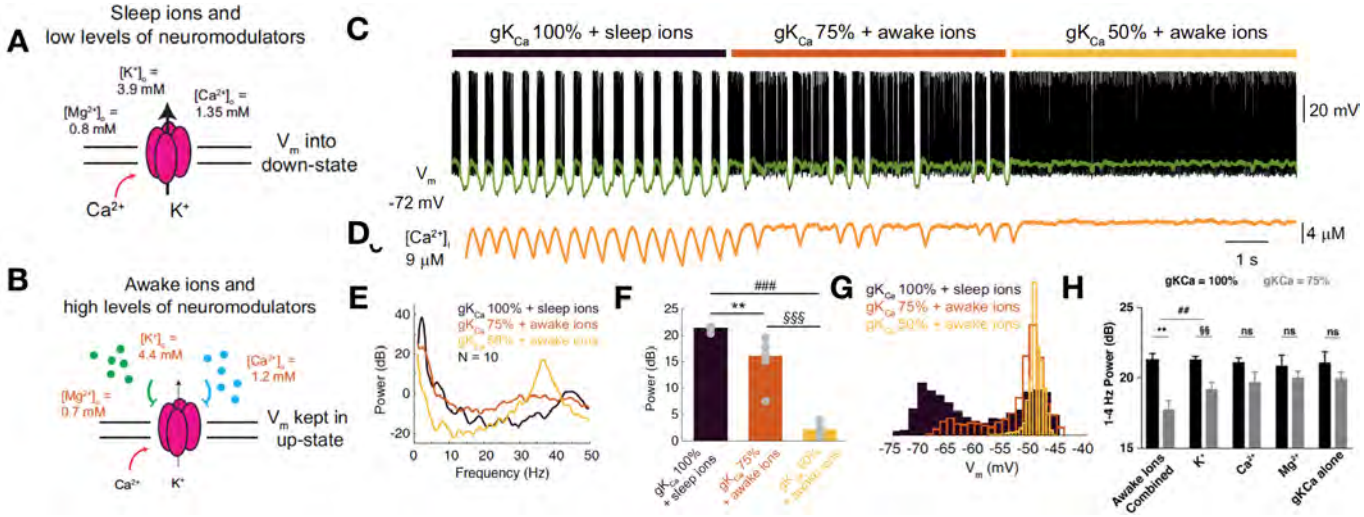

Figure 52: *A-B) Schematic diagram of speculated interaction between extracellular ion concentrations, neuromodulators and Ca^{2+}-activated K^+ channel conductance (gKCa) during sleep and wakefulness. C) Representative membrane potential (Vm) firing pattern with 100% gKCa + sleep ions ($[K^+]o$ = 3.9 mM, $[Ca^{2+}]o$ = 1.35 mM and $[Mg^{2+}]o$ = 0.8 mM), 75% gKCa + awake ions ($[K^+]o$ = 4.4 mM, $[Ca^{2+}]o$ = 1.2 mM and $[Mg^{2+}]o$ = 0.7 mM) or 50% gKCa + awake ions D) Representative ($[Ca^{2+}]i$). Parameters as in C. E) Vm frequency spectra for 100% gKCa + sleep ions, 75% gKCa + awake ions or 50% gKCa + awake ions. F) 1-4 Hz delta power. Colors correspond to intervals in C. G) Mean Vm distribution. Colors correspond to intervals in C. H) Bar graphs showing quantifications for the effect of changing gKCa from 100 to 75% in combination with shifting only one or more ion species concentration on neuronal state changes, assessed by membrane potential 1-4 Hz delta power.*

4.3.3 Transition from Quiet Awake to Active Awake Mediated by Ion Concentrations

Having demonstrated that the awake ion concentrations are permissive for shifting Vm dynamics from sleep to awake, we next moved on to investigated the two apparent awake states in greater detail. In particular we were interested in the the role of extracellular ion concentrations on this transition. For this, we speculate that an arousal-related "hyper-awake" ion composition (in addition to the sleep and awake ion compositions) might exist and could be involved in shifting Vm

into the active awake state [143, 144, 104, 145, 146]. As an estimate, we changed extracellular ions with the same magnitude as observed between sleep and awake for formulating the hypothesized hyper-awake ion concentrations (Fig. 53A)

- $[K^+]o = 4.9$ mM
- $[Ca^{2+}]o = 1.05$ mM
- $[Mg^{2+}]o = 0.6$ mM

We initially simulated the quiet awake state (75% gKCa and awake ions) and then shifted the extracellular ion concentrations to hyper-awake ions while maintaining $gKCa$ at 75% (Fig. 53B-C). We observed that with the awake ions Vm alternated between long periods of firing (upstate) and occasional silent downstates (Fig. 53B), similar to described in quiet awake rodents [141, 142]. When we shifted to hyper-awake ion concentrations we observed an almost complete annihilation of downstates and Vm was maintained in the depolarized upstate with continuous firing as a result (Fig. 53B), which resulted in a constantly elevated level of $[Ca^{2+}]i$. Analyzing these further, we found that with hyper-awake ions, the 1-4 Hz delta power significantly decreased and 25-45 Hz gamma power significantly increased (Fig. 53D-F). This result is alike what has been observed when rodents transition from the quiet to the active awake state [147, 145, 148]. Finally, the mean Vm distribution was shifted towards the depolarized upstate with hyper-awake ions, representing the lack of downstates (Fig. 53G). All of these results are in congruence with in vivo recordings obtained in awake rodents, where the active awake state is characterized by a depolarized Vm and a lack of downstates[141, 142, 138]. Taken together, these results demonstrate that subtle changes in extracellular ion concentrations are sufficient for shifting Vm dynamics from the quiet awake state to the active awake state, which recapitulates key properties of the active awake state Vm dynamics. Testing the changing ion concentrations indivudially revealed that shifting $[K^+]o$ alone was sufficient for invoking this state transition, but the combined effect of shifting all three ion species was more effect full (Fig. 53H), suggesting a biological importance of combined extracellular ion changes. Therefore we advocate that the existence of such hyper-awake ion concentrations should be investigated in future in vivo experiments, and even more important the ability to causally invoke the proposed awake state changes.

4.4 Chaotic dynamics and synchrony in neurons

At this point we had found that awake ion concentrations are permissive for shifting the state from sleep awake (Fig. 52), and that hyper-awake ion concentrations can invoke the transition from quiet to active awake (Fig. 53). However we wanted to investigate the nature of the state-dependent Vm dynamics in more physical terms, as we altered extracellular ion concentrations, to characterize if a qualitative transition did occur.

4.4.1 Transitions Between Brain States are Governed by Chaotic Dynamics

First, we performed a deterministic simulation of the sleep stat. Here we found the dynamics of Vm to be stable and periodic in the sense that the pattern was self-repeating (Fig. 54A). This therefore had to be a closed trajectory with several small loops that occurs when the neuron fires. This is best is visualized and analyzed in a 3-dimensional phase space spanned by 3 variables (we chose Vm, $[Ca^{2+}]i$ and n_K) (Fig. 54B). Thus the Vm dynamics in the sleep state is well defined

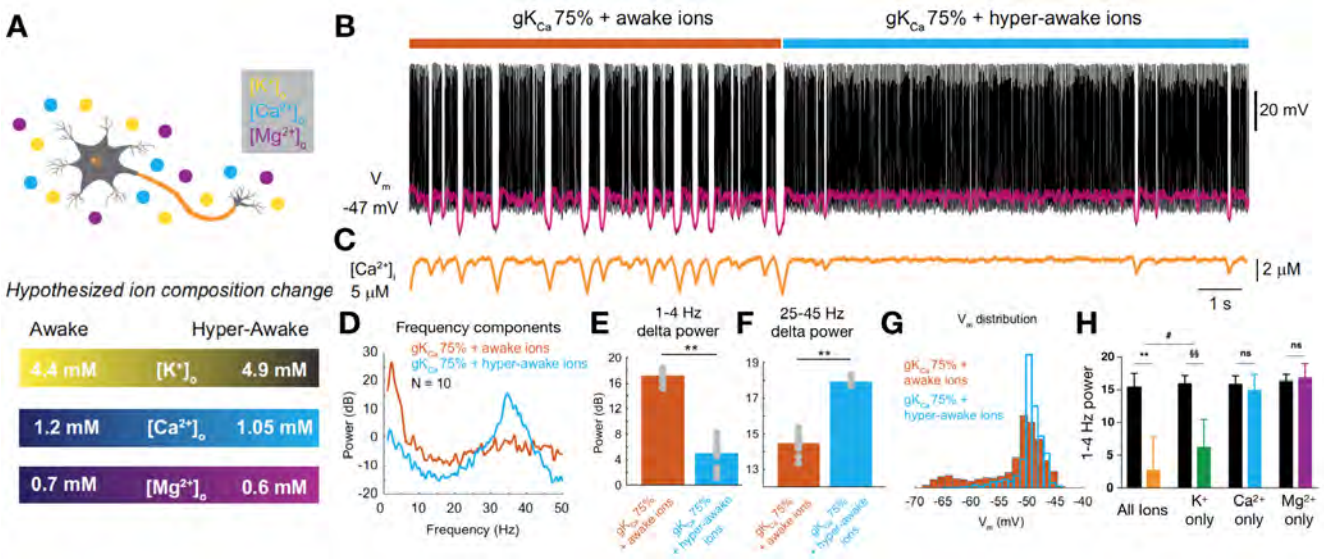

Figure 53: *A) Schematic diagram of hypothesized shift in extracellular ion concentration from awake to hyper-awake. Awake:* $[K^+]o = 4.4$ *mM,* $[Ca^{2+}]o = 1.2$ *mM and* $[Mg^{2+}]o = 0.7$ *mM. Hyper-awake:* $[K^+]o = 4.9$ *mM,* $[Ca^{2+}]o = 1.05$ *mM and* $[Mg^{2+}]o = 0.6$ *mM. B) Representative membrane potential (Vm) firing pattern with 75% gKCa + awake ions and 75% gKCa + hyper-awake ions. Below is an expansion of Vm dynamics. C) Representative* ($[Ca^{2+}]i$)*. Same parameters as in B. D) Vm frequency spectra for 75% gKCa + awake ions and 75% gKCa + hyper-awake ions. E) 1-4 Hz delta power for 75% gKCa + awake ions and 75% gKCa + hyper-awake ions. F) 25-45 Hz gamma power for 75% gKCa + awake ions and 75% gKCa + hyper-awake ions. G) Mean Vm distribution for 75% gKCa + awake ions and 75% gKCa + hyper-awake ions H) Bar graphs showing quantifications for the effect of changing only one or more ion species concentration on neuronal state changes, assessed by membrane potential 1-4 Hz delta power, while maintaining gKCa at 75%*

by regular and stable oscillations. Moving on to the awake state, we considered which ion currents are most important for changing the state from sleep to awake. From what was observed in the awake state (Fig. 51 and Fig. 52), we characterize the transition in terms of 1) the rate of which a silent downstate period is initiated, 2) the mean time duration of a spiking upstate period and 3) the SD of this measure. These numbers combined describe much of the change in Vm dynamics that happens between the sleep and awake state. By affecting only one of the currents at a time by the change in extracellular ion concentrations from sleep to awake, we found the largest ion concentrations-mediated effect was produced on the CaV-mediated current (Fig. 54C). This was even better observed if we combined the sleep to awake ion-mediated changes in CaV current with a small perturbation in gKCa (Fig. 54C). Thus, here we found that affecting only the CaV channel by sleep to awake ion concentration changes can account for much of the irregularities of the awake state, and that a similar ion-mediated effect can occur for the extrinsic AMPA receptor and this induces a big step towards the awake state (Fig. 54C).

As observed in the sections above, with the combination of 75% gKCa and awake ions, Vm dynamics are more irregular and significantly long periods of upstates and spiking can occur before a silent downstate is recovered. We hypothesized that this could be due to the fact that Vm dynamics

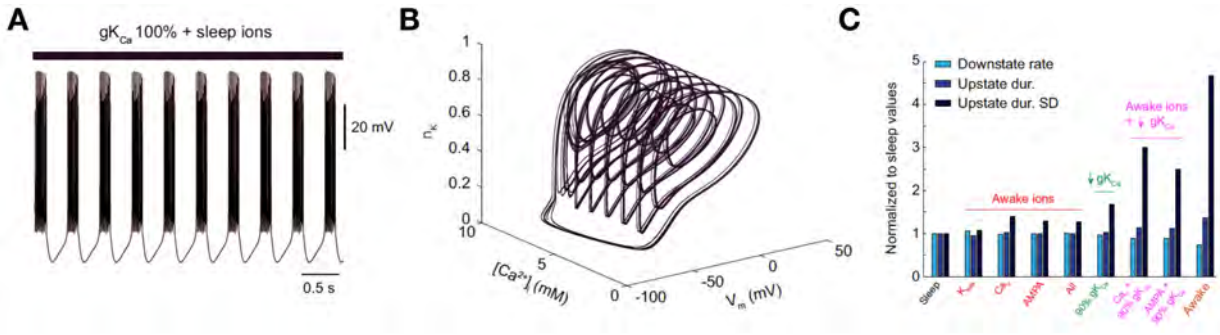

Figure 54: *A) Representative membrane potential (Vm) firing pattern in the sleep state with 100% gKCa and sleep ion composition ($[K^+]o$ = 3.9 mM, $[Ca^{2+}]o$ = 1.35 mM and $[Mg^{2+}]o$ = 0.8 mM). B) Phase space plot showing the trajectory in the sleep state. C) Measures for the affect of different ion channel-mediated currents on Vm dynamics. Light blue is the average rate of initiating a silent downstate periods. Blue is the average duration of the spiky upstate periods. Dark blue is the standard deviation in the duration of upstate periods. All measures are normalized to the sleep state..*

in the awake state was chaotic, and tested this by applying deterministic simulation with high precision. We know that deterministic chaos is defined so by the fact that two initial conditions, being infinitesimally perturbed, will have diverging trajectories as time evolves. Therefore one cycle will never repeat itself and no closed cycles can exist on a strange attractor [16]. We tested this by perturbing the initial concentration of $[Ca^{2+}]i$ by only 1 pM (10^{-12}) and found that even though Vm trajectories are very similar in the beginning, after some seconds they have completely different values (Fig. 55A). Another way of visualizing the chaotic nature of the awake state Vm dynamics can be seen in Fig. 55B, where the trajectory is shown in 3 dimensions. Here it seems that the trajectory never repeats, and that the dynamics are irregular compared to the oscillations in the sleep state. Furthermore it is evident that the trajectory "fills" up large parts of the phase space, which is a fingerprint of the fractal dimension of the strange attractor. To test if this had the signature of chaos, we calculated the difference in all dimensions between two trajectories and found that they diverge in a complex manner, but that the general trend seems to be exponential. This is what we would expect from a chaotic system with a positive lyapunov exponent [16] (Fig. 55C).

As shown in previous sections, the sleep to awake state transition that we have now characterized is likely not the end of the story and an additional active awake state exist [141, 142], that is controlled by parameter set of hyper-awake ion concentrations. We analyzed the deterministic hyper-awake Vm dynamics and found that it is a continuously spiking process with no occurrence of silent downstates (Fig. 56A), making it likely to correspond to an aroused and alert active awake state [141, 104]. Here we find that this state is not chaotic, but rather a well-defined, high frequency 3-cycle (Fig. 56B). This means, that the initial transition from the sleep state, can be regarded as a mediator between two robust states (sleep and active awake), defined by closed cycles. We consider it of great importance, that the dynamics of Vm changes from sleep to the awake state and even further into an active awake state, using effects of chaotic dynamics. To study how this chaotic state could work as a mediator between the sleep and active awake we performed

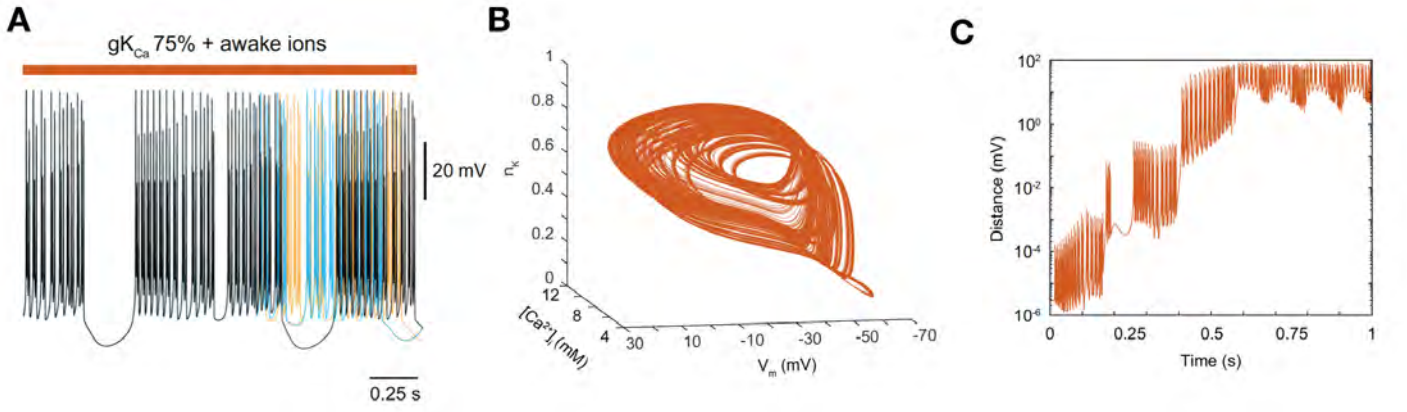

Figure 55: *A) Representative Vm firing patterns with 75% gKCa, awake ion composition ($[K^+]o$ = 4.4 mM, $[Ca^{2+}]o$ = 1.2 mM and $[Mg^{2+}]o$ = 0.7 mM) and 1 mV perturbations showing the development of different trajectories. B) Phase space plot showing the trajectory in the awake state with 75% gKCa and awake ion composition. C) Difference between two Vm trajectories in the awake state with 75% gKCa and awake ion composition*

the Vm simulation while applying white noise. Since the most striking difference between the sleep and awake states is the occurrence/lack of silent downstates, we used the number of silent periods as a measure to characterize the gradual transition from sleep to the active awake state. We investigated this for four different noise levels while we linearly perturbed the values of $[K^+]o$, $[Ca^{2+}]o$ and $[Mg^{2+}]o$ from the sleep to the hyper-awake concentrations. By using this measure, we find that the complete state transition is a continuous process for the noise levels tested, and shifting extracellular ion concentrations is sufficient to fully transition from the quiet awake to the active awake state in a smooth way.

In summary, we found that the transition from sleep to full wakefulness is modulated by changes in extracellular ion concentrations and that the sleep state is governed by a stable limit cycle whereas the quite awake state is chaotic, which ensure a smooth and robust transition between the sleep state and the active awake state.

4.5 Discussion and perspectives

It is generally believed that states of neurons can influence sensory processing and perceptions [149, 102, 102, 103, 148]. In this project, we have shown that the concentrations of extracellular ions influences the neuronal states, and that if can guide the KCa channel-mediated transition between sleep and awake. Furhtermore we found that they can themselves drive the switch from quiet awake to active awake. Thereby is the switch between sleep and awake a more robust AND gate, whereas the transition between the two awake states is more fluent and can be controlled by ions alone.

Through the simulations of the model, we showed how the state change from sleep to awake is characterized by a transition from stable cycles to chaotic dynamics. Here we argue that chaotic dynamics, mediates a smooth transition between the quiet awake and active awake state, remarkably robust to intrinsic noise.

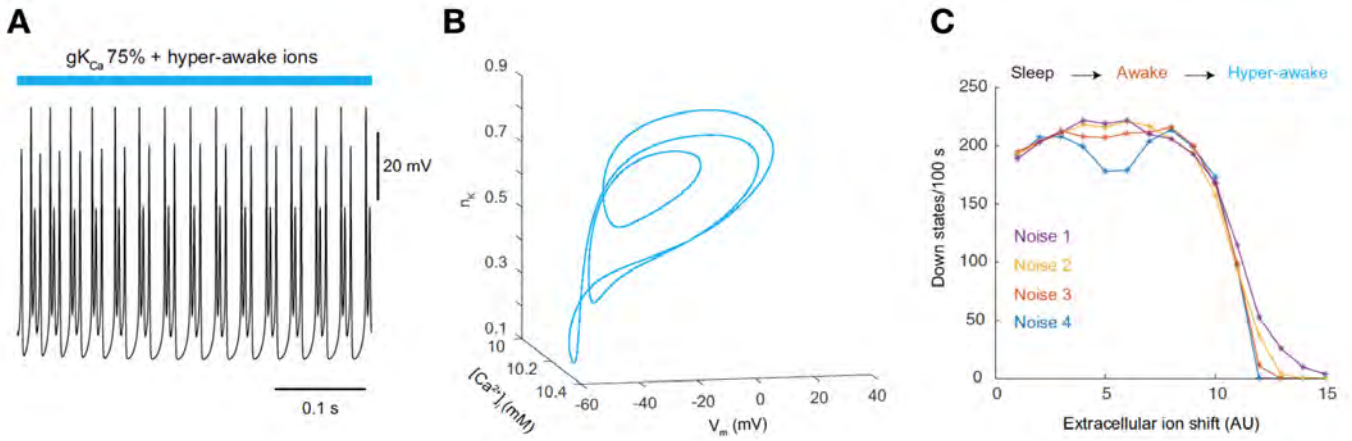

Figure 56: *A) Representative Vm firing pattern in the awake state with 75% gKCa and hyper-awake ion composition ($[K^+]o$ = 4.9 mM, $[Ca^{2+}]o$ = 1.05 mM and $[Mg^{2+}]o$ = 0.6 mM). B) Phase space plot showing the trajectory in the awake state with 75% gKCa and hyper-awake ion composition. C) Number of silent periods for a period of 100 s as the values of the ions are perturbed linearly from values for the sleep state to values of the active awake state. On the x-axis 1 corresponds to sleep state, and 9 corresponds to the awake state*

In experiments it has been shown that ion concentrations do change between different states, and studies have implicated that the ion concentrations causally drive the sleep to awake transitions [106]. However due to the intimate relation between neural activity and ionic changes, causality is extremely difficult to establish in vivo. Therefore, investigations through mathematical modelling can be helpfull, and in our model, exclusively shifting ion concentrations by the same magnitude as measured in vivo was insufficient to cause a complete sleep to awake state transition (Fig 49). This suggests that other parameters needs to change in time, in order to transition the neuron into to the awake state. This might seem as an advantageous built-in gate mechanism, since extracellular ion concentrations are affected by changes in neuronal firing [108, 109, 110, 111], and global brain states should be robust to such small ion fluctuations.

We then found that decreasing the conductance of the KCa channel is a powerful way for inducing the sleep to awake state change (Fig 51), in congruence with previous work implicating this channel as a prime mechanism for Vm downstates [139, 140, 105, 116]. Shifting to the awake ion concentrations was permissive to decreasing the conductance of the KCa channel (Fig 52); advocating that changes in the extracellular ion concentrations does affect the state transition. Changing the global environment through ion concentrations, in addition to modulating selective intrinsic ion channels, might be a simple, yet powerful, way for shifting the state of entire brain-wide neuronal networks and ultimately for changing the behavioral state. Transitions between states in living organisms are fundamental for the functions and complexity of that organism and failure to regulate these transitions properly, might be harmful for cells. In this regard, the state transition described here for neuronal Vm dynamics has the beneficial property, that it represents a gradual change between the two stereotypical behavioral states.

It is increasingly appreciated that the awake state is comprised of at least two sub-states, namely quiet awake and active awake [143, 141, 144, 103, 104, 145, 146]. Rodent studies have suggested

that the ongoing . It has been suggested that the nature of the awake state, shapes how the brain processes sensory inputs, for instance, the gain of visual-evoked responses in visual cortex is increased when neurons are in the active awake state, whereas auditory responses in auditory cortex are suppressed [143, 103, 104, 150]. This indicates that the brain state powerfully and differentially scales what sensory modalities are up- and down regulated at a given moment in time for optimizing sensory processing and neural computations. Based on this, we hypothesized, that in addition to sleep and awake extracellular ion concentrations [106], a hyper-awake ion composition might exist (Fig 53). When KCa was kept partially inhibited (75% gKCa), shifting from the awake to the hyper-awake ion concentrations produced a state change alike to what is observed when rodents transition from quiet to active [141, 138]. This means that this state transition is ion-mediated, and it was characterized by a significant increase in the high frequency spikes leading to a uni-modal Vm distribution (Fig 53). These reasults were similar to what has been observed in vivo with intracellular recordings from cortical neurons in behaving rodents. Therefore it is tempting, that the subtle concerted changes in extracellular ion concentrations, could be a key mechanism for the rapid and often-occurring state shifts in the awake brain, that allow sensory processing and neural computations to be rapidly modified based on the different situational demands.

One of the key findings in this study, is the chaotic dynamics in the quiet-awake state. We believe there are several intriguing elements in a chaotic transition to the awake stat. Firstly, since not only one, but several, parameters are changed in the sleep to awake state transition, chaotic dynamics is a clever way for the system to make a path-independent transition between the two states. Due to the never repeating trajectories, the system does not change significantly if, for example, the changes in $[Ca^{2+}]o$ occur before $[K^{+}]o$ or vice versa. By this we mean that the neuron can in chaos gradually change the statistics of the neuronal dynamics, but in a short period of time, the dynamics can be regarded as path independent. Secondly, we believe that chaotic dynamics is an important property of neurons in the awake state since one would expect that neurons in this state needs the capacity to create a variety of different combinatorial outputs on a population level. If the neuronal dynamics in the awake state were purely stable limit cycles differing in period, small differences in incoming inputs would lead to very small differences in output firing, and thus information encoding. However since they are governed by chaotic dynamics, the sensitivity to the always existing small perturbations that accompanies external stimulation, can lead to a much more complex variety of outcomes that likely is highly important and necessary for higher-order neuronal computations. Thirdly, it is intriguing to imagine that since all neurons are governed by the dynamics of a stable limit cycle in the sleep state, they have the potential to synchronize their firing outputs through their common oscillations. Now, perturbing the system could change the period of oscillations but would not necessarily destroy this activity synchrony between neurons. However, as the awake state is chaotic, this population synchrony would naturally disappear. In this way, the awake state would make each neuron more independent, since it is no longer "bounded" by the dynamics of the state, and the specific feature-selective inputs to each neuron can have a great effect on the firing output for that particular neuron in the end.

To sum up, this project uncovers an important function of extracellular ion concentrations and chaotic dynamics in neuronal state transitions. It is vital for complex organisms, that the sleep to wake transition is strictly controlled and well regulated to avoid diseases such narcolepsy or insomnia. Here, the concentration of extracellular ions can be a key parameter for neuronal state

changes and these state transitions are governed by chaotic dynamics. Concerted regulation and shifts in ion concentrations therefore expands the toolbox for controlling state-dependent activity, and thus needs to be considered as an integrated mechanism in future investigations of what determines ongoing activity and state transitions in the brain.

5 Investigation of the Spatiotemporal Landscape of Dopaminergic Denervation in the Striatum

In this section the results of that forms the basis of **paper VIII** is presented and discussed. This work was in some way initiated in early 2013, as a work on my bachelor thesis in collaboration with Hussein Nasser Awada and Jakob Kisbye Dreyer as supervisor. Here we played with the model for extracellular dopamine concentration and made some crude estimations of the landscape of dopamine neurons after denervation. This idea was revisited in the spring of 2018, where we constructed all the models used in this section. The ideas and conclusions from this project was heavily improved through discussions with Rune Rasmussen and Mogens H. Jensen.
In this project we will use a mean field model for the extracellular dopamine concentration, and examine how the dynamics gets affected as the number of neurons is decreased, in the case of different compensatory mechanisms. We introduce an abstract, stochastic firing model and by using this in the mean field model, we show how the dynamics can show oscillatory behaviour, and how the signal to noise ratio is decreased for all compensation mechanisms as denervation of neurons progresses. Next we investigate the global distribution of the remaining neurons, and inspired by existing literature, we introduce three different models to represent denervation through various diseases and stresses. We find that depending on these, this can show completely different distributions of neurons and we argue that these variations might be some of the explanation for the variety of different symptoms that is found in patients with Parkinsons Disease.

5.1 Background to Neuronal Firing and Parkinsons Disease

Parkinson's disease (PD), first described by James Parkinson in 1817, is the second most common neurodegenerative disorder [151]. The disease is diagnosed clinically based on the presence of typical motor symptoms that include bradykinesia, limb rigidity, abnormal posture, and resting tremor [152]. These symptoms primarily result from the progressive loss of dopamine (DA) neurons in the substantia nigra pars compacta (SNc) [153], and the onset of symptoms emerge when a substantial fraction of dopamine neurons (¿ 70%) are lost [154, 155]. The main projection target of the SNc DA neurons is the striatum, a nucleus within the basal ganglia that is critically involved in motor behavior and motor learning [156, 157]. Within the striatum, DA exerts its main effects on medium spiny neurons (MSNs) through metabotropic receptors, grossly grouped onto Gs-coupled D1 and Gi-coupled D2 receptors [158, 159]: D1 receptor activation increases cAMP, whereas D2 receptor activation decreases cAMP in neurons. In turn, the level of intraneuronal cAMP affects how MSNs respond to glutamatergic inputs, with increased cAMP levels associated with increased excitability and vice versa [157]. Thus, the DA signaling in the extracellular space within the striatum powerfully regulates excitability and spiking of striatal MSNs [159]. The MSNs activity is a critical component in the direct and indirect pathway, which act in opposing ways to control movements [157]. In the parkinsonian brain, striatum-projecting DA neurons and their axon terminals are progressively lost, leading to striatal DA depletion and abnormal striatal activity with time. In spite of the cardinal role of failing DA levels for the development of PD, the precise nature of the striatal DA signaling at the time when symptoms occur and during disease progression is still debated and largely unresolved. In many biological systems physiology largely follows anatomy and connectivity. For example, the analysis of the uniquely organized primary

visual part of the cerebral cortex suggested unique aspects of visual processing and sensory relay, which were subsequently confirmed experimentally. Within the field of PD research, a major emphasis has been placed on understanding the molecular mechanisms causing neurodegeneration [160], but surprisingly little attention have been given to elucidating the spatial and temporal pattern of DA neuron loss, and how this relates to DA signaling and disease development. One reason for this might be the lack of resolution for non-invasive methodologies used in patients. Current clinical data measuring dopamine transporter densities, a correlate of DA neuron density, employs imaging modalities such as SPECT [161, 162], suffering from insufficient spatial resolution to resolve the organization of DA neurons within brain regions. On the other hand, DA signals and dopaminergic neuron spiking can be recorded by invasive techniques in experimental animals [163, 164] and by determining the DA neuron density at the recording site post-mortem one can correlate DA neuron density to DA signaling. However, this lacks the temporal resolution needed to follow DA neuron density and d DA signaling during the disease onset and development in the same animals, and it only allows measuring DA signaling from one site. Thus, a detailed description of the spatial organization of DA neuron loss over time, and how this relates to DA signaling and symptoms onset, is currently lacking. Obtaining such insight might provide an explanation for why the age of disease onset, disease progression and symptoms are remarkably heterogeneous among PD patients [165, 166].

5.2 Construction of a Mathematical Model

We aim to construct a mathematical model that captures some important features of dynamics of dopamine in human striatum. Dopamine is a very important neurotransmitter, and it has been shown to have play a role in for instance movement, memory and learning [167, 168, 169, 170]. It is believed that a fundamental structure in the correct movement and initiation of actions in general, is the basal ganglia, that consists of two different pathways that originates from two Medium Spiny Neuron (MSN) populations in the striatum [171]. The direct pathway is postulated to promote movement, whereas activation of the indirect pathway is believed to inhibit it. Since dopamine affects both populations, its role as a modulatory element in the network is believed to be of fundamental importance.

In this we will focus on the concentration of extracellular dopamine in striatum and model that as a function of the release and uptake of the specific neurons. We focus on a region of space in striatum where the synapses project into and they can release vesicles of dopamine upon stimulation. However at these synapses there is also dopamine transporters, that can carry dopamine molecules from the extracellular space and back into the synapse. In this way the synapses create a dynamics of extracellular dopamine, that can change in time depending of the firing properties for the neurons and on the parameters of the synapses. Finally we introduce diffusion between synapses in a small subvolume. Even the region we consider, consists of many different cells there is an extracellular volume between these where dopamine can diffuse between the synapses. We now use the experimentally defined diffusion constant: $D^* \approx 322\mu m^2/s$ [172] and using time steps of $0.1s$, we obtain a length scale of $L \approx 10\mu m$. Therefore if we consider a small volume of space of dimensions $1000\mu m^3$, and since the density of synapses is $\rho \approx 0.1\mu m^{-3}$ [173] we consider this a standard region to be covered with 100 synapses. A schematic picture of the imagined setup is found in Fig. 57

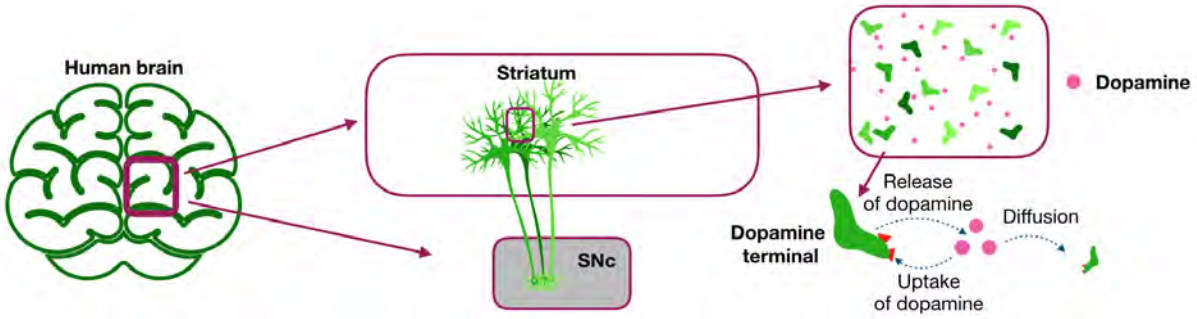

Figure 57: *Schematic figure showing the region on the human brain that this model aims to describe. We consider the region in the very center, striatum, that is covered with millions of release terminals from hundreds of thousands of neurons, having their soma in another region, substantia nigra pars compacta (SNc). We focus of a small subregion of striatum, covered with dopamine terminals that can release dopamine, but that can also absorb it back into the neuron.*

5.2.1 Approximation of Dopamine Dynamics in Mean Field Model

From the above introduction we are ready to model the dopamine concentration in the extracellular space. Here we adopt the model previously proposed by Dreyer et. al [174], where we can describe the dopamine dynamics as

$$\dot{D_A} = N\nu P\Gamma - NV_{max}\frac{D_A}{D_A + Km} + (D^*\nabla^2 D_A - \delta D_A) \tag{94}$$

Here the first term describes the addition of dopamine into the extracellular space with ν being the firing rate of a neuron, P being the release probability from a terminal on a firing neuron, N being the number of terminals in a given subspace, and Γ being the released amount. The second term is a typical Michaelis Menten uptake term, with V_{max} being the maximal uptake rate. Finally the last part represents the diffusion from other regions and the spontaneous degradation of dopamine. In healthy striatum, where N is large, both these effects are negligibly small and we will thus, if not otherwise stated, neglect these terms. It turns out that the above differential equation is solvable, so we wish to describe $D_A(t)$: Now denoting $D_A \equiv D$, $P\Gamma\nu N - VN \equiv \gamma$ and $P\Gamma\nu NK \equiv \delta$ we can write:

$$\frac{dD}{dt} = \frac{D\gamma + \delta}{D + K} \Rightarrow \int \frac{D + K}{D\gamma + \delta} dD = t + C \tag{95}$$

Thus we focus on the integral an obtains:

$$\int \frac{D + K}{D\gamma + \delta} dD = \int \frac{D}{D\gamma + \delta} dD + \int \frac{K}{D\gamma + \delta} dD \tag{96}$$

$$= \frac{K}{\gamma}\int \frac{1}{u} du + \frac{1}{\gamma^2}\int \frac{u - \delta}{u} du \tag{97}$$

$$= \frac{K}{\gamma} ln(u) + \frac{1}{\gamma^2} u - \frac{\delta}{\gamma^2} ln(u) + C \tag{98}$$

$$= \frac{D}{\gamma} + ln(D\gamma + \delta) \cdot \left(\frac{K}{\gamma} - \frac{\delta}{\gamma^2}\right) \tag{99}$$

With this we can now rewrite the equation:

$$(\gamma D + \delta) + ln(D\gamma + \delta) \cdot \Big(- KV\Big) = \gamma^2 t + \delta - C \tag{100}$$

Now setting $T = \gamma D + \delta$, $-KV = \Delta$ and $\gamma^2 t + \delta = f(t)$ we obtain:

$$T + \Delta ln(T) = f(t) - C \tag{101}$$

$$T + \Delta ln\Big(\frac{T}{\Delta}\Big) = f(t) + \Delta ln\Big(\frac{1}{\Delta}\Big) - C \tag{102}$$

$$\frac{T}{\Delta} + ln\Big(\frac{T}{\Delta}\Big) = \frac{f(t)}{\Delta} + ln\Big(\frac{1}{\Delta}\Big) - C \tag{103}$$

$$e^{T/\Delta}\frac{T}{\Delta} = \frac{e^{\frac{1}{\Delta}(f(t)-C)}}{\Delta} \tag{104}$$

$$T = \Delta W\Big(\frac{e^{\frac{1}{\Delta}(f(t)-C)}}{\Delta}\Big) \tag{105}$$

Now if we insert initial conditions and rewrite everything in terms of $D(t)$ we end up with:

$$D(t) = \frac{1}{\delta} W\Big[e^{\frac{f(t)}{\Delta}} e^{\frac{D_0\gamma}{\Delta}} \frac{(\gamma D_0 0\delta)}{\Delta}\Big]\Delta - \delta \tag{106}$$

5.2.2 Deterministic Results for Denervated Regions

Having found an expression for the concentration of D as a function of time, depending on the initial conditions, we can calculate the dopamine concentration in the steady state and during bursts and pauses. We start by calculating this for three different denervation levels, and find that while the steady state remains constant, the peak value during bursts significantly decreases and the minimum value during bursts does not reach zero for the high denervation level (Fig. 58A). We calculate the height of the pulse during the bursting period and find that this is decreasing as the number of neurons is reduced already from the early denervation and that this process is acceleration as we reach the 20% remaining neurons (Fig. 58B). Here we also find that the minimum level of dopamine during a pause, reaches zero until the region is severely denervated (Fig. 58B). We see in (Fig. 58A) that it is a trend that the rate of change gets smaller as the denervation gets more and more severe. Therefore the concentration does not reach its large peaks but it also takes longer time to decay back to the steady state. Therefore we investigated whether the integral value of dopamine following bursts and pauses remained constant, but these also decayed, in a process speeding up around the final stages of denervation (Fig. 58C).
Many compensatory mechanisms of the dopaminergic system has been reported and we investigated the effects of these. It has been suggested that when the dopaminergic neurons are removed, the dopamine transporters reduces their efficiency at which they take up dopamine [175, 176, 177]. We included this in the model as:

$$V_- \mapsto V_0(1 - \delta) \tag{107}$$

Where $\delta \in [0; 1]$ is the denervation level. Here we find that this can increase the height of the peak, but that it also increases the steady state level significantly (Fig. 58D, red trace). Another hypothesis is, that in order to keep the dopamine levels and the transient pulses, the remaining neurons increase the released dopamine levels [178, 179]. We include this in the model as:

$$\Gamma_+ \mapsto \frac{\Gamma_0}{1 - \delta} \tag{108}$$

Here we find that this does increase the height of the peak, even more than the inhibited uptake, but that this also leads to an increased steady state value (Fig. 58D, orange trace). Finally we

note that from this model, an full compensatory mechanism is to enhance both the uptake and the release so

$$V_+ \mapsto \frac{V_0}{1-\delta} \quad \text{and} \quad \Gamma_+ \mapsto \frac{\Gamma_0}{1-\delta} \tag{109}$$

Doing this, the dynamics in the deterministic model is not affected by the loss of dopaminergic neurons (Fig. 58D, brown trace).

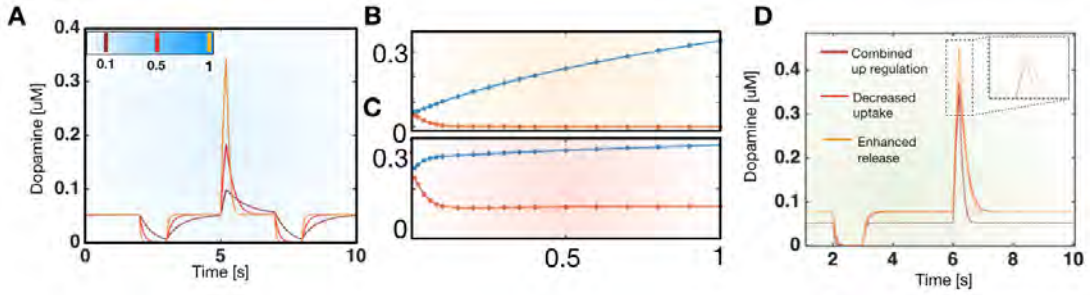

Figure 58: *A) Analytical plot for D(t) as well as simulated trace (white dots) for different denervation levels. B) Maximum value during burst (blue) and minimum value during pause (red) as a function of the remaining number of neurons C) Integral value during burst (blue) and pause (red) as a function of the remaining number of neurons. D) Analytical plot for D(t) for the combined up regulation, the inhibition of uptake and the enhanced release as described in the section.*

5.2.3 Introdcution of Stochastic Model of the Neuron Firing Pattern

In this section we will create a three parameter model that mimics the dynamics of a neuronal firing pattern. We believe that this is the simplest way to describe the process of firing patterns. We consider a population of neurons, where the i'th neuron fires with a time dependent rate given by (Fig. 59A):

$$f(t_i) = \frac{\alpha}{1 + e^{-\beta(t_i - \tau + (t_i - \frac{\sum_j S_{ij} t_j}{\sum_j S_{ij}}))}} \tag{110}$$

Here τ is a time parameter that governs the time between firings, and t_i is the time since the i'th neuron had the latest firing. S_{ij} represents the coupling between the i'th and the j'th neuron, so they have the potential to synchronize. We are interested to find the distribution of this firing and will for now keep $S_{ij} = 0$. Thus the probability that the neuron will fire in time interval $t + dt$ is

$$F(t) = \prod_{n=1}^{t/dt} \Big[1 - f(t)dt\Big] f(t)dt \tag{111}$$

Now we can use Volterras integral formula so:

$$F(t) = f(t)e^{-\int_0^t f(t')dt'} \tag{112}$$

Now solving the integral yields:

$$\alpha \int_0^t \frac{1}{1 + e^{-\beta(t'-\tau)}} dt' = \frac{\alpha}{\beta} \int_{-\beta\tau}^{\beta(t-\tau)} (1 + e^u)^{-1} du \tag{113}$$

$$= \frac{\alpha}{\beta} ln\Big[\frac{1 + e^{\beta(t-\tau)}}{1 + e^{-\beta\tau}}\Big] \tag{114}$$

Therefore the total probability distribution is

$$F(t) = \frac{1}{1+e^{-\beta(t_i-\tau)}} e^{-\frac{\alpha}{\beta} ln\left[\frac{1+e^{\beta(t-\tau)}}{1+e^{-\beta\tau}}\right]} \tag{115}$$

$$= \mathcal{C}(1+e^{\psi(t)})^{-\frac{\alpha}{\beta}-1} e^{\psi(t)} \tag{116}$$

$$\text{with} \quad \mathcal{C} = \frac{\alpha}{(1+e^{-\beta\tau})^{-\alpha/\beta}} \quad \text{and } \psi(t) = \beta(t-\tau) \tag{117}$$

The sigmoidal shape of the firing rate is shown in (Fig. 59B), and by simulating this process, we can find the distribution of times between each firing and see that it mathces perfectly with the distribution found in the above derivation (Fig. 59C). To simulate this in a fast way we want to generate randomly distributed numbers according to this distribution [180]. This is the classical way to simulate a Gillespie algorithm, where one uses the transformation method as a way to generate random numbers following a specific PDF, f(x), from random numbers uniformly distributed in the interval $[0;1]$ [181]. For this we cannot solve it exactly, but we can use a combination of the hit and miss method and the transformation method. We can in the majority of cases use the Laplace distribution and calculate random numbers from this:

$$L(t) = \frac{1}{2b} e^{-\frac{|t-\mu|}{b}} = r \quad \Rightarrow t(r) = \mu - b \cdot \text{Sgn}(r) ln(1-2|r|) \quad \text{Where } r \in]-1/2; 1/2] \tag{118}$$

We then chose a random number according to this distribution, r_t, and for that given number, we calculate a new random number, r_n, between 0 and $L(r_t)$. If $r(n) < F(r_t)$ we choose this value as the next time step. This is seen schematically in Fig. 59D. To do this we need the maximum value of F(t) which can be found:

$$d_t\Big(\frac{g(t)^{\alpha/\beta}}{g(-t)}\Big) = 0 \Rightarrow \Big(\frac{\alpha}{\beta}\Big) = \frac{1+e^{\psi(t)}}{1+e^{-\psi(t)}} \Rightarrow t_{max} = \tau - ln\Big(\frac{\alpha}{\beta}\Big)^{1/\beta} \tag{119}$$

Thus we can very fast simulate the a population of non-interacting neurons, and choose the three parameters so it captures the properties of firing rates found in vivo. Now we consider the interactions between neurons from the termS_{ij}, then the neuron can receive inputs from all the non-negative elements of the matrix S. Clearly if $S = 0$ then the neurons are all uncorrelated, and there is no rhythm to find in a large simulated population (Fig. 59E). However if we now set $S_{ij} = 1$ and let them all couple, we can get a synchronous state where they all correlate in their firings (Fig. 59F). For this setup we cannot use the next step reaction scheme described above, and we must use the classical Gillespie algorithm to generate the firing patterns [20].

(Fig. **??**A).

5.2.4 Stochastic Model Reveals How Denervation Leads to Reduced Signal to Noise Ratio

We included the firing patterns from the constructed firing model. We considered the weighted average term in the exponent to have equal weights for all neurons and defined:

$$f(t_i) = \frac{\alpha}{1+e^{-\beta(t_i-\tau+(S\frac{1}{N}\sum_1^N(t_i-t_j))}} \tag{120}$$

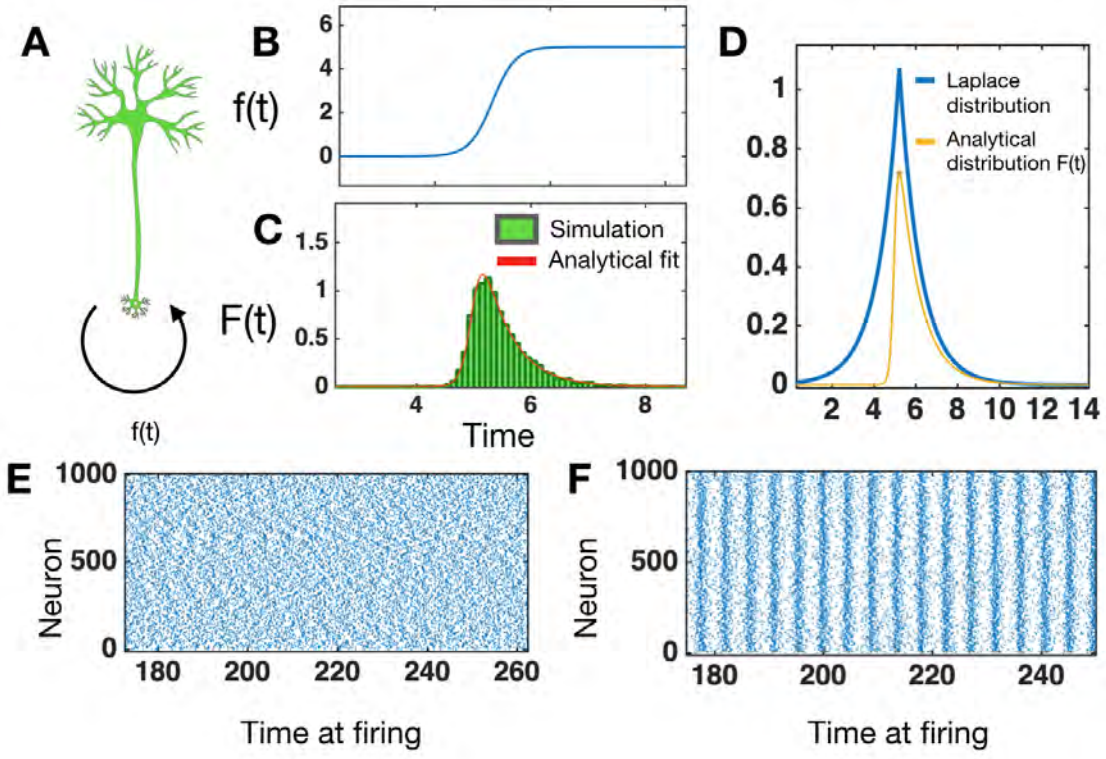

Figure 59: *A) Schematic figure showing the neuron and that fires independently of any other event as a time dependent stochastic process B) The firing rate as a function of the time since last firing. C) Distribution of times between firings, fitted with F(t) as calculated in the section. D) Figure showing how to generate random numbers following the F(t) distribution. E) Firing times for thousand neurons in the absence of couplings. F) Firing times for thousand neurons when coupling is present.*

We simulated during tonic and phasic firing signals and used the parameters

$$\alpha_{Tonic} = 1 \quad \alpha_{Phasic} = 2$$
$$\beta_{Tonic} = 3 \quad \beta_{Phasic} = 10$$
$$\tau_{Tonic} = 5 \quad \tau_{Phasic} = 1$$
$$S \in [0; 1.5]$$

In this we still considered the three different compensation mechanisms as introduced above. First we calculated the average value for D_A, as well as the standard deviation on this measure. Here we note that the standard deviation does not actually serve the purpose of reporting an uncertainty on the datapoint, since the distribution of dopamine over time is not gaussian. However it still gives a measure on the spread of the data and is worth considering since a perturbation to the spread, might interrupt signal transmission in striatum.
Calculating the average value of dopamine, we find that this is enhanced for the two independent compensation mechanisms, as well as the standard deviation is increased for denervated regions. However for both the model including no compensation as well as the combined compensation model, we find the average level to be approximately constant (Fig. 60A). If we now consider

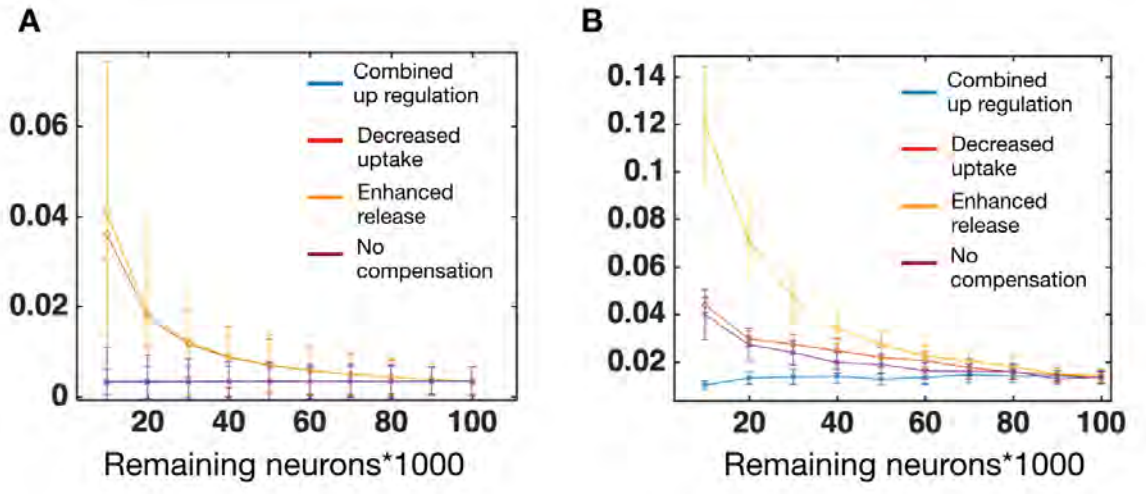

Figure 60: *A) Average value of dopamine in tonic time series as a function of number of remaining neurons. Vertically is standard deviation shown. B) Amplitude height of oscillations and the standard deviation on this number as a function of number of remaining neurons.*

the amplitude of the oscillations in the tonic firing, we find that these are enhancing for the denervated regions for both the individual compensation mechanisms as well as the one with no compensation, the oscillations are enhanced for the synchronized tonic state (Fig. 60B). Especially the compensation with an enhanced release, has a great rise in the amplitude which is due to the fact that the remaining neurons release a very high amount that gives an extreme transient peak following release.

Since we learned in the section concerning the deterministic model, that the height of the peaks could depend on the remaining number of neurons, we hypothesize that an important measure that is affected during the dopaminergic denervation is the signal to noise ratio. Here we define the short bursting periods as signal, and the noise as the standard deviation in the tonic period. We argue that there is interesting phenomena in the oscillatory behaviour in tonic firing, and therefore we do not expect that the measure of the standard deviation is intended to be zero, but the system might need to clearly separate these two, which is obtained by a clear signal. We start by considering the non-synchronized case, where the oscillatory behaviour is not found. Here we see that the signal to noise ratio is decreasing, and this is a remarkable trend for all the systems independent of the compensation (Fig. 61A). To validate this we tested this for the synchronized system, and here we found the same trend and the change in signal strength was around the same level. Thus reducing the number of neurons will make it difficult to separate a signal input from the random fluctuations arising from the variations in the firings.

5.3 Characterization of the dopaminergic Landscape Following Denervation

From results of the mean field model, we realized that the dynamics was affected by the number of remaining neurons. Experimental results has estimated the number of remaining dopaminergic neurons around the onset of PD, but almost nothing has been hypothsized on how the global

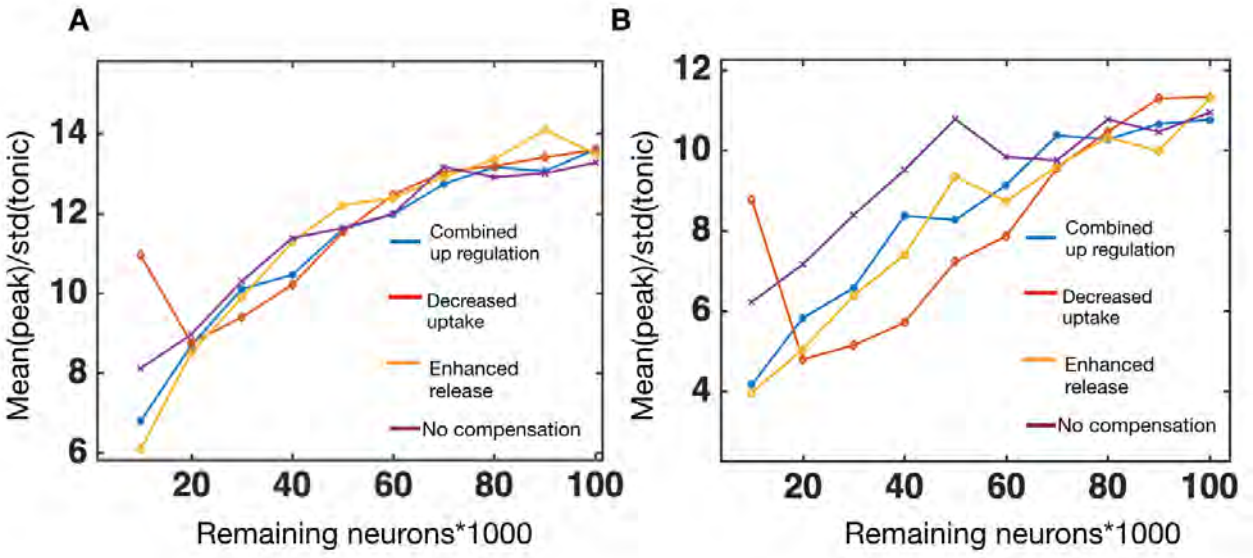

Figure 61: *A) Signal to noise ratio calculated as the mean peak height during bursts divided by the standard deviation of the data during tonic period. $S = 0$. B) Same as A, but for the synchronized case where $S = 1.5$.*

landscape is characterized when only a fraction of neurons are remaining. We wish to investigate this following different hypotheses on why neurons are degenerated. To do this, we start by "constructing" a healthy striatum, that will then later be denervated. In this we assume that striatum can be described by an ellipsoid with principal axes $a = 2.1$ cm, $b = 1.5$ cm, and $c = 0.3$ c, giving $V_T \approx 4\text{cm}^2$. The reason for this choice in geometry is simply that the shape looks very ellipsoid like from clinical pictures. Inside this volume, we now insert $N_T = 10^5$ neurons as randomly positioned dots. We assume that the axonal arbor of a dopaminergic neuron can be described as a sphere, with radius $r_d = 0.5$ mm and constant terminal density ρ_d. With these assumptions, we now have a model of human striatum, but to study the effects of denervated striatum, we need some fundamental measures.

5.3.1 Identification of Three Important Measures in Denervated Striatum

Based on the initial results of the model, we now want to characterize striatum as the neurons are denervated. Firstly, the number of remaining neurons inside the subvolume of the mean field model is important for the resulting dynamics, and we want to describe the distribution of neurons covering an arbitrary point in striatum. For the healthy model, we can estimate this analytically. We consider a region ϵ with radius $r_\epsilon << r_d$, centered at position c_ϵ. If we now placed an axonal arbor, with volume V_n randomly, the probability that ϵ would be covered by this neuron would be:

$$P(\epsilon \in V_1) = \frac{V_d}{V_T} \approx 1.25 \cdot 10^{-4} \tag{121}$$

Now assuming that all axonal arbors are placed independently, we can calculate that the probability of a region in space ϵ is covered by n neurons, given that there is N_T in total:

$$P(\{\Delta_{i\to\epsilon} \leq r_n\}|N_T) = \left(\frac{V_d}{V_T}\right)^n \left(1 - \frac{V_d}{V_T}\right)^{N_T - n} \frac{N_T!}{n!(N_T - n)!} \tag{122}$$

Here $\{\Delta_{i\to\epsilon}\}$ is the set of neurons with center closer to ϵ than r_d. We now rewrite $\frac{V_c}{V_T} \Rightarrow \frac{\frac{V_c}{V_T}N_T}{N_T}$, and since $N_T >> n$ we can make the following approximations:

$$\left(1-\frac{\frac{V_c}{V}N_T}{N_T}\right)^{N_T-n} \approx \left(1-\frac{\frac{V_c}{V_T}N_T}{N_T}\right)^{N_T} = e^{-\frac{V_d}{V_T}N_T} \text{ and } \quad \frac{N_T!}{(N_T-n)!} \approx N_T^n \tag{123}$$

Inserting these we end up at:

$$P(\{\Delta_{i\to\epsilon} \leq r_n\} = n|N_T) = e^{-\mu}\frac{\mu^n}{n!} \quad \text{where} \mu \equiv \frac{V_d}{V_T}N_T \tag{124}$$

We have thus shown that the number of neurons covering a random position in space can be estimated from a Poisson distribution, with mean proportional to the number of remaining neurons. This does not take the boundaries into account and as we move closer to the boundary, the volume where neurons can cover the small test volume ϵ get smaller. The probability of ϵ to be covered, dependent on the distance d to the boundary:

$$P(\epsilon \in V_i) = \frac{1}{V_P} \cdot \begin{cases} \frac{4\pi}{3}r_d^3 & \text{if} \quad d \geq r_d \\ (\frac{\pi}{3}(2r_d^3 + 3dr_d^2 - d^3) & \text{if} \quad d < r_d \end{cases} \tag{125}$$

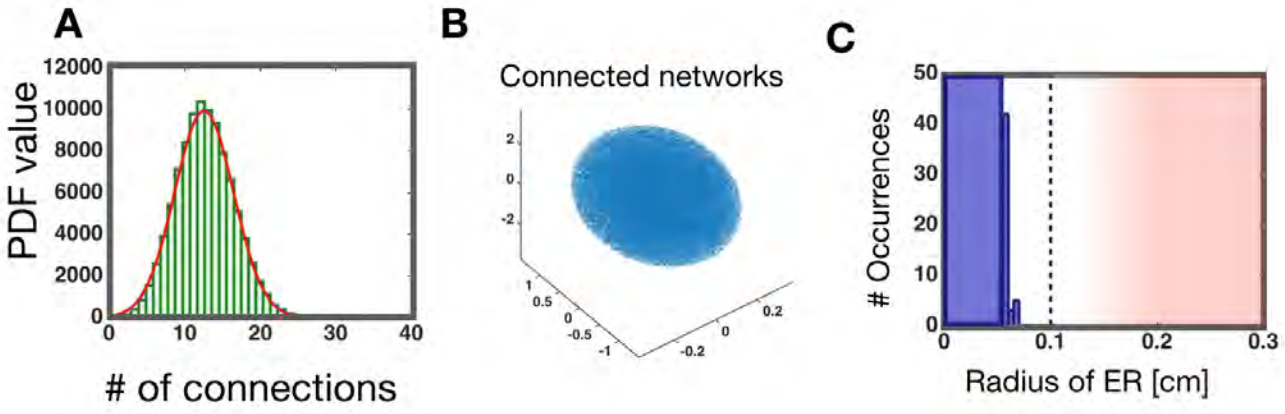

Figure 62: *A) Coverage of neurons, fitted by a poisson distribution B) Visualization of the neurons positioned in striatum and all coloured in the same color to represent the irreducibility of the healthy state. C) Distribution of the 30 largest ER, where the large blue bar represents that the numerous other empty regions, will all be smaller than these.*

This means that the mean of covering neurons is smaller at the boundary, but from this we will mainly use that we expect that the distribution of covering neurons can be described by a poissonian, which we confirm from simulations (Fig. 62A).

Next we consider the communication classes of the network of neurons. We say that two neurons i, j communicates if there is a possible path from i to j. This means that they do not need to be directly connected, but they should, indirectly could transmit information between each other. If they all communicate, we define that the network is irreducible, and we expect that this can be very important for correct signal transmission and global synchronization in striatum. To find the communication classes we computed the following algorithm:

- Pick the neuron n_1 and put it in the set S_1
- Find all its neighbours, and put these in a transient set $C = \{n_j....n_k\}$
- Pick the first element of C, put it in S_1, remove it from C, and find all its neighbours and put these into C.
- Pick the next element of C and repeat the algorithm. When C is empty the set S_1 is a collection of all neurons in communication class 1.
- After this take n_2. If $n_2 \in S_1$ go to n_3. Otherwise create the set S_2, put all the connections of n_2 in C, and repeat the algorithm as above.

To visualize this we paint each communication class in a distinct color. If we use this algorithm for the healthy striatum, we find that it is irreducible, and thus all neurons can communicate with each other. Therefore we hypothesize that it is an essential feature of functioning striatum that all neurons can communicate, transmit signals and synchronize and this might be feature that breaks down following denervation. Finally we consider the possibility that some regions in striatum gets completely denervated and we term these empty regions (ER). Here we review the original model, and since $N = 0$ we are left with

$$\dot{D_A} = D^* \nabla^2 D_A(r) - \delta D_A \tag{126}$$

Even in our model where we consider spheres of constant density, small ER volume might exist for all levels of denervation, but due to diffusion from the neighbouring regions, the steady state level remains approximately at the normal level. An analytical derivation for the situation of diffusion with decay, into an empty sphere, is found in Appendix E, and from this we define an ER to be with $r_{ER} > 1mm$, because for this value, the steady state will definitely be zero. To find the empty regions for a given number of remaining neurons, we use Voronoi tesselation, installed in MATLAB, to find all the voronoi edges, and then we scan through these edges to find the most empty region. A small review of Voronoi tesselation is found in Appendix F. By applying this method, we find that the largest empty regions in healthy striatum is significantly smaller than 1 mm, and thus we expect the concentration of DA non-zero at all points in striatum. We hypothesize that this could also be an essential feature that the steady state level of DA is does not go to zero anywhere, since this could lead to completely wrong signals for the MSNs in this region.
To sum up, we consider the following three measures to be the most important to describe the state of striatum after denervation:

- The distribution of neurons covering an arbitrary point in space
- The distribution of communication classes and specifically the largest class
- The size of empty regions where DA is degraded completely

We are going to investigate these three measures, when striatum gets denervated in three different ways.

5.3.2 Denervation I. Random Removal of Neurons Result in Low Coverage and Phase Transition in Clusters

We start by considering that each neuron is removed completely stochastically. This represents the situation where all neurons have the same probability to die, $1/r$ where r is the rate. This is

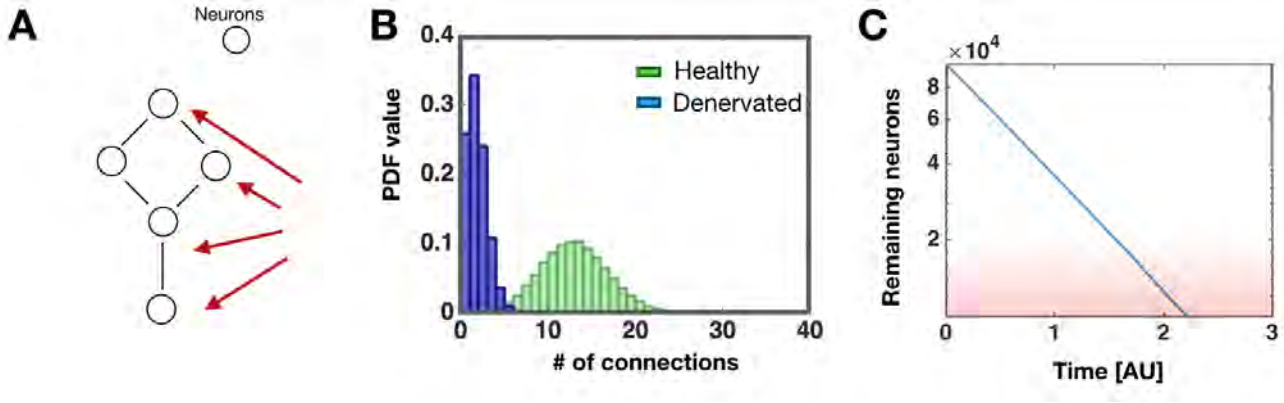

Figure 63: *A) Schematic figure showing connected neurons that all die at the same rate B) PDF of number of connections. Green: Healthy and Blue: Denervated. C) The number of remaining neurons as a function of time.*

represented schematically (Fig. 63A), where the thickness of the arrows correspond to the given rate at which neurons die, and the black lines correspond to neurons in contact with each other. In this picture, the cause of death can originate from all kinds of different events, and this is what we would term as standard ageing. In the following we treat the rate as a fixed constant, which of course is a simplification, since this rate is probably close to zero in the young stages of life. However at this critical stage, which might come during adult age, we believe this serves as a good approximation. After removing the neurons at random, leaving only 10% surviving, we investigate this denervated Striatum. We find that as expected the distribution of overlapping neurons still follow a Poisson distribution (Fig. 63B) as was the case for the healthy Striatum. We find that the majority of regions has a very low coverage, and thus the dynamics makes it difficult to transmit any large signal since the peak of the burst is decreased. An important measure is the rate at which the disease evolves, and from our point of view how the number of remaining neurons decreases as a function of time. For the age dependent model, all rates are constant and the number of remaining neurons follow an exponential model as shown in Fig. 63C. From this we move on to study the existing networks of overlapping neurons. We find that the large connected cluster (Fig. 62B) has been split into multiple small clusters with no ability to communicate and synchronise (Fig. 64A), when 10% neurons are remaining. This is quite surprising, since the coverage is rather smoothened, and by eye, one might believe that the neurons all created one communication class, however even though the vast majority overlap, they are separated into many smaller classes. Tho understand this further, we calculate the number of neurons in each communication class, and find that this scales well as a power law, with no serious out-layers (Fig. 64B). Since we at this point find many small clusters, and we know that for the healthy striatum, all neurons were indirectly connected in one cluster, we ask the question when this break-up occurs. We calculate the number of neurons in the largest cluster, and divide this by the total number of remaining neurons to find the time at which the break up occurs, and find that this happens quite dramatically when 20% of the neurons are left (Fig. 64C).

Finally, we aim to describe the possibility of completely empty regions, as studied in Section II. Considering only regions larger than 0.1 mm, we use the techniques described above, to find the

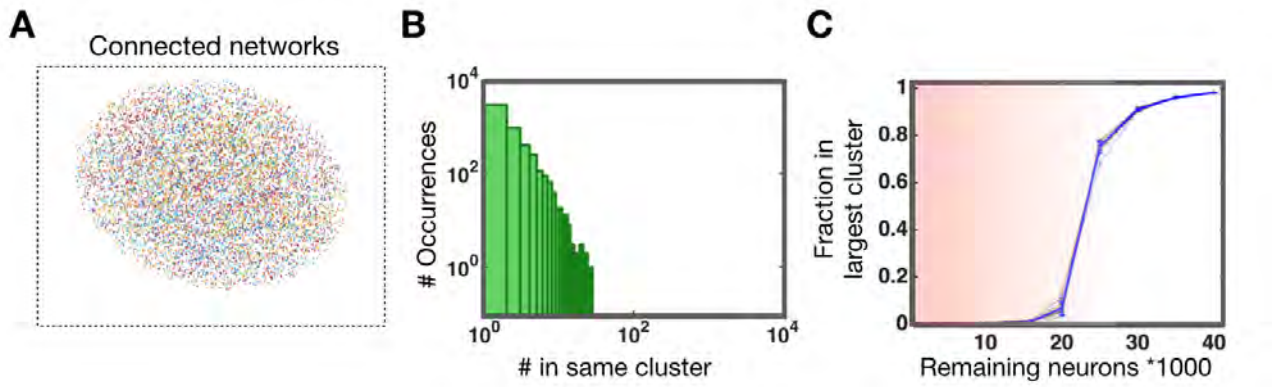

Figure 64: *A) Visualization of 10% remaining neurons. Different Colors Indicate Different Communication Classes. B) Distribution of cluster sizes. c) Number of neurons in the largest cluster divided by the total number of remaining neurons, as a function of the remaining number of neurons.*

largest uncovered regions, which are shown as black spheres in Fig. 65A. A full derivation of the probability of an empty region to occur as a function of the remaining number of neurons can be found in Appendix X. Looking at the size of these, we see that they are only just larger than the definition of empty regions, and no big outlayers exist (Fig. 65B). Therefore it is quite possible, that inside these empty regions the decresed steady state level of DA, does not harm the affected MSNs. An interesting measure in this regard is how the development on the largest empty region evolves as the neurons are removed. Taking the average of 25 independent simulations, we find that the radius of the largest empty region grows slowly, but starts to grow dramatically when less than 10% of the neurons are remaining (Fig. 65C).

5.3.3 Denervation II. Spread of Disease Result in both Functioning and Denervated Regions

Another way that the neurons can die, is by a disease spreading from a fixed number of initial cells. This is inspired by the spreading of Lewy bodies or other diseases that might spread between neurons. For simplicity we assume that all neurons that cover the same space in striatum, is also within range of disease spreading in SNc, where the soma of the neurons are placed. Therefore at each timestep, one at randomly chosen infected neuron, infects two of its randomly chosen neighbours. These neurons are now considered as infected and all infected neurons have a probability $1/b$ to die at each timestep. This is schematically shown in Fig. 66A where the infected red cell infects two neighbours that can are then prone to die. Studying this macroscopic landscape, we quickly see that each surviving neuron a higher number of neighbours compared to the random denervation (Fig. 66B) . Thus there exists patches, where the dynamics is still lively and signals can be transmitted through the dynamics as good as in the healthy striatum. We consider how the denervation evolves, and find that initially the number of neurons decreases very slowly, only to accelerate and thus decrease faster than a exponential function (Fig. 66C). This is explained by the fact that the population of infected neurons grow and therefore the time until the next

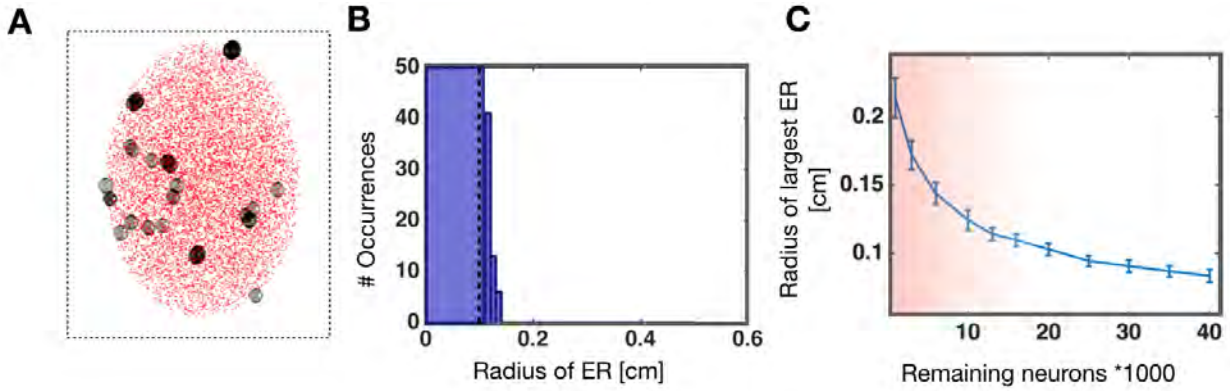

Figure 65: *A) Visualization of the remaining neurons, and black spheres represent the largest empty spaces. Note some of these might overlap. B) Distribution of the largest empty regions. The large bar represents that numerous smaller empty regions will exist. C) Size of the largest empty region, as a function of the remaining number of neurons.*

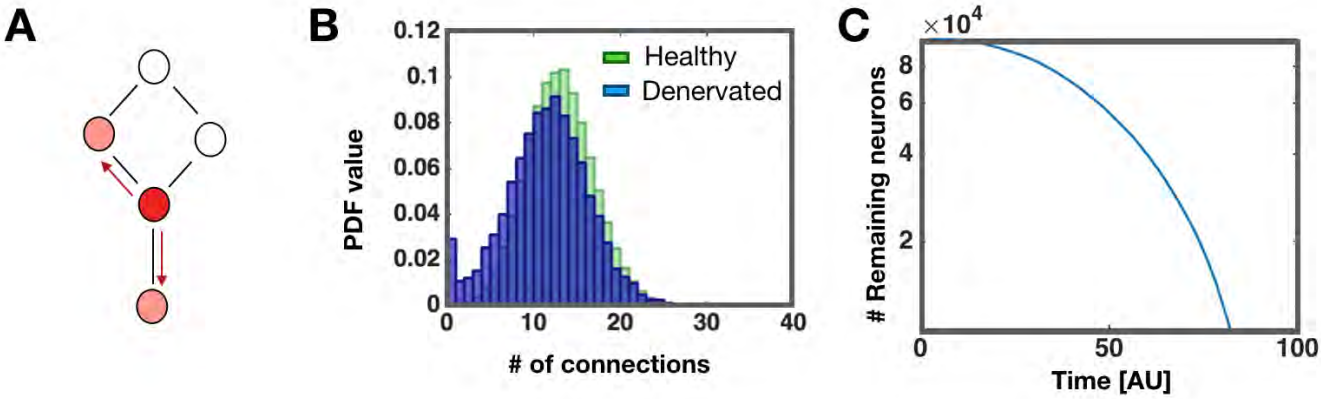

Figure 66: *A) Schematic figure showing connected neurons, where the red neuron is dying and passing the disease on to two random neighbours. B) PDF of number of connections. Green: Healthy and Blue: Denervated. C) The number of remaining neurons as a function of time.*

neuron is removed is much shorter, when the population of infected cells is large. To better understand the nature of the densely populated regions, we move on to investigate the networks of the remaining neurons. We find that the disease induced denervation has removed entire sections of the human striatum (Fig. 67A), but has left other areas unharmed. Considering the colors it is clear that there exists two large, connected regions, and that does have the ability to function as healthy tissue individually. However since they have no communication, this might results in correlated and maybe even conflicting signals further to the basal ganglia. Looking at the size distributions of these remaining networks, we see that as in the randomly denervated case, numerous tiny collections exist, but contrary to the former, this is dominated by two very large networks, that probably is responsible for the majority of outputs (Fig. 67B). Since the clusters are still large when 10% of the neurons are remaining, it is not certain if they will always be dominated by one large cluster, or split up like the age dependent denervation model. Calculating the number of

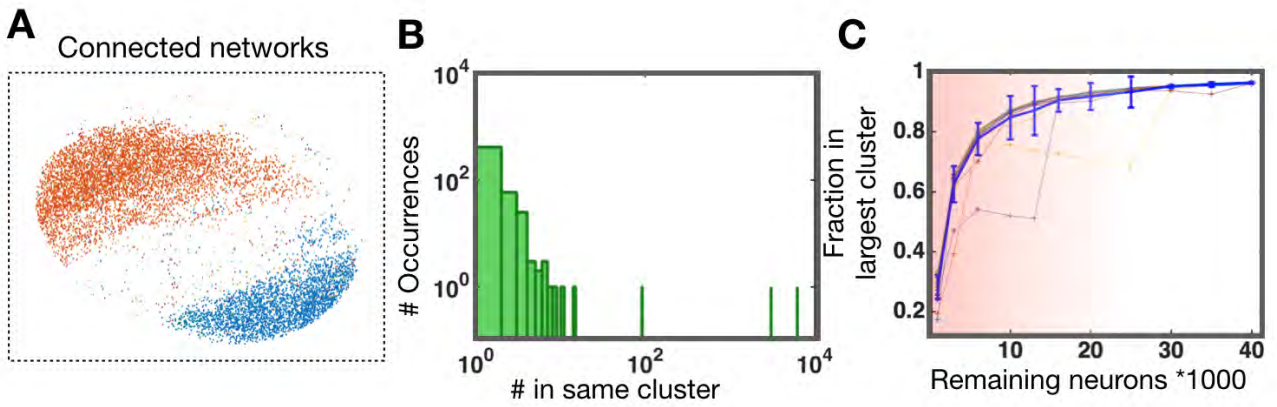

Figure 67: *A) Visualization of 10% remaining neurons. Different Colors Indicate Different Communication Classes. B) Distribution of cluster sizes. c) Number of neurons in the largest cluster divided by the total number of remaining neurons, as a function of the remaining number of neurons.*

neurons in the largest cluster, divided by the number of remaining neurons and taking the average of 25 independent simulations, we find that even though one large cluster dominates until 10% neurons are remaining, and at this point many small independent clusters emerges (Fig. 67C). Since the remaining neurons, form spatially divided clusters, it is evident that empty regions should occur. Here we find that several large empty regions exist (Fig. 68A), but due to some remaining neurons, these are still kept at a moderate level. However since these last remaining neurons are with all possibility still infected, the evolution in the size of the largest empty spaces will be rapid at this stage of the disease. With 10% surviving neurons, we see that the largest empty spaces is almost a factor of four larger than in the case for the random denervation (Fig. 68B), and inside these regions, the steady state level of DA will be zero, which of course affects down stream signalling in basal ganglia, but probably also will lead to the death of the MSNs inside these regions. We estimate the point at which these large empty regions occur, by taking the average of the largest empty region in 25 independent simulations. We find that the growth of the largest empty region is fairly slow when 40% of the neurons are left, but the absolute level is already very large. Thus the large empty regions emerges very early, but due to a few remaining neurons in the denervated space, the growth of these does not explode (Fig. 68C).

5.3.4 Denervation II. Stress Induced Removal Result in Small Unconnected Islands of High Coverage

Finally we consider a situation where the neurons die due to stress caused by upregulation. It has long been hypothesized, that one of the mechanisms that could delay the outbreak of PD, was the upregulation of DA release and uptake by the remaining neurons. In this picture, whenever one neuron dies, the total number of released molecules are decreased, but by releasing higher amounts and more often, the remaining neurons can decrease the effects of denervation for a long time. However, as it has been argued, dopaminergic neurons are already close to their maximum

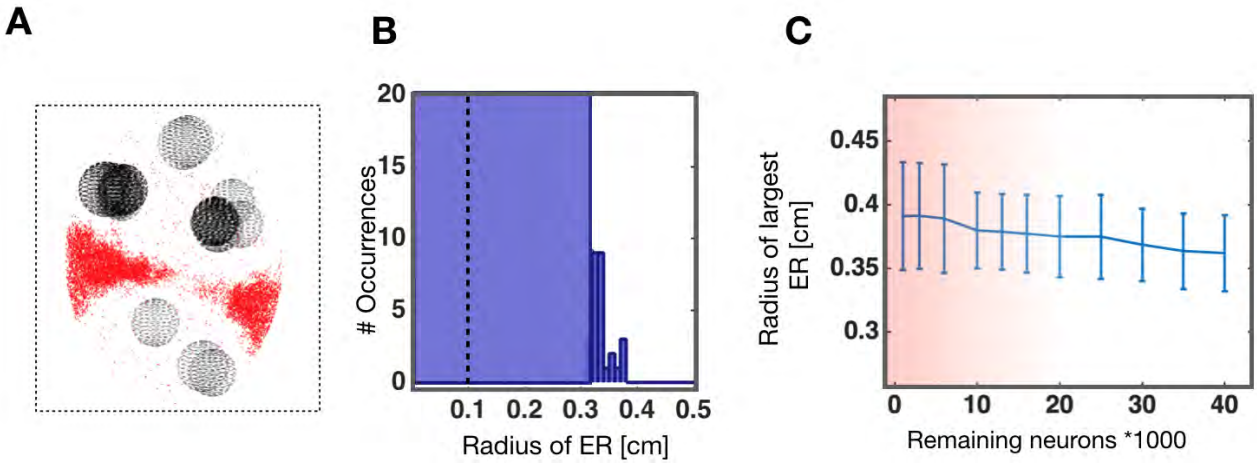

Figure 68: *A) Visualization of the remaining neurons, and black spheres represent the largest empty spaces. Note some of these might overlap. B) Distribution of the largest empty regions. The large bar represents that numerous smaller empty regions will exist. C) Size of the largest empty region, as a function of the remaining number of neurons.*

capacity, due to the high number of terminals and vast complexity of their axonal arbors [182]. Therefore we imagine the rate by which a neuron dies to be a function its number of neighbours, and thus few neurons overlapping the same area are more probable to die due to stress than many neurons overlapping the same area. This is schematically shown in Fig. 69A, where the large arrows correspond to a high rate of dying, which occurs for the neuron with fewest connections. In this "poor-gets-poorer" model, we observe that the distribution of neighbours of each existing neuron is very high (Fig. 69B). Therefore all neurons experience a situation with vivid DA dynamics and they can all transmit signals downstream to the Basal Ganglia. We calculate the rate of denervation by measuring the number of remaining neurons at different time points, and find that the neurons are removed very quickly initially, but at the late stages the rate of neuron removal are decelerating (Fig. 69C). To understand this we need to characterize this configuration of neurons from their spatial networks, and we observe that they have all split into small clusters (Fig. 70A). These clusters are demarcated from each other, and have no ability to correlate their signals and synchronize their dynamics. This also explains the deceleration found in Fig. 5C, since at the final stages some very robust islands have been created, and inside these the dynamics of others creates non-stressed conditions for the individual neurons. We argue, that even though these clusters should all be able to transmit signals through the DA dynamics, the total output that is transmitted from striatum might be non-coherent due to the isolation of all the clusters. Looking at size distributions of these, we see that no clusters with less than 10 neurons exist, and the largest cluster has around 10% of the remaining neurons (Fig. 70B). The evolution of the break-up of clusters, has a similar pattern to what was found in the age dependent denervation model, but is not as dramatic and the largest cluster keeps a population around 10% of the total population even when the striatum is almost completely denervated (Fig. 70C). Due to the separation of clusters, we expect that empty spaces are also present at this stage of denervation, and from Fig. 71A we see that large regions depleted from DA exists. Calculating the volume of these we find that the largest are around 0.35 cm in radius and thus they are so large that many MSNs are affected. We

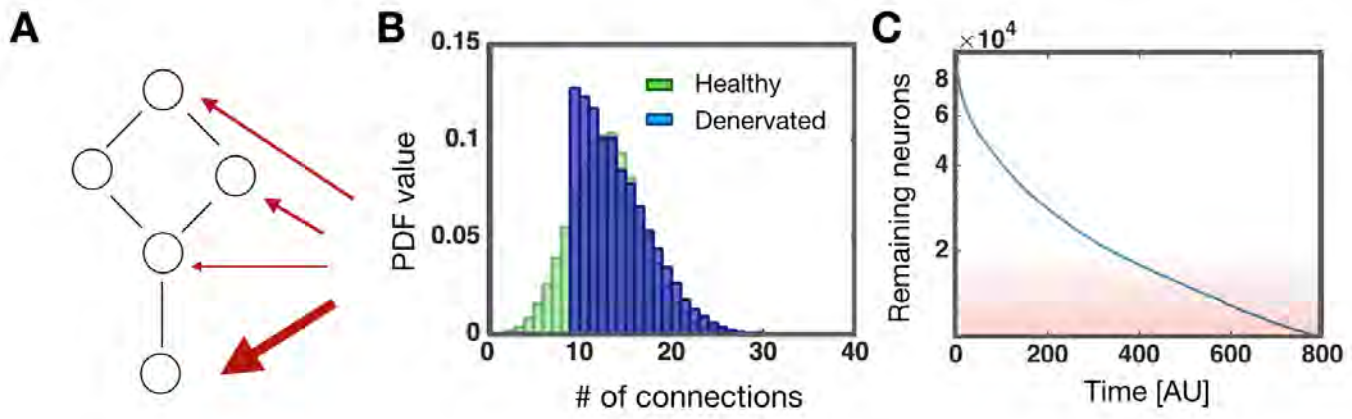

Figure 69: *A) Schematic figure showing connected neurons with removal rates depending on their number of neighbours. Here the bottom one has the highest rate to die, because it only has one connection. B) PDF of number of connections. Green: Healthy and Blue: Denervated. C) The number of remaining neurons as a function of time.*

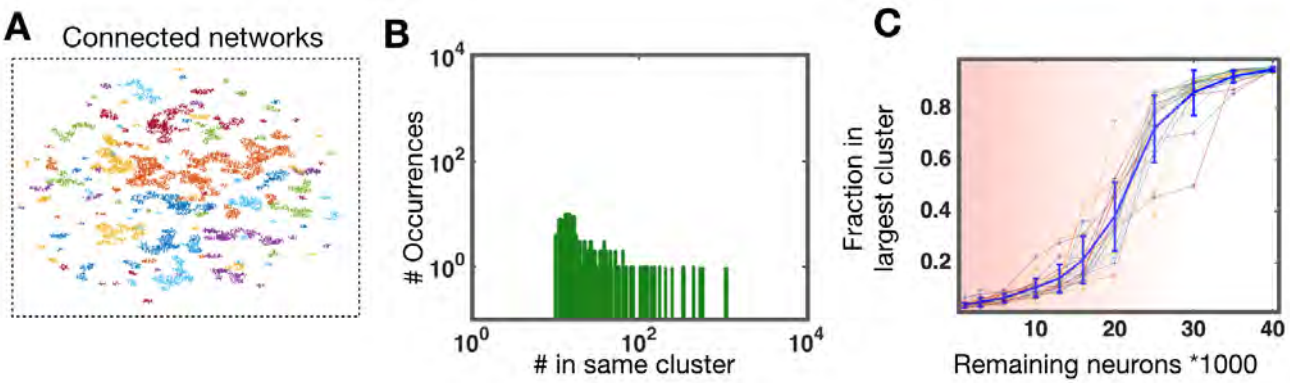

Figure 70: *A) Visualization of 10% remaining neurons. Different Colors Indicate Different Communication Classes. B) Distribution of cluster sizes. c) Number of neurons in the largest cluster divided by the total number of remaining neurons, as a function of the remaining number of neurons.*

note that these empty approximately as large as for the disease induced case and much larger than the ones arising from the age driven denervation. Compared to the disease induced denervation, we don?t expect these empty spaces to grow as quickly, since the clusters all consist of many neurons, and the removal of a single neuron does not have the same impact as when many clusters small and the removal on one neuron might cause the emergence of an empty region (Fig. 71B). From this we investigate the evolution of empty regions, and we find that they are quite low when 40% are remaining, but from this point they grow fast (Fig. 71C) and even faster than what we found for the other denervation strategies (Fig. 65C and Fig. 68C).

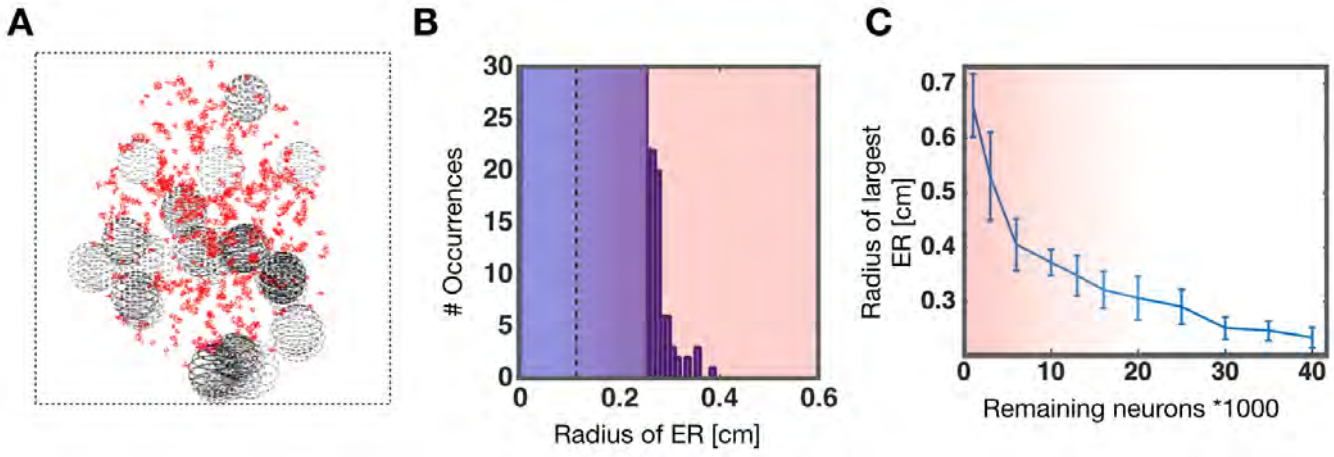

Figure 71: *A) Visualization of the remaining neurons, and black spheres represent the largest empty spaces. Note some of these might overlap. B) Distribution of the largest empty regions. The large bar represents that numerous smaller empty regions will exist. C) Size of the largest empty region, as a function of the remaining number of neurons.*

5.4 Discussion and Perspectives

DA is a key neurotransmitter involved in a variety of critical functions, and it is therefore not surprising that multiple disorders have been related to dopaminergic dysfunctions [183]. The most well known DA-related disorder is PD, which since the sixties, has been known to originate from a loss of striatal dopaminergic denervention [184]. From a scientific point of view it is fascinating that the neuronal network can resist a large denervation and that the cardinal symptoms of PD does not show up before 60% - 70% of the dopaminergic neurons are lost [154, 155, 185]. Therefore, it is likely that one or more compensation mechanisms ?exist, keep?ing the system from a breakdown, but it is highly debated whether these mechanisms occur by regulation of release or uptake of the remaining neurons, [178, 179, 175, 176, 177], mediated by changes in the receptor properties [186, 187, 188, 189], or by changed activity in other regions of the brain [190, 191].
We examined how the DA-signalling changed as the neuronal denervation progressed. Starting out by introducing the simple mean field model as previously described by Dreyer et. al 2010 [174] we examined the effects during neuronal degradation, and in this we introduced three different mechanisms of compensation. By solving the differential equation and simulating the system we found that the individual compensation mechanisms led to enhancement of the tonic DA concentration which was not the case for the the models with combined or no compensation in which the steady state level remained constant. Furthermore, we found that the height of the peak during phasic periods decreased with the level of denervation, whereas the compensation models showed enhancement and finally the combined compensation remained unaffected. We believe it is interesting that the different compensation mechanisms, all reflecting suggested mechanisms from the available literature, can result in highly different patterns of the extracellular DA-concentration, and we believe that these results could be a valuable prediction in future experiments investigating the response mechanisms to neuronal denervation.
From the deterministic description we moved on to introducing a simple model of a firing pattern

of the neuron depending on three parameters. A variety of different models of neurons already exist, where some try to model the true biophysical situation which includes a lot of parameters, where others are abstract and try to capture the dynamics in a simple way. [192]. This model is definitely on the abstract side since it does not contain any information about the neuron itself or the nature of the firing rates. However, we believe it is the simplest model which captures the dynamics of periodic spiking and therefore it can be highly applicable for future work where it is not the actual mechanisms controlling the firings in neurons that is examined, but rather the effects caused by firings in neurons, as it has been in this project. The fact that we could generate random numbers according to the distribution opens up for even faster simulations, but at the present stage this has only been done for the non-synchronized case.

Including this model in the dynamical system results in a stochastic system, and by simulating this we find that oscillations can arise in the tonic state if the neurons are coupled to each other. Analysis of this system reveals an increase in the standard deviation of the data as the denervation progresses. Furthermore, we find that the oscillations from the coupling in tonic firing has increasing amplitudes the enhanced DA-release compensation as the neuronal density decreases. However, for the system with combined compensation the amplitude decreases and thus we conclude that depending on the compensation mechanisms, the amplitudes can either be enhanced or decreased as the denervation progresses. We believe that this spectrum of responses in the amplitude is interesting and can give be fingerprint of how the dopaminergic system can deal with large levels of denervation. Furthermore, we speculate that this might differ between individuals and some might have one type of response while others might have another. However, we searched for a measure that did show the same trend for all the compensation mechanisms. Here, we found that the signal to noise ratio was always decreasing as the number of neurons decreased. This was true for all compensation models and both for the systems with synchronization and the ones without. Therefore, we hypothesize that the signal to noise ratio is a very important measure and might be related to the loss in abilities to initiate actions as observed in PD. We note that we have only considered presynaptic compensation mechanisms in this project, and it is suggestive that there should also be post synaptic compensation mechanisms in the D1 and D2 receptors. However, a low signal to noise ratio will always affect the post synaptic receptors because even if these are upregulated, the noise will just be enhanced and give rise to misinterpreted signals.

From this temporal description we moved on to study the spatial effects of denervation. Clinical measurements, investigating patients with PD, usually reports an average on the denervation level around 60-80%. However, this does not give any information about whether the remaining neurons are all gathered in one small region or whether they are completely distributed over the entire striatum. Therefore, we introduced three mechanisms of neuronal denervation, all inspired by existing literature. We decided that the most important measures would be the number of neurons for the remaining neurons, their cluster size in the remaining network, and the completely denervated areas. We found that the progression of denervation through removal of random neurons lead to a low coverage landscape, where the DA dynamics is vague and the signal to noise ratio is decreased at all points. However, the low coverage is connected to a large distribution meaning that the number areas of complete denervation were quite small. An interesting measure for this model was the sudden transition in cluster sizes occuring for around 20% remaining neurons. Until this point, the neurons are almost in one large cluster but after this they form very small and unconnected

clusters. We believe this could be a crucial change around the onset of PD since the dopaminergic network moves from a state where all neurons ?has the ability to synchronize to a state where the neurons can only communicate with a small number of other neurons. For the disease spread model, we found that the remaining neurons had been separated into subregions, but these regions were characterized by a normal distribution of neighbors. We note that this denervation model leads the the most rapid progression in the denervation since the number of infected neurons accelerates in time. On the other hand, this type of denervation will keep one dominating cluster longer than the two other denervations, and thus it can be argued that the dynamics inside the dominating cluster, can show the same effects as the healthy striatum. Finally, we examined the results for the stress induced denervation and found an interesting shift into numerous, completely divided subpopulations all with a large number of neurons covering and thus high level of dynamics and a high signal to noise ratio. All these subgroups cannot communicate with each other, and thereby this results in strong non-coordinated signals which could be linked to the motor symptoms of PD. Also, the complete division into small subgroups creates large empty regions deprived of DA, and it is this type of denervation that gives rise to the largest empty regions for the final parts of the denervation.

What happens around the onset of PD and why the symptoms only arise after a critical level of denervation has been highly debated for several decades. We have examined this problem by constructing a series of mathematical models based on assumptions from the literature. By using these, we have described how the dopaminergic landscape changes in time and space as more and more neurons are removed from the striatum. We find that depending on the mechanism of compensation and denervation some different results can arise and we believe this can explain some of the variety in symptoms and disease progression observed for PD patients. However, we also find some common features independent of the applied compensation or denervation: As the number of neurons is decreased, the signal to noise ratio will decrease, the irreducibility of the network breaks into separate clusters and empty regions start to appear. Therefore, we argue that these are the most important elements characterizing dopaminergic denervation and we believe ?they might be related to many outbreaks of PD.

6 Incorporation of Non Canonical Amino Acids in Bacteria Suggest Density Induced Translation Arrest Phenomena

In this chapter the results of **paper IV** is presented and discussed. This work was initiated during my stay at q-bio summer school in San Diego in 2015 through great scientific discussions with Yonatan Chemla. The background was the experimental results carried out by Orr Schlesinger and Yonatan Chemla, and by applying our knowledge of the system, we created a simple model, based on experimentally measured parameters from E. Coli. I formulated and constructed the model and performed the simulations of the system. The project was guided by Lital Alfonta and Mogens H. Jensen, who played an important role in the development of the model.
In this project we will start by introducing a very strong promoter and ribosome binding site to the GFP gene. Here we observe that the protein expression is very low, but we find that by introducing a codon for a non canonical amino acid early in the sequence rescues the protein production. By investigating this result, we introduce a stochastic model that describes transcription and translation simultaneously and allow for interactions of ribosomes on neighbouring mRNA strands. This model reproduces the experimental trends and we use this to make predictions about the position of the codon for the non canonical amino acid and the protein expression, that we confirm in the experiments. Finally we test these predictions on other genes, and find strong agreement between the predictions of the model and the expermental observations.

6.1 Background to Protein Synthesis in Bacteria

The synthesis of proteins, is one of the most important functions of living cells. Even in bacteria this can be quite complex, and is controlled by several mechanisms at different stages. Every stage in the process, from DNA transcription to protein folding dynamics, is tightly regulated to ensure that proteins are produced in required amounts, at the correct times and with minimal waste of energy and resources [193]. In bacteria, the transcription of DNA to mRNA and the subsequent translation into a polypeptide chain are coupled in time and space [194, 195]. Since the two processes occur simultaneously, it creates a high molecular density area, that is populated with all the components required for protein synthesis. For the dynamics of transcription and translation, the molecular crowding in the cytoplasm is important fir the ability to stabilize protein-protein interactions and to control the diffusion rates of the components involved in protein synthesis[196, 197].
A key feature of the synthesis, is the binding of a RNA polymerase to a promoter on the DNA and the ribosome to a ribosome binding site (RBS) at the mRNA. The strengths to bind at these sight, is vital for the transcription and translation initiation rates, and this in turn leads to resulting molecular densities of RNA polymerases on DNA and of ribosomes on mRNA. It has been shown that the use of a strong RBS with a high initiation rate to overexpress proteins can lead to ribosome collisions and queuing along individual mRNA strands. [198, 199]. The kinetics of translation also depend on the codon usage of the encoded gene, which is manifested by its effects on the elongation rate of the growing polypeptide chain [200, 201]. Exploited across species to control translation rates and the ribosome queues along mRNA strands, the ribosome moves at along the sequence of codons with different rates depending on the codon, in order to optimize protein synthesis. Depending on the elongation rates they dictate, the codons can be divided into different rate classes. Slower codons are more frequencly found in the first 30-50 codons of the

mRNA whereas downstream codons, however, are found to be optimized for fast elongation rates [202, 203, 204].

6.2 Experimental Results Suggests That Incorporation of Non-Canonical Amino Acids Rescues Protein Production

An interesting way to study this is by genetic code expansion through stop codon suppression [205]. This method has normally been used for applicative purposes, but can also be used as a basic research tool. We used genetic code expansion, by incorporating noncanonical amino acids (ncAAs) into the GFP protein. Here we used the UAG nonsense (stop) codon, and transformed it into a sense codon that encodes for the incorporation of an ncAA. This recoding is facilitated by introducing into a host organism an orthogonal translation system (OTS) that comprises of an orthogonal Archaeal otRNA with an anticodon corresponding to the UAG stop codon [206] (Fig. 72). The affinity of the otRNA to the tertiary complex of the ribosome A-site during translation, is significantly smaller than that of the native bacterial tRNA [207, 208]. This smaller affinity can be exploited to alter ribosomal traffic on the mRNA by decreasing the speed of translation along the mRNA. This approach could be efficiently obtained when the OTS and the native release factor (i.e., RF1) are not in direct competition for the UAG codon. That competition can be eliminated by recoding all TAG stop codons in the bacterial genome to TAA and by knocking out the RF1 gene [209] (Fig. 72). Furthermore, we use the OR2-OR1-pr-UTR1 (P70a-UTR1) expression system, based on a modified promoter (from λ PR) and RBS (fromT7 bacteriophage)[210]. This system has the highest transcription and translation initiation rates reported for an E. coli element, and so far, it has been used exclusively in vitro. We expect that its high initiation rates will generate large and unusual ribosome crowding along the transcribing mRNA. We therefore hypothesized that in the crowded environment of a polysome, a growing polypeptide chain may interact with neighboring translational components inside the polysome in a manner that can significantly retard the process. Indeed, it was previously shown that the nascent polypeptide can regulate the translation process in the ribosome by interacting with the polypeptide exit tunnel in the ribosome[211]. Such interaction may cause ribosome stalling [212] translation arrest [213] and even accelerated mRNA degradation [214]. We exploited both the incorporation of ncAAs using UAG stop codon suppression, synonymous mutations in the gene and the modular tuning of the P70a-UTR1 expression system to model and control ribosomal traffic, thus optimizing recombinant protein expression.

6.2.1 Non Canonical Amino Acid Incorporated at Position 35 Increases Production

With this experimental setup, we wanted to test the effects of expression and incorporation ncAA. In the following, all cells will have the P70a-UTR1 system unless otherwise stated (strong promoter and RBS) and WT will refer to a cell with no ncAA. We now started by measuring the production of GFP from the WT, where the nave hypothesis was that it should produce an extreme amount. In order to measure the production we measured the fluorescence for a group of population of cells, and here we found a very small production of GFP from these (Fig. 73A). In the time course we observed that the fluorescence level would initially be low and then start increasing fast and then finally settle into a steady state, meaning that the entire trajectory takes a sigmoidal shape. We

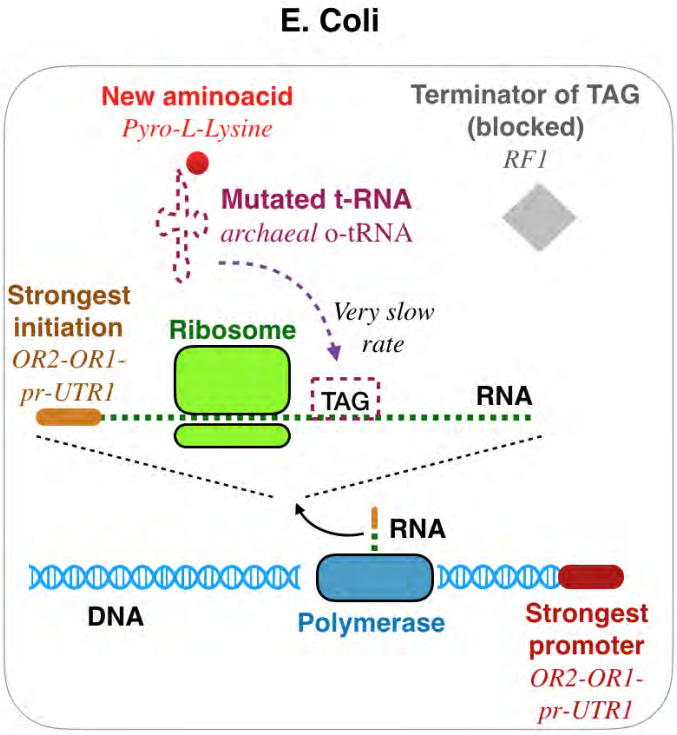

Figure 72: *A) Schematic figure showing the experimental setup of the system*

assume that the steady state level represents a lack of production in the cell culture due to lack of resources. To explore this further, we now inserted a single TAG mutation at position 35 in the GFP sequence(35TAG from hereon. TAG refers to the codon and the number defines its position in the gene). Surprisingly, we found that this produced much more GFP than the wildtype (Fig. 73A). This was highly surprising, since our only hypothesis for the effect of TAG, was a severely decreased translation rate at the given position. To investigate this further, we now tested the effects on the mRNA level and here we found a much larger mRNA level for the 35TAG(Fig. 73B), which was also surprising since the rate at which translation occurs should not be coupled to the production of mRNA. This outcome was observed not only when using a genomically recoded E. coli strain (C321Δprf1) (GRO) but also with two other E. coli strains (i.e., BL21(DE3) and DH5α). We tested the ncAA incorporation by mass spectrometry and verified that this was correct. We also ruled out the possibility that inclusion bodies or secondary mRNA structures were the source of the divergence between the WT GFP and 35TAG GFP quantities. Cryo-electron microscopy imaging of GFP revealed neither inclusion bodies nor any marked difference in bacterial shape compared to bacteria without the GFP expression plasmid Moreover, there was no difference in the mRNA structure encoding for the WT GFP and the mutant GFP. Finally we tested whether the insertion of the mutant affected the basic groth rate of the bacteria, but here we did not find any difference either. Taken together, these observations motivated our search for a more fundamental explanation related to the coupling of bacterial transcription and translation kinetics. We conclude from this that a system with extremely high levels of RBS and promoter strengths has an apparent breakdown, which can be rescued by inserting a single mutated codon with a very low rate. To explore this further we therefore moved to a mathematical model.

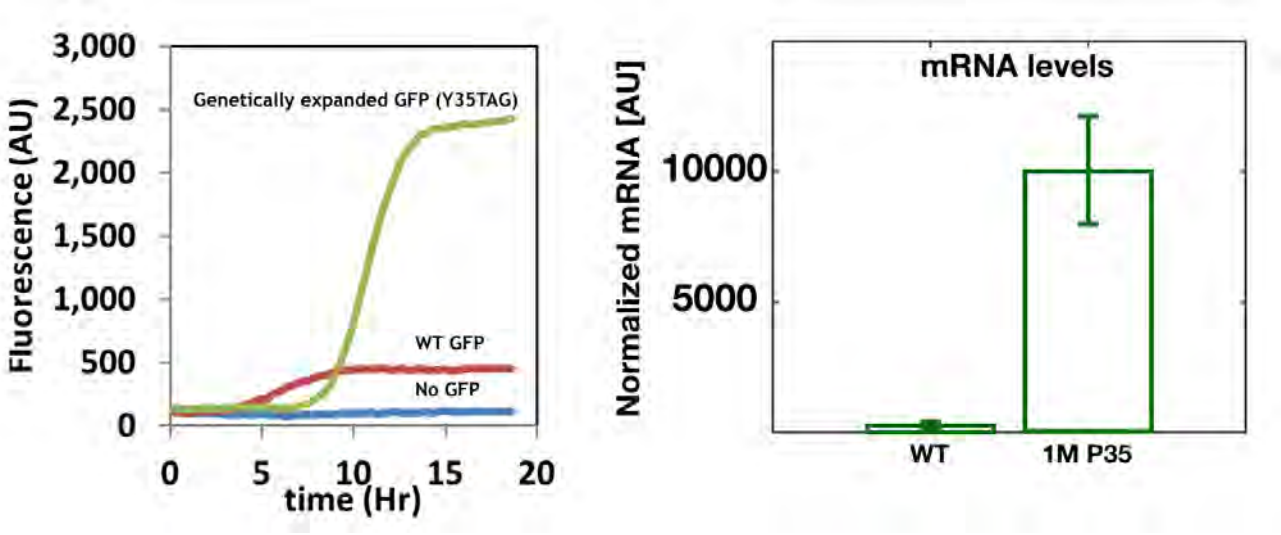

Figure 73: *A) The protein level measured through flourescence for control, WT and 1 mutation at position 35 B) The measured mRNA level for WT and 1 mutation at position 35*

6.3 Construction Of a Simple Model Relating Transcription and Translation

Herein, we propose a model to predict protein and mRNA levels that is based on a set of biochemical parameters combined with several assumptions. Model parameters: an increase in the RNA polymerase (RNAP) initiation rate (i.e., promoter "strength") leads to a decrease in the average distance between transcribing RNAP and vice versa [215] The deterministic average distance between RNAPs is given by:

$$\langle D \rangle = D_{Pol} + \frac{R_0}{R_\alpha} \tag{127}$$

Where D_{Pol} is half the length of the polymerase, R_0 is the movement rate along the DNA, and R_α is the polymerase initiation rate.

6.3.1 Movement of Polymerase and Ribosome in the Model

We consider the DNA strand of the GFP gene of length 238 codons. First the RNA-polymerase can attach to the DNA with a rate R_a given there is no other RNA-Polymerase already attached to the DNA at any of the 12 first positions, since this is the width of a RNA-Polymerase. Now this is moving on down the 238 codons that all has a rate R_0. It should be noted that because all positions on the DNA has the same rate, does not mean that the RNA-Polymerase moves at uniform velocity. First of all, in a stochastic picture, a constant rate means that the distribution of time the polymerase spends at a position before moving, is given by an exponential distribution with mean R_0, and spread. Furthermore the basic assumption that no object can share the same position, means that quickly a queuing structure will evolve, and this will leads to regions where some polymerases will move very slowly due to leading polymerases, there by chance has moved a bit slower down the strand. When the polymerase reaches the final step in the strand, it can leave the strand and release the RNA with a rate R_b (Fig. 74A). Whenever the RNA-polymerase moves

one position, it produces RNA, meaning that the length of the RNA strand will to be equal to the position of polymerase.

Whenever the length of the RNA is 12 codons, which is the width of the ribosome, a ribosome can attach to the RNA strand with rate ra. Once attached the ribosome can move at at the RNA strand. with rates $a = 35/s$, $b = 8/s$, $c = 4.5/s$ or $TAG = 0.04/s$. The ribosome can only move if there is no ribosome occupying any of the 12 codons in front of it, and if the position of the polymerase on the DNA is higher than the position of the ribosome plus 12, since otherwise the RNA strand has not been created, for the ribosome to move on (Fig. 74B). Whenever the ribosome moves down one position, a new aminoacid is added to the polypeptidechain there is growing in space.

Whenever the ribosome reaches the final position, it can leave the RNA strand with a rate ra, hereby releasing the polypeptidechain to produce a protein. From the above description, this can only happen after the polymerase polymerase has detached from the DNA strand. Therefore the final RNA stands can produce proteins, until they are degraded with a rate k_{RNA}

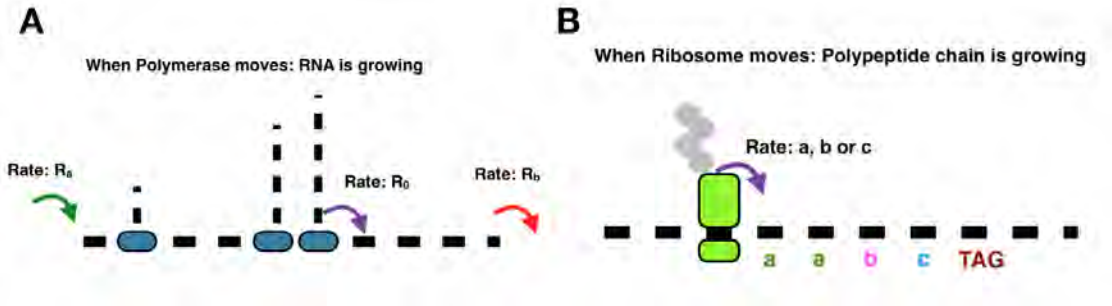

Figure 74: *A) Schematic figure showing the movement of a polymerase B) Schematic figure showing the movement of a ribosome*

6.3.2 Growth of Polypeptide Chain and Interaction Between Chains

We need to consider the resultant length of the polypeptidechain, in the situation sketched above. We consider the amino acids to be solid spheres with radius r_{aa} (Fig. 75A). Now as we add a new aminoacid, it is attached at the ribosome, and we assume that it has one point of contact with the aminoacid in front. Thus we assume that the two angles in 3 dimensions, is uniformly distributed, so

$$P(\theta) \in [-\alpha; \alpha] \quad \text{and} \quad P(\phi) \in [-\alpha; \alpha] \tag{128}$$

The resultant length of the chain can now be described by:

$$L(\theta_i, \phi_i) = 2r + \sum_{i=1}^{n} 2rcos(\theta_i)cos(\phi_i) \tag{129}$$

The avarage length of a chain of two aminoacids is thus:

$$\langle L \rangle = 2r\Big(1 + \int_{-\alpha}^{\alpha}\int_{-\alpha}^{\alpha} cos(\theta)cos(\phi)P(\theta)P(\phi)d\theta d\phi\Big) = 2r\Big[1 + \Big(\frac{sin(\alpha)}{\alpha}\Big)^2\Big] \tag{130}$$

For $\sigma_\theta = \sigma_\phi = \frac{\pi}{2}$, and a length of the amoni acid of 0.3 nm, we get an avarage constant of proportionality $\lambda = 0.12$ nm/codon. This means that the length of the polypeptidechain perpendicular

to the direction of movement of the ribosome, can be described by the linear relation, depending on the position of the ribosome, denoted n:

$$L(n) = W_r + d_{aa} + \lambda(n-1) \tag{131}$$

where W_r is the estimated height of the t_{RNA} and d_{aa} is the diameter of the first aminoacid and we assume $W_r + d_{aa} \approx 8nm$ [216]. We note that this is a highly simplified calculation, but we believe that it can prove valid during the short time, where transcription in the bacteria occurs.

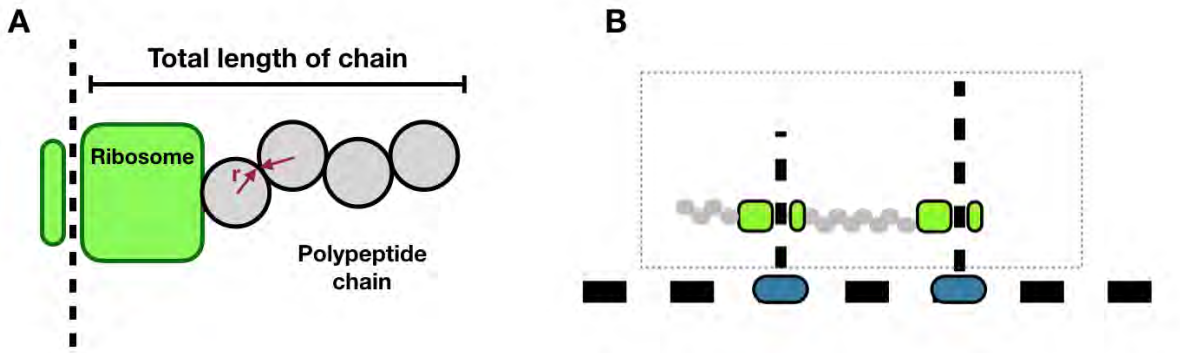

Figure 75: *A) Schematic figure showing the growth of a polypeptide B) Schematic figure showing the interaction between two ribosomes on neighbouring mRNA strands*

In bacteria, transcription and translation are coupled, i.e., as soon as the RBS on the transcribed mRNA emerges from the polymerase, the ribosome can bind to the RBS and translation begins [194] The close proximity of the two processes in time and space means that there may be interactions between them. From our model description, it can be deduced, that the distance between two ribosomes on neighouring mRNA strands, is given by the distance between polymerases. In this picture, the size of the polypeptidechain from one ribosome, can be longer than this distance between them and therefore we hypothesized that highly crowded conditions will promote high spatial ribosome density. Through interactions between these ribsosomes on separate mRNA strands, this can induce translation arrest in a process that we termed "Density Induced Translation Arrest" (DITA). This means that if a ribosome moves into a position, where the distance to the polymerase generating its own mRNA is the same as the ribosome on one of the neighbouring RNA strands interactions can occur. Now if the length of the polypeptidechain is longer than the distance between the two polymerases, the two ribosomes will be "arrested" (Fig. 75B). This arrest, causes the two ribosomes to stop moving and after transcription ends, an mRNA that has arrested ribosomes are immediately degraded. To sum up, we therefore proposed that in situations where the promoter and RBS initiation rates are large enough to create regions with high molecular density and in which the nascent polypeptide is long enough, the probability for DITA events increases. In the case of a DITA event, all the ribosomes upstream of the arrested ribosome stall, promoting translation termination and thus reducing the number of full-length proteins produced from crowded mRNA strands.

6.3.3 Description of Simulation Steps and Parameters in the Model

With this we are ready to set up the entire model as can be schematically seen in Fig. 76. We start with an empty DNA sequence of 238 codons, where a polymerase can attach with rate R_α, and then move on the DNA with uniform elongation rateR_0 [194, 215]. When the polymerase has moved a distance $L_p/2$which defines the minimal distance between polymerases, a new polymerase can attach with rate R_α. When the polymerase has produced $L_r/2$ codons, a ribosome can now attach with rate r_α. An important element is now the different elongation rates of each codon in the mRNA sequence[217, 218, 219] at which the ribosome can move along. On the basis of a previous model developed by Mitarai et al., the entire set of bacterial codons was divided into three groups based on translation rate: fast (A), medium (B) and slow (C), which correspond to elongation rates of 35, 8, and 4.5 codons per second, respectively[218]. The mutated UAG codon was assigned a new translation rate category, group (D), which had a significantly lower elongation rate of 0.04 codons per second. The rate was estimated from in vitro experiments [207] has some uncertainty, however the majority of the results of the following sections are robust for $r_D \in 0.01-0.2 codons/s$. Every time a ribosome moves, the polypeptide chain grows with λ and after each move its distance to nearest neighbours on neighbouring mRNAs is calculated and compared to the lengths of the polypeptide chain. Whenever a ribosome reaches the final codon, it can be released with rate r_β and at this point we count a new protein. From this it is clear that the ribosome can not produce any proteins during transcription. A list of all parameters is found below:

Parameters used in this study	Notation	value
Initiation rate of P70a promoter (strong)	R_α^S	$3.0/s$
Initiation rate of P70b promoter (weak)	R_α^W	$0.2/s$
Elongation rate of polymerase	R_0	$51 nt/s$
Termination rate of polymerase	R_β	$3.0/s$
Initiation rate of UTR1 (strong)	r_α^S	$1.5/s$
Initiation rate of UTR3 (weak)	r_α^W	$0.15/s$
Elongation rate of ribosome A (fast)	r_A	$35.0 codons/s$
Elongation rate of ribosome B (medium)	r_B	$8.0 codons/s$
Elongation rate of ribosome C (slow)	r_C	$4.5 codons/s$
Elongation rate of ribosome D (UAG - very slow)	r_D	$0.04 codons/s$
Termination rate of ribosome	r_β	$1/s$
mRNA half-life time	$t_{1/2}$	$60s$
Proportionality constant lambda	λ	$0.11 nm/codon$
Size of ribosome	L_r	$24 codons$
Size of polymerase	L_p	$24 codons$

To simulate this, we use the setup of Totally Asymmetric Simple Exclusion Processes, which has previously been used to study translation [220]. This means that at each step we calculate the time until next event by transforming a uniformly distributed random number to an exponentially distributed random number:

$$t_{next} = -\frac{ln(\mathcal{R})}{\sum_i a_i} \tag{132}$$

Here $\mathcal{R}$ is a standard uniformly distributed random number and the a's are defined as the rates on the mRNA. Now we determine the element that moves, by choosing a new random number and calculate the normalized cumulative sum of the rates. We pick reaction, i, if:

$$\text{if} \quad \mathcal{R} \quad \in \quad]\frac{a_{i-1}}{\sum_{j=1} a_j}, \frac{a_i}{\sum_{j=1} a_j}] \rightarrow \text{reaction i takes place} \tag{133}$$

Here we use this setup to couple transcription and translation using the real gene sequence and and take the biological measures into account. Before comparing the results from the experiments to the results from the model we started out by investigating the basic properties of the model.

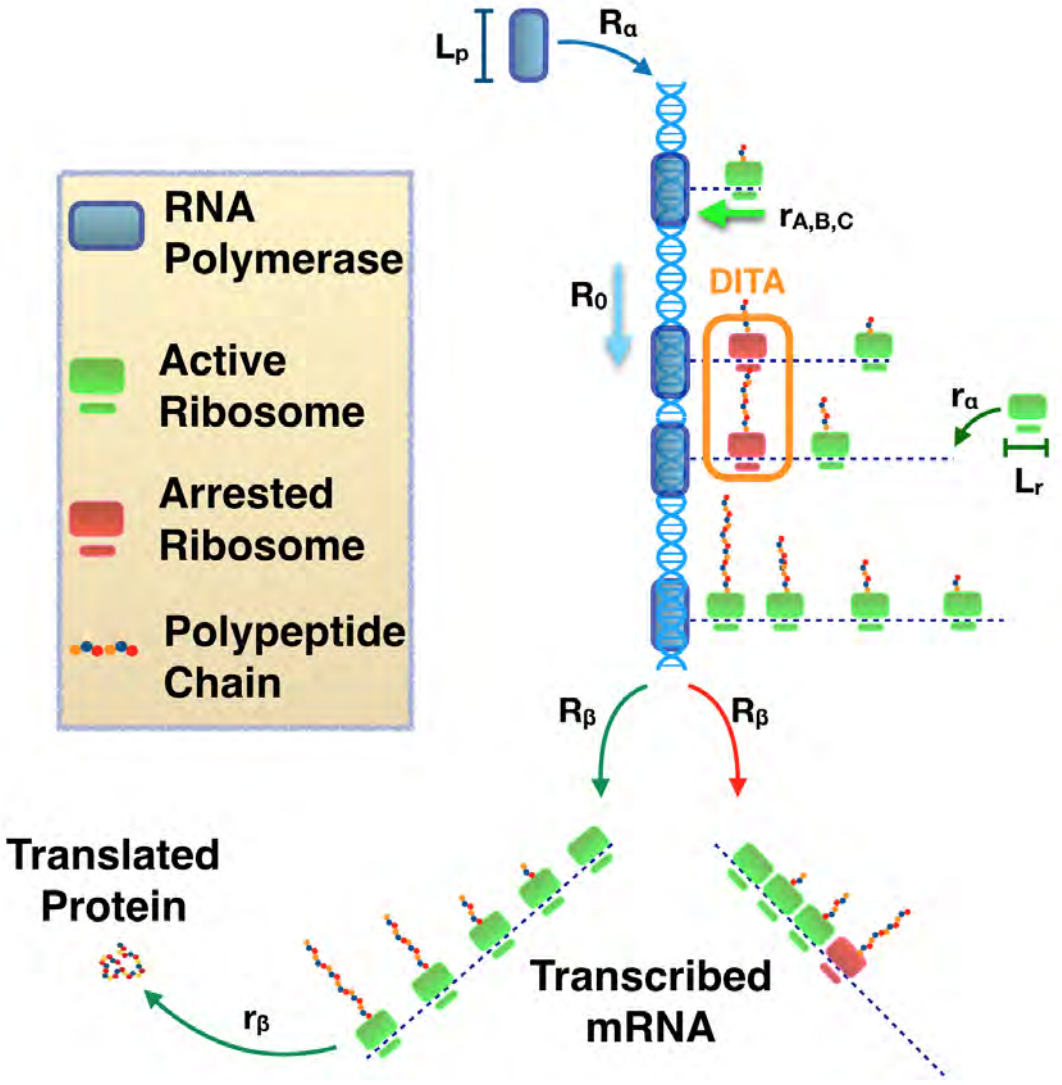

Figure 76: *Schematic figure showing the full model along with the parameters of importance.*

6.4 Stochastic Model Recapitulates Key Results From Experiments

With the setup of the model we were now ready to predict the production from different versions of the system. We will in this section change the position of the TAG mutation and change the strengths of the promoters and RBS. We will mainly take four systems into account:

- WT - strong polymerase and ribosome binding
- Y35TAG - same as WT but with mutation at position 35
- Y35TAG + D193TAG - same as WT but with mutation at positions 35 and 193
- Weak promoter - no mutations but a weak promoter
- Weak RBS - no mutations but a weak RBS

6.4.1 Early TAG Mutation Rescues Protein Expression

The first test for the model was whether it could predict the initial experimental result: The low production for the WT and the enhanced production by incorporating a TAG codon at position 35. Here we found that the results of the Gillespie algorithm simulation agreed with the experimental results for both WT and Y35TAG mutant GFP (Fig. 77A-B, red and blue curves). Thus the model suggests that WT GFP expression levels are negligible because of the high probability for DITA occurrences when a strong promoter and RBS are used. In the case of the Y35TAG mutant, the model suggests that the small translation-rate at the mutated codon serves as a "traffic light" to reduce ribosomal density downstream. Taken together, the reduction in translational density downstream of the mutated site and the low probability of a DITA event result in high yields of expressed protein. Since we suggest that the role of a traffic light is important for optimal expression efficiency the position of the mutation should be quite important. Due to its substantially slow translation rate compared to those of codons encoding for canonical amino acids, a queue of ribosomes will grow behind the reassigned stop codon. This transient stalling generated by an early mutatuin significantly reduces ribosome occupancy downstream, and thereby the chance of a DITA event. As the translation process continues, the chance that the elongating polypeptide chain will have a DITA grows. Indeed, both our experimental results and our simulations indicated that the earlier the stop codon is introduced, the lower the chance of a DITA event. Our hypothesis predicts that the closer a UAG codon is positioned to the C-terminal, the smaller will be the protein yields in a manner similar to what is observed for the WT GFP. Therefore we ran a simulation with a mutation inserted only at position 193 instead of 35. Here we found that only a fraction of what was produced for the Y35TAG system was produced, and even less than for the WT (Fig. 77B, green curve). This result is explained by the fact that whenever a ribosome is stopped at a late position, the polypeptide chain will be long enough at this point so moving ribosomes at neighbouring mRNAs can cause interactions. The reason it produces less than the WT, is that the few mRNAs that escape without any arrested ribosomes, will give a higher production than the ones with a TAG codon. To test our prediction from the model, we mutated position D193TAG in the GFP gene, and here we found that the experimental results coincided with those of the simulation, i.e., low protein levels (Fig. 77A, green curve). This result is rather surprising since it clearly shows that it it not an effect of the mutation itself but a result of the specific position in the gene. This result is in agreement with earlier reports by Tuller et al. of an early slow translating "ramp" region close to the translation initiation region [201, 202]. We note that there is a discrepancy between the experimental results and the model, since the model predicts the D193TAG to give lower expression than the WT. We believe that this might be explained by other minor effects that is beyond the scope of our simple model, and that this small discrepancy does not destroy the predictive succes of the model. Finally, we tested a combination of Y35TAG and D193TAG. The model predicted that the early mutation would decrease the translational density around the

later, thus reducing the probability of DITA in total (Fig. 77B, purple curve). Thus the double mutation would produce more than D193TAG because of an early rescue of ribosome densities and less than Y35TAG, since the produced mRNAs would have a lower production rate due to the two stalling sites. Again we tested this prediction experimentally, and found a strong correlation between experiments and the model predictions. We therefore conclude from this that our model could explain not only the initial results, but also predict the outcomes of new experiments. These results reconfirm that translation rates are crucial for high yields of protein expression. To test the model further we now also included dependencies on promoter strengths and RBS.

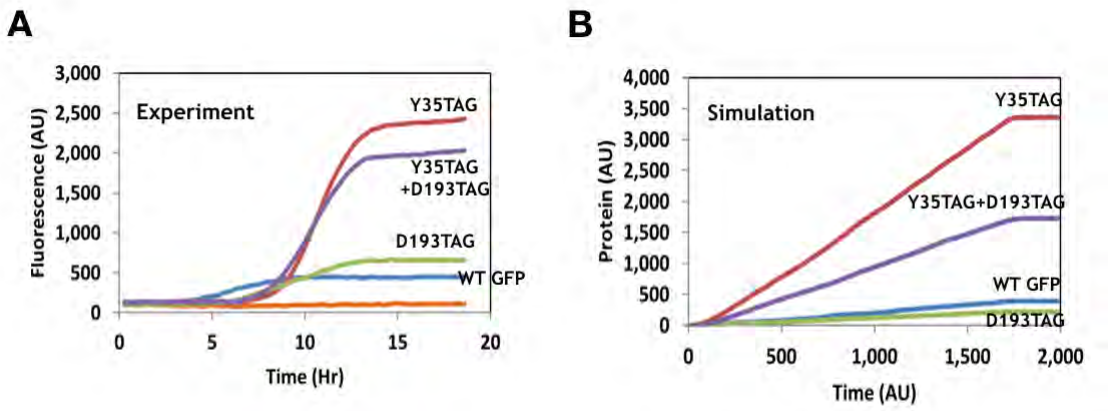

Figure 77: *A) Protein level measured experimentally through fluorescence as a function of time. Blue: WT, red: Y35TAG, green: D193TAG and purple: Y35TAG+D193TAG. B) Protein level calculated from the model. Colours as in A.*

6.4.2 Decreased Initiation Rates Rescue Protein Expression

Since the main rescue mechanism studied in the section above, was the inclusion of a low rate codon, it is tempting that a low RBS might cause an even higher production. Furthermore, if the arrest is caused by the coupled density between mRNA strands, we would believe that lowering the promoter strength as well could give an efficient way of producing proteins without reaching a density threshold. We therefore started out by investigating the effect of a weak promoter in relation to the single and double mutants. Here we tested the production rate from a finished strand with no arrested ribosomes on it. Following the decay of an mRNA, we recorded its lifetime and the number of proteins coming from this template. Here we find that the weak promoter has just as high an efficiency to as the WT, but it occurs much more frequently that an mRNA with no arrested ribosomes is produced from the weak promoter than for the WT (Fig. 78A, cyan and purple curve). Here we also find that the production rate for the single and double mutated cells to be significantly lower, due to the slow rate at the TAG site. Surprisingly, the production rate for cells with two mutations, is only slightly lower compared to the single mutation (Fig. 78A, red and blue curve). We then moved on to test how the protein production depended on the constant that governs the elongation rate of the polypeptide chain λ. We find that for very small values of λ the WT has the highest production, since no arrest events occurs in this regime. Here the weak promoters also produce more than the mutations, since the protein outcome of their

produced mRNAs is much higher than for the ones with mutations. As λ increases to the level we expect from our calculations in the sections above, the ones with a weak promoter has the highest production, and the mutated cells produce more than the WT. Finally, for the very large values of λ, arrested ribosomes occurs so frequently that the optimal production is found for the cells with TAG mutated codons (Fig. 78B). We now simulated the system with the parameters shown above, and compared the Y35TAG to the weak promoter and a weak RBS. Here we found that the weak RBS had the highest production and that the weak promoter also had a higher production than the Y35TAG. They were all significantly higher than the WT (Fig. 78C). To test this, we engineered weaker variant of the P70a promoter and the UTR1 RBS by introducing point mutations into the control regions. The use of either a weaker promoter or RBS enabled us to test whether the lowered production of the WT, was affected only by transcriptional or translational density or, as our model suggests, that both factors influence the expression density. Intuitively, the use of weaker promoter and RBS regions is expected to result in smaller amounts of synthesized protein, however, as predicted by our hypothesis and model, the counterintuitive trend was observed, according to which the weaker the control region, the higher the protein yields (Fig. 78D). Thus, by using a simple set of mutated reporter genes and incorporation of non canonical amino acids, we showed how protein synthesis yields depend, in a counterintuitive manner, on the strengths of the regulatory elements, i.e., promoter and RBS strengths, as well as on codon usage. Under the DITA assumption, we propose that the stalling of translation somewhere along an mRNA causes all upstream ribosomes to stall while all downstream ribosomes complete translation. This hypothesis also suggests that the stretch of mRNA between the DITA site and the 3' end will be more exposed to endonuclease cleavage. For that reason, we predicted that the larger the chances of DITA, the lower the mRNA levels will be, because mRNA is more exposed to endonucleases. Using the model, we determined the amount of mRNA produced by each of the mutants and compared it to the relative quantity of GFP mRNA found in mid log phase cultures of the same mutants using qPCR (Fig. 78E). A comparison of the experimental and the modeled results revealed a strong correlation, suggesting that DITA affects both protein and mRNA levels by rapidly degrading not only the mRNA, but also nascent peptides.

6.4.3 Predictions of Optimal mRNA and Protein Production Regions

From the results in the section above, it is evident that there is a correlation between the protein production and strengths of the promoter and of the RBS. This correlation has to be dependent on the inserted rates, and we are therefore inspired to investigate what combination of parameters that gives an optimal production under the DITA assumption. We therefore tested all a wide combination of promoter and RBS strengths in simulations, and reported the calculated protein production. In Fig. 79A we see the resulting heat map generated by the model, that exemplifies the intricate relationship between promoter initiation rate and ribosomal initiation rate and resulting protein levels. In this map we find that there is a certain set of conditions that will afford high protein yields, even for a combination of a very low promoter initiation rate and a high ribosomal initiation rate. From an evolutionary point of view there is therefore many different combinations that can give the desired production level. Since high mRNA levels usually correspond to high protein expression levels, it is essential to optimize protein expression for high levels of mRNA. We therefore investigate the combined mRNA levels for the same parameter set, which generates the

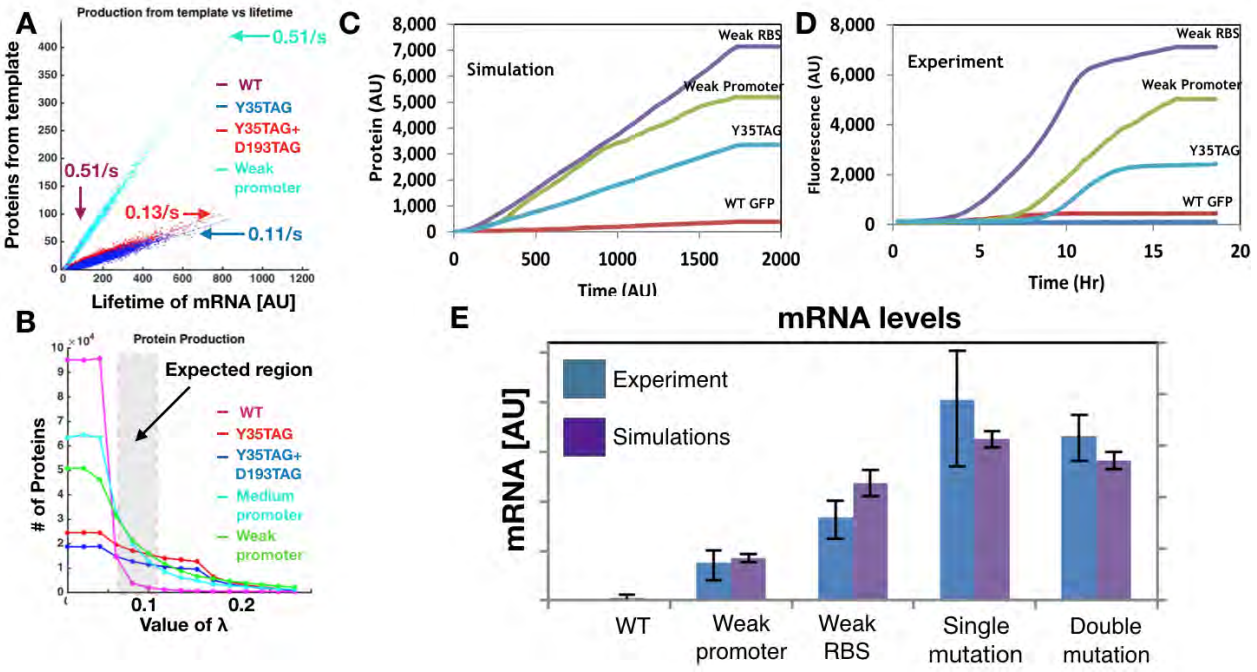

Figure 78: *A) Production from an mRNA template vs. the lifetime of the template B) The number of produced proteins in the model as a function of the elongation factor λ. C) Protein production as a function of time from the model simulation. Red: WT, Blue: Y35TAG, Green: Weak Promoter, Purple: Weak RBS. D) Protein production as a function of time from the Experiments. Red: WT, Blue: Y35TAG, Green: Weak Promoter, Purple: Weak RBS. E) mRNA levels for WT, Weak Promoter, Weak RBS, Y35TAG and Y35TAG+D193TAG.*

heat map shown in Fig. 79B. It can be seen from the map that as expected ribosomal initiation rates have a very low influence on mRNA levels, that is optimized for very low values of RBS and high values for the promoter strength. We note that the band from the heat map in Fig. 79A is still visible, and this is of importance, since this represents the highest production rate for the lowest cost in terms of produced mRNAs. Thus we hypothesize that this ratio is what would be found in many natural genes. To sum up, our experimental results as well as the model have identified a set of conditions in which mRNA levels are influenced by ribosomal initiation rates. From our hypothesis this is explained by a high spatial density of ribosomes. We do not exclude other explanations for the reduction in mRNA levels such as effect on transcription initiation by the density, or a codon bias effect [221] possibly mediated by a protein [222] However, if this is the case, then it is mutually inclusive to our hypothesis.

6.4.4 Testing of Additional Proteins Strengthens the Models Prediction Strength

To investigate the generality of our results, and to make sure that it is not specific only to GFP, we tested our model on three different genes: red fluorescent protein (mRFP1), Zymomonas mobilis alcohol dehydrogenase II (zmADH) and the B1 domain of Protein L (PL). The genes were tested under similar conditions to those used for GFP, and their exact sequence were included in the model. The mRFP1 gene was chosen because it is a reporter protein as is GFP, however, mRFP1

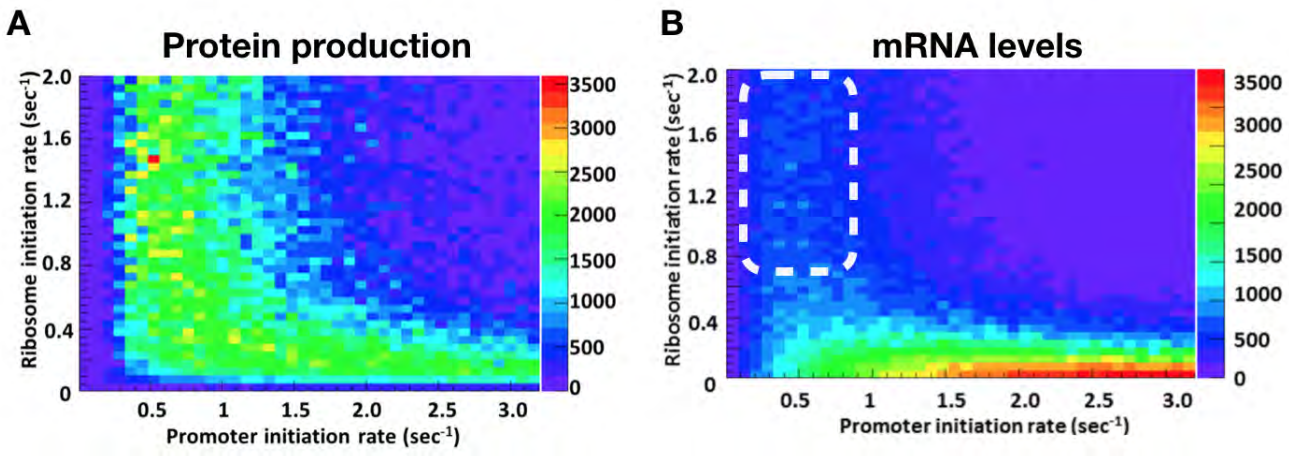

Figure 79: *A) Number of produced proteins from the model, calculated for different values of R_α and r_α. B) Number of produced mRNA strands without arrest from the model, calculated for different values of R_α and r_α. Region marked in white is the most economical region.*

shares only 26% similarity with the GFP amino acid sequence and it represents an optimized gene in terms of codon usage (it consists almost entirely of rapidly translating, i.e. A-type codons). The experimental results for mRFP1 were in a good agreement with the model simulations (Fig. 80A) and showed in general the same trends as the GFP. We note here that the combination of the very weak promoter and the slow TAG codon at position 15 has an even lower production than the WT system. From the model perspective this is because the low production of mRNA due to the promoter and low production of protein from the finished strands gives a very low output. In contrast to mRFP1, zmADH is a larger, more complex gene with lower translation rates owing to its abundance of codons from groups B and C, which attenuate the translation process and result in more complex folding dynamics. The results were once more in a good agreement with the simulations (Fig. 80B), but we observed, contrary to model predictions, a partial rescue effect when testing expression levels with a late mutation (V86TAG) compared to the WT. This finding suggests that cotranslational folding and chaperons may introduce specific points at which nascent polypeptide length is significantly reduced - an assumption that is not incorporated in the model. Thus, the special case of a late mutation can partially rescue a protein from DITA. However, once again we observe that a weak promoter increases expression for this enzyme as well, which was observed both in the model prediction and experimentally. Lastly, we measured the production from PL which is a small, 73-amino-acid polypeptide. This was chosen to test the model prediction that a protein with a relatively short polypeptide chain should have a much lower propensity for a DITA event. This is because the time where the mRNAs are aligned during transcription is much shorter, and almost all mRNA can thus escape without any arrested ribosomes. Furthermore the length of the polypeptide chains remains quite small at all times and thus interactions almost never occurs. We found that WT PL is efficiently produced at significantly greater levels than the TAG mutated variant (Fig. 80C). The results with PL is an additional experimental fingerprint, that if the polypeptide is short enough, and the time spent with mRNAs in close proximity of each other, then spatial collisions are less likely to occur. To sum up, there is good agreement between

our model predictions and the experimental results also for other proteins of different complexity, and thus it could have predictive power for several proteins and potentially in other procaryotes as well.

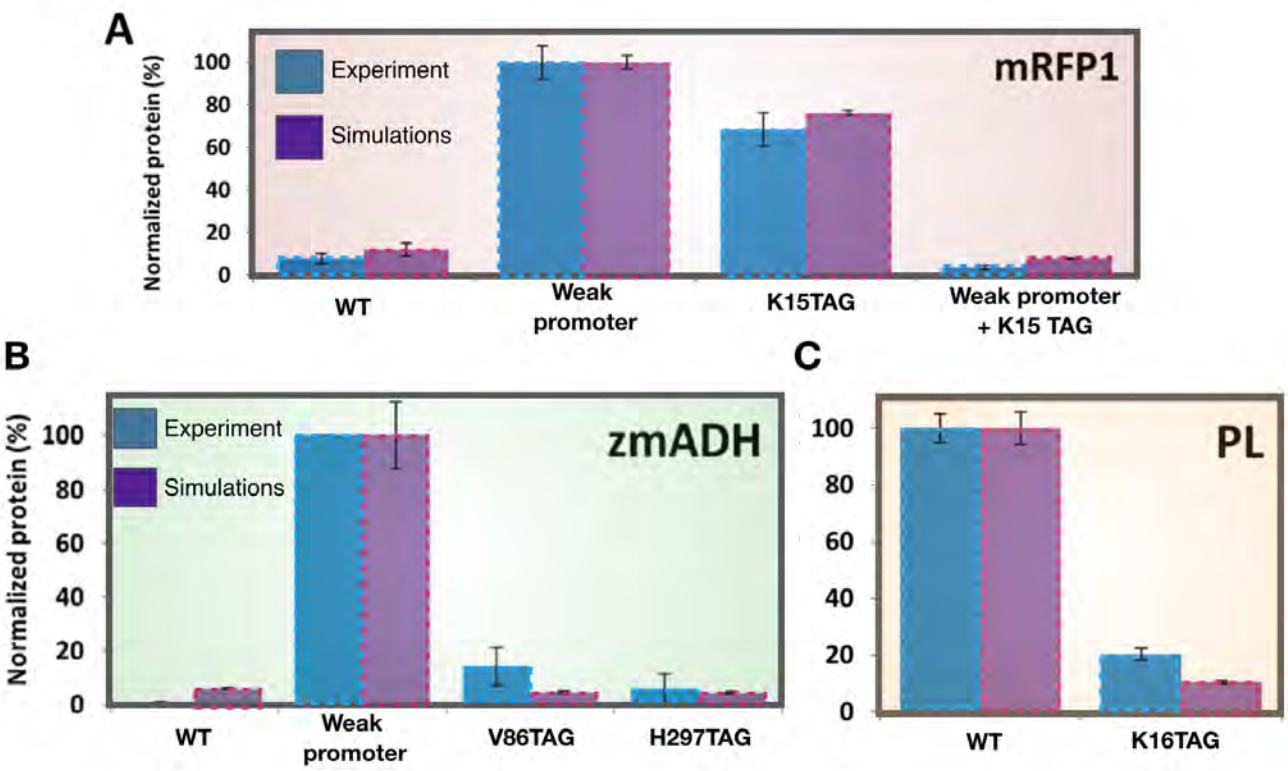

Figure 80: *A) Protein expression for mRFP1 for WT, Weak promoter, K15TAG and Weak promoter + K15TAG B) Protein expression for zmADH for WT, Weak promoter, V86TAG and H297TAG C) Protein expression for PL for WT and K16TAG*

6.5 Discussion and Perspectives

Due to the fact that we have no direct evidence to the occurrence of DITA, we wanted to test our hypothesis by exploring alternative explanations for this phenomenon. Alternative explanations that were excluded by us are: differences in protein stability between a protein with an ncAA and WT protein, differences in plasmid copy numbers, mRNA secondary structure differences, as well as ncAAs interference with fluorescence of the reporting protein, GFP. In order to demonstrate no apparent change in protein stability between WT GFP and Y35TAG GFP, two experiments were conducted: We monitored the stability of the WT and the mutant protein in a crude cell lysate over the course of 24 h, showing that both proteins were stable with no significant change in fluorescence. In the second experiment we used synonymous, slow translating codons that were consecutively mutated around position 35, demonstrating that after the addition of four and above slowly translating codons, protein yields improve significantly to yields that are even higher than that of the protein with incorporated ncAA , these important results indicate that the same protein with no structural change, but a change in the coding sequence, can be expressed with higher yields when the rate of translation slows down significantly, these results are in agreement

with a recent report of Zhong and co-workers.32 These results also show that even with a strong promoter as is being used in this study, no hindrance from plasmid replication is observed. Evidence that attests to the fact that there is no hindrance for plasmid replication due to the existence of a strong promoter are the results with PL, since this protein is very short (ca. 70 AA) it is not affected by DITA, and high yields of expression are observed for this protein even with the strong promoter . mRNA secondary structure could have accounted for the apparent differences in expression profiles between WT GFP and Y35GFP; however, an analysis of the mRNA secondary structure according to an algorithm written by Mathews and co-workers33 has shown no difference in mRNA secondary structure. The algorithm calculates mRNA secondary structure by taking into account base pairing, free energy minimization and other thermodynamic considerations. The analysis has shown that the single nucleotide change of C $\mapsto$ G has no implications on mRNAs secondary structure, hence could not explain the discrepancy in expression levels. Moreover, once ribosomes bind mRNA during translation, the secondary structure is rendered almost linear, hence the predicted secondary structure is not relevant any longer and could not account for the observed difference. In order to exclude the possibility that ncAAs may interfere in any way with GFP fluorescence, we have quantified WT and mutant GFP and thus report their quantities rather than their fluorescence. Additional possibilities were tested as well: ribosome abortion due to ribosome collisions was not excluded it could be an additional hindrance in the system but not an exclusive explanation since we could see elevated expressions of WT GFP also with a weak promoter and a strong RBS. Another possibility is that due to the strong promoter and RBS there will be an extreme consumption of translation factors (i.e., ribosomes, tRNAs, elongation factors, release factors), this possibility was excluded since it should have been seen for the much slower mutant as well (Y35PrK GFP), with the same strong promoter, multiple mRNAs will require multiple ribosomes too. Lastly, we have considered the plasmid copy number as a possible cause of low protein expression levels as is common with very strong promoters, however, our observations point to very low effect of plasmid copy numbers if any: the fact that the relatively small protein WT PL have shown high yields compared to the mutant protein using the same expression vector as for WT GFP expression, while the WT GFP have shown very small expression levels under the same conditions, contradicts the effect of plasmid copy number as the cause for low protein yields. In addition, for the same plasmid Y35PrK GFP have exhibited very high yields as well, again contradicting the effect of high plasmid copy number. Moreover, the synonymous mutations experiment, demonstrates very well that after the insertion of four synonymous "slow" translating codons in the beginning of the gene, protein expression levels are recovered, for the same plasmid, yet again demonstrating that plasmid copy number could not be the cause for low protein yields.

The ability of the model to accurately predict the expression trends of various proteins under different conditions led us to suggest that spatial expression density and DITA have significant effects on protein expression in cells. We note that our model does not take into account co-translational folding and therefore should not be applied to these cases. We would like to stress out that a natural system could not have been evolved to have such strong elements to drive higher protein expression, maybe due to DITA, hence, natural systems have evolved to prevent inefficiency and energy loss. We have used artificial transcription and translation elements as well as a recombinant GFP with a synthetic sequence to demonstrate DITA. These elements were then modified to control DITA levels. In our model the expression density of any gene relies on a

combination of four key determinants: translation initiation and termination rates, transcription initiation and termination rates, gene length and codon bias. Herein, we propose an additional hypothesis for the important roles of codon bias and genetic code redundancy. Although this effect was only observed in this study due to the use of highly efficient transcription and translation control regions, we infer that its effects could have significant, yet not always easy to observe implications, on the expression of all recombinant heterologous proteins. We propose that what is widely known as exogenous expression toxicity due to resource and energy depletion in some cases could be explained by DITA. In addition, we were able to show that by reducing the strength of the regulatory elements, we could lower expression density, resulting in a counterintuitive outcome that significantly improved protein yields. These protein expression dependencies were also observed at the mRNA levels of the various mutants, showing that it affects both cellular protein and mRNA levels, thus affecting the final quantities of protein produced. We showed that DITA occurs for several, highly dissimilar proteins, suggesting that it could be a general mechanism found in all bacteria. Moreover, our findings may also point out the importance of separating transcription and translation processes to increase the production rate of proteins, especially with longer and more complex genes. Obtaining a deep understanding of the transcription and translation processes is of an utmost importance; our findings are a novel step towards the ability to control and modify these processes, which may have a significant impact on protein expression both for fundamental research as well as for biotechnological applications.

References

[1] Steven H Strogatz. *Nonlinear dynamics and chaos: with applications to physics, biology, chemistry, and engineering*. CRC Press, 2018.

[2] VI Arnold and S Ilyashenko Yu. Dynamical systems i ed dv anosov and vi arnold. *Berlin and New York: Springer-Verlag*, 1988.

[3] DE Nelson, AEC Ihekwaba, M Elliott, JR Johnson, CA Gibney, BE Foreman, G Nelson, V See, CA Horton, DG Spiller, et al. Oscillations in nf-κb signaling control the dynamics of gene expression. *Science*, 306(5696):704–708, 2004.

[4] Alexander Hoffmann, Andre Levchenko, Martin L Scott, and David Baltimore. The iκb-nf-κb signaling module: temporal control and selective gene activation. *Science*, 298(5596):1241–1245, 2002.

[5] Galit Lahav, Nitzan Rosenfeld, Alex Sigal, Naama Geva-Zatorsky, Arnold J Levine, Michael B Elowitz, and Uri Alon. Dynamics of the p53-mdm2 feedback loop in individual cells. *Nature genetics*, 36(2):147, 2004.

[6] Octavio Mondragón-Palomino, Tal Danino, Jangir Selimkhanov, Lev Tsimring, and Jeff Hasty. Entrainment of a population of synthetic genetic oscillators. *Science*, 333(6047):1315–1319, 2011.

[7] Michael C Mackey and Leon Glass. Oscillation and chaos in physiological control systems. *Science*, 197(4300):287–289, 1977.

[8] Kim Sneppen. *Models of Life*. Cambridge University Press, 2014.

[9] Joe H Levine, Yihan Lin, and Michael B Elowitz. Functional roles of pulsing in genetic circuits. *Science*, 342(6163):1193–1200, 2013.

[10] Didier Gonze, José Halloy, and Albert Goldbeter. Robustness of circadian rhythms with respect to molecular noise. *Proceedings of the National Academy of Sciences*, 99(2):673–678, 2002.

[11] Sandeep Krishna, Mogens H Jensen, and Kim Sneppen. Minimal model of spiky oscillations in nf-κb signaling. *Proceedings of the National Academy of Sciences*, 103(29):10840–10845, 2006.

[12] Karsten Kruse and Frank Jülicher. Oscillations in cell biology. *Current opinion in cell biology*, 17(1):20–26, 2005.

[13] Ryan A Kellogg and Savaş Tay. Noise facilitates transcriptional control under dynamic inputs. *Cell*, 160(3):381–392, 2015.

[14] Benedicte Mengel, Alexander Hunziker, Lykke Pedersen, Ala Trusina, Mogens H Jensen, and Sandeep Krishna. Modeling oscillatory control in nf-κb, p53 and wnt signaling. *Current opinion in genetics & development*, 20(6):656–664, 2010.

[15] Henri Poincaré and Francis Maitland. *Science and method*. Courier Corporation, 2003.

[16] Edward N Lorenz. Deterministic nonperiodic flow. *Journal of the atmospheric sciences*, 20(2):130–141, 1963.

[17] Mogens H Jensen and Itamar Procaccia. Chaos via quasiperiodicity: Universal scaling laws in the chaotic regime. *Physical Review A*, 32(2):1225, 1985.

[18] Lev S Tsimring. Noise in biology. *Reports on Progress in Physics*, 77(2):026601, 2014.

[19] Michael B Elowitz, Arnold J Levine, Eric D Siggia, and Peter S Swain. Stochastic gene expression in a single cell. *Science*, 297(5584):1183–1186, 2002.

[20] Daniel T Gillespie. Exact stochastic simulation of coupled chemical reactions. *The journal of physical chemistry*, 81(25):2340–2361, 1977.

[21] Yang Cao, Daniel T Gillespie, and Linda R Petzold. Efficient step size selection for the tau-leaping simulation method. *The Journal of chemical physics*, 124(4):044109, 2006.

[22] Inder M Verma, Jennifer K Stevenson, Edward M Schwarz, Daniel Van Antwerp, and Shigeki Miyamoto. Rel/nf-kappa b/i kappa b family: intimate tales of association and dissociation. *Genes & development*, 9(22):2723–2735, 1995.

[23] Sankar Ghosh, Michael J May, and Elizabeth B Kopp. Nf-κb and rel proteins: evolutionarily conserved mediators of immune responses. *Annual review of immunology*, 16(1):225–260, 1998.

[24] Qiutang Li and Inder M Verma. Nf-κb regulation in the immune system. *Nature reviews immunology*, 2(10):725, 2002.

[25] Marc D Jacobs and Stephen C Harrison. Structure of an iκbα/nf-κb complex. *Cell*, 95(6):749–758, 1998.

[26] John Silke. The regulation of tnf signalling: what a tangled web we weave. *Current opinion in immunology*, 23(5):620–626, 2011.

[27] Walter Swardfager, Krista Lanctôt, Lana Rothenburg, Amy Wong, Jaclyn Cappell, and Nathan Herrmann. A meta-analysis of cytokines in alzheimer's disease. *Biological psychiatry*, 68(10):930–941, 2010.

[28] Richard M Locksley, Nigel Killeen, and Michael J Lenardo. The tnf and tnf receptor superfamilies: integrating mammalian biology. *Cell*, 104(4):487–501, 2001.

[29] Thomas D Gilmore. Introduction to nf-κb: players, pathways, perspectives. *Oncogene*, 25(51):6680, 2006.

[30] MS Hayden, AP West, and S Ghosh. Nf-κb and the immune response. *Oncogene*, 25(51):6758, 2006.

[31] V Bottero, S Withoff, and IM Verma. Nf-κb and the regulation of hematopoiesis. *Cell death and differentiation*, 13(5):785, 2006.

[32] Abul K Abbas, Andrew H Lichtman, and Shiv Pillai. *Basic immunology: functions and disorders of the immune system*. Elsevier Health Sciences, 2014.

[33] Mogens Hϕgh Jensen, Per Bak, and Tomas Bohr. Transition to chaos by interaction of resonances in dissipative systems. i. circle maps. *Physical review A*, 30(4):1960, 1984.

[34] Mogens H Jensen and Sandeep Krishna. Inducing phase-locking and chaos in cellular oscillators by modulating the driving stimuli. *FEBS letters*, 586(11):1664–1668, 2012.

[35] Vladimir Igorevich Arnol'd and André Avez. *Ergodic problems of classical mechanics*. WA Benjamin, 1968.

[36] M Høgh Jensen, Per Bak, and Tomas Bohr. Complete devil's staircase, fractal dimension, and universality of mode-locking structure in the circle map. *Physical review letters*, 50(21):1637, 1983.

[37] Arkady Pikovsky, Michael Rosenblum, and Jürgen Kurths. *Synchronization: a universal concept in nonlinear sciences*, volume 12. Cambridge university press, 2003.

[38] J Stavans, F Heslot, and A Libchaber. Fixed winding number and the quasiperiodic route to chaos in a convective fluid. *Physical Review Letters*, 55(6):596, 1985.

[39] Stuart E Brown, George Mozurkewich, and George Grüner. Subharmonic shapiro steps and devil's-staircase behavior in driven charge-density-wave systems. *Physical review letters*, 52(25):2277, 1984.

[40] EG Gwinn and RM Westervelt. Frequency locking, quasiperiodicity, and chaos in extrinsic ge. *Physical review letters*, 57(8):1060, 1986.

[41] Tony Yu-Chen Tsai, Yoon Sup Choi, Wenzhe Ma, Joseph R Pomerening, Chao Tang, and James E Ferrell. Robust, tunable biological oscillations from interlinked positive and negative feedback loops. *Science*, 321(5885):126–129, 2008.

[42] Albert Goldbeter. Computational approaches to cellular rhythms. *Nature*, 420(6912):238, 2002.

[43] Aurore Woller, Hélène Duez, Bart Staels, and Marc Lefranc. A mathematical model of the liver circadian clock linking feeding and fasting cycles to clock function. *Cell reports*, 17(4):1087–1097, 2016.

[44] Ronald A Fisher. The use of multiple measurements in taxonomic problems. *Annals of eugenics*, 7(2):179–188, 1936.

[45] Mark Maienschein-Cline, Aryeh Warmflash, and Aaron R Dinner. Defining cooperativity in gene regulation locally through intrinsic noise. *IET systems biology*, 4(6):379–392, 2010.

[46] Maria Werner, LiZhe Zhu, and Erik Aurell. Cooperative action in eukaryotic gene regulation: physical properties of a viral example. *Physical Review E*, 76(6):061909, 2007.

[47] Shai Kaplan, Anat Bren, Alon Zaslaver, Erez Dekel, and Uri Alon. Diverse two-dimensional input functions control bacterial sugar genes. *Molecular cell*, 29(6):786–792, 2008.

[48] Kim Sneppen, Sandeep Krishna, and Szabolcs Semsey. Simplified models of biological networks. *Annual review of biophysics*, 39:43–59, 2010.

[49] Paolo Tieri, Alberto Termanini, Elena Bellavista, Stefano Salvioli, Miriam Capri, and Claudio Franceschi. Charting the nf-κb pathway interactome map. *PloS one*, 7(3):e32678, 2012.

[50] Aurore Trocoli and Mojgan Djavaheri-Mergny. The complex interplay between autophagy and nf-κb signaling pathways in cancer cells. *American journal of cancer research*, 1(5):629, 2011.

[51] Keng Boon Wee, Wee Kheng Yio, Uttam Surana, and Keng Hwee Chiam. Transcription factor oscillations induce differential gene expressions. *Biophysical journal*, 102(11):2413–2423, 2012.

[52] Louise Ashall, Caroline A Horton, David E Nelson, Pawel Paszek, Claire V Harper, Kate Sillitoe, Sheila Ryan, David G Spiller, John F Unitt, David S Broomhead, et al. Pulsatile stimulation determines timing and specificity of nf-κb-dependent transcription. *Science*, 324(5924):242–246, 2009.

[53] Long Cai, Chiraj K Dalal, and Michael B Elowitz. Frequency-modulated nuclear localization bursts coordinate gene regulation. *Nature*, 455(7212):485, 2008.

[54] Jaroslav Stark, Cliburn Chan, and Andrew JT George. Oscillations in the immune system. *Immunological reviews*, 216(1):213–231, 2007.

[55] Cliburn CW Chan, Jaroslav Stark, and Andrew JT George. Analysis of cytokine dynamics in corneal allograft rejection. *Proceedings of the Royal Society of London B: Biological Sciences*, 266(1434):2217–2223, 1999.

[56] SA Rayner, WJ King, RM Comer, JD Isaacs, G Hale, AJT George, and DFP Larkin. Local bioactive tumour necrosis factor (tnf) in corneal allotransplantation. *Clinical & Experimental Immunology*, 122(1):109–116, 2000.

[57] Saku Ruohonen, Mohsen Khademi, Maja Jagodic, Hanna-Stiina Taskinen, Tomas Olsson, and Matias Röyttä. Cytokine responses during chronic denervation. *Journal of neuroinflammation*, 2(1):26, 2005.

[58] Maren Keller, Jeannine Mazuch, Ute Abraham, Gina D Eom, Erik D Herzog, Hans-Dieter Volk, Achim Kramer, and Bert Maier. A circadian clock in macrophages controls inflammatory immune responses. *Proceedings of the National Academy of Sciences*, 106(50):21407–21412, 2009.

[59] Pernille Yde, Benedicte Mengel, Mogens H Jensen, Sandeep Krishna, and Ala Trusina. Modeling the nf-κb mediated inflammatory response predicts cytokine waves in tissue. *BMC systems biology*, 5(1):115, 2011.

[60] T Bohr and G Gunaratne. Scaling for supercritical circle-maps: Numerical investigation of the onset of bistability and period doubling. *Physics Letters A*, 113(2):55–60, 1985.

[61] Andreas Piehler, Navid Ghorashian, Ce Zhang, and Savaş Tay. Universal signal generator for dynamic cell stimulation. *Lab on a Chip*, 17(13):2218–2224, 2017.

[62] Philip Dettinger, Tino Frank, Martin Etzrodt, Nouraiz Ahmed, Andreas Reimann, Christoph Trenzinger, Dirk Loeffler, Konstantinos D Kokkaliaris, Timm Schroeder, and Sava? Tay. Automated microfluidic system for dynamic stimulation and tracking of single cells. *Analytical chemistry*, 90(18):10695–10700, 2018.

[63] Axelle Amon and Marc Lefranc. Topological signature of deterministic chaos in short nonstationary signals from an optical parametric oscillator. *Physical review letters*, 92(9):094101, 2004.

[64] Robert Gilmore and Marc Lefranc. The topology of chaos, 2003.

[65] O Laptenko and C Prives. Transcriptional regulation by p53: one protein, many possibilities. *Cell death and differentiation*, 13(6):951, 2006.

[66] Edward R Kastenhuber and Scott W Lowe. Putting p53 in context. *Cell*, 170(6):1062–1078, 2017.

[67] Arnold J Levine. p53, the cellular gatekeeper for growth and division. *cell*, 88(3):323–331, 1997.

[68] Jan-Philipp Kruse and Wei Gu. Modes of p53 regulation. *Cell*, 137(4):609–622, 2009.

[69] David P Lane. Cancer. p53, guardian of the genome. *Nature*, 358:15–16, 1992.

[70] Ygal Haupt, Ruth Maya, Anat Kazaz, and Moshe Oren. Mdm2 promotes the rapid degradation of p53. *nature*, 387(6630):296, 1997.

[71] Reiko Honda, Hirofumi Tanaka, and Hideyo Yasuda. Oncoprotein mdm2 is a ubiquitin ligase e3 for tumor suppressor p53. *FEBS letters*, 420(1):25–27, 1997.

[72] Michael HG Kubbutat, Stephen N Jones, and Karen H Vousden. Regulation of p53 stability by mdm2. *Nature*, 387(6630):299, 1997.

[73] Randal S Tibbetts, Kathryn M Brumbaugh, Josie M Williams, Jann N Sarkaria, William A Cliby, Sheau-Yann Shieh, Yoichi Taya, Carol Prives, and Robert T Abraham. A role for atr in the dna damage-induced phosphorylation of p53. *Genes & development*, 13(2):152–157, 1999.

[74] Alexandre Maréchal and Lee Zou. Dna damage sensing by the atm and atr kinases. *Cold Spring Harbor perspectives in biology*, 5(9):a012716, 2013.

[75] Eric Batchelor, Alexander Loewer, Caroline Mock, and Galit Lahav. Stimulus-dependent dynamics of p53 in single cells. *Molecular systems biology*, 7(1):488, 2011.

[76] Domenico Migliorini, Eros Lazzerini Denchi, Davide Danovi, Aart Jochemsen, Manuela Capillo, Alberto Gobbi, Kristian Helin, Pier Giuseppe Pelicci, and Jean-Christophe Marine. Mdm4 (mdmx) regulates p53-induced growth arrest and neuronal cell death during early embryonic mouse development. *Molecular and cellular biology*, 22(15):5527–5538, 2002.

[77] Jason D Grier, Shunbin Xiong, Ana C Elizondo-Fraire, John M Parant, and Guillermina Lozano. Tissue-specific differences of p53 inhibition by mdm2 and mdm4. *Molecular and cellular biology*, 26(1):192–198, 2006.

[78] Shunbin Xiong, Carolyn S Van Pelt, Ana C Elizondo-Fraire, Geng Liu, and Guillermina Lozano. Synergistic roles of mdm2 and mdm4 for p53 inhibition in central nervous system development. *Proceedings of the National Academy of Sciences*, 103(9):3226–3231, 2006.

[79] Mark W Jackson and Steven J Berberich. Mdmx protects p53 from mdm2-mediated degradation. *Molecular and cellular biology*, 20(3):1001–1007, 2000.

[80] Miriam Shadfan, Vanessa Lopez-Pajares, and Zhi-Min Yuan. Mdm2 and mdmx: Alone and together in regulation of p53. *Translational cancer research*, 1(2):88, 2012.

[81] Jean-Christophe Marine and Aart G Jochemsen. Mdmx as an essential regulator of p53 activity. *Biochemical and biophysical research communications*, 331(3):750–760, 2005.

[82] GM Wahl. Mouse bites dogma: how mouse models are changing our views of how p53 is regulated in vivo. *Cell death and differentiation*, 13(6):973, 2006.

[83] Rajesh K Singh, Saravanakumar Iyappan, and Martin Scheffner. Hetero-oligomerization with mdmx rescues the ubiquitin/nedd8 ligase activity of ring finger mutants of mdm2. *Journal of Biological Chemistry*, 282(15):10901–10907, 2007.

[84] K Linke, PD Mace, CA Smith, DL Vaux, J Silke, and Catherine L Day. Structure of the mdm2/mdmx ring domain heterodimer reveals dimerization is required for their ubiquitylation in trans. *Cell death and differentiation*, 15(5):841, 2008.

[85] Sheng-hong Chen, William Forrester, and Galit Lahav. Schedule-dependent interaction between anticancer treatments. *Science*, 351(6278):1204–1208, 2016.

[86] Naama Geva-Zatorsky, Nitzan Rosenfeld, Shalev Itzkovitz, Ron Milo, Alex Sigal, Erez Dekel, Talia Yarnitzky, Yuvalal Liron, Paz Polak, Galit Lahav, et al. Oscillations and variability in the p53 system. *Molecular systems biology*, 2(1), 2006.

[87] José Reyes, Jia-Yun Chen, Jacob Stewart-Ornstein, Kyle W Karhohs, Caroline S Mock, and Galit Lahav. Fluctuations in p53 signaling allow escape from cell-cycle arrest. *Molecular cell*, 71(4):581–591, 2018.

[88] Alan J McKane and Timothy J Newman. Predator-prey cycles from resonant amplification of demographic stochasticity. *Physical review letters*, 94(21):218102, 2005.

[89] Karim ElSawy, Chandra S Verma, Thomas Leonard Joseph, David P Lane, Reidun Twarock, and Leo Caves. On the interaction mechanisms of a p53 peptide and nutlin with the mdm2 and mdmx proteins: a brownian dynamics study. *Cell Cycle*, 12(3):394–404, 2013.

[90] Dongsheng Pei, Yanping Zhang, and Junnian Zheng. Regulation of p53: a collaboration between mdm2 and mdmx. *Oncotarget*, 3(3):228, 2012.

[91] Jeremy E Purvis and Galit Lahav. Encoding and decoding cellular information through signaling dynamics. *Cell*, 152(5):945–956, 2013.

[92] Mark Wade, Yao-Cheng Li, and Geoffrey M Wahl. Mdm2, mdmx and p53 in oncogenesis and cancer therapy. *Nature Reviews Cancer*, 13(2):83, 2013.

[93] Agnieszka Gembarska, Flavie Luciani, Clare Fedele, Elisabeth A Russell, Michael Dewaele, Stéphanie Villar, Aleksandra Zwolinska, Sue Haupt, Job De Lange, Dana Yip, et al. Mdm4 is a key therapeutic target in cutaneous melanoma. *Nature medicine*, 18(8):1239, 2012.

[94] Davide Danovi, Erik Meulmeester, Diego Pasini, Domenico Migliorini, Maria Capra, Ruth Frenk, Petra de Graaf, Sarah Francoz, Patrizia Gasparini, Alberto Gobbi, et al. Amplification of mdmx (or mdm4) directly contributes to tumor formation by inhibiting p53 tumor suppressor activity. *Molecular and cellular biology*, 24(13):5835–5843, 2004.

[95] Yohko Kitayama, Taeko Nishiwaki, Kazuki Terauchi, and Takao Kondo. Dual kaic-based oscillations constitute the circadian system of cyanobacteria. *Genes & development*, 22(11):000–000, 2008.

[96] Aziz Sancar, Laura A Lindsey-Boltz, Tae-Hong Kang, Joyce T Reardon, Jin Hyup Lee, and Nuri Ozturk. Circadian clock control of the cellular response to dna damage. *FEBS letters*, 584(12):2618–2625, 2010.

[97] Michel Jacquet, Georges Renault, Sylvie Lallet, Jan De Mey, and Albert Goldbeter. Oscillatory nucleocytoplasmic shuttling of the general stress response transcriptional activators msn2 and msn4 in saccharomyces cerevisiae. *The Journal of cell biology*, 161(3):497–505, 2003.

[98] Mary-Lee Dequéant, Earl Glynn, Karin Gaudenz, Matthias Wahl, Jie Chen, Arcady Mushegian, and Olivier Pourquié. A complex oscillating network of signaling genes underlies the mouse segmentation clock. *science*, 314(5805):1595–1598, 2006.

[99] Taeko Kobayashi, Hiroaki Mizuno, Itaru Imayoshi, Chikara Furusawa, Katsuhiko Shirahige, and Ryoichiro Kageyama. The cyclic gene hes1 contributes to diverse differentiation responses of embryonic stem cells. *Genes & development*, 23(16):1870–1875, 2009.

[100] Wulfram Gerstner and Werner M Kistler. *Spiking neuron models: Single neurons, populations, plasticity*. Cambridge university press, 2002.

[101] Alan L Hodgkin and Andrew F Huxley. A quantitative description of membrane current and its application to conduction and excitation in nerve. *The Journal of physiology*, 117(4):500–544, 1952.

[102] Seung-Hee Lee and Yang Dan. Neuromodulation of brain states. *Neuron*, 76(1):209–222, 2012.

[103] Matthew J McGinley, Stephen V David, and David A McCormick. Cortical membrane potential signature of optimal states for sensory signal detection. *Neuron*, 87(1):179–192, 2015.

[104] Pierre-Olivier Polack, Jonathan Friedman, and Peyman Golshani. Cellular mechanisms of brain state–dependent gain modulation in visual cortex. *Nature neuroscience*, 16(9):1331, 2013.

[105] Mircea Steriade, I Timofeev, and F Grenier. Natural waking and sleep states: a view from inside neocortical neurons. *Journal of neurophysiology*, 85(5):1969–1985, 2001.

[106] Fengfei Ding, John O'Donnell, Qiwu Xu, Ning Kang, Nanna Goldman, and Maiken Nedergaard. Changes in the composition of brain interstitial ions control the sleep-wake cycle. *Science*, 352(6285):550–555, 2016.

[107] Florin Amzica, Marcello Massimini, and Alfredo Manfridi. Spatial buffering during slow and paroxysmal sleep oscillations in cortical networks of glial cells in vivo. *Journal of Neuroscience*, 22(3):1042–1053, 2002.

[108] J Hounsgaard and C Nicholson. Potassium accumulation around individual purkinje cells in cerebellar slices from the guinea-pig. *The Journal of physiology*, 340(1):359–388, 1983.

[109] HD Lux. Fast recording ion specific microelectrodes: Their use in pharmacoeogical studies in the cns. *Neuropharmacology*, 13(6):509–517, 1974.

[110] HD Lux and E Neher. The equilibration time course of [k+] 0 in cat cortex. *Experimental brain research*, 17(2):190–205, 1973.

[111] C Nicholson, G ten Bruggencate, Rt Steinberg, and H Stöckle. Calcium modulation in brain extracellular microenvironment demonstrated with ion-selective micropipette. *Proceedings of the National Academy of Sciences*, 74(3):1287–1290, 1977.

[112] Pei-Yu Shih, Leonid P Savtchenko, Naomi Kamasawa, Yulia Dembitskaya, Thomas J McHugh, Dmitri A Rusakov, Ryuichi Shigemoto, and Alexey Semyanov. Retrograde synaptic signaling mediated by k+ efflux through postsynaptic nmda receptors. *Cell reports*, 5(4):941–951, 2013.

[113] Flavio Fröhlich, Maxim Bazhenov, Igor Timofeev, Mircea Steriade, and Terrence J Sejnowski. Slow state transitions of sustained neural oscillations by activity-dependent modulation of intrinsic excitability. *Journal of Neuroscience*, 26(23):6153–6162, 2006.

[114] Giri P Krishnan, Gregory Filatov, Andrey Shilnikov, and Maxim Bazhenov. Electrogenic properties of the na+/k+ atpase control transitions between normal and pathological brain states. *Journal of neurophysiology*, 113(9):3356–3374, 2015.

[115] M Emin Tagluk and Ramazan Tekin. The influence of ion concentrations on the dynamic behavior of the hodgkin–huxley model-based cortical network. *Cognitive neurodynamics*, 8(4):287–298, 2014.

[116] Fumiya Tatsuki, Genshiro A Sunagawa, Shoi Shi, Etsuo A Susaki, Hiroko Yukinaga, Dimitri Perrin, Kenta Sumiyama, Maki Ukai-Tadenuma, Hiroshi Fujishima, Rei-ichiro Ohno, et al. Involvement of ca 2+-dependent hyperpolarization in sleep duration in mammals. *Neuron*, 90(1):70–85, 2016.

[117] Maxim Bazhenov, Igor Timofeev, Mircea Steriade, and Terrence J Sejnowski. Model of thalamocortical slow-wave sleep oscillations and transitions to activated states. *Journal of neuroscience*, 22(19):8691–8704, 2002.

[118] Albert Compte, Maria V Sanchez-Vives, David A McCormick, and Xiao-Jing Wang. Cellular and network mechanisms of slow oscillatory activity (¡ 1 hz) in a cortical network model. *Journal of neurophysiology*, 2003.

[119] Sean Hill and Giulio Tononi. Modeling sleep and wakefulness in the thalamocortical system. *Journal of neurophysiology*, 93(3):1671–1698, 2005.

[120] Maria V Sanchez-Vives, Maurizio Mattia, Albert Compte, Maria Perez-Zabalza, Milena Winograd, Vanessa F Descalzo, and Ramon Reig. Inhibitory modulation of cortical up states. *Journal of neurophysiology*, 104(3):1314–1324, 2010.

[121] I Timofeev, F Grenier, M Bazhenov, TJ Sejnowski, and Mircea Steriade. Origin of slow cortical oscillations in deafferented cortical slabs. *Cerebral cortex*, 10(12):1185–1199, 2000.

[122] Belén Sancristóbal, Beatriz Rebollo, Pol Boada, Maria V Sanchez-Vives, and Jordi Garcia-Ojalvo. Collective stochastic coherence in recurrent neuronal networks. *Nature Physics*, 12(9):881, 2016.

[123] Mark L Mayer, Gary L Westbrook, and Peter B Guthrie. Voltage-dependent block by mg2+ of nmda responses in spinal cord neurones. *Nature*, 309(5965):261, 1984.

[124] L_ Nowak, Pw Bregestovski, P Ascher, A Herbet, and Aa Prochiantz. Magnesium gates glutamate-activated channels in mouse central neurones. *Nature*, 307(5950):462, 1984.

[125] Abdoullah Diarra, Claire Sheldon, and John Church. In situ calibration and [h+] sensitivity of the fluorescent na+ indicator sbfi. *American Journal of Physiology-Cell Physiology*, 280(6):C1623–C1633, 2001.

[126] I Dietzel, U Heinemann, G Hofmeier, and HD Lux. Stimulus-induced changes in extracellular na+ and cl- concentration in relation to changes in the size of the extracellular space. *Experimental brain research*, 46(1):73–84, 1982.

[127] Olga Markova, Marat Mukhtarov, Eleonore Real, Yves Jacob, and Piotr Bregestovski. Genetically encoded chloride indicator with improved sensitivity. *Journal of neuroscience methods*, 170(1):67–76, 2008.

[128] Joseph Valentino Raimondo, Bradley Joyce, Louise Kay, Theresa Schlagheck, Sarah Elizabeth Newey, Shankar Srinivas, and Colin Jon Akerman. A genetically-encoded chloride and ph sensor for dissociating ion dynamics in the nervous system. *Frontiers in cellular neuroscience*, 7:202, 2013.

[129] Christine R Rose and Arthur Konnerth. Nmda receptor-mediated na+ signals in spines and dendrites. *Journal of Neuroscience*, 21(12):4207–4214, 2001.

[130] Christine R Rose and Bruce R Ransom. Intracellular sodium homeostasis in rat hippocampal astrocytes. *The Journal of physiology*, 491(2):291–305, 1996.

[131] Morten S Jensen and Yoel Yaari. Role of intrinsic burst firing, potassium accumulation, and electrical coupling in the elevated potassium model of hippocampal epilepsy. *Journal of neurophysiology*, 77(3):1224–1233, 1997.

[132] Stephen Francis Traynelis and Raymond Dingledine. Potassium-induced spontaneous electrographic seizures in the rat hippocampal slice. *Journal of neurophysiology*, 59(1):259–276, 1988.

[133] Roberto De Col, Karl Messlinger, and Richard W Carr. Conduction velocity is regulated by sodium channel inactivation in unmyelinated axons innervating the rat cranial meninges. *The Journal of physiology*, 586(4):1089–1103, 2008.

[134] RK Orkand, JG Nicholls, and SW Kuffler. Effect of nerve impulses on the membrane potential of glial cells in the central nervous system of amphibia. *Journal of neurophysiology*, 29(4):788–806, 1966.

[135] Rune Enger, Wannan Tang, Gry Fluge Vindedal, Vidar Jensen, P Johannes Helm, Rolf Sprengel, Loren L Looger, and Erlend A Nagelhus. Dynamics of ionic shifts in cortical spreading depression. *Cerebral Cortex*, 25(11):4469–4476, 2015.

[136] Bernice Grafstein. Mechanism of spreading cortical depression. *Journal of neurophysiology*, 19(2):154–171, 1956.

[137] George G Somjen. Mechanisms of spreading depression and hypoxic spreading depression-like depolarization. *Physiological reviews*, 81(3):1065–1096, 2001.

[138] Takayuki Yamashita, Aurélie Pala, Leticia Pedrido, Yves Kremer, Egbert Welker, and Carl CH Petersen. Membrane potential dynamics of neocortical projection neurons driving target-specific signals. *Neuron*, 80(6):1477–1490, 2013.

[139] David A McCormick and Anne Williamson. Convergence and divergence of neurotransmitter action in human cerebral cortex. *Proceedings of the National Academy of Sciences*, 86(20):8098–8102, 1989.

[140] David A McCormick, Zhong Wang, and John Huguenard. Neurotransmitter control of neocortical neuronal activity and excitability. *Cerebral cortex*, 3(5):387–398, 1993.

[141] Sylvain Crochet and Carl CH Petersen. Correlating whisker behavior with membrane potential in barrel cortex of awake mice. *Nature neuroscience*, 9(5):608, 2006.

[142] Matthew J McGinley, Martin Vinck, Jacob Reimer, Renata Batista-Brito, Edward Zagha, Cathryn R Cadwell, Andreas S Tolias, Jessica A Cardin, and David A McCormick. Waking state: rapid variations modulate neural and behavioral responses. *Neuron*, 87(6):1143–1161, 2015.

[143] Corbett Bennett, Sergio Arroyo, and Shaul Hestrin. Subthreshold mechanisms underlying state-dependent modulation of visual responses. *Neuron*, 80(2):350–357, 2013.

[144] Luc J Gentet, Michael Avermann, Ferenc Matyas, Jochen F Staiger, and Carl CH Petersen. Membrane potential dynamics of gabaergic neurons in the barrel cortex of behaving mice. *Neuron*, 65(3):422–435, 2010.

[145] Jacob Reimer, Emmanouil Froudarakis, Cathryn R Cadwell, Dimitri Yatsenko, George H Denfield, and Andreas S Tolias. Pupil fluctuations track fast switching of cortical states during quiet wakefulness. *Neuron*, 84(2):355–362, 2014.

[146] Edward Zagha, Amanda E Casale, Robert NS Sachdev, Matthew J McGinley, and David A McCormick. Motor cortex feedback influences sensory processing by modulating network state. *Neuron*, 79(3):567–578, 2013.

[147] Cristopher M Niell and Michael P Stryker. Modulation of visual responses by behavioral state in mouse visual cortex. *Neuron*, 65(4):472–479, 2010.

[148] Martin Vinck, Renata Batista-Brito, Ulf Knoblich, and Jessica A Cardin. Arousal and locomotion make distinct contributions to cortical activity patterns and visual encoding. *Neuron*, 86(3):740–754, 2015.

[149] Kenneth D Harris and Alexander Thiele. Cortical state and attention. *Nature reviews neuroscience*, 12(9):509, 2011.

[150] David M Schneider, Anders Nelson, and Richard Mooney. A synaptic and circuit basis for corollary discharge in the auditory cortex. *Nature*, 513(7517):189, 2014.

[151] D Hirtz, DJ Thurman, K Gwinn-Hardy, M Mohamed, AR Chaudhuri, and R Zalutsky. How common are the ?common? neurologic disorders? *Neurology*, 68(5):326–337, 2007.

[152] Joseph Jankovic. Parkinson?s disease: clinical features and diagnosis. *Journal of neurology, neurosurgery & psychiatry*, 79(4):368–376, 2008.

[153] P Damier, EC Hirsch, Y Agid, and AM Graybiel. The substantia nigra of the human brain: Ii. patterns of loss of dopamine-containing neurons in parkinson's disease. *Brain*, 122(8):1437–1448, 1999.

[154] Julian M Fearnley and Andrew J Lees. Ageing and parkinson's disease: substantia nigra regional selectivity. *Brain*, 114(5):2283–2301, 1991.

[155] Shuang Yong Ma, Matias Röyttä, Juha O Rinne, Yrjö Collan, and Urpo K Rinne. Correlation between neuromorphometry in the substantia nigra and clinical features in parkinson's disease using disector counts. *Journal of the neurological sciences*, 151(1):83–87, 1997.

[156] Ann M Graybiel and Scott T Grafton. The striatum: where skills and habits meet. *Cold Spring Harbor perspectives in biology*, 7(8):a021691, 2015.

[157] Anatol C Kreitzer and Robert C Malenka. Striatal plasticity and basal ganglia circuit function. *Neuron*, 60(4):543–554, 2008.

[158] D James Surmeier, Wen-Jie Song, and Zhen Yan. Coordinated expression of dopamine receptors in neostriatal medium spiny neurons. *Journal of neuroscience*, 16(20):6579–6591, 1996.

[159] D James Surmeier, Jun Ding, Michelle Day, Zhongfeng Wang, and Weixing Shen. D1 and d2 dopamine-receptor modulation of striatal glutamatergic signaling in striatal medium spiny neurons. *Trends in neurosciences*, 30(5):228–235, 2007.

[160] Patrick P Michel, Etienne C Hirsch, and Stéphane Hunot. Understanding dopaminergic cell death pathways in parkinson disease. *Neuron*, 90(4):675–691, 2016.

[161] Ling Wang, Qi Zhang, Huanbin Li, and Hong Zhang. Spect molecular imaging in parkinson's disease. *BioMed Research International*, 2012, 2012.

[162] Fang Ba and WR Wayne Martin. Dopamine transporter imaging as a diagnostic tool for parkinsonism and related disorders in clinical practice. *Parkinsonism & related disorders*, 21(2):87–94, 2015.

[163] Carlos A Paladini, Siobhan Robinson, Hitoshi Morikawa, John T Williams, and Richard D Palmiter. Dopamine controls the firing pattern of dopamine neurons via a network feedback mechanism. *Proceedings of the National Academy of Sciences*, 100(5):2866–2871, 2003.

[164] Tommaso Patriarchi, Jounhong Ryan Cho, Katharina Merten, Mark W Howe, Aaron Marley, Wei-Hong Xiong, Robert W Folk, Gerard Joey Broussard, Ruqiang Liang, Min Jee Jang, et al. Ultrafast neuronal imaging of dopamine dynamics with designed genetically encoded sensors. *Science*, page eaat4422, 2018.

[165] Julia C Greenland, Caroline H Williams-Gray, and Roger A Barker. The clinical heterogeneity of parkinson's disease and its therapeutic implications. *European Journal of Neuroscience*, 2018.

[166] SJG Lewis, Thomas Foltynie, Andrew D Blackwell, Trevor W Robbins, Adrian M Owen, and Roger A Barker. Heterogeneity of parkinson?s disease in the early clinical stages using a data driven approach. *Journal of Neurology, Neurosurgery & Psychiatry*, 76(3):343–348, 2005.

[167] Wolfram Schultz and Anthony Dickinson. Neuronal coding of prediction errors. *Annual review of neuroscience*, 23(1):473–500, 2000.

[168] Wolfram Schultz. Multiple dopamine functions at different time courses. *Annu. Rev. Neurosci.*, 30:259–288, 2007.

[169] Graham V Williams and Patricia S Goldman-Rakic. Modulation of memory fields by dopamine dl receptors in prefrontal cortex. *Nature*, 376(6541):572, 1995.

[170] Roy A Wise. Dopamine, learning and motivation. *Nature reviews neuroscience*, 5(6):483, 2004.

[171] Paolo Calabresi, Barbara Picconi, Alessandro Tozzi, Veronica Ghiglieri, and Massimiliano Di Filippo. Direct and indirect pathways of basal ganglia: a critical reappraisal. *Nature neuroscience*, 17(8):1022, 2014.

[172] Charles Nicholson. Interaction between diffusion and michaelis-menten uptake of dopamine after iontophoresis in striatum. *Biophysical journal*, 68(5):1699–1715, 1995.

[173] G Doucet, L Descarries, and S Garcia. Quantification of the dopamine innervation in adult rat neostriatum. *Neuroscience*, 19(2):427–445, 1986.

[174] Jakob K Dreyer, Kjartan F Herrik, Rune W Berg, and Jørn D Hounsgaard. Influence of phasic and tonic dopamine release on receptor activation. *Journal of Neuroscience*, 30(42):14273–14283, 2010.

[175] Tanya Chotibut, Deana M Apple, Rebecca Jefferis, and Michael F Salvatore. Dopamine transporter loss in 6-ohda parkinson?s model is unmet by parallel reduction in dopamine uptake. *PLoS One*, 7(12):e52322, 2012.

[176] A Jon Stoessl. Positron emission tomography in premotor parkinson's disease. *Parkinsonism & related disorders*, 13:S421–S424, 2007.

[177] John R Adams, Hinke Van Netten, Michael Schulzer, Edwin Mak, Jessamyn Mckenzie, Audrey Strongosky, Vesna Sossi, Thomas J Ruth, Chong S Lee, Matthew Farrer, et al. Pet in lrrk2 mutations: comparison to sporadic parkinson's disease and evidence for presymptomatic compensation. *Brain*, 128(12):2777–2785, 2005.

[178] Xiomara A Perez, Neeraja Parameswaran, Luping Z Huang, Kathryn T O?Leary, and Maryka Quik. Pre-synaptic dopaminergic compensation after moderate nigrostriatal damage in nonhuman primates. *Journal of neurochemistry*, 105(5):1861–1872, 2008.

[179] Michael J Zigmond, Elizabeth D Abercrombie, Theodore W Berger, Anthony A Grace, and Edward M Stricker. Compensations after lesions of central dopaminergic neurons: some clinical and basic implications. *Trends in neurosciences*, 13(7):290–296, 1990.

[180] Michael A Gibson and Jehoshua Bruck. Efficient exact stochastic simulation of chemical systems with many species and many channels. *The journal of physical chemistry A*, 104(9):1876–1889, 2000.

[181] Glen Cowan. *Statistical data analysis*. Oxford university press, 1998.

[182] J Paul Bolam and Eleftheria K Pissadaki. Living on the edge with too many mouths to feed: why dopamine neurons die. *Movement Disorders*, 27(12):1478–1483, 2012.

[183] Jean-Martin Beaulieu and Raul R Gainetdinov. The physiology, signaling, and pharmacology of dopamine receptors. *Pharmacological reviews*, 63(1):182–217, 2011.

[184] Hornykiewicz Ehringer and O Hornykiewicz. Verteilung von noradrenalin und dopamin (3-hydroxytyramin) im gehirn des menschen und ihr verhalten bei erkrankungen des extrapyramidalen systems. *Klinische Wochenschrift*, 38(24):1236–1239, 1960.

[185] Javier Blesa, Inés Trigo-Damas, Michele Dileone, Natalia Lopez-Gonzalez del Rey, Ledia F Hernandez, and José A Obeso. Compensatory mechanisms in parkinson's disease: circuits adaptations and role in disease modification. *Experimental neurology*, 298:148–161, 2017.

[186] Erwan Bezard, Christian E Gross, and Jonathan M Brotchie. Presymptomatic compensation in parkinson's disease is not dopamine-mediated. *Trends in neurosciences*, 26(4):215–221, 2003.

[187] Valtteri Kaasinen, Hanna M Ruottinen, Kjell Någren, Pertti Lehikoinen, Vesa Oikonen, and Juha O Rinne. Upregulation of putaminal dopamine d2 receptors in early parkinson's disease: a comparative pet study with [11c] raclopride and [11c] n-methylspiperone. *Journal of Nuclear Medicine*, 41(1):65–70, 2000.

[188] Jianjun Sun, Evguenia Kouranova, Xiaoxia Cui, Robert H Mach, and Jinbin Xu. Regulation of dopamine presynaptic markers and receptors in the striatum of dj-1 and pink1 knockout rats. *Neuroscience letters*, 557:123–128, 2013.

[189] Jakob K Dreyer. Three mechanisms by which striatal denervation causes breakdown of dopamine signaling. *Journal of Neuroscience*, 34(37):12444–12456, 2014.

[190] G Orieux, C Francois, J Feger, J Yelnik, M Vila, M Ruberg, Y Agid, and EC Hirsch. Metabolic activity of excitatory parafascicular and pedunculopontine inputs to the subthalamic nucleus in a rat model of parkinson's disease. *Neuroscience*, 97(1):79–88, 2000.

[191] Chaorui Huang, Chengke Tang, Andrew Feigin, Martin Lesser, Yilong Ma, Michael Pourfar, Vijay Dhawan, and David Eidelberg. Changes in network activity with the progression of parkinson's disease. *Brain*, 130(7):1834–1846, 2007.

[192] Eugene M Izhikevich. Simple model of spiking neurons. *IEEE Transactions on neural networks*, 14(6):1569–1572, 2003.

[193] Douglas F Browning and Stephen JW Busby. The regulation of bacterial transcription initiation. *Nature Reviews Microbiology*, 2(1):57, 2004.

[194] Sergey Proshkin, A Rachid Rahmouni, Alexander Mironov, and Evgeny Nudler. Cooperation between translating ribosomes and rna polymerase in transcription elongation. *Science*, 328(5977):504–508, 2010.

[195] Hui-Zhu Chen and Geoffrey Zubay. [44] prokaryotic coupled transcription?translation. In *Methods in enzymology*, volume 101, pages 674–690. Elsevier, 1983.

[196] R John Ellis. Macromolecular crowding: obvious but underappreciated. *Trends in biochemical sciences*, 26(10):597–604, 2001.

[197] Cheemeng Tan, Saumya Saurabh, Marcel P Bruchez, Russell Schwartz, and Philip LeDuc. Molecular crowding shapes gene expression in synthetic cellular nanosystems. *Nature nanotechnology*, 8(8):602, 2013.

[198] Namiko Mitarai, Kim Sneppen, and Steen Pedersen. Ribosome collisions and translation efficiency: optimization by codon usage and mrna destabilization. *Journal of molecular biology*, 382(1):236–245, 2008.

[199] Haining Jin, Asgeir Björnsson, and Leif A Isaksson. Cis control of gene expression in e. coli by ribosome queuing at an inefficient translational stop signal. *The EMBO journal*, 21(16):4357–4367, 2002.

[200] Michael A Sørensen, CG Kurland, and Steen Pedersen. Codon usage determines translation rate in escherichia coli. *Journal of molecular biology*, 207(2):365–377, 1989.

[201] Kurt Fredrick and Michael Ibba. How the sequence of a gene can tune its translation. *Cell*, 141(2):227–229, 2010.

[202] Tamir Tuller, Asaf Carmi, Kalin Vestsigian, Sivan Navon, Yuval Dorfan, John Zaborske, Tao Pan, Orna Dahan, Itay Furman, and Yitzhak Pilpel. An evolutionarily conserved mechanism for controlling the efficiency of protein translation. *Cell*, 141(2):344–354, 2010.

[203] Gina Cannarozzi, Nicol N Schraudolph, Mahamadou Faty, Peter von Rohr, Markus T Friberg, Alexander C Roth, Pedro Gonnet, Gaston Gonnet, and Yves Barral. A role for codon order in translation dynamics. *Cell*, 141(2):355–367, 2010.

[204] Tamir Tuller and Hadas Zur. Multiple roles of the coding sequence 5? end in gene expression regulation. *Nucleic acids research*, 43(1):13–28, 2014.

[205] Lei Wang, Ansgar Brock, Brad Herberich, and Peter G Schultz. Expanding the genetic code of escherichia coli. *Science*, 292(5516):498–500, 2001.

[206] Lei Wang and Peter G Schultz. A general approach for the generation of orthogonal trnas. *Chemistry & biology*, 8(9):883–890, 2001.

[207] Jinfan Wang, Marek Kwiatkowski, and Anthony C Forster. Kinetics of trnapyl-mediated amber suppression in escherichia coli translation reveals unexpected limiting steps and competing reactions. *Biotechnology and bioengineering*, 113(7):1552–1559, 2016.

[208] Chenguang Fan, Hai Xiong, Noah M Reynolds, and Dieter Söll. Rationally evolving trnapyl for efficient incorporation of noncanonical amino acids. *Nucleic acids research*, 43(22):e156–e156, 2015.

[209] Marc J Lajoie, Alexis J Rovner, Daniel B Goodman, Hans-Rudolf Aerni, Adrian D Haimovich, Gleb Kuznetsov, Jaron A Mercer, Harris H Wang, Peter A Carr, Joshua A Mosberg, et al. Genomically recoded organisms expand biological functions. *science*, 342(6156):357–360, 2013.

[210] Jonghyeon Shin and Vincent Noireaux. Efficient cell-free expression with the endogenous e. coli rna polymerase and sigma factor 70. *Journal of biological engineering*, 4(1):8, 2010.

[211] Alexander S Mankin. Nascent peptide in the ?birth canal?of the ribosome. *Trends in biochemical sciences*, 31(1):11–13, 2006.

[212] Anton A Komar. A pause for thought along the co-translational folding pathway. *Trends in biochemical sciences*, 34(1):16–24, 2009.

[213] Cheryl A Woolhead, Arthur E Johnson, and Harris D Bernstein. Translation arrest requires two-way communication between a nascent polypeptide and the ribosome. *Molecular cell*, 22(5):587–598, 2006.

[214] Takafumi Sunohara, Kaoru Jojima, Hideaki Tagami, Toshifumi Inada, and Hiroji Aiba. Ribosome stalling during translation elongation induces cleavage of mrna being translated in escherichia coli. *Journal of Biological Chemistry*, 2004.

[215] Stefan Klumpp and Terence Hwa. Growth-rate-dependent partitioning of rna polymerases in bacteria. *Proceedings of the National Academy of Sciences*, 105(51):20245–20250, 2008.

[216] Koji Tamura. Origins and early evolution of the trna molecule. *Life*, 5(4):1687–1699, 2015.

[217] Tessa EF Quax, Nico J Claassens, Dieter Söll, and John van der Oost. Codon bias as a means to fine-tune gene expression. *Molecular cell*, 59(2):149–161, 2015.

[218] Namiko Mitarai and Steen Pedersen. Control of ribosome traffic by position-dependent choice of synonymous codons. *Physical biology*, 10(5):056011, 2013.

[219] Alexandra Dana and Tamir Tuller. Mean of the typical decoding rates: a new translation efficiency index based on the analysis of ribosome profiling data. *G3: Genes, Genomes, Genetics*, 5(1):73–80, 2015.

[220] Leah B Shaw, RKP Zia, and Kelvin H Lee. Totally asymmetric exclusion process with extended objects: a model for protein synthesis. *Physical Review E*, 68(2):021910, 2003.

[221] Grégory Boël, Reka Letso, Helen Neely, W Nicholson Price, Kam-Ho Wong, Min Su, Jon D Luff, Mayank Valecha, John K Everett, Thomas B Acton, et al. Codon influence on protein expression in e. coli correlates with mrna levels. *Nature*, 529(7586):358, 2016.

[222] Aditya Radhakrishnan, Ying-Hsin Chen, Sophie Martin, Najwa Alhusaini, Rachel Green, and Jeff Coller. The dead-box protein dhh1p couples mrna decay and translation by monitoring codon optimality. *Cell*, 167(1):122–132, 2016.

[223] Rob Phillips, Julie Theriot, Jane Kondev, and Hernan Garcia. *Physical biology of the cell*. Garland Science, 2012.

[224] Vladimir Igorevich Arnol'd. *Geometrical methods in the theory of ordinary differential equations*, volume 250. Springer Science & Business Media, 2012.

[225] Vassili Gelfreich. Notes for term i. *Mathematics Institute, University of Warwick*, 2013.

[226] Vladimir I Arnol'd. Remarks on the perturbation theory for problems of mathieu type. *Russian Mathematical Surveys*, 38(4):215–233, 1983.

[227] Robert L Devaney, Peter B Siegel, A John Mallinckrodt, and Susan McKay. A first course in chaotic dynamical systems: theory and experiment. *Computers in Physics*, 7(4):416–417, 1993.

[228] David Singer. Stable orbits and bifurcation of maps of the interval. *SIAM Journal on Applied Mathematics*, 35(2):260–267, 1978.

Appendix A - Biochemical Processes

Simple Protein Dynamics

We consider a protein, T_F, and with one operator P, where the RNA polymerase can bind if there is a transcription factor present (Fig 81A). In terms of reactions it looks as the following:

$$\mathrm{T_F} + \mathrm{P} \underset{\mathrm{k_{off}}}{\overset{\mathrm{k_{on}}}{\rightleftharpoons}} \overline{PT_F}$$

with k_{on} being the rate at which binding occurs and k_{off} being the rate at which they dissociate. If we consider the equilibrium situation we have:

$$k_{on} \cdot T_F \cdot P = k_{off}\overline{PT_F}$$

From where we can get the dissociation constant defined by:

$$K = \frac{k_{off}}{k_{on}} = \frac{T_F \cdot P}{\overline{PT_F}}$$

Typically we then consider a finite number of operators, meaning that

$$P_{total} = P + \overline{PT_F}$$

Then we can use this to calculate the fraction of the occupied operator to be:

$$\frac{\overline{PT_F}}{P_{total}} = \frac{P}{P+K}$$

The dynamics would be governed by the differential equation:

$$\frac{d\overline{PT_F}}{dt} = k_{on}P \cdot T_F - k_{off}\overline{PT_F}$$

This is one of the simplest cases to describe mathematically, and usually this will be too simplified for a genetic network. But for some systems, the above description can be used in simplified models, for instance the ion channel [223].

Michaelis-Menten Kinetics

We consider the following situation (Fig 81C):

$$\mathrm{E} + \mathrm{S} \underset{\mathrm{k_2}}{\overset{\mathrm{k_1}}{\rightleftharpoons}} ES \xrightarrow{\mathrm{k_3}} E + P$$

Under the assumptions that the total amount of E is constant $E = E_0 - ES$
We have 4 components in this network so we consider the differential equations. We just consider the differential equation for $\dot{S}$:

$$\dot{S} = k_2 ES - k_1 \cdot E \cdot S = k_2 ES - k_1 \cdot (E_0 - ES) \cdot S$$

In steady state we have

$$ES = \frac{E_0 S}{\frac{k_2}{k_1} + S}$$

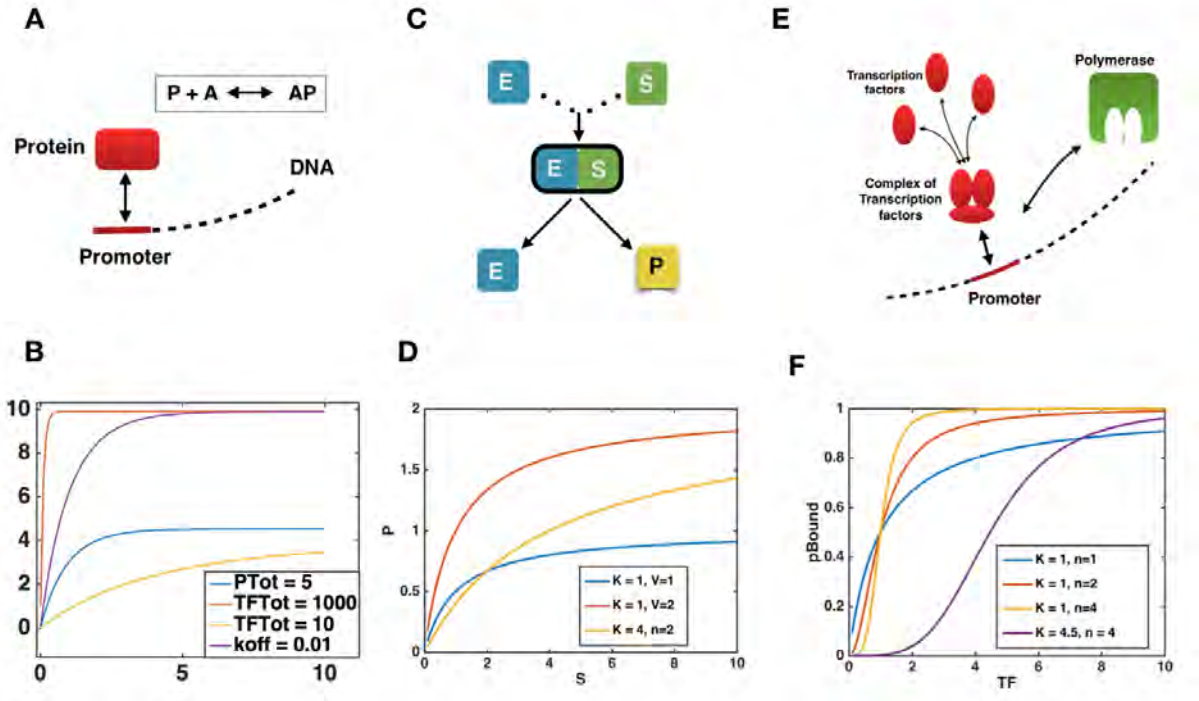

Figure 81: A) Schematic figure of the simplest promoter-Transcription factor binding. B) Time development to steady state. C) Schematic picture of Michaelis Menten situation. D) Curves showing different output values depending on K and V. E) Schematic figure of cooperativity giving rise to Hill function F) Curves showing different output values depending on K and h.

Using this expression, we can get an expression for $\dot{P}$ which is the component we want to describe:

$$\dot{P} = k_{cat}ES = V_{max}\frac{S}{k_D + S}$$

$$\text{where} \quad V_{max} = k_{cat}E_0 \quad \text{and} \quad K_D = \frac{k_2}{k_1}$$

Here V_{max} is the maximum production of the system, in the case of $S \to \infty$, and K_m corresponds to the concentration to reach half maximum. Also here the system provides possibility to describe some of the kinetics of proteins, but for many systems this is oversimplified, which is partly because many systems tend to have cooperativity between the proteins (Fig 81D).

Coorperativity in Gene Regulations

The way that transcription factors regulate the transcription is still far from well understood. However it is well established that not always are only one transcription factor needed, and quite often a complex of several transcription factors can be needed in order to efficiently bind the polymerase and start transcription. In Fig 81E we see a situation where three transcription factors are needed in order to bind the polymerase to the promoter region. To establish an equation for this, we consider the binding of n Transcription factors Tf to a position in on the genome E. We can write this process as:

$$\mathrm{n{\cdot}Tf} + \mathrm{E} \underset{\mathrm{k_2}}{\overset{\mathrm{k_1}}{\rightleftharpoons}} Tf_nE$$

From this we can define the dissociation constant as :

$$K_D^n = \frac{[Tf]^n \cdot [E]}{[Tf_nE]}$$

Now we want to consider the probability to be bound:

$$p_{bound} = \frac{[Tf_nE]}{[E] + [Tf_nE]}$$

Then we can insert the definition of the dissociation constant to obtain:

$$p_{bound} = \frac{([Tf_n]/K_d)^n}{1 + ([Tf_n]/K_d)^n} = \frac{[Tf_n]^n}{K_D^n + [Tf_n]^n}$$

In Fig 81F we see the different output of the Hill function for different values of the parameters K and n. This equation is typically used to describe the production of mRNA for a system. First of all it is important to note, that as the Hill coefficient (above n, often it is defined as h) increases, a switch like behaviour emerges for the output function. Many times in experiments, switch-like behaviours are found, and here the Hill equation is usually used to model this; also even though the theoretical value of n, is unknown [223]. One point to mention is here that even though a complex might need for instance 3 molecules theoretically, from experiments this value can often be lower. An example of this is the bind of haemoglobin that should bind 4 molecules, but where experiments give a Hill coefficient of around 3.0. The constant K, should be understood as a measure for the concentration of Transcription factors to occupy half of the binding sites. Note that the higher the value of K, the longer before the curve starts to rise.

Derivation of the saturated degradation

An important element in the model is the description of the negative feedback mechanism modelled as a so called saturated degradation term. The proces we are actually considering is the following:

$$p53 + Mdm2 \underset{k_2}{\overset{k_1}{\rightleftharpoons}} C_{p-M} \xrightarrow{k_3} \emptyset + Mdm2$$

If we now assume there is a quasi-steady state so the rate of change in the complexes can be neglected we can write:

$$k_1 \cdot (p53 - \emptyset) \cdot (Mdm2 - C_{p-M}) - k_2 C_{p-M} - k_3 C_{p-M} = 0$$

Now isolating C_{p53-M} we obtain:

$$C_{p-M} = Mdm2 \frac{(p53 - \emptyset)}{(p53 - \emptyset) + \frac{k_2 + k_3}{k_1}}$$

Since

$$\dot{\emptyset} = k_3 C_{p-M}$$

we can express the degradation of P53 through the expression:

$$\dot{p53} \approx -k_3 Mdm2 \frac{p53}{p53 + \frac{k_2 + k_3}{k_1}} = -\beta Mdm2 \frac{p53}{p53 + \gamma}$$

Appendix B - NF-κB Model (M)

The transcription factor NF-κB is very important for the mammalian protein production, since it regulates 384 genes involved in at least 572 protein-protein interactions [49]. Therefore it is very important to understand the underlying network leading to NF-κB dynamics and several models have therefore been constructed to capturethis.
In the following we describe the assumptions behind the NF-κB model [34], which is again based on previous findings [52, 11]. A schematic version of this is found in Fig 11A. In the model, we consider the NF-κB inside the nucleus (N_n), where it acts as a transcription factor for proteins, including I-κB. We describe N_n as the nuclear NF-κB concentration, I_m is the IkB mRNA level, and I is the concentration of cytoplasmic I-κB protein. In the equation for $\dot{N_n}$, the first term takes the import of NF-κB to the nucleus into account. This is however in many circumstances inhibited by NF-κB-IκB complexes formed in the cytoplasm. The second term considers the formation of these complexes in the nucleus followed by their export into the cytoplasm. The equation for I_{RNA} describes the NF-κB activated transcription of IκB m_{RNA} and the degradation of the m_{RNA} with a half-life of $ln(2)/\gamma_m$. The first term in the equation for IκB models translation of IκB m_{RNA} into IκB protein in the cytoplasm, and the second term models the TNF-triggered degradation of IκB in the cytoplasm when it is bound to NF-κB. The triggering stimulus TNF, acts by changing the level of active IκB kinase, $[IKK_a]$, which phosphorylates IκB, resulting eventually in its degradation. This degradation rate is set by the parameter α in the model. It is thus only this protein complex with IKK that can phosphorylate the NF-κB - I-κB complex and make NF-κB active again. This model assumes that there is a constant amount of IKK (IKK_{tot}), which can be in three states: active (IKK_a), inactive(IKK_i) and neutral ($IKK_{tot} - IKK_a - IKK_i$). TNF increases the rate at which neutral IKK is made active, and decreases the rate at which inactive IKK is made neutral. All the parameters used in the NF-κB model are found in the Table.

With these assumptions at hand, we formulate a system with the following five coupled differential equations:

$$\dot{N_n} = k_{Nin}(N_{tot} - N_n)\frac{K_I}{K_I + I} - k_{Iin} I \frac{N_n}{K_N + N_n} \tag{134}$$

$$\dot{I_{RNA}} = k_t N_n^2 - \gamma_m I_{RNA} \tag{135}$$

$$\dot{I} = k_{tl} I_{RNA} - \alpha IKK_a (N_{tot} - N_n)\frac{I}{K_I + I} \tag{136}$$

$$\dot{IKK_a} = k_a \cdot TNF \cdot IKK_n - k_i IKK_a \tag{137}$$

$$\dot{IKK_i} = k_i IKK_a - k_p IKK_i \frac{k_{A20}}{k_{A20} + [A20] \cdot TNF} \tag{138}$$

$$IKK_n = [IKK]_{tot} - IKK_a - IKK_i \tag{139}$$

$$TNF = 0.5 + A\sin(\frac{2\pi}{T}t) \tag{140}$$

Parameter in paper	Default value
k_{Nin}	5.4 min^{-1}
k_{Iin}	0.018 min^{-1}
k_t	1.03 $(\mu\text{M})^{-1}.\text{min}^{-1}$
k_{tl}	0.24 min^{-1}
K_I	0.035 μM
K_N	0.029 μM
γ_m	0.017 min^{-1}
α	1.05 $(\mu\text{M})^{-1}.\text{min}^{-1}$
N_{tot}	1. μM
k_a	0.24 min^{-1}
k_i	0.18 min^{-1}
k_p	0.036 min^{-1}
k_{A20}	0.0018 μM
$[IKK]_{tot}$	2.0 μM
$[A20]$	0.0026 μM

Table 1: Default values of parameters in the model. The first 9 are from Ref. [11] and the next 4 from Ref. [52]. $[IKK]_{tot}$ and $[A20]$ were chosen in order to obtain sustained spiky oscillations with frequency in the range 0.3–1 hr^{-1} when $[TNF]$ is kept fixed at 0.5 (the actual frequency obtained with these values is $\nu_0 = 1/1.8\ hr^{-1}$.)

Appendix C - Results for the sine circle map

In this section we will recreate and review the most important results for the sine circle map that serves as inspiration for our study of coupled oscillators.

Poincare section

In general we can write any equation on the torus as:

$$\begin{aligned}\dot{\mathbf{z}} =& v(\mathbf{z}) \quad z \in \mathcal{R}^2 \\ & \text{with } v(\mathbf{z} + 2\pi e_1) = v(\mathbf{z} + 2\pi e_2) = v(\mathbf{z})\end{aligned}$$

The curves of this system, coincide with the integral curves of the non-autonumous system:

$$\frac{dx}{dt} = f(x,t) \quad \text{with } f(x + 2\pi, t) = f(x, t + 2\pi) = f(x,t)$$

Now we evaluate this function every time $t = 2\pi$. This means we want to map the x-axis onto itself and associate the point $(x, 0)$ with $t = 2\pi$ given that the initial condition was $(x_0, 0)$. This we define as the successor function (called monodromy mapping). If we now adopt this formalism we make some definitions of the monodromy mapping, that is now a 1D map:

$$A(x) = x + a(x) \quad a(x + 2\pi) = a(x) \quad a'(x) > -1$$

We have the definitions:

- The trajectory of a point under the action of a diffeomorphism of a space onto itself all the points visited in all iterations.
- A periodic point has a finite trajectory and we define the number of elements in the trajectory as the period p.
- The multiplicity of a cycle with period p, is the degeneracy of any point in this cycle.

The cycles are our main focus, and we define their rotation number:

$$\mu = \frac{1}{2\pi} \lim_{k \to \infty} \frac{A^k(x)}{k}$$

Important insight was reached by Henri Poincare in his study of limicycles, when he proved, that for a homoeomorphism, A, there is a limit to this rotation number and that it is *independent* of the initial point x_0. The rotation number for the differential equation introduced above, is the same as for the monodromy mapping [2].

We consider in the results of this thesis, a similar form of the monodromy map in higher dimensions to be a Poincare section, defined as a surname section of n-1 dimensions for a system in n dimensions. To study the properties of the 1D map, we introduce and study the behaviour of the sine circle map:

$$\theta_{n+1} = \theta_n + \Omega - \epsilon sin(\theta_n)$$

Here we consider one oscillator with phase θ that has modulus 2π. This means that θ_n in the phase after n rotations. This oscillator is now coupled to an external oscillator with frequency Ω,

through a coupling with constant ϵ. In the following we will usually use the equivalent description of the map:

$$x \mapsto x + a + \epsilon sin(x)$$

Note that the value of the external frequency is not dependent on the internal oscillator.

No Coupling

We start by considering the case of uncoupled oscillators where $\epsilon = 0$.
A dynamical with two noninteracting oscillations with frequencies q and p will form a closed cycle, if the rotation number p/q is rational. In this case the period of the cycle is 2π and thus is $2\pi/a$ is rational, the map will show a repeating pattern.
As an example of a closed trajectory we consider $a = 4/3\pi$ and let $x_0 = 0$. For $\epsilon = 0$, we obtain the first phases

$$x_0 = 0 \mapsto x_1 = 4.1888 \mapsto x_2 = 2.0944 \mapsto x_3 = 2\pi$$

This means that after three rotations of the *external* oscillator, the internal oscillator are back at the same point, but it has gone through 2 rotations. This can be seen if we sum the phases. In this way we define, that the coupling is 2/3.
Since couplings exist for all rational rotation numbers, and there are infinitely many rational numbers, one should believe that a randomly chosen parameter would have a rational rotation number. However it turns out that the Lebesgue measure of the rational numbers are zero, compared the irrational numbers that has a Lebesgue measure of 1. This is due to the fact that all the rationals are countable, whereas the reals are uncountable, leading to the fact that if one chooses a random diffeomorphism it will have an irrational rotation number with probability 1 [224] The Lebesgue measure of an open set S, that contains N intervals $[a_i, b_i]$ is defined by:

$$L = \sum_{i}^{N} (b_i - a_i) \tag{141}$$

A good way to realize that the rationals have Lebesgue measure 0, is that a point has lebesgue measure 0. Then summing all the points of measure 0, still give a measure of 0. Following the proof sketched in [1], we will now show that the real numbers are uncountable, whereas the rationals are countable: Proof that all the real numbers are uncountable:
We use proof by contradiction. If we now assume that they are countable, then every number should be in the list, that could be wrtitten of the form:

$$x_i = 0.x_{11}x_{12}x_{13}...$$

We will now construct a number r that is not in the list.

$$r = 0.\bar{x_{11}}\bar{x_{12}}\bar{x_{13}}...$$

This means that it's first digit is anything other than the first digit of x_1, it's second anything other than the second of x_2 and so on. Then we have constructed a number that is not on the list and thus the real numbers are between 0 and 1 are uncountable. Thus all real numbers are

uncountable. And thus the irrational numbers are uncountable. Proof that all the rational numbers are countable:
We setup an infinite matrix, structured in a way, so the ij'th element has the value i/j. Now since there is a structure in this, we can create a sets so:

$$\begin{aligned} l_1 &= 1 \\ l_2 &= \{\frac{2}{1}, \frac{1}{2}\} \\ l_3 &= \{\frac{3}{1}, \frac{2}{2}, \frac{1}{3}\} \\ &\vdots \\ l_n &= \{\frac{n}{1}, \frac{n-1}{2}, ..., \frac{2}{n-1}, , \frac{1}{n}\} \end{aligned}$$

Following the sets, starting from 1, we can always reach any rational number within a finite number of steps. Thus the rationals are countable. So at this point we have argued that for two oscillators with no coupling, there rotational number is irrational. Now all integral curves of the equation

$$\frac{dx}{dt} = \omega \quad \omega \text{ is irrational}$$

are dense on the torus, which means that they are not closed. I Denjoys theorem from 1932, states that a diffeomorphism with irrational rotation number μ, is equivalent to a rotation of the circle by an irrational number, which proved that irrational rotation numbers have quasi periodic trajectories. A quasi periodic trajectory means that the trajectory never repeats itself, and the trajectory is thus infinite.

Weak Coupling

The sine circle map is continuously differentiable and when $\epsilon < 1$ it is easy to see that the derivative $f'(x) = 1 + \epsilon cos(x) > 0$. for all x.
Now the inverse function theorem states that the map is also invertible and the inverse is also continuously differentiable [225]. This means that the map is a diffeomorphism, for which Poincares theorem is valid and thus is the rotation number independent on the initial point x_0.
We observed that for the case of $\epsilon = 0$ the probability of choosing a diffeomorphism with irrational rotation number was equal 1, given the Lebesgue measure of the irrationals. However as the coupling strength grows, the width of the Arnold tongues grow. But even for $\epsilon > 0$, the irrationals are not rapidly approximated by the rationals, especially those of large denominator. Vladimir Arnold proved that for an irrational rotation number μ, there is always a $C > 0$ such that:

$$|\mu - \frac{p}{q}| \geq Cq^{-2-\epsilon} \tag{142}$$

This means that the area of resonance tongues in the Arnold tongue diagram in a small neighbourhood is quite small compared to the entire neighbourhood [224]. This was the background for the definition of the later denoted Arnold tongues. However the resonance curves do grow in width as the coupling strength increases $0 < \epsilon < 1$, and they bend in structure. As was stated in the definition for the rotation number, the limit does exist and is not dependent on the initial condition.

As the coupling strength ϵ increases, the wider the range of coupling to a specific tongue will be. If we consider the 1/1 resonance tongue, we can relatively easy find the width of the resonance family by considering a fixed point since:

$$x + 2\pi = x + a + \epsilon sin(x) \quad \rightarrow a - 2\pi + \epsilon sin(x) = 0$$

This has a solution if:

$$\epsilon sin(3\pi/2) \leq a \leq \epsilon sin(\pi/2)$$

defining the max and min values of the sine function. To obtain a proper description of the width of the tongues for cycles of higher period is very difficult, but in his work as a student in 1959, Vladimir Arnold showed that for the resonance family $\mu = 1/2$, the width of the tongue could be expressed as:

$$a = \pi \pm \frac{\epsilon^2}{4} + \mathcal{O}(\epsilon^4) \tag{143}$$

Here he also argued that the width of the tongues of the resonance family would scale as

$$W \approx \epsilon^q \quad \text{for} \epsilon \rightarrow 0 \tag{144}$$

But not before 1983 in his article for Kolmogorovs 80th birthday was he able to produce a proper proof of this statement [226]. In this famous proof about the width of the Arnold tongues scales as $\approx \epsilon^q$, Vladimir Arnold end with an interesting remark:
A diffeomorphism of the circle can have many cycles. Is the number of isolated cycles of a diffeomorphism given by a trigonometric polynomial bounded by a constant depending only on the degree of the polynomial? This question can be regarded as an analogue of the question in Hilberts 16^{th} problem on the number of limit cycles of a polynomial differential equation. It has not even been solved for the diffeomorphisms $x \mapsto x + a + bcos(x)$. Conversely, the asymptotic expressions obtained above for the boundaries of domains of existence of cycles does have analogues in the theory of differential equations with a polynomial right-hand side. An important development was Jakobsens' theorem, stating that:
Every diffeomorphism in the two-parameter family

$$f_{\epsilon,a} : y \mapsto t + a + \epsilon sin(y) \tag{145}$$

has no more than two cycles
Here we can check the stability of the cycles and easy find that one has $\frac{dx_{n+1}}{dx_n} < 1 \quad \rightarrow$ stable and one has $\frac{dx_{n+1}}{dx_n} > 1 \quad \rightarrow$ unstable. Combining this with Jakobsens theorem we can state that for $\epsilon < 1$ no overlapping resonance families will emerge.
We now test a small section to see whether other members of the resonance family will grow as expected. We therefore considered a small intervals of values for a, so $a \in [0.617; 0.717]$, and simulated values of ϵ in the interval $\epsilon \in]0; 1]$. Often one is interested in studying the resonance families for a fixed coupling strength, and this type of plot is denoted a Devil's staircase. In Fig 82A these are considered. Combining values of a and ϵ, we obtain an Arnold tongue plot is visualised in Fig 82B, where we the regions grow, that it is the rationals with the smallest denominator that are by far the largest. The largest is therefore the 2/3 region, and we estimate the width of as a

function of a coupling strength and find (Fig 82C):

$$g(w) = \alpha w^{\beta} \Rightarrow b = 2.8 \pm 0.01 \tag{146}$$

These simulations therefore give a crude estimate of the width which almost follows the growth for small ϵ.

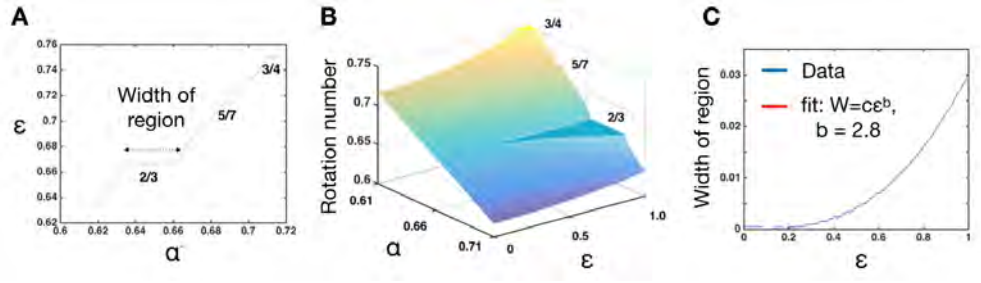

Figure 82: *A) Devils staircase showing rotation number as a function of the external frequency a. B) Arnold tongue plot showing rotation number as a function of the external frequency a and ϵ C) The width of the 2/3 region as a function of ϵ and fitted by a powerlaw*

Overlapping Regime

As the Arnold Tongues grow continuously, eventually regions will emerge where different Arnold Tongues start to overlap. If we consider the overlap of two resonance families, for instance the 2/3 and the 5/7, then in principle all families of the rationals in between would be expected also to overlap. In principle they could all coexist, which means that the limit in the definition of the rotation number *would* depend on the initial conditions. Otherwise one or more resonances could take up the entire space, meaning that some of the families has lost their stability. The third possibility is that no stable cycles are present when the tongues start to overlap.

For $\epsilon > 1$, Jakobsons theorem does no longer apply, since here the map is not invertible, meaning that it is no longer a diffeomorphism.

Theoretically we can argue that there can maximally be 2 stable cycles. We use the Schwarzian derivative given by:

$$Sf(x) = \frac{f'''(x)}{f'(x)} - \frac{3}{2}\left(\frac{f''(x)}{f'(x)}\right) \tag{147}$$

Inserting this in the expression for the sine circle map we get:

$$Sf(x) = \frac{-2\epsilon(cos(x) + \epsilon) - (\epsilon sin(x))^2}{2(1 + cos(x))^2} \tag{148}$$

we see that it is only strictly negative if $\epsilon > 1$. Now if the Schwarzian derivative is negative, then one can show that the function f, cannot have a positive local minima or a negative local maxima[227]. If we now suppose that the Schwarzian derivative is negative, then there is a theorem stating that if x_0 is a stable periodic point of f, then either the immediate basin of attraction of x_0 extends from ∞ to $-\infty$, or else there is a critical point of f whose orbit is attracted to the orbit of x_0 [228].

Now we can easlily see that the sine circle map becomes bimodal for $\epsilon > 1$ since the derivative

$1 + \epsilon cos(x)$ here is equal to zero at two critical points. And since at least one of the critical points will be attracted to a stable periodic point, then no more than two periodic cycles can exist. Simulations show that if we increase the coupling strength to 2.3 then we see in Fig 83A that *two stable cycles exist*, which would never happen for the homeomorphism.
To check this dependency on the initial conditions, we simulate 10000 initial conditions for x_0 and in Fig 83B we see the rotation numbers dependency on the initial condition is rather complex. But since these two stable cycles do occur, it should then be possible to jump from one cycles to another. This is investigated by adding gaussian noise to the system, so the update now is like:

$$x \mapsto x + a + \epsilon sin(x) + \mathcal{N}(0, 0.002)$$

The result is seen inFig 83C, where it is seen clearly that the transitions between the states occur.

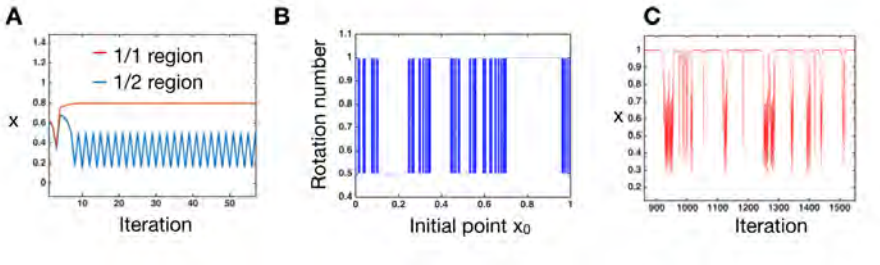

Figure 83: *A) Values of x, starting from two different initial conditions B) The calculated rotation number as a function of the initial point x_0. C) Stochastic simulation showing x as a function of the iteration number*

Period Doublings and Chaos

For $\epsilon = 1$ the map is still invertible, however the differentiated is no longer non-zero everywhere since $1 - cos(\pi) = 0$, and thus it is still a homeomorphism, for which the rotation number should be independent of the initial point. At this point the full devils staircase has previously been studied [33], and it is found that the resonances form a cantor set of fractal dimension ≈ 0.87, which is the universal measure for which transitions into chaos can occur.
When the value of ϵ increases above 1, the theorems used in the sections above are no longer valid, since the map is no longer invertible. Here period doublings occurs, meaning that a cycle changes in integers multiplied with the nominator and denominator but the rotation number stays the same.
Chaos is defined by a positive lyapunov constant. For a 1D map, we define the lyapunov constant as:

$$\lambda(f, x) = \lim_{n\to\infty} \frac{1}{n} log|(f^n)'(x)| \tag{149}$$

$$\to \lim_{n\to\infty} \frac{1}{n} \sum_{k=1}^{n-1} |f'(x_k)| \tag{150}$$

This means we can calculate the lyapunov function for a series of points starting from x_0, but in principle when calculating the lyapunov exponent, one should consider *all* initial conditions.

However in many practical uses, one can remember that the qualitative meaning of the lyapunov constant is that trajectories starting from almost the same initial conditions are departing from eachother. it is given that two trajectories part from each other

$$|\delta Z_n| \approx e^{\lambda n} |\delta Z_0| \tag{151}$$

In a previously study of an annulus map [17], this has been found to grow like:

$$\lambda \approx (K - K_c)^{\beta} \quad \rightarrow \quad \beta \approx 0.95 \tag{152}$$

There are several routes to chaos, and here we have seen that one of them is through couplings that through period doublings goes into chaos. This should thus be a basic property in all systems of one oscillator coupled to an externally driven oscillator. Both chaotic and quasiperiodic trajectories never repeat themselves, meaning that they are dense on the torus. However a small perturbation for a quasiperiodic trajectory does not cause the distance between trajectories will grow, as is the case for the chaotic trajectory.

Appendix D - Extended Averaged-Neuron model

We consider the membrane potential (V_m) given by:

$$\frac{dV}{dt} = -\frac{1}{C}(\sum I_{Ext}) - \frac{1}{AC}((\sum I_{Int}))$$

$$\text{intrinsic} \in [Leak, Na_V, K_V, K_{A-type}, K_{SI}, Ca_V, K_{Ca}, NaP, K_{IR}]$$

$$\text{extrinsic} \in [NMDA, AMPA, GABA_A]$$

The units on the left side is mV/ms, but the extrinsic currents are in units of uA whereas the intrinsic currents are in nA, and therefore the first should be multiplied by 1000. This reduces to 10, since we multiply with A, that should be in cm^2 and should thus be divided by 100.

Intrinsic Channel Conductances

For the leak channel we have:

$$I_{Leak} = g_{Leak}(V - V_{Leak}) \tag{153}$$

$$g_{Leak} = 0.03573 \quad mS/cm^2 \quad V_{Leak} = \frac{RT}{zF}\ln\Big(\frac{p_K[K]_o + p_{Na}[Na]_o + p_{Cl}[Cl]_i}{p_K[K]_i + p_{Na}[Na]_i + p_{Cl}[Cl]_o}\Big)$$

$$R = 8.314472 \quad J/K/mol \quad T = 310 \quad kelvins \quad z = valence_{ion} \quad F = 9.64853399x10^4 \quad C/mol$$

For the voltage-gated sodium channel we have:

$$I_{Na_V} = g_{Na_V} m_{Na_V}^3 h_{Na_V}(V - V_{Na}) \tag{154}$$

$$m_{Na_V} = \frac{\alpha_m}{\alpha_m + \beta_m} \qquad \begin{cases} \alpha_m = 0.1\frac{V+33}{1-e^{-(V+33)/10}} \\ \beta_m = 4e^{-(V+53.7)/12} \end{cases}$$

$$\dot{h}_{Na_V} = 4(\alpha_h(1 - h_{Na_V}) - \beta_h h_{Na_V}) \qquad \begin{cases} \alpha_h = 0.07e^{-(V+50)/10} \\ \beta_h = \frac{1}{1+e^{-(V+20)/10}} \end{cases}$$

$$g_{Na_V} = 12.2438 \quad mS/cm^2 \quad V_{Na} = \frac{RT}{zF}\ln\Big(\frac{[Na]_o}{[Na]_i}\Big)$$

For the voltage-gated potassium channel we have:

$$I_{K_V} = g_{K_V} n_K^4 (V - V_K) \tag{155}$$

$$\dot{n}_{K_V} = 4(\alpha_h(1 - h_{K_V}) - \beta_h h_{K_V}) \qquad \begin{cases} \alpha_n = 0.01\frac{V+34}{1-e^{-(V+34)/10}} \\ \beta_n = 0.125e^{-(V+44)/25} \end{cases}$$

$$g_{K_V} = 2.61868 \quad mS/cm^2 \quad V_K = \frac{RT}{zF}\ln\Big(\frac{[K]_o}{[K]_i}\Big)$$

For the fast A-type potassium channel we have:

$$
\begin{aligned}
I_{A-type} =& g_{A-type} m_{A-type}^3 h_{A-type} (V - V_K) \\
& m_{A-type} = \frac{1}{1 + e^{-(V+50)/20}} \\
& \dot{h}_{A-type} = \frac{h_{A-type\infty} - h_A - type}{\tau_{hA-type}} \\
& h_{A-type\infty} = \frac{1}{1 + e^{(V+80)/6}} \\
& g_{A-type} = 1.79259 \quad mS/cm^2 \quad \tau_{hA-type} = 15ms \quad V_K = \frac{RT}{zF} \ln\Big(\frac{[K]_o}{[K]_i}\Big)
\end{aligned}
\tag{156}
$$

For the slowly inactivating potassium channel we have:

$$
\begin{aligned}
I_{K_{SI}} =& g_{K_{SI}} m_{K_{SI}} (V - V_K) \\
& m_{K_{SI}} = \frac{h_{m_{K_{SI}\infty}} - m_{K_{SI}}}{\tau_{mK_{SI}}} \\
& m_{K_{SI}\infty} = \frac{1}{1 + e^{-(V+34)/6.6}} \\
& \tau_{mK_{SI}} = \frac{8}{e^{-(V+55)/30} + e^{(V+55)/30}} \\
& g_{K_{SI}} = 0.0350135 \quad mS/cm^2 \quad V_K = \frac{RT}{zF} \ln\Big(\frac{[K]_o}{[K]_i}\Big)
\end{aligned}
\tag{157}
$$

For the voltage-gated calcium channel we have:

$$
\begin{aligned}
I_{Ca_V} =& g_{Ca_V} m_{Ca_V\infty}^2 (V - V_{Ca}) \\
& m_{Ca_V\infty} = \frac{1}{1 + e^{(V+20)/9)}} \\
& g_{Ca_V} = 0.0256867 \quad mS/cm^2 \quad V_{Ca} = \frac{RT}{zF} \ln\Big(\frac{[Ca]_o}{[Ca]_i}\Big)
\end{aligned}
\tag{158}
$$

For the calcium-dependent potassium channel we have:

$$
\begin{aligned}
I_{K_{Ca}} =& g_{K_{Ca}} m_{K_{Ca}\infty} (V - V_K) \\
& m_{K_{Ca}\infty} = \frac{1}{1 + \frac{K_D}{[Ca]_i}^{3.5}} \\
& \dot{[Ca]}_i = -\alpha_{Ca}(10 \cdot AI_{Ca} + I_{NMDA}) - \frac{[Ca]_i}{\tau_{Ca}} \\
& g_{K_{Ca}} = 2.34906 \quad mS/cm^2 \quad K_D = 30\mu M \quad \tau_{Ca} = 121.403ms \quad V_K = \frac{RT}{zF} \ln\Big(\frac{[K]_o}{[K]_i}\Big)
\end{aligned}
\tag{159}
$$

For the persistent sodium channel we have:

$$
\begin{aligned}
I_{NaP} =& g_{NaP} m_{NaP\infty} (V - V_{Na}) \\
& m_{NaP\infty} = \frac{1}{1 + e^{-(V+55.7)/7.7}} \\
& g_{NaP} = 0.0717984 \quad mS/cm^2 \quad V_{Na} = \frac{RT}{zF} \ln\Big(\frac{[Na]_o}{[Na]_i}\Big)
\end{aligned}
\tag{160}
$$

For the inwardly rectifying potassium channel we have:

$$\begin{aligned} I_{K_{IR}} =& g_{K_{IR}} h_{K_{IR}\infty}(V - V_K) \\ & h_{K_{IR}\infty} = \frac{1}{1 + e^{(V+75)/4}} \\ & g_{K_{IR}} = 0.0166454 \quad mS/cm^2 \quad V_K = \frac{RT}{zF}\ln\Big(\frac{[K]_o}{[K]_i}\Big) \end{aligned} \tag{161}$$

Extrinsic Channel Conductances

We start by defining the saturating function

$$f(V) = \frac{1}{1 + e^{-(V-20)/2)}}$$

We now consider the AMPA receptor:

$$\begin{aligned} I_{AMPA} =& g_{AMPA} s_{AMPA}(V - V_{AMPA}) \\ & \dot{s_{AMPA}} = 3.48 f(V) - \frac{s_{AMPA}}{\tau_{AMPA}} \\ & g_{AMPA} = 0.513425 \quad \mu S/cm^2 \quad V_{AMPA} = \frac{RT}{zF}\ln\Big(\frac{p_K[K]_o + p_{Na}[Na]_o}{p_K[K]_i + p_{Na}[Na]_i}\Big) \end{aligned} \tag{162}$$

For the NMDA receptor we have:

$$\begin{aligned} I_{NMDA} =& \frac{1.1}{1.0 + [Mg]_o/8.0mM} g_{NMDA} s_{NMDA}(V - V_{NMDA}) \\ & \dot{s_{NMDA}} = 0.5 x_{NMDA}(1 - s_{NMDA}) - \frac{s_{NMDA}}{\tau_{sNMDA}} \\ & \dot{x_{NMDA}} = 3.48 f(V) - \frac{x_{NMDA}}{\tau_{xNMDA}} \\ & g_{NMDA} = 0.00434132 \quad \mu S/cm^2 \quad V_{NMDA} = \frac{RT}{zF}\ln\Big(\frac{p_K[K]_o + p_{Na}[Na]_o + p_{Ca}[Ca]_o}{p_K[K]_i + p_{Na}[Na]_i + p_{Ca}[Cl]_i}\Big) \end{aligned} \tag{163}$$

For the GABA_A receptor we have:

$$\begin{aligned} I_{GABA_A} =& g_{GABA_A} s_{GABA_A}(V - V_{GABA}) \\ & \dot{s_{GABA_A}} = f(V) - \frac{s_{GABA_A}}{\tau_{sGABA_A}} \\ & g_{GABA_A} = 0.00252916 \quad \mu S/cm^2 \quad V_{GABA} = \frac{RT}{zF}\ln\Big(\frac{[Cl]_i}{[Cl]_o}\Big) \end{aligned} \tag{164}$$

Ion Concentrations

We used the following intra- and extracellular ion concentrations:

$$[Na]_o = 140 \quad mM \quad [Na]_i = 7 \quad mM$$

$$[K]_o = [3.5; 3.9; 4.4; 4.9; 8; 14] \quad mM \quad [K]_i = 7 \quad mM$$

$$[Ca]_o = [1.05; 1.2; 1.35] \quad mM \quad [Ca]_i = -\alpha_{Ca}(10 \cdot AI_{Ca} + I_{NMDA}) - \frac{[Ca]i}{\tau_{Ca}} \quad \mu M$$

$$[Cl]_o = 140 \quad mM \quad [Cl]_i = 10 \quad mM$$

$$[Mg]_o = [0.6; 0.7; 0.8] \quad mM$$

Appendix E - Diffusion in a sphere

We then consider the effects of diffusion in a region where no dopaminergic terminals are left, but where the MSN neurons still are workin. Mathematically this corresponds to a situation where a sphere of radius r is surrounded by a large region with steady state DA level C_0 (Fig. A2A). This means we wish to solve the diffusion equation in spherical coordinates:

$$\frac{\partial C(r,t)}{\partial t} = D\Big(\frac{\partial^2 C(r,t)}{\partial r^2} + \frac{1}{r}\frac{\partial C(r,t)}{\partial r}\Big) \tag{165}$$

With boundary conditions: (166)

$$C(a,t) = C_0, \quad C(0,t) = 0, \quad C(r,0) = 0 \quad (r < a) \tag{167}$$

Using a proper substitiution, and laplace transformation, one can show that the concentration is described by:

$$C(r,t) = C_s \cdot \Big(1 + \frac{2a}{\pi r}\sum_{n=1}^{\infty}\frac{(-1)^n}{n} sin(\frac{2\pi r}{a}) e^{-D\frac{n^2\pi^2 t}{a}}\Big) \tag{168}$$

However we have so far not encountered the decay of dopamine, that in healthy striatum is a negligible quantity. However in this situation it becomes of great importance, so we actually want to solve:

$$\frac{\partial C(r,t)}{\partial t} = D\Big(\frac{\partial^2 C(r,t)}{\partial r^2} + \frac{r}{r}\frac{\partial C(r,t)}{\partial r}\Big) - kC(r,t) \tag{169}$$

This solution is easily obtained from the above result, through the relation:

$$C(r,t) = k\int_0^t C_1(r,t')e^{-kt'}dt' + C_1(r,t)e^{-kt} \tag{170}$$

so we find that the concentration in an empty region can be described by:

$$C(r,t) = C_s + \frac{2kC_s a}{\pi r}\sum_{n=1}^{\infty}\frac{(-1)^n}{n}\cdot \tag{171}$$

$$sin(\frac{n\pi r}{a})\Big(\frac{k}{X}(1 - e^{-Xt}) + e^{-Xt}\Big) \quad X \equiv \frac{Dn^2\pi^2}{a^2} \tag{172}$$

Based on this result we can see in Fig. A2B, how this in time reaches a steady state, and how this steady state value drops to a very low value for empty regions with radius larger than 0.03 cm.

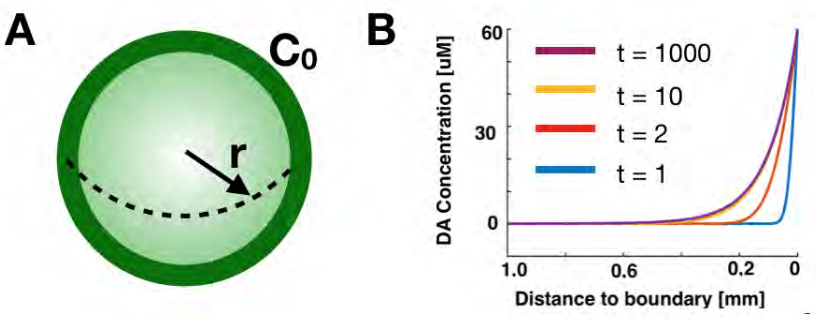

Figure 84: *A) Model showing high dopamine level at the boundary of an empty region. B) Profiles showing the dopamine concentration at different distances to the boundary after certain time steps*

Appendix F - Voronoi tesselation

Consider a space, X, with distance function, $d(x, P_i)$ and some points, P_i (Fig 85A). We define the most empty space as the largest sphere one can draw, without meeting one of the N points. Therefore we search for the centre of this sphere, that is the mark, whose distance to the point nearest point, is larger than any other marks distance to its nearest point. Mathematically we formulate the mark x^* as:

$$x^* = \max\Big\{\min\{d(x, P_j)\}\Big\}$$
$$x^* = \min\Big(x \in X | \partial_x(\min\{d(x, P_j)\}) = 0\Big)$$

Finding this mark is a surprisingly tedious task, and using brute force Monte Carlo techniques takes very long computational time and give low precision, since we search for a minimum in 3D, but filled with local minima created by all points. To enhance both precision and calculation time, we use the concept of Voronoi Diagrams. A Voronoi cell, R_k is defined as the set of all points, whose distance to P_k is not greater than their distance to any of the other sites P_j (Fig 85B). Thus the formal definition for a Voronoi diagram is:

$$R_K = \Big\{x \in X | d(x, P_k) \leq d(x, P_j) \quad \text{for all } k \neq j\Big\}$$

Therefore, using this definition, the most empty point must be one of edges where different Voronoi cells intersect, and we search for the most empty point in the set of all Voronoi cell edges (Fig A3B). Since the points represent areas in our calculations, the actual empty space is significantly smaller and is calculated by subtracting the diameter of the covered area by one neuron, from the calculated empty space (Fig 85C). Using this technique we find all the empty regions inside the area. However, since some of the edges meet outside the circle, the most empty regions on the boundary are not found. Therefore by searching for points on the boundary as well, we find the most empty regions in that set (Fig 85B) and comparing this with the empty spaces found using Voronoi diagrams, we find the most empty space unambiguously.

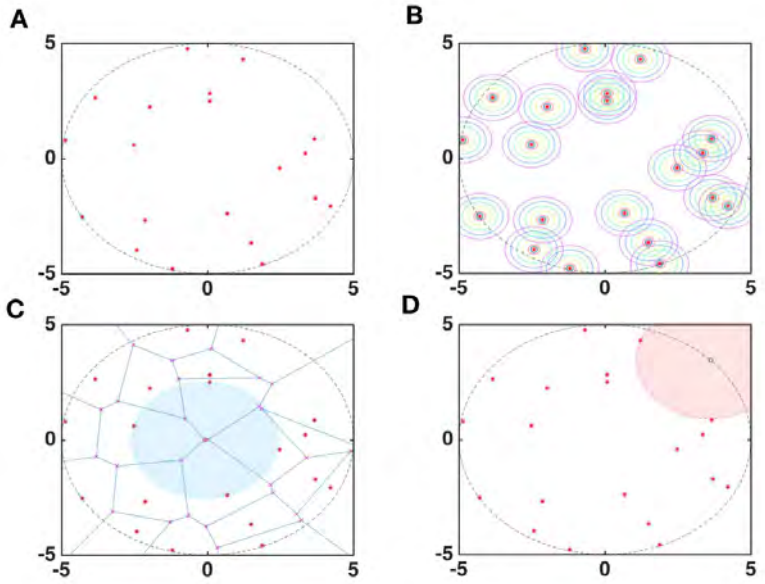

Figure 85: A) 20 points randomly positioned inside a circle B) Voronoi diagram for the generated points. Points, x, denote the edges. Shaded area show the largest empty space. C) Neurons cover some area. Shaded area show the largest empty space within the covered areas. D) Largest empty space from the boundary.

Appendix G - The evolution of empty regions

The question is now, if such empty spaces can arise while there is still many neurons remaining. The calculation of these dead spaces, does not follow a simple distribution, and the question we ask is therefore the following: After N neurons what is the most desolate point i.e. from what point in space can we draw the largest sphere without meeting terminals from another neuron? To calculate this we use the theory of Voronoi tessellation, where each neuron is given a volume in form of a polyhedron, which is created to define that inside this polyhedron all points are closest to the given neuron. This means that either one of these edges, or (which will typically be the case) a point on the boundary, must be the most desolate spot in the putamen and satisfies our criteria.

The calculation of this distribution will be very complex, especially since the probability to be covered is not the same everywhere. We note that we look for one specific spot out of many, and thus we expect this to be an example of an extreme value type distribution, or a Gumbel distribution. The Gumbel distribution is given by:

$$P(r_{max}|\beta,\mu) = \frac{1}{\beta}e^{-(z+e^{-z})} \quad \text{where} \quad z = \frac{r_{max}-\mu}{\beta} \tag{173}$$

To test this, we simulate 1000 samples, and calculate the largest empty space. As seen in fig **??**, the fit is very good, and we conclude that the distribution of largest empty spaces is described by a Gumbel Distribution. What we would really like though is to know the probability that the largest empty space is less than a certain threshold. This is done by calculating:

$$P(r_{max} < k) = \int_{-\infty}^{R} \frac{1}{\beta}e^{-(z+e^{-z})}dr \quad \text{where} \quad z \equiv \frac{r-\mu}{\beta} \tag{174}$$

This integral is easily evaluated using substitution, and we find that the probability of the largest empty space having being larger than R is given by:

$$S(x) \equiv P(r_{max} > R) = 1 - e^{-e^{-w}} \quad \text{where} \quad w = \frac{R-\mu}{\beta} \tag{175}$$

Furthermore, for the Gumbel distribution, the mean is given by:

$$E(r_{max}|N) = \mu + \lambda\beta \quad \text{where} \quad \lambda \approx 0.5772 \quad \text{(Eulers constant)} \tag{176}$$

This means that for the given two parameters, β and μ, the probability that the largest empty space will be smaller than a given quantity is found by the above formula. Therefore in order to describe this system, we must be able to find the relation between these parameters, and the remaining number of neurons.

Fitting the values obtained from the fit to the Gumbel distribution, we find that both parameters can be calculated, depending on the number of remaining neurons, and we can describe:

$$\beta(N) = a_\beta N^{-b_\beta} \quad \text{with} \quad a_\beta = 0.014, b_\beta = 0.43,$$

$$\mu(N) = a_\mu \cdot b_\mu^{-N^{c_\mu}} \quad \text{with} \quad a_\mu = 0.94, b_\mu = 1.55, c_\mu = 0.21$$

This means that the largest empty region follows a well defined statistical evolution as a function of the remaining neurons.

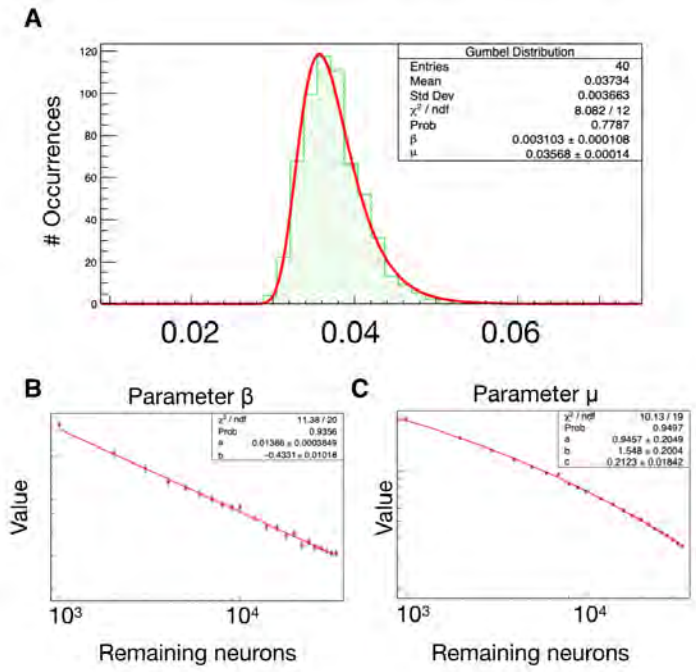

Figure 86: *A) Distribution of the largest empty region with a Gumbel distribution fitted. B) The parameter value of β as a function of the remaining number of neurons C) The parameter value of μ as a function of the remaining number of neurons*

Article

Cell Systems

Noise Induces Hopping between NF-κB Entrainment Modes

Graphical Abstract

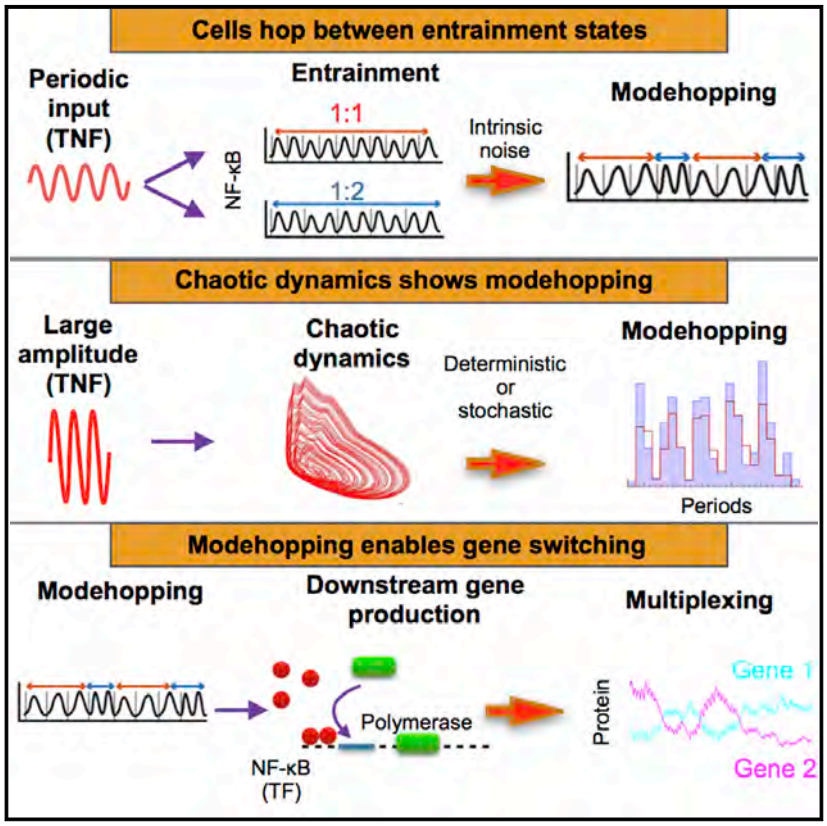

Highlights

- Periodic TNF stimulation leads to hopping between NF-κB entrainment modes
- For regions of overlapping Arnold tongues, intrinsic noise leads to mode-hopping
- Chaotic dynamics is characterized by frequent mode-hopping
- Mode-hopping suggests mechanism for the cell to regulate protein production

Authors

Mathias Heltberg, Ryan A. Kellogg, Sandeep Krishna, Savaş Tay, Mogens H. Jensen

Correspondence

tays@uchicago.edu (S.T.), mhjensen@nbi.ku.dk (M.H.J.)

In Brief

Oscillations and noise drive many processes in biology, but how both affect the activity of the transcription factor NF-κB is not understood. This paper describes "cellular mode-hopping," phenomenon in which NF-κB exhibits noise-driven jumps between defined frequency modes. The authors suggest that mode-hopping is a mechanism by which different NF-κB-dependent genes under frequency control can be expressed at different times.

Heltberg et al., 2016, Cell Systems *3*, 532–539
December 21, 2016
http://dx.doi.org/10.1016/j.cels.2016.11.014

OPEN ACCESS
CellPress

Cell Systems
Article

Noise Induces Hopping between NF-κB Entrainment Modes

Mathias Heltberg,[1,6] Ryan A. Kellogg,[2,6,7] Sandeep Krishna,[1,3] Savaş Tay,[2,4,5,*] and Mogens H. Jensen[1,8,*]
[1]Niels Bohr Institute, University of Copenhagen, 2100 Copenhagen, Denmark
[2]Department of Biosystems Science and Engineering, ETH Zürich, 8092 Zürich, Switzerland
[3]Simons Center for the Study of Living Machines, National Center for Biological Sciences, Bangalore 560065, Karnataka, India
[4]Institute for Molecular Engineering, University of Chicago, Chicago, IL 60637, USA
[5]Institute for Genomics and Systems Biology, University of Chicago, Chicago, IL 60637, USA
[6]Co-first author
[7]Present address: Department of Genetics, Stanford University School of Medicine, Stanford, CA 94305, USA
[8]Lead Contact
*Correspondence: tays@uchicago.edu (S.T.), mhjensen@nbi.ku.dk (M.H.J.)
http://dx.doi.org/10.1016/j.cels.2016.11.014

SUMMARY

Oscillations and noise drive many processes in biology, but how both affect the activity of the transcription factor nuclear factor κB (NF-κB) is not understood. Here, we observe that when NF-κB oscillations are entrained by periodic tumor necrosis factor (TNF) inputs in experiments, NF-κB exhibits jumps between frequency modes, a phenomenon we call "cellular mode-hopping." By comparing stochastic simulations of NF-κB oscillations to deterministic simulations conducted inside and outside the chaotic regime of parameter space, we show that noise facilitates mode-hopping in all regimes. However, when the deterministic system is driven by chaotic dynamics, hops between modes are erratic and short-lived, whereas in experiments, the system spends several periods in one entrainment mode before hopping and rarely visits more than two modes. The experimental behavior matches our simulations of noise-induced mode-hopping outside the chaotic regime. We suggest that mode-hopping is a mechanism by which different NF-κB-dependent genes under frequency control can be expressed at different times.

INTRODUCTION

Oscillation is a conserved dynamic feature of many biological systems. Increasingly oscillation is appreciated to play a role in transcriptional processes in the living cell, given the large number of transcriptional regulators now observed to exhibit oscillation or pulsing (Levine et al., 2013; Gonze et al., 2002). Noise is a core feature of biological systems, and it impacts variability and timing of oscillatory transcriptional regulators (Eldar and Elowitz, 2010; Elowitz et al., 2002). However, the roles of oscillation and noise in gene regulation are still incompletely understood.

Periodic inputs may lead to entrainment of oscillators, a phenomenon where the oscillatory process locks, in frequency and phase, to the external signal. Canonical examples of entrainment in physics include pendulum clocks and lasers; in these systems there exists well-developed theory describing how two oscillators can couple in the way that one external (that is, an independent periodic input) couples to an internal oscillator. The output of the internal oscillator depends on the coupling to the external and to the difference in frequency between the two. When they couple, we call it entrainment, and these regions of entrainment grow with increasing amplitude of the external oscillator. This is depicted schematically in Figure 1. On the horizontal axis is the frequency of the external oscillator (here tumor necrosis factor [TNF]) while on the vertical axis is it is amplitude. These entrainment regions are called Arnold tongues (Jensen et al., 1984); they are indicated as regions of green, red, and yellow. In the case of entrainment between the internal (here nuclear factor κB [NF-kB]) and external oscillator, we observe the widening of the tongues.

However, it is unclear whether biological oscillators can exhibit behaviors that are similarly complex. Recently, it was shown in single mammalian cells that periodic cytokine inputs entrain the nuclear localization oscillations of NF-κB (Kellogg and Tay, 2015) (schematized in Figure 2A), a transcription factor that plays a central role in environmental sensing and the immune response. In this earlier work, noise (i.e., the dynamic variability in molecular interactions), was demonstrated to synergistically enhance the ability of NF-κB oscillations to entrain to periodic cytokine input from the environment. Specifically, it was observed that noise increased NF-kB oscillation amplitude and gene expression under periodic stimulation. Nonetheless, how noise interacts with both the periodic input and the oscillator itself to mediate entrainment in signaling networks like NF-κB is not yet clear. Here, we demonstrate that noise facilitates a phenomenon we call "mode-hopping": NF-κB oscillations remain entrained but switch spontaneously between two frequencies. This phenomenon qualitatively resembles mode-hopping behavior observed in lasers, another form of oscillator (Mork et al., 1990). We suggest that mode-hopping may diversify the expression patterns of frequency-modulated genes.

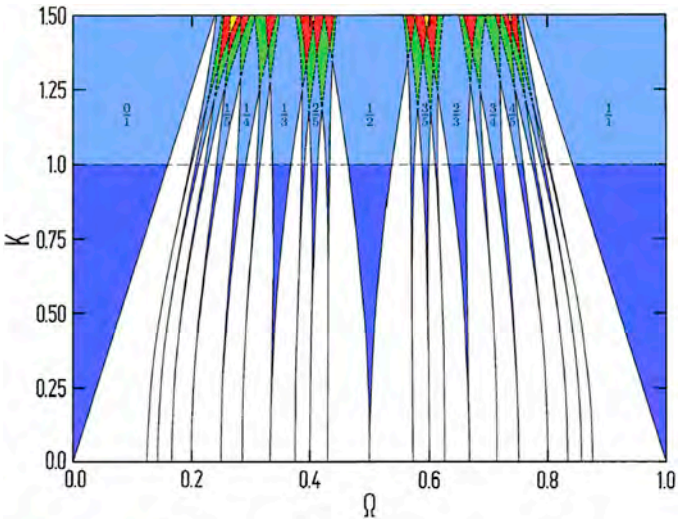

Figure 1. Schematic Diagram of Arnold Tongues

On the horizontal axis is the frequency (Ω) of the external (TNF) oscillator and the vertical axis is its amplitude (K). The blue regions are ones in which the internal and external oscillators are entrained, the numbers attached to each region describes the frequency ratio for the entrainment. The white regions show intermixed quasi-periodic and periodic behavior, too finely intermingled to be separated by our plot. The dashed line indicate where the tiniest tongues start to overlap. The green, red, and yellow regions show overlapping behavior, but now also including a chaotic element (Jensen et al., 1984).

RESULTS

Mode-Hopping in Entrained NF-κB Oscillations under Fluctuating TNF Input

In cells, the extracellular ligand TNF initiates a series of intracellular processes that can produce oscillations in the concentration of nuclear NF-κB under specific conditions. Specifically, TNF activates IκB kinase (IKK), which causes the NF-κB transcription factor to enter the cell nucleus and regulate gene expression including upregulation of IκB negative feedback (schematized in Figure 2A) (Krishna et al., 2006). When TNF is delivered periodically, the fraction of NF-κB localized within the nucleus oscillates with a natural oscillation period of 90–100 min (Kellogg and Tay, 2015). Accordingly, we previously showed that NF-κB oscillations can synchronize across the population and entrain cells to the TNF input, and noise was found to facilitate entrainment and efficient gene expression (Kellogg and Tay, 2015). For example, TNF with a 180-min period can entrain NF-κB at a 90-min period for a 1:2 (input:oscillator) locking or entrainment mode (schematized in Figure 2B) (original observation described in Kellogg and Tay [2015]). These regions are defined as Arnold tongues, and the entrainment is schematized in Figure 2B.

Our current investigation began with repeating the observations described in Kellogg and Tay (2015). Using microfluidic cell culture, we delivered periodic TNF stimulation to fibroblasts and recorded dynamics of NF-κB nuclear localization by live cell fluorescence microscopy. Not only did we confirm that NF-κB oscillations occur, we also observed that they show spontaneous frequency jumps and transitions between locking modes during the time course of periodic stimulation for some external forcing periods (Figure 2C). Specifically, these transitions involve apparent spontaneous changes in amplitude (Figure 2D) and doubling and halving of the oscillation frequency over time (Figure 2E); borrowing from the literature on Martin et al. (1997), we refer to this phenomenon as mode-hopping. Compared to 90 min TNF input where cells entrain almost exclusively at the 1:1 locking mode, at 150 min, the average cell spends equal time in 1:1 and 1:2 modes. For 180 min input, the average cell spends the most time in the 2:1 mode but also ~30% of time in the 1:1 mode (Figure 2F). The appearance of multiple entrainment modes during the time course suggests that the system is in the overlapping Arnold tongue regions (schematized in Figures 2B and 2D). It is understood in physics that in noise-free (i.e., deterministic) systems, spontaneous transitions between locking modes cannot occur before the multiple overlaps within the Arnold tongue regions cause a transition into chaos (Jensen et al., 1984). However, whether and how transitions between entrainment modes can spontaneously occur in a noisy system like the NF-κB network is not clear; if these transitions occur, it is not clear what drives them. To answer these questions, we turned to simulation.

Noise Induces NF-κB Frequency Jumps between Entrainment Modes

First, we considered the differential equations model (Jensen and Krishna, 2012), described in the STAR Methods, that captures the essential features of NF-κB behavior. We started by deterministically simulating this model's behavior in response to oscillatory inputs of different periods and amplitudes; in aggregate, these simulations define the Arnold tongue regions of this model within parameter space. For the NF-κB system, the structure of the tongues is not symmetric, and overlapping regimes of tongues start at quite low amplitudes (Jensen and Krishna, 2012; Kellogg and Tay, 2015) (Figure 3A). As expected, we observed that when NF-κB oscillations are simulated deterministically within the overlapping Arnold tongue regions of parameter space (as defined by the amplitude and frequency of external oscillator), oscillations settle in different entrained states depending on the initial conditions (Figures 3B and 3C; see the STAR Methods for details of the simulations). Mathematically speaking, this means that more than one limit cycle exists, and depending on the basins of attraction, a trajectory decay be attracted to one of the limit cycles. Mode-hopping was, however, not observed, because transitions between stable states do not occur for the deterministic system. This is at the very heart of deterministic systems; once an initial position is defined, that trajectory will be followed, and if the system is inside a basin of attraction, it cannot leave this state.

Next, we considered whether noise could mediate mode-hopping and frequency jumps in NF-κB oscillations by adding noise to our simulations using the Gillespie algorithm (Gillespie, 1977) while keeping the average concentrations of NF-κB and other molecules the same. In these stochastic simulations, we find that transitions between entrained states do indeed occur and show mode-hopping events similar to experimental observations (Figures 3D). These transitions are more easily observed if we look at the periods, where it is clear that they make transitions between states (Figure 3E). Another way to study this phenomena is to look at the trajectory in the three-dimensional phase space spanned by NF-κB, I-κB mRNA, and I-κB (the

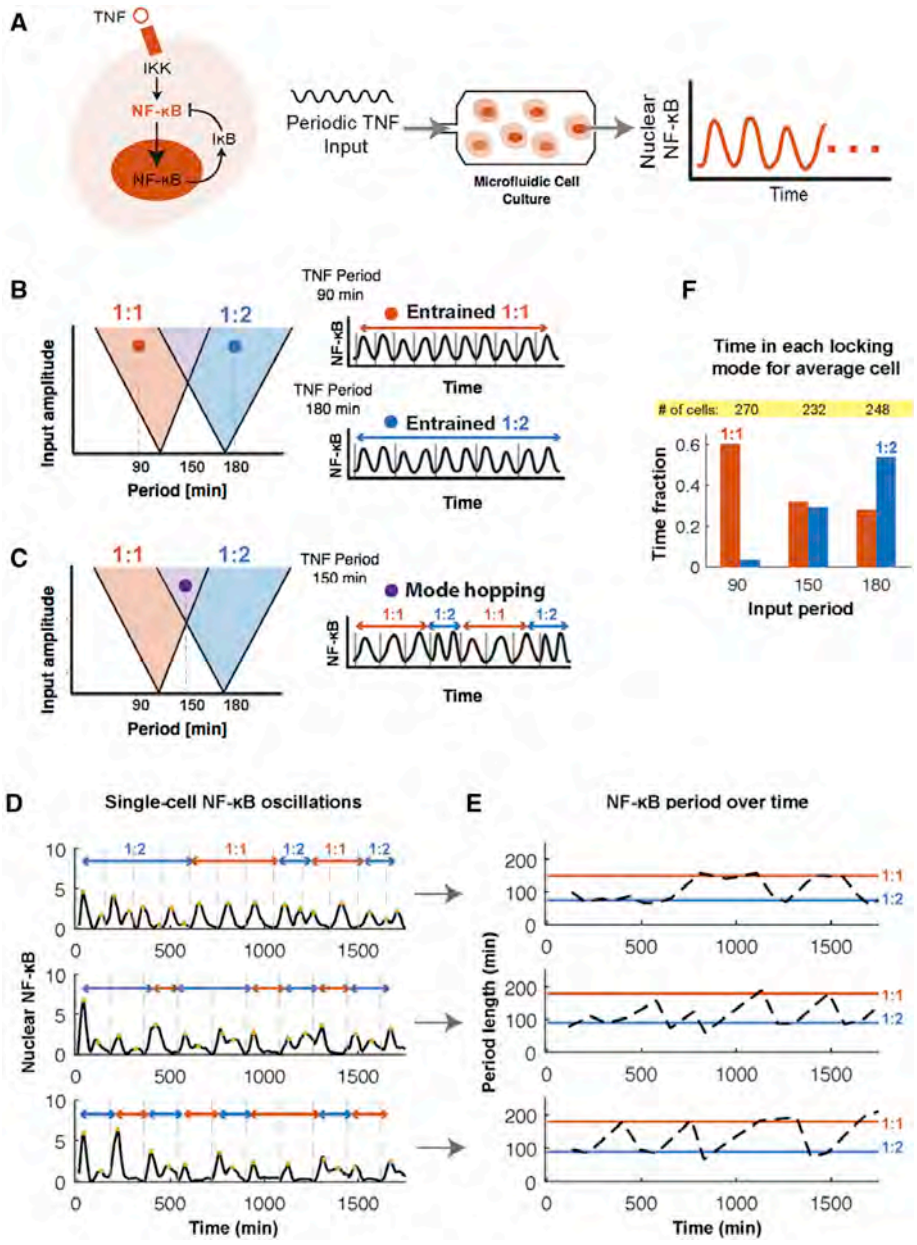

Figure 2. Experimentally Measured Frequency Jumps (Mode-Hopping) in NF-κB Oscillations

(A) TNF activates IKK and NF-κB, causing IκB negative feedback leading to oscillations in NF-κB nuclear translocation. We apply periodic TNF input using microfluidics and monitor nuclear NF-κB oscillation dynamics using live cell fluorescence imaging.

(B) Periodic forcing of an oscillator leads to entrainment visualized by regions called Arnold tongues. In the 1:1 NF-κB entrainment mode (orange region), the NF-κB period matches the 90-min period of the fluctuating TNF input. In the 1:2 entrainment mode (blue region), there is one TNF input cycle for every two cycles of the NF-κB oscillation.

(C) In overlapping Arnold tongue regions, multiple entrainment modes are possible. Here, noise may enable spontaneous transitions between entrainment modes as observed in experiments.

(D) Three examples of mode-hopping in single-cell NF-κB traces. Timing of TNF input is indicated by vertical gray dashed lines.

(E) Plots of NF-κB oscillation period versus time. Colors indicate intervals in entrainment 1:1 (orange) and 1:2 (blue) modes.

(F) Comparison of time an average cell spends in each entrainment mode, for differing TNF input frequencies.

variables in the first three differential equations presented in the STAR Methods). This presents a quite intuitive way of thinking of the mode-hopping; the trajectory oscillates with two different radii, and this gives rise to the two different periods of oscillation (Figure 3F). Based on these analyses, we conclude that noise mediates hopping between entrainment modes and could serve as a mechanism in the cell to produce quick switching of NF-κB oscillation frequency.

To understand this observation in a more detailed way, we simulated different noise levels by controlling the volume and number of molecules in the simulation. We find that as noise is increased (smaller simulation volume and hence smaller number of molecules), mode-hopping transitions happen more often with more entrainment modes visited. In this sense, increasing the noise tends to broaden the Arnold tongues of the system (Figures 3G–3I). Systems with little noise, in contrast, usually spend very long times in one entrained state, and we find that the system tends to be more in a high period state for small noise compared to large noise. We also find that systems with high noise jump quickly and spend approximately the same time in each entrained state (Figure 3J). Together, these simulations demonstrate that noise is able to reproduce the mode-hopping frequency transitions that we observe in experiments. The mode-hopping seen in the overlapping tongue region is reminiscent of the noise-induced hopping one would observe in a classical bistable system but with the states defined by frequencies and amplitudes of oscillations. Next, we investigated whether mode-hopping is restricted to stochastic systems in the early overlapping regime, or systems operating close to the chaotic regime may also exhibit mode-hopping within the Arnold tongue regions and how this was related to the (deterministic)transition into chaos.

Mode-Hopping Is a Characteristic Feature for Noisy and Chaotic Systems

When the amplitude of the driving TNF oscillation is increased, we move up in the Arnold tongue diagram (Figure 4A), which leads the deterministic system into a chaotic regime (Jensen et al., 1984). Deterministic chaos is characterized by a trajectory in phase space that never repeats itself and has the property that two trajectories starting from slightly different initial conditions diverge exponentially in time (Lorenz, 1963). Chaotic states are reached for larger TNF amplitudes where many tongues overlap

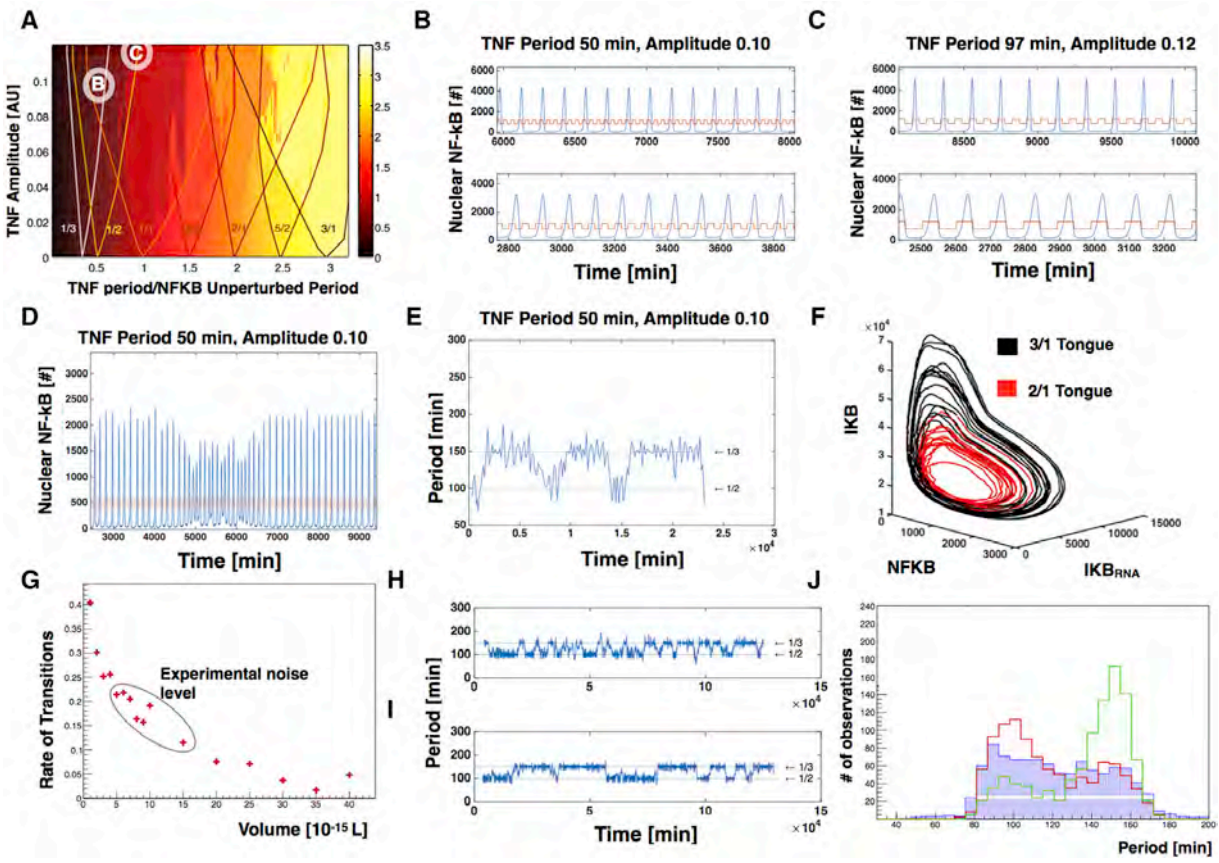

Figure 3. Noise Induces Mode-Hopping in Overlapping Arnold Tongue Regions

(A) Arnold tongue diagram for a deterministic model of NF-κB oscillations driven by a periodic square pulse of TNF. Note that the amplitude is dimensionless. The colors show the ratio of the observed NF-κB frequency to the driving TNF frequency as defined in the color bar (right) (Jensen and Krishna 2012).

(B and C) Deterministic simulations of NF-κB behavior conducted within regions of parameter space that exist within the overlapping region between Arnold tongues. The simulations shown in (B) were conducted using the parameters in the region of space labeled "B" in Figure 2A, the simulations shown in (C) were conducted using the parameters in the region of space labeled "C" in Figure 2A. Red traces indicate TNF input frequency (50 min in B, 97 min in C; all amplitudes are 0.1 AU); blue traces describe the behavior of NF-κB.

(D) Stochastic (Gillespie) simulation of NF-κB behavior conducted within region of parameter space labeled "B" in Figure 2A. Red traces indicate TNF input frequency (period of 50 min; amplitude of 0.1 AU); blue traces describe the be the behavior of NF-κB.

(E) Additional visualization of the data shown in (D) where the period between successive NF-κB peaks is plotted as a function of time. The horizontal lines correspond to integer multiples of the time period of the driving TNF oscillation.

(F) The trajectories of individual simulations conducted as in (D), plotted in a phase space that describes IKB, IKB_{RNA}, and NK-kB values. Colors indicate the different entrained states the trajectory visits.

(G) The number of transitions between frequency modes per thousand oscillations as a function of simulation volume; simulated noise decreases with increasing volume; data are taken from simulations analogous to the one shown in (D) but conducted at different cell volumes. The rate of transitions that corresponds to what is found in the experiments are shown in the red circle.

(H and I) Additional visualizations of the data shown in (G) where the period between successive NF-κB peaks is plotted as a function of time. The horizontal lines correspond to integer multiples of the time period of the driving TNF oscillation.

(J) The distribution of periods is shown, and we see that they peak around integer multiples of the TNF period, and when noise decreases, the system spends longer times in the high period sta.

(Figure 4A). We characterized the behavior of the NF-κB oscillator near this region of parameter space.

As we increase the amplitude of the TNF oscillations, but before chaos sets in, a variety of interesting phenomena occur. For example, one of these known as period doubling, where it takes two oscillations peak NF-κB amplitude (Figure 4B). Even in the early onset of chaos, transient and unstable limit-cycle behaviors can be found (Figure 4C), but these are quite rare and disappear as we increase the amplitude of the TNF oscillations even further. Using the same tools we used to characterize noise-induced mode-hopping, if we study NF-κB oscillations in the chaotic system, that we observe oscillations starting in almost the same initial conditions will diverge after a few oscillations (Figure 4D). This is typical for chaotic systems and defined by the positive Lyapunov constant of the system. Reproducible tendencies, however, remain. When we study the periods of the NF-κB oscillator in period space under these conditions, we observe that even though they do not produce a clean pattern, they are always close to the integer values of the external periods, which are indicated by the lines (Figure 4E). This can be seen more clearly in the three-dimensional space spanned by NF-κB, I-κB mRNA, and I-κB, where we can see

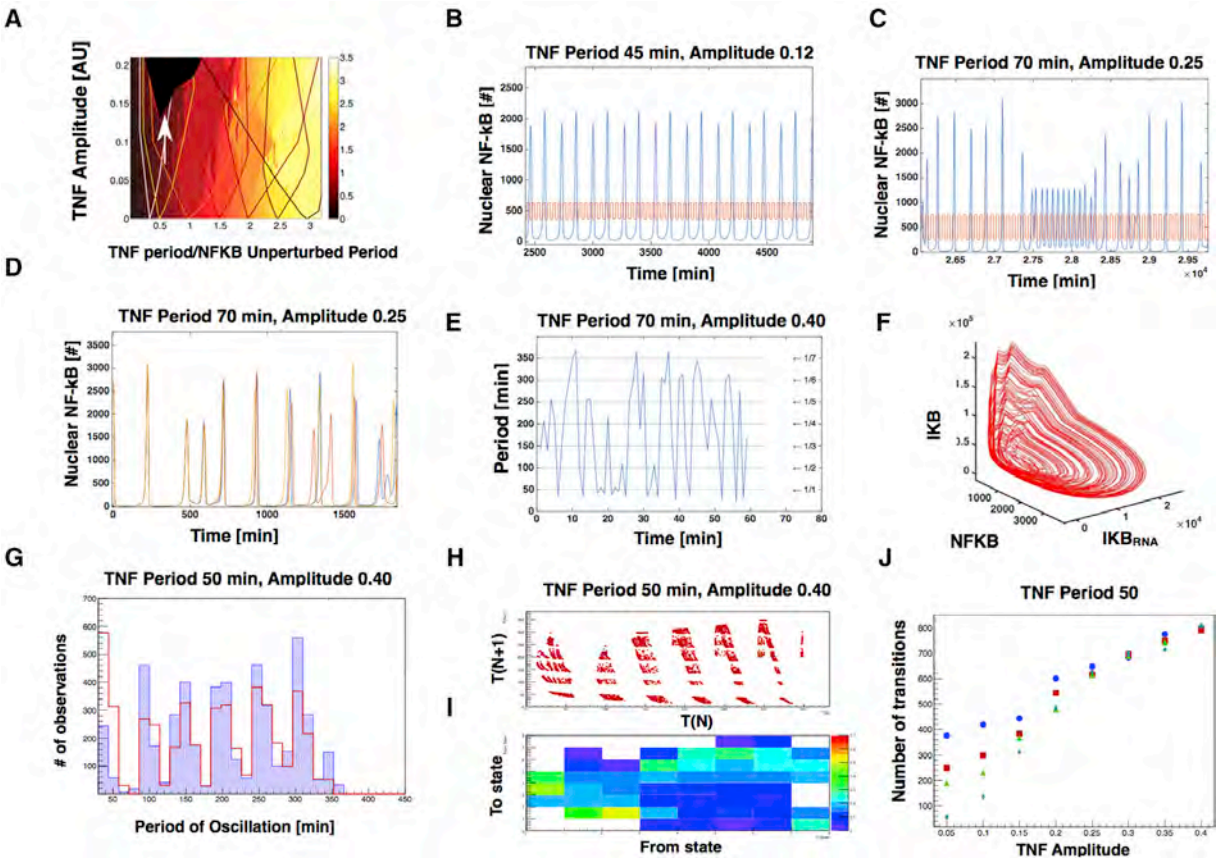

Figure 4. Deterministic Chaos in NF-κB Oscillation Manifests as Mode-Hopping

(A) Arnold tongue diagram for a deterministic model of NF-kB, same as Figure 2A, but with TNF amplitude spanning a larger range, including the onset of chaos (black section, indicated by the white arrow).

(B and C) Before the onset of chaos, interesting phenomena arise for the deterministic system, including period doublings (B) and transient oscillations in unstable limit cycles (C), which are however quite rare.

(D) For very large amplitudes in the chaotic regime, trajectories starting from very similar initial conditions diverge quickly in time. The different colors show trajectories for initial conditions differing only in one molecule; they remain close for a while but eventually diverge exponentially.

(E) Additional visualization of the data shown in (D) where the period between successive NF-κB peaks is plotted as a function of time. The horizontal lines correspond to integer multiples of the time period of the driving TNF oscillation.

(F) Trajectory of oscillations in (D) in phase space for IKB, IKB_{RNA}, and NK-kB.

(G) Distribution of time periods for a simulation of 1,000 oscillations. The red indicates the distribution of periods for the deterministic simulation, and the blue indicates the distribution for stochastic simulation. Same parameters were used in the simulations.

(H and I) Additional visualization of the structure in chaotic mode-hopping. The period to period correlation plot is shown in (H) and a transition heatmap (I) showing the probability of going from each entrained state to other entrained states, exhibiting no clear correlation between the jumps of states.

(J) The number of transitions (over an interval of thousand oscillations) between entrained states for different noise levels, as a function of the external amplitude. Blue, $V = 1 \times 10^{-15}$ L; red, $V = 2 \times 10^{-15}$ L; green, $V = 5 \times 10^{-15}$ L; cyan, $V = 15 \times 10^{-15}$ L.

the trajectories are ordered in small bands (Figure 4F). Moreover, looking at 1,000 oscillations, we find that the distribution of periods is sharply peaked around integer multiples of the TNF period (Figure 4G). However, these behaviors are not reminiscent of mode-hopping as described above.

Next, we asked whether adding noise to the chaotic system could induce mode-hopping. We find that when the driving TNF oscillation is such that the deterministic system would exhibit chaos, then adding noise to our simulations does not reduce the entrainment of the NF-κB oscillations (Figure 4G). Moreover, for the high amplitude driving shown in Figures 4D–4F, we find that noise does produce trajectory hops between many entrained modes. When we plot the period-to-period correlation of these oscillators (Figure 4H), we find that all periods belong to well-defined tongues, as indicated by the layered structure of the plot. One might expect that the mode-hopping will occur between neighboring tongues, however, in Figure 4I, we show that jumps between distant tongues also occur frequently. In this sense, chaotic dynamics might be regarded as random transitions between various tongues, rather between specific oscillations with particular amplitudes and frequencies. Chaos and noise, therefore, both manifest as increasingly frequent mode-hopping as noise is increased or one moves deeper into the chaotic regime by increasing the amplitude of external TNF oscillations (Figure 4J). In fact, in the presence of noise, it is difficult to distinguish between the system being inside or outside the chaotic regime from the probability of exhibiting entrainment or the probability distribution of being in the various possible entrained states (Figure 4G). Notably, however, in the presence of noise, mode-hopping is already observed for small

TNF amplitudes (Figure 3E) and is found for all higher TNF amplitudes, which is a much larger region of parameter space than the deterministic system, where chaos only sets in for larger amplitudes (Figure 4A).

There are important differences, however, between the dynamics of noise-induced mode-hopping below the transition into chaos and deterministic chaos above the transition. Comparing Figure 3E (noise-induced mode-hopping) and Figure 4E (mode-hopping within the chaotic regime), it is seen that the noise-induced mode-hopping only makes jumps between two states and usually remains in the same state for a few periods (Figure 3E), whereas the chaotic dynamics jumps between many different states and usually does not spend more than one period in each state (Figures 4E and 4J). These observations raise the question of whether the NF-κB mode-hopping seen in living cells is induced by noise or a function of a deterministic system operating above the transition to chaos. In experimentally observed NF-κB trajectories in living cells, we see that the system spends several periods in each entrained state and rarely visits more than two entrainment modes (Figure 2F and simulations from Figures 3E, 3H, and 3I). This suggests that, in experiments, the system sits in a region of parameter space where the Arnold tongues overlap but below the transition to chaos. More sophisticated ways exist to distinguish between chaos and randomness in dynamical trajectories (Amon and Lefranc, 2004), but we believe our arguments above are sufficient to suggest that the experimental NF-κB system has a relatively high level of noise and operates in the overlapping tongue region but below the transition to chaos.

Mode-Hopping Enables Cells to Switch between High and Low Gene Production States

One potential advantage of oscillatory transcription factor dynamics is differential regulation of frequency-sensitive promoters. Frequency modulation and frequency-sensitive gene regulation occurs in the Crz1 system, ERK signaling, hormone regulation, and is speculated to exist in NF-κB immune signaling (Albeck et al., 2013; Ashall et al., 2009; Cai et al., 2008; Krishna et al., 2006; Mengel et al., 2010; Waite et al., 2009; Wee et al., 2012). Previously, Cai et al. (2008) showed that frequency modulation can ensure a proportional expression of multiple genes having different promoter characteristics. Our observations prompt the question: how could mode-hopping facilitate regulation of diverse frequency-sensitive genes?

When oscillations of NF-κB switch between two tongues, frequency and amplitude of the oscillations change (Figure 5B), and this can alter the expression of different downstream genes that have NF-κB as a transcriptional regulator. Frequency-dependent NF-κB transcriptional regulation, in turn, may be achieved through altered binding affinity and cooperativity (Wee et al., 2012). As an example of this mechanism, we consider two genes, gene 1 and gene 2, regulated differentially by NF-κB (Figure 5A). NF-κB binds with high affinity and low cooperativity to the *cis*-regulatory region controlling expression of gene 1 and with low affinity and high cooperativity to the region controlling gene 2. The expression level of the two genes for different constant levels of NF-κB are shown in Figure 5C, along with the NF-κB oscillations in the 1/2 and 1/3 tongues (shown vertically) that demonstrates the differing range of NF-κB concentration produced during these oscillations (higher frequency results in a smaller maximum NF-κB level). Gene 1, having a higher affinity for NF-κB, has high expression for oscillations of both the frequencies shown in Figure 5C. In contrast, for the low affinity gene 2, Figure 5C shows that the expression level is low for the 1/2 tongue, because of its lower amplitude oscillations, and substantially higher for the 1/3 tongue that has a higher amplitude. In Figures 5D and 5E, the protein production from gene 1 and gene 2 is plotted as a function of time for each individual tongue and in the case of mode-hopping. Figure 5F shows that, in contrast to constant regulation across multiple genes, mode-hopping allows different regulation across different frequency-sensitive promoters at different times. A list of the applied parameter values can be found in the second table of the STAR Methods

The cell's ability to switch between high and low production states for different, defined subsets genes, as shown in Figure 5F, is what we define here as "multiplexing." The mechanism could, in principle, act together with, or in addition to, other mechanisms of multiplexing. Such mechanisms may allow the cell to dedicate its resources to producing one specific gene/protein at a given time, rather than a broad repertoire of genes/proteins at a time. Even though of random nature, this mode-hopping can be controlled in a statistical way by the cell. Changing the frequency or amplitude of TNF will change the position in the Arnold tongues and thus the probability of being in one state as opposed to the other. For instance, a TNF with amplitude below overlap of Arnold tongues would stay in one state, while going to an overlap with competition between different states, would allow for frequent mode-hopping. In this way, the cell can use the Arnold tongues to upregulate the time in different states without completely losing the possibility of jumping between states. We note that this mechanism is not necessarily the only, or even the main, functional effect of noise in protein dynamics inside the cell but rather points out how this stochastic nature can be used in an advantageous and regulatory way.

DISCUSSION

Oscillations in gene regulatory networks are known to control transcriptional specificity and efficiency (Kellogg and Tay, 2015; Levine et al., 2013; Wee et al., 2012). We have shown here experimentally that entrained NF-κB oscillations in single cells exhibit jumps in frequency under high amplitude fluctuating TNF stimulation, a phenomenon we called "mode-hopping." During these frequency jumps, cells maintain entrainment with the TNF input; this suggests that the system functions in the region of overlapping Arnold tongues. Previous studies have demonstrated that well entrained oscillations result in certain genes having higher expression (Kellogg and Tay, 2015). Within the overlapping Arnold tongue region of parameter space, a gene may exhibit two types of entrained oscillations, which we call entrainment modes. The presence of multiple entrainment modes may diversify biological functions. For example, oscillatory transcriptional control is using frequency modulation to control gene expression output and specificity (Ashall et al., 2009; Cai et al., 2008). Genes differ in affinity and cooperativity characteristics, which consequently determines sensitivity to frequency and amplitude of

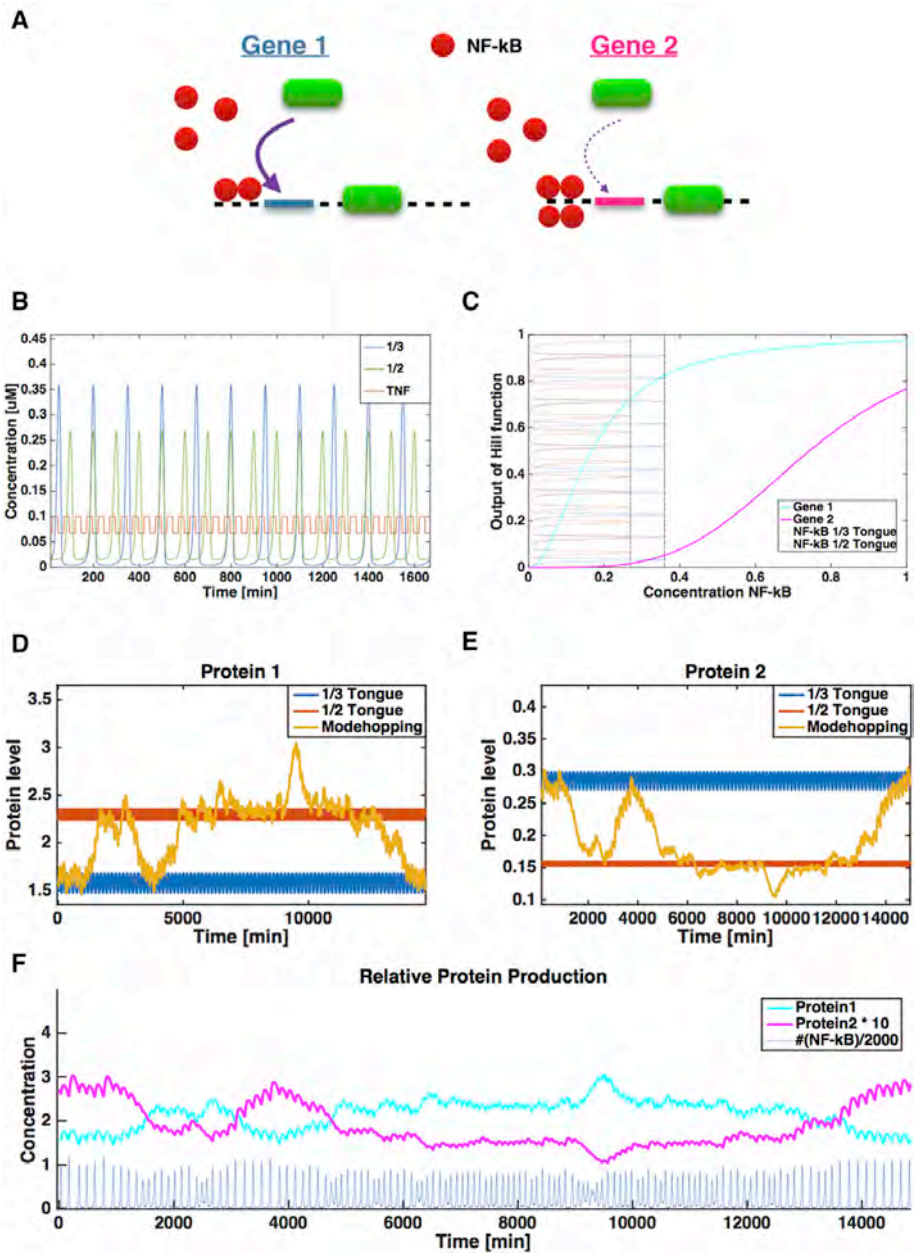

Figure 5. Mode-Hopping Switches between High and Low Gene Production States

(A) Schematic figure of the downstream network for the two genes with distinct properties. The green oval represents RNA polymerase, which is recruited by NF-κB binding to a *cis*-regulatory region upstream of each gene. For gene 1, NF-κB binds to this region with high affinity and low cooperativity, while for gene 2 it binds with low affinity and high cooperativity.

(B) NF-κB oscillation at two frequencies reflecting two different locking modes, tongue 1/2 and tongue 1/3.

(C) Output of the Hill function for the mRNA production for each gene for a fixed level of NF-κB plotted as a function of NF-κB level. Oscillations from (B) are plotted vertically to indicate the range of NF-κB concentration oscillations in each tongue produce.

(D and E) Plots of gene expression output for gene 1 (D) and gene 2 (E).

(F) The expressed protein levels for the two different gene families. The cyan curve shows protein production for gene 1 and the magenta curve shows protein production for gene 2 (although multiplied by a factor 10). The blue shows the corresponding NF-κB oscillations used in to produce the protein production.

NF-κB regulation (Figure 5A). Therefore, changing NF-κB entrainment states causes switching between high and low gene production over time. For genes that are differentially sensitive to NF-κB frequency and amplitude, mode-hopping switches activation on and off for multiple genes over time (Figure 5E). This temporally multiplexed gene regulation contrasts to regulation under unchanging NF-κB oscillation, which drives expression across multiple genes equally over time.

This work uncovers a function for noise in gene regulation that, to the best of our knowledge, has not been previously reported. NF-κB activates hundreds of genes, requiring mechanisms for controlling relative expression level and specificity under fluctuating environmental signals. As we show, noise-induced jumps in NF-κB oscillation frequency can cause temporal switching between genes with diverse promoter characteristics over time. This method of gene regulation could facilitate management of amino acid or other metabolic factors by dedicating resources to synthesis of a defined subset of proteins at one time. Cellular mode-hopping therefore expands the toolbox of single cells to control the dynamics, specificity, and efficiency of gene expression and protein production.

STAR★METHODS

Detailed methods are provided in the online version of this paper and include the following:

- KEY RESOURCES TABLE
- CONTACT FOR REAGENT AND RESOURCE SHARING
- EXPERIMENTAL MODEL AND SUBJECT DETAILS
- METHOD DETAILS
  - Cell Culture and Live Cell Imaging
  - Mathematical Modeling
  - Multiplexing Model

AUTHOR CONTRIBUTIONS

R.A.K. and S.T. conducted the experiments. M.H., S.K., and M.H.J. developed the models and performed the numerical simulations. M.H., R.A.K., S.K., S.T., and M.H.J. wrote the paper.

ACKNOWLEDGMENTS

S.K. thanks the Simons Foundation for funding. We are grateful to Jordi Garcia-Ojalvo for valuable discussions about gene regulation. We thank Kristian Moss-Bendtsen for discussions. M.H. and M.H.J. acknowledge support from the Danish Council for Independent Research and StemPhys DNRF Center of Excellence (DNRF116). This work is supported by an ERC Starting Grant (SingleCellDynamics), the NIH (R01 GM117134-01), Schweizerischer Nationalfonds, and a SystemsX research grant to S.T.

Received: June 23, 2016
Revised: September 29, 2016
Accepted: November 30, 2016
Published: December 21, 2016

REFERENCES

Albeck, J.G., Mills, G.B., and Brugge, J.S. (2013). Frequency-modulated pulses of ERK activity transmit quantitative proliferation signals. Mol. Cell *49*, 249–261.

Amon, A., and Lefranc, M. (2004). Topological signature of deterministic chaos in short nonstationary signals from an optical parametric oscillator. Phys. Rev. Lett. *92*, 094101.

Ashall, L., Horton, C.A., Nelson, D.E., Paszek, P., Harper, C.V., Sillitoe, K., Ryan, S., Spiller, D.G., Unitt, J.F., Broomhead, D.S., et al. (2009). Pulsatile stimulation determines timing and specificity of NF-kappaB-dependent transcription. Science *324*, 242–246.

Brun, R., and RAdemakers, F. (1997). ROOT An Object Oriented Data Analysis Framework. Phys Rev A. *389*, 81–86.

Cai, L., Dalal, C.K., and Elowitz, M.B. (2008). Frequency-modulated nuclear localization bursts coordinate gene regulation. Nature *455*, 485–490.

Eldar, A., and Elowitz, M.B. (2010). Functional roles for noise in genetic circuits. Nature *467*, 167–173.

Elowitz, M.B., Levine, A.J., Siggia, E.D., and Swain, P.S. (2002). Stochastic gene expression in a single cell. Science *297*, 1183–1186.

Gillespie, D.T. (1977). Exact stochastic simulation of coupled chemical reactions. J. Phys. Chem. *81*, 2340–2361.

Gonze, D., Halloy, J., and Goldbeter, A. (2002). Robustness of circadian rhythms with respect to molecular noise. Proc. Natl. Acad. Sci. USA *99*, 673–678.

Jensen, M.H., and Krishna, S. (2012). Inducing phase-locking and chaos in cellular oscillators by modulating the driving stimuli. FEBS Lett. *586*, 1664–1668.

Jensen, M.H., Bak, P., and Bohr, T. (1984). Transition to chaos by interaction of resonances in dissipative systems. I. Circle maps. Phys. Rev. A *30*, 1960–1969.

Kellogg, R.A., and Tay, S. (2015). Noise facilitates transcriptional control under dynamic inputs. Cell *160*, 381–392.

Kellogg, R.A., Gómez-Sjöberg, R., Leyrat, A.A., and Tay, S. (2014). High-throughput microfluidic single-cell analysis pipeline for studies of signaling dynamics. Nat. Protoc. *9*, 1713–1726.

Krishna, S., Jensen, M.H., and Sneppen, K. (2006). Minimal model of spiky oscillations in NF-kappaB signaling. Proc. Natl. Acad. Sci. USA *103*, 10840–10845.

Levine, J.H., Lin, Y., and Elowitz, M.B. (2013). Functional roles of pulsing in genetic circuits. Science *342*, 1193–1200.

Lorenz, E.N. (1963). Deterministic nonperiodic flow. J. Atmos. Sci. *20*, 130–141.

Martin, K.I., Clarkson, W.A., and Hanna, D.C. (1997). Self-suppression of axial mode hopping by intracavity second-harmonic generation. Opt. Lett. *22*, 375–377.

Mengel, B., Hunziker, A., Pedersen, L., Trusina, A., Jensen, M.H., and Krishna, S. (2010). Modeling oscillatory control in NF-κB, p53 and Wnt signaling. Curr. Opin. Genet. Dev. *20*, 656–664.

Mork, J., Semkow, M., and Tromborg, B. (1990). Measurement and theory of mode hopping in external cavity lasers. Electron. Lett. *26*, 609–610.

Tay, S., Hughey, J.J., Lee, T.K., Lipniacki, T., Quake, S.R., and Covert, M.W. (2010). Single-cell NF-kappaB dynamics reveal digital activation and analogue information processing. Nature *466*, 267–271.

Waite, E., Kershaw, Y., Spiga, F., and Lightman, S.L. (2009). A glucocorticoid sensitive biphasic rhythm of testosterone secretion. J. Neuroendocrinol. *21*, 737–741.

Wee, K.B., Yio, W.K., Surana, U., and Chiam, K.H. (2012). Transcription factor oscillations induce differential gene expressions. Biophys. J. *102*, 2413–2423.

STAR★METHODS

KEY RESOURCES TABLE

REAGENT or RESOURCE	SOURCE	IDENTIFIER
Chemicals, Peptides, and Recombinant Proteins		
TNF	Life Technologies	PMC3014
Experimental Models: Cell Lines		
p65-DsRed/H2B-GFP 3T3 mouse fibroblasts	Tay et al., 2010	N/A
Software and Algorithms		
ROOT	Brun and RAdemakers, 1997	https://root.cern.ch/documentation
Simulations made in c++	This Paper	
MATLAB 6.1	The MathWorks Inc. 2010	https://se.mathworks.com/products/matlab/
Gillespie Algorithm	Gillespie, 1977	
Cellprofiler	http://cellprofiler.org/	
Other		
Automated microfluidic cell culture system	Kellogg et al., 2014	N/A
DMEM	Life Technologies	cat. no. 32430-027
FBS	Sigma-Aldrich	cat. no. F2442-500ML

CONTACT FOR REAGENT AND RESOURCE SHARING

Further information and requests for reagents may be directed to, and will be fulfilled by the corresponding author Mogens Høgh Jensen (mhjensen@nbi.ku.dk).

EXPERIMENTAL MODEL AND SUBJECT DETAILS

Mouse (3T3) fibroblasts expressing near-endogenous p65 levels were described previously (Tay et al., 2010; Kellogg and Tay, 2015). Briefly, p65−/− mouse 3T3 fibroblasts were engineered to express p65-DsRed under control of 1.5kb p65 promoter sequence (Tay et al., 2010). The cell line was clonally derived to express at p65-DsRed at lowest detectable level to preserve near endogenous expression (Tay et al., 2010). Addition of ubiquitin-promoter driven H2B-GFP expression provided a nuclear label to facilitate automated tracking and image processing.

METHOD DETAILS

Cell Culture and Live Cell Imaging

Automated microfluidic cell culture and periodic TNF stimulation was performed as previously described (Kellogg et al., 2014; Tay et al., 2010; Kellogg and Tay, 2015). In vitro cultures were maintained in DMEM (Life Technologies, cat. no. 32430-027) and FBS (Sigma-Aldrich, cat. no. F2442-500ML). Prior to seeding in the microfluidic device, NIH 3T3 fibroblasts were cultured in (DMEM + 10% (vol/vol) FBS). Cells were passaged 1:10 every 3 days to not exceed 80% confluency. Standard culture conditions of 5% CO2 and 37°C were maintained using an incubation chamber during culturing and throughout imaging experiments.

Briefly the live cell microscopy experiments proceeded as follows: microfluidic chambers were fibronectin treated and seeded with cells at approximately 200 cells/chamber. Cells were allowed to grow for one day with periodic media replenishment until 80% confluence. To stimulate cells, media equilibrated to 5% CO2 and containing the desired TNF amount was delivered to chambers, leading to a step increase in TNF concentration. To produce periodic TNF signals, chambers were washed with media containing TNF at the desired intervals. Chambers were imaged at 5-6 min intervals. DsRed and GFP channels were acquired using a Leica DMI6000B widefield microscope at 20x magnification with a Retiga-SRV CCD camera (QImaging) using Leica L5 and Y3 filters to acquire GFP and DsRED signals, respectively and a Leica EL6000 mercury metal halide light source.

Mathematical Modeling

We consider the model, previously published by Jensen and Krishna (2012), of the NF-kB, defined by the 5 coupled differential equations given as:

$$\frac{dN_n}{dt} = k_{Nin}(N_{tot} - N_n)\frac{K_I}{K_I + I} - k_{lin} I \frac{N_n}{K_N + N_n}$$

$$\frac{dI_m}{dt} = k_t N_n^2 - \gamma_m I_m$$

$$\frac{dI}{dt} = k_{tl} I_m - \alpha [IKK]_a (N_{tot} - N_n)\frac{I}{K_I + I}$$

$$\frac{d[IKK]_a}{dt} = k_a [TNF]\left([IKK]_{tot} - [IKK]_a - [IKK]_i\right) - k_i [IKK]_a$$

$$\frac{d[IKK]_i}{dt} = k_i [IKK]_a - k_p [IKK]_i \frac{k_{A20}}{k_{A20} + [A20][TNF]}$$

The background and the underlying assumptions for this model, is previously published and the relevant discussions in this regard are presented in that paper (Jensen and Krishna, 2012). All the parameters in the model is seen in the table below. The first nine are from Krishna et al. (2006) and the following four from Ashall et al. (2009).

Parameter	Default value
k_{Nin}	5.4 min^{-1}
k_{lin}	0.018 min^{-1}
k_t	1.03 (μM) · min^{-1}
k_{tl}	0.24 min^{-1}
K_I	0.035 μM
K_N	0.029 μM
γ_m	0.018 min^{-1}
α	1.05 (μM) · min^{-1}
N_{tot}	1.0 μM
k_a	0.24 min^{-1}
k_i	0.18 min^{-1}
k_p	0.036 min^{-1}
k_{A20}	0.0018 μM
$[IKK]_{tot}$	2.0 μM
[A20]	0.0026 μM

Multiplexing Model

Protein and mRNA production by these genes is described by the following equations:

$$\dot{m}_i = \gamma_i \frac{N^{h_i}}{K_i^h + N^{h_i}} - \delta_i m_i$$

$$\dot{P}_i = \Gamma_i m_i - \Delta_i P_i$$

Here the m_i represents the mRNA of species *i*, and P_i represents the protein level of species *i*. As can be seen from Figure 5A, the two genes differ only in two parameters, the affinity of the binding represented by K_i and the cooperativity represented by hill

coefficient h_i. γ_i describes the mRNA production per time, δ_i is the decay of mRNA per time, Γ_i is the protein production per time and Δ_i is the decay of the protein per time. All parameters in this model is found in the table below:

Parameter	Default Value Gene 1	Default Value Gene 2
K	1.0 #molecules	1.0 #molecules
h	2.0	4.0
γ	4.0 #molecules · min^{-1}	4.0 #molecules · min^{-1}
Γ	2.0 min^{-1}	2.0 min^{-1}
δ	2.0 min^{-1}	2.0 min^{-1}
Δ	0.3 min^{-1}	0.3 min^{-1}

QUANTIFICATION AND STATISTICAL ANALYSIS

CellProfiler software (http://cellprofiler.org) and custom MATLAB software was used to automatically track cells and quantify NF-κB translocation, and automated results were manually compared with images to ensure accuracy prior to further analysis. NF-κB activation was quantified as mean nuclear fluorescence intensity normalized by mean cytoplasm intensity. For peak analysis data were smoothed (MATLAB function *smooth*) followed by peak detection (MATLAB function *mspeaks*). Peaks were filtered based on reaching a threshold 10% of maximum intensity.

DATA AND SOFTWARE AVAILABILITY

Software

All simulations were performed using scripts written in c++ and MATLAB. All data-analysis were performed from scripts written in python and using the ROOT software.

All scripts used for simulation and data analysis from the model, will be available upon request to Mathias Luidor Heltberg (heltberg@nbi.ku.dk)

Algorithms

All deterministic simulations were performed using Runge-Kutta 4th order simulations. All stochastic simulations were performed using the Gillespie algorithm (Gillespie, 1977). We considered 10 possible reactions given from the 10 different terms in the 5 differential equations.

Time Correlations in Mode Hopping of Coupled Oscillators

Mathias L. Heltberg,[1,2] Sandeep Krishna,[1,2] and Mogens H. Jensen[1,2]

[1] *The Niels Bohr Institute, University of Copenhagen*
[2] *Simons Centre for the Study of Living Machines, National Centre for Biological Sciences, Bangalore, India*

(Dated: February 10, 2017)

We study the dynamics in a system of coupled oscillators when Arnold Tongues overlap. By varying the initial conditions, the deterministic system can be attracted to different limit cycles. Adding external noise, the mode hopping between different states become a dominating part of the dynamics. We simplify the system through a Poincare section, and derive a 1D model to describe the dynamics. We explain that for some parameter values of the external oscillator, the time distribution of occupancy in a state is exponential and thus memoryless. In the general case, on the other hand, it is a sum of exponential distributions characteristic of a system with time correlations.

Keywords: Coupled oscillators, mode hopping, Arnold tongues, Poincare sections, time correlations.

Introduction

Leo Kadanoff was a giant pioneer in the field of dynamical systems and chaos theory and was a fantastic inspiration for many of us collaborating with him over the years. With this paper we wish to honor the legacy of Leo by presenting a study of mode locking phenomena in a system with two characteristic frequencies, a topic that interested Leo for many years [1–3]. We analyse the hopping between limit cycles using Poincare sections, another topic that was of close interest to Leo.

Already in 1676, the dutch physicist Christian Huygens [4] observed that the dynamics of two coupled clocks resulted in synchronization [5]. This is one of the oldest non-linear phenomena ever to be described, and despite many attempts [6], the dynamics of a system of coupled oscillators is still far from completely understood. A classical example of this consists of two self-sustained oscillators where an external oscillator is weakly coupled to an internal oscillator. Systems of this character can show surprisingly complex bevaviour [3], only parts of which are understood due to the pioneering work of Vladimir Arnold [7]: in regions called Arnold Tongues, these oscillators become synchronized, or entrained, to each other. In recent years, synchronization of coupled oscillators has been found in a variety of physical systems from fluids [2] to quantum mechanical devices [8, 9], and during the last 10 years this has also been observed in many biological processes such as cell cycles [10, 11, 13], gene regulatory dynamics in synthetic populations [12], and protein oscillations in single cells [14], in particular oscillations in the transcription factor NF-κ B [15–18]. An important, but less well-understood, aspect is the dynamics in regions where two or more Arnold tongues overlap [19]. Here different synchronization are possible; mathematically, the trajectory in phase space can be attracted to different stable limit cycles depending on initial conditions.

Model of protein oscillations: limit cycles and Poincare section

In this study we consider a network of 5 coupled differential equations, describing the dynamics of the important transcription factor NF-κB, previously published in[20]. Here we consider the concentration of a molecule, that has a fixed concentration N_x, whose *active* form is described by x. This indirectly starts production of the molecule z, mediated through the variable y. As z increase the activation level of x decrease, leading to a negative feedback mechanism resulting in oscillations. A molecule, that has fixed concentration w, can assume three states, u, v and $w-u-v$ and the active form, u. It can lead to degradation of z, which again make x active. The activation of u is mediated by a periodically varying component, described by τ. A schematic version of the network can be found in Figure 1A. The equations now take the following form:

$$
\begin{aligned}
\dot{x} &= V_x(N_x - x)\frac{K_z}{K_z + z} - V_z \cdot z\frac{x}{K_x + x} \\
\dot{y} &= \Gamma_y x^2 - \Delta_y y \\
\dot{z} &= \Gamma_z \cdot y - \Delta_z \cdot u \cdot (N_x - x)\frac{z}{K_z + z} \\
\dot{u} &= \Gamma_u \cdot \tau \cdot w - \Delta_u \cdot u \\
\dot{v} &= \Gamma_v \cdot u - V_v \cdot v\frac{K_A}{K_A + A_{20}\tau} \\
\tau &= 0.5 + A\sin\Big(\frac{2\pi}{T}t\Big) \\
w &= N_{uv} - u - v
\end{aligned}
$$

Here all the capital letters refer to fixed parameters of the model, whereas lowercase letters refer to variables.

In order to study the system, we define a Poincare section at $x = 1500$ allowing us to perform discrete analysis on the 4 other variables and the time of each period [21]. For a set of external parameters corresponding to a region where two Arnold Tongues overlap, we find that the deterministic system can settle into different limit cycles (Figure 1B), where typically the period of the internal oscillator is an integer times the period of the external oscillator (in principle other limit cycles exist, but it is harder to find the initial conditions and paramater values that produce them). Dynamical systems of multi-stability have been studied in many aspects [22, 23], usually through the coupling of separate attractors, but the arise of multi-stability through the overlapping of Arnold tongues, has not been thoroughly investigated and serve as an interesting system to study the appearance and disappearance of different stable limit-cycles. Interestingly, we find that when we add noise to the system (by using the Gillespie algorithm to simulate the system [24]), transitions between these co-

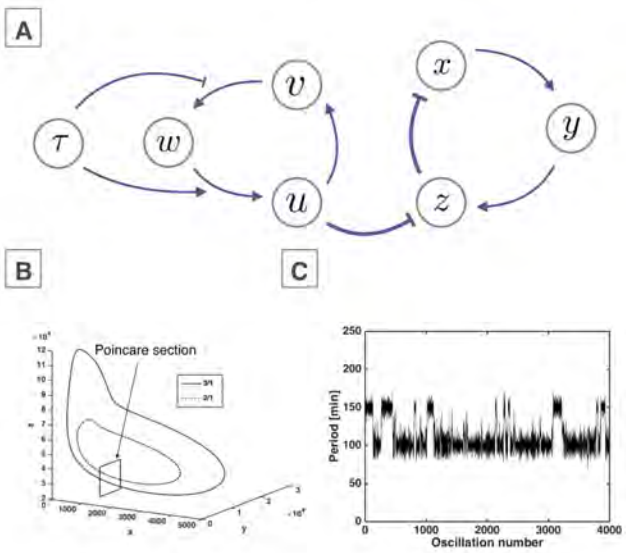

Figure 1: A) Schematic figure showing the network, that give rise to the equations in the model B) The two stable limit cycles for the deterministic system with external oscillator parameters T = 50 min and A = 0.1. Shown here is the phase space of variables x, y, and z, and the Poincare section we use in our analysis. C) Fluctuations in the time period for this system in the presence of noise; external oscillator parameters are T = 50 min and A = 0.1.

existing limit cycles is observed (Figure 1C). This phenomena we describe as *mode hopping*, reflecting that the trajectory inside the Poincare section hops between different entrainment modes. Our goal is to describe the time correlations between transitions in this system with a discrete time model, using information extracted from the Poincare section. Transitions are of course only possible when noise is added to the system. The noise makes it difficult to determine every transition with complete precision, but combining studies of the deterministic system with sufficiently long stochastic time-series to generate enough statistics, we will be able to make conclusions about the nature of these transitions.

Distribution of noise in the Poincare section

We begin by studying the distribution of positions on the Poincare section after precisely one period of oscillation, where all trajectories started at the same initial point in the Poincare section. Mathematically speaking we want to find the distribution $P(x_i^n \mid x_i^{n-1} = \mu_i)$, where x_i^n is the position of the ith variable on the Poincare section after n periods of the oscillation, given that the position in the Poincare section after $n-1$ oscillations was μ_i (the period is also regarded as a variable). From our simulations, we find that, independent of the starting position μ_i, the distribution of time period of the oscillation is Gaussian (Figure 2A), and that its standard deviation, σ, to a good approximation, can be treated as constant (Figure 2B). Furthermore, we observed the same for every other variable and thus, to a good approximation, we can describe P as a multivariate Gaussian:

$$P(\boldsymbol{x} \mid \boldsymbol{x_0} = \boldsymbol{\mu}) = \frac{1}{\sqrt{2\pi}^5 \sqrt{|\boldsymbol{V}|}} e^{-\frac{1}{2}\left[(\tilde{\boldsymbol{x}}-\tilde{\boldsymbol{\mu}})\boldsymbol{V}^{\boldsymbol{1}}(\boldsymbol{x}-\boldsymbol{\mu})\right]}$$

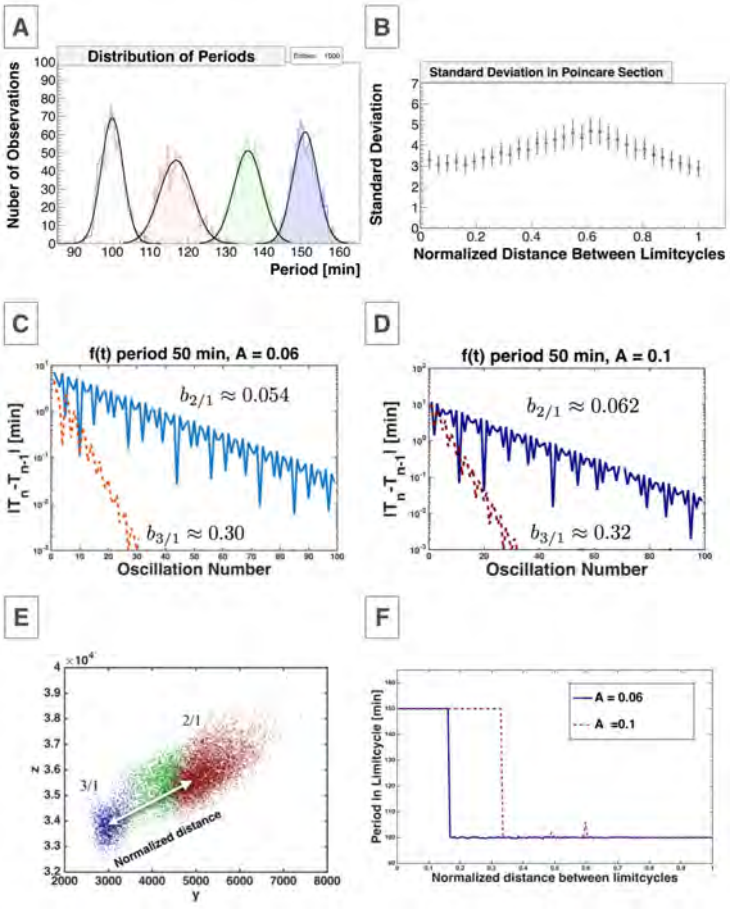

Figure 2: A) Gaussian fits for the distribution of periods after one trajectory started at 4 different initial positions in the Poincare section. B) Value of the standard deviation of the Gaussian fit at different positions in the Poincare section. The normalized distance is here defined as the norm of a vector from the position in phase space of one limit cycle to the other limit cycle, when they intersect with the Poincare section. C-D) Absolute value difference between period and previous period, as the trajectories decay into the limit cycle. The parameter b is the exponential decay constant. E) 10^4 points from stochastic simulation used as initial values for deterministic simulation. After 10 oscillations blue has period greater than 145 min and red has period smaller than 105 min. Green refers to points between these values. F) Width of the basin of attraction for different values of the amplitude of the external oscillator after 40 oscillations.

Thus, within the Poincare section, the system can be described as a deterministic trajectory with Gaussian noise. This observation is of great importance, and to use this further, we study how a trajectory with initial position perturbed from the limit cycle, is attracted to the given limit cycle within the Poincare section, which in general depends on the possibly complex geometry of the basin of attraction of the limit cycle. We first consider the absolute value of the difference between the period and the period of the previous oscillation in deterministic simulations. We find that this quantity exhibits a complicated structure, but overall goes to zero with an exponential decay as the limit cycle is approached (Figure 2C-D). We find that independent of the initial condition, but for fixed parameters of the external oscillator, the exponential decay has the same decay constant, that changes slightly, as the external parameters change (Figure 2C-D). The non-smooth structure arises from the coupling between variables and is reminiscent of a damped harmonic oscillator, but in our subsequent analysis we will treat this as a negligible effect

on top of the basic exponential decay characteristic to each basin of attraction.

To finish the description, we must locate the boundary between each basin of attraction. Starting from various initial conditions, we need to map which limit cycle each initial conditions settles into. In order to choose sensible initial positions, we take 10^4 recorded points from a stochastic simulation, and use these as initial conditions. After 10 oscillations, we find that the majority have settled into one of the two limit cycles, but some are still unsettled (Figure 2E). This seems to an result of an unstable 5/2 Arnold tongue. We note importantly that the basins are not riddled, but to good approximation can be regarded as divided in groups. To simplify this we consider the shortest distance between the two stable limit cycles in the Poincare section, and consider the points in between as initial conditions. Figure 2F shows that after 40 oscillations, all trajectories have settled into one of the two stable limit cycles, and that as we increase the amplitude of the external oscillator, the basin of attraction for one basin grows, whereas the other decreases. Thus, for a given set of external parameters, we can approximate the width of the basin of attraction compared to the standard deviation of the Gaussian noise. Changing the amplitude of the external oscillator would change the probability to be in one of the limit cycles for the stochastic system and thus change the average number of oscillations before leaving the given entrained state.

A model for the dynamics in the Poincare section

At this point we have argued that for a fixed set of parameters of the external oscillator, the decay into a limit cycle for the internal oscillator follows exponential decay with a constant depending on the basin of attraction. Secondly, the boundaries, and therefore width, of this basin are determined by the external parameters. Thirdly, the next position in phase space inside the Poincare section is Gaussian distributed with a characteristic standard deviation determined by the noise in the system.

From these results, we thus create a simple, discrete 1D model, that should be able to qualitatively explain the results we find for the dynamics for the stochastic system. We imagine a measure, d_n, that defines the distance to the center of the limitcycle inside a given basin of attraction. We consider the 1D map:

$$d_n = d_{n-1}\Delta = d_0\Delta^n = d_0 e^{ln(\Delta)n} \tag{0.1}$$

Now we add Gaussian noise to the system, so the update is:

$$d_n = d_{n-1}\Delta + \mathcal{N}(0,\sigma) = \mathcal{N}(d_{n-1}\Delta, \sigma), \tag{0.2}$$

where $\mathcal{N}$ defines the normal distribution with parameters given in the argument. A schematic version of this simple model, is shown in figure 3A. We are now interested in knowing the probability density function, $P(d_n)$. This can thus be described as:

$$P(d_n) = P(d_n|d_{n-1})P(d_{n-1}) \tag{0.3}$$

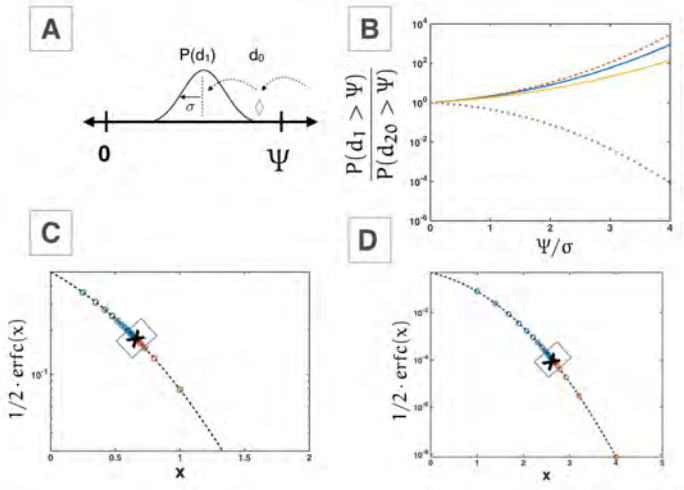

Figure 3: A) Schematic cartoon of the 1D model. B) Ratio between the probability to leave the state after the first jump and after 20 jumps (in steady state), plotted for the different parameters and initial positions in the model. C) The probability to leave the state, plotted on the error function. Orange starting from $d_0 = 0$ and blue starting from $d_0 = \Psi$. $\Psi/\sigma = 1$. The cross indicates the steady state. D) The probability to leave the state, plotted on the error function. Orange starting from $d_0 = 0$ and blue starting from $d_0 = \Psi$. $\Psi/\sigma = 4$. The cross indicates the steady state.

We start by considering the position after one jump, given the initial position is d_0, described by:

$$P(d_1) = \frac{1}{\sqrt{2\pi}\sigma} e^{-\frac{1}{2}\left(\frac{d_1 - \Delta d_0}{\sigma}\right)^2}$$

Now we want to calculate the distribution for the position after the second step. To calculate this we are thus (to avoid too many ds we define $d = d_0$, $y = d_1$ and $x = d_2$) solving the integral:

$$\begin{aligned} P(x) &= \frac{1}{\sqrt{2\pi}\sigma_1\sigma_2}\int_{-\infty}^{\infty} e^{-\frac{1}{2}\left(\frac{x-\Delta y}{\sigma_1}\right)^2} e^{-\frac{1}{2}\left(\frac{y-\Delta d}{\sigma_2}\right)^2} dy \\ &= \mathcal{N}\Big(\Delta^2 d, \sqrt{\sigma_1^2 + \sigma_2^2\Delta^2}\Big). \end{aligned}$$

As this holds for every step, we can iterate from the first jump d_1. That is, the PDF of the nth jump becomes:

$$P(d_n) = \frac{1}{\sqrt{2\pi}\sigma_n} e^{-\frac{1}{2}\left(\frac{d_n - \Delta^n d_0}{\sigma_n}\right)^2}$$

$$\text{where} \quad \sigma_n = \sigma\sqrt{\sum_{i=0}^{n-1}\Delta^{2i}} = \sigma\sqrt{\frac{1-\Delta^{2n}}{1-\Delta^2}}.$$

Now in order to consider transitions between basins of attraction, we must consider the probability that the distance d is larger than the boundary of the basin, defined as Ψ. Thus:

$$\begin{aligned} P(d_n > \Psi) &= \int_{\Psi}^{\infty} \frac{1}{\sqrt{2\pi}\sigma_n} e^{-\frac{1}{2}\left(\frac{x-\Delta^n d_0}{\sigma_n}\right)^2} dx \\ &= \frac{1}{2}\mathrm{erfc}\Big(\frac{\Psi - \Delta^n d_0}{\sigma_n}\Big) \end{aligned}$$

From this we can also see that this will always reach a steady state, where the probability of leaving (i.e., a tran-

sition out of the basin of attraction) will be:

$$\lim_{n\to\infty} P(d_n > \Psi) = \lim_{n\to\infty} \Big(\frac{1}{2}\Big[\mathrm{erfc}\Big(\frac{\Psi - \Delta^n d_0}{\sigma_n}\Big)\Big]\Big) = \frac{1}{2}\Big[\mathrm{erfc}\Big(\frac{\Psi}{\sigma}\sqrt{1-\Delta^2}\Big)\Big]$$

This means that the probability of leaving will, in steady state, be highly dependent on the relation between Ψ and σ, but independent of the initial position d_0. The probability to leave the state in the first jump, however, will always be dependent on the initial position. If we assume $d_0 = \Psi$ we obtain:

$$P(d_1 > \Psi | d_0 = \Psi) = \frac{1}{2}\Big[\mathrm{erfc}\Big(\frac{\Psi}{\sigma}(1-\Delta)\Big)\Big],$$

which shows that the probability to leave in the first jump is higher than in the steady state. If we consider $d_0 = 0$ we obtain:

$$P(d_1 > \Psi | d_0 = 0) = \frac{1}{2}\Big[\mathrm{erfc}\Big(\frac{\Psi}{\sigma}\Big)\Big],$$

which shows that the probability to leave in the first jump is lower than in the steady state.
With these results, we have an interesting measure, the ratio between the probability of leaving in the first iteration, divided by the probability of leaving in the steady state. This ratio is plotted in figure 3B for different values of Δ and different initial positions. Another visualization of this is the probability to leave for each step, depending on the initial condition, for $\Psi/\sigma = 1$ (Figure 3C) and for $\Psi/\sigma = 4$ (Figure 3D).

We now proceed to calculate the probability distribution for the first time to leave the entrained state, J_1, meaning the first time the distance will be greater than Ψ:

$$P(J_1 = n) = \frac{1}{2^n}\Big[1 - \mathrm{erf}\Big(\frac{\Psi - \Delta^n d_0}{\sigma_n}\Big)\Big]\prod_{j=1}^{n-1}\mathrm{erf}\Big(\frac{\Psi - \Delta^j d_0}{\sigma_j}\Big). \tag{0.4}$$

Assuming that $d_0 = \Psi$ we can reduce the above expression:

$$P(J_1 = n | d_0 = \Psi) = \tag{0.5}$$

$$\frac{1}{2^n}\mathrm{erfc}\Big(\frac{\Psi}{\sigma}\sqrt{1-\Delta^2}\sqrt{\frac{1-\Delta^n}{1+\Delta^n}}\Big)\prod_{j=1}^{n-1}\mathrm{erf}\Big(\frac{\Psi}{\sigma}\sqrt{1-\Delta^2}\sqrt{\frac{1-\Delta^j}{1+\Delta^j}}\Big). \tag{0.6}$$

From this expression, it should be deduced, that the argument depending on n will converge to one, meaning that the probability to jump out will quickly reach a steady state. In the steady state there is always the same probability to jump out, and the distribution describing a discrete event with the same probability will be the exponential distribution.

Approximation to the distribution

As we observed in the above expressions and in figure 3C-D, it takes several iterations to reach the steady state, and we expect that these initial probabilities can be described by a single exponential distribution. Therefore, we expect that the distribution of oscillations in one limit cycle before transition, can be described by a sum of two exponential distributions:

$$f(n) = \overset{\text{Initialposition}}{Ae^{-bn}} + \overset{\text{SteadyState}}{Ce^{-dn}}$$
$$\text{where} \quad n \equiv d_n > \Psi \wedge d_{n-1}..d_1 \leq \Psi.$$

Testing this assumption, we now try to compare simulations on the 1D model with the real system. For both systems we start at $d_0 = \Psi$, i.e., on the border of the basin of attraction, defined from the normalized distance between the limit cycles (Figure 4A-B), and at $d_0 = 0$, i.e., at the center of the limit cycle (Figure 4C-D). In these simulations, we define that the trajectory leaves the entrained state when the period becomes closer to the period in the other limit cycle. Even though these simulations cannot be compared quantitatively, since the 1D model does not take the cycles of the decay into account, they do have the same qualitative description of the dependence on initial positions, and are well described by the suggested function. The interpretation of the above result is as follows: The first several oscillations follows a distribution of either decreasing (if $d_0 = \Psi$) or increasing (if $d_0 = 0$) probability of transition out of the entrained state, before reaching the steady state probability. In the steady state, this should follow an exponential distribution since there is at each iteration the same probability to leave, which can be seen from the fact that the exponential decay, if the first fraction of the plot is neglected, has exactly the same slope independent of the initial position. However, the effect of the initial effect conditions is captured in the first part of the fit, where we find that these effects can be estimated by adding another exponential function.

Long time dynamics

Now we want to study the long term dynamics, and estimate the distribution of number of oscillations in one limit cycle, before leaving the limit cycle. As seen in figure 1B, there clearly are transitions between states, but to define exactly when the trajectory is out of the basin of attraction of a specific limit cycle can be difficult. We here use Fisher's discriminant, implemented in MATLAB, to separate the points, and classify them between different states [25]. From the model we expect the distribution to reach a steady state after some trajectories in the same limit cycle, but having much higher probability to leave the state in the early rounds, as we usually enter a new state close to the boundary. We again expect the distribution to fit the sum of two exponentials, where the first position in the basin of attraction follows a distribution but is always close to the boundary of the basin. This is confirmed in figure 5A, where we have also plotted the best exponential and stretched exponential fit. From figure 4B the other limit cycle in this experiment also follows the sum of two exponentials, and that this state is a little different from the one shown in 5A, due to the Δ of this state is higher. Now if the value of Ψ/σ can be estimated to be small, the effective dynamics is however imagined to be closer to an exponential distribution as the ratio shown in Figure 3B gets smaller. Now from the model we estimate that we would have more exponential like fits, if we:
a) Decreased external period (causing smaller Ψ)

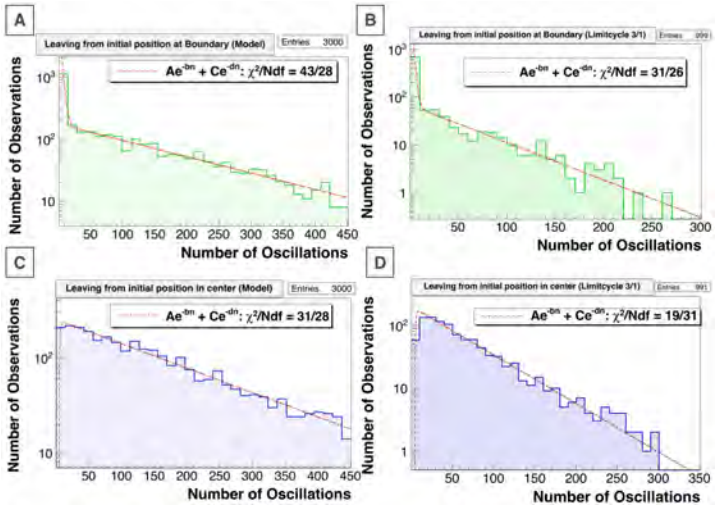

Figure 4: A) Distribution of number of jumps before leaving the state for the model. Initial position $d_0 = \Psi$. B) Distribution of number of jumps before leaving the state for the simulated system. Initial position around the boundary. C) Distribution of number of jumps before leaving the state for the model. Initial position $d_0 = 0$. D) Distribution of number of jumps before leaving the state for the simulated system. Initial position in the center of the limit cycle.

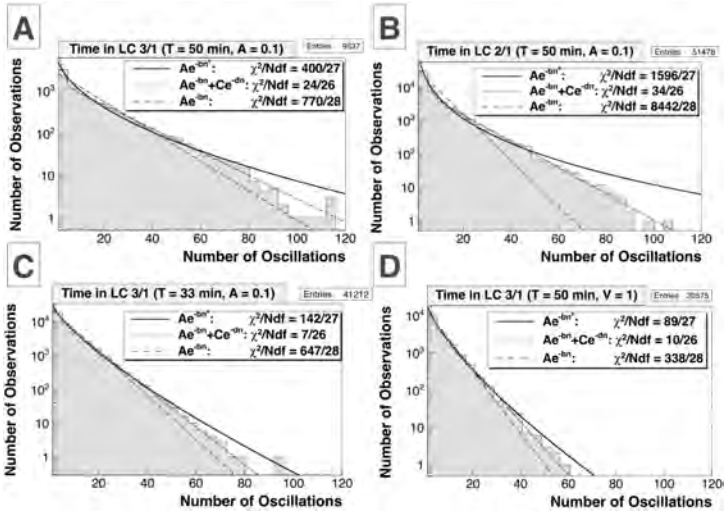

Figure 5: A) Distribution of oscillations in 3/1 state for totally 600000 oscillations. Parameters of external oscillator is T = 50 min and A = 0.1. V = $2 \cdot 10^{-14}$L. B) Distribution of periods for the 2/1 limit cycle. From the model perspective this distribution is different from A) in the value of Δ. Same parameters used. C) Distribution of oscillations in 3/1 limit cycle. for external parameters T = 33 min and A = 0.1. D) Distribution of periods for the 3/1 limit cycle. Parameters of external oscillator is T = 50 min and A = 0.1. V = $1 \cdot 10^{-14}$L

b) Decreased external amplitude (causing smaller Ψ)
c) Decreased Volume = Larger noise (causing larger σ)
Lowering the amplitude of the external oscillator, effectively decreases the distance between the two limit cycles and transitions between limit cycles should be more frequent, as the noise level remains constant. This prediction is confirmed in figure 5C where the probability of leaving the limit cycle in the steady state is higher than in figure 5A-B. Also we note that this distribution is much closer to being exponential than the figures above, which was predicted by the results in figure 3. In the same manner we expect that if we keep the width of the basin constant, meaning we fix the parameters of the external oscillator, but we add more noise to the system, similar effects should be observed. In figure 5D we see that if we increase the noise of the system, the probability to leave the state increases in the steady state, and the distribution is again closer to an exponential distribution than before. This means that we have obtained an understanding, not only of why the distribution of time in one state follows two exponentials, but also how the parameters in this distribution change, as we change the external parameters.

Conclusion

We have shown how the dynamics of a system of coupled oscillators, in the overlapping Arnold Tongue regime, can show bistable behaviour, and how the statistics for the transitions between limit cycles can be controlled by changing the parameters of the external oscillator. We have observed how the distribution of the number of oscillations in each state tends to look exponential in some parameter ranges, while in others looks very stretched. We showed that this behaviour is reproduced in a simple 1D system, derived from the behaviour within Poincare section of the system, leading us to a useful description of the dynamics as a sum of two exponential functions. We believe that these results can be used to describe the dynamics of many synchronized oscillating systems in the presence of noise, even when the basins of attraction are divided by several regions.

SK thanks the Simons Foundation for funding. MLH and MHJ acknowledge support from the Danish Council for Independent Research and Danish National Research Foundation through StemPhys Center of Excellence, grant number DNRF116.

[1] Jensen, M.H., Kadanoff, L.P., Krishna, S.: Universal behaviour of coupled oscillators: lessons for biology preprint (2016).

[2] Stavans, J., Heslot, F., Libchaber, A.: Fixed winding number and the quasiperiodic route to chaos in a convective fluid, Phys. Rev. Lett. **55**, 596-599 (1985); Jensen, M.H., Kadanoff, L.P., Libchaber, A., Procaccia, I., Stavans, J.: Global Universality at the Onset of Chaos: Results of a Forced Rayleigh Benard experiment, Phys.Rev.Lett. **55**, 2798-2801 (1985).

[3] Jensen, M.H., Bak, P., Bohr, T.: Complete devil's staircase, fractal dimension and universality of mode-locking structure in the circle map, Phys. Rev. Lett. **50**, 1637-1639 (1983); Jensen, M.H., Bak, P., Bohr, T.: Transition to chaos by interaction of resonances in dissipative systems. I. Circle maps, Phys. Rev. A **30**, 1960-1969 (1984).

[4] Huygens, C.: *A copy of the letter on this topic to the Royal Society of London appears in (1893) (Nijhoff, M., Ed.), Ouevres Completes de Christian Huygens, vol. 5, p. 246, Societe Hollandaise des Sciences, The Hague, The Netherlands. 1989.*

[5] Pikovsky, A., Rosenblum. M., Kurths, J.: *Synchronization: a universal concept in nonlinear sciences* Cambridge University Press, Cambridge (2003).

[6] Ramirez, J.P., Olvera, L.A., Nijmeijer, H., Alvarez, J.: Scientific Reports **6**, 23580 (2016).

[7] Arnold, V.I., Avez, A.: *Ergodic Problems of Classical Mechanics*, Addison-Wesley (1989).

[8] Brown, S.E., Mozurkewich, G., Gruner, G.: Subharmonic Shapiro Steps and Devil's-Staircase Behavior in Driven Charge-Density-Wave Systems, Phys. Rev. Lett. **52**, 2277-2380 (1984).

[9] Gwinn, E.G., Westervelt, R.M.: Frequency Locking, quasiperiodicity, and Chaos in Extrinsic Ge, Phys. Rev. Lett. **57** 1060-1063 (1986).

[10] Tsai, T.Y., Choi, Y.S., Ma, W., Pomerening, J.R., Tang, C., Ferrell Jr., J.E.: Robust, tunable biological oscillations from interlinked positive and negative feedback loops, Science **321**, 126-129 (2008)

[11] Goldbeter, A.: Computational approaches to cellular rhythms", Nature 420, 238-245 (2002).

[12] Mondragon-Palomino, O., Danino, T., Selimkhanov, J., Tsimring, L., Hasty, J.: Entrainment of a Population of Synthetic Genetic Oscillators, Science **333** 1315-1319 (2011).

[13] Woller, A., Duez, H., Staels, B., Lefranc, M.: A Mathematical Model of the Liver Circadian Clock Linking Feeding and Fasting Cycles to Clock Function, Cell Reports **17**, 1087-1097 (2016)

[14] Mengel, B., Hunziker, A., Pedersen, L., Trusina, A., Jensen, M.H., Krishna, S.: Modeling oscillatory control in NF-kB, p53 and Wnt signaling, Current Opinion in Genetics and Development **20**, 656-664 (2010).

[15] Hoffmann, A., Levchenko, A., Scott, M.L., Baltimore, D.: The IκB-NF-κB signaling module: temporal control and selective gene activation, Science **298**, 1241-1245 (2002).

[16] Nelson, D.E. et. al: Oscillations in nf-κb signaling control the dynamics of gene expression, Science **306**, 704-708 (2004).

[17] Krishna, S., Jensen, M.H., Sneppen, K.: Spiky oscillations in NF-kappaB signalling, Proc.Nat.Acad.Sci. **103**, 10840-10845 (2006).

[18] Tay, S., Kellogg, R.: Noise facilitates transcriptional control under dynamic inputs, Cell. **160**, 381-392 (2015).

[19] Heltberg, M.L., Kellogg, R.A., Krishna, S., Tay, S., Jensen, M.H.: Noise induces hopping between NF-κB entrainment modes, Cell Systems, Dec. (2016).

[20] Jensen, M.H., Krishna, S.: Inducing phase-locking and chaos in cellular oscillators by modulating the driving stimuli, FEBS Letters **586**, 1664-1668 (2012).

[21] Strogatz, S. H. : *Dynamical Systems and Chaos* Westview Press, Cambridge MA 02142 (2000). pp 278-279.

[22] Sun, H., Scott, S.K., Showalter, K.: *Uncertain destination dynamics* Physical Review E **60**4: (1999)

[23] Hens, C., Dana, S.K., Feudel, U.: *Extreme multistability: Attractor manipulation and robustness* Chaos: An Interdisciplinary Journal of Nonlinear Science **25**5 (2015):

[24] Gillespie, D. T. : *Exact stochastic simulation of coupled chemical reactions* The Journal of Physical Chemistry, 81(25), 2340 - 2361. http://doi.org/10.1021/j100540a008 (1977)

[25] Fisher, R. A. : *The use of multiple measurements in taxonomic problems* Annals of Eugenics **7**: 179 - 188. (1936)

Appendix A

Description of the biological model

The network of the transcription factor NF-κB is very important for the mammalian protein production, and several models have therefore been constructed to capture the essential dynamics

Here we use the NF-κB model, published in 2012 by Jensen and Krishna. In this model, we consider the NF-κB inside the nucleus, acting as a transcription factor for a great variety of different proteins, including I-κB. This forms a complex with NF-κB, making it unable to enter the nucleus, which means it is inactive. In order to create a time delay, the equation for the I-κB RNA is added, which gives a three node network. Now we consider the protein complex IKK, that can phosphorylate the NF-κB - I-κB complex and thus make NF-κB active again. We assume that there IKK can be in three states: active, neutral and inactive. Furthermore we assume that is a finite amount of both NF-κB and I-κB, but nothing is spontaneously degraded. With these assumptions at hand, we describe the system by the five coupled differential equations:

$$\dot{N_n} = k_{Nin}(N_{tot} - N_n)\frac{K_I}{K_I + I} - k_{Iin} I \frac{N_n}{K_N + N_n}$$

$$\dot{I_{RNA}} = k_t N_n^2 - \gamma_m I_{RNA}$$

$$\dot{I} = k_{tl} I_{RNA} - \alpha I K K_a (N_{tot} - N_n)\frac{I}{K_I + I}$$

$$\dot{IKK_a} = k_a f(t)([IKK]_{tot} - IKK_a - IKK_i) - k_i IKK_a$$

$$\dot{IKK_i} = k_i IKK_a - k_p IKK_i \frac{k_{A20}}{k_{A20} + [A20]f(t)}$$

$$f(t) = 0.5 + A\sin(\frac{2\pi}{T}t)$$

The parameters in the mode can be seen in the table below.

Original Parameter	Parameter in paper	Default value
k_{Nin}	V_x	5.4 min^{-1}
k_{Iin}	V_z	0.018 min^{-1}
k_t	Γ_y	1.03 $(\mu\text{M})^{-1}.\text{min}^{-1}$
k_{tl}	Γ_z	0.24 min^{-1}
K_I	K_z	0.035 μM
K_N	K_x	0.029 μM
γ_m	Δ_y	0.017 min^{-1}
α	Δ_z	1.05 $(\mu\text{M})^{-1}.\text{min}^{-1}$
N_{tot}	N_x	1. μM
k_a	Γ_u	0.24 min^{-1}
k_i	Δ_u	0.18 min^{-1}
k_p	V_v	0.036 min^{-1}
k_{A20}	K_A	0.0018 μM
$[IKK]_{tot}$	w	2.0 μM
$[A20]$	A_{20}	0.0026 μM

Table I: Default values of parameters in the model. $[IKK]_{tot}$ and $[A20]$ were chosen in order to obtain sustained spiky oscillations with frequency in the range 0.3–1 hr^{-1} when $[TNF]$ is kept fixed at 0.5 (the actual frequency obtained with these values is $\nu_0 = 1/1.8\ hr^{-1}$.)

Appendix B

Implementation of Gillespie algorithm

In the Gillespie algorithm we consider a volume V, with a spatially uniform mixture of N chemical species that can react through M different reactions, $R_1 ... R_M$. The number of each of the species is denoted $X_1 ... X_N$. At $t = 0$, we thus consider the initial number of molecules and calculates all reactions. The first goal is now to calculate the PDF, for the time until the next reaction occur

We consider the probability that the next reaction is of type ϵ, and it occurs in the time-interval $[t + \tau, t + \tau + dt]$. We therefore consider:

$$P(\tau, \epsilon)d\tau = \overset{\text{No reaction in } [t, t+\tau]}{P_{not}(\tau)} \cdot \overset{\text{Reaction } \epsilon \text{ occurs}}{R_\epsilon d\tau}$$

Therefore we want to describe $P_{not}(\tau)$ in terms of the rates. Since at each timestep ϵ, the probability for no reaction to appear is:

$$P_{not}(dt) = 1 - \sum_{i=1}^{N} R_i dt$$

We can thus define $\tau \equiv n \cdot dt$ and then:

$$P_{not}(\tau) = P_{not}(dt)^n = \left(1 - \sum_{i=1}^{N} R_i \frac{\tau}{n}\right)^n = e^{-r\tau}$$

$$\text{where} \quad r \equiv \sum_{i=1}^{N} R_i$$

This means that we should generate a random number according to the exponential distribution, and a random number according to a uniform distribution. Here we can use the transformation method, and we can then create the update process, where at each step we jump a step in time τ to next reaction, and picks the reaction according to r. Schematically the Gillespie algorithm can be described as:

- Pick two random numbers, ν_1 and ν_2. Calculate time until next reaction:

$$\tau = -\frac{ln(\nu_1)}{r}$$

Pick the next reaction:

$$\epsilon = \frac{\sum_{i=1}^{k-1} r_i}{\sum_{j=1}^{n} r_j} < \nu_2 \leq \frac{\sum_{i=1}^{k} r_i}{\sum_{j=1}^{n} r_j}$$

- Update the system according to the chosen reaction.

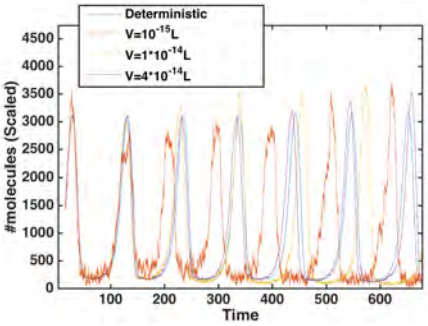

Figure 6: Trajectories starting from the same initial conditions for different noise levels. Here oscillations in the variable x

In this way the system can be updated, and adjusting the reactions to each time step. As can be seen in the figure, changing the volume, changes the noise level, since we have two fixed concentrations in the model and therefore the considered number of molecules change. In the limit of a high number of molecules, this should be very close to deterministic.

Biochemistry

Communication

pubs.acs.org/biochemistry

Expanding the Genetic Code of a Photoautotrophic Organism

Yonatan Chemla,[†] Mor Friedman,[†] Mathias Heltberg,[‡] Anna Bakhrat,[†] Elad Nagar,[§] Rakefet Schwarz,[§] Mogens Høgh Jensen,[‡] and Lital Alfonta*[,†]

[†]Department of Life Sciences and Ilse Katz Institute for Nanoscale Science and Technology, Ben-Gurion University of the Negev, Beer-Sheva 84105, Israel

[‡]Niels Bohr Institute, University of Copenhagen, Blegdamsvej 17, 2100 Copenhagen, Denmark

[§]The Mina and Everard Goodman Faculty of Life Sciences, Bar-Ilan University, Ramat-Gan 5290002, Israel

Supporting Information

ABSTRACT: The photoautotrophic freshwater cyanobacterium *Synechococcus elongatus* is widely used as a chassis for biotechnological applications as well as a photosynthetic bacterial model. In this study, a method for expanding the genetic code of this cyanobacterium has been established, thereby allowing the incorporation of unnatural amino acids into proteins. This was achieved through UAG stop codon suppression, using an archaeal pyrrolysyl orthogonal translation system. We demonstrate incorporation of unnatural amino acids into green fluorescent protein with 20 ± 3.5% suppression efficiency. The introduced components were shown to be orthogonal to the host translational machinery. In addition, we observed that no significant growth impairment resulted from the integration of the system. To interpret the observations, we modeled and investigated the competition over the UAG codon between release factor 1 and pyl-tRNA$_{CUA}$. On the basis of the model results, and the fact that 39.6% of the stop codons in the *S. elongatus* genome are UAG stop codons, the suppression efficiency in *S. elongatus* is unexpectedly high. The reason for this unexpected suppression efficiency has yet to be determined.

Cyanobacteria play a significant role on earth as aquatic primary producers and oxygen generators and are crucial in CO_2 fixation. Cyanobacteria are also prolific producers of natural products and unique enzymes[1] that are being systematically improved for biotechnological purposes.[2] *Synechococcus elongatus* sp. PCC7942 (*S. elongatus*) is a free-living, freshwater cyanobacterium strain. This strain is relatively simple to culture, is characterized by high biomass production, and can be easily genetically manipulated. By these virtues, *S. elongatus* has been utilized for a myriad of applications. Among these are biofuel production,[3] renewable energy,[4] and CO_2 reduction.[5] *S. elongatus* is also used as a model organism for studies of circadian rhythm,[6] biofilm formation,[7] carbon fixation,[8] and photosynthesis.[9] In recent years, multiple genetic tools and methods have been developed to facilitate *S. elongatus* genetic manipulation. However, while in the past 15 years, genetic code expansion tools were introduced and improved in *Escherichia coli*,[10] Actinobacteria,[11] *Caenorhabditis elegans*,[12] *Drosophila*,[13] and mammalian cells,[14] they were not adapted for cyanobacteria.

The most notable advantage of genetic code expansion is the ability to incorporate, site-specifically, a synthetic amino acid of choice aimed to introduce new chemical or physical properties into a desired protein. The common strategy utilized for this is stop codon suppression, using an archaeal orthogonal translation system (OTS) that does not cross-react with the host native tRNAs and tRNA synthetases. The archaea *Methanosarcina mazei* (*Mm*) were found to genetically encode pyrrolysine with the utilization of the UAG stop codon as a sense codon. This process is enabled by a unique *Mm*-pyrrolysyl tRNA synthetase (PylRS) and *Mm*-tRNA$_{CUA}^{pyl}$ (pyl-tRNA)[15] pair. Once cloned, this pair was used to incorporate more than 100 synthetic unnatural amino acids (UAAs) into proteins in the three different kingdoms of life[16] and was demonstrated to be incorporated in vivo and in vitro.[17] For these reasons, the pyl-orthogonal pair was chosen as a candidate for attempting to expand the genetic code of *S. elongatus*.

Herein, we aim to introduce and develop a general method for incorporation of UAAs into proteins in the cyanobacterium *S. elongatus*. To achieve this, the pyrrolysyl orthogonal translation system (pyl-OTS) was cloned to a pCB4 shuttle vector (Table S1), and the resulting construct was named pCOTS-pyl. In addition, a model protein for genetic code expansion, GFP Y35TAG, was cloned, resulting in pCOTS-pyl-35TAG-GFP, whereas the UAA was incorporated using the UAG stop codon as a sense codon, replacing tyrosine. Furthermore, a second genetic construct was designed for genomic recombination of the pyl-OTS into the *S. elongatus* chromosome (Figure S1). In this strain, the target gene, GFP, was expressed from the pES94-35TAG-GFP plasmid (Table S1). This genomically modified strain was named 7942-PO. In both cases, GFP was expressed under the P$_{cpcB1}$ promoter[18] and T$_{cpcA}$ terminator (Figure 1a) and PylRS was expressed under the P$_{rbcL}$ promoter and terminator. The pyl-tRNA was expressed under the *S. elongatus* Leu-tRNA$_{CAG}$ promoter and terminator, which were extracted from the *S. elongatus* genome (Figure 1b) (sequences are available in the Supporting Information). The two *S. elongatus* variants, pCOTS-pyl-

Received: February 15, 2017
Revised: April 9, 2017
Published: April 10, 2017

DOI: 10.1021/acs.biochem.7b00131
Biochemistry 2017, 56, 2161−2165

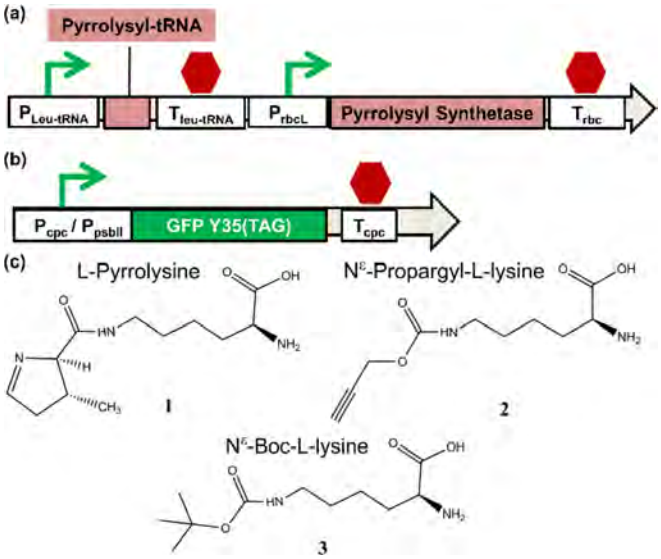

Figure 1. Genetic code expansion constructs that allow incorporation of UAAs into proteins in *S. elongatus*. (a) Genetic map of the OTS. (b) Genetic map for protein expression. (c) UAAs mentioned in this study.

35TAG-GFP and 7942-PO, were selected by antibiotic markers and validated by sequencing.

PylRS is a promiscuous enzyme as it was shown to recognize several UAAs in addition to its original substrate shown in Figure 1c, 1-pyrrolysine (**1**). Two of these UAAs are shown in Figure 1c: N^{ε}-propargyl-L-lysine (**2**) that allows a "click" reaction[19] and N^{ε}-boc-L-lysine (**3**) that is being used as a protected amino acid in bioorthogonal chemical conjugation reactions.[20] UAAs **2** and **3** were chosen to be incorporated as a general proof of concept for the genetically expanded *S. elongatus*. Either **2** or **3** was added to the growing bacterial cultures, containing either one of the genetic constructs, for incorporation into GFP(Y35TAG). To test the OTS in *S. elongatus*, we have grown the transformed cells in the absence of a UAA as a negative control. As a positive control, we have transformed the pCOTS-pyl-GFP-WT vector encoding the wild-type GFP gene. The incorporation of both **2** and **3** into GFP was successful, while no synthesis of protein was observed in the absence of a UAA (Figure 2a). To ensure the orthogonality of the pyl-tRNA in the *S. elongatus* cell, a genetic construct with only pyl-tRNA and the reporter Y35TAG GFP gene in the absence of the PylRS gene (pCOTS-ΔPylRS-GFP) was transformed and cultured in the presence of **2**. No expression of the reporter protein was observed (Figure S2), which led us to conclude that no endogenous tRNA synthetase can aminoacylate pyl-tRNA.

Aiming to optimize the growth conditions of *S. elongatus*, we examined variable UAA concentrations (Figure S3) and UAA addition at different OD_{750} values (Figure S4). The optimum was found to be 1 mM UAA, and the optimal OD_{750} for UAA addition was 0.01. Next, the optimal OD_{750} for bacterial harvesting was found to be at an OD_{750} of 1.1 (Figure S5). After optimization, the efficiency of the systems was evaluated. We have measured the UAA-incorporated GFP concentrations compared to the concentration of WT GFP (Figure 2b). This comparison is termed suppression efficiency. It is an indirect measurement of the ability of the OTS to reassign, at a specific site, the original "meaning" of the UAG codon. The pCOTS-pyl system exhibited up to 20 ± 3.5% suppression efficiency with yields of up to 15 μg/L (of original culture), while the 7942-PO system exhibited only 2% suppression efficiency with yields of up to 1.5 μg/L. Both systems resulted in relatively low yields; nonetheless, the vector-based pCOTS-pyl system showed results significantly better than those of the genome recombination system, and thus, further experiments were performed primarily with this system. Yields were further increased by changing the GFP expression promoter, p_{cpcB1}, to the *S. elongatus* P_{psbII} promoter. This change improved the yields by a factor of 5 and resulted in yields of 375 and 75 μg/L [for WT and Y35(**2**)-GFP, respectively], with 22 ± 7.5% suppression efficiency (Figure 2c and Figure S6). In the future, protein yields can be increased by improving the combination of promoter strength, ribosome binding site strength, and adaptation of coding sequence to that of *S. elongatus* as was recently shown by us in *E. coli*.[21]

To validate the selectivity of UAA incorporation, the molecular masses of produced proteins were measured using electrospray ionization mass spectrometry (ESI-MS) (Figure 2d). The experimentally observed masses of the Y35(**2**) mutant and WT GFP were within 1 Da of the calculated masses.

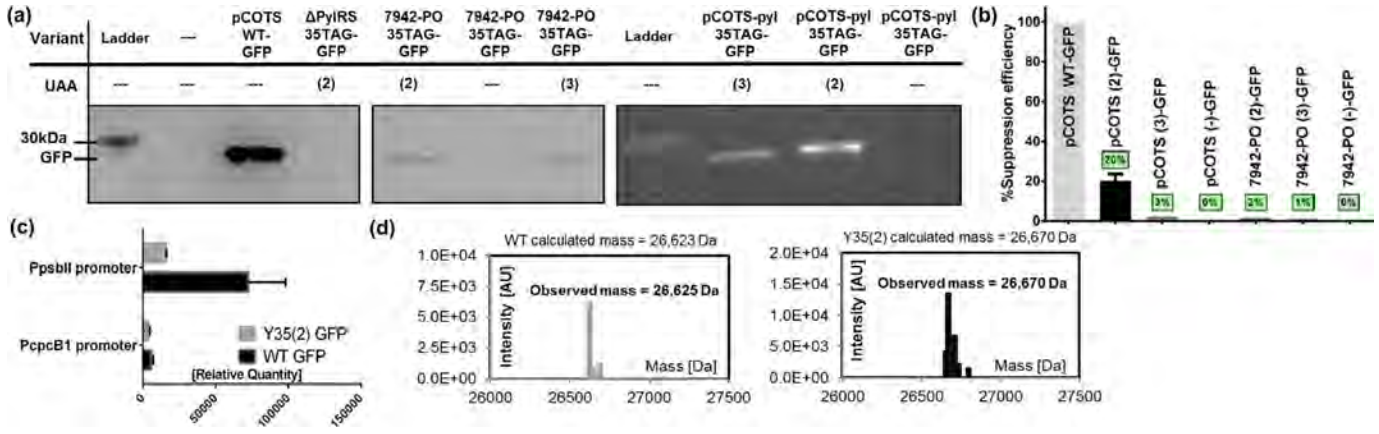

Figure 2. Incorporation of UAAs into GFP. (a) Representative Western blot analysis of GFP expression in *S. elongatus* variants, using different vectors, in the presence or absence of either **2** or **3**. (b) Suppression efficiencies of the different GFP variants relative to WT GFP expression. (c) Densitometry analysis comparing WT and Y35(**2**)-GFP expression levels between two promoters. (d) Mass spectrometry (electrospray ionization mass spectrometry with liquid chromatography) results for WT-GFP (gray) and Y35(**2**)-GFP (black).

DOI: 10.1021/acs.biochem.7b00131
Biochemistry 2017, 56, 2161−2165

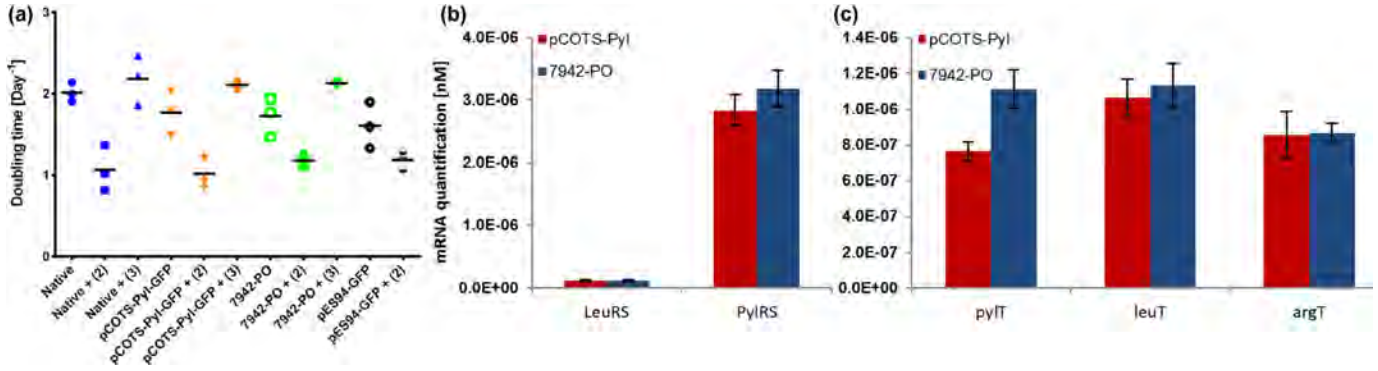

Figure 3. (a) Doublings per day of the different *S. elongatus* variants in the presence or absence of **2** or **3**. (b) Quantitative polymerase chain reaction (qPCR)-determined quantities of PylRS and LeuRS mRNA in *S. elongatus*. (c) qPCR quantities of pyl-tRNA, leu-tRNA$_{CAG}$, and arg-tRNA$_{CCT}$.

Observing these masses, we concluded that the UAA is selectively incorporated into GFP (Figure S7).

As pyl-tRNA suppresses the UAG stop codon, it should compete with release factor 1 (RF1) for the translation or termination of transcribed genes of *S. elongatus*. In fact, it was found that *S. elongatus* utilizes TAG termination in 39.6% of its open reading frames (ORFs), compared to only 7.4% in *E. coli*.[22] Hence, the important question of whether translation termination is being suppressed in TAG terminating genes arises, and if so, what are its adverse effects on the host organism if any? It is reasonable to assume that if the signal for the correct termination of almost 40% of the genes in *S. elongatus* is compromised, even to the smallest extent, *S. elongatus* growth should be impaired. This argument is emphasized when taking into account the fact that many of the photosystem genes terminate with TAG. To test this, the log-phase doubling times of the different strains in the presence or absence of different UAAs were followed (Figure 3a). It was found that pCOTS-pyl and 7942-PO variants, supplied with 1 mM **3**, did not show any significant reduction in growth rates (measured as the number of doublings of the population density per day) compared to that of native *S. elongatus* (1.9 ± 0.3 and 1.9 ± 0.4 day^{-1} for pCOTS-pyl and 7942-PO variants, respectively, compared to 2.0 ± 0.1 day^{-1} for the native form). However, the same variants, supplied with **2**, suffered a significant reduction in the number of doublings of the population density of 40−50% per day (1.0 ± 0.2 and 1.2 ± 0.1 day^{-1}, respectively).

The same reduction is observed when supplying native *S. elongatus* with **2**, 1.0 ± 0.2 day^{-1} compared to the value of 2.0 ± 0.1 day^{-1} of native *S. elongatus* in the absence of **2**. These results lead us to conclude that very low, if any, toxicity stems from the introduction of the OTS into this strain of cyanobacteria, while significant levels of toxicity stem from the introduction of **2** into *S. elongatus*. To further investigate the source of the toxicity of **2**, native and pCOTS-pyl strains were supplied with both **2** and L-lysine in equimolar quantities; in these cases, no toxicity was observed (data not shown). Therefore, we suspected that the cause of the toxicity is interference with the lysine synthesis metabolic pathway.

To better characterize the orthogonal translation system, the mRNA expression level of PylRS was measured using RT-PCR and was compared to that of the native leucine tRNA synthetase, which is a highly abundant synthetase (Figure 3b). The expression level of pyl-tRNA was also measured and compared to that of the most used leu-tRNA$_{CAG}$ and the least used arg-tRNA$_{CCT}$ (Figure 3c). The results suggest that the level of expression of the pyl-tRNA is relatively low and should be increased to improve the efficiency of the system. Counterintuitively, while the genomically recombined system shows an increased level of expression of the OTS, its efficiency is lower, and at present, we have no explanation for this intriguing observation. Finally, we tested the incorporation of **2** into different sites in GFP (Figure 4a) and simultaneously into multiple sites; however, multiple incorporation was undetectable (Figure S9).

The suppression efficiency achieved in this study was ∼20%, despite the low cellular concentration of pyl-tRNA and high

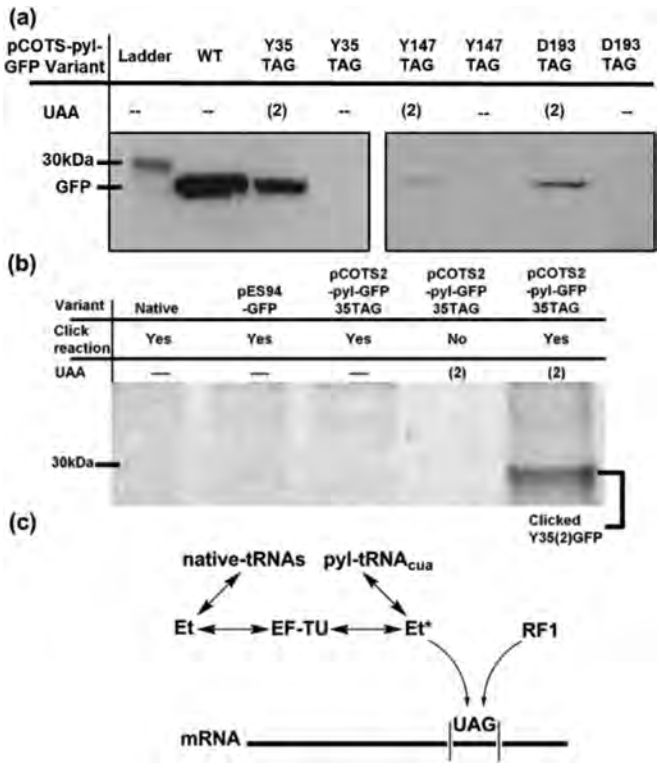

Figure 4. (a) Representative Western blot of *S. elongatus* lysates containing GFP variants with TAG mutations at different sites. (b) Representative fluorescent (excitation at 532 nm and emission at 575 nm) sodium dodecyl sulfate−polyacrylamide gel electrophoresis gel loaded with *S. elongatus* lysates that underwent click reaction to TAMRA-azide. (c) Scheme of the RF1 and pyl-tRNA competition model in which Et and Et* stand for the complex of the elongation factor (EF-Tu) bound to endogenous aminoacylated tRNAs and pyl-tRNA, respectively.

DOI: 10.1021/acs.biochem.7b00131
Biochemistry 2017, 56, 2161−2165

levels of RF1 needed for termination of ∼40% of ORFs in the *S. elongatus* genome. As a comparison, in *E. coli*, where the extent of genomic TAG termination is ∼7%, the initial suppression efficiency was <8%[23] and has gradually improved to 60%.[24] Given the suppression efficiencies, in *E. coli* and in *S. elongatus*, we expected that the off-target native chromosomal genes terminating with TAG would be suppressed with similar efficiencies. The system developed in this study allowed the exploration of this prediction in a bacterial strain with significant UAG termination usage. As described above, *S. elongatus* does not exhibit any significant difference in growth rates with and without an aminoacylated pyl-tRNA; this implies that there is no significant UAG suppression in chromosomal genes.

To test if this lack in toxicity is unique to *S. elongatus*, we examined two *E. coli* strains (DH5α and BL21) transformed with pEVOL-pyl-OTS and supplied with **2** or **3** (Figure S10); no reduction in growth rates was observed in either form of *E. coli*. The toxicity could possibly be alleviated by the use of multiple stop signals downstream from the suppressed UAG stop codon, but if this is the case, it should be expected that the UAA will be incorporated into those suppressed UAG sites. To test this claim directly and to evaluate one possible downstream application of the presented system, both *E. coli* and *S. elongatus* were cultured with vectors harboring pyl-OTS and **2**. The cultures were lysed and underwent a "click" reaction between proteins incorporated with **2** and a TAMRA-azide fluorescent dye. The fluorescent gels of the reaction products were analyzed (Figure 4b and Figures S11 and S12). The incorporation of **2** could be detected only in Y35TAG GFP, while no significant incorporation was observed in off-target proteins that terminate with TAG. Granted, it could be that the efficiency of the click reaction as well as the low suppression efficiency of the Pyl-tRNA will not afford a signal that is strong enough to be detected; however, in *S. elongatus*, strongly expressed photosystem components terminate with UAG. Taken together, these results may imply the existence of a mechanism by which the organism avoids unwarranted read-through events; this observation is in agreement with previous studies in *E. coli*.[25,26] The intriguing bias in suppression has also been recently observed in *E. coli* and HEK293T cells and was attributed to context effects, an increased level of degradation due to incorrect termination, and low expression levels of the off-target genes.[27,28] One of the causes of context dependence was shown to be that the identity of the fourth nucleotide in the 3′ end of the UAG codon affects the affinity of the suppressor or the terminator for the UAG codon.[29] Another hypothesis suggested that the position of the UAG codon in the gene may also affect local ribosomal density that, in turn, will influence protein expression.[21] Furthermore, and in agreement with these findings, Ozer et al. showed that RF1 has no observable influence on near-cognate pyl-tRNA mis-suppression of the UAG codon.[30] However, while these factors may play a part in this bias, we find it unlikely that they account for the apparently complete absence of pyl-tRNA suppression in the chromosomal genes of *S. elongatus*.

To further characterize this phenomenon, we modeled the cellular competition between RF1 and pyl-tRNA over the UAG codon in *E. coli* (Figure 4c). The competition between native tRNAs and pyl-tRNA over the elongation factor (EF-Tu) was calculated. It was done by using the reported affinity between EF-Tu and both pyl-tRNA[31] and native tRNAs,[32] it also took into account the approximate cellular concentrations of these molecules. This revealed the steady-state concentration of EF-Tu molecules bound to aminoacylated pyl-tRNA (Et*). Next, the competition over the UAG codon between Et* and RF1 could be assessed using their measured affinities (detailed in the Supporting Information). Our results show that RF1 should outcompete the pyl-$tRNA_{CUA}$ by more than 3 orders of magnitude (RF1 is ∼1365 times more likely to react with a UAG codon, according to the model). This explains the fact that no reduction in generation time was observed in *E. coli* or *S. elongatus*.

However, the model predicts that the suppression efficiencies should be negligible (<0.1%). This calculation for *E. coli* is in direct contradiction with the observed data by 2.5 orders of magnitude. Considering the significant abundance of UAG termination in *S. elongatus* compared to *E. coli*, and the correlation between stop codon usage and RF1 abundance,[22] the model results are further contradictory to our finding that the suppression efficiency is 20% in *S. elongatus*. These results stipulate the existence of a mechanism that reduces the level of premature stop codon termination. The existence of such a mechanism suggests an evolutionarily selective advantage by reducing the level of premature termination by nonsense mutations or translation errors, which requires further investigation.

In conclusion, this study reports a facile method of genetic code expansion in the cyanobacterium *S. elongatus*. The incorporation of UAAs was demonstrated by incorporating **2** or **3** into three different sites of GFP as a proof of concept. This protein augmentation ability combined with the unique attributes of cyanobacteria should give rise to many new applications, such as single-molecule studies in cyanobacteria with site-specifically labeled proteins, coupling of the photosynthetic system to modified proteins of interest, and large-scale production of proteins with unique new properties utilizing the solar energy harvested by these bacteria.

■ ASSOCIATED CONTENT

Supporting Information

The Supporting Information is available free of charge on the ACS Publications website at DOI: 10.1021/acs.biochem.7b00131.

Biochemical model, methods, additional figures, and gene sequences (PDF)

■ AUTHOR INFORMATION

Corresponding Author

*E-mail: alfontal@bgu.ac.il.

ORCID

Lital Alfonta: 0000-0002-3805-8625

Funding

This research was supported in part by ERC Grant 260647.

Notes

The authors declare no competing financial interest.

■ ACKNOWLEDGMENTS

We thank Eden Ozer for assistance with "click" experiments and Michael Shaferman, Orr Schlesinger, Rami Parnassa, and Ashok Bhagat for providing assistance and advice.

DOI: 10.1021/acs.biochem.7b00131
Biochemistry 2017, 56, 2161−2165

REFERENCES

(1) Kehr, J. C., Gatte Picchi, D., and Dittmann, E. (2011) *Beilstein J. Org. Chem. 7*, 1622−1635.
(2) Bernstein, H., et al. (2016) *mBio 7*, e00949-16.
(3) Dexter, J., and Fu, P. (2009) *Energy Environ. Sci. 2*, 857−864.
(4) Quintana, N., Van Der Kooy, F., Van De Rhee, M. D., Voshol, G. P., and Verpoorte, R. (2011) *Appl. Microbiol. Biotechnol. 91*, 471−490.
(5) Atsumi, S., Higashide, W., and Liao, J. C. (2009) *Nat. Biotechnol. 27*, 1177−1180.
(6) Cohen, S. E., and Golden, S. S. (2015) *Microbiol. Mol. Biol. Rev. 79*, 373−385.
(7) Parnasa, R., Nagar, E., Sendersky, E., Reich, Z., Simkovsky, R., Golden, S., and Schwarz, R. (2016) *Sci. Rep. 6*, 32209.
(8) Savage, D. F., Afonso, B., Chen, A. H., and Silver, P. A. (2010) *Science 327*, 1258−1261.
(9) Nelson, N., and Junge, W. (2015) *Annu. Rev. Biochem. 84*, 659−683.
(10) Wang, L., Brock, A., Herberich, B., and Schultz, P. G. (2001) *Science 292*, 498−500.
(11) He, J., Van Treeck, B., Nguyen, H. B., and Melançon, C. E. (2016) *ACS Synth. Biol. 5*, 125−132.
(12) Greiss, S., and Chin, J. W. (2011) *J. Am. Chem. Soc. 133*, 14196−14199.
(13) Bianco, A., Townsley, F. M., Greiss, S., Lang, K., and Chin, J. W. (2012) *Nat. Chem. Biol. 8*, 748−750.
(14) Liu, W., Brock, A., Chen, S., Chen, S., and Schultz, P. G. (2007) *Nat. Methods 4*, 239−244.
(15) Srinivasan, G., James, C. M., and Krzycki, J. A. (2002) *Science 296*, 1459−1462.
(16) Dumas, A., Lercher, L., Spicer, C. D., and Davis, B. G. (2015) *Chem. Sci. 6*, 50−69.
(17) Chemla, Y., Ozer, E., Schlesinger, O., Noireaux, V., and Alfonta, L. (2015) *Biotechnol. Bioeng. 112*, 1663−1672.
(18) Sawaki, H., Sugiyama, T., and Omata, T. (1998) *Plant Cell Physiol. 39*, 756−761.
(19) Thirumurugan, P., Matosiuk, D., and Jozwiak, K. (2013) *Chem. Rev. 113*, 4905−4979.
(20) Nguyen, D. P., Alai, M. M. G., Virdee, S., and Chin, J. W. (2010) *Chem. Biol. 17*, 1072−1076.
(21) Schlesinger, O., Chemla, Y., Heltberg, M., Ozer, E., Marshall, R., Noireaux, V., Jensen, M. H., and Alfonta, L. (2017) *ACS Synth. Biol.*, DOI: 10.1021/acssynbio.7b00019.
(22) Korkmaz, G., Holm, M., Wiens, T., and Sanyal, S. (2014) *J. Biol. Chem. 289*, 30334−30342.
(23) Ryu, Y., and Schultz, P. G. (2006) *Nat. Methods 3*, 263−266.
(24) Chatterjee, A., Xiao, H., and Schultz, P. G. (2012) *Proc. Natl. Acad. Sci. U. S. A. 109*, 14841−14846.
(25) Eggertsson, G., and Söll, D. (1988) *Microbiol. Rev. 52*, 354−374.
(26) Johnson, D. B. F., et al. (2011) *Nat. Chem. Biol. 7*, 779−786.
(27) Uttamapinant, C., Howe, J. D., Lang, K., Beránek, V., Davis, L., Mahesh, M., Barry, N. P., and Chin, J. W. (2015) *J. Am. Chem. Soc. 137*, 4602−4605.
(28) Kipper, K., Lundius, E. G., Curic, V., Nikic, I., Lemke, E. A., Wiessler, M., and Elf, J. (2017) *ACS Synth. Biol. 6*, 233−255.
(29) Smolskaya, S., Zhang, Z. J., and Alfonta, L. (2013) *PLoS One 8*, e68363.
(30) Ozer, E., Chemla, Y., Schlesinger, O., Aviram, H., Riven, I., Haran, G., and Alfonta, L. (2017) *Biotechnol. Bioeng. 114*, 1065−1073.
(31) Wang, J., Kwiatkowski, M., and Forster, A. C. (2016) *Biotechnol. Bioeng. 113*, 1552−1559.
(32) Ieong, K., Pavlov, M. Y., Kwiatkowski, M., Ehrenberg, M., and Forster, A. C. (2014) *RNA 20*, 632−643.

DOI: 10.1021/acs.biochem.7b00131
Biochemistry 2017, 56, 2161−2165

ACS SyntheticBiology

Research Article

pubs.acs.org/synthbio

Tuning of Recombinant Protein Expression in *Escherichia coli* by Manipulating Transcription, Translation Initiation Rates, and Incorporation of Noncanonical Amino Acids

Orr Schlesinger,[†,#] Yonatan Chemla,[†,#] Mathias Heltberg,[‡,#] Eden Ozer,[†] Ryan Marshall,[§] Vincent Noireaux,[§] Mogens Høgh Jensen,[*,‡] and Lital Alfonta[*,†]

[†]Department of Life Sciences and Ilse Katz Institute for Nanoscale Science and Technology, Ben-Gurion University of the Negev, PO Box 653, Beer-Sheva 8410501, Israel

[‡]Niels Bohr Institute, University of Copenhagen, Blegdamsvej 17, 2100 Copenhagen, Denmark

[§]School of Physics and Astronomy, University of Minnesota, Minneapolis, Minnesota 55455, United States

Supporting Information

ABSTRACT: Protein synthesis in cells has been thoroughly investigated and characterized over the past 60 years. However, some fundamental issues remain unresolved, including the reasons for genetic code redundancy and codon bias. In this study, we changed the kinetics of the *Eschrichia coli* transcription and translation processes by mutating the promoter and ribosome binding domains and by using genetic code expansion. The results expose a counterintuitive phenomenon, whereby an increase in the initiation rates of transcription and translation lead to a decrease in protein expression. This effect can be rescued by introducing slow translating codons into the beginning of the gene, by shortening gene length or by reducing initiation rates. On the basis of the results, we developed a biophysical model, which suggests that the density of co-transcriptional-translation plays a role in bacterial protein synthesis. These findings indicate how cells use codon bias to tune translation speed and protein synthesis.

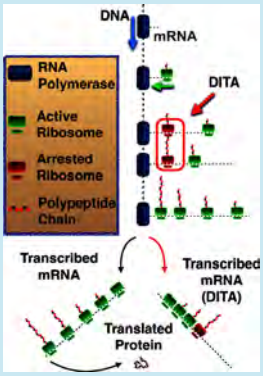

KEYWORDS: *protein translation initiation, transcription initiation, genetic code expansion, rates of translation, codon bias*

Protein synthesis, one of the most important and complex functions of living cells, is controlled by several mechanisms. Every stage in the process, from DNA transcription to protein folding dynamics, is tightly regulated to ensure that proteins are produced in required amounts, at the correct times and with minimal waste of energy and resources.[1] In bacteria, the transcription of DNA to mRNA and the subsequent translation into a polypeptide chain are coupled in time and space.[2,3] The two processes occur simultaneously, which creates a high molecular density area populated with all the components required for protein synthesis. For the dynamics of transcription and translation, such molecular crowding in the cytoplasm plays an important role by stabilizing protein−protein interactions and by controlling the diffusion rates of the components involved in protein synthesis.[4,5] The molecular densities of RNA polymerases on DNA and of ribosomes on mRNA are known to depend on the transcription and translation initiation rates, which, in turn, are determined by the strengths of the promoter and of the ribosome binding site (RBS). For example, it was shown that the use of a strong RBS with a high initiation rate to overexpress proteins can lead to ribosome collisions and queuing along individual mRNA strands. These queues can generate interference between adjacent translating ribosomes, significantly lowering the yields and efficiency of protein expression.[6,7] The nature of possible interactions that may occur between ribosomes on adjacent mRNA strands, however, is not clear.

The kinetics of translation also depend on the codon usage of the encoded gene, which is manifested by its effects on the elongation rate of the growing polypeptide chain.[8,9] Exploited across species to control translation rates and the ribosome queues along mRNA strands, codon bias is used to optimize protein synthesis and folding. Depending on the elongation rates they dictate, codons can be divided into different rate classes. Slower codons are found to be more favorably encoded for in the first 30−50 codons of the mRNA, thus resulting in ribosome crowding near the translation initiation site. Downstream codons, however, are found to be optimized for fast elongation rates.[10−12] These findings give rise to several questions: Why is translation that occurs close to the translation initiation site slow? Is this slow translation rate related to the density of the molecular environment in the vicinity of the cotranscriptional−translation event?

Although normally used for applicative purposes,[13] genetic code expansion through stop codon suppression constitutes an effective, basic research tool to shed light on these questions. One approach of genetic code expansion, the incorporation of

Received: January 17, 2017
Published: February 23, 2017

DOI: 10.1021/acssynbio.7b00019
ACS Synth. Biol. 2017, 6, 1076−1085

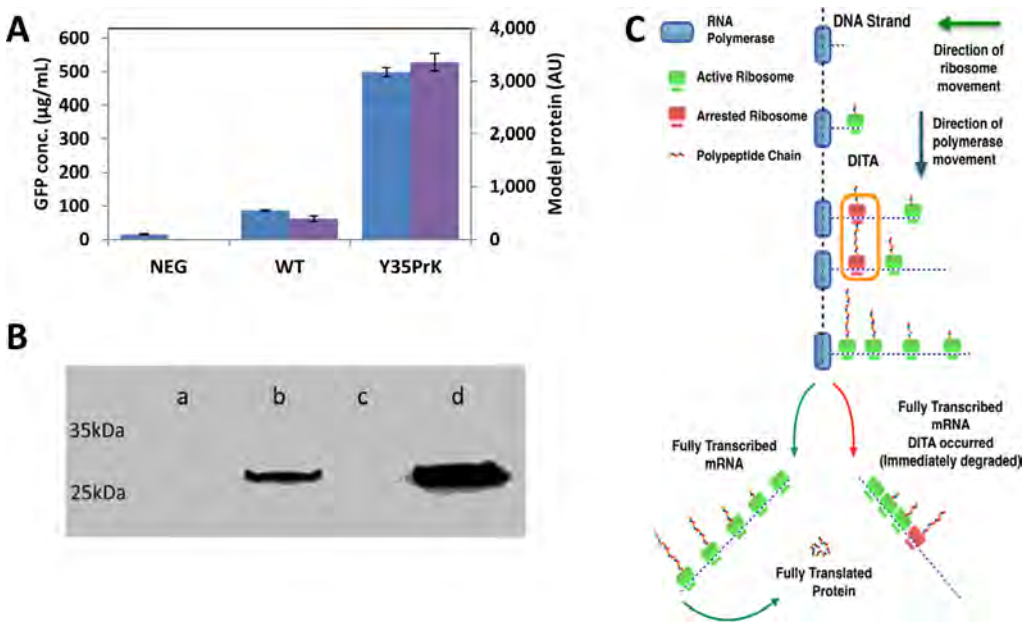

Figure 1. GFP expression using the P70a-UTR1 system. (A) Comparison of the experimental results (blue bars) with the modeled protein quantities (purple bars). (B) Western blot analysis using anti-GFP antibody of GFP expression in C321.ΔA.exp: w/o plasmids (a) pBEST-p70a-UTR1-GFP WT (b) and Y35PrK mutant in the absence and presence of PrK in the growth medium (lanes c and d, respectively). (C) Schematic presentation of the hypothesized DITA phenomenon.

noncanonical amino acids (ncAAs) into proteins, typically exploits the UAG nonsense (stop) codon, essentially transforming it into a sense codon that encodes for the incorporation of an ncAA. This recoding is facilitated by introducing into a host organism an orthogonal translation system (OTS) that comprises of an orthogonal Archaeal o-tRNA with an anticodon corresponding to the UAG stop codon and an orthogonal amino-acyl-tRNA synthetase (o-aaRS) that selectively recognizes the ncAA of choice and aminoacylates its cognate $tRNA_{CUA}$.[14] The affinity of the o-tRNA to the tertiary complex of the ribosome A-site during translation, is significantly smaller than that of the native bacterial tRNA.[15,16] This smaller affinity can be exploited to alter ribosomal traffic on the mRNA by decreasing the speed of translation along the mRNA. This approach could be efficiently realized when the OTS and the native release factor (*i.e.*, RF1) are not in direct competition for the UAG codon. That competition can be eliminated by recoding all TAG stop codons in the bacterial genome to TAA and by knocking out the RF1 gene.[17]

Here we use the OR2-OR1-pr-UTR1 (P70a-UTR1) expression system, based on a modified lambda PR promoter and the T7 bacteriophage RBS,[18] to perform genetic code expansion. This system has the highest transcription and translation initiation rates reported for an *E. coli* element, and so far, it has been used exclusively *in vitro*. Its high initiation rates promote large and unusual ribosome crowding along the transcribing mRNA. We therefore hypothesized that in the crowded environment of a polysome, a growing polypeptide chain may interact with neighboring translational components inside the polysome in a manner that can significantly retard the process. Indeed, it was previously shown that the nascent polypeptide can regulate the translation process in the ribosome by interacting with the polypeptide exit tunnel in the ribosome.[19] Such interaction may cause ribosome stalling,[20] translation arrest[21] and even accelerated mRNA degradation.[22] We exploited both the incorporation of ncAAs using UAG stop codon suppression, synonymous mutations in the gene and the modular tuning of the P70a-UTR1 expression system to model and control ribosomal traffic, thus optimizing recombinant protein expression.

RESULTS

WT GFP Exhibits Smaller Expression Levels Compared to GFP with an ncAA Incorporated at Position 35. Compared to its *in vitro* expression, the *in vivo* expression of the WT GFP (WT GFP stands for a protein without incorporated ncAAs) using the strongest *E. coli* promoter so far reported (P70a-UTR1)[18] was unexpectedly weak (Figures 1A, 1B lane b). This outcome was observed not only when using a genomically recoded *E. coli* strain (C321Δ*prf1*) (GRO),[17] but also with two other *E. coli* strains (*i.e.*, BL21(DE3) and DH5α). However, expression in the GRO strain of the same protein, in which a tyrosine residue at position 35 has been replaced with a nonsense stop codon (UAG), led to large and unexpected quantities of mutant GFP with the ncAA Propargyl-L-Lysine (PrK) incorporated into position 35 (Figures 1A, 1B lane d). Correct ncAA incorporation was verified by mass spectrometry (LC-ESI-MS) as well as by MS/MS analysis of peptide fragments (Figure S1).

To understand these initial observations, we first ruled out the possibility that inclusion bodies or secondary mRNA structures were the source of the divergence between the WT GFP and 35TAG GFP quantities. Cryo-electron microscopy (Cryo-EM) imaging of GFP revealed neither inclusion bodies nor any marked difference in bacterial shape compared to Cryo-EM images of bacteria without the GFP expression plasmid (Figures S2A, S2B). Moreover, there was no difference in the mRNA structure encoding for the WT GFP and the mutant GFP (Figures S2C, S2D). We used two different plasmid vectors to express the mutant Y35TAG GFP: one encoding for the mutated protein and one encoding the Pyrrolysine orthogonal translation system (Pyl-OTS), which is the machinery for the ncAA incorporation. To exclude the

DOI: 10.1021/acssynbio.7b00019
ACS Synth. Biol. 2017, 6, 1076−1085

possibility that the pEVOL Pyl-OTS plasmid contributed to the unusual overexpression of the mutated reporter protein, we demonstrated that pEVOL Pyl-OTS has no particular effect on the expression of WT GFP (Figure S2E). Taken together, these observations motivated our search for a more fundamental explanation related to the coupling of bacterial transcription and translation kinetics.

Density Induced Translation Arrest Model Predictions Corresponds to Counterintuitive Protein Expression Patterns. Herein, we propose a model to predict protein and mRNA levels that is based on a set of biochemical parameters combined with several assumptions. Model parameters: an increase in the RNA polymerase (RNAP) initiation rate (*i.e.*, promoter "strength") leads to a decrease in the average distance between transcribing RNAP and *vice versa*.[23] The deterministic average distance between RNAPs, $\langle D \rangle$, is governed by eq 1 (the equation and its solutions are presented in Figures S3A, S3B):

$$\langle D \rangle = D_{\text{pol}} + \frac{R_0}{R_\alpha} \tag{1}$$

where R_α is the RNAP initiation rate and R_0 is the RNAP elongation rate anywhere on the gene, while D_{Pol} is the size of the RNAP, which defines the minimal distance between polymerases. The use of the Gillespie stochastic algorithm imposed a distribution of RNAP velocities around the simplified elongation rate: R_0. This creates a stochastic distribution of the distances between RNAPs and even creates queues of adjacent RNAPs. As the average distance between RNAPs decreases, the density of mRNAs being synthesized along the DNA strand increases and the average distance between adjacent mRNAs decreases. We named this promoter dependent mRNA density along DNA "transcriptional density" (Figure S3E).

The initiation rate of translation depends on the properties of the ribosome binding site (RBS). As the ribosomal translation initiation rate increases, the average distance between the ribosomes translating the same mRNA template becomes shorter. The average distance, $\langle d \rangle$, is governed by ribosome size d_{rib}, the initiation rate r_α and the elongation rate for each codon i given by r_i'. Considering that the time for each step is given by $\langle t \rangle = \frac{1}{r'_i}$ the average distance (in number of codons) can be simplified and expressed by eq 2 (the equation and its solutions are presented in Figures S3C, S3D):

$$\langle d \rangle = d_{\text{rib}} + N + t_n \tag{2}$$

where

$$t_n = \frac{\frac{1}{r_\alpha} - \sum_{i=12}^{N} \frac{1}{r'_i}}{r_{N+1}}$$

and N fulfills

$$\sum_{i=12}^{N} \frac{1}{r'_i} < \frac{1}{r_\alpha} < \sum_{i=12}^{N+1} \frac{1}{r'_i}$$

Note that r'_i and r_α units are $[s^{-1}]$, whereas r_i units are [codons $\times$ s^{-1}].

Another factor to include in the model is the different elongation rates of each codon in the mRNA sequence.[24−26] On the basis of a previous model developed by Mitarai *et al.*, the entire set of bacterial codons was divided into three groups based on translation rate—fast (A), medium (B) and slow (C)—which correspond to elongation rates of 35, 8, and 4.5 codons per second, respectively[25] (Figure S3F). To these canonical codons we added the new noncanonical UAG codon (in the GRO strain its only translated by the o-tRNA). The UAG codon was assigned a new translation rate category, group (D), which had a significantly lower elongation rate of 0.04 codons per second. The rate was estimated from in vitro experiments[15] and even though this value has some uncertainty to it, it is at present our best estimate. Moreover, the model based simulated results are quite robust to large perturbations around this estimate. For example, the main observation being that by using an early TAG mutation, significantly more protein is being produced compared to WT GFP. These yields are still achieved for values of a UAG rate ranging between 0.01−0.2 codons/s. Like the case of the RNAP stochastic velocity, the ribosome also moves in a stochastic-probabilistic manner. This means that in addition to the 4 rate groups the actual ribosome velocity is governed by rate distributions for each codon around the group mean. Finally, we included "translational density", defined as the density of ribosomes along an mRNA. The length of the growing nascent polypeptide is directly proportional to the position of the ribosome along the mRNA relative to the translation initiation site.

In bacteria, transcription and translation are coupled, *i.e.*, as soon as the RBS on the transcribed mRNA emerges from the RNAP, the ribosome binds the RBS and translation begins.[2] The close proximity of the two processes in time and space means that there may be interactions between them. Accordingly, we hypothesized that highly crowded conditions will promote spatial ribosome density, thus inducing translation arrest in a process that we termed "Density Induced Translation Arrest" (DITA). We propose that in cases in which the promoter and RBS initiation rates are large enough to create regions with high molecular density and in which the nascent polypeptide is long enough, the probability for DITA events increases. In the case of a DITA event, all the ribosomes upstream of the arrested ribosome stall, promoting translation termination and thus reducing the number of full-length proteins produced from crowded mRNA strands (Figure 1C).

Next, we characterized our system's model parameters (described in detail in the methods section and listed in Table S2). The GFP gene was mapped and the codons were assigned to one of the four codon rate groups (A−D). The ribosome elongation rate is governed by each codon during translation. The average RNAP transcription rate was assumed to be constant.[2,27] Lastly, the length of the growing nascent polypeptide could not be determined *a priori* since its folding dynamics and interactions with the ribosome are unknown to us. For this reason, we chose the simplest possible approach and we added an empirical constant of proportionality, λ, which governs the length of the polypeptide protruding from its parent ribosome (Figure S3H). This approach allowed us to predict, for a given gene, which transcription-translation instances will generate a full-length protein and, as a result, the protein production rate.

The results of the Gillespie algorithm simulation agreed with the experimental results for both WT and Y35TAG mutant GFP (Figure 1A). The model suggests that WT GFP expression levels are negligible because of the high probability for DITA occurrences when a strong promoter and RBS, such as P70a and UTR1, respectively, are used. In the case of the Y35TAG GFP mutant, the model suggests that the small-

DOI: 10.1021/acssynbio.7b00019
ACS Synth. Biol. 2017, 6, 1076−1085

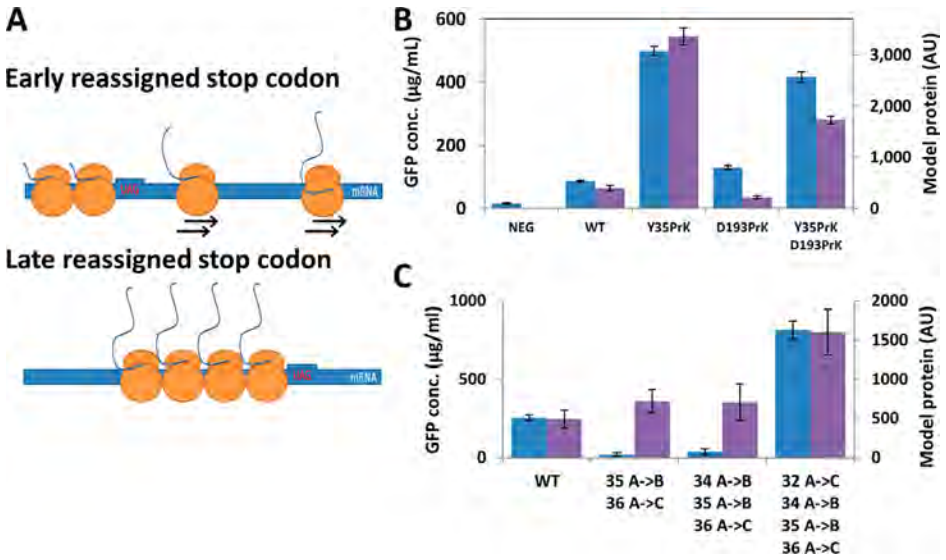

Figure 2. The "rescue effect" caused by ncAA incorporation and the associated attenuation in transcription rate is position dependent as well as "slow translating" codon dependent. (A) Schematic presentation of the ribosome queue caused by UAG codons at various positions along the mRNA. In early introduced UAG codons, the nascent polypeptide is relatively short and the ribosome traffic downstream of the codon is low, reducing the chance of spatial ribosome density. However, with later UAG codons, the nascent peptide is longer and has more chances to interact with other molecules in the polysome due to the ribosomal queue caused by the slow rate of the UAG codon. (B) Comparison of the experimental results (blue bars) with the modeled protein amounts (purple bars). (C) WT GFP expression upon introduction of synonymous mutations around position 35. Experimental results (blue bars) and modeled protein quantities (purple bars) show a significant increase in expression after the introduction of the 4th synonymous mutation.

translation-rate UAG codon (group D) inserted in this position serves as a "traffic light" that reduces ribosomal density downstream. Taken together, the reduction in translational density downstream of the UAG codon and the low probability of a DITA event result in high yields of expressed protein.

Early Reassigned Amber Stop Codon Rescues Protein Expression As Predicted by the Model. In the proposed model, we suggest that a suppressed UAG stop codon functions as a traffic light, thus its position along the mRNA is of importance. Due to its substantially slower ncAA incorporation kinetics compared to those of codons encoding for canonical amino acids, a queue of ribosomes will grow behind the reassigned stop codon. The transient stalling generated by an early UAG codon significantly reduces ribosome occupancy downstream, thereby reducing the chance of a DITA event (Figure 2A). As the translation process continues, the chance that the elongating polypeptide chain will have a DITA grows. Indeed, both our experimental results and our simulations indicated that the earlier the stop codon is introduced, the lower the chance of a DITA event. For cases in which both promoter and RBS are strong, our hypothesis predicts that the closer a UAG codon is positioned to the C-terminal, the smaller will be the protein yields in a manner similar to what is observed for the WT GFP. Indeed, the choice of a late D193TAG site in the simulation resulted in high DITA levels and small protein yields compared to those in the Y35TAG GFP mutant and protein yields equal to that of the WT protein. To test our prediction, we mutated position D193TAG in GFP. The experimental results coincided with those of the simulation, *i.e.*, low protein levels (Figure 2B). Note that D193TAG GFP is a permissive mutation site, as compared *in vitro*[28,29] to the WT and Y35PrK mutant expression (Figure S4A). The relationship between the position of the UAG codon and the protein expression levels was simulated (Figure S4B) revealing that only the first 37 codons enable rescue of protein levels. This result is in agreement with our experimental results and with earlier reports by Tuller *et al.* of an early slow translating "ramp" region close to the translation initiation region.[9,10]

Next, we tested the influence of adding an early UAG codon to a mutant that already contains a late mutation (Y35TAG +D193TAG). The model predicted that the early mutation would decrease the translational density around the later UAG stop codon, thus reducing the probability of DITA and conferring a rescue mechanism on protein levels. The expression levels of the double mutant Y35TAG+D193TAG GFP, its protein expression kinetics and the final yields with the different mutants predicted *in silico* and tested *in vivo* showed high correlation and a clear rescue effect on protein expression (Figure 2B).

Observing these results, we wanted to test whether the rescue effect could be achieved with synonymous (silent) sense codon mutations. Hence, we have tried to mutate the codons around the early Y35 site in the WT GFP gene to slower synonymous codons. As an example; tyrosine 35 was mutated from TAC (group A) to TAT (group B). When tested *in silico*, we predicted that at least four slow translating codon mutations (two A → B mutations and two A → C mutations) should be introduced in order to increase protein yields (Figure 2C, purple bars). We tested our predictions experimentally and only when four slow translating codon mutations were introduced, the WT GFP expression was rescued and showed significant increase in expression levels (Figure 2C, blue bars). When two or three slow codon mutations were introduced, the expression levels of WT GFP were only basal levels in both the simulation and the experiments. These results reconfirm that translation rates are crucial for high yields of recombinant protein expression.

Slower Transcription and Translation Initiation Rates Rescue Protein Expression. The use of weaker variants of

DOI: 10.1021/acssynbio.7b00019
ACS Synth. Biol. 2017, 6, 1076−1085

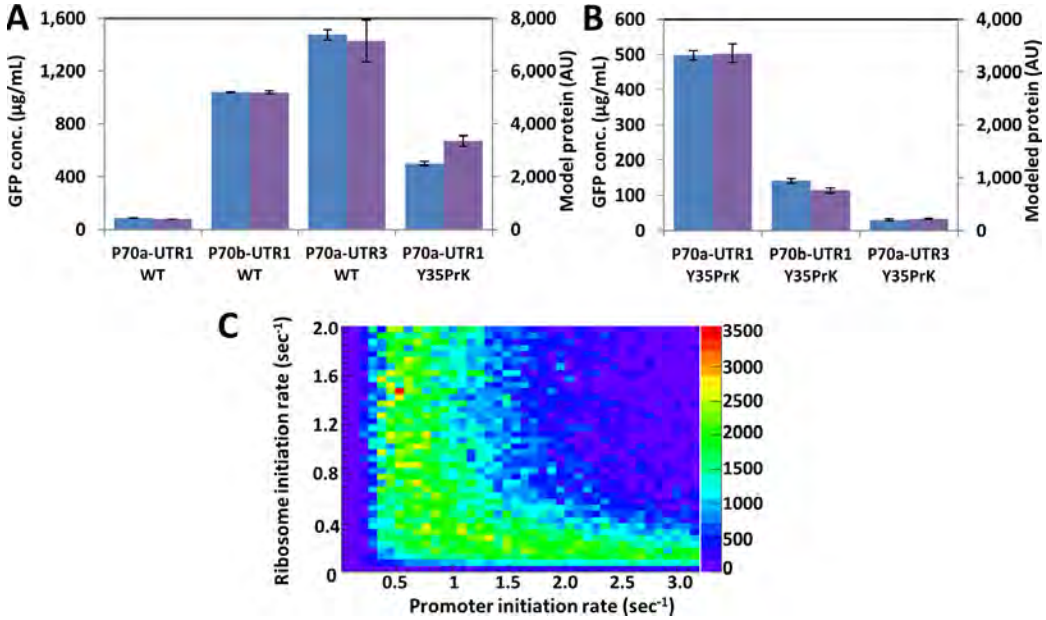

Figure 3. Smaller initial transcription and translation rates decrease the probability of DITA. (A) Comparison of the experimental results (blue bars) with the modeled protein amounts (purple bars) of WT GFP expression under the control of promoter and RBS with variable initiation rates. (B) Comparison of the expression of GFP Y35PrK mutant under the control of different control regions. Experimental and the modeled results, shown in blue and purple bars, respectively. (C) Heat map of the expected amounts of WT GFP protein using different combinations of transcription and translation initiation rates.

both promoter and RBS to increase the average distances between adjacent mRNAs and between translating ribosomes, respectively, should reduce the probability of DITA and increase protein expression. We engineered weaker variant of the P70a promoter and the UTR1 RBS by introducing point mutations into the control regions. *In vitro* transcription and translation experiments showed that the transcription initiation rate of the weaker promoter variant, P70b, was about 20 times smaller than that of the P70a promoter (Figure S5A). *In vitro* tests of the weak RBS variant UTR3 found that its translation initiation rate was 10 times smaller than that of the original UTR1 (Figure S5B). Our use of either a weaker promoter or RBS enabled us to test whether DITA is affected only by transcriptional or translational density or, as our model suggests, that both factors influence the expression density, the chances for DITA and thus, the amount of expressed protein. Intuitively, the use of weaker promoter and RBS regions is expected to result in smaller amounts of synthesized protein. However, as predicted by our hypothesis and model, the counterintuitive trend was observed, according to which the weaker the control region, the higher the protein yields. This finding is true both for the weaker promoter and RBS variant, P70b-UTR1 and P70a-UTR3, respectively (Figure 3A, purple bars). Experimental tests of this prediction showed that the weakened variants yielded up to 20 times more protein than the strong promoter-RBS construct (Figure 3A, blue bars), suggesting that DITA can be mitigated by increasing either the spacing of RNAP on DNA or ribosomal spacing on mRNA. Notably, when the same experiment was performed with the Y35TAG GFP mutant it showed the opposite trend, both experimentally as well as by simulation, where a weaker control region yielded less protein (Figure 3B). Thus, by using a simple set of mutated reporter genes and incorporation of non canonical amino acids, we showed how protein synthesis yields depend, in a counterintuitive manner, on the strengths of the regulatory elements, *i.e.*, promoter and RBS strengths, as well as on codon usage. Figure 3C is a heat map generated by the model that exemplifies the intricate relationship between promoter initiation rate and ribosomal initiation rate and resulting protein levels, it could be seen from this heat map that there is a certain set of conditions that will afford high protein yields, even for a combination of a very low promoter initiation rate and a high ribosomal initiation rate.

An Analysis of Mutants and Initiation Rate Variants Suggests That DITA Influences mRNA Levels. Under the DITA assumption, we propose that the stalling of translation somewhere along an mRNA causes all upstream ribosomes to stall while all downstream ribosomes complete translation. This hypothesis also suggests that the stretch of mRNA between the DITA site and the 3′ end will be more exposed to endonuclease cleavage. For that reason, we predicted that the larger the chances of DITA, the lower the mRNA levels will be, because mRNA is more exposed to endonucleases. Using the model, we determined the amount of mRNA produced by each of the mutants and compared it to the relative quantity (RQ) of GFP mRNA found in mid log phase cultures of the same mutants using qPCR (Figure 4A). A comparison of the qPCR and the modeled results revealed a strong correlation, suggesting that DITA affects both protein and mRNA levels by rapidly degrading not only the mRNA, but also nascent peptides. Since high mRNA levels usually correspond to high protein expression levels, it is essential to optimize protein expression for high levels of mRNA while maintaining the half-life of mRNA by avoiding DITA. This can be accomplished by exploiting the optimal regions, in terms of transcription and translation initiation rates, for maintaining a high level of GFP mRNA and by using regulatory elements that are strong enough but calibrated to prevent DITA under high expression density conditions. The heat map shown in Figure 4B is a result of a simulation of different initiation rates of the promoter and ribosomes and their influence on mRNA levels. It can be seen from the map that as expected ribosomal initiation rates have a

DOI: 10.1021/acssynbio.7b00019
ACS Synth. Biol. 2017, 6, 1076−1085

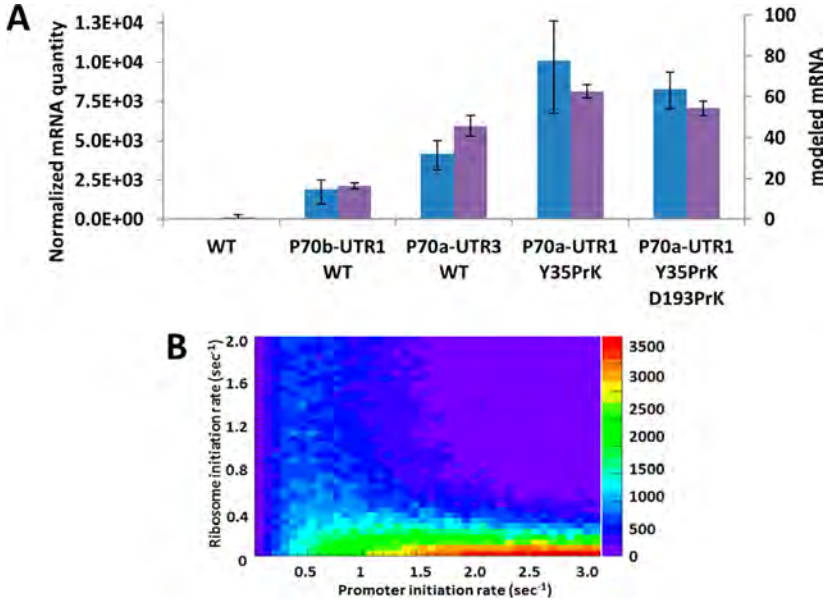

Figure 4. mRNA levels are also affected by DITA. (A) Comparison of the relative quantities of GFP mRNA transcripts found in mid log phase cultures and (blue bars) with the modeled mRNA quantities (purple bars). (B) Heat map of the expected amounts of GFP mRNA transcripts using different combinations of transcription and translation initiation rates.

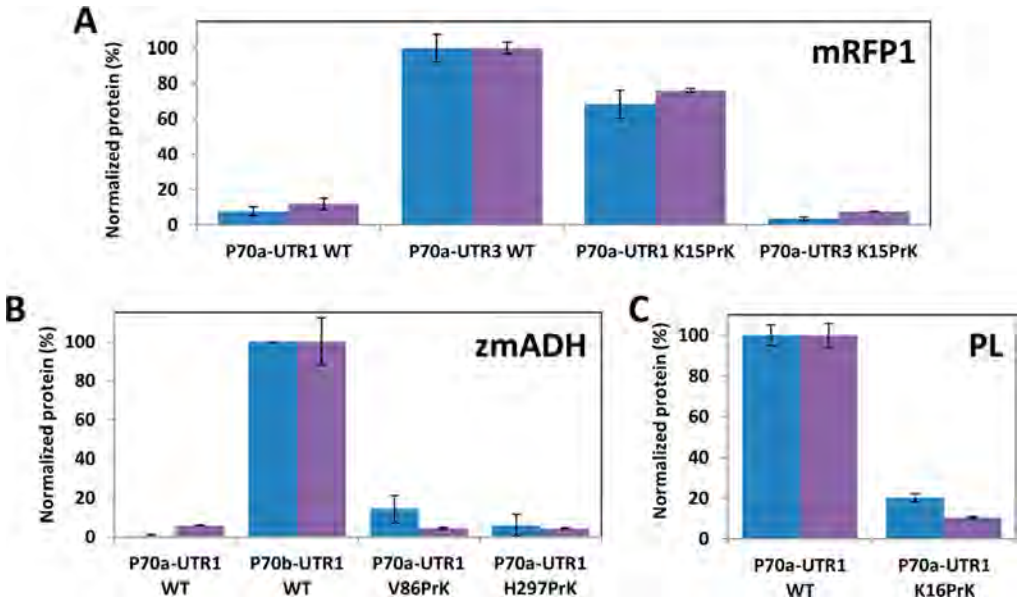

Figure 5. DITA is not limited to GFP and can be seen in other genes expressed using the P70a-UTR1 system and its variants. (A) Experimental (blue bars) and modeled (purple bars) protein levels of a codon optimized WT and K15PrK mRFP1. (B) Experimental (blue bars) and modeled (purple bars) normalized expression levels of zmADH. (C) Experimental (blue bars) and modeled (purple bars) normalized expression levels of WT and K16PrK protein L (PL).

very low influence on mRNA levels, however, our experimental results as well as the model have identified a set of conditions in which mRNA levels are influenced by ribosomal initiation rates. We do not exclude other explanations for the reduction in mRNA levels such as effect on transcription initiation by the density, or a codon bias effect[30] possibly mediated by a protein.[31] However, if this is the case, then it is mutually inclusive to our hypothesis.

Testing Additional Proteins Supports the Generality of the DITA Phenomenon. To investigate whether the proposed phenomenon is a general mechanism and that it is not specific to GFP, we tested our model on three different genes: red fluorescent protein (mRFP1), *Zymomonas mobilis* alcohol dehydrogenase II (*zmADH*) and the B1 domain of Protein L (PL), which is a small, 73-amino-acid polypeptide. The mRFP1 gene was chosen because it is a reporter protein as is GFP, however, mRFP1 shares only 26% similarity with the GFP amino acid sequence (sequences are available in the SI section), and it represents an optimized gene in terms of codon usage (it consists almost entirely of rapidly translating codons (A-type codons). The genes were tested under similar conditions to those used for GFP. The experimental results for mRFP1 were in a good agreement with the model simulations (Figure 5A). This protein has shown the same trends as GFP both in the model and in the experiments. In contrast to mRFP1, *zmADH* is a larger, more complex gene

DOI: 10.1021/acssynbio.7b00019
ACS Synth. Biol. 2017, 6, 1076−1085

with lower translation rates owing to its abundance of codons from groups B and C, which attenuate the translation process and result in more complex folding dynamics. The results were once more in a good agreement with the simulations (Figure 5B), but we observed, contrary to model predictions, a partial rescue effect when testing expression levels with a late mutation (V86TAG). Still, a weaker promoter has given higher expression for this enzyme as well, which was observed both in the model prediction and experimentally. This observation is evidence that our model does not account for all factors that influence transcription/translation. Moreover, this finding suggests that cotranslational folding and chaperons may introduce bifurcation points at which nascent polypeptide length is significantly reduced. Thus, the special case of a late mutation can rescue a protein from DITA. Lastly, PL was chosen to test the model prediction that a protein with a relatively short polypeptide chain should have a much lower propensity for a DITA event (Figure S3A–D). Indeed, because it is a small protein, WT PL is efficiently produced at significantly greater levels than the TAG mutated variant (Figure 5C). The results with PL are additional experimental evidence that if the polypeptide is short enough, spatial collisions are less likely to occur although density is very high. The good agreement found between our model simulation and the experimental results for other proteins suggest that our proposed model is applicable not only to GFP.

DISCUSSION

Due to the fact that we have no direct evidence to the occurrence of DITA, we wanted to test our hypothesis by exploring alternative explanations for this phenomenon. Alternative explanations that were excluded by us are: differences in protein stability between a protein with an ncAA and WT protein, differences in plasmid copy numbers, mRNA secondary structure differences, as well as ncAAs interference with fluorescence of the reporting protein, GFP. In order to demonstrate no apparent change in protein stability between WT GFP and Y35TAG GFP, two experiments were conducted: We monitored the stability of the WT and the mutant protein in a crude cell lysate over the course of 24 h, showing that both proteins were stable with no significant change in fluorescence (Figure S6). In the second experiment we used synonymous, slow translating codons that were consecutively mutated around position 35, demonstrating that after the addition of four and above slowly translating codons, protein yields improve significantly to yields that are even higher than that of the protein with incorporated ncAA (Figure 2C), these important results indicate that the same protein with no structural change, but a change in the coding sequence, can be expressed with higher yields when the rate of translation slows down significantly, these results are in agreement with a recent report of Zhong and co-workers.[32] These results also show that even with a strong promoter as is being used in this study, no hindrance from plasmid replication is observed. Evidence that attests to the fact that there is no hindrance for plasmid replication due to the existence of a strong promoter are the results with PL, since this protein is very short (*ca.* 70 AA) it is not affected by DITA, and high yields of expression are observed for this protein even with the strong promoter (Figure 5C). mRNA secondary structure could have accounted for the apparent differences in expression profiles between WT GFP and Y35GFP; however, an analysis of the mRNA secondary structure according to an algorithm written by Mathews and co-workers[33] has shown no difference in mRNA secondary structure. The algorithm calculates mRNA secondary structure by taking into account base pairing, free energy minimization and other thermodynamic considerations. The analysis has shown that the single nucleotide change of C → G (Figure S2C,D) has no implications on mRNA's secondary structure, hence could not explain the discrepancy in expression levels. Moreover, once ribosomes bind mRNA during translation, the secondary structure is rendered almost linear, hence the predicted secondary structure is not relevant any longer and could not account for the observed difference. In order to exclude the possibility that ncAAs may interfere in any way with GFP fluorescence, we have quantified WT and mutant GFP and thus report their quantities rather than their fluorescence.

Additional possibilities were tested as well: ribosome abortion due to ribosome collisions was not excluded it could be an additional hindrance in the system but not an exclusive explanation since we could see elevated expressions of WT GFP also with a weak promoter and a strong RBS (Figure 3A). Another possibility is that due to the strong promoter and RBS there will be an extreme consumption of translation factors (*i.e.*, ribosomes, tRNAs, elongation factors, release factors), this possibility was excluded since it should have been seen for the much slower mutant as well (Y35PrK GFP), with the same strong promoter, multiple mRNAs will require multiple ribosomes too. Lastly, we have considered the plasmid copy number as a possible cause of low protein expression levels as is common with very strong promoters, however, our observations point to very low effect of plasmid copy numbers if any: the fact that the relatively small protein WT PL have shown high yields compared to the mutant protein using the same expression vector as for WT GFP expression, while the WT GFP have shown very small expression levels under the same conditions, contradicts the effect of plasmid copy number as the cause for low protein yields. In addition, for the same plasmid Y35PrK GFP have exhibited very high yields as well, again contradicting the effect of high plasmid copy number. Moreover, the synonymous mutations experiment (shown in Figure 2C), demonstrates very well that after the insertion of four synonymous "slow" translating codons in the beginning of the gene, protein expression levels are recovered, for the same plasmid, yet again demonstrating that plasmid copy number could not be the cause for low protein yields.

CONCLUSIONS

The ability of the model to accurately predict the expression trends of various proteins under different conditions led us to suggest that spatial expression density and DITA have significant effects on protein expression in cells. We note that our model does not take into account co-translational folding and therefore should not be applied to these cases. We would like to stress out that a natural system could not have been evolved to have such strong elements to drive higher protein expression, maybe due to DITA, hence, natural systems have evolved to prevent inefficiency and energy loss. We have used artificial transcription and translation elements as well as a recombinant GFP with a synthetic sequence to demonstrate DITA. These elements were then modified to control DITA levels. In our model the expression density of any gene relies on a combination of four key determinants: translation initiation and termination rates, transcription initiation and termination rates, gene length and codon bias. Herein, we propose an additional hypothesis for the important roles of codon bias and

DOI: 10.1021/acssynbio.7b00019
ACS Synth. Biol. 2017, 6, 1076–1085

genetic code redundancy. Although this effect was only observed in this study due to the use of highly efficient transcription and translation control regions, we infer that its effects could have significant, yet not always easy to observe implications, on the expression of all recombinant heterologous proteins. We propose that what is widely known as exogenous expression toxicity due to resource and energy depletion in some cases could be explained by DITA. In addition, we were able to show that by reducing the strength of the regulatory elements, we could lower expression density, resulting in a counterintuitive outcome that significantly improved protein yields. These protein expression dependencies were also observed at the mRNA levels of the various mutants, showing that it affects both cellular protein and *mRNA* levels, thus affecting the final quantities of protein produced. We showed that DITA occurs for several, highly dissimilar proteins, suggesting that it could be a general mechanism found in all bacteria. Moreover, our findings may also point out the importance of separating transcription and translation processes to increase the production rate of proteins, especially with longer and more complex genes. Obtaining a deep understanding of the transcription and translation processes is of an utmost importance; our findings are a novel step towards the ability to control and modify these processes, which may have a significant impact on protein expression both for fundamental research as well as for biotechnological applications.

EXPERIMENTAL PROCEDURES

GFP and mRFP1 Quantification and Purity Assessment. GFP and mRFP1 fluorescence were measured during overnight incubation at 37 °C. ncAA mutants were supplemented with PrK in a final concentration of 2 mM of ncAA. The various mutants were grown in 96 well plates while OD600 and fluorescence were measured every 20 min for up to 20 h. GFP and mRFP1 fluorescence were measured with the respective excitation/emission wavelengths of 488/510 nm and 584/607 nm. GFP mutants were purified using nickel affinity chromatography, and the resulting samples were measured using a commercial Bradford assay (Thermo Scientific, Waltham, MA). Western blot analysis was used to verify the integrity of fluorescence as a measure of protein quantity when comparing the various mutants and to eliminate the possibility of fluorescence reduction due to ncAA incorporation. For Western blot analysis, goat anti-GFP and donkey antigoat (HRP-conjugated) antibodies were used as primary and secondary antibodies (Santa Cruz, CA, USA), respectively.

GFP Purification and Mass Spectrometry. For the LC−MS validation of PrK incorporation, nickel affinity chromatography purification (IMAC) of 6xhis-tagged GFP was performed. Overnight cultures of 100 mL were lysed using BugBuster protein extraction reagent (Novagen, WI, USA) and 6xHis tagged GFP was purified from the crude lysate using His-Bind nickel affinity chromatography resin (Novagen). The protein-containing eluted fraction was concentrated using a 10 kDa cutoff Vivaspin concentrator (Sartorius, Göttingen, Germany) to a final concentration of 2 mg/mL. The resulting concentrated fraction was analyzed by LC−MS (Finnigan Surveyor Autosampler Plus/LCQ Fleet (Thermo Scientific, Waltham, MA), using Chromolith monolithic column (EMD Millipore). The results were analyzed using Xcallibur (Thermo) and Promass (Novatia) software. MS/MS analysis was performed using standard protocols for in-gel trypsin digestion and desalting using ZipTip μC18 (EMD Millipore). The desalted peptides were analyzed on an LTQ/Orbitrap mass spectrometer (Thermo). Collision induced dissociation (CID) was used to analyze ions of interest for tandem mass spectrometry.

***Zymomonas mobilis* Alcohol Dehydrogenase (zmADH) Expression and Quantification.** Cultures of C321.ΔA.exp harboring the pBEST-zmADH plasmid with the various mutants were incubated at 37 °C. Cultures intended for ncAA incorporation were also supplemented with PrK at a final concentration of 2 mM. zmADH expression was analyzed by quantifying ADH activity in the samples.[34] The results were also semiquantitatively verified by densitometry analysis of a Western blot of the different mutants. Blotting was done using anti His-tag antibodies made in mice (Santa Cruz, CA, USA). The Western blot results were analyzed using ImageJ software.[35]

B1 Domain of Protein L (PL) Expression and Quantification. The PL gene was subcloned to the pBEST P70a-UTR1 vector. The K16TAG mutant was created using site-directed mutagenesis (primer sequences can be found in the SI section). The two variants were transformed separately into C321Δ*Prf1*.EXP already harboring the pEVOL-Pyl OTS plasmid. The cultures were incubated overnight at 37 °C in LB media supplemented with 2 mM of propargyl-L-lysine. The OD of the cultures was calibrated and lysis was performed using the protocol supplied with the BugBuster Reagent (Novagen, WI, USA). A sample of each lysate was loaded onto SDS-PAGE (WT sample was diluted by a factor of 10) and then blotted using anti His-Tag antibodies produced in mice (Santa Cruz, CA, USA). The Western blot results were analyzed using imageJ software[35] and the conversion to molar concentration was done using a calibration curve.

mRNA Quantification. A GeneJET RNA purification kit (Thermo Scientific, Waltham, MA, USA) was used to extract total RNA from bacterial cultures during midexponential phase. cDNA samples were synthesized from RNA samples using iScript cDNA synthesis kit (Biorad, Hercules, CA, USA). qPCR was performed using KAPA SYBR FAST qPCR Kit (KapaBiosystems, Wilmington, MA, USA) with the recommended relative calibration curve protocol, in the StepOnePlus Real-Time PCR System (Thermo Scientific, Waltham, MA, USA).

Modeling the Expression Density under the DITA Assumption. The system was modeled in a 2D temporal-spatial model and was simulated using a Gillespie algorithm. All the parameters used in the model are detailed in Supporting Information Table S2. The parameters were assessed and determined from literature and from experimentation as described in detail in the supporting experimental procedures section. The computational simulation enabled the assessment of mRNA and protein production kinetics and statistical assessment of the propensity for density induced translation arrest under different parameter regimes. Detailed explanation about the construction of the model including literature sources, and experiments along with the computational simulation code are available in the SI section.

ASSOCIATED CONTENT

Supporting Information

The Supporting Information is available free of charge on the ACS Publications website at DOI: 10.1021/acssynbio.7b00019.

DOI: 10.1021/acssynbio.7b00019
ACS Synth. Biol. 2017, 6, 1076−1085

Additional experimental procedures; Supporting figures, tables and gene sequences (PDF)
Complete code of the model (PDF)
Constants used in the model (PDF)

AUTHOR INFORMATION

Corresponding Authors

*E-mail: mhjensen@nbi.ku.dk. Phone: +45-353-25371. Fax: +45-353-25425.
*E-mail: alfontal@bgu.ac.il. Phone: +972-8-6479066. Fax: +972-8-6479576.

ORCID

Orr Schlesinger: 0000-0002-2648-6235
Lital Alfonta: 0000-0002-3805-8625

Author Contributions

#O.S., Y.C. and M.H. contributed equally.

Notes

The authors declare no competing financial interest.

ACKNOWLEDGMENTS

We would like to thank the following for their valuable contributions: Prof. Gilad Haran for providing us the PL gene, Prof. Yuval Shoham for providing the zmADH gene, Prof. Edward Lemke for providing us with pEVOL-PylRS plasmid, Dr. Namiko Mitarai for fruitful discussions and Prof. Kim Sneppen for invaluable advice. ERC−SG number 260647 (L.A.), The Danish Council for Independent Research (M.H.J. and M.H.) and Office of Naval Research award number N00014-13-1-0074 (V.N.) are gratefully acknowledged.

REFERENCES

(1) Browning, D. F., and Busby, S. J. (2004) The regulation of bacterial transcription initiation. *Nat. Rev. Microbiol. 2*, 57−65.
(2) Proshkin, S., Rahmouni, A. R., Mironov, A., and Nudler, E. (2010) Cooperation between translating ribosomes and RNA polymerase in transcription elongation. *Science 328*, 504−508.
(3) Chen, H.-Z., and Zubay, G. (1983) Prokaryotic coupled transcription−translation. *Methods Enzymol. 101*, 674−690.
(4) Ellis, R. J. (2001) Macromolecular crowding: obvious but underappreciated. *Trends Biochem. Sci. 26*, 597−604.
(5) Tan, C., Saurabh, S., Bruchez, M. P., Schwartz, R., and Leduc, P. (2013) Molecular crowding shapes gene expression in synthetic cellular nanosystems. *Nat. Nanotechnol. 8*, 602−608.
(6) Mitarai, N., Sneppen, K., and Pedersen, S. (2008) Ribosome collisions and translation efficiency: optimization by codon usage and mRNA destabilization. *J. Mol. Biol. 382*, 236−245.
(7) Jin, H., Björnsson, A., and Isaksson, L. A. (2002) Cis control of gene expression in E. coli by ribosome queuing at an inefficient translational stop signal. *EMBO J. 21*, 4357−4367.
(8) Sørensen, M. A., Kurland, C. G., and Pedersen, S. (1989) Codon usage determines translation rate in Escherichia coli. *J. Mol. Biol. 207*, 365−377.
(9) Fredrick, K., and Ibba, M. (2010) How the sequence of a gene can tune its translation. *Cell 141*, 227−229.
(10) Tuller, T., Carmi, A., Vestsigian, K., Navon, S., Dorfan, Y., Zaborske, J., Pan, T., Dahan, O., Furman, I., and Pilpel, Y. (2010) An evolutionarily conserved mechanism for controlling the efficiency of protein translation. *Cell 141*, 344−354.
(11) Cannarozzi, G., Schraudolph, N. N., Faty, M., von Rohr, P., Friberg, M. T., Roth, A. C., Gonnet, P., Gonnet, G., and Barral, Y. (2010) A role for codon order in translation dynamics. *Cell 141*, 355−367.
(12) Tuller, T., and Zur, H. (2015) Multiple roles of the coding sequence 5′ end in gene expression regulation. *Nucleic Acids Res. 43*, 13−28.
(13) Wang, L., Brock, A., Herberich, B., and Schultz, P. G. (2001) Expanding the genetic code of Escherichia coli. *Science 292*, 498−500.
(14) Wang, L., and Schultz, P. G. (2001) A general approach for the generation of orthogonal tRNAs. *Chem. Biol. 8*, 883−890.
(15) Wang, J., Kwiatkowski, M., and Forster, A. C. (2016) Kinetics of tRNA Pyl-mediated amber suppression in Escherichia coli translation reveals unexpected limiting steps and competing reactions. *Biotechnol. Bioeng. 113*, 1552−1559.
(16) Fan, C., Xiong, H., Reynolds, N. M., and Söll, D. (2015) Rationally evolving tRNA Pyl for efficient incorporation of non-canonical amino acids. *Nucleic Acids Res. 43*, e156−e156.
(17) Lajoie, M. J., Rovner, A. J., Goodman, D. B., Aerni, H. R., Haimovich, A. D., Kuznetsov, G., Mercer, J. A., Wang, H. H., Carr, P. A., Mosberg, J. A., Rohland, N., Schultz, P. G., Jacobson, J. M., Rinehart, J., Church, G. M., and Isaacs, F. J. (2013) Genomically recoded organisms expand biological functions. *Science 342*, 357−360.
(18) Shin, J., and Noireaux, V. (2010) Efficient cell-free expression with the endogenous E. Coli RNA polymerase and sigma factor 70. *J. Biol. Eng. 4*, 8.
(19) Mankin, A. S. (2006) Nascent peptide in the "birth canal" of the ribosome. *Trends Biochem. Sci. 31*, 11−13.
(20) Komar, A. A. (2009) A pause for thought along the co-translational folding pathway. *Trends Biochem. Sci. 34*, 16−24.
(21) Woolhead, C. A., Johnson, A. E., and Bernstein, H. D. (2006) Translation arrest requires two-way communication between a nascent polypeptide and the ribosome. *Mol. Cell 22*, 587−598.
(22) Sunohara, T., Jojima, K., Tagami, H., Inada, T., and Aiba, H. (2004) Ribosome stalling during translation elongation induces cleavage of mRNA being translated in Escherichia coli. *J. Biol. Chem. 279*, 15368−15375.
(23) Klumpp, S., and Hwa, T. (2008) Growth-rate-dependent partitioning of RNA polymerases in bacteria. *Proc. Natl. Acad. Sci. U. S. A. 105*, 20245−20250.
(24) Quax, T. E. F., Claassens, N. J., Söll, D., and van der Oost, J. (2015) Codon bias as a means to fine-tune gene expression. *Mol. Cell 59*, 149−161.
(25) Mitarai, N., and Pedersen, S. (2013) Control of ribosome traffic by position-dependent choice of synonymous codons. *Phys. Biol. 10*, 56011.
(26) Dana, A., and Tuller, T. (2015) Mean of the typical decoding rates: a new translation efficiency index based on the analysis of ribosome profiling data. *G3: Genes, Genomes, Genet. 5*, 73−80.
(27) Klumpp, S., and Hwa, T. (2008) Stochasticity and traffic jams in the transcription of ribosomal RNA: Intriguing role of termination and antitermination. *Proc. Natl. Acad. Sci. U. S. A. 105*, 18159−18164.
(28) Chemla, Y., Ozer, E., Schlesinger, O., Noireaux, V., and Alfonta, L. (2015) Genetically expanded cell-free protein synthesis using endogenous Pyrrolysyl orthogonal translation system. *Biotechnol. Bioeng. 112*, 1663−1672.
(29) Ozer, E., Chemla, Y., Schlesinger, O., Aviram, H. Y., Riven, I., Haran, G., and Alfonta, L. (2016) In vitro suppression of two different stop codons. *Biotechnol. Bioeng.*, DOI: 10.1002/bit.26226.
(30) Boël, G., Letso, R., Neely, H., Price, W. N., Wong, K.-H., Su, M., Luff, J. D., Valecha, M., Everett, J. K., Acton, T. B., Xiao, R., Montelione, G. T., Aalberts, D. P., and Hunt, J. F. (2016) Codon influence on protein expression in E. coli correlates with mRNA levels. *Nature 529*, 358−363.
(31) Radhakrishnan, A., Chen, Y.-H., Martin, S., Alhusaini, N., Green, R., and Coller, J. (2016) The DEAD-Box protein dhh1p couples mrna decay and translation by monitoring codon optimality. *Cell 167*, 122−132.
(32) Zhong, C., Wei, P., and Zhang, Y.-H. P. (2016) Enhancing functional expression of codon-optimized heterologous enzymes in Escherichia coli BL21(DE3) by selective introduction of synonymous rare codons. *Biotechnol. Bioeng.*, DOI: 10.1002/bit.26238.

DOI: 10.1021/acssynbio.7b00019
ACS Synth. Biol. 2017, 6, 1076−1085

(33) Mathews, D. H., Disney, M. D., Childs, J. L., Schroeder, S. J., Zuker, M., and Turner, D. H. (2004) Incorporating chemical modification constraints into a dynamic programming algorithm for prediction of RNA secondary structure. *Proc. Natl. Acad. Sci. U. S. A. 101*, 7287−7292.
(34) Amir, L., Carnally, S. A., Rayo, J., Rosenne, S., Melamed Yerushalmi, S., Schlesinger, O., Meijler, M. M. M., and Alfonta, L. (2013) Surface display of a redox enzyme and its site-specific wiring to gold electrodes. *J. Am. Chem. Soc. 135*, 70−73.
(35) Abramoff, M. D., Magalhães, P. J., and Ram, S. J. (2004) Image processing with ImageJ. *Biophotonics Int. 11*, 36−42.

DOI: 10.1021/acssynbio.7b00019
ACS Synth. Biol. 2017, 6, 1076−1085

Article

Cell Systems

Chaotic Dynamics Mediate Brain State Transitions, Driven by Changes in Extracellular Ion Concentrations

Graphical Abstract

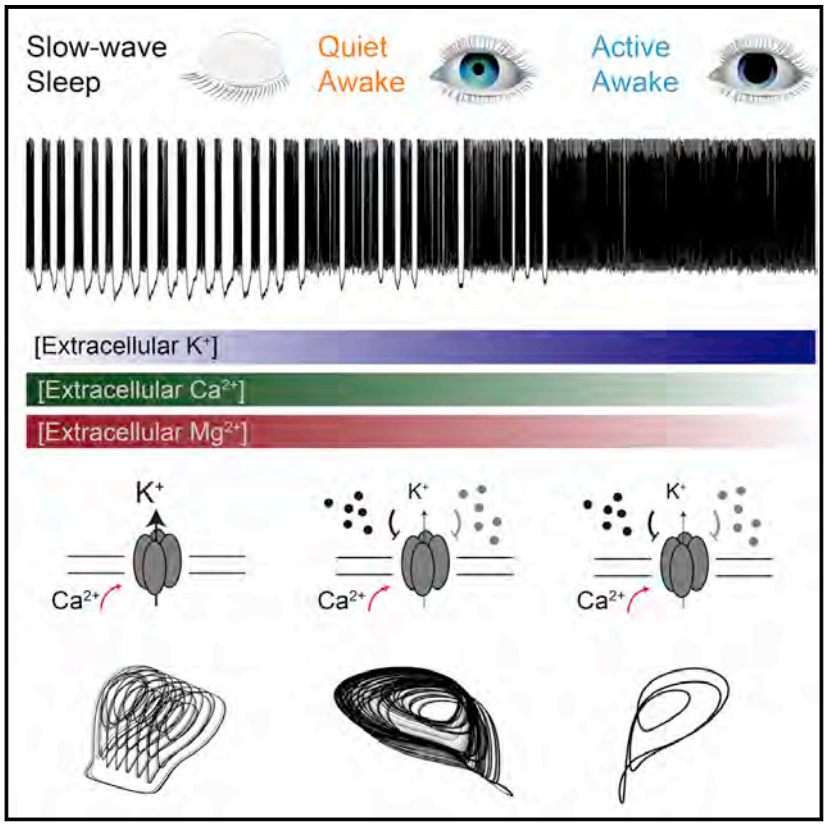

Highlights

- The Averaged-Neuron model is extended to include extracellular ionic changes
- *In vivo* sleep- and wake-dependent neuronal firing patterns are recapitulated
- Extracellular ionic changes lower the threshold for transitioning to wakefulness
- Chaotic dynamics create a smooth transition between different activity states

Authors

Rune Rasmussen, Mogens H. Jensen, Mathias L. Heltberg

Correspondence

runerasmussen@dandrite.au.dk (R.R.), heltberg@nbi.ku.dk (M.L.H.)

In Brief

By extending the Averaged-Neuron model to include changes in extracellular ion concentrations, Rasmussen et al. show that transitions between states of sleep and wakefulness are facilitated by ionic changes and governed by chaotic dynamics, which ensure smooth and robust transitions.

Rasmussen et al., 2017, Cell Systems *5*, 1–13
December 27, 2017
https://doi.org/10.1016/j.cels.2017.11.011

CellPress

Please cite this article in press as: Rasmussen et al., Chaotic Dynamics Mediate Brain State Transitions, Driven by Changes in Extracellular Ion Concentrations, Cell Systems (2017), https://doi.org/10.1016/j.cels.2017.11.011

Cell Systems
Article

Chaotic Dynamics Mediate Brain State Transitions, Driven by Changes in Extracellular Ion Concentrations

Rune Rasmussen,[1,3,*] Mogens H. Jensen,[2] and Mathias L. Heltberg[2,3,4,*]
[1]The Danish Research Institute of Translational Neuroscience – DANDRITE, Nordic EMBL Partnership for Molecular Medicine, Department of Biomedicine, Aarhus University, 8000 Aarhus C, Denmark
[2]Niels Bohr Institute, University of Copenhagen, 2100 Copenhagen, Denmark
[3]These authors contributed equally
[4]Lead Contact
*Correspondence: runerasmussen@dandrite.au.dk (R.R.), heltberg@nbi.ku.dk (M.L.H.)
https://doi.org/10.1016/j.cels.2017.11.011

SUMMARY

Previous studies have suggested that changes in extracellular ion concentrations initiate the transition from an activity state that characterizes sleep in cortical neurons to states that characterize wakefulness. However, because neuronal activity and extracellular ion concentrations are interdependent, isolating their unique roles during sleep-wake transitions is not possible *in vivo*. Here, we extend the Averaged-Neuron model and demonstrate that, although changes in extracellular ion concentrations occur concurrently, decreasing the conductance of calcium-dependent potassium channels initiates the transition from sleep to wakefulness. We find that sleep is governed by stable, self-sustained oscillations in neuronal firing patterns, whereas the quiet awake state and active awake state are both governed by irregular oscillations and chaotic dynamics; transitions between these separable awake states are prompted by ionic changes. Although waking is indicative of a shift from stable to chaotic neuronal firing patterns, we illustrate that the properties of chaotic dynamics ensure that the transition between states is smooth and robust to noise.

INTRODUCTION

During transition from sleep to awake, the brain passes from a state that attenuates sensory inputs to one that often amplifies them (Lee and Dan, 2012; McGinley et al., 2015b; Polack et al., 2013). How this transition between states occurs is still incompletely understood, both at the level of the brain and at the level of the neurons that must implement the transition in a smooth and robust way.

Cortical neurons are known to exhibit three distinct physiological and behavioral states that characterize the transition from sleep to active wakefulness. Specifically, slow-wave sleep is characterized by oscillating periods of synaptic barrages (also called "upstates") and silence ("downstates") (Steriade et al., 2001). It is understood that this behavior reflects oscillations in membrane potential (V_m) and therefore the neuron's susceptibility to input. In wakefulness, these downstates are suppressed and V_m is maintained closer to threshold. Although the classic view holds that oscillations are restricted to slow-wave sleep, recent studies have demonstrated that a quiet awake state is also characterized by low-frequency V_m oscillations. Once actively awake, however, movement and arousal suppress these oscillations, and V_m is depolarized tonically, making neurons sensitive to inputs and prone to firing. Despite our understanding of the neuronal behaviors that are indicative of transitions from slow-wave sleep to quiet awake to active awake, the underlying mechanisms that initiate these transitions remain unclear.

Recently it was proposed that changes in extracellular ion concentrations ($[K^+]_o$, $[Ca^{2+}]_o$, and $[Mg^{2+}]_o$) control activity patterns during sleep and wakefulness, and that ionic changes are sufficient to shift the state from sleep to awake (Ding et al., 2016). However, given that changes in neural activity also strongly affect extracellular ion concentrations (Amzica et al., 2002; Hounsgaard and Nicholson, 1983; Lux, 1974; Lux and Neher, 1973; Nicholson et al., 1977), it is not possible to unequivocally distinguish cause and consequence *in vivo*. For example, both spiking and excitatory barrages, which originate within the neuron itself, increase $[K^+]_o$ (Hounsgaard and Nicholson, 1983; Shih et al., 2013), making it difficult to experimentally assess causality. A remedy for solving this issue is modeling and simulations (Fröhlich et al., 2006; Krishnan et al., 2015; Tagluk and Tekin, 2014; Tatsuki et al., 2016). The ability to maintain parameters constant, thereby reducing variable space dimensionality, is a powerful tool for interrogating the impact of changes in both intracellular and extracellular ion concentrations on V_m dynamics and state transitions, as well as for formulating hypotheses and predictions for future experimental investigations.

An important step toward successfully modeling the neuronal dynamics in a simple manner, is the Averaged-Neuron model, which recently has been proposed (Tatsuki et al., 2016). This model is inspired by previously constructed neural-network models (Bazhenov et al., 2002; Chen et al., 2012; Compte et al., 2003; Hill and Tononi, 2005; Sanchez-Vives et al., 2010; Timofeev et al., 2000), but simplifies the enormous complexity of these by performing a mean-field approximation of a

Please cite this article in press as: Rasmussen et al., Chaotic Dynamics Mediate Brain State Transitions, Driven by Changes in Extracellular Ion Concentrations, Cell Systems (2017), https://doi.org/10.1016/j.cels.2017.11.011

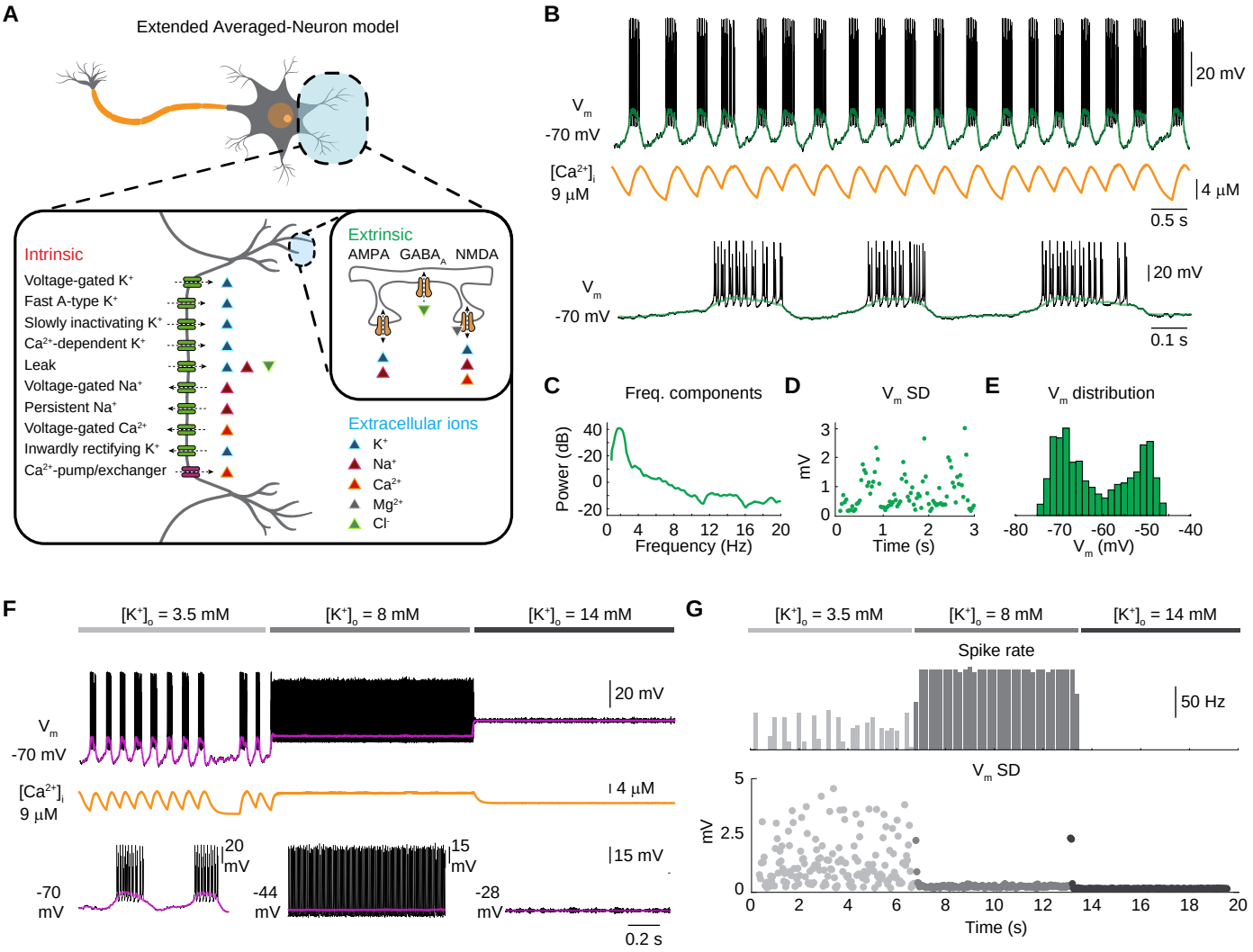

Figure 1. Implementing Ion Concentrations in the Averaged-Neuron Model

(A) Schematic diagram of the extended Averaged-Neuron model containing intrinsic ion channel conductances and Ca^{2+} pumps, extrinsic synaptic ion channel conductances, and extracellular ion concentrations.

(B) Representative slow-wave sleep membrane potential (V_m) firing pattern and intracellular Ca^{2+} concentration ($[Ca^{2+}]_i$) with the initial extracellular ion concentration parameter set ($[K^+]_o$ = 3.5 mM, $[Ca^{2+}]_o$ = 1.5 mM, and $[Mg^{2+}]_o$ = 1.1 mM). Below is an expansion of V_m dynamics.

(C) V_m frequency spectra.

(D) SD of mean V_m (spikes removed).

(E) Mean V_m distribution.

(F) Representative V_m firing pattern and $[Ca^{2+}]_i$ with 3.5, 8, or 14 mM $[K^+]_o$. Below is an expansion of V_m dynamics.

(G) Upper: Spike rate versus time for 3.5, 8, or 14 mM $[K^+]_o$. Lower: SD of mean V_m for 3.5, 8, and 14 mM $[K^+]_o$.

See also Figure S1.

population of neurons to construct an Averaged-Neuron model. The framework of the model is based on the existence of different ion channels and is mathematically described in a Hodgkin-Huxley manner; all contribute to the total change in V_m. As a first-order approximation, it is assumed that the averaged-neuron can interact with itself (directly or indirectly) through excitatory or inhibitory synaptic currents. Furthermore, intrinsic currents exist as depolarizing Na^+ and Ca^{2+} currents and hyperpolarizing K^+ currents. This polarization affects the V_m through nine different intrinsic channels (Figure 1A).

Here, we extend the Averaged-Neuron model to explicitly treat the changes in extracellular ion concentrations that occur during the sleep-wake cycle. We demonstrate how decreasing the conductance of the Ca^{2+}-dependent K^+ channel, in combination with physiological changes in $[K^+]_o$, $[Ca^{2+}]_o$, and $[Mg^{2+}]_o$, initiates state transitions in neuronal firing patterns. We find that sleep is dominated by a stable limit cycle, resulting in self-sustained, stable firing patterns, whereas wakefulness is governed by irregular oscillations and chaotic dynamics. As the ion concentrations are changed, the firing patterns become more dominated by long high-frequency upstate periods, and we predict that a state change from quiet to active awake can be induced by subtle changes in extracellular ion concentrations. Finally, we discuss how the fundamental properties of chaotic dynamics can ensure smooth transitions between brain states in the presence of intrinsic noise.

RESULTS

Implementing Dynamic Ion Concentration Dependencies in the Averaged-Neuron Model

As a starting point for investigating the influence of extracellular ion concentrations on neuronal states, we first implemented and extended the Averaged-Neuron model (Tatsuki et al., 2016). In this model, a single neuron feeds back onto itself directly and indirectly, through synaptic excitatory and inhibitory conductances (AMPA, NMDA, and $GABA_A$ receptors) (Figure 1A). In addition to synaptic conductances, the Averaged-Neuron model includes the following intrinsic conductances, either depolarizing or hyperpolarizing V_m: voltage-gated (Na_V) and persistent (NaP) Na^+ channels, voltage-gated (Ca_V) Ca^{2+} channels, voltage-gated (K_V), leak (K_{Leak}), fast A-type ($K_{A\text{-}type}$), inwardly rectifying (K_{IR}), slowly inactivating (K_{Sl}), and Ca^{2+}-dependent (K_{Ca}) K^+ channels, and finally a Ca^{2+}-pump/exchanger expelling Ca^{2+} ions from the intracellular compartment (Tatsuki et al., 2016) (Figure 1A). For all of these conductances, we adapted the full parameter set from the original Averaged-Neuron model published by Tatsuki et al. (2016). The original Averaged-Neuron model did not consider changes in extracellular ion concentrations as variables but as fixed constants. We extended the Averaged-Neuron model by introducing extracellular and intracellular ion concentration dependencies by implementing Nernst and Goldman-Hodgkin-Katz equations for calculating reversal potentials for all receptors and channels. We also added a $[Mg^{2+}]_o$ dependency for the NMDA receptor that satisfies the criteria that higher $[Mg^{2+}]_o$ leads to lower current (Mayer et al., 1984; Nowak et al., 1984) (Figure 1A). A detailed formal description of the extended Averaged-Neuron model is provided in the STAR Methods and the code is available on GitHub (https://github.com/Neurune/IonsAndChaos).

First, we simulated V_m in time with an initial extracellular ion concentration parameter set of $[K^+]_o$ = 3.5 mM, $[Ca^{2+}]_o$ = 1.5 mM, and $[Mg^{2+}]_o$ = 0.8 mM. The remaining intra- and extracellular ion concentrations were maintained constant, and values were based on previous *in vivo* and *in vitro* experimental measurements (Diarra et al., 2001; Dietzel et al., 1982; Markova et al., 2008; Raimondo et al., 2013; Rose and Konnerth, 2001; Rose and Ransom, 1996). We found that the model remarkably closely recapitulated previous recordings obtained from neurons during slow-wave sleep (simply referred to as sleep from here on) (Steriade et al., 2001) (Figure 1B). The extended Averaged-Neuron model generated wave forms of slow oscillatory patterns, consisting of alternating periods of V_m depolarization and spiking (upstates) and V_m hyperpolarization and silence (downstates). This oscillatory pattern was also present in the modeled intracellular Ca^{2+} concentration ($[Ca^{2+}]_i$), with upstates generating a ~8 μM rise in $[Ca^{2+}]_i$ (Figure 1B). The preferential slow V_m oscillations were evident when analyzing frequency components for ten simulations, showing a high prevalence of 1–4 Hz delta power (Figure 1C). The moving SD of the mean V_m (spikes removed) varied between 0.1 and 3 mV (Figure 1D), similar to the seminal recordings obtained by Steriade et al. (2001). Finally, mean V_m showed a clear bimodal distribution, with peaks around −70 and −50 mV, reflecting the equal presence of up- and downstates separated by ~20 mV (Figure 1E).

To assess the validity of our implemented ion concentration dependencies in the extended Averaged-Neuron model, we sought to test the effect of increasing $[K^+]_o$ from 3.5 to 8 to 14 mM. The resting V_m of neurons is mainly determined by K^+-permeable conductances, and V_m is highly sensitive to changes in $[K^+]_o$ (Fröhlich et al., 2008). Thus, we expected drastic V_m changes when pushing $[K^+]_o$ to the biological extremes if our model was valid. When increasing $[K^+]_o$ from 3.5 to 8 mM, we observed a qualitative change in V_m dynamics. The alternating up- and downstates disappeared, and instead V_m was maintained depolarized and the neuron fired continuously at rates of ~100 Hz, giving rise to a tonic elevation in $[Ca^{2+}]_i$ at ~9 μM (Figures 1F and 1G). This finding is in congruence with *in vitro* slice experiments, inducing epileptic seizure activity by increasing $[K^+]_o$ to 7.5 or 8.5 mM in the external media (Jensen and Yaari, 1997; Traynelis and Dingledine, 1988). Further elevating $[K^+]_o$ to 14 mM depolarized V_m even more but also completely abolished action potential firing, releasing the tonic $[Ca^{2+}]_i$ elevation (Figures 1F and 1G). This effect is likely explained by depolarization-induced conductance blockage, where Na_V channels are kept hostage in the inactivated configuration, resulting in the inability of the neuron to fire (De Col et al., 2008; Orkand et al., 1966). This observed effect appears similar to what is seen during *in vivo* cortical spreading depression, where $[K^+]_o$ reaches levels above 12 mM (Enger et al., 2015), leading to annihilation of neural activity in the affected brain area (Grafstein, 1956; Somjen, 2001, 2002, 2004). An example of how V_m dynamics are also modulated by extreme shifts in $[Ca^{2+}]_o$ is provided in Supplemental Information (Figure S1).

Overall, these results demonstrate that the extended Averaged-Neuron model very closely recapitulates cardinal properties of V_m dynamics during sleep and is expectedly sensitive to changes in extracellular ion concentrations.

Shifting from Sleep to Awake Ion Concentrations Induces No Apparent State Transition

It was recently suggested that changes in extracellular ion concentrations ($[K^+]_o$, $[Ca^{2+}]_o$, and $[Mg^{2+}]_o$) control state-dependent activity patterns during sleep and wakefulness, and that ion shifts are sufficient to mediate the transition from sleep to awake (Ding et al., 2016). However, due to the intimate relation between neural activity and ionic changes, establishing causality *in vivo* is non-trivial.

To investigate the effect of ion concentration changes on sleep to awake transitions in the extended Averaged-Neuron model, we used the previously measured extracellular ion concentrations during sleep ($[K^+]_o$ = 3.9 mM, $[Ca^{2+}]_o$ = 1.35 mM, and $[Mg^{2+}]_o$ = 0.8 mM) and awake ($[K^+]_o$ = 4.4 mM, $[Ca^{2+}]_o$ = 1.2 mM, and $[Mg^{2+}]_o$ = 0.7 mM) (Ding et al., 2016) (Figure 2A). With sleep ions, V_m dynamics closely recapitulated sleep with alternating up- and downstates. When we switched to awake ions, no apparent change in V_m dynamics was obvious, except a subtle tendency for more spikes per upstate (Figure 2B). When we analyzed V_m frequency components, we found no significant difference in 1–4 Hz delta power between sleep (21.2 ± 0.24 dB) and awake ions (20.4 ± 0.62 dB) ($p = 0.08$, Student's t test, n = 10 simulations) (Figures 2C and 2D). Also mean V_m SD, a frequently used indicator for neuronal state (McGinley et al., 2015a; Steriade et al., 2001; Yamashita et al.,

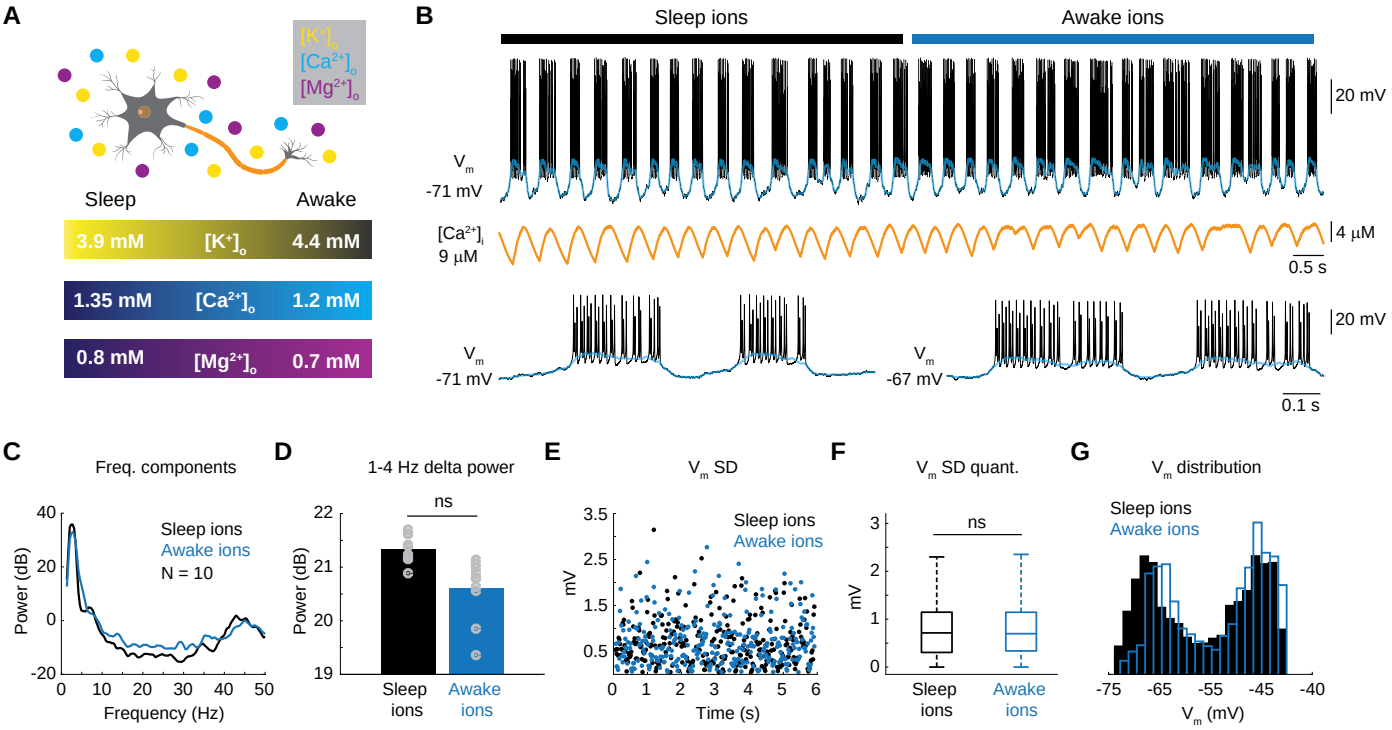

Figure 2. Shifting from Sleep to Awake Extracellular Ion Concentrations Does Not Induce State Change

(A) Schematic diagram of extracellular ion concentrations used. Sleep: $[K^+]_o$ = 3.9 mM, $[Ca^{2+}]_o$ = 1.35 mM, and $[Mg^{2+}]_o$ = 0.8 mM. Awake: $[K^+]_o$ = 4.4 mM, $[Ca^{2+}]_o$ = 1.2 mM, and $[Mg^{2+}]_o$ = 0.7 mM.

(B) Representative membrane potential (V_m) firing pattern and intracellular Ca^{2+} concentration ($[Ca^{2+}]_i$) with sleep and awake ion composition. Below is an expansion of V_m dynamics.

(C) V_m frequency spectra for sleep and awake ion composition.

(D) 1–4 Hz delta power for sleep and awake ion composition (non-significant [ns] p = 0.08, Student's t test, n = 10 simulations).

(E) SD of mean V_m (spikes removed) with sleep or awake ion composition.

(F) Boxplot for SD of mean V_m with sleep or awake ion composition. Center line is the median, box limits are 25th and 75th percentiles, and whiskers are maximum and minimum values (ns p = 0.089, Student's t test, n = 10 simulations).

(G) Mean V_m distribution with sleep or awake ion composition.

See also Figure S2.

2013), was similar for sleep (0.77 ± 0.62 mV) and awake ions (0.78 ± 0.58 mV) (p = 0.089, Student's t test, n = 10 simulations) (Figures 2E and 2F). Finally, mean V_m showed a clear bimodal distribution with both sleep and awake ion concentrations (Figure 2G).

Taken together, shifting the extracellular concentrations of K^+, Ca^{2+}, and Mg^{2+} with the same magnitude as measured *in vivo* during sleep and awake failed to induce a cortical state transition, suggesting that ion changes of this magnitude alone are not sufficient to produce a transition from sleep to awake. To exclude that these findings were not merely a special case of one parameter set, we evaluated the effect of switching from sleep to awake ion concentrations, but with varying values of model parameters. These analyses showed the same overall result, as with the initial parameter set (Figure S2) thus substantiating our initial conclusion.

Partially Inhibiting the K_{Ca} Channel Induces Sleep to Awake State Transition

Early seminal and more recent work has implicated the K_{Ca} channel in V_m activity patterns observed during sleep and wakefulness (Steriade et al., 1993; Tatsuki et al., 2016). Following a rise in $[Ca^{2+}]_i$ this channel activates and generates an outward K^+ current, hyperpolarizing V_m. In this way, the K_{Ca} channel was proposed as a key component for generating downstates during sleep (Steriade et al., 1993). In contrast, with elevated levels of neuromodulators (acetylcholine, norepinephrine, serotonin, and histamine) as seen during wakefulness (Lee and Dan, 2012), the K_{Ca} channel is partially inhibited (McCormick and Williamson, 1989; McCormick et al., 1993), and this could potentially induce the sleep to awake transition by preventing the occurrence of downstates (Steriade et al., 1993).

During our sleep V_m simulations, we observed a close relation between mean V_m and $[Ca^{2+}]_i$ oscillations with a 0.12 s lag for $[Ca^{2+}]_i$ (Figure 3A). This led us to analyze the relation between $[Ca^{2+}]_i$ and the K_{Ca} current. Not surprisingly, we found a −0.013 s lag between $[Ca^{2+}]_i$ and K_{Ca} currents (Figure 3B). The largest K_{Ca} currents occurred when mean V_m was most depolarized, and V_m rapidly hyperpolarized following peak K_{Ca} currents (Figure 3C), suggesting that K_{Ca}-mediated outward currents could be key for generating downstates.

To assess the role of the K_{Ca} channel and to mimic the elevation in neuromodulator levels seen during wakefulness (Lee and Dan, 2012; McCormick and Williamson, 1989), we reduced the

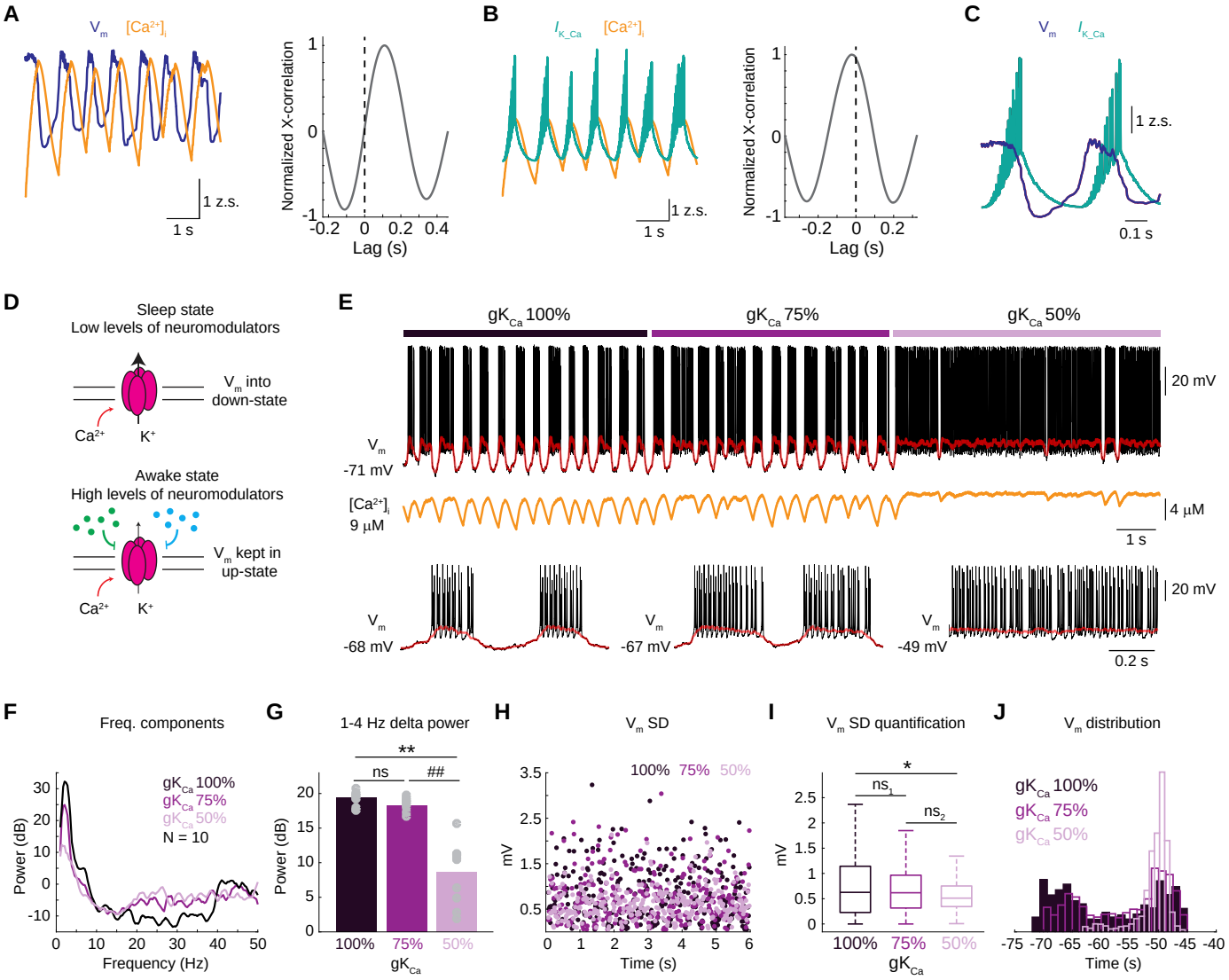

Figure 3. Partially Inhibiting Ca^{2+}-Activated K^+ Channel Can Induce Sleep to Awake State Change

(A) Left: Relation between membrane potential (V_m) and intracellular Ca^{2+} concentration ($[Ca^{2+}]_i$). Right: Cross-correlation between V_m and $[Ca^{2+}]_i$.

(B) Left: Relation between Ca^{2+}-activated K^+ channel current (I_{K_Ca}) and $[Ca^{2+}]_i$. Right: Cross-correlation between I_{K_Ca} and $[Ca^{2+}]_i$.

(C) Relation between V_m and I_{K_Ca}.

(D) Schematic diagram of speculated sleep and awake state and neuromodulator-mediated decrease of Ca^{2+}-activated K^+ channel conductance (gK_{Ca}).

(E) Representative V_m firing pattern and $[Ca^{2+}]_i$ with 100%, 75%, or 50% gK_{Ca}. Below is an expansion of V_m dynamics.

(F) V_m frequency spectra for 100%, 75%, and 50% gK_{Ca}.

(G) 1–4 Hz delta power for 100%, 75%, and 50% gK_{Ca} (non-significant [ns], p = 0.383, **p = 0.0069, ##p = 0.0083, one-way ANOVA, n = 10 simulations).

(H) SD of mean V_m (spikes removed) with 100%, 75%, and 50% gK_{Ca}.

(I) Boxplot for SD of mean V_m with 100%, 75%, and 50% gK_{Ca}. Center line is the median, box limits are 25th and 75th percentiles, and whiskers are maximum and minimum values (ns_1 p = 0.875, *p = 0.0262, ns_2 p = 0.065, one-way ANOVA, n = 10 simulations).

(J) Mean V_m distribution for 100%, 75%, and 50% gK_{Ca}.

See also Figure S3.

conductance of the K_{Ca} channel (gK_{Ca}) over time (100% = 2.3 mS/cm^2, 75% = 1.73 mS/cm^2, and 50% = 1.15 mS/cm^2). This simulation was performed with the sleep ion concentrations being maintained throughout. When reducing gK_{Ca} to 75%, we observed only a tendency toward a state change, with longer upstates and fewer downstates, whereas reducing gK_{Ca} to 50% produced a clear state change, almost completely preventing V_m from entering downstates, thereby producing tonic firing (Figure 3E). This qualitative interpretation was supported when quantified. Decreasing gK_{Ca} to 75% non-significantly reduced 1–4 Hz delta power (p = 0.383, one-way ANOVA, n = 10 simulations), whereas 50% significantly reduced delta power (p = 0.0069, one-way ANOVA, n = 10 simulations). Mean V_m SD was similar between 100% (0.74 ± 0.55 mV) and 75% gK_{Ca} (0.67 ± 0.46 mV) (p = 0.875, one-way ANOVA, n = 10 simulations), but significantly reduced with 50% gK_{Ca} (0.59 ± 0.32 mV) (p = 0.0262, one-way ANOVA, n = 10 simulations) (Figures 3H and 3I). Finally, mean V_m distributions for 100% and 75% gK_{Ca} appeared bimodal, whereas the 50% gK_{Ca} distribution was uni-modal (Figure 3J).

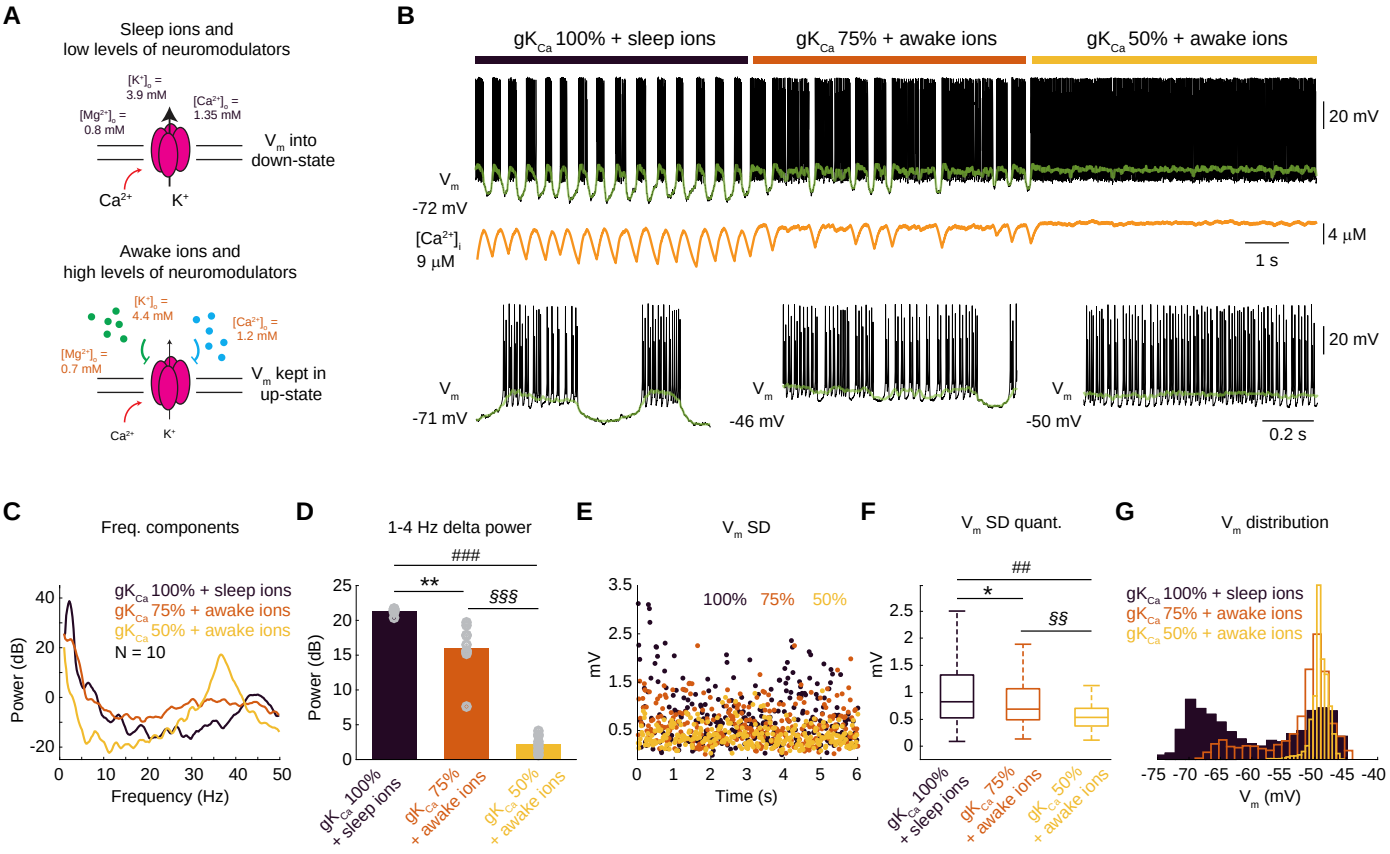

Figure 4. Awake Ion Concentrations Lowers the Threshold for Sleep to Awake State Change

(A) Schematic diagram of speculated interaction between extracellular ion concentrations, neuromodulators, and Ca^{2+}-activated K^+ channel conductance (gK_{Ca}) during sleep and wakefulness.

(B) Representative membrane potential (V_m) firing pattern and intracellular Ca^{2+} concentration ($[Ca^{2+}]_i$) with 100% gK_{Ca} + sleep ions ($[K^+]_o$ = 3.9 mM, $[Ca^{2+}]_o$ = 1.35 mM, and $[Mg^{2+}]_o$ = 0.8 mM), 75% gK_{Ca} + awake ions ($[K^+]_o$ = 4.4 mM, $[Ca^{2+}]_o$ = 1.2 mM, and $[Mg^{2+}]_o$ = 0.7 mM) or 50% gK_{Ca} + awake ions. Below is an expansion of V_m dynamics.

(C) V_m frequency spectra for 100% gK_{Ca} + sleep ions, 75% gK_{Ca} + awake ions, or 50% gK_{Ca} + awake ions.

(D) 1–4 Hz delta power for 100% gK_{Ca} + sleep ions, 75% gK_{Ca} + awake ions, or 50% gK_{Ca} + awake ions (**p = 0.026, $^{###}$p < 0.0001, §§§p < 0.0001, one-way ANOVA, n = 10 simulations).

(E) SD of mean V_m (spikes removed) for 100% gK_{Ca} + sleep ions, 75% gK_{Ca} + awake ions, or 50% gK_{Ca} + awake ions.

(F) Boxplot for SD of mean V_m for 100% gK_{Ca} + sleep ions, 75% gK_{Ca} + awake ions, or 50% gK_{Ca} + awake ions. Center line is the median, box limits are 25th and 75th percentiles, and whiskers are maximum and minimum values (*p = 0.011, $^{##}$p = 0.0062, §§p = 0.0018, one-way ANOVA, n = 10 simulations).

(G) Mean V_m distribution for 100% gK_{Ca} + sleep ions, 75% gK_{Ca} + awake ions, or 50% gK_{Ca} + awake ions.

See also Figure S4.

To illuminate if changing gK_{Ca} is the most efficient way to induce the awake state, we performed a bifurcation analysis (i.e., gradual change in parameter values). This revealed that the parameter of gK_{Ca} was the most important parameter for creating state change in firing dynamics (Figure S3). Changing the conductance of almost all other channels had very little effect, except for the parameter gCa_V, which also had the potential to create a transition, but this was still less potent than gK_{Ca} (Figure S3).

Overall, these results demonstrate that the K_{Ca} channel most likely plays a dominant role in sleep V_m activity patterns, and inhibiting this channel, assumedly via increased levels of neuromodulators, is sufficient to induce a transition to the awake state. However, decreasing the conductance of this channel by 25% was not sufficient to invoke a full state transition, suggesting a threshold level for when the state is shifted from sleep to wakefulness.

Awake Ion Concentrations Lower the Threshold for Sleep to Awake State Transition

Although changing extracellular ions from sleep to awake concentrations was not in itself sufficient to induce a state transition (Figures 2 and S2), we speculate if awake ions could lower the threshold for invoking the K_{Ca} channel-dependent state change and in this way be permissive and modulatory on state changes (Figure 4A).

To investigate this, we changed the extracellular ions from sleep to awake concentrations while reducing gK_{Ca} to 75% and 50% as in the previous section (Figure 3). In contrast to Figure 3, when we reduced gK_{Ca} to 75% in the presence of awake ions, we observed a state transition with V_m kept in the upstate for long periods and with few downstates (Figure 4B). As before, when reducing gK_{Ca} to 50%, the state change was pronounced, with V_m tonically depolarized and the neuron continuously firing (Figure 4B). We now found a significant reduction in 1–4 Hz delta

power with the combination of 75% gK_{Ca} and awake ions ($p = 0.026$, one-way ANOVA, n = 10 simulations), as well as with 50% gK_{Ca} and awake ions ($p < 0.0001$, one-way ANOVA, n = 10 stimulations) (Figures 4C and 4D). The prevalence of delta power was significantly smaller with 50% gK_{Ca} compared with 75% gK_{Ca} ($p < 0.0001$, one-way ANOVA, n = 10 simulation) (Figure 4D), likely reflecting that wakefulness comprises two states (i.e., quiet awake and active awake) (Crochet and Petersen, 2006; McGinley et al., 2015b). Further supporting a permissive effect of awake ions on the sleep to awake transition was the significant decrease in mean V_m SD from 100% gK_{Ca} and sleep ions (0.81 ± 0.15 mV) to 75% K_{Ca} and awake ions (0.64 ± 0.13 mV) ($p = 0.011$, one-way ANOVA, n = 10 simulations). Reducing gK_{Ca} to 50% with awake ions caused a significant decrease in mean V_m SD to (0.51 ± 0.07 mV) ($p = 0.0062$, one-way ANOVA, n = 10 simulations), significantly smaller than with 75% gK_{Ca} ($p = 0.0018$, one-way ANOVA, n = 10 simulations), again pointing to multiple awake states (Figure 4F). Finally, the mean V_m distribution was shifted toward uni-modality with 75% gK_{Ca} and awake ions, and this was even more apparent with 50% gK_{Ca} and awake ions (Figure 4G).

Taken together, these data suggest that the awake ion concentrations reduce the threshold for invoking a sleep to awake state transition, and thereby are permissive on this state change. We found that $[K^+]_o$ is the most potent mediator of this ion-concentration-mediated effect, but the combined concurrent shift in all three ion species triggers the greatest sleep to awake state change (Figure S4). What is more, the results point to and support current *in vivo* evidence that the awake state comprises multiple sub-states, with differences in delta oscillations and mean V_m dynamics.

Subtle Change in Extracellular Ion Concentrations Shifts the State from Quiet Awake to Active Awake

After demonstrating that the awake ion concentrations are permissive for shifting V_m dynamics from sleep to awake (Figures 4 and S4), we next investigated the two apparent awake states in greater detail, and in particular the role of extracellular ion concentrations on the transition from the quiet awake to active awake state. For this, we speculate that an arousal-related "hyper-awake" ion composition (in addition to the sleep and awake ion compositions) might exist and could be involved in shifting V_m into the active awake state (Bennett et al., 2013; Crochet and Petersen, 2006; Gentet et al., 2010; McGinley et al., 2015a; Polack et al., 2013; Reimer et al., 2014; Zagha et al., 2013). As an estimate, we changed extracellular ions with the same magnitude as observed between sleep and awake for formulating the hypothesized hyper-awake ion concentrations ($[K^+]_o$ = 4.9 mM, $[Ca^{2+}]_o$ = 1.05 mM, and $[Mg^{2+}]_o$ = 0.6 mM) (Figure 4A).

We initially simulated the quiet awake state (75% gK_{Ca} and awake ions) and then selectively shifted the extracellular ion concentrations to hyper-awake ions while maintaining gK_{Ca} at 75% (Figures 5A and 5B). We observed that with awake ions, V_m alternated between long periods of firing (upstate) and occasional silent downstates (Figure 5B), similar to what is described in quiet awake rodents (Crochet and Petersen, 2006; McGinley et al., 2015a; Yamashita et al., 2013). When we shifted to hyper-awake ion concentrations, we observed an annihilation of downstates, and V_m was maintained in the depolarized upstate with continuous firing as a result (Figure 5B). We next analyzed these two V_m states further. We found that with hyper-awake ions, 1–4 Hz delta power significantly decreased ($p = 0.002$, Student's t test, n = 10 simulations) and 25–45 Hz gamma power significantly increased ($p = 0.0023$, Student's t test, n = 10 simulations) (Figures 5C–5E). This result is similar to what has been observed when rodents transition from the quiet to the active awake state (Niell and Stryker, 2010; Reimer et al., 2014; Vinck et al., 2015). With hyper-awake ions, mean V_m was significantly more depolarized than with awake ions (−49.38 ± 0.11 mV and −52.62 ± 0.23 mV; $p = 0.002$, Student's t test, n = 10 simulations) (Figure 5F), keeping V_m closer to the firing threshold. Finally, mean V_m distribution was shifted toward the depolarized upstate with hyper-awake ions, representing the lack of downstates (Figure 5G). All of these results are in congruence with *in vivo* recordings obtained in awake rodents, where the active awake state is characterized by a depolarized V_m and a lack of downstates (Crochet and Petersen, 2006; McGinley et al., 2015a; Yamashita et al., 2013).

Taken together, these results demonstrate that subtle changes in extracellular ion concentrations are sufficient for shifting V_m dynamics from the quiet awake state to the active awake state. Shifting to the hypothesized hyper-awake ion concentrations recapitulated key properties of the active awake state V_m dynamics, including increased gamma oscillations and depolarized V_m. Further analysis revealed that shifting $[K^+]_o$ alone was sufficient for invoking this state transition, but the combined effect of shifting all three ion species was greater (Figure S5), suggesting a biological importance of concerted extracellular ion changes. We advocate that the existence of such hyper-awake ion concentrations should be investigated in future *in vivo* experiments, as well as its ability to causally invoke the proposed awake state changes.

Transitions between Brain States Are Governed by Chaotic Dynamics

After finding that awake ion concentrations are permissive for shifting the state from sleep awake (Figure 4), and that hyper-awake ion concentrations can invoke the transition from quiet to active awake (Figure 5), we next investigated the state-dependent properties of V_m dynamics in more analytical and physical terms, as we altered extracellular ion concentrations.

First, we performed a detailed simulation of the sleep state, where in the deterministic system we found spikes and V_m oscillations to be stable and periodic in the sense that the pattern was self-repeating, and small perturbations in the initial conditions did not make the trajectories diverge (Figure 6A). This therefore had to be a closed trajectory with several small loops that occur when the neuron fires, which is best visualized in a three-dimensional phase space spanned by three variables (V_m, Ca^{2+}, and n_K) (Figure 6B). This means that V_m dynamics in the sleep state is well defined by regular and stable oscillations, exactly as what one would expect from a synchronous system.

Next, we considered which ion currents are most important for changing the state from sleep to awake. From what was observed in the awake state (Figures 3 and 4), we characterize the transition in terms of (1) the rate at which a silent downstate period is initiated, (2) the mean time duration of a spiking upstate period, and

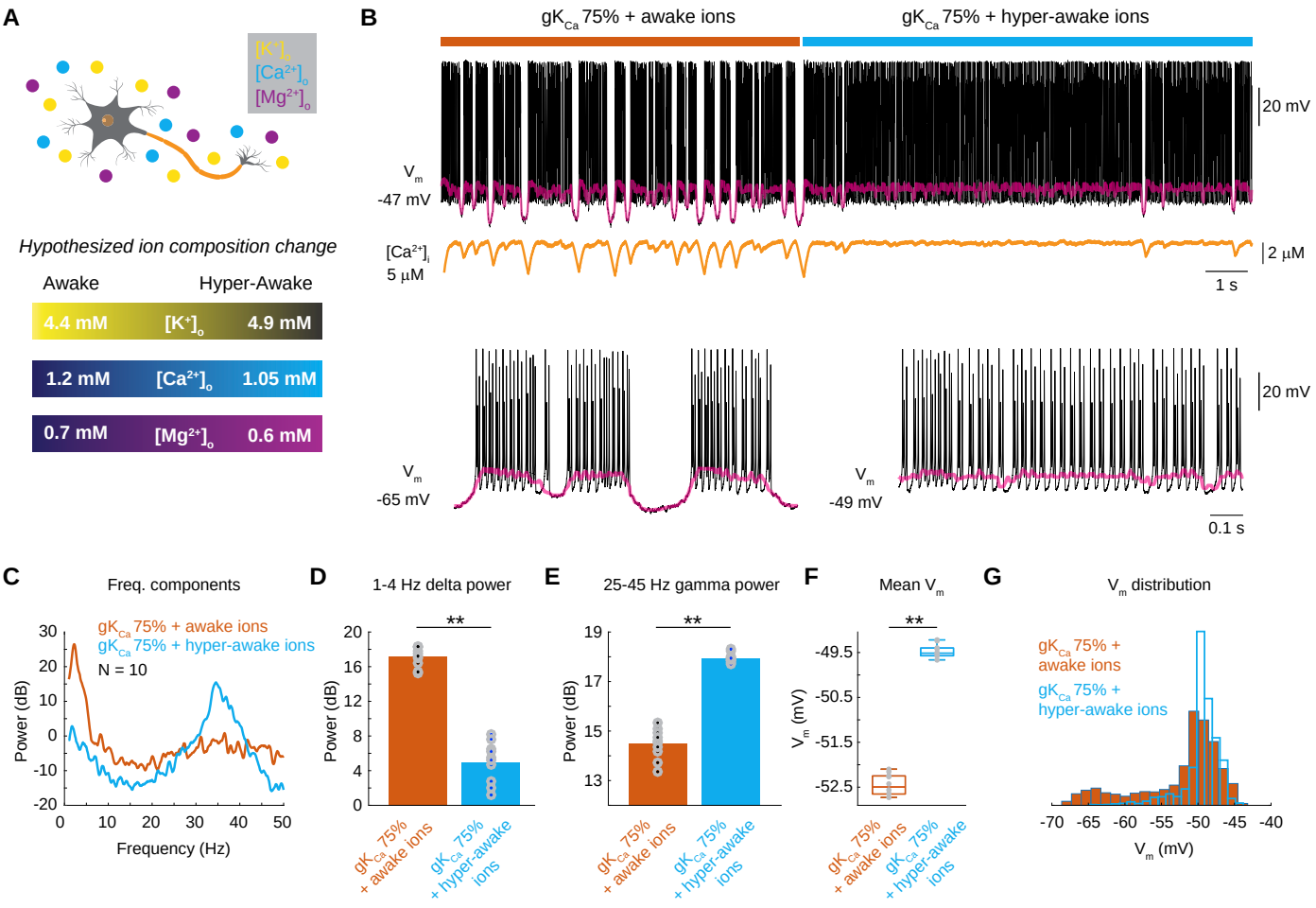

Figure 5. Transition between Two Awake States Can Be Controlled by Extracellular Ion Concentrations

(A) Schematic diagram of hypothesized shift in extracellular ion concentration from awake to hyper-awake. Awake: $[K^+]_o$ = 4.4 mM, $[Ca^{2+}]_o$ = 1.2 mM, and $[Mg^{2+}]_o$ = 0.7 mM. Hyper-awake: $[K^+]_o$ = 4.9 mM, $[Ca^{2+}]_o$ = 1.05 mM, and $[Mg^{2+}]_o$ = 0.6 mM.

(B) Representative membrane potential (V_m), firing pattern, and intracellular Ca^{2+} concentration ($[Ca^{2+}]_i$) with 75% gK_{Ca} + awake ions and 75% gK_{Ca} + hyper-awake ions. Below is an expansion of V_m dynamics.

(C) V_m frequency spectra for 75% gK_{Ca} + awake ions and 75% gK_{Ca} + hyper-awake ions.

(D) 1–4 Hz delta power for 75% gK_{Ca} + awake ions and 75% gK_{Ca} + hyper-awake ions (**p = 0.002, Student's t test, n = 10 simulations).

(E) 25–45 Hz gamma power for 75% gK_{Ca} + awake ions and 75% gK_{Ca} + hyper-awake ions (**p = 0.0023, Student's t test, n = 10 simulations).

(F) Boxplot for mean V_m for 75% gK_{Ca} + awake ions and 75% gK_{Ca} + hyper-awake ions. Center line is the median, box limits are 25th and 75th percentiles, and whiskers are maximum and minimum values (**p = 0.002, Student's t test, n = 10 simulations).

(G) Mean V_m distribution for 75% gK_{Ca} + awake ions and 75% gK_{Ca} + hyper-awake ions.

See also Figure S5.

(3) the SD of this measure. These numbers combined describe much of the change in V_m dynamics that happens between the sleep and awake state. By affecting only one of the currents at a time by the change in extracellular ion concentrations from sleep to awake, we found the largest ion-concentration-mediated effect was produced on the Ca_V-mediated current (Figure 6C). This was even better observed if we combined the sleep to awake ion-mediated changes in Ca_V current with a small perturbation in gK_{Ca} (Figure 6C). Thus, here we found that affecting only the Ca_V channel by changes in sleep to awake ion concentration can account for much of the irregularities of the awake state, and that a similar ion-mediated effect can occur for the extrinsic AMPA receptor, and this induces a big step toward the awake state (Figure 6C). We also show that decreasing gK_{Ca} is the most important factor in moving V_m dynamics toward the awake state, but that changes in extracellular ion concentrations amplify this effect markedly (Figure 6C).

As observed in the sections above, transition from the sleep to the awake state could be invoked by a 25% reduction in gK_{Ca} and a concomitant change to awake ion concentrations (Figure 4). With the combination of 75% gK_{Ca} and awake ions, V_m dynamics are more irregular and significantly long periods of upstates and spiking can occur before a silent downstate is recovered (Figure 4B). This suggests that V_m dynamics in the awake state is chaotic, meaning that the phase space has a strange attractor. Deterministic chaos is defined by the fact that two initial conditions, being infinitesimally perturbed, will have diverging trajectories as time evolves, and that one cycle will never repeat itself and therefore no closed cycles exist on a strange attractor (Lorenz, 1963) (Box 1). We tested this by

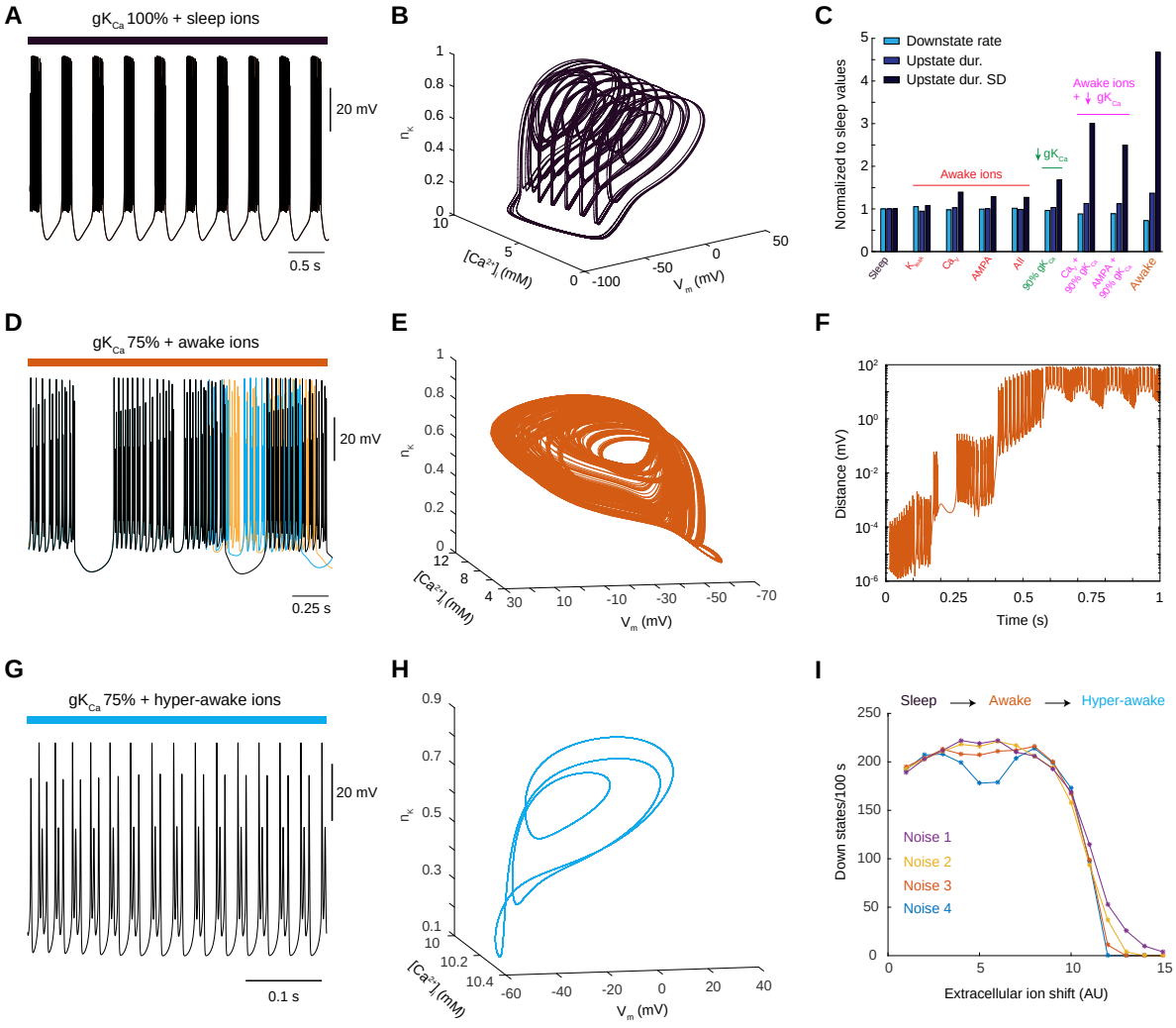

Figure 6. Transition from Sleep to Wakefulness Is Governed by Chaotic Dynamics

(A) Representative membrane potential (V_m) firing pattern in the sleep state with 100% gK_{Ca} and sleep ion composition ($[K^+]_o$ = 3.9 mM, $[Ca^{2+}]_o$ = 1.35 mM, and $[Mg^{2+}]_o$ = 0.8 mM).

(B) Phase space plot showing the trajectory in the sleep state.

(C) Measures for the effect of different ion channel-mediated currents on V_m dynamics. Light blue is the average rate of initiating a silent downstate periods. Blue is the average duration of the spiky upstate periods. Dark blue is the SD in the duration of upstate periods. All measures are normalized to the sleep state.

(D) Representative V_m firing patterns with 75% gK_{Ca}, awake ion composition ($[K^+]_o$ = 4.4 mM, $[Ca^{2+}]_o$ = 1.2 mM, and $[Mg^{2+}]_o$ = 0.7 mM) and 1 mV perturbations showing the development of different trajectories.

(E) Phase space plot showing the trajectory in the awake state with 75% gK_{Ca} and awake ion composition.

(F) Difference between two V_m trajectories in the awake state with 75% gK_{Ca} and awake ion composition.

(G) Representative V_m firing pattern in the awake state with 75% gK_{Ca} and hyper-awake ion composition ($[K^+]_o$ = 4.9 mM, $[Ca^{2+}]_o$ = 1.05 mM, and $[Mg^{2+}]_o$ = 0.6 mM).

(H) Phase space plot showing the trajectory in the awake state with 75% gK_{Ca} and hyper-awake ion composition.

(I) Number of silent periods for a period of 100 s as the values of $[K^+]_o$, $[Ca^{2+}]_o$, and $[Mg^{2+}]_o$ are perturbed linearly from values for the sleep state to values of the active awake state. On the x axis, 1 corresponds to the sleep state and 9 corresponds to the awake state.

perturbing the initial concentration of $[Ca^{2+}]_i$ by only 1 pM (10^{-12}), and even though V_m trajectories are very similar in the beginning, after some seconds they are completely different (Figure 6D). Another way of visualizing the chaotic nature of the awake state V_m dynamics can be seen in Figure 6E, where the trajectory is shown in three dimensions. Here, it seems that the trajectory never repeats and that the dynamics are irregular compared with the regular oscillations in the sleep state. To test if this had the signature of chaos, we calculated the difference in all dimensions between two trajectories and found that they diverge in a complex manner that seems however to be on top of a general exponential diverging, which is what we would expect from a chaotic system (Lorenz, 1963) (Figure 6F).

As shown in previous sections, the sleep to awake state transition that we have now characterized is likely not the end of the story, and an additional active awake state exists (Crochet and Petersen, 2006; McGinley et al., 2015b) (Figures 4 and 5). Furthermore, we hypothesize that a parameter set of hyper-awake ion concentrations exist (Figure 5A). As in Figure 5, we observed that with hyper-awake ions, V_m dynamics is a

Please cite this article in press as: Rasmussen et al., Chaotic Dynamics Mediate Brain State Transitions, Driven by Changes in Extracellular Ion Concentrations, Cell Systems (2017), https://doi.org/10.1016/j.cels.2017.11.011

Box 1. What Is Chaos?

Chaos is a well-defined mathematical concept that occurs in non-linear dynamical systems with three or more dimensions. It is defined by the property that two initial conditions infinitesimally apart exhibit exponentially diverging trajectories as time evolves. Such systems are deterministic in the sense that if one knows the initial state of the system exactly, then the trajectory will be the same every time it is initiated in that state. Chaos is thus a mathematical definition that should not be confused with the use of chaos in normal language. Furthermore, it is important to distinguish chaos from randomness or stochasticity in general. Randomness normally refers to non-deterministic responses due to stochastic noise, which in principle appears in any system of nature. The effects of stochasticity can sometimes be negligible but may, in some cases, give rise to a different dynamics than seen in a deterministic system. Examples of this can be sustained oscillations or multi-stability. Since systems always exhibit some uncertainty, the initial conditions in a system are never completely known and therefore chaotic systems, from a practical point of view, might appear random since it is impossible to predict the dynamical outcome.

continuously spiking process with no occurrence of silent downstates (Figure 6G), which likely correspond to an aroused and alert active awake state (Crochet and Petersen, 2006; Polack et al., 2013). We find that this state is not chaotic, but rather a well-defined, high-frequency three cycle (Figure 6H). This means that the initial transition from the sleep state can be regarded as a mediator between two robust states (sleep and active awake) defined by closed cycles. We consider it of great importance that the dynamics of V_m changes from sleep to the awake state and even further into an active awake state, using effects of chaotic dynamics, and how these changes are sensitive to subtle changes in extracellular ion concentrations.

Next, we performed the V_m simulation while applying white noise, which in the awake state, with awake ions, gives rise to V_m dynamics as shown in Figure 6D. Since stochasticity is present in every system and intrinsic biological noise is assumed to appear around the ion channels, noise is a very import element in this region where multi-stable solutions seem to arise. Since the most striking difference between the sleep and awake states is the occurrence/lack of silent downstates, we used the number of silent periods as a measure to characterize the gradual transition from sleep to the active awake state. We investigated this for four different noise levels while we linearly perturbed the values of $[K^+]_o$, $[Ca^{2+}]_o$, and $[Mg^{2+}]_o$ from the sleep to the hyper-awake concentrations. As can be observed from Figure 6I, the complete state transition in this measure is a continuous process for the noise levels tested, and shifting extracellular ion concentrations is sufficient to fully transition from the quiet awake to the active awake state.

In summary, we found that the transition from sleep to full wakefulness is modulated by changes in extracellular ion concentrations. Moreover, we show that if extracellular ions change, for instance if $[K^+]_o$ is either below or above 3.9 and 4.5 mM, respectively, the dynamics of the system is determined by a stable limit cycle with several smaller loops included, whereas for $[K^+]_o$ within the range of 3.9 and 4.5 mM, the system is chaotic, which can ensure a smooth and robust transition between the sleep state and the active awake state.

DISCUSSION

Neuronal states powerfully influence sensory processing and perceptions (Harris and Thiele, 2011; Lee and Dan, 2012; Lee et al., 2014; McGinley et al., 2015a; Vinck et al., 2015). Here, we have shown that the concentrations of extracellular ions influence K_{Ca} channel-mediated sleep to awake transitions and can themselves drive the switch from quiet awake to active awake. We demonstrate that the state change from sleep to awake is characterized by the transition from stable to chaotic dynamics, and argue that chaotic dynamics mediates a smooth transition between the quiet awake and active awake state, remarkably robust to intrinsic noise.

Previous studies have causally implicated ion concentrations in sleep to awake transitions (Ding et al., 2016). However, due to the intimate relation between neural activity and ionic changes, causality is difficult to establish *in vivo*. In our model, exclusively shifting ion concentrations by the same magnitude as measured *in vivo* was insufficient to cause a complete sleep to awake state transition (Figures 2, 6C, and S2), suggesting that other parameters need to change in time in order to transition the neuron into to the awake state, and that ion concentration changes are not causal for this state transition. This might seem as an advantageous built-in gate mechanism, since extracellular ion concentrations are affected by even slight changes in neuronal firing (Hounsgaard and Nicholson, 1983; Lux, 1974; Lux and Neher, 1973; Nicholson et al., 1977), and global brain states should be robust to such small ion fluctuations, not causing the system to constantly cycle between sleep and awake.

We determined that decreasing the conductance of the K_{Ca} channel is a powerful way to induce the sleep to awake state change (Figures 3, 6C, and S3), in congruence with previous work implicating this channel as a prime mechanism for V_m downstates (McCormick and Williamson, 1989; McCormick et al., 1993; Steriade et al., 1993; Tatsuki et al., 2016). Shifting to the awake ion concentrations was permissive to decreasing the conductance of the K_{Ca} channel (Figures 4, 6C, and S4), advocating that subtle changes in extracellular ion concentrations can lower the threshold for how much ion channel modulation is required to shift the state. Changing the global environment surrounding neurons, in addition to modulating selective intrinsic ion channels, might be a simple, yet powerful, way to shift the state of entire brain-wide neuronal networks and ultimately for changing the behavioral state.

In more abstract terms, transitions between states in living organisms are fundamental for the functions and complexity of that organism. However, it is often speculated that very rapid state changes might be harmful for cells, since they might not be able to adapt properly and fast enough to the new dynamics. In this regard, the state transition described here for neuronal V_m dynamics has the beneficial property that it represents a gradual

and smooth change between the two stereotypical behavioral states, sleep and wakefulness. Furthermore, the chaotic nature of the phase space even guarantees the smoothness for a range of different intrinsic noise levels, which ensures that neurons can transition between states in a controlled and noise-robust manner when this is needed and appropriate.

It is increasingly appreciated that the awake state is comprised of at least two sub-states, namely quiet awake and active awake, related to the level of arousal and motor behavior (Bennett et al., 2013; Crochet and Petersen, 2006; Gentet et al., 2010; McGinley et al., 2015a; Polack et al., 2013; Reimer et al., 2014; Zagha et al., 2013). Rodent studies have suggested that the ongoing awake state shapes how the brain processes incoming sensory inputs. For example, the gain of visual-evoked responses in the visual cortex is increased when neurons are in the active awake state, whereas auditory responses in the auditory cortex are suppressed (Bennett et al., 2013; McGinley et al., 2015a; Polack et al., 2013; Schneider et al., 2014). This indicates that the brain state powerfully and differentially scales what sensory modalities are up- and downregulated at a given moment in time for optimizing sensory processing and neural computations, making it important to understand at the mechanistic level what determines brain states and the transition between them.

Here, we hypothesized that in addition to sleep and awake extracellular ion concentrations (Ding et al., 2016), a hyper-awake ion composition might exist (Figures 5, 6, and S5). When K_{Ca} was kept partially inhibited (75% gK_{Ca}), shifting from the awake to the hyper-awake ion concentrations produced a state change similar to what is observed when rodents transition from quiet to active (Crochet and Petersen, 2006; Yamashita et al., 2013) (Figures 5, 6, and S5). This ion-mediated state change was characterized by a decrease in delta power, an increase in gamma power, V_m depolarization, and a uni-modal V_m distribution (Figure 5); similar to what has been observed *in vivo* with intracellular recordings from cortical neurons in behaving rodents. We predict that subtle concerted changes in extracellular ion concentrations could be a key mechanism for the rapid and often-occurring state shifts in the awake brain, allowing sensory processing and neural computations to be rapidly modified based on the different situational demands. Whether our hypothesized shifts in extracellular ion concentrations do occur in the awake brain during active behavior and states of elevated arousal, as well as whether this ionic shift is primary or secondary to neural activity, will be interesting and important to resolve in future experiments.

We consider the frequency and length of the silent downstate periods a key signature defining the different dynamics in the two awake states (Figure 6I). It can be argued that in the active awake state, V_m is sustained depolarized and only high-frequency spikes occur, and one might entertain the speculative hypothesis that this is required for rapid responses to incoming barrages of sensory stimuli and for decision making. In this case, one would ideally avoid the hyperpolarized silent downstates and in general slow oscillations in the V_m. From a dynamical systems point of view, this means that the trajectory should not visit a large part of the phase space. Since this is the case for a chaotic system, the fact that the chaotic dynamics disappears in the active awake state can be regarded as a beneficial mechanism that ensures the occurrence of only high-frequency spikes and maintains V_m close to the firing threshold, keeping the neuron in a state for optimal responsiveness to sensory inputs from the periphery. We note that from a theoretical point of view, it is possible to imagine a stable limit cycle that can guarantee a smooth transition. In this picture, the temporal period between downstates gets shorter and shorter as the parameters change in the quiet awake state, for it to completely disappear in the end in the hyper-awake state. However, we believe there are several intriguing elements in a chaotic transition to the awake state in this neuronal state transition. Firstly, since not only one, but several, parameters are changed in the sleep to awake state transition, chaotic dynamics is a clever way for the system to make a path-independent transition between the two states. Due to the never-repeating trajectories, the system does not change significantly if, for example, the changes in $[Ca^{2+}]_o$ occur before $[K^+]_o$ or vice versa. This would normally not be the case for a stable limit cycle, and thus the chaotic transition makes the transition to the awake state change more robust. Secondly, we believe that chaotic dynamics is an important property of neurons in the awake state since one would expect that neurons in this state need the capacity to create a variety of different combinatorial outputs on a population level. If the neuronal dynamics in the awake state were purely stable limit cycles differing in period, small differences in incoming inputs would lead to very small differences in output firing, and thus information encoding. However, since they are governed by chaotic dynamics, the sensitivity to the always existing small perturbations that accompany external stimulation, can lead to a much more complex variety of outcomes that are likely highly important and necessary for higher-order neuronal computations. Thirdly, it is intriguing to imagine that since all neurons are governed by the dynamics of a stable limit cycle in the sleep state, they have the potential to synchronize their firing outputs through their common oscillations. Now, perturbing the system could change the period of oscillations but would not necessarily destroy this activity synchrony between neurons. However, as the awake state is chaotic, this population synchrony would naturally disappear. In this way, the awake state would make each neuron more independent, since it is no longer "bound" by the dynamics of the state, and the specific feature-selective inputs to each neuron can have a great effect on the firing output for that particular neuron in the end.

This work uncovers an important function of extracellular ion concentrations and chaos dynamics in neuronal state transitions that, to the best of our knowledge, has not been previously reported. The transition between global brain states needs to be strictly controlled and well regulated to avoid risky diseases such narcolepsy or insomnia. As we show, the concentration of extracellular ions is a key parameter for neuronal state changes, and these state transitions are governed by chaotic dynamics. Concerted regulation and shifts in ion concentrations therefore expand the toolbox available to the brain for controlling state-dependent activity, and thus need to be considered as an integrated mechanism in future investigations of what determines ongoing activity and state transitions in the brain.

STAR★METHODS

Detailed methods are provided in the online version of this paper and include the following:

- KEY RESOURCES TABLE
- CONTACT FOR REAGENT AND RESOURCE SHARING
- EXPERIMENTAL MODEL AND SUBJECT DETAILS
  - Description of the Extended Averaged-Neuron Model
- METHOD DETAILS
  - Membrane Potential (V_m) Analysis
- DATA AND SOFTWARE AVAILABILITY
  - Software
  - Algorithms
- QUANTIFICATION AND STATISTICAL ANALYSIS
- ADDITIONAL RESOURCES

SUPPLEMENTAL INFORMATION

Supplemental Information includes five figures and can be found with this article online at https://doi.org/10.1016/j.cels.2017.11.011.

ACKNOWLEDGMENTS

M.L.H. and M.H.J. acknowledge support from the Danish Council for Independent Research and Danish National Research Foundation through StemPhys Center of Excellence, grant number DNRF116. R.R. acknowledges support from the European Research Council Starting Grant "CIRCUITASSEMBLY" contract 638730 to Keisuke Yonehara.

AUTHOR CONTRIBUTIONS

Conceptualization, R.R. and M.L.H.; Methodology, R.R., M.H.J., and M.L.H.; Investigation, R.R., M.H.J., and M.L.H.; Writing, R.R. and M.L.H.; Visualization, R.R. and M.L.H.

Received: June 16, 2017
Revised: September 7, 2017
Accepted: November 20, 2017
Published: December 13, 2017

REFERENCES

Amzica, F., Massimini, M., and Manfridi, A. (2002). Spatial buffering during slow and paroxysmal sleep oscillations in cortical networks of glial cells in vivo. J. Neurosci. *22*, 1042–1053.

Bazhenov, M., Timofeev, I., Steriade, M., and Sejnowski, T.J. (2002). Model of thalamocortical slow-wave sleep oscillations and transitions to activated States. J. Neurosci. *22*, 8691–8704.

Bennett, C., Arroyo, S., and Hestrin, S. (2013). Subthreshold mechanisms underlying state-dependent modulation of visual responses. Neuron *80*, 350–357.

Chen, J.-Y., Chauvette, S., Skorheim, S., Timofeev, I., and Bazhenov, M. (2012). Interneuron-mediated inhibition synchronizes neuronal activity during slow oscillation. J. Physiol. *590*, 3987–4010.

Compte, A., Sanchez-Vives, M.V., McCormick, D.A., and Wang, X.-J. (2003). Cellular and network mechanisms of slow oscillatory activity and wave propagations in a cortical network model. J. Neurophysiol. *89*, 2707–2725.

De Col, R., Messlinger, K., and Carr, R.W. (2008). Conduction velocity is regulated by sodium channel inactivation in unmyelinated axons innervating the rat cranial meninges. J. Physiol. *586*, 1089–1103.

Crochet, S., and Petersen, C.C.H. (2006). Correlating whisker behavior with membrane potential in barrel cortex of awake mice. Nat. Neurosci. *9*, 608–610.

Diarra, A., Sheldon, C., and Church, J. (2001). In situ calibration and $[H^+]$ sensitivity of the fluorescent Na+ indicator SBFI. Am. J. Physiol. Cell Physiol. *280*, C1623–C1633.

Dietzel, I., Heinemann, U., Hofmeier, G., and Lux, H.D. (1982). Stimulus-induced changes in extracellular Na^+ and C^{l-} concentration in relation to changes in the size of the extracellular space. Exp. Brain Res. *46*, 73–84.

Ding, F., O'Donnell, J., Xu, Q., Kang, N., Goldman, N., and Nedergaard, M. (2016). Changes in the composition of brain interstitial ions control the sleep-wake cycle. Science *352*, 550–555.

Enger, R., Tang, W., Vindedal, G.F., Jensen, V., Johannes Helm, P., Sprengel, R., Looger, L.L., and Nagelhus, E.A. (2015). Dynamics of ionic shifts in cortical spreading depression. Cereb. Cortex *25*, 4469–4476.

Fröhlich, F., Bazhenov, M., Timofeev, I., Steriade, M., and Sejnowski, T.J. (2006). Slow state transitions of sustained neural oscillations by activity-dependent modulation of intrinsic excitability. J. Neurosci. *26*, 6153–6162.

Fröhlich, F., Bazhenov, M., Iragui-Madoz, V., and Sejnowski, T.J. (2008). Potassium dynamics in the epileptic cortex: new insights on an old topic. Neuroscientist *14*, 422–433.

Gentet, L.J., Avermann, M., Matyas, F., Staiger, J.F., and Petersen, C.C.H. (2010). Membrane potential dynamics of GABAergic neurons in the barrel cortex of behaving mice. Neuron *65*, 422–435.

Grafstein, B. (1956). Mechanism of spreading cortical depression. J. Neurophysiol. *19*, 154–171.

Harris, K.D., and Thiele, A. (2011). Cortical state and attention. Nat. Rev. Neurosci. *12*, 509–523.

Hill, S., and Tononi, G. (2005). Modeling sleep and wakefulness in the thalamocortical system. J. Neurophysiol. *93*, 1671–1698.

Hounsgaard, J., and Nicholson, C. (1983). Potassium accumulation around individual Purkinje cells in cerebellar slices from the Guinea-pig. J. Physiol. *340*, 359–388.

Jensen, M.S., and Yaari, Y. (1997). Role of intrinsic burst firing, potassium accumulation, and electrical coupling in the elevated potassium model of hippocampal epilepsy. J. Neurophysiol. *77*, 1224–1233.

Krishnan, G.P., Filatov, G., Shilnikov, A., and Bazhenov, M. (2015). Electrogenic properties of the Na^+/K^+ ATPase control transitions between normal and pathological brain states. J. Neurophysiol. *113*, 3356–3374.

Lee, S.H., and Dan, Y. (2012). Neuromodulation of brain states. Neuron *76*, 209–222.

Lee, A.M., Hoy, J.L., Bonci, A., Wilbrecht, L., Stryker, M.P., and Niell, C.M. (2014). Identification of a brainstem circuit regulating visual cortical state in parallel with locomotion. Neuron *83*, 455–466.

Lorenz, E.N. (1963). Deterministic nonperiodic flow. J. Atmos. Sci. *20*, 130–141.

Lux, H.D. (1974). Fast recording ion specific microelectrodes: their use in pharmacological studies in the CNS. Neuropharmacology *13*, 509–517.

Lux, H.D., and Neher, E. (1973). The equilibration time course of $[K^+]_o$ in cat cortex. Exp. Brain Res. *17*, 190–205.

Markova, O., Mukhtarov, M., Real, E., Jacob, Y., and Bregestovski, P. (2008). Genetically encoded chloride indicator with improved sensitivity. J. Neurosci. Methods *170*, 67–76.

Mayer, M.L., Westbrook, G.L., and Guthrie, P.B. (1984). Voltage-dependent block by Mg^{2+} of NMDA responses in spinal cord neurones. Nature *309*, 261–263.

McCormick, D.A., and Williamson, A. (1989). Convergence and divergence of neurotransmitter action in human cerebral cortex. Proc. Natl. Acad. Sci. USA *86*, 8098–8102.

McCormick, D.A., Wang, Z., and Huguenard, J. (1993). Neurotransmitter control of neocortical neuronal activity and excitability. Cereb. Cortex *3*, 387–398.

McGinley, M.J., David, S.V., and McCormick, D.A. (2015a). Cortical membrane potential signature of optimal states for sensory signal detection. Neuron *87*, 179–192.

McGinley, M.J., Vinck, M., Reimer, J., Batista-Brito, R., Zagha, E., Cadwell, C.R., Tolias, A.S., Cardin, J.A., and McCormick, D.A. (2015b). Waking state:

rapid variations modulate neural and behavioral responses. Neuron *87*, 1143–1161.

Mitra, P., and Bokel, H. (2008). Observed Brain Dynamics (Oxford University Press).

Nicholson, C., Bruggencate, G.T., Steinberg, R., and Stöckle, H. (1977). Calcium modulation in brain extracellular microenvironment demonstrated with ion-selective micropipette. Proc. Natl. Acad. Sci. USA *74*, 1287–1290.

Niell, C.M., and Stryker, M.P. (2010). Modulation of visual responses by behavioral state in mouse visual cortex. Neuron *65*, 472–479.

Nowak, L., Bregestovski, P., Ascher, P., Herbet, A., and Prochiantz, A. (1984). Magnesium gates glutamate-activated channels in mouse central neurones. Nature *307*, 462–465.

Orkand, R.K., Nicholls, J.G., and Kuffler, S.W. (1966). Effect of nerve impulses on the membrane potential of glial cells in the central nervous system of amphibia. J. Neurophysiol. *29*, 788–806.

Polack, P.O., Friedman, J., and Golshani, P. (2013). Cellular mechanisms of brain state–dependent gain modulation in visual cortex. Nat. Neurosci. *16*, 1331–1339.

Raimondo, J., Joyce, B., Kay, L., Schlagheck, T., Newey, S.E., Srinivas, S., and Akerman, C.J. (2013). A genetically-encoded chloride and pH sensor for dissociating ion dynamics in the nervous system. Front. Cell. Neurosci. *7*, 202.

Rasmussen, R., Nedergaard, M., and Petersen, N.C. (2016). Sulforhodamine 101, a widely used astrocyte marker, can induce cortical seizure-like activity at concentrations commonly used. Sci. Rep. *6*, 30433.

Reimer, J., Froudarakis, E., Cadwell, C.R., Yatsenko, D., Denfield, G.H., and Tolias, A.S. (2014). Pupil fluctuations track fast switching of cortical states during quiet wakefulness. Neuron *84*, 355–362.

Rose, C.R., and Konnerth, A. (2001). NMDA receptor-mediated Na^+ signals in spines and dendrites. J. Neurosci. *21*, 4207–4214.

Rose, C.R., and Ransom, B.R. (1996). Intracellular sodium homeostasis in rat hippocampal astrocytes. J. Physiol. *491* (Pt 2), 291–305.

Sanchez-Vives, M.V., Mattia, M., Compte, A., Perez-Zabalza, M., Winograd, M., Descalzo, V.F., and Reig, R. (2010). Inhibitory modulation of cortical up states. J. Neurophysiol. *104*, 1314–1324.

Schneider, D.M., Nelson, A., and Mooney, R. (2014). A synaptic and circuit basis for corollary discharge in the auditory cortex. Nature *513*, 189–194.

Shih, P.Y., Savtchenko, L.P., Kamasawa, N., Dembitskaya, Y., McHugh, T.J., Rusakov, D.A., Shigemoto, R., and Semyanov, A. (2013). Retrograde synaptic signaling mediated by K^+ efflux through postsynaptic NMDA receptors. Cell Rep. *5*, 941–951.

Somjen, G.G. (2001). Mechanisms of spreading depression and hypoxic spreading depression-like depolarization. Physiol. Rev. *81*, 1065–1096.

Somjen, G.G. (2002). Ion regulation in the brain: implications for pathophysiology. Neuroscientist *8*, 254–267.

Somjen, G.G. (2004). Ions in the Brain: Normal Function, Seizures, and Stroke (Oxford University Press).

Steriade, M., Amzica, F., and Nuñez, A. (1993). Cholinergic and noradrenergic modulation of the slow (approximately 0.3 Hz) oscillation in neocortical cells. J. Neurophysiol. *70*, 1385–1400.

Steriade, M., Timofeev, I., and Grenier, F. (2001). Natural waking and sleep states: a view from inside neocortical neurons. J. Neurophysiol. *85*, 1969–1985.

Tagluk, M.E., and Tekin, R. (2014). The influence of ion concentrations on the dynamic behavior of the Hodgkin–Huxley model-based cortical network. Cogn. Neurodyn. *8*, 287–298.

Tatsuki, F., Sunagawa, G.A., Shi, S., Susaki, E.A., Yukinaga, H., Perrin, D., Sumiyama, K., Ukai-Tadenuma, M., Fujishima, H., Ohno, R., et al. (2016). Involvement of Ca^{2+}-dependent hyperpolarization in sleep duration in mammals. Neuron *90*, 70–85.

Timofeev, I., Grenier, F., Bazhenov, M., Sejnowski, T.J., and Steriade, M. (2000). Origin of slow cortical oscillations in deafferented cortical slabs. Cereb. Cortex *10*, 1185–1199.

Traynelis, S.F., and Dingledine, R. (1988). Potassium-induced spontaneous electrographic seizures in the rat hippocampal slice. J. Neurophysiol. *59*, 259–276.

Vinck, M., Batista-Brito, R., Knoblich, U., and Cardin, J.A. (2015). Arousal and locomotion make distinct contributions to cortical activity patterns and visual encoding. Neuron *86*, 740–754.

Yamashita, T., Pala, A., Pedrido, L., Kremer, Y., Welker, E., and Petersen, C.C. (2013). Membrane potential dynamics of neocortical projection neurons driving target-specific signals. Neuron *80*, 1477–1490.

Zagha, E., Casale, A.E., Sachdev, R.N., McGinley, M.J., and McCormick, D.A. (2013). Motor cortex feedback influences sensory processing by modulating network state. Neuron *79*, 567–578.

Please cite this article in press as: Rasmussen et al., Chaotic Dynamics Mediate Brain State Transitions, Driven by Changes in Extracellular Ion Concentrations, Cell Systems (2017), https://doi.org/10.1016/j.cels.2017.11.011

STAR★METHODS

KEY RESOURCES TABLE

REAGENT or RESOURCE	SOURCE	IDENTIFIER
Software and Algorithms		
Simulations made in c++	This Paper	
MATLAB 6.1	The MathWorks Inc. 2010	https://se.mathworks.com/products/matlab/
Chronux 2.0 Toolbox	Chronux	https://chronux.org/
fcn, d02cjx and d02cjw library packages in Fortran	The NAG Library, The Numerical Algorithms Group (NAG), Oxford, United Kingdom	www.nag.com

CONTACT FOR REAGENT AND RESOURCE SHARING

Further information and requests for resources should be directed to and will be fulfilled by the Lead Contact, Mathias L. Heltberg (heltberg@nbi.ku.dk).

EXPERIMENTAL MODEL AND SUBJECT DETAILS

Description of the Extended Averaged-Neuron Model

We consider the membrane potential (V_m) given by:

$$\frac{dV}{dt} = -\frac{1}{C}\left(\sum I_{Ext}\right) - \frac{1}{AC}\left(\left(\sum I_{Int}\right)\right)$$

$$\text{intrinsic} \in \left[Leak, Na_V, K_V, K_{A-type}, K_{SI}, Ca_V, K_{Ca}, NaP, K_{IR}\right]$$

$$\text{extrinsic} \in [NMDA, AMPA, GABA_A]$$

The units on the left side is mV/ms, but the extrinsic currents are in units of uA whereas the intrinsic currents are in nA, and therefore the first should be multiplied by 1000. This reduces to 10, since we multiply with A, that should be in cm^2 and should thus be divided by 100.

Intrinsic Channel Conductances

For the leak channel we have:

$$I_{Leak} = g_{Leak}(V - V_{Leak})$$

$$g_{Leak} = 0.03573\ mS/cm^2 \quad V_{Leak} = \frac{RT}{zF}\ln\left(\frac{p_K[K]_o + p_{Na}[Na]_o + p_{Cl}[Cl]_i}{p_K[K]_i + p_{Na}[Na]_i + p_{Cl}[Cl]_o}\right) \qquad \text{(Equation 1)}$$

$$R = 8.314472\ J/K/mol \quad T = 310\ kelvins \quad z = valence_{ion} \quad F = 9.64853399x10^4\ C/mol$$

For the voltage-gated sodium channel we have:

$$I_{Na_V} = g_{Na_V} m_{Na_V}^3 h_{Na_V}(V - V_{Na})$$

$$m_{Na_V} = \frac{\alpha_m}{\alpha_m + \beta_m} \qquad \begin{cases} \alpha_m = 0.1\dfrac{V+33}{1-e^{-(V+33)/10}} \\ \beta_m = 4e^{-(V+53.7)/12} \end{cases}$$

$$\dot{h}_{Na_V} = 4\left(\alpha_h\left(1 - h_{Na_V}\right) - \beta_h h_{Na_V}\right) \qquad \begin{cases} \alpha_h = 0.07e^{-(V+50)/10} \\ \beta_h = \dfrac{1}{1+e^{-(V+20)/10}} \end{cases} \qquad \text{(Equation 2)}$$

$$g_{Na_V} = 12.2438\ mS/cm^2 \quad V_{Na} = \frac{RT}{zF}\ln\left(\frac{[Na]_o}{[Na]_i}\right)$$

For the voltage-gated potassium channel we have:

$$I_{K_V} = g_{K_V} n_K^4 (V - V_K)$$
$$\dot{n}_{K_V} = 4\left(\alpha_h\left(1 - h_{K_V}\right) - \beta_h h_{K_V}\right) \quad \begin{cases} \alpha_n = 0.01\dfrac{V+34}{1-e^{-(V+34)/10}} \\ \beta_n = 0.125e^{-(V+44)/25} \end{cases} \qquad \text{(Equation 3)}$$
$$g_{K_V} = 2.61868\ mS/cm^2 \quad V_K = \frac{RT}{zF}\ln\left(\frac{[K]_o}{[K]_i}\right)$$

For the fast A-type potassium channel we have:

$$I_{A-type} = g_{A-type} m_{A-type}^3 h_{A-type} (V - V_K)$$
$$m_{A-type} = \frac{1}{1+e^{-(V+50)/20}}$$
$$\dot{h}_{A-type} = \frac{h_{A-type\infty} - h_A - type}{\tau_{hA-type}} \qquad \text{(Equation 4)}$$
$$h_{A-type\infty} = \frac{1}{1+e^{(V+80)/6}}$$
$$g_{A-type} = 1.79259\ mS/cm^2 \quad \tau_{hA-type} = 15ms \quad V_K = \frac{RT}{zF}\ln\left(\frac{[K]_o}{[K]_i}\right)$$

For the slowly inactivating potassium channel we have:

$$I_{K_{SI}} = g_{K_{SI}} m_{K_{SI}} (V - V_K)$$
$$m_{K_{SI}} = \frac{h_{m_{K_{SI}\infty}} - m_{K_{SI}}}{\tau_{mK_{SI}}}$$
$$m_{K_{SI}\infty} = \frac{1}{1+e^{-(V+34)/6.6}} \qquad \text{(Equation 5)}$$
$$\tau_{mK_{SI}} = \frac{8}{e^{-(V+55)/30} + e^{(V+55)/30}}$$
$$g_{K_{SI}} = 0.0350135\ mS/cm^2 \quad V_K = \frac{RT}{zF}\ln\left(\frac{[K]_o}{[K]_i}\right)$$

For the voltage-gated calcium channel we have:

$$I_{Ca_V} = g_{Ca_V} m_{Ca_V\infty}^2 (V - V_{Ca})$$
$$m_{Ca_V\infty} = \frac{1}{1+e^{(V+20)/9}} \qquad \text{(Equation 6)}$$
$$g_{Ca_V} = 0.0256867\ mS/cm^2 \quad V_{Ca} = \frac{RT}{zF}\ln\left(\frac{[Ca]_o}{[Ca]_i}\right)$$

For the calcium-dependent potassium channel we have:

$$I_{K_{Ca}} = g_{K_{Ca}} m_{K_{Ca}\infty} (V - V_K)$$
$$m_{K_{Ca}\infty} = \frac{1}{1+\dfrac{K_D^{3.5}}{[Ca]_i}}$$
$$\left[\dot{Ca}\right]_i = -\alpha_{Ca}(10 \cdot AI_{Ca} + I_{NMDA}) - \frac{[Ca]_i}{\tau_{Ca}} \qquad \text{(Equation 7)}$$
$$g_{K_{Ca}} = 2.34906\ mS/cm^2 \quad K_D = 30\mu M \quad \tau_{Ca} = 121.403ms \quad V_K = \frac{RT}{zF}\ln\left(\frac{[K]_o}{[K]_i}\right)$$

For the persistent sodium channel we have:

$$I_{NaP} = g_{NaP} m_{NaP\infty} (V - V_{Na})$$
$$m_{NaP\infty} = \frac{1}{1 + e^{-(V+55.7)/7.7}}$$
$$g_{NaP} = 0.0717984 \ mS/cm^2 \quad V_{Na} = \frac{RT}{zF} \ln\left(\frac{[Na]_o}{[Na]_i}\right)$$

(Equation 8)

For the inwardly rectifying potassium channel we have:

$$I_{K_{IR}} = g_{K_{IR}} h_{K_{IR}\infty} (V - V_K)$$
$$h_{K_{IR}\infty} = \frac{1}{1 + e^{(V+75)/4}}$$
$$g_{K_{IR}} = 0.0166454 \ mS/cm^2 \quad V_K = \frac{RT}{zF} \ln\left(\frac{[K]_o}{[K]_i}\right)$$

(Equation 9)

Extrinsic Channel Conductances

We start by defining the saturating function

$$f(V) = \frac{1}{1 + e^{-(V-20)/2)}}$$

We now consider the AMPA receptor:

$$I_{AMPA} = g_{AMPA} s_{AMPA} (V - V_{AMPA})$$
$$\dot{s}_{AMPA} = 3.48 f(V) - \frac{s_{AMPA}}{\tau_{AMPA}}$$
$$g_{AMPA} = 0.513425 \ \mu S/cm^2 \quad V_{AMPA} = \frac{RT}{zF} \ln\left(\frac{pK[K]_o + pNa[Na]_o}{pK[K]_i + pNa[Na]_i}\right)$$

(Equation 10)

For the NMDA receptor we have:

$$I_{NMDA} = \frac{1.1}{1.0 + [Mg]_o/8.0mM} g_{NMDA} s_{NMDA} (V - V_{NMDA})$$
$$\dot{s}_{NMDA} = 0.5 x_{NMDA} (1 - s_{NMDA}) - \frac{s_{NMDA}}{\tau_{sNMDA}}$$
$$\dot{x}_{NMDA} = 3.48 f(V) - \frac{x_{NMDA}}{\tau_{xNMDA}}$$
$$g_{NMDA} = 0.00434132 \ \mu S/cm^2 \quad V_{NMDA} = \frac{RT}{zF} \ln\left(\frac{pK[K]_o + pNa[Na]_o + pCa[Ca]_o}{pK[K]_i + pNa[Na]_i + pCa[Ca]_i}\right)$$

(Equation 11)

For the $GABA_A$ receptor we have:

$$I_{GABA_A} = g_{GABA_A} s_{GABA_A} (V - V_{GABA})$$
$$\dot{s}_{GABA_A} = f(V) - \frac{s_{GABA_A}}{\tau_{sGABA_A}}$$
$$g_{GABA_A} = 0.00252916 \ \mu S/cm^2 \quad V_{GABA} = \frac{RT}{zF} \ln\left(\frac{[Cl]_i}{[Cl]_o}\right)$$

(Equation 12)

Ion Concentrations

We used the following intra- and extracellular ion concentrations:

$$[Na]_o = 140 \ mM \quad [Na]_i = 7 \ mM$$
$$[K]_o = [3.5; 3.9; 4.4; 4.9; 8; 14] \ mM \quad [K]_i = 7 \ mM$$
$$[Ca]_o = [1.05; 1.2; 1.35] \ mM \quad [Ca]_i = -\alpha_{Ca}(10 \cdot Al_{Ca} + I_{NMDA}) - \frac{[Ca]i}{\tau_{Ca}} \ \mu M$$
$$[Cl]_o = 140 \ mM \quad [Cl]_i = 10 \ mM$$
$$[Mg]_o = [0.6; 0.7; 0.8] \ mM$$

METHOD DETAILS

Membrane Potential (V_m) Analysis

V_m frequency component analysis was performed using procedures in MATLAB similar to previously described (Rasmussen et al., 2016). For exploring frequency-domain dynamics we used the *mtspectrumc* function, a multi-taper method implemented in the Chronux 2.0 toolbox, an open-source, MATLAB-based toolbox available at http://chronux.org/ (Mitra and Bokel, 2008). For this analysis we used a padding factor of 2, time-bandwidth product of 3 and 5 tapers. For determining power content we used the *bandpower* function and afterwards the *pow2db* functions in MATLAB. All power measurements are reported in units of decibel unless otherwise stated. For removing spikes from the simulated V_m, yielding the mean V_m, we median filtered the raw V_m (window size: 80 ms). V_m standard deviation was determined over a 200 ms moving window.

DATA AND SOFTWARE AVAILABILITY

Software

All simulations were performed using scripts written in Fortran, C++ and MATLAB. All data-analysis were performed from scripts written in MATLAB and python using the ROOT software. Figures were composed in Adobe Illustrator. All scripts used for simulation and data analysis from the model, will be available upon reasonable request to Mathias L. Heltberg (heltberg@nbi.ku.dk).

Algorithms

All deterministic simulations were performed using the fcn, d02cjx and d02cjw library packages in Fortran and tested by a similar script written in c++. All stochastic simulations were performed by scripts written in c++, and using the Mersenne Twister to draw random numbers.

QUANTIFICATION AND STATISTICAL ANALYSIS

Statistical testing was carried out in MATLAB. All group comparisons were performed using two-sided parametric paired Student's t test. For comparisons of multiple groups the parametric repeated measures One-way ANOVA with a Geisser-Greenhouse correction and a Dunnett's multiple comparisons correction was used. Lower-case 'n' refers to the number of simulations and is noted in the manuscript text, figure legends and on figure panels whenever appropriate. Statistical significance was considered with P-values less than 0.05. When a statistical test was used, the precise P-value is noted in the manuscript text, and depicted in figures with asterisks: * $P < 0.05$, ** $P < 0.01$, *** $P < 0.001$.

ADDITIONAL RESOURCES

The custom code for the extended Averaged-Neuron model is publicly available online at https://github.com/Neurune/IonsAndChaos.

nature COMMUNICATIONS

ARTICLE

https://doi.org/10.1038/s41467-018-07932-1 OPEN

On chaotic dynamics in transcription factors and the associated effects in differential gene regulation

Mathias L. Heltberg[1], Sandeep Krishna[2] & Mogens H. Jensen[1]

The control of proteins by a transcription factor with periodically varying concentration exhibits intriguing dynamical behaviour. Even though it is accepted that transcription factors vary their dynamics in response to different situations, insight into how this affects downstream genes is lacking. Here, we investigate how oscillations and chaotic dynamics in the transcription factor NF-κB can affect downstream protein production. We describe how it is possible to control the effective dynamics of the transcription factor by stimulating it with an oscillating ligand. We find that chaotic dynamics modulates gene expression and up-regulates certain families of low-affinity genes, even in the presence of extrinsic and intrinsic noise. Furthermore, this leads to an increase in the production of protein complexes and the efficiency of their assembly. Finally, we show how chaotic dynamics creates a heterogeneous population of cell states, and describe how this can be beneficial in multi-toxic environments.

[1] Niels Bohr Institute, University of Copenhagen, Blegdamsvej 17, DK-2100 Copenhagen, Denmark. [2] Simons Centre for the Study of Living Machines, National Centre for Biological Sciences-TIFR, GKVK Campus, Bellary Road, Bangalore 560065, India. Correspondence and requests for materials should be addressed to S.K. (email: sandeep@ncbs.res.in) or to M.H.J. (email: mhjensen@nbi.dk)

The regulation and control of protein production is a vital element in all living organisms. This process can be highly complicated, involving a large number of steps. However, despite stochastic fluctuations, life is characterised by a high level of organisation indicative of very precise regulation. A thorough understanding of the mechanisms and interactions that maintain the precision of regulation is absent, but the prospect of discerning and ultimately controlling the production of specific proteins is one of the great goals in the field of systems biology.

Control of transcription is a ubiquitous means of regulating gene expression, but it has only recently been appreciated that transcription factor dynamics might be important for gene regulation. For instance, oscillations have been observed in key transcriptional factors, such as the p53 tumour suppressor or NF-κB, which regulates numerous genes involved in immune response[1–7]. Debate continues about the functional role, if any, of these oscillations, but it is clear that altering the dynamics of these transcription factors differentially affects downstream genes[1,2,4,8].

Oscillatory dynamics is the prerequisite for many complex phenomena—and in the present study for the onset of chaotic dynamics. Chaos refers to complex, apparently unpredictable, dynamics that even simple deterministic dynamical systems can produce (see section What is chaos?). A universal way to achieve chaos is by driving a nonlinear oscillator (say the NF-κB system) by an external periodic signal (e.g., by periodically varying a cytokine-like tumor necrosis factor (TNF) that triggers NF-κB oscillations). When the external driving signal has low amplitude oscillations, it can entrain or synchronise the nonlinear oscillator, i.e., if TNF is varied within certain frequency ranges it will force the NF-κB oscillations to occur with the externally imposed frequency[8,9]. As the amplitude of TNF oscillations is increased, the range of frequencies for which it can entrain NF-κB becomes larger—these expanding synchronisation regions of the external amplitude–frequency parameter space are called Arnold tongues[10–12]. Such entrainment/synchronisation[13] has been observed in many different physical systems, from fluids[14] to quantum mechanical devices[15,16], and now also in biological processes, such as cell cycles[17–19], and gene regulatory dynamics in synthetic populations[20]. The dynamics gets even more complex as the amplitude of the external driving signal increases further. First, Arnold tongues start overlapping, which means the nonlinear oscillator can exist in more than one entrained state with different frequencies (termed modes), and even small amounts of intrinsic or extrinsic noise can cause it to hop between these modes. Such mode-hopping has been observed in the NF-κB system when driven by a periodically varying TNF signal of sufficiently high amplitude[21]. When the external amplitude is increased even further, then chaotic dynamics is predicted[11,12].

In this paper, we study the possible implications of oscillatory and chaotic dynamics of a transcription factor, such as NF-κB, on the downstream genes it controls. We compare the expression of genes with different affinities to the transcription factor, and show that chaotic dynamics has differential effects on genes with different affinites. This can be exploited, for instance, to up-regulate certain proteins, or specific protein complexes. We also show how chaotic dynamics can generate heterogeneity in a cell population that can provide a selective advantage in multi-toxic environments. Our work provides a theoretical framework to study the effects of dynamically varying transcription factors, and we believe it constitutes one of the first investigations into how chaotic dynamics might influence genetic regulation in living cells.

Results

The model. Our investigation starts with a model of the transcription factor NF-κB that is known to exhibit oscillatory dynamics[3,9,22]. A schematic version of this is found in Fig. 1a and a full description is presented in the Supplementary Note 1. In this deliberately simplified model, the oscillations arise from a single negative feedback loop between NF-κB and its inhibitor IkBα, and can be triggered by TNF via the activation of the IkB kinase (IKK). We then allow TNF to oscillate. This system exhibits Arnold tongues (shown schematically in Fig. 1c), which are regions of parameter space where the NF-κB oscillation is entrained to the external TNF oscillation[9], i.e., it locks on to the external signal's frequency and phase. Outside the Arnold tongues there is no synchronisation. It is straightforward to add intrinsic noise to this system by explicitly modelling the randomness in binding/unbinding of proteins, phosphorylation, as well as transcriptional and translation processes using the Gillespie algorithm[23] (see Supplementary Note 2 and Supplementary Figure 1C for details). Figure 1c right panel shows that this system exhibits single-mode oscillations (for low amplitude TNF oscillations), mode-hopping (intermediate amplitude) and chaos (high amplitude) in this system, as was first noted in ref. [21]. Note that changes in a single parameter are sufficient to obtain all these different dynamics.

To the above model, we now add genes that are regulated by NF-κB, following the approach of Mengel et al. [4]. We assume that NF-κB can bind to an enhancer or operator region, and can form complexes to bind the RNA polymerase, with different affinity, depending on the gene (schematically shown in Fig. 1d). We describe the transcription and translation of each gene, labelled $i = 1, 2, 3,\ldots$, using the differential equations:

$$\dot{m}_i = \gamma_i \frac{N^{h_i}}{N^{h_i} + K_i^{h_i}} - \delta_i m_i, \quad (1)$$

$$\dot{P}_i = \Gamma_i m_i - \Delta_i P_i. \quad (2)$$

Here, the m_i represent the mRNA level transcribed from gene i, and P_i represents the concentration of proteins produced from the correspnding mRNA. The first term in the equation for the mRNA is known as a Hill function; the canonical way to describe the protein production for genes governed by transcription factors where each gene has a specific Hill coefficient and effective affinity[4,24–27].

The effective affinity K_i is a parameter that combines the strength of binding of the transcription factor to the operator/enhancer region, the strength of binding of RNA polymerase to the promoter and transcription factor, as well as the effect of DNA looping that may be needed to bring the enhancer/operator close to the promoter region. Operationally, K_i sets the concentration of NF-κB that results in 50% of maximal gene expression enhancement. The Hill coefficient h_i is a measure of the cooperativity of the transcription factor at that gene. A thorough description of this is presented in Supplementary Note 3, and representations of the sigmoidally shaped curves are shown in Supplementary Figure 1. γ_i and Γ_i are the maximal transcription and translation rates for the gene, while δ_i and Δ_i are inversely proportional to the half-lives of the mRNA and protein, respectively. While all these parameters affect the behaviour of genes described by these equations, the affinity K_i is particularly important. In particular, as we will demonstrate in subsequent sections, high-affinity genes (HAGs) with low K_i behave quite differently from low-affinity genes (LAGs) with high K_i. In Fig. 1e the values of the Hill function $N^h/(K^h + N^h)$ as NF-

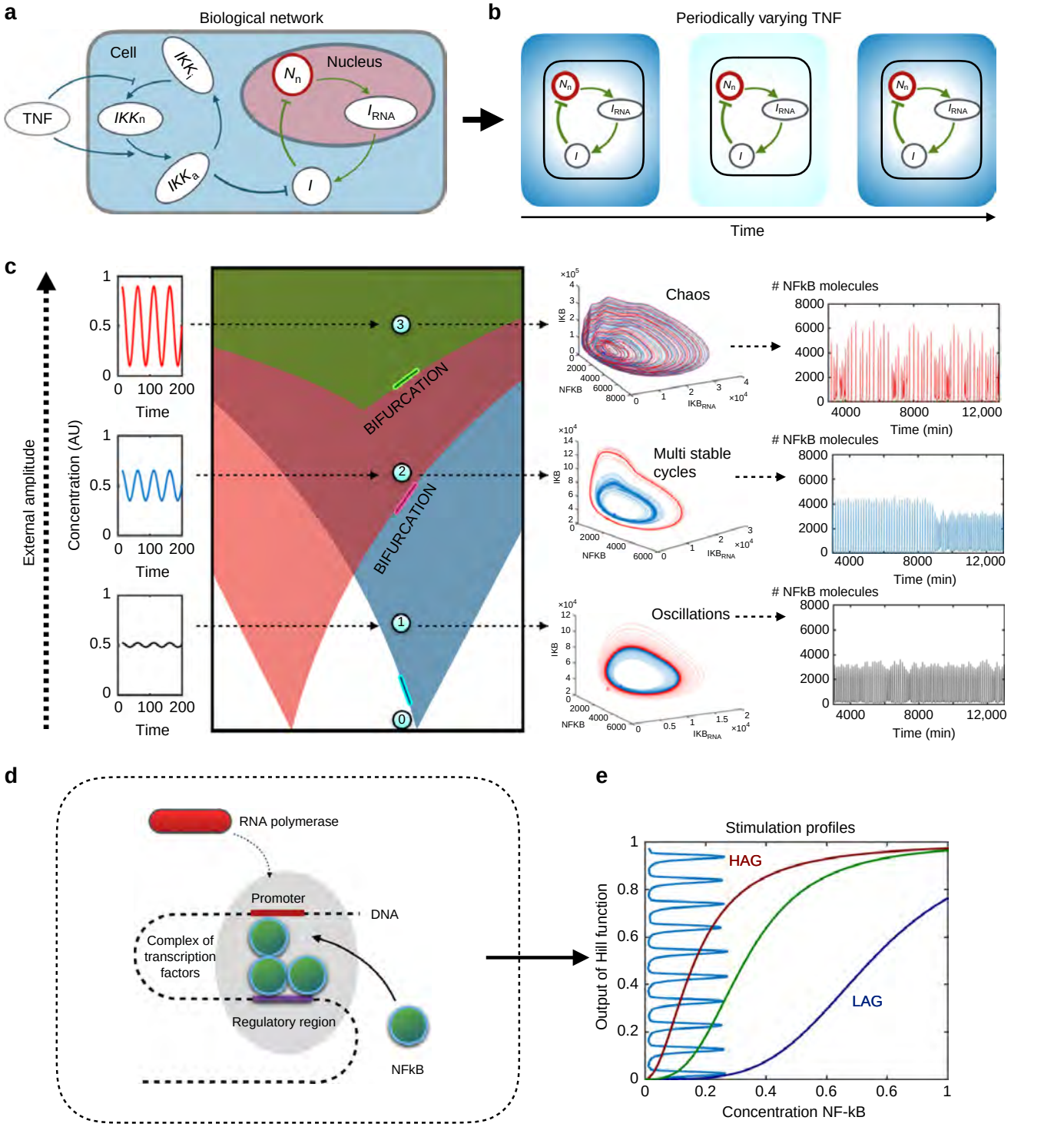

Fig. 1 Dynamics from coupled oscillators and emergence of chaos. **a** Schematic picture of a simplified NF-κ B network with a single negative feedback loop which can generate oscillations. **b** Schematic picture of oscillations in the external TNF concentration, represented by the changing shade of blue. **c** Dynamics that emerges when the NF-kB system is driven by a periodic TNF signal. The left panel shows schematically that there are Arnold tongues, triangular regions of the TNF amplitude-period parameter space where NF-kB oscillations can be synchronised to the TNF signal. Outside the Arnold tongues, e.g. point 0, there is no synchronisation. As TNF amplitude increase the Arnold tongues start overlapping and the behaviour becomes more complex. Keeping the TNF period fixed (here we used $T = 50$ min), as we increase the the TNF amplitude we enter three distinct states: Point 1: A single Arnold tongue, only allowing one oscillation state. Point 2: Overlap of Arnold tongues, allowing two stable oscillation states. The presence of noise can cause transitions (mode-hopping). Point 3: Chaotic dynamics, with apparently unpredictable trajectories. The trajectories corresponding to these points are shown in in the middle panels. Red and blue trajectories correspond to two different initial conditions in a deterministic simulation. The rightmost panels show the dynamics of NF-κ B vs. time in stochastic simulations where intrinsic noise is implemented using the Gillespie algorithm. **d** Schematic figure of the polymerase binding for genes that have NF-κB (green spheres) as a transcription factor. **e** Profile of the Hill function in Eq. (2) for different values of affinity and cooperativity. Red: $h = 2$ and $K = 1.0$ (HAG). Purple: $h = 4$ and $K = 4.5$ (LAG). Green: Example of intermediate values with $h = 3$ and $K = 2.0$ (MAG). Vertically, light blue: a representative NF-κB oscillation

κB level N varies are shown, along with a typical single-mode NF-κB oscillation. It is clear from the figure that the same NF-κB oscillation would be expected to excit HAGs and LAGs to different levels.

What is chaos? When we speak of chaos, we refer to deterministic chaos. Deterministic means that if one knows the initial state of the system exactly, then the dynamical trajectory will be the same every time it is initiated in that state. However, any two initial conditions infinitesimally apart will have exponentially diverging trajectories as time proceeds making it practically impossible to predict the future dynamics—hence chaos[28–31]. It is important to note that the unpredictability of chaos does not arise from stochasticity—the latter refers to a non-deterministic system with noise. Noise is observed in most real-world systems and can often result in very different dynamics than the deterministic version of the same system. For example, noise can cause transitions between different states which would never occur if the system were deterministic. Thus, both deterministically chaotic and noisy systems exhibit unpredictability of their future trajectories, but for very different underlying reasons.

Chaos enhances LAGs. We simulate our model of the NF-κB system, with periodically varying TNF and intrinsic noise, along with downstream genes with different affinities and cooperativities. We then measure the average protein concentration associated with each gene over timescales much longer than the half-lives of the mRNA and proteins. This long-term average is the simplest measure of the effect of NF-κB oscillations on gene expression. As shown in Fig. 2, we find that as TNF amplitude increases, we obtain very different behaviour for HAGs, LAGs and genes with intermediate affinity (MAGs). As described above and in Fig. 1, as TNF amplitude is increased, keeping its frequency fixed, the NF-κB dynamics is first a single-mode oscillation (point 1 in Fig. 1c), then exhibits mode-hopping (point 2 in Fig. 1c) and finally chaos (point 3 in Fig. 1c) for high amplitude TNF. The ranges of TNF amplitude which exhibit these three qualitatively different dynamics are indicated in Fig. 2a–c.

The chaotic regime shows the differential behaviour of the different genes most clearly. The HAG has a linearly decreasing average protein level as TNF amplitude is increased, while the LAG shows exactly the opposite. The MAG exhibits much less variation with TNF amplitude. It is interesting that genes under control of NF-κB can thus be designed to have increasing, decreasing, as well as relatively flat response to variation of a single parameter. The increasing (decreasing) trend that is seen for LAGs (HAGs) within the chaotic regime is also seen across the entire range of TNF amplitudes, going from single-mode oscillations through mode-hopping to chaos. However, within the first two regimes the response is relatively flat with major change happening only near the transition between regimes. Overall, we see that both HAGs and LAGs could exhibit fold-changes on the order of two-fold, which we believe should be observable in experiments, while MAGs could lie within experimental error and thus appear effectively unresponsive to TNF amplitude.

A mathematical analysis of this behaviour provides some intuition to understand why HAGs and LAGs respond so differently: The long-term average protein level is essentially proportional to the average of the Hill function over the same long timescale: $\langle P\rangle \sim \left\langle \frac{N^h}{K^h+N^h}\right\rangle$. For HAGs, K is small, and to lowest order in K/N, $\langle P\rangle \sim 1 - K^h\left\langle \frac{1}{N^h}\right\rangle$. In contrast, for LAGs, K is large, and $\langle P\rangle \sim \frac{\langle N^h\rangle}{K^h}$ (see Supplementary Note 4 for further details). The averages $\langle N^h\rangle$ and $\langle 1/N^h\rangle$ depend on the probability distribution of NF-κB values over a long time series. This distribution is typically unimodal, but is asymmetric and has a long right tail (see Supplementary Figure 2K–L). Now $\langle N^h\rangle$ is largely dominated by this right tail, especially for large h. Thus, if the right tail of this distribution became more prominent as TNF amplitude was increased, we would expect $\langle N^h\rangle$ to increase and this would explain why LAGs show an increasing average protein level, while $\langle 1/N^h\rangle$ in contrast is dominated by the other end of the probability distribution, i.e., very low values of N. Thus, if the probability of NF-κB spending time at low concentrations increased with TNF amplitude, then $\langle 1/N^h\rangle$ would increase, and the average protein level of LAGs would decrease. Supplementary Figure 2K–L shows that this is indeed what happens to the probability distribution of NF-κB as TNF amplitude is increased—both within the chaotic regime, as well as across single-mode oscillations, mode-hopping and chaos. Thus, we conclude that the differential control of HAGs vs. LAGs is directly caused by the broadening of the range of NF-κB levels as one goes deeper into the chaotic regime. The increase of peak NF-κB levels and the decrease of minimum NF-κB levels are both necessary for such differential control.

Robustness to variations in parameters and noise. We tested our central result from the previous section at other TNF frequencies (see the heatmaps in Fig. 2j–l and Supplementary Figure 2A–F) and, for TNF time period in the range 30–120 min, we found the same trends in average protein levels, as a function of TNF amplitude.

Since biological systems are often characterised by large fluctuations and much noise, we also varied the level of intrinsic noise in the NF-κB system by varying the effective volume of the system. Decreasing the volume leads to larger fluctuations, but as shown in Fig. 2d–f, the average protein levels are quite robust to such increases of intrinsic noise. The mode-hopping region is of specific interest to changes in noise, since these affect the rate at which the system jumps from one entrained state to another[32]. The chaotic regime, in contrast, already exhibits many hallmarks of randomness even in the absence of noise, so adding noise does not affect the behaviour much.

Next, we also wanted to include extrinsic noise into the variation of TNF. In experimental procedures, as well as in vivo, it is of course very likely that there will be considerable stochasticity in the TNF signal. Could such fluctuations mask the differential control of genes, especially in the chaotic regime? We added Langevin noise to the periodic TNF waveform at a sufficiently high level to smear out the predominant frequency in a Fourier spectrum of the noisy waveform (see Supplementary Figure 2G-H). We found that this did not affect our results—NF-κB still showed the same transition from single-mode oscillation to mode-hopping to chaos as TNF amplitude was increasing, and HAGs and LAGs showed the same opposite trends in average protein level as in the absence of TNF noise (Fig. 2g–i). As with intrinsic noise, the extrinsic noise had most effect in the mode-hopping regime and minimal effect in the chaotic regime.

Finally, we also found that our results were unchanged when we used non-sinusoidal waveforms for TNF (Supplementary Figure 2I), and when we varied the Hill coefficient (Supplementary Figure 2J). Thus, these results show that the enhancement of LAGs in chaotic dynamics is robust to both internal and external noise, and this effect is a striking feature of chaos in transcription factors for a large set of parameters.

Chaos increases efficiency in protein complex formation. In eukaryotic cells, many functions are carried out by complexes of proteins that are constructed from multiple subunits, for

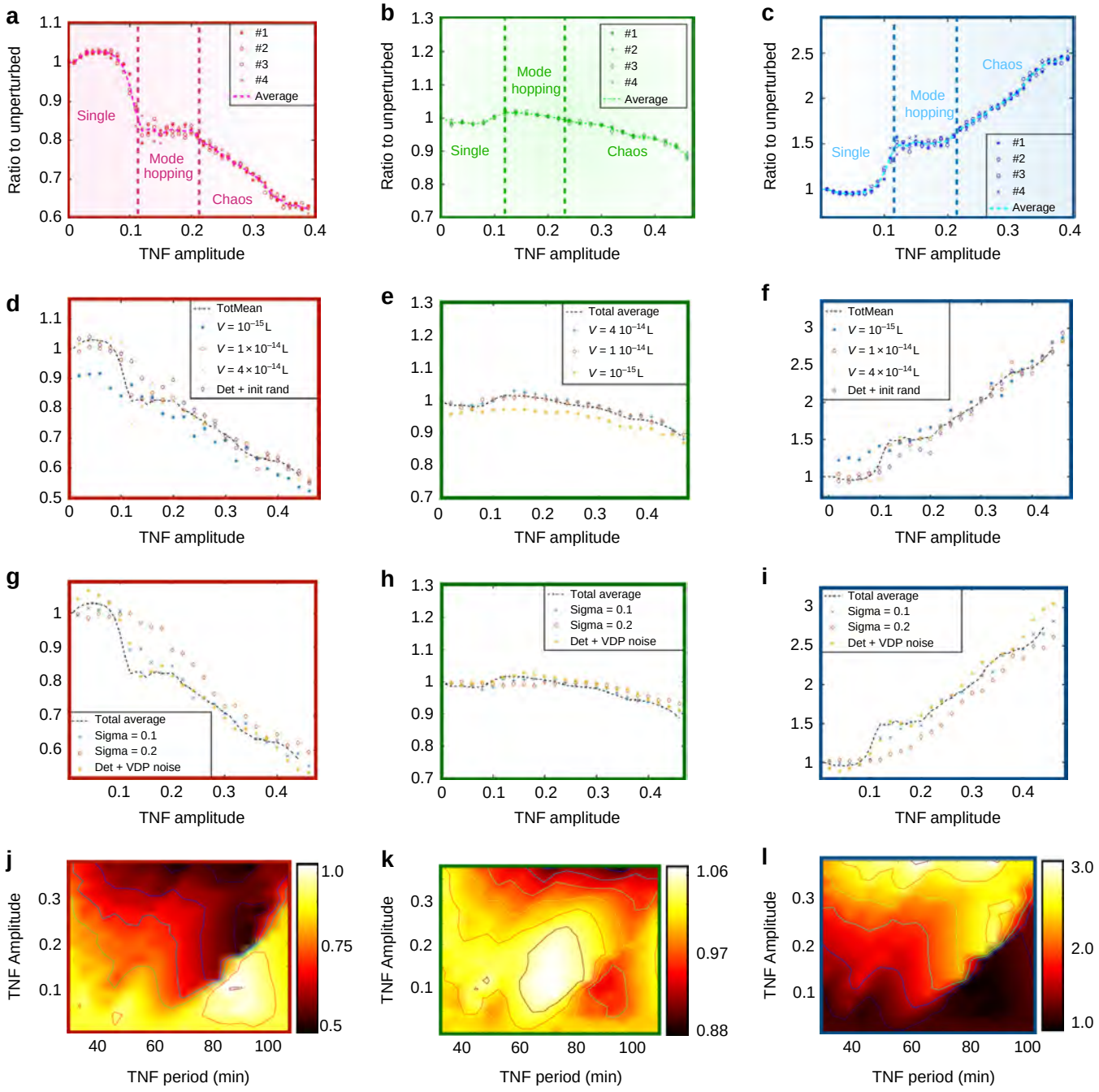

Fig. 2 Effects of chaos on protein production. **a** The average protein level from an HAG ($K = 4.5$, $h = 4$), for different values of the TNF amplitude. We performed four separate simulations of duration $5*10^5$ min. and show their individual means and the mean of these four combined. We used $V = 2*10^{-14}L$ and $T = 50$ min. Results for other periods are found in SI. **b** Same as **a** but for MAG ($K = 2$, $h = 3$). **c** Same as **a** but for LAG ($K = 1$, $h = 2$). **d** The average production from the HAG for different intrinsic noise levels. We performed simulations of duration $1*10^5$ min each datapoint and used the total mean as calculated in **a**–**c**. Here $T = 50$ min. **e** Same as **d** but for the MAG. **f** Same as **d** but for the LAG. **g** The average production from the HAG for different extrinsic noise levels. We performed simulations of duration $1*10^5$ min each datapoint and used the total mean as calculated in **a** and **b**. We added Langevin noise to the oscillator and used $\dot{r} = r(1 - r)$ and $\dot{\theta} = \nu$, and in the last dataseries (yellow *) we used the Van der Pol oscillator with noise as a perturbation to TNF (see Supplementary Note 4). Here $T = 50$ min. **h** Same as **g** but for the MAG. **i** Same as **g** but for the LAG. **j** The average production from the HAG, for different values of the TNF amplitude and period. The bright colours indicate the maximal average protein levels, while the dark colours correspond to low average protein levels. **k** Same as **j** but for the MAG. **l** Same as **j** but for the LAG

instance haemoglobin, that consists of four subunits from two genes that are located on different chromosomes. A study of the NF-κB interactome found that amongst 384 genes that are regulated by NF-κB there were 572 protein–protein interactions[33]. While these complexes have not been deeply investigated, we expect at least some will have a functional role. For instance, there seems to be evidence that NF-κB controls autophagy via multiple pathways, including the up-regulation of both Beclin 1 and A20, which interact with each other inhibiting Beclin 1 ubiquitination, and thereby repressing autophagy[34]. Therefore, we tested how the concentration of protein complexes, whose subunits were encoded by NF-κB controlled genes, was altered as the NF-κB dynamics became chaotic and the LAGs were up regulated.

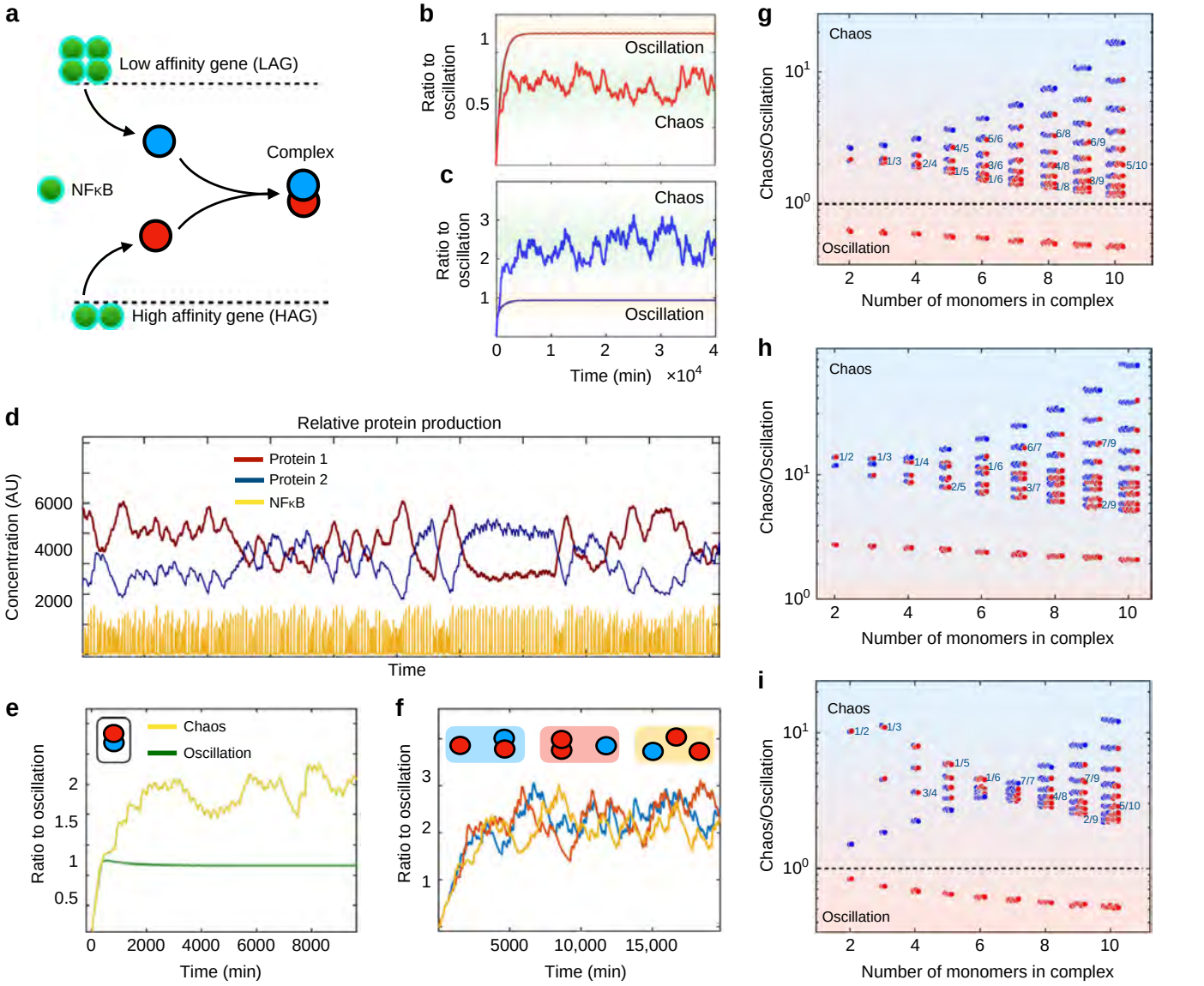

Fig. 3 Effects of chaos on protein complex formation. **a** Schematic picture of how LAG and HAG encoded proteins may form protein complexes. **b** Protein concentration for HAG ($K = 1$, $h = 2$) with oscillatory and chaotic dynamics, respectively. $T_{TNF} = 50$ min. **c** Protein concentration for LAG with ($K = 4.5$, $h = 4$) oscillatory and chaotic dynamics, respectively. $T_{TNF} = 50$ min. **d** Time series of NF-κB (yellow) and the corresponding protein level. Red: Level of HAG protein. Blue: Level of LAG protein (multiplied by 20). $T_{TNF} = 50$ min. **e** Concentration of a heterogenous two-protein complex (shown upper left) with oscillatory and chaotic dynamics respectively. **f** Concentration of a heterogenous three-protein complex in chaotic dynamics depending on the hierarchical assembly (shown above). **g** Relative concentration for complexes of different compositions. The *y*-axis show the concentration in chaos divided by the concentration in the oscillatory regime, and the black line show where these are equal. **h** Relative concentration per NF-κB for complexes of different compositions measured by the fraction $\frac{\langle C_{N,n_H} \rangle}{\langle \mathrm{NFkB} \rangle}$. Same axis as in **g**. **i** Relative concentration per unused subunits for complexes of different compositions measured by the fraction $\frac{\langle C_{N,n_H} \rangle}{\sum_{i=1}^{N} \langle P_i \rangle}$. Same axis as in **g**. For **g**–**i**, the exact ratios are found in the tables in Supplementary Note 5

We first consider a complex that consists of two subunits. In this case, the model has the following additional equations, where P_1 and P_2 represent the concentrations of the two proteins and $C_{2,1}$ the concentration of the complex:

$$\dot{P}_1 = \Gamma_1 m_1 - \lambda_C P_1 P_2 - \Delta_1 P_1, \quad (3)$$

$$\dot{P}_2 = \Gamma_2 m_2 - \lambda_C P_1 P_2 - \Delta_2 P_2, \quad (4)$$

$$\dot{C}_{2,1} = \lambda_C P_1 P_2 - \Delta C_{2,1}. \quad (5)$$

In the following we will, in order to keep things as simple and transparent as possible, keep the values of the parameters λ and Δ fixed even though these could easily differ between complexes. An exploitation of the effects of the entire parameter space will be interesting to pursue in future work, but is beyond the scope of this paper. Obviously if the two subunits are both HAG proteins, the complex has the highest average level in the oscillatory regime, while if it consists of two LAG proteins, the highest average level will be found in the chaotic regime (Fig. 3b, c). However, if the complex is heterogeneous and consists of one HAG and one LAG subunit, as shown schematically in Fig. 3a, the result is not as obvious. Simulating the above equations for a heterogenous complex, we

find a significantly higher level of the complex in the chaotic regime, as seen in Fig. 3e.

We then test larger complexes. The concentration of the protein complex C_{n,n_H} consisting of n subunits, of which n_H are from an HAG and the rest from an LAG, is modelled by

$$\dot{C}_{n,n_H} = \lambda \prod_{i=1}^{n} P_i - \Delta_n C_{n,n_H}. \quad (6)$$

For $n = 3$ and $n_H = 2$, we found that the production was also highest in the chaotic regime and, before moving further, we tested whether the outcome was different if all complexes combined randomly (yellow curve in Fig. 3f), or if there was a hierarchical structure in the assembly (blue and red curves in Fig. 3f). As we see in Fig. 3f the outcome is quite similar, and we could therefore focus on the non-hierarchical assembly of complexes, calculated as shown above. We subsequently tested for $n \in [2–10]$ and in each case we tried with all different different combinations of HAG and LAG subunits. Unexpectedly, we find that all heterogeneous complexes exhibit a higher average lvel in the chaotic regime (Fig. 3g). This means that only homogenous HAG complexes would be present at a high level in the single-mode oscillatory regime. One might ask, whether this is simply the result of higher mean levels of NF-κB. Therefore, we normalised the concentration of the complexes by the mean NF-κB concentration—when this ratio is large we will say the complexes are produced more efficiently. As seen in Fig. 3h, all complexes are produced more efficiently in the chaotic regime—even the homogenous HAG complexes. Another economical argument for the cell is that if only the complexes are of importance, then it is necessary to minimise the number of unused subunits. In Fig. 3i, we see the ratio between the average concentration of complexes to the concentration of unused subunits. This ratio too is largest in the chaotic regime for all complexes, except those made only from HAG proteins. Thus, a chaotically varying transcription factor not only up regulates LAGs, but also results in higher and more economical production of protein complexes composed of subunits from different genes.

Chaos generates advantageous population heterogeneity. We now consider how the dynamics of NF-κB can affect a population of cells. In the following, we consider the deterministic NF-κB system, and study a population of N independent cells that are affected by the same oscillating TNF stimulus. In all simulations, cells have randomly distributed initial conditions, i.e., the NF-κB oscillations in different cells are not initially synchronised. Within each cell, we will track one LAG and one HAG; parameters are chosen so that the two corresponding proteins have the same average protein level. In Fig. 4a–d we see that when NF-κB is in a single-mode oscillatory state, the average level of both Protein 1 and Protein 2 is homogenous across the population, whereas if NF-κB is mode-hopping then the distribution of protein levels across the populaiton is bimodal. In the chaotic regime, the distribution is broad and heterogenous for both proteins (Fig. 4e, f), but the LAG has on average a higher expression in this state (for $\mathrm{TNF}_{\mathrm{Period}} = 95$ min, we note a special tail, which is caused by the occurrence of some high-frequency oscillations).

Such heterogeneity in a cell population can provide a selective advantage when the population is exposed to some potentially lethal stresses. Imagine each cell in the population is exposed to two toxic drugs at concentrations D_1 and D_2. We assume that at each time step each cell is killed with probability

$$\mathcal{P}_{\mathrm{Die}} = \mathcal{P}_0 \left(\frac{D_1^h}{D_1^h + P_1^h} + \frac{D_2^h}{D_2^h + P_2^h} \right). \quad (7)$$

This describes a situation where the two proteins P_1 and P_2 are stress-responders that can help the cell survive stressed conditions. $\mathcal{P}_0$ represents the probability that the drugs kill in the absence of the protective proteins. We consider the case where P_1 is encoded by an HAG and P_2 by an LAG, both under control of NF-κB.

First we consider the situation where only one of these drugs is present, shown in Fig. 4g, h. When only Drug 1 is added in a high amount, cells where NF-κB is in a single-mode oscillating state will have a higher survival rate than cells where NF-κB is mode-hopping or chaotic. This is what one would expect from Fig. 3, since HAG proteins are on average at higher levels in the single-mode oscillatory state. When only Drug 2 is added in a high amount, cells in chaotic states will have a slightly higher survival rate, but due to large fluctuations, these cells will also eventually die due to temporary low levels of Protein 2. Now we consider what will happen to the system if both drugs are added in a comparable amounts. We test four different patterns of adding the drugs (Fig. 4i–l) and find that the cells in the chaotic state will have significantly higher survival rate compared to the others. In the Supplementary Note 6, we provide some mathematical arguments for these results and here we also show tests of the robustness of these results, and here we found similar results as shown above (Supplementary Figure 3). From this we conclude that in the presence of multiple toxic drugs, a population of cells is better off having a large heterogeneity in gene expression and up regulating the LAGs and thus up regulating the product of genes. This is obtained in the chaotic regime for NF-κB dynamics and this enhances the survival rate.

Discussion

Transcription factors are known to have different dynamics, depending on external conditions, but how this may be exploited to differentially control downstream genes is not well understood. We have shown how dynamically varying transcription factors can differentially regulate genes based on an effective affinity that characterises the interaction between the gene and the transcription factor. In particular, we suggest that chaotic dynamics can produce differential control of high vs. LAGs, down regulating the former while simultaneously up regulating the latter. We show that this can be used not only to control single non-interacting genes, but also for upregulating specific complexes of proteins and generating useful heterogeneities in cell populations.

Our results are derived from a model of the NF-κB system. Such models have been used to explain numerous experimentally observed features of NF-κB oscillations[3,35], and therefore form a good basis for our exploration of the effects on downstream genes. Our model has already successfully predicted the existence of mode-hopping for a range of TNF amplitudes[21]. Since chaotic behaviour within overlapping Arnold tongues is such a fundamental feature of driven nonlinear oscillators[11,12,36], we are confident that NF-κB driven by sufficiently large TNF amplitudes will exhibit deterministic chaos. However, an experimental realisation of our model[37,38] would necessarily be subject to various sources of noise and stochasticity, and it is not obvious that deterministically chaotic behaviour can be practically discerned in the presence of such fluctuations. Fortunately, many sophisticated methods exist that allow chaos to be distinguished from noise

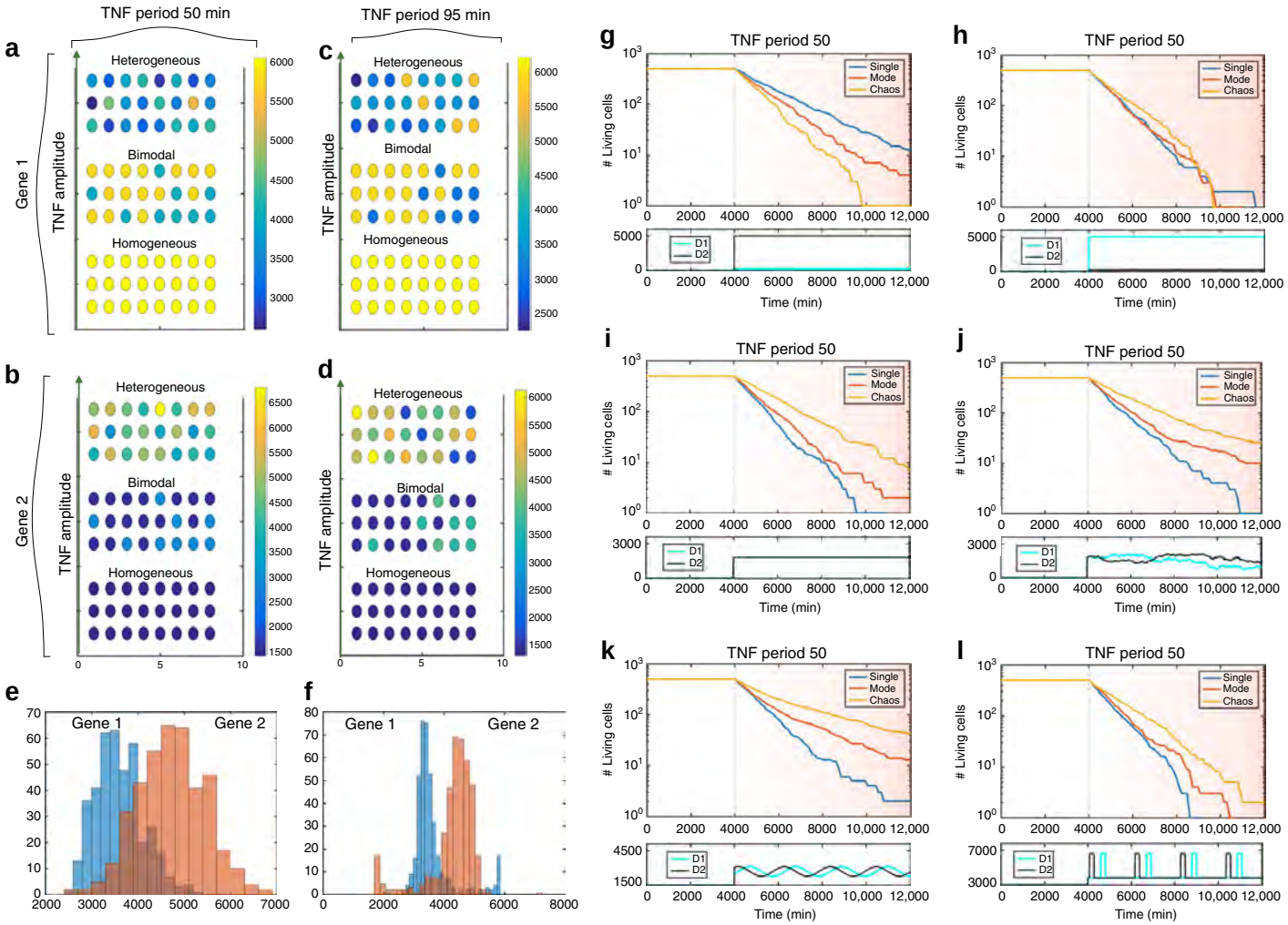

Fig. 4 Population heterogeneity emerges from chaos. **a** Protein concentration from an HAG with $K = 1$, $h = 2$ and external TNF period 50 min. Bottom: The concentration corresponding to a single-mode oscillation; TNF amplitude: 0.04. Middle: The concentration corresponding to mode-hopping; TNF amplitude: 0.12. Top: The concentration corresponding to chaos; TNF amplitude: 0.36. **b** Protein concentration from an LAG with $K = 4.5$, $h = 4$. TNF period 50 min. TNF amplitudes are identical to those used in **a**. **c** Protein concentration from the HAG. TNF period 95 min. Bottom: The concentration corresponding to a single-mode oscillation; TNF amplitude: 0.1. Middle: The concentration corresponding to mode-hopping; TNF amplitude: 0.2. Top: The concentration corresponding to chaos; TNF amplitude: 0.4. **d** Protein concentration from the LAG. TNF period 95 min. TNF amplitudes are identical to those used in **c**. **e** Distribution of protein concentrations in the chaotic state (TNF period: 50 min, TNF amplitude: 0.36). **f** Distribution of protein concentrations in the chaotic state (TNF period: 95 min, TNF amplitude: 0.4). **g** Number of surviving cells vs. time (drug is added at $T = 4000$ min). $D1 = 6000$, $D2 = 0$. **h** Same as **g** with $D1 = 0$, $D2 = 6000$. **i** Same as **g** with $D1 = D2 = 3000$. **j** Same as **g** with $\dot{D}_{1+2} = \mathcal{N}(0, 100.0)$ and $D_{1+2}(0) = 3000$. The panel below shows a specific trajectory on this pattern. In general D_1 is above D_2 50% of the times and vice versa. **k** Same as **g** with $D_{1+2}(t) = 3000 + 1500 \cdot \sin\left(\frac{t}{5000} + \Omega\right)$. **l** Same as **g** with $D_{1+2}(t) = 7000$ if $\sin\left(\frac{t}{5000} + \Omega\right) > 0.95$ and otherwise $D_{1+2}(t) = 3000$

without requiring unreasonably long time series; see for example refs. [39,40]. Once chaos is found in the NF-κB system, the next step of testing whether HAGs respond differently from LAGs can be tackled using genes that have previously investigated in the regime where NF-κB shows single-mode oscillations[1,8]. Since the expression level of some of these genes track NF-κB oscillations closely, while others track the mean NF-κB levels, it is likely that these genes already span a range of affinity values[4]. The robustness of our results to many parameter values suggests that these genes may be directly used to study the chaotic regime, without worrying too much about details, such as their maximal transcription/translation rates or the stabilities of the mRNA and proteins they encode.

Our model uses periodic variation of TNF to produce complex dynamics of NF-κB. Uncovering conditions where TNF naturally varies periodically and thereby entrains the NF-κB oscillations would add substantial weight to our results. Oscillatory dynamics is believed to be of importance to several processes in the immune system[41] and there exists evidence that TNF does indeed vary in a pulsatile or periodic manner in some situations[42–45], as well as mathematical models that attempt to explain the underlying mechanisms[42,46], but it is unclear whether these natural oscillations entrain NF-κB. The positive feedback between NF-κB and TNF that has been hypothesised to produce travelling waves of TNF is perhaps the most promising scenario we are aware of where periodic TNF modulation may occur naturally[46].

Chaotic dynamics has thus far been underestimated as a means for controlling genes, perhaps because of its unpredictability. Our work shows that deterministic chaos potentially expands the toolbox available for single cells to control gene expression dynamically and specifically. We hope this will inspire theoretical and experimental exploration of the presence and utility of chaos in living cells.

Methods

Simulations. All deterministic simulations were performed by numerically integrating the dynamical equations using the Runge–Kutta fourth-order method, and for optimisation reasons, some of the equations were simulated using Euler integration. Whenever Euler integration was used it was tested that it generated similar results as the Runge–Kutta fourth-order method. For all stochastic simulations of NF-kB dynamics, we used the Gillespie algorithm[23]. For noise in the external TNF oscillations we used Langevin simulations of the different oscillations.

Regions of chaos. To find the regions of parameter space that exhibit chaotic dynamics, we first computed the standard deviation in the NF-kB amplitudes from each time series, and found the parameter points at which this grew discontinuously, as we increased the TNF amplitude. Within these regions, we further tested for chaos by calculating the divergence of trajectories that started at almost identical initial points, using deterministic simulations. Parameter regions where such trajectories diverged exponentially were labelled as regions exhibiting chaos.

Code availability. All computer code is available upon request at heltberg@nbi.ku.dk or mhjensen@nbi.dk. The majority of scripts can also be found at https://github.com/Mathiasheltberg/ChaoticDynamicsInTranscriptionFactors.

Data availability

All the data in this paper, was generated using deterministic and stochastic simulations. All scripts to generate the data are available upon request at heltberg@nbi.ku.dk or mhjensen@nbi.dk. The majority of scripts can also be found at https://github.com/Mathiasheltberg/ChaoticDynamicsInTranscriptionFactors.

Received: 1 May 2018 Accepted: 23 November 2018
Published online: 08 January 2019

References

1. Hoffmann, A., Levchenko, A., Scott, M. L. & Baltimore, D. The IκB-NF-κB signaling module: temporal control and selective gene activation. *Science* **298**, 1241–1245 (2002).
2. Nelson, D. E. et al. Oscillations in NF-κB signaling control the dynamics of gene expression. *Science* **306**, 704–708 (2004).
3. Krishna, S., Jensen, M. H. & Sneppen, K. Spiky oscillations in NF-κB signalling. *Proc. Natl Acad. Sci. USA* **103**, 10840–10845 (2006).
4. Mengel, B. et al. Modeling oscillatory control in NF-κB, p53 and Wnt signaling. *Curr. Opin. Genet. Dev.* **20**, 656–664 (2010).
5. Levine, JoeH., Lin, H. & Elowitz, M. Functional roles of pulsing in genetic circuits. *Science* **342**, 1193–1200 (2013).
6. Gonze, D., Halloy, J. & Goldbeter, A. Robustness of circadian rhythms with respect to molecular noise. *Proc. Natl Acad. Sci. USA* **99**, 673–678 (2002).
7. Lahav, G. et al. Dynamics of the p53-Mdm2 feedback loop in individual cells. *Nat. Genet.* **36**, 147 (2004).
8. Tay, S. & Kellogg, R. Noise facilitates transcriptional control under dynamic inputs. *Cell* **160**, 381–392 (2015).
9. Jensen, M. H. & Krishna, S. Inducing phase-locking and chaos in cellular oscillators by modulating the driving stimuli. *FEBS Lett.* **586**, 1664–1668 (2012).
10. Arnold, V. I. & Avez, A. *Ergodic Problems of Classical Mechanics* (Addison-Wesley, New York, 1989).
11. Jensen, M. H., Bak, P. & Bohr, T. Complete devil's staircase, fractal dimension and universality of mode-locking structure in the circle map. *Phys. Rev. Lett.* **50**, 1637–1639 (1983).
12. Jensen, M. H., Bak, P. & Bohr, T. Transition to chaos by interaction of resonances in dissipative systems. I. Circle maps. *Phys. Rev. A* **30**, 1960–1969 (1984).
13. Pikovsky, A., Rosenblum, M. & Kurths, J. *Synchronization: A Universal Concept in Nonlinear Sciences*. (Cambridge University Press, Cambridge, 2003).
14. Stavans, J., Heslot, F. & Libchaber, A. Fixed winding number and the quasiperiodic route to chaos in a convective fluid. *Phys. Rev. Lett.* **55**, 596–599 (1985).
15. Brown, S. E., Mozurkewich, G. & Gruner, G. : Subharmonic Shapiro steps and devil's-staircase behavior in driven charge-density-wave systems. *Phys. Rev. Lett.* **52**, 2277–2380 (1984).
16. Gwinn, E. G. & Westervelt, R. M. Frequency locking, quasiperiodicity, and chaos in extrinsic Ge. *Phys. Rev. Lett.* **57**, 1060–1063 (1986).
17. Tsai, T. Y. et al. Robust, tunable biological oscillations from interlinked positive and negative feedback loops. *Science* **321**, 126–129 (2008).
18. Goldbeter, A. Computational approaches to cellular rhythms. *Nature* **420**, 238–245 (2002).
19. Woller, A., Duez, H., Staels, B. & Lefranc, M. A mathematical model of the liver circadian clock linking feeding and fasting cycles to clock function. *Cell Rep.* **17**, 1087–1097 (2016).
20. Mondragon-Palomino, O., Danino, T., Selimkhanov, J., Tsimring, L. & Hasty, J. Entrainment of a population of synthetic genetic oscillators. *Science* **333**, 1315–1319 (2011).
21. Heltberg, M. L., Kellogg, R. A., Krishna, S., Tay, S. & Jensen, M. H. Noise induces hopping between NF-κB entrainment modes. *Cell Syst.* **3**, 532–539 (2016).
22. Ashall, L. et al. Pulsatile stimulation determines timing and specificity of NF-B-dependent transcription. *Science* **324**, 242 (2009).
23. Gillespie, D. T. Exact stochastic simulation of coupled chemical reactions. *J. Phys. Chem.* **81**, 2340–2361 (1977).
24. Maienschein-Cline, M., Warmflash, M. A. & Dinner, A. R. Defining cooperativity in gene regulation locally through intrinsic noise. *IET Syst. Biol.* **4.6**, 379–392 (2010).
25. Werner, M., Zhu, L. & Aurell, E. Cooperative action in eukaryotic gene regulation: physical properties of a viral example. *Phys. Rev. E* **76**, 061909 (2007).
26. Kaplan, S., Bren, A., Zaslaver, A., Dekel, E. & Alon, U. Diverse two-dimensional input functions control bacterial sugar genes. *Mol. Cell* **29**, 786–792 (2008).
27. Sneppen, K., Krishna, S. & Semsey, S. Simplified models of biological networks. *Annu. Rev. Biophys.* **39**, 43–59 (2010).
28. Poincaré, H. *Science and Method*, 68 (Courier Corporation, Dover Publications, Mineola, New York, 2013).
29. Lorenz, E. N. Deterministic nonperiodic flow. *J. Atmos. Sci.* **20**, 130–141 (1963).
30. Jensen, M. H., Kadanoff, L. P., Libchaber, A., Procaccia, I. & Stavans, J. Global Universality at the onset of chaos: results of a forced Rayleigh Benard experiment. *Phys. Rev. Lett.* **55**, 2798–2801 (1985).
31. Strogatz, S. H. *Dynamical Systems and Chaos*, 278–279 (Westview Press, Boulder, Colorado, 2000).
32. Heltberg, M. L., Krishna & Jensen, M. H. Time Correlations in mode hopping of coupled oscillators. *J. Stat. Phys.* **167**, 792–805 (2017).
33. Tieri, P. et al. Charting the NF-kB pathway interactome map. *PLoS One* **7**, e32678 (2012).
34. Trocoli, A. & Djavaheri-Mergny, M. The complex interplay between autophagy and NF-kB signaling pathways in cancer cells. *Am. J. Cancer Res.* **391**, 629–649 (2011).
35. Basak, S., Behar, M. & Hoffmann, A. Lessons from mathematically modeling the NF-kB pathway. *Immunol. Rev.* **246**, 221–238 (2012).
36. Bohr, T. & Gunaratne, G. Scaling for supercritical circle maps: numerical investigation of the onset of bistability and period doubling. *Phys. Lett.* **113A**, 55 (1985).
37. Piehler, A., Ghorashian, N., Zhang, C. & Tay, S. Universal signal generator for dynamic cell stimulation. *Lab Chip* **17**, 2218–2224 (2017).
38. Dettinger, P. et al. Automated microfluidic system for dynamic stimulation and tracking of single cells. *Anal. Chem.* **90**, 10695–10700 (2018).
39. Amon, A. & Lefranc, M. Topological signature of deterministic chaos in short nonstationary signals from an optical parametric oscillator. *Phys. Rev. Lett.* **92**, 094101 (2004).
40. Gilmore, R. & Lefranc, M. *The Topology of Chaos* (John Wiley and Sons Ltd., New York, 2002).
41. Stark, J., Chan, C. & George, A. J. Oscillations in the immune system. *Immunol. Rev.* **216**, 213–231 (2007).
42. Chan, C. C. W., Stark, J. & George, A. J. T. Analysis of cytokine network dynamics in corneal allograft rejection. *Proc. R. Soc. B* **266**, 2217–2223 (1999).
43. Rayner, S. A. et al. Local bioactive tumour necrosis factor (TNF) in corneal allotransplantation. *Clin. Exp. Immunol.* **122**, 109–116 (2000).
44. Ruohonen, S. et al. Cytokine responses during chronic denervation. *J. Neuroinflamm.* **2**, 26 (2005).
45. Keller, M. et al. A circadian clock in macrophages controls inflammatory immune responses. *Proc. Natl Acad. Sci. USA* **106**, 21407–21412 (2009).
46. Yde, P., Mengel, B., Jensen, M. H., Krishna, S. & Trusina, A. Modeling the NF-κB mediated inflammatory response predicts cytokine waves in tissue. *BMC Syst. Biol.* **5**, 115 (2011).

Acknowledgements

We are grateful Jordi Garcia-Ojalvo, Namiko Mitarai, Andrew Oates and Ala Trusina for valuable discussions. S.K. thanks the NCBS-TIFR and the Simons Foundation for funding. M.L.H. and M.H.J. acknowledge support from the Danish Council for Independent Research and Danish National Research Foundation through StemPhys Center of Excellence, grant number DNRF116.

Author contributions

M.L.H., S.K. and M.H.J. developed the models. M.L.H. performed the numerical simulations. M.L.H., S.K. and M.H.J. wrote the paper.

Additional information

Supplementary Information accompanies this paper at https://doi.org/10.1038/s41467-018-07932-1.

Competing interests: The authors declare no competing interests.

Reprints and permission information is available online at http://npg.nature.com/reprintsandpermissions/

Publisher's note: Springer Nature remains neutral with regard to jurisdictional claims in published maps and institutional affiliations.

Inferring leading interactions in the p53 network through live-cell imaging and modeling

Mathias Heltberg[1,2*], Sheng-hong Chen[2, 3*], Alba Jimenez[2], Mogens H. Jensen[1+], Galit Lahav[2+],

Affiliations:

[1]Niels Bohr Institute, University of Copenhagen, 2100 Copenhagen, Denmark

[2]Department of Systems Biology, Harvard Medical School, Boston, MA, USA

[3] Institute of Molecular Biology, Academia Sinica, Taipei, Taiwan

[*]Co-first author

[+]Correspondence: galit@hms.harvard.edu, mhjensen@nbi.ku.dk

Highlights

- A model of autonomous p53-Mdm2 oscillator was built to examine regulatory functions of Mdmx in p53 dynamics.
- Mathematical modeling reveals that enhanced p53 degradation instead of transcriptional inhibition is the most critical function of Mdmx.
- Mdm2-dependent degradation of p53 is facilitated by Mdmx and hindered by ATR after damage.

Abstract

The tumor suppressor protein p53 is a master regulator of stress responses. In non-stressed conditions it is maintained at low levels due to its suppression by the oncogenes Mdm2 and Mdmx. Earlier work in single cells revealed that depletion of Mdmx leads to two phases of p53 dynamics; an initial post-mitotic pulse followed by oscillations. The mechanism leading to this complex dynamical behavior is unknown. In addition, while the structure of the p53/Mdm2/Mdmx network is well known, we still lack a detailed, quantitative understanding of their functional interactions under various conditions. Here, we developed a simple mathematical model of the p53/Mdm2/Mdmx system and investigated which of their known interactions quantitatively affects different features of p53 dynamics. We found that the Mdm2-dependent degradation of p53, facilitated by Mdmx, is the most critical interaction regulating p53 dynamics in non-stressed conditions. Further, we used our model to predict p53 behavior following DNA damage in Mdmx depleted cells. We then acquired new live single-cell data to constrain the model and identified specific regulatory mechanisms responsible for the DNA-damage dose-dependent and -independent features of p53 dynamics. Our integrated imaging with modeling approach provided a new model for p53 dynamics and suggested specific Mdmx-mediated suppressive mechanisms for regulating oscillations in the p53 system. Similar approaches can be applied to reveal the most impactful interactions regulating the dynamics of key proteins in additional systems in human cells.

Introduction

Decades of research in molecular biology and biochemistry led to the identification of the key molecular players that sense and transfer cellular information, and to the assembly of complicated networks describing the interactions between them. Such biological maps often include interac-

tions collected from a large number of studies performed across different conditions. The specific interactions that are functional and dominate the response in each condition, as well as the role of these interactions in triggering the right outcome, often remain elusive. In addition, interactions between genes or proteins in biological networks are represented as a static drawing of binary (inhibitory or activating) arrows connecting different components of the network. To fully understand how information is processed in cells, one needs to move beyond the static description of networks' structure into developing a quantitative understanding of their contributions and behavior in response to different intracellular and extracellular inputs.

One approach for identifying and quantifying functional interactions in biological networks is to investigate the dynamics of key proteins within the network, and use this information for the development of mathematical modeling capturing their behavior (Purvis and Lahav, 2013, Ronen et al., 2002, Jacquet et al,. 2003; Hao and O'Shea, 2012, Tay et al., 2012; Batchelor et al., 2011; Hunziker et al., 2010; Geva-Natorsky et al., 2006; Cirit et al., 2010, Lee et al., 2014; Mengel et al., 2010; Tiana et al., 2002). Such dynamical data are complementary to the information originally used to describe biological networks, and have great potential to provide new insights into the relationship between network structure and its function. Furthermore, such insights are crucial for better understanding the underlying causes of disease, and for developing therapeutics that quantitatively target protein dynamics (Behar et al., 2013). Here we used the complex dynamics of the tumor suppressor protein p53 in single cells together with modeling to identify dominant interactions in the network controlling p53 and the relative contribution of these interactions in triggering specific dynamical outcomes under basal and DNA damage conditions.

p53 is a transcription factor and a master regulator of stress responses. In non-stressed conditions, the p53 protein is maintained at low levels due to its suppression by the oncogenes Mdm2 and Mdmx (Wade et al., 2013). The circuit describing the interactions between p53, Mdm2 and MdmX is complex (Figure 1A). First, the core of this circuit includes a negative feedback loop between p53 and Mdm2 (Genes Dev. 1993 Jul;7(7A):1126-32. The p53-mdm-2 autoregulatory feedback loop.)(Lahav et al., 2004; Bar-Or et al., 2000); p53 activates the transcription of Mdm2, while Mdm2 negatively regulates p53 stability by promoting its ubiquitination and degradation (Oncogene. 1998 Nov 12;17(19):2543-7. Mdm2 association with p53 targets its ubiquitination.). The oncogene Mdmx feeds into both of these interactions between p53 and Mdm2. (Figure 1A) (Barboza et al., 2008; Karni-Schmidt et al., 2016; ElSawy et al., 2013). On the one hand, Mdmx catalyzes Mdm2-mediated p53 ubiquitination and degradation through its heterodimerization with Mdm2 (Wang et al., 2011) (Figure 1A, blue arm). On the other hand, Mdmx suppresses p53 transcriptional activity through its competitive binding with transcriptional cofactors to p53 trans-activation domain (Pei et al., 2012) (Figure 1A, orange arm). This high connectivity and multiplicity of interactions between p53, Mdm2 and Mdmx make it difficult to detangle the relative contribution of each arrow under different conditions (Mancini et al., 2010).

The dynamics of p53 following manipulation of its key regulators can serve as a platform for identifying functional leading interactions, and how quantitatively they regulate p53. It was recently discovered that suppression of Mdmx triggers complicated two-phase dynamics of p53 in single cells (Chen et al., 2016); in the first phase, p53 undergoes a pulse following cell division. In the second phase, p53 shows a series of undamped oscillations. The mechanism leading to p53 biphasic dynamics following Mdmx suppression is unknown. In addition, p53 oscillations during the second phase of the response to Mdmx suppression resembled (both in frequency and amplitude) the previously described p53 oscillations in response to DNA damage (Chen et al., 2016; Batchelor et al., 2008). However, the previous molecular mechanisms suggested for p53 oscillations did not incorporate Mdmx regulation on p53 and Mdm2 (Purvis et al., 2012; Batchelor et al., 2011; Geva-Natorsky et al., 2006; Lahav et al., 2004; Batchelor et al., 2008). Therefore, the relative quantitative contribution of the interactions between p53/Mdm2 and Mdmx (Figure 1A) in controlling p53 dynamics remain not known.

Here we infer and quantify the leading interactions between p53, Mdm2 and Mdmx through a combination of time-lapse single-cell imaging and computational modeling. The complicated dynamics of p53 following Mdmx depletion (Chen et al., 2016) prompted us to develop a plausible mathematical model for the p53 signaling network. Using the model to simulate p53 dynamics we predicted its behavior under various conditions and validated these temporal dynamics experimentally. We further used these experiments to constrain the model and its parameters allowing us to propose a quantitative mechanism for how p53 and Mdm2 are regulated by Mdmx and the upstream DNA damage signal, and to identify the most critical interactions controlling p53 dynamics in basal conditions and in response to DNA damage.

Results

I. Identifying quantitative features of p53 dynamics and activity following Mdmx depletion

The dynamics of p53 in response to Mdmx depletion in single cells is complex. Our first goal was to identify specific quantitative features of these dynamics in order to guide the mathematical analysis. Depletion of Mdmx leads to two phases of p53 dynamics (Chen et al., 2016). In the first phase, p53 undergoes a high-amplitude pulse following mitosis (Figure 1B, grey region). In the second phase, p53 shows a series of low amplitude oscillations (Figure 1B, yellow region).

We first characterized p53 dynamics during the initial response of the system (Figure 1B, grey region). Because this first phase is triggered after mitosis, we performed an in-silico alignment of all individual single-cell p53 dynamics to the time of cell division. The average population trace (Figure 1C, green trace) shows a strong post-mitotic pulse, while the low-amplitude oscillations are masked by the mean value. Note that the small peak preceding mitosis is due to an increase in auto-fluorescence seen in all channels. From this in-silico alignment we found the average initial pulse (Figure 1D) to be symmetric, i.e. showing identical increasing and decreasing slopes (Figure 1E) and with a maximal amplitude approximately three times larger than the basal level prior to

Mdmx depletion (Figure 1D). Further, we found that the distribution of amplitudes across individual cell traces can be well described by fitting it to a gamma distribution (Figure 1F).

We next characterized p53 dynamics during the second-phase of the response, when it exhibits oscillations (Figure 1B, yellow region). We calculated the Fourier spectrum of individual cell traces as distinct time series. The power spectrum of individual cells confirms that p53 oscillations are well defined and regular, having a frequency of approximately 0.3/hour (Figure 1G). The power spectrum (Figure 1G, y-axis) also provides an estimate of the corresponding amplitude in the best-fitted sinusoidal frequency. As an alternative way to measure the amplitude of oscillations, we used an independent algorithm that estimated the oscillatory amplitude as the distance from each peak to the two neighboring valleys. From this single cell measurements we plotted the distribution of amplitudes during the oscillatory phase which was also well described by a gamma distribution (Figure 1H). Using the most probable amplitude and frequency defined from these algorithms, we showed that a sinusoidal function with these parameters agrees well with the experimentally observed oscillations in single-cells (Figure 1I), showing the regularity of p53 oscillations. Note that the amplitude shows a higher variation than the frequency, which was relatively stable as was previously reported for p53 oscillations post DNA damage (Geva-Natorsky et al., 2006; Reyes et al., 2018).

In order to quantitatively determine the role Mdmx has on p53's transcriptional activity (Figure 1A, orange arm), we compared the ratio of Mdm2 to p53 in individual cells, before and after Mdmx depletion using immunofluorescence (Figure 1J). We found that depletion of Mdmx shifts the mean of the distribution to a higher value, meaning that more Mdm2 proteins are produced per p53 protein when Mdmx is depleted. This finding agrees with previous studies suggesting that Mdmx suppresses p53 transcriptional activity (ElSawy et al., 2013; Pei et al., 2012).

Following these sets of observations and measurements, we identified three key quantitative features of p53 dynamics and activity following Mdmx depletion: (I) an initial high amplitude symmetric pulse; (II) sustained low-amplitude oscillations; (III) a shift in the Mdm2/p53 distribution (Figure 1K). Next, we used these quantitative features to guide us in developing a mathematical model of p53 and Mdm2 regulation by Mdmx.

II. Mathematical model points to the specific functional interactions regulating p53 dynamics by Mdmx in non-stressed conditions.

In order to asses the effect of Mdmx onto the core p53-Mdm2 network, we first developed a minimal model of the p53-Mdm2 feedback-loop using the two ordinary differential equations below:

$$\frac{d}{dt}[p53] = \alpha - \beta \cdot [Mdm2]\frac{[p53]}{\gamma + [p53]}$$

$$\frac{d}{dt}[Mdm2] = \psi \cdot [p53(t - \tau_{Del})] - \delta \cdot [Mdm2]$$

In this model, p53 is produced at a constant rate (α) and degraded upon binding to Mdm2 through a saturated degradation process (β, γ), whereas Mdm2 is produced proportionally to the p53 level (ψ) and degraded through a first-order decay process (δ) (Figure 2A). We restricted the model to include a minimal number of parameters, as no cooperativity is assumed (e.g. use of Hill coefficients). We used numerical analysis to choose appropriate values for each biological parameter (SI, sections I and II). Particularly, in order to recapitulate p53 oscillatory behavior, we found that a time delay (T*Del*) mimicking the transcription and translation processes in the cell is required for oscillations to occur. Thus, these two equations serve as a minimal model for p53 oscillatory behavior.

We use this minimal model to investigate the potential interactions between Mdmx and the p53-Mdm2 feedback. Mdmx can potentially affect p53 degradation, interfere with p53 transcriptional activity or modify the time-delay for Mdm2 production (Figure 1A). To model these potential effects, we introduced a series of parameters λ_i that we refer to as impact factors. Impact factors λ_1 and λ_2 account for Mdmx's effect on p53 degradation affecting biological parameters (β) and (γ) respectively (Figure 2B) while λ_3 and λ_4 account for Mdmx's effect on p53 transcriptional activity (ψ) and time delay (T_{Del}) respectively (Figure 2C).

$$\beta \rightarrow \beta(1 + \lambda_1[Mdmx])$$
$$\gamma \rightarrow \gamma(1 + \lambda_2[Mdmx])$$
$$\psi \rightarrow \psi(1 - \lambda_3[Mdmx])$$
$$\tau_{Del} \rightarrow \tau_{Del}(1 + \lambda_4[Mdmx])$$

Our goal is to investigate which potential interaction of Mdmx best recapitulates the quantitative features of p53 dynamics following Mdmx depletion. For that, we tested the effect of each impact factor separately. We simulated p53 dynamics using a range of values for each factor (Figure 2D-G) and assesed whether the simulations reproduced the experimentally observed p53 dynamics.

We found that incorporating impact factor λ_1 led to the best fit to p53 dynamics following Mdmx depletion. Before Mdmx depletion, all tested values of λ_1 led to a steady state level of p53, with higher λ_1 leading to lower basal levels of p53 (Figure 2D). After Mdmx depletion, a large pulse is observed followed by oscillations (Figure 2D). It is noted that, as λ_1 increases, so does the height of the initial pulse. However the amplitude of oscillations does not vary with λ_1. Interestingly, incorporating impact factor λ_2 leads to p53 oscillations after depletion but does not reproduce the initial high-amplitude pulse of p53 (Figure 2F). Last, introducing either impact factors λ_3 or λ_4 results in oscillatory p53 behavior before Mdmx depletion, which does not fit our experimental ob-

servations (Figure 2E and 2G). Based on these simulations, we concluded impact factor λ_1, which accounts for the role of Mdmx in enhancing p53 degradation by Mdm2, is critical for generating p53 biphasic dynamics and can recapitulate the first two key features of p53 dynamics following Mdmx depletion (i.e. an initial pulse followed by sustained low-amplitude oscillations).

In order to better understand the role of impact factor λ_1 on p53 dynamics we used tools of dynamical systems theory. We visualized how the phase portrait of the p53-Mdm2 network is affected by λ_1. As we explored a wide range of λ_1 values, we observed that small values can lead to oscillations before Mdmx depletion. As λ_1 increases, oscillations dampen, see the progressive narrowing of the limit cycle in Figure 2H. This observation further strengthens our previous choice of λ_1 values for p53 simulations, with values high enough to reproduce the observed p53 steady-state levels before Mdmx depletion (Figure 2D). A second phase portrait of the p53-Mdm2 system drawn after Mdmx depletion shows how the system transitions from a steady state (green zone) to an oscillatory regime (red zone) (Figure 2D and Figure 2I). The transition occurs through an initial pulse which is described by the colored trajectories in Figure 2I. For increasing values of λ_1, the trajectory takes a longer path to reach the oscillatory regime. The length of the trajectory corresponds to the height of the initial pulse, thus explaining how increasing values of λ_1 lead to higher amplitudes of the initial pulse (Figure 2D).

We next investigated whether the effect of Mdmx on p53 degradation through impact factor λ_1 can also capture the third quantitative feature of p53 dynamics; the shift in the ratio between Mdm2/p53 (Figure 1J and 1K). We found that incorporating λ_1 alone is insufficient for accounting for this shift as was observed experimentally (compare Figure 1J to Figure 2J). In order to capture the shift, we chose to test the effect of impact factor λ_3, which accounts for the direct effect of Mdmx on Mdm2 transcription by p53 (parameter ψ) and therefore is a good candidate to affect the ratio of Mdm2/p53 (see SI). From the immunofluorescence data, we extracted the average ratio of Mdm2/p53 both in the control and Mdmx depleted cells. These values can be used to set the bounds for the value of λ_3. We predicted that values of λ_1 equal to 3 and λ_3 equal to 0.15 could capture the shift in the Mdmx/p53 distribution (see detailed analysis in SI). Indeed, the resulting distribution when considering both factors shifted after Mdmx depletion as was experimentally observed (compare Figure 1J to Figure 2K). In order to test whether including λ_3 affected any of the quantitative features λ_1 could recapitulate, we further tested the amplitude of the initial p53 pulse as a function of λ_1 for different values of λ_3. We found that the amplitude of the pulse is almost solely defined by the value of λ_1 (Figure 2L). Therefore, a high value of λ_1 ($\lambda_1 = 3.0$) is chosen to maintain p53 at steady state before Mdmx depletion and a small value of λ_3 ($\lambda_3 = 0.15$) is chosen to capture the shift in the Mdmx/p53 distribution.

Combining both impact factors (λ_1 and λ_3) at the fixed values mentioned above, we simulated the system with internal and external noise (applying Chemical Langevin equation) to examine its robustness. We confirmed a robust biphasic dynamics of p53 after Mdmx depletion in the presence

of noise that accurately captured the experimental behavior in single cells (Figure 2M). Taken together our mathematical analysis shows that the Mdmx-mediated p53 degradation through impact factor λ_1 and Mdmx-mediated regulation of p53 activity through impact factor λ_3 are sufficient for capturing the three quantitative features of p53 biphasic dynamics following Mdmx depletion including the initial high amplitude pulse, the low amplitude oscillations and the shifted distribution of Mdm2/p53 with increased variance.

III. Simulation of the model predicts the effect of Mdmx on p53 dynamics after DNA damage

Having optimized λ_1 and λ_3 to mimic the observed p53 dynamics before and after Mdmx depletion, we propose a unified model of the core p53-Mdm2-Mdmx feedback. We now aim to apply this model to investigate the effect of DNA damage on p53, particularly the potential p53 dynamics that result from combining Mdmx depletion and DNA damage.

We aim at studying the biological response to DNA damage after UV-radiation. UV-radiation results in activated ATR, a PI3 kinase-related kinase that stabilizes p53 through inhibitory phosphorylation of Mdm2. We thus expanded our model to incorporate the effect of DNA damage through ATR activation. To more accurately reflect the biological response to DNA damage, we introduced a function that describes ATR dynamics following UV-radiation (Figure S2). ATR activity reaches a maximal UV dose-dependent level right after radiation then decays exponentially representing the repair of DNA damage (FigureS3). Further, we modeled ATR inhibition of Mdm2-mediated p53 degradation through two impact factors (κ1 and κ2) (Figure 3A):

$$\beta_{Mdmx} \rightarrow \beta_{Mdmx}(1 - \frac{ATR}{ATR + \kappa_1})$$
$$\gamma \rightarrow \gamma(1 - \frac{ATR}{ATR + \kappa_2})$$

Note that β_{Mdmx} refers to the initial value of β now being affected by Mdmx through impact factor λ_1. We used our extended model to compare the effects of UV-radiation alone (Figure 3B, D) to that of Mdmx depletion followed by UV-radiation (Figure 3C, E). We introduced three doses of UV-radiation through three different values of κ_1 and κ_2 (see Methods).

It was previously shown experimentally that the p53 dynamics in response to UV radiation consists of a large pulse with an amplitude that scales with UV dose (Batchelor et al., 2011). In Figures 3B to 3E, we observed that only impact factor κ_1 had a strong effect on the amplitude of the UV-triggered p53 pulse. Specifically, ATR activation (through its effect on κ_1) led to a single p53 pulse with an amplitude that scaled with κ_1 value (Figure 3B). In contrast, activation of ATR through κ_2 led to oscillations with no initial p53 pulse across all tested values (Figure 3D, E). This

suggests that ATR inhibition of Mdm2-mediated p53 degradation occurs through impact factor κ1 that affects β (degradation of p53 by Mdm2).

Interestingly, when we consider the effect of ATR through impact factor κ1 in cells with Mdmx suppression, we found the amplitude and duration of the UV-induced pulse to be higher (Figure 3C) compared to those with UV-radiation alone (Figure 3B). Furthermore, the model predicted that in Mdmx depleted cells the initial pulse caused by UV-radiation is followed by a series of p53 oscillations (Figure 3C).

We next analyzed how different UV doses might affect the slope (Figure 3F) and amplitude (Figure 3G) of the UV-triggered initial p53 pulse. Simulation of the model using a range of values for κ_1 suggests that both the slope and height of the initial p53 pulse increase with the dose of UV-radiation (Figure 3F, G). A similar trend was predicted for Mdmx depleted cells, although the model also predicts that the slope and amplitude of the p53 initial pulse will be higher in these cells (Figures 3F and G; blue curves).

Lastly, we tested how different UV doses might affect the amplitude of p53 oscillations following the initial p53 pulse in response to UV in Mdmx depleted cells. The model simulations measure the relative increase in the oscillatory amplitude after UV as we vary κ_1 and κ_2 independently (Figure 3H). First, we observe that impact factor κ_2 holds a stronger effect in changing the oscillatory amplitude. Second, for all values of impact factors κ_1 and κ_2, the amplitude of p53 oscillations following UV is independent of the UV dose. Taken together our model suggests that a combined treatment of Mdmx depletion followed by UV radiation will lead to a large p53 pulse (Figures 3C, 3G) followed by oscillations (Figures 3C, 3H). In addition, our model predicts that the UV-triggered p53 oscillations will have higher amplitude compared to the oscillations prior to UV (Figures 3C, 3G).

IV. Experimental data confirming the effect of Mdmx on p53 dynamics in response to UV

We next tested experimentally whether our mathematical model could predict the potential p53 dynamics that result from combining Mdmx depletion and DNA damage. Cells were exposed to UV alone (8 J/m^2 or 16 J/m^2) (upper single-cell p53 traces in Figure 4A and Figure 4B) or to UV after Mdmx depletion (lower single-cell p53 traces in Figure 4A and Figure 4B). Single-cell p53 traces are colored according to their dynamic behavior: before treatment (white region), initial response (grey region) and long-term response (yellow region); and the average population behavior is shown in Figures 4C and 4D.

We first characterized the first phase of p53 dynamics, a pulse triggered by UV. As was previously observed (Batchelor et al., 2011), when cells are subjected to UV-radiation alone, p53 shows a single pulse with an amplitude that increases with dose (upper single-cell traces Figure 4A, B and

red traces Figure 4C, D). When UV-radiation is combined with Mdmx depletion, this initial pulse shows a larger amplitude and duration (Figure 4A, B, F, H). Note that, as predicted by our model, an increase in the UV dose leads to a larger slope (Figure 3H, Figure 4E, G) and higher amplitude of the pulse (Figure 3G, Figure 4F, H).

We next characterized the long-term response of p53 dynamics. In agreement with our model predictions, in the combined treatment (UV and Mdmx depletion), the initial single pulse was followed by oscillations with higher amplitude compared to before UV treatment (lower single-cell traces Figures 4A and 4B). In order to characterize the series of oscillations observed in Mdmx-depleted cells following the initial UV-triggered pulse, we calculated the Fourier spectrum (Figures 4I and 4J) and distribution of amplitudes (Figures 4K and 4L) for both UV doses. While the frequencies of the oscillations were similar to the oscillations resulting from Mdmx depletion alone (compare Figure 1G with Figures 4I and 4J), the amplitude of oscillations was approximately two times larger compared to the amplitude resulting from Mdmx depletion alone (in Figure 4 K & 4L compare gamma fits in yellow from of Figure 1H with current gamma fits in blue). For both observations, the maintenance of the oscillatory frequency and the increase in oscillatory amplitude were independent of the UV-dose. Note that, the increase in the oscillatory amplitude is in agreement with the predictions generated by our model (compare Figure 3B with Figure 3C).

The main features of p53 dynamics in response to Mdmx depletion combined with UV-radiation (an enhanced UV-triggered initial pulse followed by large-amplitude oscillations) were all captured in our model. Following the strong agreement between our model and experimental results, we concluded that the effect ATR has on Mdm2-mediated degradation of p53 through impact parameter β is the function that dominates the p53 dynamical response following DNA damage.

Indeed, we found that the Mdm2-dependent degradation of p53 (facilitated by Mdmx and hindered by ATR) is the most critical interaction regulating p53 dynamics both in non-stressed conditions and following DNA damage. A final model that captures the dependencies of parameters (β) and (ψ) to Mdmx and ATR can be found in the Supplementary Information.

V. Discussion

How dynamics of signaling molecules emerge through interacting components in space and time remains an unresolved question. Here we investigated the regulation of p53 dynamics through a combination of single-cell imaging and mathematical modeling. Specifically, we focused on the role of Mdmx in regulating p53 dynamics in both non-stressed conditions and after DNA damage. Our previous observation of p53 oscillations in the absence of DNA damage inspired us to construct a minimal mathematical model of the p53-Mdm2 signaling system with minimum free parameters and no nonlinearity.

Using three prototypic features of the p53 dynamics as the guidelines, we simulated the effect of each Mdmx-mediated molecular mechanism in regulating p53 dynamics using the minimal p53-Mdm2 model. By comparing experimental results with simulations, we proposed that Mdmx-mediated p53 degradation plays a major role in regulating p53 biphasic dynamics. It is tempting to speculate that Mdmx's main function could be to maintain p53 levels at low steady state by constantly catalyzing Mdm2-mediated p53 ubiquitination. In non-stressed conditions, p53 undergoes a single pulsatile induction during G1/S cell cycle phase (Loewer et al., 2010). Thus, it is possible that ubiquitination activity of the Mdmx/Mdm2 complex toward p53 is rhythmic and is the lowest during the G1/S cell cycle phase. In support of this hypothesis, Mdm2 has been implicated in regulating cell cycle progression by targeting cell-cycle machineries (Frum et al., 2009; Giono et al., 2017). It remains to be tested if the same mechanism applies to Mdmx.

UV radiation has been shown to induce a graded p53 response (Batchelor et al., 2011). However, it is unclear how signaling proteins shape the UV-induced p53 pulse. After Mdmx suppression, the p53 pulse showed higher slope and amplitude following UV-irradiation (Figures 4E, 4G, and 4H), suggesting an inhibitory role of Mdmx via modulation of the slope and height of the p53 pulse. Interestingly, ths inhibitory effect is not obvious when a low UV dose (8 J/m^2) was applied to cells (Figure 4F). It is possible that there is a technical challenge in quantifying a mild increase in amplitude due to the low basal level of p53. Alternatively, the amplitute could be dampened by unknown signaling proteins and this dampening effect is relieved at high UV dose.

How signal-specific p53 dynamics emerge and specify transcriptional programs for cellular decision remains elusive. It has been shown that p53 oscillations are flexible in amplitute but robust in period (Chen et al., 2016). It remains unclear if different amplitudes of p53 oscillations activate distinct transcriptional programs and therefore encode distinct biological information for cell state determination (Purvis and Lahav 2013). The fact that ATR activation leads to a higher amplitude of p53 oscillations provides a plausible approach to further dissect functions of p53 amplitude. From the dynamics point of view, Mdmx acts as a key suppressor of p53 oscillations in both non-stressed conditions and after gamma-irradiation (Chen et al., 2016). It remains to be tested if other cellular signals modulate p53 dynamics through regulating Mdmx stability or its binding to p53. Clinically, Mdmx overexpression is observed in multiple cancers (Wade et al., 2013; Gembarska et al., 2012; Danovi et al., 2004). Thus, it would be interesting to further investigate the role of Mdmx in regulating p53 dynamics in *MDMX* overexpressed cancers as well as cancers with wild type *TP53*.

Oscillatory dynamics are widely observed in various biological processes including circadian rhythm (Kitayama et al., 2008; Sancar et al., 2010), immune response (Hoffmann et al., 2002; Nelson et al., 2004), stress response (Jacquet et al., 2003; Lahav et al., 2004) and development (Dequéant et al., 2006; Kobayashi et al., 2009). To understand how these oscillations emerge and what biological functions are encoded in these oscillations, it is critical to take multifaceted quantitative approaches. Here, we took an integrative approach combining single-cell quantitative

imaging with mathematical modeling to identify key regulatory mechanisms underlying p53 dynamics. Our study provides an example to examine mechanisms responsible for signaling dynamics by developing a minimal mathematical platform based on quantitative perturbations of signaling dynamics in single cells. This platform can be the basis to study p53 dynamics in various biological contexts in the future.

Material and methods:

Cell Culture and UV radiation

MCF7 cells were grown in RPMI + 10% fetal bovine serum (FBS) supplemented with selective antibiotics (400 μg/ml G418, 5 μg/ml blasticidin, and 0.5 μg/ml puromycin) when needed. The MCF7 p53 reporter cell line have been previously described (Giorgio Gaglia, Yinghu Guana, Jagesh V. Shaha, and Galit Lahav. Activation and control of p53 tetramerization in individual living cells PNAS, 2013). UV was delivered to cells using a UV lamp with a rate of 1.5 $J/m^2/s$. All UV were performed in a single burst.

Reagents

Antibodies were used against Mdm2 (SMP14, Santa Cruz), p53 (DO1 and FL-393, Santa Cruz). Small interfering RNAs targeting MDMX (sequences: AGCCCTCTCTATGATATGCTA and GACCACGAGACGGGAACATTA) from Qiagen were used for MDMX knockdown. Two siRNAs show qualitatively identical results. For all MDMX knockdowns, 5nM of siRNA was used unless stated otherwise.

Live-Cell Microscopy

Cells were grown in RPMI without phenol red and riboflavin + 10% FBS in poly-D-lysine coated glass-bottom plates (MatTek Coporation) for two days before imaging. We used Nikon Eclipse TE-2000 inverted microscope with a 20× plan apo objective (NA 0.75) with a Hammamatsu Orca ER camera. The microscope was equipped with an environmental chamber controlling temperature, atmosphere (5% CO2), and humidity. Images were acquired every 30 min for 24-72 hr controlled by MetaMorph Software (Molecular Devices). Image analysis was done with ImageJ (NIH) and Matlab (MathWorks).

Immunofluorescence

Cells were grown on glass-bottom plates (MatTek Coporation) coated with poly-D-lysine and fixed with 4% paraformaldehyde. Cells were permeabilized in PBS/1% Triton for 5 min, blocked with 2% BSA, incubated with primary antibody overnight, washed, and incubated with secondary antibody coupled to either Alexa488 or Alexa647 for one hour. After washing, cells were stained with DAPI and embedded in imaging media (20mM Tris-HCl, ph8.0, 2.5% DABCO and 80% Glycerol). Images were acquired with a 20× plan apo objective (NA 0.75) with the appropriate filter sets. Image analysis was done with CellProfiler. At least fifty thousand cells were measured per condition.

Choice in the range of values for impact factors

The range of values for impact factors in Figure s 2D-G and 3B-E were chosen taking into account how each factor affected p53 dynamics. The ranges explored allow for the correct visualization of p53 levels. The ranges explored correspond to three-fold changes as follows: λ_1: (1; 2; 3), λ_2: (2; 4; 6), λ_3 (0.25; 0.5; 0.75), λ_4 (0.5; 1; 1.5), $\kappa 1$: (0.1; 0.25; 1) and $\kappa 2$: (0.01; 0.025; 0.1). Fourier spectrums of Figures 1G, 4I and 4J were calculated using a Matlab FFT algorithm.

Figure 1

A) Schematic diagram of Mdmx regulating p53. Mdmx acts to inhibit the p53-Mdm2 oscillator through two arms: degradation of p53 through catalyzing Mdm2-mediated ubiquitination (blue left arm) and inhibition of p53 transcriptional activity (orange right arm).

B) Four representative single-cell time series of p53 dynamics following Mdmx depletion. The grey region indicates the initial pulse while the yellow region highlights the sustained oscillations.

C) p53 population dynamics obtained by averaging individual cell traces over time. Green bold line and green shaded areas correspond to mean and standard deviation respectively. Individual p53 traces were aligned based on the time of cell division.

D) Mean value of the initial peak following Mdmx depletion.

E) Increasing (Rise) and decreasing (Fall) slopes of the initial p53 pulse.

F) Histogram showing the distribution of amplitudes of the initial p53 pulse. Fitted gamma distribution in red.

G) Fourier spectrum of the sustained oscillations. The red dots mark the highest Fourier signal for each individual cell. The height of the peak correspond to the amplitude of the most dominant frequency of oscillation.

H) Histogram showing the distribution of amplitudes of the oscillatory phase.

I) Comparison of a single cell oscillatory expression (green) to a modelled sinusoidal oscillation (red) with amplitude and frequency corresponding to the most probable values of the Fourier spectrum in Figure 1G.

J) Distribution of the Mdm2/p53 ratio before (black) and after (red) Mdmx depletion based on the immunofluorescent staining of Mdm2 and p53 in single cells. Before (mean=1.26; sd=0.14) and after MdmX depletion (mean=1.38; sd=0.23). Vertical lines show the corresponding mean values.

K) Characteristic features of p53 dynamics following Mdmx depletion. A large initial pulse (I) is followed by sustained oscillations (II). A shift in the ratio between Mdm2 and p53 (III).

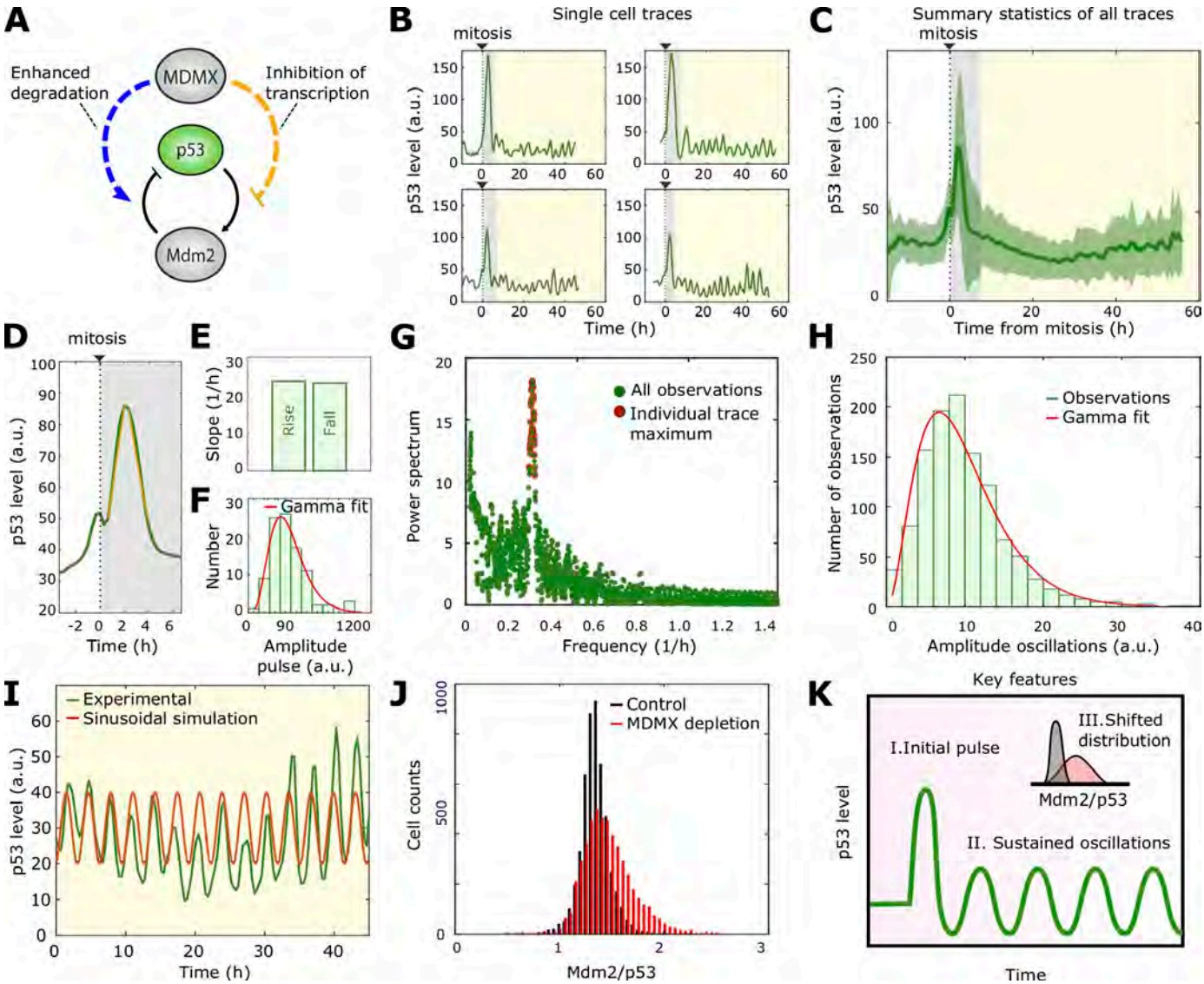
A
Enhanced degradation
MDMX
Inhibition of transcription
p53
Mdm2
B
Single cell traces
mitosis
p53 level (a.u.)
Time (h)
C
Summary statistics of all traces
mitosis
p53 level (a.u.)
Time from mitosis (h)
D
mitosis
p53 level (a.u.)
Time (h)
E
Slope (1/h)
Rise
Fall
F
Gamma fit
Number
Amplitude pulse (a.u.)
G
All observations
Individual trace maximum
Power spectrum
Frequency (1/h)
H
Observations
Gamma fit
Number of observations
Amplitude oscillations (a.u.)
I
Experimental
Sinusoidal simulation
p53 level (a.u.)
Time (h)
J
Control
MDMX depletion
Cell counts
Mdm2/p53
K
Key features
I.Initial pulse
III.Shifted distribution
Mdm2/p53
II. Sustained oscillations
p53 level
Time

Figure 2

A) Schematics of the p53-Mdm2 negative feedback loop with the parameters (β, γ, ψ, T_{Del}) in our mathematical model.

B) Possible mechanisms for Mdmx-mediated p53 degradation through enhancing Mdm2-mediated p53 poly-ubiquitination.

C) Possible mechanism of Mdmx-mediated inhibition of p53 transcriptional activity through competitive binding.

D) Effects of Mdmx through impact factor λ_1 on parameter β. Before Mdmx depletion, λ_1 values for blue, red and yellow curves respectively: (1; 2; 3). After Mdmx depletion, λ_1 is set to zero.

E) Effects of Mdmx through impact factor λ_3 on parameter γ. Before Mdmx depletion, λ_3 values for blue, red and yellow curves respectively: (0.25; 0.5; 0.75). After Mdmx depletion, λ_3 is set to zero.

F) Effects of Mdmx through impact factor λ_2 on parameter ψ. Before Mdmx depletion, λ_2 values for blue, red and yellow curves respectively: (2; 4; 6). After Mdmx depletion, λ_2 is set to zero.

G) Effects of Mdmx through impact factor λ_4 on parameter T_{Del}. Before Mdmx depletion, λ_4 values for blue, red and yellow curves respectively: (0.5; 1; 1.5). After Mdmx depletion, λ_4 is set to zero.

H) Evolution of the p53-Mdm2 behavior in phase space when λ_1 increases. Increase in λ_1 drives the limit cycle towards a fixed point.

I) Evolution of the p53-Mdm2 behavior in phase space when λ_1 increases. Increase in λ_1 enhances the amplitude of the initial pulse.

J) Simulations of the distribution of Mdm2/p53 before (black) and after (red) Mdmx depletion, taking into account λ_1 alone (λ_1 =3; λ_3 =0). Mdmx depletion (λ_1 =0; λ_3 =0). Before (mean=1.30; sd=0.11) and after MdmX depletion (mean=1.32; sd=0.22).

K) Simulations of the distribution of Mdm2/p53 before (black) and after (red) Mdmx depletion, taking into account both λ_1 and λ_3 (λ_1 =3; λ_3 =0.15). Mdmx depletion (λ_1 =0; λ_3 =0). Before (mean=1.11; sd=0.09) and after MdmX depletion (mean=1.32; sd=0.22).

L) Amplitude of the initial pulse for distinct combinations of λ_1 and λ_3. λ_3 values for balck, blue, red and yellow dots respectively: (0; 0.25; 0.5; 0.75).

M) 100 simulations of p53 dynamics with Langevin noise before and after Mdmx depletion. We used λ_1 = 3, λ_2 = 0, λ_3 = 0.15, λ_4 = 0. The yellow line represents the deterministic trajectory.

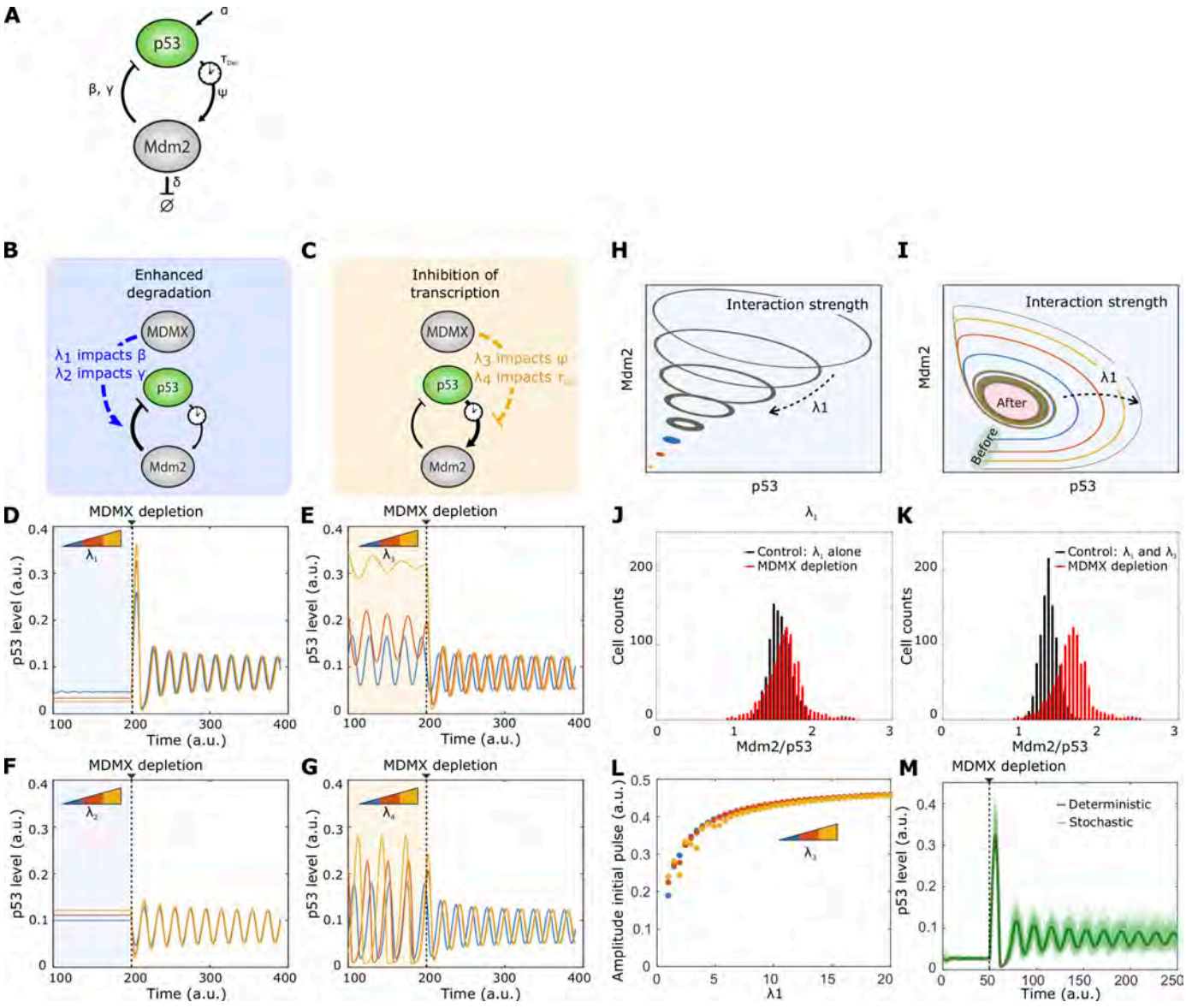
A
p53
Mdm2
α
β, γ
ψ
δ
B
Enhanced degradation
MDMX
λ1 impacts β
λ2 impacts γ
p53
Mdm2
C
Inhibition of transcription
MDMX
λ3 impacts ψ
λ4 impacts τ
p53
Mdm2
H
Interaction strength
Mdm2
p53
λ1
I
Interaction strength
Mdm2
p53
λ1
After
Before
D
MDMX depletion
p53 level (a.u.)
Time (a.u.)
E
MDMX depletion
p53 level (a.u.)
Time (a.u.)
J
Control: λ1 alone
MDMX depletion
Cell counts
Mdm2/p53
K
Control: λ1 and λ3
MDMX depletion
Cell counts
Mdm2/p53
F
MDMX depletion
p53 level (a.u.)
Time (a.u.)
G
MDMX depletion
p53 level (a.u.)
Time (a.u.)
L
Amplitude initial pulse (a.u.)
λ1
M
MDMX depletion
Deterministic
Stochastic
p53 level (a.u.)
Time (a.u.)

Figure 3

A) Schematics of the p53-Mdm2 system with regulation by Mdmx and ATR. ATR inhibits Mdm2-mediated p53 degradation through two impact factors (κ1 or κ2)

B, D) p53 dynamics before and after UV-radiation with ATR effects through B) κ1 or D) κ2.

C, E) p53 dynamics with Mdmx depletion followed by UV-radiation when considering ATR effects through C) κ1 or E) κ2.

B-E) Before UV, κ1 and κ2 are set to zero. After UV, κ1 values for blue, red and yellow curves respectively: (0.1; 0.25; 1) and κ2 values for blue, red and yellow curves respectively: (0.01; 0.025; 0.1).

F) Slope of the p53 initial pulse with increasing UV dose.

G) Amplitude of the p53 initial pulse with increasing UV dose.

H) Amplitude of the p53 sustained oscillations after the initial pulse for different levels of κ2, blue, red and yellow curves respectively: (0.01; 0.025; 0.1) and κ1 fixed (1).

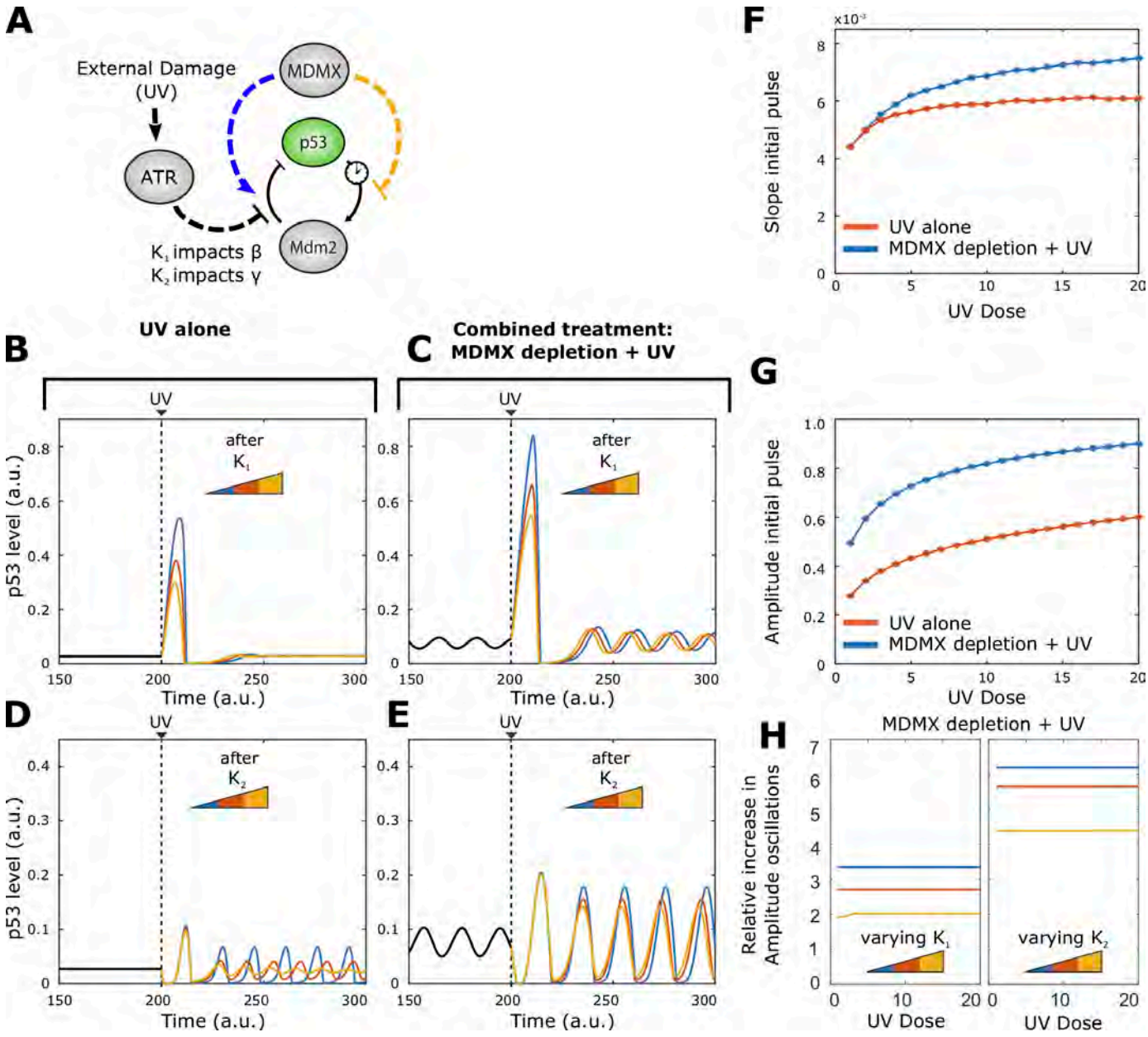
A
External Damage
(UV)
MDMX
p53
ATR
Mdm2
K1 impacts β
K2 impacts γ
B
UV alone
C
Combined treatment:
MDMX depletion + UV
UV
after
K1
p53 level (a.u.)
Time (a.u.)
D
E
after
K2
F
Slope initial pulse
x10-3
UV alone
MDMX depletion + UV
UV Dose
G
Amplitude initial pulse
H
MDMX depletion + UV
Relative increase in
Amplitude oscillations
varying K1
varying K2

Figure 4

A-B) Four representative single-cell time series of p53 dynamics (before treatment (white region), initial response (grey region) and long-term response (yellow region) following UV-radiation (8 and 16 J/m^2 respectively). The bottom two panels show prior Mdmx depletion.

C-D) Mean p53 dynamics trajectories (bold lines) ± std deviation (shaded areas) before and after UV-radiation radiation (8 and 16 J/m^2 respectively). Red traces corresponds to p53 under UV only. Blue traces show p53 dynamics with prior Mdmx depletion followed by UV.

E-F) Slope (E) and amplitude (F) of the p53 initial pulse after UV-radiation (8 J/m2) without (red) and with Mdmx depletion (blue).

G-H) Slope (G) and amplitude (H) of the p53 initial pulse after UV-radiation (16 J/m2) without (red) and with Mdmx depletion (blue).

I-J) Fourier spectrum of the sustained oscillatory phase (I, J) after UV-radiation (8 and 16 J/m^2 respectively).

K-L) Distribution of amplitudes of the p53 oscillations (K, L) following UV-radiation (8 and 16 J/m^2 respectively).

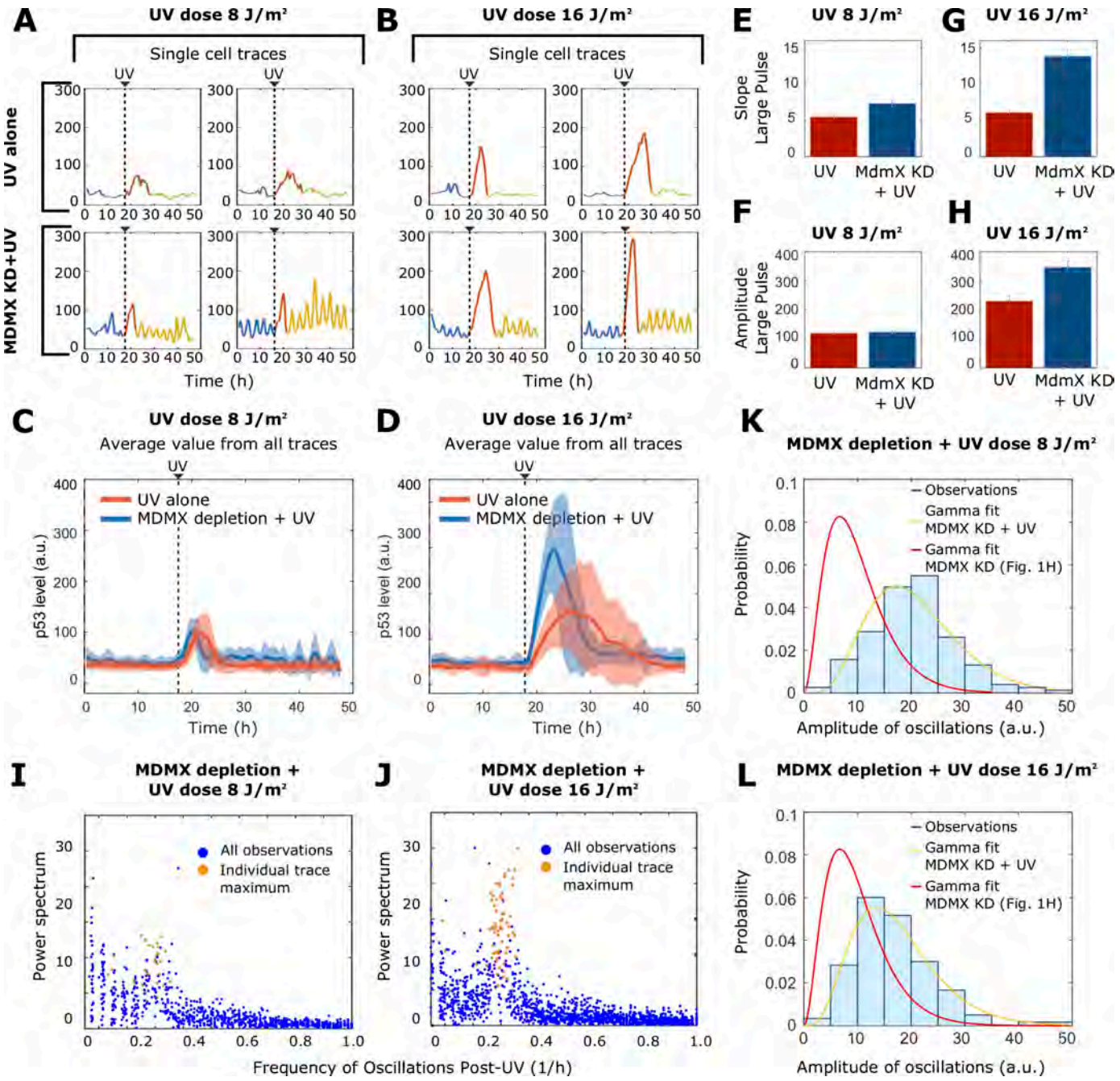
A
UV dose 8 J/m²
Single cell traces
UV alone
MDMX KD+UV
UV
Time (h)
B
UV dose 16 J/m²
Single cell traces
Time (h)
E
UV 8 J/m²
Slope Large Pulse
UV
MdmX KD + UV
G
UV 16 J/m²
F
UV 8 J/m²
Amplitude Large Pulse
H
UV 16 J/m²
C
UV dose 8 J/m²
Average value from all traces
UV alone
MDMX depletion + UV
p53 level (a.u.)
Time (h)
D
UV dose 16 J/m²
Average value from all traces
K
MDMX depletion + UV dose 8 J/m²
Observations
Gamma fit MDMX KD + UV
Gamma fit MDMX KD (Fig. 1H)
Probability
Amplitude of oscillations (a.u.)
I
MDMX depletion + UV dose 8 J/m²
All observations
Individual trace maximum
Power spectrum
Frequency of Oscillations Post-UV (1/h)
J
MDMX depletion + UV dose 16 J/m²
L
MDMX depletion + UV dose 16 J/m²

References

1. Purvis, J. E., Lahav, G. (2013). Encoding and Decoding Cellular Information through Signaling Dynamics. *Cell*. **152**, 945–956
2. Purvis, J. E., Karhohs, K. W., Mock, C., Batchelor, E., Loewer, A., and Lahav, G. (2012). p53 dynamics control cell fate. *Science*, ***336***(6087), 1440-1444.
3. Ronen, M., Rosenberg, R., Shraiman, B. I., and Alon, U. (2002). Assign-ing numbers to the arrows: parameterizing a gene regulation network by using accurate expression kinetics. *Proceedings of the national academy of sciences*, ***99***(16), 10555-10560.
4. Jacquet, M., Renault, G., Lallet, S., De Mey, J., and Goldbeter, A. (2003). Oscillatory nucleocytoplasmic shuttling of the general stress response transcriptional activators Msn2 and Msn4 in Saccharomyces cerevisiae. *The Journal of cell biology*, ***161***(3), 497-505.
5. Hao, N., and O'shea, E. K. (2012). Signal-dependent dynamics of transcription factor translocation controls gene expression. *Nature structural & molecular biology*, ***19***(1), 31.
6. Tay, S., Hughey, J. J., Lee, T. K., Lipniacki, T., Quake, S. R., & Covert, M. W. (2010). Single-cell NF-κB dynamics reveal digital activation and analogue information processing. *Nature*, ***466***(7303), 267.
7. Batchelor, E., Loewer, A., Mock, C., and Lahav, G. (2011). Stimulus-dependent dynamics of p53 in single cells. *Molecular systems biology*, ***7***(1), 488.
8. Hunziker, A., Jensen, M. H., & Krishna, S. (2010). Stress-specific response of the p53-Mdm2 feedback loop. *BMC systems biology*, ***4***(1), 94.
9. Geva-Zatorsky, N., Rosenfeld, N., Itzkovitz, S., Milo, R., Sigal, A., Dekel, E., Yarnitzky, T., Liron, Y., Polak, P., Lahav, G. and Alon, U., (2006). Oscillations and variability in the p53 system. *Molecular systems biology*, ***2***(1).
10. Cirit, M., Wang, C. C., and Haugh, J. M. (2010). Systematic quantification of negative feedback mechanisms in the extracellular signal-regulated kinase (ERK) signaling network. *Journal of Biological Chemistry*, ***285***(47), 36736-36744.
11. Lee, R. E., Walker, S. R., Savery, K., Frank, D. A., and Gaudet, S. (2014). Fold change of nuclear NF-κB determines TNF-induced transcription in single cells. *Molecular cell*, ***53***(6), 867-879.
12. Mengel, B., Hunziker, A., Pedersen, L., Trusina, A., Jensen, M. H., and Krishna, S. (2010). Modeling oscillatory control in NF-κB, p53 and Wnt signaling. *Current opinion in genetics & development*, ***20***(6), 656-664.
13. Tiana, G., Jensen, M. H., and Sneppen, K. (2002). Time delay as a key to apoptosis induction in the p53 network. *The European Physical Journal B-Condensed Matter and Complex Systems*, ***29***(1), 135-140.
14. Behar, M., Barken, D., Werner, S. L., and Hoffmann, A. (2013). The dynamics of signaling as a pharmacological target. *Cell*, ***155***(2), 448-461.
15. Wade, M., Li, Y. C., and Wahl, G. M. (2013). MDM2, MDMX and p53 in oncogenesis and cancer therapy. *Nature Reviews Cancer*, ***13***(2), 83.
16. Lahav, G., Rosenfeld, N., Sigal, A., Geva-Zatorsky, N., Levine, A. J., Elowitz, M. B., and Alon, U. (2004). Dynamics of the p53-Mdm2 feedback loop in individual cells. *Nature genetics*, ***36***(2), 147.
17. Bar-Or, R. L., Maya, R., Segel, L. A., Alon, U., Levine, A. J., and Oren, M. (2000). Generation of oscillations by the p53-Mdm2 feedback loop: a theoretical and experimental study. *Proceedings of the National Academy of Sciences*, ***97***(21), 11250-11255.
18. Barboza, J. A., Iwakuma, T., Terzian, T., El-Naggar, A. K., and Lozano, G. (2008). Mdm2 and Mdm4 loss regulates distinct p53 activities. *Molecular Cancer Research*, ***6***(6), 947-954.
19. Karni-Schmidt, O., Lokshin, M., and Prives, C. (2016). The roles of MDM2 and MDMX in cancer. *Annual Review of Pathology: Mechanisms of Disease*, ***11***, 617-644.
20. ElSawy, K., Verma, C. S., Joseph, T. L., Lane, D. P., Twarock, R., and Caves, L. (2013). On the interaction mechanisms of a p53 peptide and nutlin with the MDM2 and MDMX proteins: a Brownian dynamics study. *Cell Cycle*, ***12***(3), 394-404.
21. Wang, X., Wang, J., and Jiang, X. (2011). MdmX protein is essential for Mdm2 protein-mediated p53 polyubiquitination. *Journal of Biological Chemistry*, ***286***(27), 23725-23734.
22. Pei, D., Zhang, Y., and Zheng, J. (2012). Regulation of p53: a collaboration between Mdm2 and Mdmx. *Oncotarget*, ***3***(3), 228..
23. Mancini, F., Di Conza, G., Monti, O., Macchiarulo, A., Pellicciari, R., Pontecorvi, A., and Moretti, F. A. B. I. O. L. A. (2010). Puzzling over MDM4–p53 network. *The international journal of biochemistry & cell biology*, ***42***(7), 1080-1083.
24. Chen, S. H., Forrester, W., and Lahav, G. (2016). Schedule-dependent interaction between anticancer treatments. *Science*, ***351***(6278), 1204-1208.
25. Batchelor, E., Mock, C. S., Bhan, I., Loewer, A., and Lahav, G. (2008). Recurrent initiation: a mechanism for triggering p53 pulses in response to DNA damage. *Molecular cell*, ***30***(3), 277-289.

26. Reyes, J., Chen, J. Y., Stewart-Ornstein, J., Karhohs, K. W., Mock, C. S., and Lahav, G. (2018). Fluctuations in p53 signaling allow escape from Cell-Cycle arrest. *Molecular cell*, ***71***(4), 581-591.
27. Loewer, A., Batchelor, E., Gaglia, G., and Lahav, G. (2010). Basal dynamics of p53 reveal transcriptionally attenuated pulses in cycling cells. *Cell*, ***142***(1), 89-100..
28. Frum, R., Ramamoorthy, M., Mohanraj, L., Deb, S., and Deb, S. P. (2009). MDM2 controls the timely expression of cyclin A to regulate the cell cycle. *Molecular Cancer Research*, 1541-7786.
29. Giono, L. E., Resnick-Silverman, L., Carvajal, L. A., St Clair, S., & Manfredi, J. J. (2017). Mdm2 promotes Cdc25C protein degradation and delays cell cycle progression through the G2/M phase. *Oncogene*, ***36***(49), 6762.
30. Gembarska, A., Luciani, F., Fedele, C., Russell, E.A., Dewaele, M., Villar, S., Zwolinska, A., Haupt, S., De Lange, J., Yip, D. and Goydos, J. (2012). MDM4 is a key therapeutic target in cutaneous melanoma. *Nature medicine*, ***18***(8), p.1239.
31. Danovi, D., Meulmeester, E., Pasini, D., Migliorini, D., Capra, M., Frenk, R., de Graaf, P., Francoz, S., Gasparini, P., Gobbi, A. and Helin, K. (2004). Amplification of Mdmx (or Mdm4) directly contributes to tumor formation by inhibiting p53 tumor suppressor activity. *Molecular and cellular biology*, ***24***(13), pp.5835-5843.
32. Kitayama, Y., Nishiwaki, T., Terauchi, K., and Kondo, T. (2008). Dual KaiC-based oscillations constitute the circadian system of cyanobacteria. *Genes & development*, ***22***(11), 000-000.
33. Sancar, A., Lindsey-Boltz, L. A., Kang, T. H., Reardon, J. T., Lee, J. H., and Ozturk, N. (2010). Circadian clock control of the cellular response to DNA damage. *FEBS letters*, ***584***(12), 2618-2625.
34. Hoffmann, A., Levchenko, A., Scott, M. L., and Baltimore, D. (2002). The IκB-NF-κB signaling module: temporal control and selective gene activation. *Science*, ***298***(5596), 1241-1245.
35. Nelson, D.E., Ihekwaba, A.E.C., Elliott, M., Johnson, J.R., Gibney, C.A., Foreman, B.E., Nelson, G., See, V., Horton, C.A., Spiller, D.G. and Edwards, S.W. (2004). Oscillations in NF-κB signaling control the dynamics of gene expression. *Science*, ***306***(5696), 704-708.
36. Dequéant, M. L., Glynn, E., Gaudenz, K., Wahl, M., Chen, J., Mushegian, A., and Pourquié, O. (2006). A complex oscillating network of signaling genes underlies the mouse segmentation clock. *Science*, ***314***(5805), 1595-1598.
37. Kobayashi, T., Mizuno, H., Imayoshi, I., Furusawa, C., Shirahige, K., and Kageyama, R. (2009). The cyclic gene Hes1 contributes to diverse differentiation responses of embryonic stem cells. *Genes & development*, ***23***(16), 1870-1875.